For Reference

NOT TO BE TAKEN FROM THIS ROOM

For Reference

NOT TO BE TAKEN FROM THIS ROOM

Ex libris
Universitatis
Albertaensis

QUAECUMQUE VERA

The University of Alberta
Printing Department
Edmonton, Alberta

Digitized by the Internet Archive
in 2022 with funding from
University of Alberta Libraries

https://archive.org/details/Walkinshaw1970

Thesis
1970
#82D

THE UNIVERSITY OF ALBERTA

LINEAR FORCED RESPONSE OF THIN ELASTIC PLATES AND SHALLOW SPHERICAL SHELLS WITH REGULAR POLYGONAL BOUNDARIES

by

© DOUGLAS S. WALKINSHAW

A THESIS
SUBMITTED TO THE FACULTY OF GRADUATE STUDIES
IN PARTIAL FULFILMENT OF THE REQUIREMENTS FOR THE DEGREE
OF DOCTOR OF PHILOSOPHY

DEPARTMENT OF MECHANICAL ENGINEERING

EDMONTON, ALBERTA

SPRING, 1970

Thesis
1970
42 D

UNIVERSITY OF ALBERTA

FACULTY OF GRADUATE STUDIES

The undersigned certify that they have read, and recommend to the Faculty of Graduate Studies for acceptance, a thesis entitled "LINEAR FORCED RESPONSE OF THIN ELASTIC PLATES AND SHALLOW SPHERICAL SHELLS WITH REGULAR POLYGONAL BOUNDARIES" submitted by DOUGLAS S. WALKINSHAW in partial fulfilment of the requirements for the degree of Doctor of Philosophy.

ABSTRACT

Approximate solutions are presented for the linear isothermal response to symmetric dynamic loading of viscously damped thin homogeneous isotropic elastic plates and shallow spherical shells having regular polygonal boundaries. Normal modes of vibration are determined with the aid of the boundary collocation technique, and modal participation functions, necessary for forced solutions, are calculated by employing numerical integration. The solutions are applicable to elastically built-in plates and shells with time-dependent edge conditions. Numerical solutions are provided for a large number of polygonal plates and shells subjected to uniform and central point loads for a variety of edge conditions. Theoretical and experimental results are compared for a square plate and a shallow spherical shell with an hexagonal boundary subject to blast loading.

ACKNOWLEDGMENTS

The author wishes to thank Dr. J. S. Kennedy for his supervision of this thesis and his invaluable guidance and encouragement during the course of this investigation.

The assistance of Mr. B. G. Laidlaw, Defence Research Establishment Suffield (DRES), throughout the entire investigation was essential to the completion of this work and is gratefully acknowledged.

Appreciation is expressed to Dr. G. H. S. Jones, the author's former supervisor at DRES, who made this research possible, and to Dr. G. AE. Oravas, McMaster University, who provided the aluminium dome for the shell experiment.

This work was supported by the Defence Research Board, DRES, and the University of Alberta. Thanks are due to the staff of DRES who participated in this investigation; in particular to Mr. N. A. Bannister who aided with the digital computer work and to Mrs. C.S. Duthie who aided with the typing. Thanks are due also to Mr. A. S. Aggarwal, University of Alberta, who assisted with the computer work.

Finally, the author would like to express deep gratitude to his wife for her continuing assistance and encouragement throughout the work.

TABLE OF CONTENTS

ABSTRACT iii

ACKNOWLEDGMENTS iv

TABLE OF CONTENTS v

LIST OF FIGURES xi

LIST OF TABLES xx

ABBREVIATIONS xxvi

NOMENCLATURE xxvii

CHAPTER 1 INTRODUCTION 1

1.1 Objectives 1

1.2 Discussion of Literature for Plates 3

1.2.1 Experimental Results 3

1.2.2 Exact Theoretical Solutions 4

1.2.3 Approximate Theoretical Solutions 5

1.3 Discussion of Literature for Shallow Spherical Shells 10

1.3.1 Linear Vibrations 12

1.3.2 Buckling 16

CHAPTER 2 PLATE THEORY 19

2.1 Governing Equations 19

2.2 Free Undamped Motion 21

2.2.1 General Solution 21

2.2.2 Edge Conditions 24

2.3 Forced Motion 29
2.3.1 General Solution 29
2.3.2 Initial Conditions 32
2.3.3 Modal Participation Functions .. 33

CHAPTER 3 SHELL THEORY 40
3.1 Governing Equations 40
3.2 Free Undamped Motion 43
3.2.1 General Solution 43
3.2.2 Boundary Conditions 47
3.2.3 Auxiliary Edge Conditions 58
3.3 Forced Motion 60
3.3.1 General Solution 60
3.3.2 Initial Conditions 63
3.3.3 Modal Participation Functions .. 64

CHAPTER 4 PLATE NUMERICAL RESULTS 71
4.1 Eigenvalues, Eigenvectors and Modal Participation Functions 71
4.2 Effect of Boundary Shape on Symmetric Eigenvalues 85
4.3 Symmetric Mode Shapes and Modal Participation Functions 89

4.4 Central Displacement 95

CHAPTER 5 EXPERIMENTAL COMPARISON WITH THEORY FOR A SQUARE PLATE 108

5.1 Procedure 108

5.1.1 Experimental Plate 108

5.1.2 Static Response 112

5.1.3 Transient Response 114

5.2 Theoretical and Experimental Results ... 121

5.2.1 Theoretical Elastically Clamped Square Plate 121

5.2.2 Transient Pressures 125

5.2.3 Damping 130

5.2.4 Displacement 140

5.2.5 Strain 147

5.2.6 Stress Couples 155

CHAPTER 6 SHELL NUMERICAL RESULTS 168

6.1 Transverse Vibrations of Thin Shallow Shells with Homogeneous Edge Conditions 168

6.1.1 Simply Supported Shells with Sliding Clamped Edges 176

6.1.2 Simply Supported Shells 181

6.1.3 Clamped Shells 186

6.1.4 Other Edge Conditions 190

6.2 Edge Condition Satisfaction 200

6.3 Series Convergence 207

6.4 Auxiliary Edge Conditions 210

CHAPTER 7 EXPERIMENTAL COMPARISON WITH THEORY FOR A SHALLOW SPHERICAL SHELL ENCLOSING AN HEXAGONAL BASE 220

7.1 Procedure 220

7.1.1 Experimental Shell 220

7.1.2 Natural Frequencies 237

7.1.3 Transient Response 240

7.2 Theoretical Frequencies and Central Displacements for Different Shell Spherical Curvatures and Edge Conditions 250

7.3 Theoretical and Experimental Results for Trial 1 251

7.3.1 Natural Frequencies and Mode Shapes 251

7.3.2 Transient Pressures 260

7.3.3 Transient Response 262

7.4 Theoretical and Experimental Results for Trial 2 281

7.4.1 Natural Frequencies 281

7.4.2 Transient Pressures 283
7.4.3 Transient Response 283

CHAPTER 8 OBSERVATIONS, CONCLUSIONS AND RECOMMENDATIONS 294
8.1 Observations and Conclusions 294
8.1.1 Theoretical Analysis of Plates .. 294
8.1.2 Comparison of Theoretical Predictions and Experimental Results for a Square Plate 296
8.1.3 Theoretical Analysis of Shells .. 298
8.1.4 Comparison of Theoretical Predictions and Experimental Results for a Shallow Shell with an Hexagonal Base 302
8.2 Recommendations 305

BIBLIOGRAPHY 310

APPENDIX A SECTIONAL RESULTANTS 328
A.1 Plate Sectional Resultants 328
A.2 Shell Sectional Resultants 331

APPENDIX B ORTHOGONALITY OF EIGENVECTORS 334
B.1 Orthogonality of Plate Eigenvectors 334
B.2 Orthogonality of Shell Eigenvectors 336

APPENDIX C COMPUTER PROGRAMS 338

C.1 Plate Program 338

C.2 Shell Program 364

LIST OF FIGURES

2.1 Thin Regular Polygonal Plates with p Sides ... 23

2.2 Vector Diagram Showing Relation of Boundary Coordinates v, s to Interior Coordinates r,θ . 25

2.3 Vector Diagram of Plate Element Showing Sectional Resultants 27

4.1 Boundary Collocation for a Square Plate 72

4.2a Symmetric Mode Shapes for the Characteristic Segments of Regular Polygonal Plates with 3 and 4 Sides 91

4.2b Symmetric Mode Shapes for the Characteristic Segments of Regular Polygonal Plates with 5 and 6 Sides 92

4.2c Symmetric Mode Shapes for the Characteristic Segments of Regular Polygonal Plates with 7 and 8 Sides 93

4.2d Symmetric Mode Shapes for the Characteristic Segments of Regular Polygonal Plates with 9 and 12 Sides 94

4.3 Theoretical Undamped Center Deflections of Some Clamped Polygonal Plates vs.Time 107

5.1 Plate Mounting Assembly 109

5.2 Plate Instrumentation 113

5.3 Plate Static Testing Arrangement 115

5.4 Instrumentation Bunker for Six-Foot Diameter Shock Tube 122

5.5 Block Diagram of Plate Transient Response Instrumentation 123

5.6 Typical Theoretical and Measured Pressure vs. Time for a 1.5 lb. Shot for Face-on Loading in Six-Foot Diameter Shock Tube 131

5.7 Plate Experimental Radial Strain at $\rho = 0.377$, $\theta = 15°$, sector 1 and Pressure vs. Time for a 1.5 lb. Shot 133

5.8 Plate Experimental Radial Strain at $\rho = 0.377$, $\theta = 15°$, sector 1 and Pressure vs. Time for a 6.0 lb. Shot 134

5.9 Theoretical Variation of Static Central Displacement with Clamping Factor β_1^1 for a Square Plate 141

5.10 Plate Theoretical and Experimental Central Displacement vs. Time for a 0.5 lb. Shot 143

5.11 Plate Theoretical and Experimental Central Displacement vs. Time for a 1.5 lb. Shot 143

5.12 Plate Experimental Static and Maximum Dynamic Central Displacements vs. Load 145

5.13 Plate Experimental Ratio of Maximum Dynamic Edge Displacement-to-Central Displacement vs. Load 145
5.14 Plate Experimental Bending and Membrane Strains vs. Time at $\rho = 0.047$, $\Theta = 0°$ for a 1.5 lb. Shot 148
5.15 Plate Experimental Maximum Dynamic Bending Strains vs. Load at $\rho = 0.778$, $\Theta = 45°$ 153
5.16 Plate Experimental Maximum Dynamic Membrane Strains vs. Load at $\rho = 0.778$, $\Theta = 45°$ 153
5.17 Static and Maximum Dynamic Plate Experimental Flexural Stress Couples vs. Load at $\rho = 0.047$, $\Theta = 0°$ 156
5.18 Plate Static Experimental and Maximum Dynamic Experimental and Theoretical Flexural Stress Couples on $\Theta = 0°$ for a 1.5 lb. Shot 157
5.19 Plate Static Experimental and Maximum Dynamic Experimental and Theoretical Flexural Stress Couples on $\Theta = 15°$ for a 1.5 lb. Shot 158
5.20 Plate Static Experimental and Maximum Dynamic Experimental and Theoretical Flexural Stress Couples on $\Theta = 30°$ for 1.5 lb. Shot 159

5.21 Plate Static Experimental and Maximum Dynamic Experimental and Theoretical Flexural Stress Couples on Θ = 45° for a 1.5 lb. Shot 160

5.22 Plate Experimental and Theoretical Flexural Stress Couples vs. Time at $\rho = 0.0471$, $\Theta = 0°$ and $\rho = 0.0707$, $\Theta = 0°$, respectively, for a 1.5 lb. Shot 163

5.23 Plate Experimental and Theoretical Flexural Stress Couples vs. Time at $\rho = 0.3771$, $\Theta = 0°$ for a 1.5 lb. Shot 164

5.24 Plate Experimental and Theoretical Flexural Stress Couples vs. Time at $\rho = 0.5657$, $\Theta = 45°$ for a 1.5 lb. Shot 165

5.25 Plate Experimental and Theoretical Flexural Stress Couples vs. Time at $\rho = 0.7778$, $\Theta = 45°$ for a 1.5 lb. Shot 166

6.1 Symmetric Mode Shapes for the Characteristic Segment of a Clamped Shallow Spherical Shell with 12 Sides and $a/R = 0.102331$, $a/h = 10.2331$ and $\nu = 0.3$ 191

6.2 Symmetric Mode Shapes for the Characteristic Segment of a Clamped Shallow Spherical Shell with 6 Sides and $a/R = 0.390625$, $a/h = 66.667$ and $\nu = 0.33$ 192

6.3 Symmetric Mode Shapes for the Characteristic Segment of a Clamped Shallow Spherical Shell with Sliding Free Edges Having 6 Sides and $a/R = 0.390625$, $a/h = 66.667$ and $\nu = 0.33$ 199

6.4 Numerical Satisfaction of Vanishing Transverse Edge Displacement for a Clamped Shallow Spherical Shell with 6 Sides and $a/R = 0.390625$, $a/h = 66.667$ and $\nu = 0.33$ 202

6.5 Numerical Satisfaction of Vanishing Normal Slope for a Clamped Shallow Spherical Shell with 6 Sides and $a/R = 0.390625$, $a/h = 66.667$ and $\nu = 0.33$ 203

6.6 Numerical Satisfaction of Vanishing Tangential Edge Shear for a Clamped Shallow Spherical Shell with 6 Sides and $a/R = 0.390625$, $a/h = 66.667$ and $\nu = 0.33$ 204

6.7 Numerical Satisfaction of Vanishing Tangential Edge Strain for a Clamped Shallow Spherical Shell with 6 Sides and $a/R = 0.390625$, $a/h = 66.667$ and $\nu = 0.33$ 205

7.1a Shell Test Assembly 221

7.1b Shell Test Assembly 222

7.2 Back View of Shell Mounted in Shock Tube for Trial 1 225

7.3 Front View of Shell Mounted in Shock Tube for Trial 1 226
7.4 Front View of Shell Mounted in Shock Tube for Trial 2 228
7.5 Back View of Shell Mounted in Shock Tube for Trial 2 230
7.6 Experimental Shell Middle Surface Profile for Trial 2 232
7.7 Variation of Experimental Shell Radius of Curvature R with Radius ρ for Trial 2 233
7.8a Shell Instrumentation 235
7.8b Shell Instrumentation 236
7.9 Acoustic Excitation Equipment 241
7.10 Block Diagram of Shell Acoustic Excitation Instrumentation 242
7.11 Schlieren Photographs Showing Air Shock Front Reflection by a Cylindrical Surface in 2 x 12 in. Shock Tube 244
7.12 Variation of Measured Pressure vs. Time Over a Cylindrical Surface in 2 x 12 in. Shock Tube 244
7.13 Vibration of Acoustically Excited Shell at Apex for Trial 1 253
7.14 Vibration of Acoustically Excited Shell at r = 16", Θ = 0° and r = 21", Θ = 0°, Sector 3, for Trial 1 254

7.15 Vibration of Acoustically Excited Shell at Boundary of Sector 3 for Trial 1 255

7.16 Some Experimental and Theoretical Shell Mode Shapes for Trial 1 261

7.17 Shell Experimental Central Back Strain and Pressure vs. Time for Trial 1 263

7.18 Shell Theoretical Static and Maximum Dynamic Transverse Displacements on Θ = 0° 265

7.19 Shell Maximum Dynamic Experimental and Theoretical Sectional Resultants on Θ = 0° for Trial 1 267

7.20 Shell Maximum Dynamic Experimental and Theoretical Sectional Resultants on Θ = 10° for Trial 1 268

7.21 Shell Maximum Dynamic Experimental and Theoretical Section Resultants on Θ = 20° for Trial 1 269

7.22 Shell Maximum Dynamic Experimental and Theoretical Sectional Resultants on Θ = 30° for Trial 1 270

7.23 Shell Experimental and Theoretical Central Displacement vs. Time for Trial 1 273

7.24 Shell Experimental and Theoretical Sectional Resultants vs. Time at $\rho = 0$, $\Theta = 0°$ and $\rho = 0.06$, $\Theta = 0°$, respectively, for Trial 1 .. 274

7.25 Shell Experimental and Theoretical Sectional Resultants vs. Time at $\rho = 0.24$, $\Theta = 30°$ for Trial 1 275

7.26 Shell Experimental and Theoretical Sectional Resultants vs. Time at $\rho = 0.48$, $\Theta = 10°$ for Trial 1 276

7.27 Shell Experimental and Theoretical Sectional Resultants vs. Time at $\rho = 0.64$, $\Theta = 30°$ for Trial 1 277

7.28 Shell Experimental and Theoretical Sectional Resultants vs. Time at $\rho = 0.72$, $\Theta = 20°$ for Trial 1 278

7.29 Shell Experimental and Theoretical Sectional Resultants vs. Time at $\rho = 0.84$, $\Theta = 0°$ for Trial 1 279

7.30 Vibration of Acoustically Excited Shell for Trial 2 282

7.31 Shell Experimental and Theoretical Central Transverse Displacement and Experimental Edge In-plane Displacement vs. Time for Trial 2 284

7.32 Shell Experimental and Theoretical Sectional Resultants vs. Time at $\rho = 0$, $\Theta = 0°$ and $\rho = 0.06$, $\Theta = 0°$, respectively, for Trial 2 ... 286

7.33 Shell Experimental and Theoretical Sectional Resultants vs. Time at $\rho = 0.24$, $\theta = 30°$ for Trial 2 287

7.34 Shell Experimental and Theoretical Sectional Resultants vs. Time at $\rho = 0.48$, $\theta = 10°$ for Trial 2 288

7.35 Shell Experimental and Theoretical Sectional Resultants vs. Time at $\rho = 0.64$, $\theta = 30°$ for Trial 2 289

7.36 Shell Experimental and Theoretical Sectional Resultants vs. Time at $\rho = 0.72$, $\theta = 20°$ for Trial 2 290

7.37 Shell Experimental and Theoretical Sectional Resultants vs. Time at $\rho = 0.84$, $\theta = 0°$ for Trial 2 291

C.1 Flow Diagram of Plate Computer Program 347

LIST OF TABLES

4.1 Symmetric Eigenvalues and Modal Participation Functions for Clamped Polygonal Plates 74
4.2 Symmetric Eigenvalues and Modal Participation Functions for Simply Supported Polygonal Plates . 75
4.3a Eigenvalues, Modal Participation Functions and Eigenvectors for a Clamped Plate With 3 Sides ... 77
4.3b Eigenvalues, Modal Participation Functions and Eigenvectors for a Clamped Plate With 4 Sides ... 77
4.3c Eigenvalues, Modal Participation Functions and Eigenvectors for a Clamped Plate With 5 Sides ... 78
4.3d Eigenvalues, Modal Participation Functions and Eigenvectors for a Clamped Plate With 6 Sides ... 78
4.3e Eigenvalues, Modal Participation Functions and Eigenvectors for a Clamped Plate With 7 Sides ... 79
4.3f Eigenvalues, Modal Participation Functions and Eigenvectors for a Clamped Plate With 8 Sides ... 79
4.3g Eigenvalues, Modal Participation Functions and Eigenvectors for a Clamped Plate With 9 Sides ... 80
4.3h Eigenvalues, Modal Participation Functions and Eigenvectors for a Clamped Plate With 12 Sides .. 80

4.4a Eigenvalues, Modal Participation Functions and Eigenvectors for a Simply Supported Plate With 3 Sides 81

4.4b Eigenvalues, Modal Participation Functions and Eigenvectors for a Simply Supported Plate With 4 Sides 81

4.4c Eigenvalues, Modal Participation Functions and Eigenvectors for a Simply Supported Plate With 5 Sides 82

4.4d Eigenvalues, Modal Participation Functions and Eigenvectors for a Simply Supported Plate With 6 Sides 82

4.4e Eigenvalues, Modal Participation Functions and Eigenvectors for a Simply Supported Plate With 7 Sides 83

4.4f Eigenvalues, Modal Participation Functions and Eigenvectors for a Simply Supported Plate With 8 Sides 83

4.4g Eigenvalues, Modal Participation Functions and Eigenvectors for a Simply Supported Plate With 9 Sides 84

4.4h Eigenvalues, Modal Participation Functions and Eigenvectors for a Simply Supported Plate With 12 Sides 84

4.5 Symmetric Eigenvalues for Clamped Polygonal Plates of Equal Area 87

4.6 Symmetric Eigenvalues for Simply Supported Polygonal Plates of Equal Area 88

4.7 Modal Participation Functions for Uniformly Loaded Clamped Polygonal Plates 96

4.8 Modal Participation Functions for Uniformly Loaded Simply Supported Polygonal Plates 97

4.9 Static Center Modal Deflections of Uniformly Loaded Clamped Polygonal Plates 100

4.10 Static Center Modal Deflections of Uniformly Loaded Simply Supported Polygonal Plates 101

4.11 Static Center Modal Deflections of Centrally Point Loaded Clamped Polygonal Plates 102

4.12 Static Center Modal Deflections of Centrally Point Loaded Simply Supported Polygonal Plates . 103

5.1 Eigenvalues, Modal Participation Functions and Central Displacements for Uniformly Loaded Elastically Clamped Square Plates 124

5.2 Theoretical Frequencies of the Experimental Plate for Various Degrees of Elastic Clamping .. 126

5.3 Plate Transient Pressures 127

5.4 Plate Theoretical Air Damping on One Surface ... 137

5.5 Plate Experimental Viscous Damping 138

5.6 Plate Experimental Fundamental Frequencies 147
5.7 Plate Experimental Bending and Membrane Strains for Uniform Static Load of 10 psi 149
5.8 Plate Experimental Maximum Bending and Membrane Strains for Uniform Blast Load, q_o = 8.6 psi and t_o = 0.033 sec. 150
6.1 Symmetric Eigenvalues and Modal Participation Functions for Simply Supported Shallow Spherical Shells With Sliding Clamped Edges Having 4, 5 and 6 Sides 178
6.2 Symmetric Frequencies and Static Central Modal Deflections for Uniformly Loaded Simply Supported Shallow Spherical Shells with Polygonal and Circular Boundaries and Equivalent Surface Areas 183
6.3 Symmetric Eigenvalues and Modal Participation Functions for Simply Supported Shallow Spherical Shells with 6, 12 and 15 Sides 185
6.4 Symmetric Frequencies of Clamped Shallow Spherical Shells with Polygonal and Circular Boundaries and Equivalent Surface Areas 187
6.5 Symmetric Eigenvalues and Modal Participation Functions for Clamped Shallow Spherical Shells with 6, 12 and 15 Sides 189

6.6 Symmetric Eigenvalues and Modal Participation Functions for Simply Supported Shallow Spherical Shells with Sliding Free Edges having 4, 5, 6 and 12 Sides 194
6.7 Symmetric Eigenvalues and Modal Participation Functions for Clamped Shallow Spherical Shells with Sliding Free Edges having 4, 5, 6 and 12 Sides 195
6.8 Symmetric Eigenvalues and Modal Participation Functions for Clamped Shallow Spherical Shells with Sliding Clamped Edges having 4, 5 and 6 Sides 196
6.9 Functional Series Convergence for the Third Mode of Response of a Uniformly Loaded Clamped Shell with 6 Sides 208
6.10 Solutions for $\bar{g}^{\ell}(\rho,\theta)$ and $\bar{h}^{\ell}(\rho,\theta)$ for Auxiliary Edge Conditions 212
6.11 Coefficients $E^{j,2}_{pn}(p)$ for Auxiliary Edge Conditions $L_1[\bar{g}^2(\tilde{\rho},\tilde{\theta})] = 0$, $\frac{a}{D} L_2[\bar{g}^2(\tilde{\rho},\tilde{\theta})] = 1$ 213
6.12 Coefficients $E^{j,2}_{pn}(p)$ for Auxiliary Edge Conditions $L_1[\bar{g}^2(\tilde{\rho},\tilde{\theta})] = 0$, $L_3[\bar{g}^2(\tilde{\rho},\tilde{\theta})] = -1$ 214

6.13 Coefficients $F^{j,1}_{pn}(p,\nu)$ for Auxiliary Edge Conditions $\frac{1}{Eh} L_4[\bar{h}^1(\tilde{\rho},\tilde{\Theta})] = 1$, $L_5[\bar{h}^1(\tilde{\rho},\tilde{\Theta})] = 0$ ... 215

6.14 Coefficients $F^{1,2}_{0}(\nu)$ for Auxiliary Edge Conditions $L_4[\bar{h}^2(\tilde{\rho},\tilde{\Theta})] = 0$, $L_5[\bar{h}^2(\tilde{\rho},\tilde{\Theta})] = 1$ 215

6.15 Coefficients $F^{j,1}_{pn}(p,\nu)$ for Auxiliary Edge Conditions $\frac{1}{Eh} L_6[\bar{h}^1(\tilde{\rho},\tilde{\Theta})] = 1$, $L_5[\bar{h}^1(\tilde{\rho},\tilde{\Theta})] = 0$ ... 216

6.16 Coefficients $F^{j,2}_{pn}(p,\nu)$ for Auxiliary Edge Conditions $L_6[\bar{h}^2(\tilde{\rho},\tilde{\Theta})] = 0$, $L_5[\bar{h}^2(\tilde{\rho},\tilde{\Theta})] = -1$ 217

7.1 Theoretical Modal Frequencies and Static Central Displacements for Uniformly Loaded Experimental Shell 252

7.2 Shell Experimental and Theoretical Natural Frequencies for Trial 1 258

C.1 Explanation of Computer Data for Plates 342

C.2 Functions of Plate Computer Program Subroutines . 346

C.3 Modifications of Plate Computer Data for Shells . 367

ABBREVIATIONS

DRES	Defence Research Establishment Suffield
Eq(s).	Equation(s)
Fig(s).	Figure(s)
A-D	analogue-to-digital
a.c.	alternating current
d.c.	direct current
( )E±( )	$(\ )10^{\pm(\ )}$
$\mu\varepsilon$	microstrain; $1\ \mu\varepsilon \equiv 1\ \varepsilon \times 10^{-6}$
psi	pounds per square inch; psi = psig unless stated otherwise
ips	inches per second
fps	feet per second
lb.	pound(s)
in.	inch(es)
deg.	degree(s)
cps	cycles per second; 1 cps ≡ 1 hertz
sec.	second(s)
msec.	millisecond(s); 1 msec. ≡ 1 sec. x 10^{-3}
nsec.	nanosecond(s); 1 nsec. ≡ 1 sec. x 10^{-9}

NOMENCLATURE

A list of all important symbols in the text is given here. Symbols which are introduced in some sections of the text but which are not referred to later are not included. Some of the symbols may have different meanings in different sections, however these have been clearly defined in each section and should not be confusing to the reader.

a	radius of circle circumscribing regular polygonal boundary
a_o	radius of circle inscribing regular polygonal boundary
R	radius of curvature of middle surface of shell
h	thickness
p	number of boundary sides
E	modulus of elasticity
ν	Poisson's ratio
γ	mass per unit volume
m	mass per unit area, $m \equiv \gamma h$
D	flexural rigidity, $D \equiv Eh^3/[12(1 - \nu^2)]$
r	radial polar coordinate
ρ	dimensionless radial polar coordinate, $\rho \equiv r/a$
θ	angular polar coordinate
$\tilde{\rho}, \tilde{\theta}$	polar coordinates of boundary points

L	number of collocation points on the characteristic segment boundary
θ_0	central angle of characteristic segment, $\theta_0 \equiv \pi/p$ radians
v,s	Cartesian boundary coordinates normal and tangential to the edge, respectively
n	transverse coordinate normal to the middle surface; also used as an integer ranging from 0 to ∞ in the functional series solutions which describe each mode of response
t	time
q	transverse load intensity per unit area, $q \equiv q_0\bar{q}(\rho)\cos pm\theta \; Q(t)$ where m is any integer
q_0	reference transverse load intensity per unit area; for blast loads q_0 is the peak reflected overpressure; for static loads q_0 is the static overpressure
$\bar{q}$	normalized transverse load distribution in the radial direction
Q	normalized transverse load transient
P	concentrated central transverse load, $P \equiv P_0Q(t)$
P_0	reference concentrated central transverse load
t_0	duration of positive phase of transverse load
∇^2	Euler-Laplace differential operator, $\nabla^2 \equiv \frac{\partial^2}{\partial r^2} + \frac{1}{r}\frac{\partial}{\partial r} + \frac{1}{r^2}\frac{\partial^2}{\partial \theta^2}$ when operating on functions of r and θ, $\nabla^2 \equiv \frac{\partial^2}{\partial \rho^2} + \frac{1}{\rho}\frac{\partial}{\partial \rho} + \frac{1}{\rho^2}\frac{\partial^2}{\partial \theta^2}$ when operating on functions of ρ and θ
k_i	dimensionless eigenvalue of i-th mode of vibration

ω_i	circular frequency of i-th mode of vibration, $\omega_i \equiv (k_i/a)^2\sqrt{D/m}$ for plates, $\omega_i \equiv \sqrt{(1/\gamma)[(D/h)(k_i/a)^4 + E/R^2]}$ for shells
λ_i	shell constant associated with i-th mode, $\lambda_i \equiv Eh/(maR\omega_i^2)$
ω_i^d	damped circular frequency of i-th mode of vibration, $\omega_i^d \equiv \sqrt{\omega_i^2 - \zeta_i^2}$
ζ_i	coefficient of viscous damping associated with the i-th mode of vibration, ζ_i/ω_i is the ratio of damping to critical damping
w	transverse displacement
η	dimensionless transverse displacement, $\eta \equiv w/a$
$\bar{\eta}^i$	transverse displacement eigenvector of the i-th mode of vibration associated with the homogeneous edge conditions
F	stress function
ξ	dimensionless stress function, $\xi \equiv F/Eha^2$
$\bar{\xi}^i$	stress function eigenvector of the i-th mode of vibration associated with the homogeneous edge conditions
η_1, ξ_1	dimensionless transverse displacement and stress function, respectively, associated with the homogeneous edge conditions
$\bar{e}^\ell, \bar{f}^\ell$	time functions associated with the ℓ-th nonhomogeneous edge conditions in functions of transverse displacement and stress function, respectively
$\bar{g}^\ell, \bar{h}^\ell$	dimensionless transverse displacement and stress function, respectively, associated with $\bar{e}^\ell$ and $\bar{f}^\ell$, respectively

A^{i}_{pn} , B^{i}_{pn} , C^{i}_{pn} , D^{i}_{pn}	integration constants associated with the i-th mode of vibration and determined from the homogeneous edge conditions
$E^{1,\ell}_{pn}$, $E^{2,\ell}_{pn}$	integration constants determined from the ℓ-th nonhomogeneous auxiliary edge condition in transverse displacement
$F^{1,\ell}_{pn}$, $F^{2,\ell}_{pn}$	integration constants determined from the ℓ-th nonhomogeneous auxiliary edge condition in stress function
$\chi^{i}_{1}/\chi^{i}_{0}$	modal participation function of the i-th mode of vibration for uniform loads associated with the homogeneous edge conditions
$(\chi^{i}_{1}/\chi^{i}_{0})_{0}$	modal participation function of the i-th mode of vibration for uniform loads associated with the homogeneous edge conditions and calculated using only the zero-order terms of $\bar{\eta}^{i}$
$(\chi^{i}_{1})_{p}/\chi^{i}_{0}$	modal participation function of the i-th mode of vibration for central point loads associated with the homogeneous edge conditions
$(\chi^{i}_{1}/\chi^{i}_{0})_{a}$	modal participation function of the i-th mode of vibration for uniform loads associated with the homogeneous edge conditions and calculated using nodal areas
$\chi^{\ell,i}_{2}$, $\chi^{\ell,i}_{3}$	modal participation functions of the i-th mode of vibration associated with the homogeneous edge conditions and the ℓ-th nonhomogeneous edge conditions
u_{α_1}	in-plane displacement component in the α_1 direction, where $\alpha_1 = r,\Theta,v,s$
$F_{\alpha_1\alpha_2}$	stress resultant component per unit length which is positive on the positive α_1 element face in the α_2 direction, where $\alpha_1,\alpha_2=r,\Theta,n,v,s$

$M_{\alpha_1\alpha_2}$	stress couple component per unit length with a vectorial component (right hand rule) which is positive on the positive α_1 element face in the α_2 direction, where $\alpha_1, \alpha_2 = r, \theta, v, s$
$\varepsilon^{\alpha_3}_{\alpha_1\alpha_2}$	strain component which is positive on the positive α_1 element face in the α_2 direction, where $\alpha_1, \alpha_2 = r, \theta, n, v, s$ and $\alpha_3 = m, b,$ (blank), indicating membrane, bending and membrane plus bending strain, respectively
W	dimensionless static central transverse displacement for uniform loads, $W = \sum_i W_i = wD/(q_o a_o^4)$
W_i	dimensionless static central transverse displacement for uniform loads associated with the i-th mode of vibration
W^P	dimensionless static central transverse displacement for central point loads, $W^P = \sum_i W^P_i = wD/(P_o a_o^2)$
W^P_i	dimensionless static central transverse displacement for central point loads associated with the i-th mode of vibration
W^e	dimensionless static central transverse displacement for uniform loads, $W^e = wD/[q_o(\rho^e a)^4]$
$W^{P,e}$	dimensionless static central transverse displacement for central point loads, $W^{P,e} = wD/[P_o(\rho^e a)^2]$
ρ^e	dimensionless bounding radius of a surface having the same area as that of the surface bounded by a particular regular polygon
β^i_1	coefficient of edge clamping relating $\partial w(\tilde{\rho}, \tilde{\theta})/\partial v$ to $M_{vs}(\tilde{\rho}, \tilde{\theta})$ for the i-th mode of vibration
β^i_2	coefficient of edge clamping relating $F_{vs}(\tilde{\rho}, \tilde{\theta})$ to $\varepsilon_{ss}(\tilde{\rho}, \tilde{\theta})$ for the i-th mode of vibration

$J_n(x)$	standardized n-th order Bessel function of the first kind of argument x
$Y_n(x)$	standardized n-th order Bessel function of the second kind of argument x
$I_n(x)$	standardized n-th order modified Bessel function of the first kind of argument x
$K_n(x)$	standardized n-th order modified Bessel function of the second kind of argument x
$L_1 \ldots L_6$	linear homogeneous differential operators of order 2 or lower defined in Eqs. (3.20a) through (3.20f)

CHAPTER 1

INTRODUCTION

1.1 Objectives

The purpose of this thesis is to present approximate theoretical solutions for the free and forced linear transverse vibrations of thin homogeneous isotropic elastic plates and spherical shells of constant thickness, both having regular polygonal boundaries. The theory gives the linear viscously damped response of these plates and shells to arbitrary transient symmetrically distributed overpressures for a wide variety of homogeneous and time-dependent edge conditions.

Theoretical frequencies, mode shapes and modal participation functions for uniform loads and central point loads have been tabulated for many different simply supported and clamped polygonal plates. Since the numerical application of this theory requires extensive use of a digital computer, it was impractical to tabulate results for shallow shells having all of the geometrical properties and edge conditions which might be of interest. However, a sufficient number of different shells have been analysed to establish some general

effects of variations in the shell geometrical properties and edge conditions on the natural frequencies and modal participation functions. Computer programs which calculate free vibration and forced response of these plates and shells are included. These programs are written in Fortran IV language for use on IBM 360/67 and 1130 (with modifications) digital computers.

It is a major purpose of this thesis to present detailed comparisons between transient experimental and theoretical stress resultants (forces) and stress couples (moments), obtained from the response to air blast overpressures of a square plate and a shallow shell with an hexagonal boundary. These comparisons reveal some of the limitations of the theory and some of the difficulties which may be encountered when an attempt is made to correlate simultaneously both magnitudes and frequencies of the sectional resultants for practical applications. The effect of variations in shell geometry from the ideal, especially in radius of curvature, is considered to play an important part in the forced response of thin shallow shells.

1.2 Discussion of Literature for Plates

Literature representing some of the different analytical approaches to the solution of the linear transverse flexural vibrations of elastic plates is summarized in this section. From this survey it is evident that while much work has been done on free vibrations of plates, theoretical forced response has been computed for only a few plate shapes and detailed experimental results for the forced response characteristics of a complete plate are lacking.

1.2.1 Experimental Results. Lassiter and Hess [1][1] studied the response of a clamped rectangular plate to random acoustic loading, measuring strain at one position only, at the middle of the short side. They concluded that for flat panels there is a nonlinearity involving a stiffening spring constant and for curved panels the nonlinearity involves a decreasing spring constant. They found, also, that combined structural and air damping was independent of panel thickness but increased rapidly with stress at higher stress levels.

---

[1] Numbers in square brackets [ ] refer to references in Bibliography.

Crocker [2,3] has studied the response of rectangular panels to normal and travelling sonic booms and to step and oscillating shock waves. He showed that contributions of higher modes to bending strains (in the direction of the longest sides of length a) are significant, particularly as the panel aspect ratio a/b (where b is the length of the shortest sides) is increased. He compared the experimental and theoretical center transient bending strain of a clamped 4.5 x 2.5 in. panel subjected to a N wave and found fair agreement.

Arising from the present work, Walkinshaw and Kennedy [4] have given the approximate theoretical solution for the forced response of polygonal plates subject to homogeneous edge conditions and compared experimental and theoretical transient central displacements and moments at different positions for an elastically clamped square plate subjected to air blast loads.

1.2.2 Exact Theoretical Solutions. Exact solutions for the free linear vibrations of circular plates have been obtained for various edge conditions. Radially symmetric free vibrations were analysed first by Poisson [5]. Later Kirchoff [6] calculated non-axisymmetric frequencies for a circular plate with free

edges. Airey [7] and Rayleigh [8] analysed free vibrations for various edge conditions. Mindlin [9] showed the effect of neglecting rotatory inertia and transverse shear, termed the thickness-shear mode effect, on higher modes of vibration. Coupling of the thickness-shear mode with the higher flexural modes is shown by Deresiewicz and Mindlin [10] for the axisymmetric vibrations of a circular plate with free edges and by Deresiewicz [11] for the axisymmetric vibrations of a circular plate with clamped edges. Raju [12] calculated the natural frequencies of annular plates with a variety of edge conditions at the inner and outer boundaries. Reid [13] analysed free vibration motion of a circular plate subjected to an initial displacement and velocity distribution and Harris [14] solved the free vibrations of a circular plate having a lenticular thickness variation.

Forced motion of circular plates undergoing symmetrical deformation has been analysed by Sneddon [15] for an artificial boundary condition using integral-transforms. Response of clamped circular plates has been analysed by Flynn [16] for impulsive

loads and by Reismann [17] for concentrated harmonically oscillating loads. McLeod and Bishop [18] have calculated the forced symmetrical and nonsymmetrical vibrations of circular plates subjected to a central force or a line force at any radius and of annular plates subjected to moment excitation at free and pinned edges and force excitation at free and sliding edges. Weiner [19] has analysed the forced motion of an elastically built-in circular plate under concentric ring loading, central loading and uniformly distributed loading. Reismann and Greene [20] have analysed the forced motions of circular and annular plates subject to general stationary or time-dependent boundary conditions using the "improved theory" which includes the effect of transverse shear deformation and rotatory inertia. Their comparison of central displacements and central and edge moments calculated by the classical and improved methods for a clamped circular plate reveals the increasing importance of the shear deformation with increasing thickness-to-radius ratio h/a and decreasing ratio of central area uniformly loaded to plate area. They concluded that the improved theory should be used for

uniformly loaded plates having a thickness ratio $h/a > 0.1$ and showed that the central displacements predicted by the classical theory will be too small both for static and dynamic loads.

Exact solutions for the linear vibrations of rectangular plates with simply supported edges have been given by Rayleigh [8] and Timoshenko [21]. Voight [22] obtained an exact solution for the free vibration of a rectangular plate simply supported along one pair of parallel edges and free at the other two edges. Mindlin, Shacknow and Deresiewicz [23] investigated the influence of rotatory inertia and shear deformation on the flexural vibrations of rectangular plates with all edges simply supported and with two parallel edges simply supported and the other two free.

1.2.3 Approximate Theoretical Solutions. Approximate solutions have been obtained for the linear transverse flexural vibrations of elastic plates having complex geometrical and material properties subject to a variety of boundary conditions. A more complete summary of approximate procedures than is presented by this review is given by Desai [24] and expanded by Meirovitch [25].

Ritz [26] introduced the energy approach, in which the calculus of variations is used to find the minimum of potential energy for self-adjoint systems, for free vibrations of rectangular plates with edge conditions other than having all sides simply supported. Natural frequencies of a square plate with free edges were found by Ritz [27] using the energy technique. Using the energy approach, Iguchi extended his earlier work [28] to find natural frequencies of rectangular plates with various length-to-width ratios and edge conditions [29]. Young [30] used the Ritz method to calculate natural frequencies of rectangular plates for various edge conditions and Ota and Hamada [31] used this approach to obtain fundamental frequencies of simply supported rectangular plates clamped along portions of the edges.

Nowacki [32] analysed the free vibrations of a clamped rectangular plate by obtaining an integral equation from compatibility of a series of clamped strips. Nowacki [33] has given a solution for the linear forced flexural response of a rectangular plate with simply supported edges subjected to uniform or concentrated loads using Greene's function and the orthogonality condition.

Tölke [34] introduced the boundary collocation technique, which can be used to satisfy arbitrary edge conditions for plates of any shape, for the static solution of square plates with clamped, simply supported and free edges. This technique has been employed by Conway [35], who introduced the nomenclature "point-matching", and by Leissa [36] to obtain the fundamental frequencies of some regular polygonal plates. Conway and Farnham [37] used this technique to obtain fundamental frequencies of some polygonal plates and Chen and Pickett [38] have developed some computer programs to obtain natural frequencies for plates of any shape subject to any boundary conditions.

Free vibrations have been analysed using the Ritz energy method for rectangular and skew cantilever plates by Barton [39], for triangular cantilever plates by Anderson [40] and for some irregularly shaped plates with square and circular holes by Rao and Pickett [41].

Reipert [42] extended the Levy method to analyse vibrations of polygonal plates resting on elastic foundations subject to transverse and in-plane loads and various boundary conditions.

Solecki [43] employed Fourier transforms to obtain the free vibrations of freely-supported four sided plates with two opposite parallel rectilinear sides and two other sides of arbitrary shape.

Shahady, Passarelli and Laura [44] used complex variable theory to map conformally various plate shapes onto a unit circle to obtain the fundamental frequencies of vibration of these plates.

Pandalai and Patel [45] analysed natural frequencies of vibration of circular plates having different material properties in the radial and circumferential directions. Salzman and Patel [46] analysed the asymmetric natural vibrations of orthotropic circular plates with variable thickness using the method of Frobenius.

Dawe [47] applied the discrete element displacement method to predict changes in natural frequencies of lateral vibration due to axial and biaxial in-plane loading for some simply supported and clamped rectangular plates.

1.3 Discussion of Literature for Shallow Spherical Shells.

Literature representing some of the analytical

solutions for the vibrations of shallow spherical shells is summarized in this section. A more extensive review of the analytical methods of analysis for free vibration and transient linear elastic response of general thin shells is given by Kalnins [48]. It is evident that although much work has been done on computing natural frequencies of shallow spherical shells with circular boundaries, theoretical forced response of these shells has been computed for only a few different edge conditions and thinness and shallowness parameters. Since most available experimental verification of shell frequencies and mode shapes have been done during stability investigations, some literature on the buckling of shallow spherical shells is included. Discrepancies between the theoretical and experimental results given for the buckling of shallow shells indicate that the effects of imperfections in shell geometry and the inability to satisfy idealized edge conditions exactly should be studied experimentally for linear vibrations. No detailed experimental and theoretical comparisons for the linear forced response of shallow shells could be found in the literature.

1.3.1 Linear Vibrations. An exact solution for the asymmetric free vibrations of shallow shells with clamped edges was formulated by Reissner [49] who evaluated an approximate fundamental frequency using the Rayleigh-Ritz procedure. Later, Reissner [50] showed that longitudinal or in-plane inertia could be neglected in solving for the transverse free vibrations of shallow shells, thereby reducing the problem to the solution of two simultaneous differential equations involving a stress function and the transverse displacement rather than three simultaneous differential equations in the three displacement components. Using this approximation, Reissner calculated the frequencies of simply supported shallow shells of rectangular plan with sliding edges. Neglecting longitudinal inertia, Reissner [51] determined axisymmetrical natural frequencies of shallow shells with both clamped and free edges, and forced vibrations of an infinite shallow shell with a point load at the apex. Free transverse vibrations of shallow spherical shells with free edges were analysed by Johnson and Reissner [52].

Naghdi [53] derived the differential equations for the linear response of thin shallow elastic shells including the effect of transverse shear deformation. Kalnins and Naghdi [54] gave an analysis for the coupled longitudinal (torsionless) and transverse asymmetric vibrations of shallow spherical shells. The differential equations governing vibrations of shallow spherical shells including the coupling effects of longitudinal, transverse and rotatory inertia, and transverse shear deformation were given by Kalnins [55], who calculated the frequency equation for a clamped shallow spherical cap from these differential equations. Free nonsymmetric and axisymmetric vibrations of clamped shallow spherical shells, including some mode shapes, were computed by Kalnins [56]. He showed that neglecting longitudinal inertia resulted in the omission of an infinite number of in-plane inertia modes but that transverse vibration frequencies computed by the classical method were quite accurate and essentially uncoupled from the in-plane frequencies.

Van Fo Fy [57] introduced two auxiliary

functions for shallow spherical shells with longitudinal inertia neglected, thereby reducing the two simultaneous differential equations in stress function and transverse displacement to two simpler uncoupled differential equations, the solution of which reduces to the solution obtained by Reissner [50].

Lee [58] analysed the axisymmetric vibrations of a shallow spherical shell with a heavy mass at the apex and Pandalai and Dym [59] showed that for practical purposes the transverse shear force can be neglected in the calculation of the axisymmetric natural frequencies of a shallow spherical cap.

Koplik and Yu [60] studied the axisymmetric vibrations of homogeneous and sandwich shallow spherical caps with clamped edges including the thickness-shear effect. They showed that the frequencies of the higher modes of vibration of homogeneous and sandwich caps can be calculated from the uncoupled equations of clamped circular plates as the shell curvature affects only the lower frequencies, and that the thickness-shear effect can be ignored for homogeneous caps. Koplik and Yu gave an approximate solution for the axisymmetric vibrations of clamped spherical caps [61]

and analysed the torsional vibrations of homogeneous and sandwich spherical caps and plates with clamped and free edges [62].

Lock, Whittier and Malcom [63] showed that the nonsymmetric transverse vibrations of a clamped shallow spherical shell depend upon a single shell geometric parameter, and that the eigenvalues of the higher modes converge to the clamped plate eigenvalues.

The response of shallow viscoelastic spherical shells to arbitrary time-dependent axisymmetric loads has been studied by Naghdi and Orthwein [64]. Neglecting longitudinal inertia, they solved the differential equations for unlimited shallow shells and shallow shell segments using Laplace and Hankel transforms. Van Fo Fy and Buibol [65] obtained a solution for shallow spherical shells, neglecting longitudinal inertia, subject to a harmonic axisymmetric transverse load. Kraus and Kalnins [66] derived a general solution for arbitrary elastic shells subjected to time-dependent surface loads, for which the free vibration characteristics are known, using spectral representation or normal modes. They

also showed that for a shallow spherical shell with simply supported edges having a base circle-to-thickness ratio of 20 and a half angle of opening of 15 degrees, three symmetric modes usually are required for the transient response to a suddenly applied uniform pressure while for a hemispherical shell with the same thinness parameter, fifteen modes are required. The method of analysis for obtaining the response of shallow spherical shells subjected to transient surface, edge and thermal loads using spectral representation has been outlined by Kraus [67]. Reismann and Culkowski [68] have obtained a solution for a clamped shallow spherical shell subjected to an impulse uniformly distributed over a central area including the effect of shear deformation and rotatory inertia.

1.3.2 Buckling. Hossack [69], in the course of an experimental investigation on the nonlinear behaviour of shallow spherical shells subjected to static overpressures, suggested that shells manufactured by spinning are subject to residual stresses and variations in thickness. He stated that the clamped edge condition is almost impossible to achieve

in practice and that attempts to attain it will induce random forces and moments and, in any case, in most engineering applications the behaviour of a shallow cap would approximate that of a freely supported shell even when some measure of restraint is provided. Hossack found for some freely supported caps that experimental bending strains agreed more closely with theory than did the membrane strains.

In experiments on dynamic buckling of clamped shallow spherical shells under uniform pressure pulse loading, Humphreys, Roth and Zatlers [70] found that maximum prebuckling deflections exceeded the theoretical predictions of Budiansky and Roth [71] by as much as 100 per cent.

Huang [72] suggested that when the shell height-to-thickness ratio exceeds a certain value, initial geometric imperfections or disturbances during deformation would cause the axisymmetric deformation of clamped shallow spherical shells to bifurcate to asymmetric deformation at some prebuckling pressure. Using this assumption, Huang, predicted lower buckling pressures for these shells which, however, were still not conservative in comparison to

experimental values.

Archer and Famili [73] adopted the vibration method of stability analysis to theoretically predict static buckling pressures for clamped shallow spherical shells. This method is based on the fact that the frequency of the buckling mode, which can be predicted by Huang's theory [72], diminishes from the free vibration values given by Kalnins [56] to zero frequency when the shell is loaded at the buckling overpressure. Okubo and Whittier [74] applied this nondestructive method of determining the static buckling pressure to some clamped shallow spherical shells. They found that the experimental frequency of the axisymmetric buckling mode, predicted as the failure mode by Huang, was slightly lower than the value predicted by the method of Archer and Famili at all static overpressures for all shells tested. They suggested that radius of curvature variations in the experimental shells as well as thickness deviations might explain the discrepancies.

CHAPTER 2

PLATE THEORY

2.1 Governing Equations

The fundamental differential equation of motion given by Poisson [5] and Kirchoff [6] for thin elastic plates subjected to linear isothermal deformation by a normal dynamic massless loading function $q(r,\theta,t)$ with viscous damping included, neglecting the effects of rotatory inertia and transverse shear, is

$$D\,\nabla^4 w(r,\theta,t) + 2\zeta m\,\frac{\partial w(r,\theta,t)}{\partial t} + m\frac{\partial^2 w(r,\theta,t)}{\partial t^2} = q(r,\theta,t). \qquad (2.1)$$

In this equation w is the transverse displacement of the middle plane of the plate, ζ is the coefficient of viscous damping, m is the mass per unit area, $D = Eh^3/[12(1 - \nu^2)]$ is the flexural rigidity, h is the plate thickness, E is the modulus of elasticity, ν is Poisson's ratio, r and θ are the radial and angular polar coordinates, t is time, and $\nabla^2 = \frac{\partial^2}{\partial r^2} + \frac{1}{r}\frac{\partial}{\partial r} + \frac{1}{r^2}\frac{\partial^2}{\partial \theta^2}$ when operating on $w(r,\theta,t)$.

Introducing the dimensionless parameters $\eta = \frac{w}{a}$ and $\rho = \frac{r}{a}$, where a is the radius of the circle

circumscribing a regular polygonal plate, Eq. (2.1) becomes

$$D \nabla^4 \eta(\rho,\theta,t) + 2\zeta m a^4 \frac{\partial \eta(\rho,\theta,t)}{\partial t} + m a^4 \frac{\partial^2 \eta(\rho,\theta,t)}{\partial t^2} =$$

$$= a^3 q(\rho,\theta,t), \qquad (2.2)$$

where $\nabla^2 = \frac{\partial^2}{\partial \rho^2} + \frac{1}{\rho}\frac{\partial}{\partial \rho} + \frac{1}{\rho^2}\frac{\partial^2}{\partial \theta^2}$ when operating on $\eta(\rho,\theta,t)$.

In the interest of obtaining the most general solution, the possibility of time-dependent nonhomogeneous edge conditions is included. A solution of Eq. (2.2) for nonhomogeneous boundary conditions which depend on functions of time $\bar{e}^{\ell}(t)$ is assumed in the form [25]

$$\eta(\rho,\theta,t) = \eta_1(\rho,\theta,t) + \sum_{\ell=1}^{c} \bar{g}^{\ell}(\rho,\theta)\, \bar{e}^{\ell}(t), \qquad (2.3)$$

where c = 4 for a plate with interior and exterior boundaries and c = 2 for a plate possessing only an exterior boundary. The functions $\bar{g}^{\ell}(\rho,\theta)$ are chosen to make the boundary conditions expressed in terms of $\eta_1(\rho,\theta,t)$ homogeneous. Substituting Eq. (2.3) into Eq. (2.2)yields

$$D\,\nabla^4\eta_1(\rho,\theta,t) + 2\zeta m a^4 \frac{\partial\eta_1(\rho,\theta,t)}{\partial t} + m a^4 \frac{\partial^2\eta_1(\rho,\theta,t)}{\partial t^2} =$$

$$= a^3 q(\rho,\theta,t) - D\sum_{\ell=1}^{c} \overset{\ell}{\bar{e}}(t)\,\nabla^4\overset{\ell}{\bar{g}}(\rho,\theta) - 2\zeta m a^4 \sum_{\ell=1}^{c} \frac{d\overset{\ell}{\bar{e}}(t)}{dt}\,\overset{\ell}{\bar{g}}(\rho,\theta) -$$

$$- m a^4 \sum_{\ell=1}^{c} \frac{d^2\overset{\ell}{\bar{e}}(t)}{dt^2}\,\overset{\ell}{\bar{g}}(\rho,\theta). \qquad (2.4)$$

2.2 Free Undamped Motion

2.2.1 General Solution.

The homogeneous equation of the undamped system

$$\nabla^4\eta_1(\rho,\theta,t) + \frac{m a^4}{D}\,\frac{\partial^2\eta_1(\rho,\theta,t)}{\partial t^2} = 0 \qquad (2.5)$$

can be solved by the separation of variables technique

$$\eta_1(\rho,\theta,t) = \bar{\eta}(\rho,\theta)\exp(i\omega t),$$

where ω is the undamped circular frequency. Substitution into Eq. (2.5) gives two simpler differential equations of the form

$$(\nabla^2 + k^2)\,\bar{\eta}_1(\rho,\theta) = 0 \qquad (2.6)$$

and

$$(\nabla^2 - k^2)\,\bar{\eta}_2(\rho,\theta) = 0, \qquad (2.7)$$

where

$$k^2 = a^2\sqrt{\frac{m}{D}}\;\omega.$$

For linear problems

$$\bar{\eta}(\rho,\theta) = \bar{\eta}_1(\rho,\theta) + \bar{\eta}_2(\rho,\theta).$$

Love [75] showed that solutions for equations of this type can be given as

$$\bar{\eta}(\rho,\theta) = \sum_{n=0}^{\infty} \bar{V}_n(\rho) \begin{cases}\cos n\theta \\ \sin n\theta\end{cases}.$$

Consequently the general solution of Eq. (2.3) is given by

$$\bar{\eta}(\rho,\theta) = \sum_{n=0}^{\infty} [A_n J_n(k\rho) + B_n I_n(k\rho) + C_n Y_n(k\rho) + D_n K_n(k\rho)] \begin{cases}\cos n\theta \\ \sin n\theta\end{cases}, \qquad (2.8)$$

where A_n, B_n, C_n and D_n are integration constants, J_n and Y_n are Bessel functions of the first and second kind, respectively, and I_n and K_n are modified Bessel functions of the first and second kind, respectively. Restricting the solution to plates possessing no interior boundaries yields

$$C_n = D_n = 0$$

and applying the solution to plates of regular polygonal shape possessing p-ply rotational geometric periodicity as shown in Fig. 2.1 yields for symmetric response[1]

---

[1] This assumption of symmetric response restricts the loading function to be of the form $q(\rho,\theta,t) = q_o\bar{q}(\rho)\cos pm\theta\ Q(t)$, where q_o is a reference pressure and m is any integer.

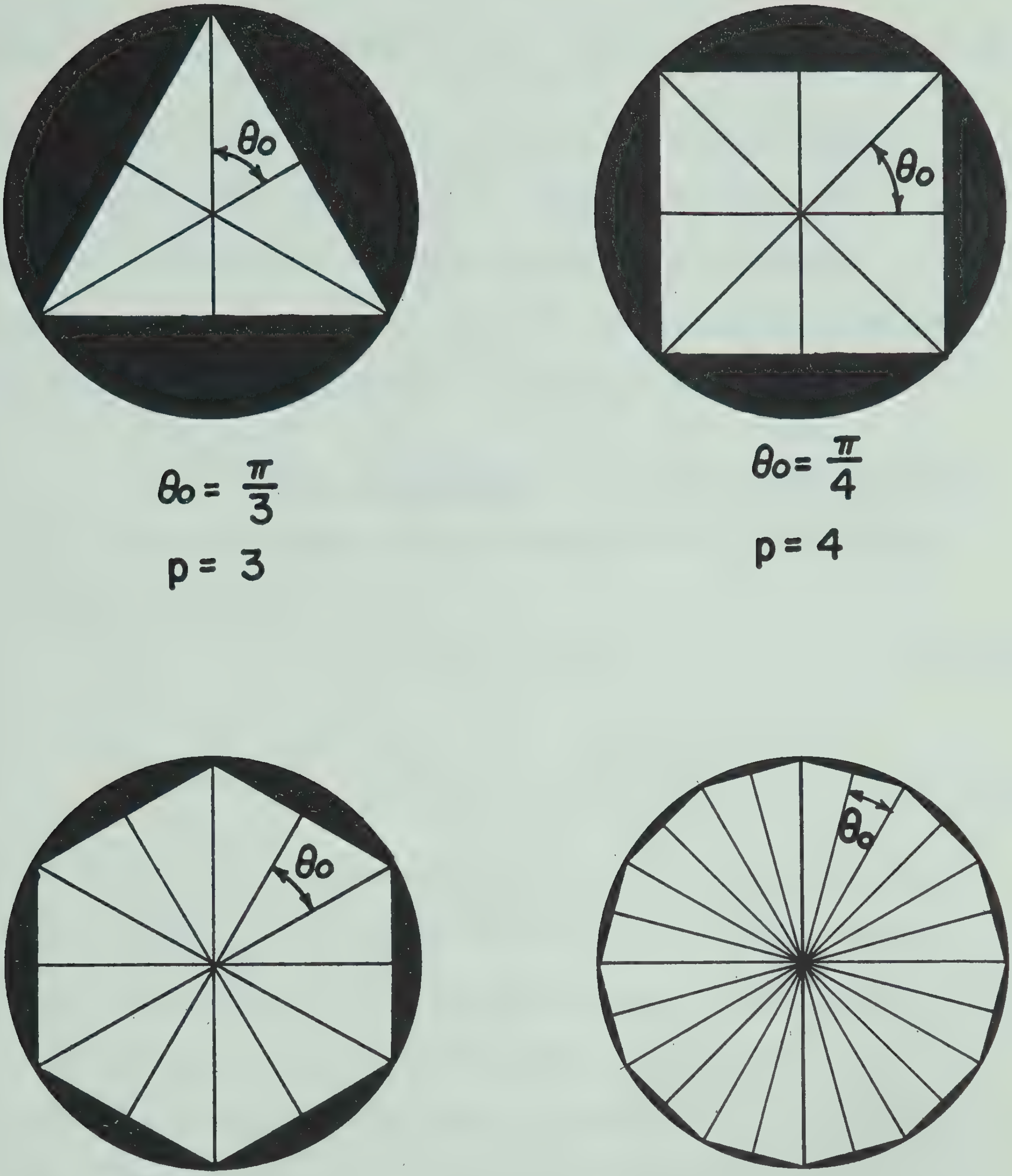

$\theta_0 = \frac{\pi}{3}$

$p = 3$

$\theta_0 = \frac{\pi}{4}$

$p = 4$

$\theta_0 = \frac{\pi}{6}$

$p = 6$

$\theta_0 = \frac{\pi}{12}$

$p = 12$

FIG. 2.1 Thin Regular Polygonal Plates with p sides

[illegible]

$$\bar{\eta}(\rho,\theta) = \sum_{n=0}^{\infty} [A_{pn} J_{pn}(k\rho) + B_{pn} I_{pn}(k\rho)] \cos pn\theta. \qquad (2.9)$$

θ is 0 and π/p radians, respectively, along radial lines which pass through the boundary center and corners. Consequently, the response is symmetric about these radial lines if $\eta(\theta)$ is chosen to vary as $\cos pn\theta$, since $\partial\eta(\rho,0)/\partial\theta = \partial\eta(\rho,\pi/p)/\partial\theta = 0$.

2.2.2 Edge Conditions. The homogeneous edge conditions which must be satisfied for an elastically built-in plate are

$$\eta(\tilde{\rho},\tilde{\theta}) = 0 \qquad (2.10a)$$

and

$$M_{vs}(\tilde{\rho},\tilde{\theta}) = \beta_1 \frac{\partial\eta(\tilde{\rho},\tilde{\theta})}{\partial v}, \qquad (2.10b)$$

where $\tilde{\rho}$ and $\tilde{\theta}$ are the coordinates of boundary points. In Eq. (2.10b) $M_{vs}(\tilde{\rho},\tilde{\theta})$ is the flexural stress couple vector tangential to the boundary and β_1 is the edge spring constant of proportionality ranging from zero for a simply supported plate to infinity for a clamped plate. The boundary and interior coordinate systems are shown in Fig. 2.2. The associated nonhomogeneous time-dependent edge conditions will be dealt with in

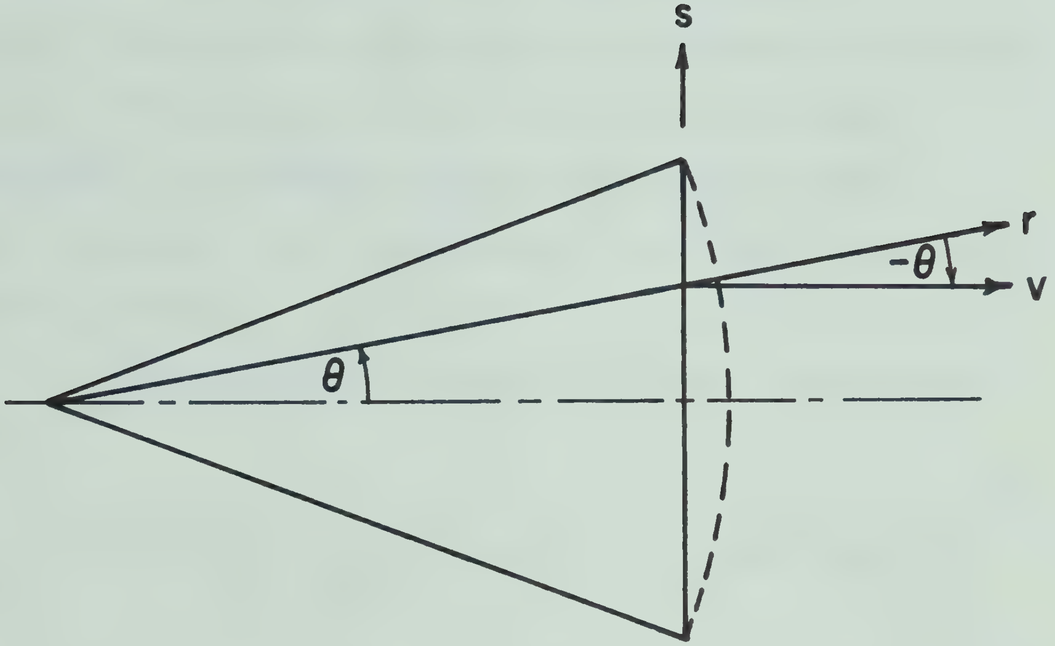

FIG. 2.2 Vector Diagram Showing Relation of Boundary Coordinates v, s to Interior Coordinates r, θ

Chapter 3.

Since at the present time an exact solution for this problem is not available for the edge restraints in Eq. (2.10a) and (2.10b), Tölke's boundary collocation method [34] is employed, whereby a rigorous satisfaction of the prescribed boundary conditions is collocated for a number of discrete points located on the boundary of one of the rotationally periodic segments of the plate.

Expressing Eq. (2.10b) in polar coordinates yields

$$M_{r\theta}(\tilde{\rho},\tilde{\theta})\cos^2\tilde{\theta} - M_{\theta r}(\tilde{\rho},\tilde{\theta})\sin^2\tilde{\theta} + M_{rr}(\tilde{\rho},\tilde{\theta})\sin 2\tilde{\theta} =$$

$$= \beta_1\left[\frac{\partial\eta(\tilde{\rho},\tilde{\theta})}{\partial\rho}\cos\tilde{\theta} - \frac{1}{\tilde{\rho}}\frac{\partial\eta(\tilde{\rho},\tilde{\theta})}{\partial\theta}\sin\tilde{\theta}\right] \qquad (2.10c)$$

The flexural stress couple components $M_{r\theta}$ and $M_{\theta r}$, the torsional stress couple components M_{rr} and $M_{\theta\theta}$ and the transverse shear stress resultant components F_{rn} and $F_{\theta n}$, which are shown in Fig. 2.3, can be expressed by

$$M_{r\theta} = -\frac{D}{a}\left[\frac{\partial^2\eta}{\partial\rho^2} + \nu\left(\frac{1}{\rho^2}\frac{\partial^2\eta}{\partial\theta^2} + \frac{1}{\rho}\frac{\partial\eta}{\partial\rho}\right)\right], \qquad (2.11a)$$

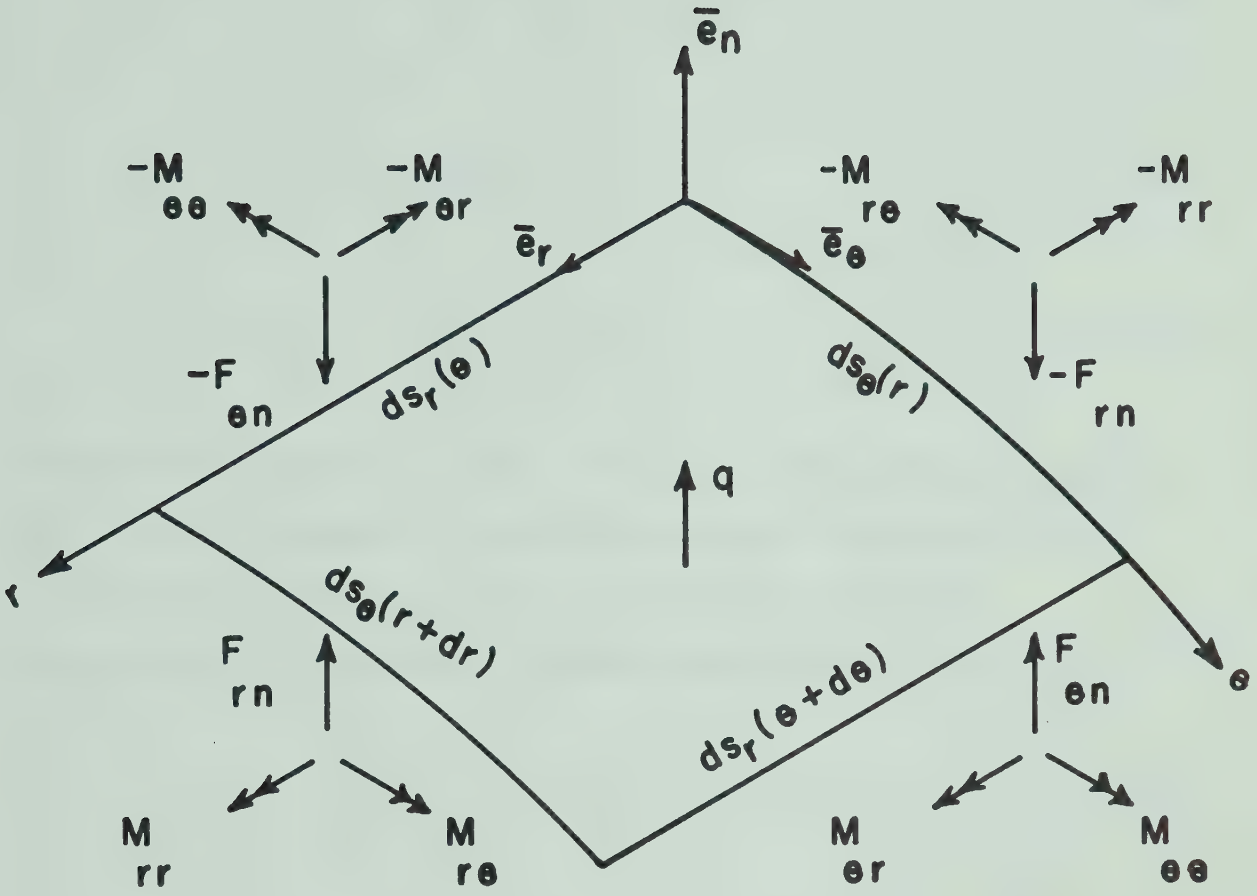

FIG. 2.3 Vector Diagram of Plate Element Showing Sectional Resultants

$$M_{\theta r} = \frac{D}{a}\left[\frac{1}{\rho^2}\frac{\partial^2\eta}{\partial\theta^2} + \frac{1}{\rho}\frac{\partial\eta}{\partial\rho} + \nu\frac{\partial^2\eta}{\partial\rho^2}\right], \tag{2.11b}$$

$$M_{rr} = -M_{\theta\theta} = \frac{D(1-\nu)}{a}\left[\frac{\partial}{\partial\rho}\left(\frac{1}{\rho}\frac{\partial\eta}{\partial\theta}\right)\right], \tag{2.11c}$$

$$F_{rn} = -\frac{D}{a^2}\frac{\partial}{\partial\rho}(\nabla^2\eta), \tag{2.11d}$$

$$F_{\theta n} = -\frac{D}{\rho a^2}\frac{\partial}{\partial\theta}(\nabla^2\eta). \tag{2.11e}$$

Substitution of Eqs. (2.9) and (2.11) into Eqs. (2.10a) and (2.10c) produces linear homogeneous equations, the solution of which will yield an infinite set of eigenvalues k_i and their associated eigenvectors. Thus

$$\sum_{n=0}^{\infty}[A^i_{pn}\,\psi_1 + B^i_{pn}\,\psi_2] = 0, \tag{2.10a*}$$

$$\sum_{n=0}^{\infty}[A^i_{pn}\,(\psi_5 - \beta^i_1\frac{a}{D}\psi_3) + B^i_{pn}\,(\psi_6 - \beta^i_1\frac{a}{D}\psi_4)] = 0. \tag{2.10c*}$$

The coefficients in the boundary equations (2.10a*) and (2.10c*) are

$$\psi_1 = J_{pn}(\tilde{\mu})\cos pn\tilde{\theta},$$

$$\psi_2 = I_{pn}(\tilde{\mu})\cos pn\tilde{\theta},$$

$$\psi_3 = k_i J'_{pn}(\tilde{\mu}) \cos \tilde{\theta} \cos pn\tilde{\theta} + \frac{pn}{\tilde{\rho}} J_{pn}(\tilde{\mu}) \sin \tilde{\theta} \sin pn\tilde{\theta},$$

$$\psi_4 = k_i I_{pn}(\tilde{\mu}) \cos \tilde{\theta} \cos pn\tilde{\theta} + \frac{pn}{\tilde{\rho}} I_{pn}(\tilde{\mu}) \sin \tilde{\theta} \sin pn\tilde{\theta},$$

$$\begin{aligned}\psi_5 = &-[k_i^2 J''_{pn}(\tilde{\mu}) - \nu(\frac{pn}{\tilde{\rho}})^2 J_{pn}(\tilde{\mu}) + \nu(\frac{k_i}{\tilde{\rho}}) J'_{pn}(\tilde{\mu})] \cos^2\tilde{\theta} \cos pn\tilde{\theta} + \\ &+[\nu k_i^2 J''_{pn}(\tilde{\mu}) - (\frac{pn}{\tilde{\rho}})^2 J_{pn}(\tilde{\mu}) + (\frac{k_i}{\tilde{\rho}}) J'_{pn}(\tilde{\mu})] \sin^2\tilde{\theta} \cos pn\tilde{\theta} - \\ &- (1 - \nu)[\frac{pn}{\tilde{\rho}^2} J_{pn}(\tilde{\mu}) - k_i(\frac{pn}{\tilde{\rho}}) J'_{pn}(\tilde{\mu})] \sin 2\tilde{\theta} \sin pn\tilde{\theta},\end{aligned}$$

$$\begin{aligned}\psi_6 = &- [k_i^2 I''_{pn}(\tilde{\mu}) - \nu(\frac{pn}{\tilde{\rho}})^2 I_{pn}(\tilde{\mu}) + \nu(\frac{k_i}{\tilde{\rho}}) I'_{pn}(\tilde{\mu})] \cos^2\tilde{\theta} \cos pn\tilde{\theta} + \\ &+ [\nu k_i^2 I''_{pn}(\tilde{\mu}) - (\frac{pn}{\tilde{\rho}})^2 I_{pn}(\tilde{\mu}) + (\frac{k_i}{\tilde{\rho}}) I'_{pn}(\tilde{\mu})] \sin^2\tilde{\theta} \cos pn\tilde{\theta} - \\ &- (1 - \nu)[\frac{pn}{\tilde{\rho}^2} I_{pn}(\tilde{\mu}) - k_i(\frac{pn}{\tilde{\rho}}) I'_{pn}(\tilde{\mu})] \sin 2\tilde{\theta} \sin pn\tilde{\theta},\end{aligned}$$

where $\tilde{\mu} = k_i\tilde{\rho}$.

2.3 Forced Motion

2.3.1 General Solution. The classical method of spectral representation in which the dependent variables are expanded in an infinite series of normal modes of free vibration is assumed for $\eta_1(\rho,\theta,t)$, defined by Eq. (2.4), in the

form

$$\eta_1(\rho,\theta,t) = \sum_{i=1}^{\infty} \bar{\eta}^i(\rho,\theta)\, T^i(t), \tag{2.12}$$

where

$$\bar{\eta}^i(\rho,\theta) = \sum_{n=0}^{\infty} [A^i_{pn} J_{pn}(k_i\rho) + B^i_{pn} I_{pn}(k_i\rho)]\cos pn\theta \tag{2.13}$$

and $T^i(t)$ is usually referred to as the modal participation factor. Substituting Eq. (2.12) into Eq. (2.4) and simplifying yields

$$\sum_{i=1}^{\infty} \left[\frac{d^2T^i(t)}{dt^2} + 2\zeta_i \frac{dT^i(t)}{dt} + \omega_i^2 T^i(t)\right]\bar{\eta}^i(\rho,\theta) =$$

$$= \frac{q_o}{ma}\bar{q}(\rho)\cos pm\theta\, Q(t) - \frac{D}{ma^4}\sum_{\ell=1}^{2} \bar{e}^\ell(t)\, \nabla^4 \bar{g}^\ell(\rho,\theta) -$$

$$- 2\zeta_i \sum_{\ell=1}^{2} \frac{d\bar{e}^\ell(t)}{dt}\bar{g}^\ell(\rho,\theta) - \sum_{\ell=1}^{2} \frac{d^2\bar{e}^\ell(t)}{dt^2}\bar{g}^\ell(\rho,\theta). \tag{2.14}$$

Here it is assumed, as is done by Meirovitch [25], that the eigenvalues k_i and the eigenvectors $\bar{\eta}^i$ associated with the homogeneous equation of the undamped system, Eq. (2.5), satisfy the nonhomogeneous equation with viscous damping included, Eq. (2.4)

Multiplying both sides of Eq. (2.14) by $\bar{\eta}^j(\rho,\theta)$, integrating over the plate characteristic segment area and applying the condition of orthogonality of the eigenvectors pointed out by Rayleigh [8] and shown in Appendix B.1,

yields

$$\frac{d^2T^i(t)}{dt^2} + 2\,\zeta_i \frac{dT^i(t)}{dt} + \omega_i^2\, T^i(t) = \frac{\chi_1^i}{\chi_0^i}\frac{q_o}{ma}\,Q(t) -$$

$$- 2\zeta_i \sum_{\ell=1}^{2} \frac{d\bar{e}^{\ell}(t)}{dt}\,\frac{\chi_3^{\ell,i}}{\chi_0^i} - \sum_{\ell=1}^{2} \frac{d^2\bar{e}^{\ell}(t)}{dt^2}\,\frac{\chi_3^{\ell,i}}{\chi_0^i}\,, \qquad (2.15)$$

where

$$\chi_0^i = \int_0^{\theta o}\int_0^{\frac{\cos\theta o}{\cos\theta}} \rho[\bar{\eta}^i(\rho,\theta)]^2\, d\rho\, d\theta, \qquad (2.16)$$

$$\chi_1^i = \int_0^{\theta o}\int_0^{\frac{\cos\theta o}{\cos\theta}} \rho\bar{\eta}^i(\rho,\theta)\ \bar{q}(\rho)\ \cos p m\theta\ d\rho\, d\theta, \qquad (2.17)$$

$$\chi_3^{\ell,i} = \int_0^{\theta o}\int_0^{\frac{\cos\theta o}{\cos\theta}} \rho\bar{g}^{\ell}(\rho,\theta)\ \bar{\eta}^i(\rho,\theta)\ d\rho\, d\theta \qquad (2.18)$$

and

$$\theta_o = \frac{\pi}{p}.$$

Eq. (2.15) has been simplified by arbitrarily choosing

$\bar{g}^{\ell}(\rho,\theta)$ as solutions of the biharmonic equation in the form

$$\bar{g}^{\ell}(\rho,\theta) = \sum_{n=0}^{\infty}\left[E_{pn}^{1,\ell}\rho^{pn} + E_{pn}^{2,\ell}\rho^{pn+2}\right]\cos pn\theta\ , \quad \ell=1,2\ldots \tag{2.19}$$

This is permissible since these auxiliary edge condition functions are not unique, as Meirovitch [25] points out.

2.3.2 Initial Conditions. The solution of Eq. (2.15) for $\zeta_i < \omega_i$ is

$$T^{i}(t) = \exp(-\zeta_i t)\left\{\frac{1}{\omega_i^d}\left[\frac{dT^{i}(0)}{dt} + \zeta_i T^{i}(0)\right]\sin\omega_i^d t + \right.$$

$$\left. + T^{i}(0)\cos\omega_i^d t\right\} + [1/(\omega_i^2\chi_0^i)]\ [(q_o/ma)\chi_1^i G_1^i(t) -$$

$$- 2\zeta_i\sum_{\ell=1}^{2}\chi_3^{\ell,i}\, G_3^{\ell,i}(t) - \sum_{\ell=1}^{2}\chi_3^{\ell,i}\, G_4^{\ell,i}(t)], \tag{2.20}$$

where

$$G_1^i(t) = (\omega_i^2/\omega_i^d)\int_0^t Q(\tau)\exp[-\zeta_i(t-\tau)]\sin\omega_i^d(t-\tau)\,d\tau, \tag{2.21a}$$

$$G_3^{\ell,i}(t) = (\omega_i^2/\omega_i^d)\int_0^t \frac{d\bar{e}^{\ell}(\tau)}{d\tau}\exp[-\zeta_i(t-\tau)]\ \times$$

$$\times\ \sin\omega_i^d(t-\tau)\,d\tau, \tag{2.21b}$$

$$G_4^{\ell,i}(t) = (\omega_i^2/\omega_i^d) \int_0^t \frac{d^2\bar{e}^\ell(\tau)}{d\tau^2} \exp[-\zeta_i(t-\tau)] \times$$

$$\times \sin \omega_i^d (t-\tau)\, d\tau \qquad (2.21c)$$

and $\omega_i^d = \sqrt{\omega_i^2 - \zeta_i^2}$ is the damped circular frequency of the i-th mode.

If the plate is initially assumed to be at rest and to have undergone no transverse displacement, then

$$\eta(\rho,\theta,0) = 0\,, \qquad (2.22a)$$

$$\frac{\partial\eta(\rho,\theta,0)}{\partial t} = 0 \qquad (2.22b)$$

and the free part of the solution, Eq. (2.20), vanishes leaving

$$T^i(t) = [1/(\omega_i^2\, \chi_0^i)]\, [(q_o/ma)\, \chi_1^i\, G_1^i\,(t) -$$

$$- 2\zeta_i \sum_{\ell=1}^{2} \chi_3^{\ell,i}\, G_3^{\ell,i}(t) - \sum_{\ell=1}^{2} \chi_3^{\ell,i}\, G_4^{\ell,i}(t)] \qquad (2.23)$$

2.3.3 Modal Participation Functions.

Substituting Eqs. (2.13) and (2.19) into Eqs. (2.16) through (2.18) yields the expressions for the modal

participation functions

$$\chi_0^{i} = [A_0^{i}]^2 \phi_1 + [B_0^{i}]^2 \phi_2 + 2 A_0^{i} B_0^{i} \phi_3 +$$

$$+ \sum_{n=1}^{\infty} \{ [A_{pn}^{i}]^2 \phi_4 + [B_{pn}^{i}]^2 \phi_5 + 2 A_{pn}^{i} B_{pn}^{i} \phi_{10} \} , \qquad (2.24a)$$

$$\chi_1^{i} = A_0^{i} \phi_7 + B_0^{i} \phi_8 + \sum_{n=1}^{\infty} [A_{pn}^{i} \phi_9 + B_{pn}^{i} \phi_{10}], \qquad (2.24b)$$

$$\chi_3^{\ell,i} = E_0^{1,\ell} [A_0^{i} \phi_{11} + B_0^{i} \phi_{12}] + E_0^{2,\ell} [A_0^{i} \phi_{13} + B_0^{i} \phi_{14}] +$$

$$+ \sum_{n=1}^{\infty} \{ E_{pn}^{1,\ell} [A_{pn}^{i} \phi_{15} + B_{pn}^{i} \phi_{16}] + E_{pn}^{2,\ell} [A_{pn}^{i} \phi_{17} + B_{pn}^{i} \phi_{18}]\}.$$

(2.24c)

In evaluating χ_0^{i} and $\chi_3^{\ell,i}$, terms involving products of functions of different orders n have been neglected. This simplification is exact only for circular boundaries and introduces errors which will increase in magnitude with the deviation of the nodal lines from circles concentric about the plate center. The accuracy of this simplification is checked for some numerical examples in Chapter 4.

Evaluation of the coefficients $\phi_1 \ldots \phi_{18}$ involves integration over ρ and θ. The integration over ρ can be carried out exactly as shown by McLachlan [76], for example, however the integration over θ must be carried out numerically. If the terms involving products of functions of different orders n had not been neglected in Eq. (2.22), then formulas for their associated ϕ-coefficients suitable for polygonal plates with any number of sides could have been solved only by numerically integrating over both coordinates ρ and θ.

For a load distributed uniformly over the plate surface $\bar{q}(\rho) \cos p m \theta = 1$ and the coefficients $\phi_1 \ldots \phi_{18}$ are:

$$\phi_1 = \frac{\cos^2 \theta o}{2} \int_0^{\theta o} [J_0^2(\mu_o) + J_1^2(\mu_o)] \frac{d\theta}{\cos^2 \theta} ,$$

$$\phi_2 = \frac{\cos^2 \theta o}{2} \int_0^{\theta o} [I_0^2(\mu_o) - I_1^2(\mu_o)] \frac{d\theta}{\cos^2 \theta} ,$$

$$\phi_3 = \frac{\cos \theta o}{2k_i} \int_0^{\theta o} [J_0(\mu_o) I_1(\mu_o) + J_1(\mu_o) I_0(\mu_o)] \frac{d\theta}{\cos \theta} ,$$

$$\phi_4 = \frac{\cos^2\theta o}{2} \int_0^{\theta o} \left\{ [J'_{pn}(\mu_o)]^2 + J^2_{pn}(\mu_o) \left[1 - \left(\frac{pn}{k_i}\right)^2 \times \right.\right.$$

$$\left.\left. \times \frac{\cos^2\theta}{\cos^2\theta o}\right]\right\} \frac{\cos^2 pn\theta}{\cos^2\theta}\, d\theta,$$

$$\phi_5 = \frac{\cos^2\theta o}{2} \int_0^{\theta o} \left\{ -[I'_{pn}(\mu_o)]^2 + I^2_{pn}(\mu_o) \left[1 + \left(\frac{pn}{k_i}\right)^2 \times \right.\right.$$

$$\left.\left. \times \frac{\cos^2\theta}{\cos^2\theta o}\right]\right\} \frac{\cos^2 pn\theta}{\cos^2\theta}\, d\theta,$$

$$\phi_6 = \frac{\cos^2\theta o}{2k_i} \int_0^{\theta o} [J_{pn}(\mu_o)\, I'_{pn}(\mu_o) - J'_{pn}(\mu_o)\, I_{pn}(\mu_o)] \times$$

$$\times \frac{\cos^2 pn\theta}{\cos\theta}\, d\theta,$$

$$\phi_7 = \frac{\cos\theta o}{k_i} \int_0^{\theta o} \frac{J_1(\mu_o)}{\cos\theta}\, d\theta,$$

$$\phi_8 = \frac{\cos\theta o}{k_i} \int_0^{\theta o} \frac{I_1(\mu_o)}{\cos\theta}\, d\theta,$$

$$\phi_9 = \frac{2}{k_i} \sum_{\alpha=0}^{\infty} \cos\theta_o \int_0^{\theta o} J_{pn+2\alpha+1}(\mu_o) \frac{\cos pn\theta}{\cos\theta} d\theta -$$

$$- \frac{2}{k_i} \sum_{\alpha=0}^{\infty} (\alpha+1) \int_0^{\theta o} J_{pn+2\alpha+2}(\mu_o) \cos pn\theta \, d\theta \, ,$$

$$\phi_{10} = \frac{2}{k_i} \sum_{\alpha=0}^{\infty} (-1)^{\alpha} \cos\theta_o \int_0^{\theta o} I_{pn+2\alpha+1}(\mu_o) \frac{\cos pn\theta}{\cos\theta} d\theta -$$

$$- \frac{2}{k_i} \sum_{\alpha=0}^{\infty} (-1)^{\alpha} (\alpha+1) \int_0^{\theta o} I_{pn+2\alpha+2}(\mu_o) \cos pn\theta \, d\theta \, ,$$

$$\phi_{11} = \frac{\cos\theta o}{k_i} \int_0^{\theta o} J_1(\mu_o) \frac{d\theta}{\cos\theta} ,$$

$$\phi_{12} = \frac{\cos\theta o}{k_i} \int_0^{\theta o} I_1(\mu_o) \frac{d\theta}{\cos\theta} ,$$

$$\phi_{13} = \frac{\cos^3\theta o}{k_i} \int_0^{\theta o} J_1(\mu_o) \frac{d\theta}{\cos^3\theta} - \frac{2}{k_i^2} \cos^2\theta o \int_0^{\theta o} J_2(\mu_o) \frac{d\theta}{\cos^2\theta} ,$$

$$\phi_{14} = \frac{\cos^3\theta o}{k_i} \int_0^{\theta o} I_1(\mu_o) \frac{d\theta}{\cos^3\theta} - \frac{2}{k_i^2} \cos^2\theta o \int_0^{\theta o} I_2(\mu_o) \frac{d\theta}{\cos^2\theta} \, ,$$

$$\phi_{15} = \frac{(\cos\ \theta o)^{pn+1}}{k_i} \int_0^{o} J_{pn+1}(\mu_o) \frac{\cos^2 pn\theta}{(\cos\ \theta)^{pn+1}} \, d\theta,$$

$$\phi_{16} = \frac{(\cos\ \theta o)^{pn+1}}{k_i} \int_0^{\theta o} I_{pn+1}(\mu_o) \frac{\cos^2 pn\theta}{(\cos\ \theta)^{pn+1}} \, d\theta,$$

$$\phi_{17} = \frac{(\cos\ \theta o)^{pn+3}}{k_i} \int_0^{\theta o} J_{pn+1}(\mu_o) \frac{\cos^2 pn\theta}{(\cos\ \theta)^{pn+3}} \, d\theta - \frac{2}{k_i^2} \times$$

$$\times (\cos\ \theta o)^{pn+2} \int_0^{\theta o} J_{pn+2}(\mu_o) \frac{\cos^2 pn\theta}{(\cos\ \theta)^{pn+2}} \, d\theta,$$

$$\phi_{18} = \frac{(\cos\ \theta o)^{pn+3}}{k_i} \int_0^{\theta o} I_{pn+1}(\mu_o) \frac{\cos^2 pn\theta}{(\cos\ \theta)^{pn+3}} \, d\theta - \frac{2}{k_i^2} \times$$

$$\times (\cos\ \theta o)^{pn+2} \int_0^{\theta o} I_{pn+2}(\mu_o) \frac{\cos^2 pn\theta}{(\cos\ \theta)^{pn+2}} \, d\theta,$$

where $\mu_o = k_i \dfrac{\cos \theta o}{\cos \theta}$.

For a concentrated load $P = P_o Q(t)$ at the plate center, P_o replaces q_o in Eq. (2.19) and the coefficients for χ_1^i become

$$\phi_7 = \phi_8 = 1/(2pa^2) \ ,$$

$$\phi_9 = \phi_{10} = 0 \ .$$

The values for ϕ_7 and ϕ_8 contain the divisor $2pa^2$ since χ_0^i is evaluated for the plate characteristic segment area with a circumscribing radius of unity rather than the complete plate area with a circumscribing radius a.

CHAPTER 3

SHELL THEORY

3.1 Governing Equations

The differential equations governing the linear transverse vibrations of shallow spherical shells subjected to linear isothermal viscously damped deformation by a normal dynamic massless load $q(r,\theta,t)$, neglecting the effects of transverse shear and rotatory and longitudinal inertia, are

$$\nabla^4 F(r,\theta,t) - \frac{Eh}{R}\nabla^2 w(r,\theta,t) = 0, \tag{3.1a}$$

$$D\,\nabla^4 w(r,\theta,t) + \frac{1}{R}\nabla^2 F(r,\theta,t) + 2\zeta m\frac{\partial w(r,\theta,t)}{\partial t} + {} + m\frac{\partial^2 w(r,\theta,t)}{\partial t^2} = q(r,\theta,t). \tag{3.1b}$$

In Eqs. (3.1a) and (3.1b) w is the transverse displacement, F is the stress function, ζ is the coefficient of viscous damping, m is the mass per unit area, $D = Eh^3 / [12(1-\nu^2)]$ is the flexural rigidity, E is the modulus of elasticity, h is the shell thickness, ν is Poisson's ratio, R is the radius of curvature of the shell middle surface, r and θ are radial and angular polar coordinates, t is time and $\nabla^2 = \frac{\partial^2}{\partial r^2} + \frac{1}{r}\frac{\partial}{\partial r} + \frac{1}{r^2}\frac{\partial^2}{\partial \theta^2}$ when operating on functions of r and θ.

Introducing the dimensionless parameters

$\eta = \frac{w}{a}$, $\xi = \frac{F}{Eha^2}$ and $\rho = \frac{r}{a}$ where a is the radius of the circle circumscribing the shell's regular polygonal base, Eqs. (3.1a) and (3.1b) become

$$\nabla^4\xi(\rho,\theta,t) - \frac{a}{R}\nabla^2\eta(\rho,\theta,t) = 0, \tag{3.2a}$$

$$D\,\nabla^4\eta(\rho,\theta,t) + \frac{Eh}{R}a^3\nabla^2\xi(\rho,\theta,t) + 2a^4\zeta m\,\frac{\partial\eta(\rho,\theta,t)}{\partial t} + $$

$$+ ma^4\,\frac{\partial^2\eta(\rho,\theta,t)}{\partial t^2} = a^3q(\rho,\theta,t), \tag{3.2b}$$

where $\nabla^2 = \frac{\partial^2}{\partial\rho^2} + \frac{1}{\rho}\frac{\partial}{\partial\rho} + \frac{1}{\rho^2}\frac{\partial^2}{\partial\theta^2}$ when operating on functions of ρ and θ.

A solution of Eqs. (3.2a) and (3.2b) for non-homogeneous boundary conditions which depend on functions of time $\bar{e}^{\ell}(t)$ and $\bar{f}^{\ell}(t)$ is assumed in the form

$$\eta(\rho,\theta,t) = \eta_1(\rho,\theta,t) + \sum_{\ell=1}^{c}\bar{g}^{\ell}(\rho,\theta)\bar{e}^{\ell}(t), \tag{3.3a}$$

$$\xi(\rho,\theta,t) = \xi_1(\rho,\theta,t) + \sum_{\ell=1}^{c}\bar{h}^{\ell}(\rho,\theta)\bar{f}^{\ell}(t), \tag{3.3b}$$

where c=4 for a shell with interior and exterior boundaries and c=2 for a shell possessing only an exterior boundary. The functions $\bar{g}^{\ell}(\rho,\theta)$ and $\bar{h}^{\ell}(\rho,\theta)$ are chosen to make the boundary conditions expressed in terms of $\eta_1(\rho,\theta,t)$ and $\xi_1(\rho,\theta,t)$ homogeneous.

Substituting Eqs. (3.3a) and (3.3b) into Eqs. (3.2a) and (3.2b) yields

$$\nabla^4\xi_1(\rho,\theta,t) - \frac{a}{R}\nabla^2\eta_1(\rho,\theta,t) = -\sum_{\ell=1}^{c}\bar{f}^{\ell}(t)\nabla^2\bar{h}^{\ell}(\rho,\theta) + \frac{a}{R}\sum_{\ell=1}^{c}\bar{e}^{\ell}(t)\nabla^2\bar{g}^{\ell}(\rho,\theta), \tag{3.4a}$$

$$D\,\nabla^4\eta_1(\rho,\theta,t) + \frac{Eh}{R}a^3\nabla^2\xi_1(\rho,\theta,t) + 2a^4\zeta m\frac{\partial\eta_1(\rho,\theta,t)}{\partial t} + ma^4\frac{\partial^2\eta_1(\rho,\theta,t)}{\partial t^2} = a^3q(\rho,\theta,t) - D\sum_{\ell=1}^{c}\bar{e}^{\ell}(t)\nabla^4\bar{g}^{\ell}(\rho,\theta) - \frac{Eh}{R}a^3\sum_{\ell=1}^{c}\bar{f}^{\ell}(t)\nabla^2\bar{h}^{\ell}(\rho,\theta) - 2a^4\zeta m\sum_{\ell=1}^{c}\frac{d\bar{e}^{\ell}(t)}{dt}\bar{g}^{\ell}(\rho,\theta) - ma^4\sum_{\ell=1}^{c}\frac{d^2\bar{e}^{\ell}(t)}{dt^2}\bar{g}^{\ell}(\rho,\theta). \tag{3.4b}$$

3.2 Free Undamped Motion

3.2.1 General Solution. The homogeneous equations of the undamped system

$$\nabla^4\xi_1(\rho,\theta,t) - \frac{a}{R}\nabla^2\eta_1(\rho,\theta,t) = 0, \tag{3.5a}$$

$$D\,\nabla^4\eta_1(\rho,\theta,t) + \frac{Eh}{R}a^3\,\nabla^2\xi_1(\rho,\theta,t) + ma^4\,\frac{\partial^2\eta_1(\rho,\theta,t)}{\partial t^2} = 0, \tag{3.5b}$$

can be solved by the separation of variables technique

$$\eta_1(\rho,\theta,t) = \bar{\eta}(\rho,\theta)\,\exp(i\omega t), \tag{3.6a}$$

$$\xi_1(\rho,\theta,t) = \bar{\xi}(\rho,\theta)\,\exp(i\omega t), \tag{3.6b}$$

and by introducing the auxiliary functions used by Van Fo Fy [57]

$$\bar{\eta}(\rho,\theta) = \nabla^2[U(\rho,\theta) + \lambda V(\rho,\theta)]\ , \tag{3.7a}$$

$$\bar{\xi}(\rho,\theta) = V(\rho,\theta) + \frac{a}{R}U(\rho,\theta)\ , \tag{3.7b}$$

where $\lambda = Eh/maR\omega^2$ and ω is the undamped circular frequency. Substitution into Eqs. (3.5a) and (3.5b) gives

$$\left[1 - \frac{Eh}{mR^2\omega^2}\right]\nabla^4V(\rho,\theta) = 0, \tag{3.8a}$$

$$\nabla^2[(\nabla^4 - k^4)U(\rho,\theta) + \lambda\nabla^4 V(\rho,\theta)] = 0, \qquad (3.8b)$$

where $k^4 = \dfrac{a^4}{D}[m\omega^2 - \dfrac{Eh}{R^2}]$.

If k=0, then $\omega = \sqrt{Eh/mR^2}$, $\lambda = R/a$ and Eq. (3.8a) is identically satisfied for all $V(\rho,\theta)$ while Eq. (3.8b) reduces to

$$\nabla^8[U(\rho,\theta) + \frac{R}{a}V(\rho,\theta)] = 0, \ k=0. \qquad (3.9)$$

The solution of Eq. (3.9) for a shell having no interior boundary and a regular polygonal exterior boundary possessing p-ply rotational geometric periodicity is

$$U(\rho,\theta) + \frac{R}{a}V(\rho,\theta) =$$

$$= \sum_{n=0}^{\infty}\left[C^1_{pn}\,\rho^{pn+2} + D^1_{pn}\,\rho^{pn}\right]\begin{Bmatrix}\cos pn\theta \\ \\ \sin pn\theta\end{Bmatrix}, \ k=0, \qquad (3.10)$$

where C^1_{pn} and D^1_{pn} are integration constants. Substituting Eq. (3.9) into Eqs. (3.7a) and (3.7b) yields

$$\bar{\eta}(\rho,\theta) = 4\left(\frac{R}{a}\right)\sum_{n=0}^{\infty}(pn+1)\,C_{pn}\,\rho^{pn}\begin{Bmatrix}\cos pn\theta \\ \\ \sin pn\theta\end{Bmatrix}, \ k=0, \qquad (3.11a)$$

$$\bar{\xi}(\rho,\theta) = \sum_{n=0}^{\infty} \left[C_{pn}\, \rho^{pn+2} + D^2_{pn}\, \rho^{pn}\right]\begin{Bmatrix}\cos pn\theta\\ \sin pn\theta\end{Bmatrix},\ k=0, \tag{3.11b}$$

where $C_{pn} = \frac{a}{R} C^1_{pn}$ and $D^2_{pn} = \frac{a}{R} D^1_{pn}$.

If $k \neq 0$, then Eqs. (3.8a) and (3.8b) reduce to two uncoupled differential equations in U and V

$$\nabla^4 V(\rho,\theta) = 0, \tag{3.12a}$$

$$\nabla^2[\nabla^4 - k^4]U(\rho,\theta) = 0. \tag{3.12b}$$

The solution of Eqs. (3.12a) and (3.12b) for a shell having no interior boundary and a regular polygonal exterior boundary possessing p-ply rotational geometric periodicity is

$$V(\rho,\theta) = \sum_{n=0}^{\infty} \left[C_{pn}\, \rho^{pn+2} + E_{pn}\, \rho^{pn}\right]\begin{Bmatrix}\cos pn\theta\\ \sin pn\theta\end{Bmatrix}, \tag{3.13a}$$

$$U(\rho,\theta) = \sum_{n=0}^{\infty} \left[A_{pn}\, J_{pn}(k\rho) + B_{pn}\, I_{pn}(k\rho) + F_{pn}\, \rho^{pn}\right]\begin{Bmatrix}\cos pn\theta\\ \sin pn\theta\end{Bmatrix}, \tag{3.13b}$$

where A_{pn}, B_{pn}, C_{pn}, E_{pn} and F_{pn} are integration constants and J_{pn} and I_{pn} are Bessel functions of the first kind of order pn.

Substituting Eqs. (3.13a) and (3.13b) into

Eqs. (3.7a) and (3.7b) and restricting the solution to symmetric response[1] yields

$$\bar{\eta}(\rho,\theta) = \sum_{n=0}^{\infty} \Big[- k^2 A_{pn} J_{pn}(k\rho) + k^2 B_{pn} I_{pn}(k\rho) + $$

$$+ 4\lambda(pn+1) C_{pn} \rho^{pn}\Big] \cos pn\theta, \qquad (3.14a)$$

$$\bar{\xi}(\rho,\theta) = \sum_{n=0}^{\infty} \Big[\frac{a}{R} A_{pn} J_{pn}(k\rho) + \frac{a}{R} B_{pn} I_{pn}(k\rho) + $$

$$+ C_{pn} \rho^{pn+2} + D_{pn} \rho^{pn}\Big] \cos pn\theta. \qquad (3.14b)$$

These solutions for $\bar{\eta}(\rho,\theta)$ and $\bar{\xi}(\rho,\theta)$ are valid for all k since they reduce to the solutions given in Eqs. (3.11a) and (3.11b) for $k = 0$ where

$D_o^2 = \frac{a}{R} A_o + \frac{a}{R} B_o + D_o$ and $D_{pn}^2 = D_{pn}$ for $n \geq 1$.

---

[1] The assumption of symmetric response restricts the loading function to be of the form $q = q_o\, \bar{q}(\rho) \cos pm\theta\, Q(t)$, where q_o is a reference pressure and m is any integer.

3.2.2 *Boundary Conditions*. The theoretical solution, which is based on supplementing the force and moment equilibrium equations by the force and moment compatibility relations, yields the transverse displacement and stress function. In-plane displacements u_v and u_s must be determined by integration of the strain-displacement relations. This integration yields expressions for the in-plane displacements in terms of the stress function and integration functions which could not be determined.[1] Consequently, edge conditions which could be expressed in terms of the in-plane displacements if the alternate theoretical approach [54] had been used, are expressed in terms of other known functions.

Time-dependent edge conditions which can be satisfied approximately by the collocation technique are:

(a) Elastically Clamped Edge[2]

$$L_1[\eta(\tilde{\rho},\tilde{\theta},t)] = \eta(\tilde{\rho},\tilde{\theta},t) = \bar{\bar{e}}^1(t) \ , \qquad (3.15a)$$

---

[1] It was discovered at a late date that expressions for the in-plane displacements had been obtained for static loads by Reissner [97] and Fettahlioğlu [98].

[2] The edge conditions used for the stress function are equivalent to satisfying $u_s(\tilde{\rho},\tilde{\theta}) = 0$ but not $u_v(\tilde{\rho},\tilde{\theta}) = 0$ as will be explained in Section 6.1.

$$L_2^*[\eta(\tilde\rho,\tilde\theta,t)] = L_2[\eta(\tilde\rho,\tilde\theta,t)] - \beta_1 L_3[\eta(\tilde\rho,\tilde\theta,t)] =$$

$$= M_{vs}(\tilde\rho,\tilde\theta,t) - \beta_1 \frac{\partial\eta(\tilde\rho,\tilde\theta,t)}{\partial v} = \bar e^2(t) - \beta_1 \bar e^3(t) = \bar e^{2*}(t), \tag{3.15b}$$

$$L_4[\xi(\tilde\rho,\tilde\theta,t)] = F_{vs}(\tilde\rho,\tilde\theta,t) = \bar f^1(t), \tag{3.15c}$$

$$L_5[\xi(\tilde\rho,\tilde\theta,t)] = \varepsilon_{ss}(\tilde\rho,\tilde\theta,t) = \bar f^2(t). \tag{3.15d}$$

(b) Elastically Clamped Edge on Rollers

$$L_1[\eta(\tilde\rho,\theta,t)] = \bar e^1(t), \tag{3.15a}$$

$$L_2^*[\eta(\tilde\rho,\tilde\theta,t)] = \bar e^{2*}(t), \tag{3.15b}$$

$$L_6[\xi(\tilde\rho,\tilde\theta,t)] = F_{vv}(\tilde\rho,\tilde\theta,t) = \bar f^1(t), \tag{3.16a}$$

$$L_4^*[\xi(\tilde\rho,\tilde\theta,t)] = L_4[\xi(\tilde\rho,\tilde\theta,t)] + \beta_2 L_5[\xi(\tilde\rho,\tilde\theta,t)] =$$

$$= F_{vs}(\tilde\rho,\tilde\theta,t) + \beta_2 \varepsilon_{ss}(\tilde\rho,\tilde\theta,t) = \bar f^2(t) +$$

$$+ \beta_2 \bar f^3(t) = \bar f^{2*}(t). \tag{3.16b}$$

In Eqs. (3.15a) through (3.15d), (3.16a) and (3.16b) M_{vs} is the flexural stress couple vector tangential to the boundary, F_{vs} is the in-plane shear stress resultant, F_{vv} is the in-plane normal stress resultant, ε_{ss} is the in-plane normal strain tangential to the boundary and $\tilde\rho$ and $\tilde\theta$ are the coordinates of boundary points. The boundary and interior coordinate systems are shown in

Fig. 2.2. In Eq. (3.15b) β_1 ranges from zero for a shell unrestricted against edge rotation to infinity for a shell completely restricted against edge rotation. In Eq. (3.16b) β_2 ranges from zero for a shell unrestricted against edge extension to infinity for a shell completely restricted against edge extension. The operators L_1 to L_6 are linear homogeneous operators of order two or lower.

Expressing the functions in Eqs. (3.15b) through (3.15d), (3.16a) and (3.16b) in polar coordinates yields

$$\frac{\partial \eta}{\partial v} = \frac{\partial \eta}{\partial \rho} \cos\theta - \frac{1}{\rho}\frac{\partial \eta}{\partial \theta} \sin \theta, \tag{3.17a}$$

$$F_{vv} = F_{rr} \cos^2\theta + F_{\theta\theta} \sin^2\theta + F_{r\theta} \sin 2\theta, \tag{3.17b}$$

$$F_{vs} = \frac{1}{2}(F_{rr} - F_{\theta\theta}) \sin 2\theta + F_{r\theta} \cos 2\theta, \tag{3.17c}$$

$$\varepsilon_{ss} = \varepsilon_{rr} \sin^2\theta + \varepsilon_{\theta\theta} \cos^2\theta + \varepsilon_{r\theta} \sin 2\theta, \tag{3.17d}$$

$$M_{vs} = M_{r\theta} \cos^2\theta - M_{\theta r} \sin^2\theta + M_{rr} \sin 2\theta. \tag{3.17e}$$

Some of the stress resultant and stress couple components are shown in Fig. 2.3. The other vectorial components of the stress resultants and strains use the same kinematic subscript notation indicated in this figure.

For plane stress, strain can be expressed as

$$\varepsilon_{rr} = \frac{1}{Eh}[F_{rr} - \nu F_{\theta\theta}], \tag{3.18a}$$

$$\varepsilon_{\theta\theta} = \frac{1}{Eh}[F_{\theta\theta} - \nu F_{rr}], \tag{3.18b}$$

$$\varepsilon_{r\theta} = \frac{1+\nu}{Eh} F_{r\theta} . \tag{3.18c}$$

Stress resultants and stress couples can be expressed in terms of the dimensionless transverse displacement and stress functions as

$$F_{\theta\theta} = Eh \frac{\partial^2 \xi}{\partial \rho^2} , \tag{3.19a}$$

$$F_{rr} = Eh\left[\frac{1}{\rho} \frac{\partial \xi}{\partial \rho} + \frac{1}{\rho^2} \frac{\partial^2 \xi}{\partial \theta^2}\right], \tag{3.19b}$$

$$F_{r\theta} = F_{\theta r} = - Eh\left[\frac{\partial}{\partial \rho}\left(\frac{1}{\rho} \frac{\partial \xi}{\partial \theta}\right)\right], \tag{3.19c}$$

$$M_{r\theta} = - \frac{D}{a}\left[\frac{\partial^2 \eta}{\partial \rho^2} + \nu\left(\frac{1}{\rho^2} \frac{\partial^2 \eta}{\partial \theta^2} + \frac{1}{\rho} \frac{\partial \eta}{\partial \rho}\right)\right], \tag{3.19d}$$

$$M_{\theta r} = \frac{D}{a}\left[\frac{1}{\rho^2} \frac{\partial^2 \eta}{\partial \theta^2} + \frac{1}{\rho} \frac{\partial \eta}{\partial \rho} + \nu \frac{\partial^2 \eta}{\partial \rho^2}\right] , \tag{3.19e}$$

$$M_{rr} = - M_{\theta\theta} = \frac{D}{a} (1-\nu)\left[\frac{\partial}{\partial \rho} \left(\frac{1}{\rho} \frac{\partial \eta}{\partial \theta}\right)\right] . \tag{3.19f}$$

Substituting Eqs. (3.17a) through (3.17e), (3.18a) through (3.18c) and (3.19a) through (3.19f) into Eqs.

(3.15a) through (3.15d), (3.16a) and (3.16b) yields the expressions for the operators L_1 to L_6 when operating on functions of ρ and θ.

$$L_1 = 1, \tag{3.20a}$$

$$\begin{aligned} \frac{a}{D} L_2 = &- \cos^2\theta \left[\frac{\partial^2}{\partial\rho^2} + \nu \left(\frac{1}{\rho^2} \frac{\partial^2}{\partial\theta^2} + \frac{1}{\rho} \frac{\partial}{\partial\rho} \right) \right] - \\ &- \sin^2\theta \left[\frac{1}{\rho^2} \frac{\partial^2}{\partial\theta^2} + \frac{1}{\rho} \frac{\partial}{\partial\rho} + \nu \frac{\partial^2}{\partial\rho^2} \right] + \\ &+ \sin 2\theta \, (1-\nu) \left[\frac{\partial}{\partial\rho} \left(\frac{1}{\rho} \frac{\partial}{\partial\theta} \right) \right], \end{aligned} \tag{3.20b}$$

$$L_3 = \cos\theta \frac{\partial}{\partial\rho} - \frac{\sin\theta}{\rho} \frac{\partial}{\partial\theta}, \tag{3.20c}$$

$$\begin{aligned} \frac{1}{Eh} L_4 = &\frac{1}{2} \sin 2\theta \left[\frac{1}{\rho} \frac{\partial}{\partial\rho} + \frac{1}{\rho^2} \frac{\partial^2}{\partial\theta^2} - \frac{\partial^2}{\partial\rho^2} \right] - \\ &- \cos 2\theta \left[\frac{\partial}{\partial\rho} \left(\frac{1}{\rho} \frac{\partial}{\partial\theta} \right) \right], \end{aligned} \tag{3.20d}$$

$$\begin{aligned} L_5 = &\sin^2\theta \left[\frac{1}{\rho} \frac{\partial}{\partial\rho} + \frac{1}{\rho^2} \frac{\partial^2}{\partial\theta^2} - \nu \frac{\partial^2}{\partial\rho^2} \right] + \\ &+ \cos^2\theta \left[\frac{\partial^2}{\partial\rho^2} - \frac{\nu}{\rho} \frac{\partial}{\partial\rho} - \frac{\nu}{\rho^2} \frac{\partial^2}{\partial\theta^2} \right] - \\ &- (1+\nu) \sin 2\theta \left[\frac{\partial}{\partial\rho} \left(\frac{1}{\rho} \frac{\partial}{\partial\theta} \right) \right], \end{aligned} \tag{3.20e}$$

$$\frac{1}{Eh} L_6 = \sin^2\theta \frac{\partial^2}{\partial\rho^2} + \cos^2\theta\left[\frac{1}{\rho}\frac{\partial}{\partial\rho} + \frac{1}{\rho^2}\frac{\partial^2}{\partial\theta^2}\right] -$$

$$- \sin 2\theta \frac{\partial}{\partial\rho}\left(\frac{1}{\rho}\frac{\partial}{\partial\theta}\right). \qquad (3.20f)$$

Substituting Eqs. (3.3a) and (3.3b) into Eqs. (3.15a) through (3.15d) and setting

$$L_1[\bar{g}^1(\tilde{\rho},\tilde{\theta})] = 1, \quad L_2^*[\bar{g}^1(\tilde{\rho},\tilde{\theta})] = 0, \qquad (3.21a)$$

$$L_1[\bar{g}^2(\tilde{\rho},\tilde{\theta})] = 0, \quad L_2^*[\bar{g}^2(\tilde{\rho},\tilde{\theta})] = 1, \qquad (3.21b)$$

$$L_4[\bar{h}^1(\tilde{\rho},\tilde{\theta})] = 1, \quad L_5[\bar{h}^1(\tilde{\rho},\tilde{\theta})] = 0, \qquad (3.21c)$$

$$L_4[\bar{h}^2(\tilde{\rho},\tilde{\theta})] = 0, \quad L_5[\bar{h}^2(\tilde{\rho},\tilde{\theta})] = 1, \qquad (3.21d)$$

yields homogeneous "elastically clamped edge" conditions in η_1 and ξ_1

$$L_1[\eta_1(\tilde{\rho},\tilde{\theta})] = 0, \qquad (3.22a)$$

$$L_2^*[\eta_1(\tilde{\rho},\tilde{\theta})] = 0, \qquad (3.22b)$$

$$L_4[\xi_1(\tilde{\rho},\tilde{\theta})] = 0, \qquad (3.22c)$$

$$L_5[\xi_1(\tilde{\rho},\tilde{\theta})] = 0. \qquad (3.22d)$$

Similarly, substituting Eqs. (3.3a) and (3.3b) into Eqs. (3.15a), (3.15b), (3.16a) and (3.16b) and setting

$$L_1[\bar{g}^1(\tilde{\rho},\tilde{\theta})] = 1, \quad L_2^*[\bar{g}^1(\tilde{\rho},\tilde{\theta})] = 0, \qquad (3.21a)$$

$$L_1[\bar{g}^2(\tilde{\rho},\tilde{\theta})] = 0, \quad L_2^*[\bar{g}^2(\tilde{\rho},\tilde{\theta})] = 1, \tag{3.21b}$$

$$L_6[\bar{h}^1(\tilde{\rho},\tilde{\theta})] = 1, \quad L_4^*[\bar{h}^1(\tilde{\rho},\tilde{\theta})] = 0, \tag{3.23a}$$

$$L_6[\bar{h}^2(\tilde{\rho},\tilde{\theta})] = 0, \quad L_4^*[\bar{h}^2(\tilde{\rho},\tilde{\theta})] = 1, \tag{3.23b}$$

yields homogeneous "elastically clamped edge on rollers" conditions in η_1 and ξ_1

$$L_1[\eta_1(\tilde{\rho},\tilde{\theta})] = 0, \tag{3.22a}$$

$$L_2^*[\eta_1(\tilde{\rho},\tilde{\theta})] = 0, \tag{3.22b}$$

$$L_6[\xi_1(\tilde{\rho},\tilde{\theta})] = 0, \tag{3.24a}$$

$$L_4^*[\xi_1(\tilde{\rho},\tilde{\theta})] = 0. \tag{3.24b}$$

Substitution of Eqs. (3.14a) and (3.14b) into Eqs. (3.22a) through (3.22d), (3.24a) and (3.24b) produces the linear homogeneous equations

$$\sum_{n=0}^{\infty}[A_{pn}^{i}\,\psi_1 + B_{pn}^{i}\,\psi_2 + C_{pn}^{i}\,\psi_3] = 0, \tag{3.22a*}$$

$$\sum_{n=0}^{\infty}\Big\{A_{pn}^{i}\,[\psi_7 - (\beta_1^{i}a/D)\psi_4] + B_{pn}^{i}\,[\psi_8 - (\beta_1^{i}a/D)\psi_5] + $$
$$+ C_{pn}^{i}\,[\psi_9 - (\beta_1^{i}a/D)\psi_6]\Big\} = 0, \tag{3.22b*}$$

$$\sum_{n=0}^{\infty} [A^i_{pn} \psi_{10} + B^i_{pn} \psi_{11} + C^i_{pn} \psi_{12} + D^i_{pn} \psi_{13}] = 0, \qquad (3.22c^*)$$

$$\sum_{n=0}^{\infty} [A^i_{pn} \psi_{14} + B^i_{pn} \psi_{15} + C^i_{pn} \psi_{16} + D^i_{pn} \psi_{17}] = 0, \qquad (3.22d^*)$$

$$\sum_{n=0}^{\infty} [A^i_{pn} \psi_{18} + B^i_{pn} \psi_{19} + C^i_{pn} \psi_{20} + D^i_{pn} \psi_{21}] = 0, \qquad (3.24a^*)$$

$$\sum_{n=0}^{\infty} \{A^i_{pn} [\psi_{10} + (\beta^i_2/Eh) \psi_{14}] + B^i_{pn}[\psi_{11} + (\beta^i_2/Eh) \psi_{15}] +$$

$$+ C^i_{pn}[\psi_{12} + (\beta^i_2/Eh) \psi_{16}] + D^i_{pn}[\psi_{13} + (\beta^i_2/Eh)\psi_{17}]\} =$$

$$= 0. \qquad (3.24b^*)$$

The coefficients $\psi_1 \ldots \psi_{21}$ are:

$$\psi_1 = - k^2_i J_{pn} (\tilde{\mu}) \cos pn\tilde{\theta},$$

$$\psi_2 = k^2_i I_{pn} (\tilde{\mu}) \cos pn\tilde{\theta},$$

$$\psi_3 = 4\lambda_i (pn+1) \tilde{\rho}^{pn} \cos pn\tilde{\theta},$$

$$\psi_4 = - k^3_i J'_{pn}(\tilde{\mu}) \cos \tilde{\theta} \cos pn\tilde{\theta} - k^2_i \left(\frac{pn}{\tilde{\rho}}\right) J_{pn} (\tilde{\mu}) \sin \tilde{\theta} \sin pn\tilde{\theta},$$

$$\psi_5 = k^3_i I'_{pn} (\tilde{\mu}) \cos \tilde{\theta} \cos pn\tilde{\theta} + k^2_i \left(\frac{pn}{\tilde{\rho}}\right) I_{pn} (\tilde{\mu}) \sin \tilde{\theta} \sin pn\tilde{\theta},$$

$$\psi_6 = 4\lambda_i pn(pn+1)\tilde{\rho}^{pn-1}[\cos \tilde{\theta} \cos pn\tilde{\theta} + \sin \tilde{\theta} \sin pn\tilde{\theta}],$$

$$
\begin{aligned}
\psi_7 = {} & k_i^2 \left\{\left[k_i^2 J''_{pn}(\tilde{\mu}) - \nu\left(\frac{pn}{\tilde{\rho}}\right)^2 J_{pn}(\tilde{\mu}) + \right.\right. \\
& \left. + \nu\left(\frac{k_i}{\tilde{\rho}}\right) J'_{pn}(\tilde{\mu})\right] \cos^2\tilde{\theta} \cos pn\tilde{\theta} + \left[\nu k_i^2 J''_{pn}(\tilde{\mu}) - \right. \\
& \left. - \left(\frac{pn}{\tilde{\rho}}\right)^2 J_{pn}(\tilde{\mu}) + \left(\frac{k_i}{\tilde{\rho}}\right) J'_{pn}(\tilde{\mu})\right] \sin^2\tilde{\theta} \cos pn\tilde{\theta} - \\
& \left. - (1 - \nu)\left[\left(\frac{pn}{\tilde{\rho}^2}\right) J_{pn}(\tilde{\mu}) - k_i\left(\frac{pn}{\tilde{\rho}}\right) J'_{pn}(\tilde{\mu})\right] \sin 2\tilde{\theta} \sin pn\tilde{\theta}\right\},
\end{aligned}
$$

$$
\begin{aligned}
\psi_8 = {} & - k_i^2 \left\{\left[k_i^2 I''_{pn}(\tilde{\mu}) - \nu\left(\frac{pn}{\tilde{\rho}}\right)^2 I_{pn}(\tilde{\mu}) + \right.\right. \\
& \left. + \nu\left(\frac{k_i}{\tilde{\rho}}\right) I'_{pn}(\tilde{\mu})\right] \cos^2\tilde{\theta} \cos pn\tilde{\theta} + \left[\nu k_i^2 I''_{pn}(\tilde{\mu}) - \right. \\
& \left. - \left(\frac{pn}{\tilde{\rho}}\right)^2 I_{pn}(\tilde{\mu}) + \left(\frac{k_i}{\tilde{\rho}}\right) I'_{pn}(\tilde{\mu})\right] \sin^2\tilde{\theta} \cos pn\tilde{\theta} - \\
& \left. - (1 - \nu)\left[\left(\frac{pn}{\tilde{\rho}^2}\right) I_{pn}(\tilde{\mu}) - k_i\left(\frac{pn}{\tilde{\rho}}\right) I'_{pn}(\tilde{\mu})\right] \sin 2\tilde{\theta} \sin pn\tilde{\theta}\right\},
\end{aligned}
$$

$$
\begin{aligned}
\psi_9 = {} & 4\lambda_i (1 - \nu) pn[1 - (pn)^2]\tilde{\rho}^{pn-2}[\cos 2\tilde{\theta} \cos pn\tilde{\theta} + \\
& + \sin 2\tilde{\theta} \sin pn\tilde{\theta}],
\end{aligned}
$$

$$
\begin{aligned}
\psi_{10} = {} & \frac{1}{2}\left(\frac{a}{R}\right)\left\{\left[\left(\frac{k_i}{\tilde{\rho}}\right) J'_{pn}(\tilde{\mu}) - \left(\frac{pn}{\tilde{\rho}}\right)^2 J_{pn}(\tilde{\mu}) - k_i^2 J''_{pn}(\tilde{\mu})\right] \sin 2\tilde{\theta} \cos pn\tilde{\theta} + \right. \\
& \left. + 2\left[k_i \left(\frac{pn}{\tilde{\rho}}\right) J'_{pn}(\tilde{\mu}) - \left(\frac{pn}{\tilde{\rho}^2}\right) J_{pn}(\tilde{\mu})\right] \cos 2\tilde{\theta} \sin pn\tilde{\theta}\right\},
\end{aligned}
$$

$$\psi_{11} = \frac{1}{2}\left(\frac{a}{R}\right)\left\{\left[\left(\frac{k_i}{\tilde{\rho}}\right) I'_{pn}(\tilde{\mu}) - \left(\frac{pn}{\tilde{\rho}}\right)^2 I_{pn}(\tilde{\mu}) -\right.\right.$$

$$\left. - k_i^2 I''_{pn}(\tilde{\mu})\right] \sin 2\tilde{\theta} \cos pn\tilde{\theta} + 2\left[k_i\left(\frac{pn}{\tilde{\rho}}\right) I'_{pn}(\tilde{\mu}) -\right.$$

$$\left.\left. - \left(\frac{pn}{\tilde{\rho}^2}\right) I_{pn}(\tilde{\mu})\right] \cos 2\tilde{\theta} \sin pn\tilde{\theta}\right\},$$

$$\psi_{12} = \tilde{\rho}^{pn}\; pn(pn + 1)(\cos 2\tilde{\theta} \sin pn\tilde{\theta} - \sin 2\tilde{\theta} \cos pn\tilde{\theta}),$$

$$\psi_{13} = \tilde{\rho}^{pn-2}\; pn(pn - 1)(\cos 2\tilde{\theta} \sin pn\tilde{\theta} - \sin 2\tilde{\theta} \cos pn\tilde{\theta}),$$

$$\psi_{14} = \frac{a}{R}\left\{\left[\left(\frac{k_i}{\tilde{\rho}}\right) J'_{pn}(\tilde{\mu}) - \left(\frac{pn}{\tilde{\rho}}\right)^2 J_{pn}(\tilde{\mu}) - \nu\, k_i^2 J''_{pn}(\tilde{\mu})\right] \sin^2\tilde{\theta} \cos pn\tilde{\theta} +\right.$$

$$+ \left[k_i^2 J''_{pn}(\tilde{\mu}) - \nu\left(\frac{k_i}{\tilde{\rho}}\right) J'_{pn}(\tilde{\mu}) + \nu\left(\frac{pn}{\tilde{\rho}}\right)^2 J_{pn}(\tilde{\mu})\right] \cos^2\tilde{\theta} \cos pn\tilde{\theta} +$$

$$\left. + (1 + \nu)\left[k_i\left(\frac{pn}{\tilde{\rho}}\right) J'_{pn}(\tilde{\mu}) - \left(\frac{pn}{\tilde{\rho}^2}\right) J_{pn}(\tilde{\mu})\right] \sin 2\tilde{\theta} \sin pn\tilde{\theta}\right\},$$

$$\psi_{15} = \frac{a}{R}\left\{\left[\left(\frac{k_i}{\tilde{\rho}}\right) I'_{pn}(\tilde{\mu}) - \left(\frac{pn}{\tilde{\rho}}\right)^2 I_{pn}(\tilde{\mu}) - \nu\, k_i^2 I''_{pn}(\tilde{\mu})\right] \sin^2\tilde{\theta} \cos pn\tilde{\theta} +\right.$$

$$+ \left[k_i^2 I''_{pn}(\tilde{\mu}) - \nu\left(\frac{k_i}{\tilde{\rho}}\right) I'_{pn}(\tilde{\mu}) + \nu\left(\frac{pn}{\tilde{\rho}}\right)^2 I_{pn}(\tilde{\mu})\right] \cos^2\tilde{\theta} \cos pn\tilde{\theta} +$$

$$\left. + (1 + \nu)\left[k_i\left(\frac{pn}{\tilde{\rho}}\right) I'_{pn}(\tilde{\mu}) - \left(\frac{pn}{\tilde{\rho}^2}\right) I_{pn}(\tilde{\mu})\right] \sin 2\tilde{\theta} \sin pn\tilde{\theta}\right\},$$

$$\psi_{16} = (pn + 1)\tilde{\rho}^{pn} \{[(pn + 2) + \nu(pn - 2)] \cos^2\tilde{\theta} \cos pn\tilde{\theta} -$$

$$- [(pn - 2) + \nu(pn + 2)]\sin^2\tilde{\theta} \cos pn\tilde{\theta} + pn(1 + \nu) \sin 2\tilde{\theta} \times$$

$$\times \sin pn\tilde{\theta}\},$$

$$\psi_{17} = (1 + \nu)pn(pn - 1)\tilde{\rho}^{pn-2} [\cos 2\tilde{\theta} \cos pn\tilde{\theta} + \sin 2\tilde{\theta} \sin pn\tilde{\theta}],$$

$$\psi_{18} = \frac{a}{R} \left\{\left[\left(\frac{k_i}{\tilde{\rho}}\right) J'_{pn}(\tilde{\mu}) - \left(\frac{pn}{\tilde{\rho}}\right)^2 J_{pn}(\tilde{\mu})\right] \cos^2\tilde{\theta} \cos pn\tilde{\theta} +\right.$$

$$+ k_i^2 J''_{pn}(\tilde{\mu}) \sin^2\tilde{\theta} \cos pn\tilde{\theta} +$$

$$\left. + \left[\left(\frac{pn}{\tilde{\rho}^2}\right) J_{pn}(\tilde{\mu}) - k_i\left(\frac{pn}{\tilde{\rho}}\right) J'_{pn}(\tilde{\mu})\right] \sin 2\tilde{\theta} \sin pn\tilde{\theta}\right\},$$

$$\psi_{19} = \frac{a}{R} \left\{\left[\left(\frac{k_i}{\tilde{\rho}}\right) I'_{pn}(\tilde{\mu}) - \left(\frac{pn}{\tilde{\rho}}\right)^2 I_{pn}(\tilde{\mu})\right] \cos^2\tilde{\theta} \cos pn\tilde{\theta} +\right.$$

$$+ k_i^2 I''_{pn}(\tilde{\mu}) \sin^2\tilde{\theta} \cos pn\tilde{\theta} +$$

$$\left. + \left[\left(\frac{pn}{\tilde{\rho}^2}\right) I_{pn}(\tilde{\mu}) - k_i\left(\frac{pn}{\tilde{\rho}}\right) I'_{pn}(\tilde{\mu})\right] \sin 2\tilde{\theta} \sin pn\tilde{\theta}\right\},$$

$$\psi_{20} = \tilde{\rho}^{pn} \{[pn + 2 - (pn)^2] \cos^2\tilde{\theta} \cos pn\tilde{\theta} +$$

$$+ (pn + 1)(pn + 2) \sin^2\tilde{\theta} \cos pn\tilde{\theta} - pn(pn + 1) \sin 2\tilde{\theta} \sin pn\tilde{\theta}\},$$

$$\psi_{21} = pn(1 - pn)\tilde{\rho}^{pn-2} [\cos 2\tilde{\theta} \cos pn\tilde{\theta} + \sin 2\tilde{\theta} \sin pn\tilde{\theta}],$$

where $\tilde{\mu} = k_i \tilde{\rho}$.

3.2.3 Auxiliary Edge Conditions. The choice of functions $\bar{g}^{\ell}(\rho,\theta)$ and $\bar{h}^{\ell}(\rho,\theta)$ which satisfy the auxiliary edge conditions formulated in Eqs. (3.21a) through (3.21d), (3.23a) and (3.23b) is not unique, as Meirovitch [25] points out. It is convenient to choose

$$\bar{g}^{\ell}(\rho,\theta) = \sum_{n=0}^{\infty}\left[E_{pn}^{1,\ell}\rho^{pn} + E_{pn}^{2,\ell}\rho^{pn+2}\right]\cos pn\theta, \quad \ell = 1,2, \qquad (2.19,\ 3.25a)$$

$$\bar{h}^{\ell}(\rho,\theta) = \sum_{n=0}^{\infty}\left[F_{pn}^{1,\ell}\rho^{pn+2} + F_{pn}^{2,\ell}\rho^{pn+4}\right]\cos pn\theta, \quad \ell = 1,2, \qquad (3.25b)$$

where the constants $E_{pn}^{j,\ell}$ and $F_{pn}^{j,\ell}$ are solved approximately by applying the boundary collocation technique to satisfy the auxiliary edge conditions.

Applying the operators $L_1 \ldots L_6$ given in Eqs. (3.20a) through (3.20f) to the functions $\bar{g}^{\ell}(\rho,\theta)$ and $\bar{h}^{\ell}(\rho,\theta)$ yields

$$L_1[\bar{g}^{\ell}(\tilde{\rho},\tilde{\theta})] = \sum_{n=0}^{\infty}\left[E_{pn}^{1,\ell}\psi_1^* + E_{pn}^{2,\ell}\psi_2^*\right], \qquad (3.26a)$$

$$\frac{a}{D} L_2[\bar{g}^{\ell}(\tilde{\rho},\tilde{\theta})] = \sum_{n=0}^{\infty}\left[E_{pn}^{1,\ell}\psi_3^* + E_{pn}^{2,\ell}\psi_4^*\right], \qquad (3.26b)$$

$$L_3[\bar{g}^{\ell}(\tilde{\rho},\tilde{\theta})] = \sum_{n=0}^{\infty}\left[E_{pn}^{1,\ell}\psi_5^* + E_{pn}^{2,\ell}\psi_6^*\right], \qquad (3.26c)$$

$$\frac{1}{Eh} L_4[\bar{h}^{\ell}(\tilde{\rho},\tilde{\theta})] = \sum_{n=0}^{\infty}\left[F_{pn}^{1,\ell}\psi_7^* + F_{pn}^{2,\ell}\psi_8^*\right], \qquad (3.26d)$$

$$L_5[\bar{h}^{\ell}(\tilde{\rho},\tilde{\theta})] = \sum_{n=0}^{\infty} [F_{pn}^{1,\ell} \psi_9^* + F_{pn}^{2,\ell} \psi_{10}^*], \qquad (3.26e)$$

$$\frac{1}{Eh} L_6[\bar{h}^{\ell}(\tilde{\rho},\tilde{\theta})] = \sum_{n=0}^{\infty} [F_{pn}^{1,\ell} \psi_{11}^* + F_{pn}^{2,\ell} \psi_{12}^*]. \qquad (3.26f)$$

The coefficients $\psi_1^* \ldots \psi_{12}^*$ are:

$$\psi_1^* = \tilde{\rho}^{pn} \cos pn\tilde{\theta},$$

$$\psi_2^* = \tilde{\rho}^{pn+2} \cos pn\tilde{\theta},$$

$$\psi_3^* = - pn(pn - 1)(1 - \nu)\tilde{\rho}^{pn-2} [\cos 2\tilde{\theta} \cos pn\tilde{\theta} + \sin 2\tilde{\theta} \sin pn\tilde{\theta}],$$

$$\psi_4^* = (pn + 1) \tilde{\rho}^{pn} \Big\{-[(pn + 2) - \nu(pn - 2)]\cos^2\tilde{\theta} \cos pn\tilde{\theta} +$$

$$+ [(pn - 2) - \nu(pn + 2)]\sin^2\tilde{\theta} \cos pn\tilde{\theta} -$$

$$- pn(1 - \nu) \sin 2\tilde{\theta} \sin pn\tilde{\theta}\Big\},$$

$$\psi_5^* = pn\, \tilde{\rho}^{pn-1} [\cos \tilde{\theta} \cos pn\tilde{\theta} + \sin \tilde{\theta} \sin pn\tilde{\theta}],$$

$$\psi_6^* = \tilde{\rho}^{pn+1} [(pn + 2) \cos \tilde{\theta} \cos pn\tilde{\theta} + pn \sin \tilde{\theta} \sin pn\tilde{\theta}],$$

$$\psi_7^* = \tilde{\rho}^{pn}\, pn(pn + 1)[\cos 2\tilde{\theta} \sin pn\tilde{\theta} - \sin 2\tilde{\theta} \cos pn\tilde{\theta}],$$

$$\psi_8^* = \tilde{\rho}^{pn+2} \Big\{ pn(pn + 3) \cos 2\tilde{\theta} \sin pn\tilde{\theta} -$$

$$- [(pn)^2 + 3pn + 4] \sin 2\tilde{\theta} \cos pn\tilde{\theta}\Big\},$$

$$\begin{aligned}\psi^*_9 = \tilde{\rho}^{pn}(pn + 1)\Big\{&[(pn + 2) + \nu(pn - 2)] \cos^2\tilde{\theta} \cos pn\tilde{\theta} - \\ &- [(pn - 2) + \nu(pn + 2)] \sin^2\tilde{\theta} \cos pn\tilde{\theta} + \\ &+ (1 + \nu)pn \sin 2\tilde{\theta} \sin pn\tilde{\theta}\Big\},\end{aligned}$$

$$\begin{aligned}\psi^*_{10} = \tilde{\rho}^{pn+2}\Big\{&[(pn + 4)(pn + 3) + \nu(pn)^2 - \\ &- \nu(pn + 4)] \cos^2\tilde{\theta} \cos pn\tilde{\theta} + [(pn + 4) - (pn)^2 - \\ &- \nu(pn + 4)(pn + 3)]\sin^2\tilde{\theta} \cos pn\tilde{\theta} + \\ &+ (1 + \nu)\, pn\, (pn + 3) \sin 2\tilde{\theta} \sin pn\tilde{\theta}\Big\},\end{aligned}$$

$$\psi^*_{11} = \tilde{\rho}^{pn}(pn + 1)\Big\{[2 - pn \cos 2\tilde{\theta}] \cos pn\tilde{\theta} + pn \sin 2\tilde{\theta} \sin pn\tilde{\theta}\Big\},$$

$$\begin{aligned}\psi^*_{12} = \tilde{\rho}^{pn+2}\Big\{&(pn + 4)(pn + 3) \sin^2\tilde{\theta} \cos pn\tilde{\theta} + \\ &+ [(pn + 4) - (pn)^2] \cos^2\tilde{\theta} \cos pn\tilde{\theta} + \\ &+ pn(pn + 3)\sin 2\tilde{\theta} \sin pn\tilde{\theta}\Big\}.\end{aligned}$$

Substitution of Eqs. (3.26a) through (3.26f) into Eqs. (3.21a) through (3.21d), (3.23a) and (3.23b) yields linear nonhomogeneous equations, the solution of which yields the functions $\bar{g}^1(\rho,\theta)$, $\bar{g}^2(\rho,\theta)$, $\bar{h}^1(\rho,\theta)$ and $\bar{h}^2(\rho,\theta)$ which are required for the time-dependent edge conditions given in Eqs. (3.15a) through (3.15d), (3.16a) and (3.16b).

3.3 Forced Motion

3.3.1 General Solution.

Series solutions for Eqs. (3.4a) and (3.2b) are assumed in the form

$$\eta_1(\rho,\theta,t) = \sum_{i=1}^{\infty} \bar{\eta}^i(\rho,\theta)\, T^i(t), \tag{3.27a}$$

$$\xi_1(\rho,\theta,t) = \sum_{i=1}^{\infty} \bar{\xi}^i(\rho,\theta)\, T^i(t), \tag{3.27b}$$

where

$$\bar{\eta}^i(\rho,\theta) = \sum_{n=0}^{\infty} \Big[-k_i^2 A^i_{pn} J_{pn}(k_i\rho) + k_i^2 B^i_{pn} I_{pn}(k_i\rho) + + 4\lambda_i (pn+1)\, C^i_{pn}\, \rho^{pn} \Big] \cos pn\theta, \tag{3.28a}$$

$$\bar{\xi}^i(\rho,\theta) = \sum_{n=0}^{\infty} \Big[\frac{a}{R} A^i_{pn} J_{pn}(k_i\rho) + \frac{a}{R} B^i_{pn} I_{pn}(k_i\rho) + + C^i_{pn}\, \rho^{pn+2} + D^i_{pn}\, \rho^{pn} \Big] \cos pn\theta. \tag{3.28b}$$

Substituting Eqs. (3.27a) and (3.28b) into Eq. (3.4b) and simplifying using Eqs. (3.5b), (3.6a) and (3.6c) yields

$$\sum_{i=1}^{\infty} m \left[\omega_i^2\, T^i(t) + 2\zeta_i \frac{dT^i(t)}{dt} + \frac{d^2T^i(t)}{dt^2} \right] \bar{\eta}^i(\rho,\theta) =$$

$$= (1/a) q_o\, \bar{q}(\rho) \cos pm\theta\, Q(t) - (D/a^4) \sum_{\ell=1}^{2} \bar{e}^{\ell}(t)\ \times$$

$$\times\ \nabla^4 \bar{g}^{\ell}(\rho,\theta) - (Eh/aR) \sum_{\ell=1}^{2} \bar{f}^{\ell}(t)\, \nabla^2 \bar{h}^{\ell}(\rho,\theta) -$$

$$- 2\zeta_i\, m \sum_{\ell=1}^{2} \frac{d\bar{e}^{\ell}(t)}{dt}\, \bar{g}^{\ell}(\rho,\theta) - m \sum_{\ell=1}^{2} \frac{d^2\bar{e}^{\ell}(t)}{dt^2}\, \bar{g}^{\ell}(\rho,\theta). \tag{3.29}$$

The term $\nabla^4 \bar{g}^\ell(\rho,\theta)$ vanishes in Eq. (3.29) since $\bar{g}^\ell(\rho,\theta)$, Eq. (3.25a), has been chosen as a solution of the biharmonic equation. Multiplying both sides of Eq. (3.29) by $\bar{\eta}^j(\rho,\theta)$, integrating over the characteristic shell segment area and applying the condition of orthogonality of the eigenvectors shown in Appendix B.2, yields

$$\begin{aligned}\frac{d^2T^i(t)}{dt^2} + 2\zeta_i \frac{dT^i(t)}{dt} + \omega_i^2 T^i(t) = (1/\chi_o^i)\Bigg[&(q_o/ma)\ Q(t)\ x \\ &x\ \chi_1^i - (Eh/maR) \sum_{\ell=1}^{2} \bar{f}^\ell(t)\ \chi_2^{\ell,i} - \\ &- 2\zeta_i \sum_{\ell=1}^{2} \frac{d\bar{e}^\ell(t)}{dt} \chi_3^{\ell,i} - \sum_{\ell=1}^{2} \frac{d^2\bar{e}^\ell(t)}{dt^2} \chi_3^{\ell,i}\Bigg].\end{aligned} \qquad (3.30)$$

Using the restriction applicable to shallow shells, that $\sqrt{1-\rho^2(\frac{a}{R})^2} \simeq 1$ for $0 \le \rho \le a$, permits the integration to be carried out over the projected area of the shell. Thus modal participation functions can be written

$$\chi_o^i = \int_0^{\theta o} \int_0^{\frac{\cos\theta o}{\cos\theta}} \rho[\bar{\eta}^i(\rho,\theta)]^2 d\rho d\theta, \qquad (3.31a)$$

$$\chi_1^{i} = \int_0^{\theta o} \int_0^{\frac{\cos\theta o}{\cos\theta}} \rho\, \bar{\eta}^{i}(\rho,\theta)\, \bar{q}(\rho) \cos pm\theta \, d\rho \, d\theta, \qquad (3.31b)$$

$$\chi_2^{\ell,i} = \int_0^{\theta o} \int_0^{\frac{\cos\theta o}{\cos\theta}} \rho \nabla^2 \bar{h}^{\ell}(\rho,\theta)\, \bar{\eta}^{i}(\rho,\theta) \, d\rho \, d\theta, \qquad (3.31c)$$

$$\chi_3^{\ell,i} = \int_0^{\theta o} \int_0^{\frac{\cos\theta o}{\cos\theta}} \rho\, \bar{g}^{\ell}(\rho,\theta)\, \bar{\eta}^{i}(\rho,\theta) \, d\rho \, d\theta, \qquad (3.31d)$$

where $\theta o = \pi/p$.

3.3.2 *Initial Conditions*. The solution of Eq. (3.30) for $\zeta_i < \omega_i$ is

$$T^{i}(t) = \exp(-\zeta_i t)\left\{ \frac{1}{\omega_i^{d}} \left[\frac{dT^{i}(0)}{dt} + \zeta_i T^{i}(0) \right] \sin \omega_i^{d} t + T^{i}(0) \cos \omega_i^{d} t \right\} + \left[1/(\omega_i^2 \chi_0^{i}) \right] \left[(q_o/ma) \times \chi_1^{i} G_1^{i}(t) - (Eh/maR) \sum_{\ell=1}^{2} \chi_2^{\ell,i} G_2^{\ell,i}(t) - 2\zeta_i \sum_{\ell=1}^{2} \chi_3^{\ell,i} G_3^{\ell,i}(t) - \sum_{\ell=1}^{2} \chi_3^{\ell,i} G_4^{\ell,i}(t) \right], \qquad (3.32)$$

where

$$G_1^{i}(t) = (\omega_i^2/\omega_i^{d}) \int_0^{t} Q(\tau) \exp[-\zeta_i (t - \tau)] \times \sin \omega_i^{d}(t - \tau)\, d\tau, \qquad (2.21a,\ 3.33a)$$

$$G_2^{\ell,i}(t) = (\omega_i^2/\omega_i^d) \int_0^t \bar{f}^{\ell}(\tau) \exp[-\zeta_i(t-\tau)] \times$$

$$\times \sin \omega_i^d (t-\tau)\, d\tau, \qquad (3.33b)$$

$$G_3^{\ell,i}(t) = (\omega_i^2/\omega_i^d) \int_0^t \frac{d\bar{e}^{\ell}(\tau)}{d\tau} \exp[-\zeta_i(t-\tau)] \times$$

$$\times \sin \omega_i^d (t-\tau)\, d\tau, \qquad (2.21b, 3.33c)$$

$$G_4^{\ell,i}(t) = (\omega_i^2/\omega_i^d) \int_0^t \frac{d^2\bar{e}^{\ell}(\tau)}{d\tau^2} \exp[-\zeta_i(t-\tau)] \times$$

$$\times \sin \omega_i^d (t-\tau)\, d\tau, \qquad (2.21c, 3.33d)$$

and

$\omega_i^d = \sqrt{\omega_i^2 - \zeta_i^2}$ is the damped circular frequency of the i-th mode.

3.3.3 Modal Participation Functions. The modal participation functions are obtained by substituting the expressions for $\bar{\eta}^i$, Eq. (3.28a), and for $\bar{g}^{\ell}$ and $\bar{h}^{\ell}$, Eqs. (3.25a) and (3.25b) respectively, into Eqs. (3.31a) to (3.31d).

In evaluating χ_0^i, $\chi_2^{\ell,i}$ and $\chi_3^{\ell,i}$, terms involving

products of functions of different orders n are neglected in the integration. This property is true only for shells with circular boundaries. The errors introduced for shells with polygonal boundaries should increase, just as for plates, with the deviation of the nodal lines from circles concentric about the apex. This deviation of the nodal lines from the circular shape generally increases with decreasing number of boundary sides and increasing mode number. The resulting modal participation functions are

$$\overset{i}{X}_0 = \left[\overset{i}{A}_0\right]^2 \phi_1 + \left[\overset{i}{B}_0\right]^2 \phi_2 + \left[\overset{i}{C}_0\right]^2 \phi_3 + 2\overset{i}{A}_0 \overset{i}{B}_0 \phi_4 + + 2 \overset{i}{A}_0 \overset{i}{C}_0 \phi_5 + 2 \overset{i}{B}_0 \overset{i}{C}_0 \phi_6 + \sum_{n=1}^{\infty} \Big\{ \left[\overset{i}{A}_{pn}\right]^2 \phi_7 + + \left[\overset{i}{B}_{pn}\right]^2 \phi_8 + \left[\overset{i}{C}_{pn}\right]^2 \phi_9 + 2 \overset{i}{A}_{pn} \overset{i}{B}_{pn} \phi_{10} + + 2 \overset{i}{A}_{pn} \overset{i}{C}_{pn} \phi_{11} + 2 \overset{i}{B}_{pn} \overset{i}{C}_{pn} \phi_{12}\Big\}, \qquad (3.34a)$$

$$\overset{i}{X}_1 = \overset{i}{A}_0 \phi_{13} + \overset{i}{B}_0 \phi_{14} + \overset{i}{C}_0 \phi_{15} + + \sum_{n=1}^{\infty} \left[\overset{i}{A}_{pn} \phi_{16} + \overset{i}{B}_{pn} \phi_{17} + \overset{i}{C}_{pn} \phi_{18}\right], \qquad (3.34b)$$

$$X_2^{\ell,i} = 4\,F_0^{1,\ell}\left[A_0^i\,\phi_{13} + B_0^i\,\phi_{14} + C_0^i\,\phi_{15}\right] +$$

$$+ 16\,F_0^{2,\ell}\left[A_0^i\,\phi_{19} + B_0^i\,\phi_{20} + C_0^i\,\phi_{21}\right] +$$

$$+ \sum_{n=1}^{\infty}\left\{ 4(pn + 1)\,F_{pn}^{1,\ell}\left[A_{pn}^i\,\phi_{22} + B_{pn}^i\,\phi_{23} +\right.\right.$$

$$\left. + C_{pn}^i\,\phi_{24}\right] + 8(pn + 2)\,F_{pn}^{2,\ell}\left[A_{pn}^i\,\phi_{25} +\right.$$

$$\left.\left. + B_{pn}^i\,\phi_{26} + C_{pn}^i\,\phi_{27}\right]\right\}, \qquad (3.34c)$$

$$X_3^{\ell,i} = E_0^{1,\ell}\left[A_0^i\,\phi_{13} + B_0^i\,\phi_{14} + C_0^i\,\phi_{15}\right] + E_0^{2,\ell}\ \times$$

$$\times\left[A_0^i\,\phi_{19} + B_0^i\,\phi_{20} + C_0^i\,\phi_{21}\right] +$$

$$+ \sum_{n=1}^{\infty}\left\{ E_{pn}^{1,\ell}\left[A_{pn}^i\,\phi_{22} + B_{pn}^i\,\phi_{23} + C_{pn}^i\,\phi_{24}\right] +\right.$$

$$\left. + E_{pn}^{2,\ell}\left[A_{pn}^i\,\phi_{25} + B_{pn}^i\,\phi_{26} + C_{pn}^i\,\phi_{27}\right]\right\}. \qquad (3.34d)$$

The coefficients $\phi_{13} \ldots \phi_{18}$ are dependent on the load distribution function $\bar{q}(\rho,\theta)$. For a load distributed uniformly over the shell plan surface area, $\bar{q}(\rho)\cos pm\theta = 1$, and the coefficients $\phi_1 \ldots \phi_{27}$ are:

$$\phi_1 = k_i^4 \frac{\cos^2\theta_o}{2} \int_0^{\theta_o} \left[J_1^2(\mu_o) + J_0^2(\mu_o) \right] \frac{d\theta}{\cos^2\theta} ,$$

$$\phi_2 = k_i^4 \frac{\cos^2\theta_o}{2} \int_0^{\theta_o} \left[- I_1^2(\mu_o) + I_0^2(\mu_o) \right] \frac{d\theta}{\cos^2\theta} ,$$

$$\phi_3 = 4\lambda_i^2 \sin 2\theta_o ,$$

$$\phi_4 = - k_i^3 \frac{\cos\theta_o}{2} \int_0^{\theta_o} \left[J_0(\mu_o)\, I_1(\mu_o) + I_0(\mu_o)\, J_1(\mu_o) \right] \frac{d\theta}{\cos\theta} ,$$

$$\phi_5 = - 4k_i\lambda_i \cos\theta_o \int_0^{\theta_o} J_1(\mu_o) \frac{d\theta}{\cos\theta} ,$$

$$\phi_6 = 4k_i\lambda_i \cos\theta_o \int_0^{\theta_o} I_1(\mu_o) \frac{d\theta}{\cos\theta} ,$$

$$\phi_7 = k_i^4 \frac{\cos^2\theta_o}{2} \int_0^{\theta_o} \left\{ J'^{\,2}_{pn}(\mu_o) + \left[1 - \left(\frac{pn}{\mu_o} \right)^2 \right] J^2_{pn}(\mu_o) \right\} \times$$

$$\times \frac{\cos^2 pn\theta}{\cos^2\theta}\, d\theta ,$$

$$\phi_8 = k_i^4 \frac{\cos^2\theta_o}{2} \int_0^{\theta_o} \left\{ - I'^{\,2}_{pn}(\mu_o) + \left[1 + \left(\frac{pn}{\mu_o} \right)^2 \right] I^2_{pn}(\mu_o) \right\} \times$$

$$\times \frac{\cos^2 pn\theta}{\cos^2\theta}\, d\theta ,$$

$$\phi_9 = 8\lambda_i^2 (pn + 1) (\cos\theta_o)^{2pn+2} \int_0^{\theta_o} \frac{\cos^2 pn\theta}{(\cos\theta)^{2pn+2}}\, d\theta ,$$

$$\phi_{10} = - k_i^3 \frac{\cos\theta_o}{2} \int_0^{\theta_o} \left[J_{pn}(\mu_o)\, I'_{pn}(\mu_o) - I_{pn}(\mu_o)\, J'_{pn}(\mu_o) \right] \times$$

$$\times \frac{\cos^2 pn\theta}{\cos\theta}\, d\theta,$$

$$\phi_{11} = - 4k_i \lambda_i (pn + 1) (\cos\theta_o)^{pn+1} \int_0^{\theta_o} J_{pn+1}(\mu_o) \frac{\cos^2 pn\theta}{(\cos\theta)^{pn+1}}\, d\theta,$$

$$\phi_{12} = 4k_i \lambda_i (pn + 1) (\cos\theta_o)^{pn+1} \int_0^{\theta_o} I_{pn+1}(\mu_o) \frac{\cos^2 pn\theta}{(\cos\theta)^{pn+1}}\, d\theta,$$

$$\phi_{13} = - k_i \cos\theta_o \int_0^{\theta_o} J_1(\mu_o) \frac{d\theta}{\cos\theta},$$

$$\phi_{14} = k_i \cos\theta_o \int_0^{\theta_o} I_1(\mu_o) \frac{d\theta}{\cos\theta},$$

$$\phi_{15} = \lambda_i \sin 2\theta_o,$$

$$\phi_{16} = - 2k_i \cos\theta_o \sum_{\alpha=0}^{\infty} \int_0^{\theta_o} J_{pn+2\alpha+1}(\mu_o) \frac{\cos pn\theta}{\cos\theta}\, d\theta +$$

$$+ 4 \sum_{\alpha=0}^{\infty} (\alpha + 1) \int_0^{\theta_o} J_{pn+2\alpha+2}(\mu_o) \cos pn\theta\, d\theta,$$

$$\phi_{17} = 2k_i \cos\theta_o \sum_{\alpha=0}^{\infty} (-1)^{\alpha} \int_0^{\theta_o} I_{pn+2\alpha+1}(\mu_o) \frac{\cos pn\theta}{\cos\theta}\, d\theta -$$

$$- 4 \sum_{\alpha=0}^{\infty} (-1)^{\alpha} (\alpha + 1) \int_0^{\theta_o} I_{pn+2\alpha+2}(\mu_o) \cos pn\theta\, d\theta,$$

$$\phi_{18} = 4\lambda_i \left(\frac{pn + 1}{pn + 2}\right) (\cos\theta_o)^{pn+2} \int_0^{\theta_o} \frac{\cos pn\theta}{(\cos\theta)^{pn+2}}\, d\theta,$$

$$\phi_{19} = - k_i \cos^3\theta_o \int_0^{\theta_o} J_1(\mu_o) \frac{d\theta}{\cos^3\theta} + 2 \cos^2\theta_o \int_0^{\theta_o} J_2(\mu_o) \frac{d\theta}{\cos^2\theta},$$

$$\phi_{20} = k_i \cos^3\theta_o \int_0^{\theta_o} I_1(\mu_o) \frac{d\theta}{\cos^3\theta} - 2 \cos^2\theta_o \int_0^{\theta_o} I_2(\mu_o) \frac{d\theta}{\cos^2\theta},$$

$$\phi_{21} = \frac{\lambda_i}{6} \sin 2\theta_o (1 + 2 \cos^2\theta_o),$$

$$\phi_{22} = - k_i (\cos\theta_o)^{pn+1} \int_0^{\theta_o} J_{pn+1}(\mu_o) \frac{\cos^2 pn\theta}{(\cos\theta)^{pn+1}}\, d\theta,$$

$$\phi_{23} = k_i (\cos\theta_o)^{pn+1} \int_0^{\theta_o} I_{pn+1}(\mu_o) \frac{\cos^2 pn\theta}{(\cos\theta)^{pn+1}}\, d\theta,$$

$$\phi_{24} = 2\lambda_i (\cos\theta_o)^{2pn+2} \int_0^{\theta_o} \frac{\cos^2 pn\theta}{(\cos\theta)^{2pn+2}}\, d\theta,$$

$$\phi_{25} = - k_i (\cos\theta_o)^{pn+3} \int_0^{\theta_o} J_{pn+1}(\mu_o) \frac{\cos^2 pn\theta}{(\cos\theta)^{pn+3}} d\theta +$$

$$+ 2(\cos\theta_o)^{pn+2} \int_0^{\theta_o} J_{pn+2}(\mu_o) \frac{\cos^2 pn\theta}{(\cos\theta)^{pn+2}} d\theta,$$

$$\phi_{26} = k_i (\cos\theta_o)^{pn+3} \int_0^{\theta_o} I_{pn+1}(\mu_o) \frac{\cos^2 pn\theta}{(\cos\theta)^{pn+3}} d\theta -$$

$$- 2(\cos\theta_o)^{pn+2} \int_0^{\theta_o} I_{pn+2}(\mu_o) \frac{\cos^2 pn\theta}{(\cos\theta)^{pn+2}} d\theta,$$

$$\phi_{27} = 2\lambda_i \left(\frac{pn + 1}{pn + 2}\right) (\cos\theta_o)^{2pn+4} \int_0^{\theta_o} \frac{\cos^2 pn\theta}{(\cos\theta)^{2pn+4}} d\theta.$$

For a concentrated load $P = P_oQ(t)$ at the shell apex, P_o replaces q_o in Eq. (3.32) and the coefficients for χ_1^i become

$$\phi_{13} = - \phi_{14} = - k_i^2/(2pa^2),$$

$$\phi_{15} = 4\lambda_i/(2pa^2),$$

$$\phi_{16} = \phi_{17} = \phi_{18} = 0.$$

CHAPTER 4

PLATE NUMERICAL RESULTS

4.1 Eigenvalues, Eigenvectors and Modal Participation Functions

In the practical execution of the boundary collocation technique, it is necessary to assume convergence of the series solution for the transverse displacement eigenvectors, Eq. (2.13). Using this assumption, symmetric eigenvalues for various clamped and simply supported polygonal plates were obtained by employing machine computation using 16 figure accuracy to search for the roots of a series of linear homogeneous equations of the form of Eqs. (2.10a*) and (2.10c*) where the summation with respect to n is truncated.

Collocation points were regularly spaced on the boundary of each plate. A typical set of nine boundary collocation points for a square plate is shown in Fig. 4.1. Edge condition Eqs. (2.10a*) and (2.10c*) were satisfied at points 1, 3, 4, 5, 6, 7, and 8. Eq. (2.10c*) was satisfied at point 2 and Eq. (2.10a*) was satisfied at point 9. Edge condition Eq. (2.10c*) was

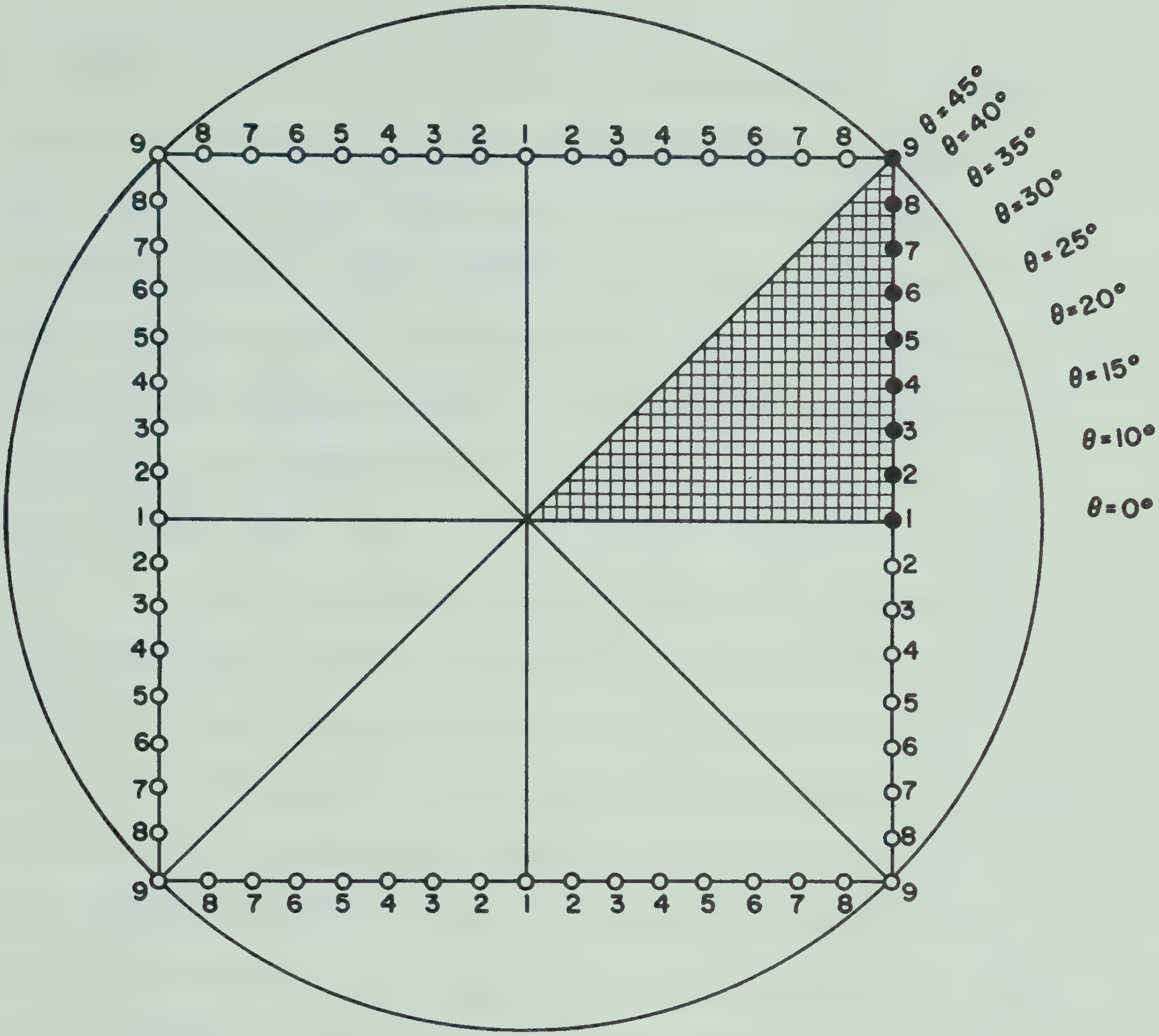

● POINT ON CHARACTERISTIC PLATE SEGMENT AT WHICH BOUNDARY CONDITIONS ARE SATISFIED IN NUMERICAL SOLUTION.

○ POINT AT WHICH BOUNDARY CONDITIONS ARE AUTOMATICALLY SATISFIED DUE TO PLATE'S ROTATIONAL PERIODICITY.

FIG. 4.1 Boundary Collocation for a Square Plate

not satisfied at point 9 since in practice it is often difficult to predict its value at the plate corners. Edge conditions were satisfied in a similar manner for the other plates. Consequently, an equal number of simultaneous boundary equations and unknown integration constants was obtained with L collocation points on the boundary of the characteristic plate segment for n ranging from 0 to (L-2).

The convergence of the symmetric eigenvalues k_i to the values given in Tables 4.1 and 4.2 was checked for each polygonal plate by increasing the number of collocation points used in the truncated series solution until the minimum number required to obtain these values was determined. It was found that fundamental eigenvalues for simply supported plates with from 7 to 12 sides as well as some of the higher modal eigenvalues, especially for 9 and 12 sides, were less convergent than the eigenvalues obtained for other plates, sometimes having significant variations in the third figure. Errors in these eigenvalues might have been caused by the Poisson's ratio effect which is explained in Section 4.2. Fundamental eigenvalues previously obtained by Conway [35], Leissa [36] and Conway and Farnham [37] for some of the plates using the boundary collocation technique agree to two or three figure accuracy with the

Table 4.1

Symmetric Eigenvalues and Modal Participation Functions for Clamped Polygonal Plates

	Number of Sides p								
	3	4	5	6	7	8	9	12	∞[1]
k_1	5.745	4.2418 4.2414[2] 4.243[3]	3.784	3.576	3.463	3.394	3.349	3.279	3.1962
x_1^1/x_0^1	0.276	1.581	1.618	1.617	1.616	1.615	1.615	1.615	
$a^2(x_1^1)_p/x_0^1$	0.851	2.784	2.295	2.058	1.933	1.858	1.809	1.735	
k_2	9.920	8.130	7.395	7.027	6.818	6.69	6.60	6.47	6.3064
x_1^2/x_0^2	-0.64E-2[4]	-1.026	-1.295	-1.305	-1.30	-1.30	-1.30	-1.29	
$a^2(x_1^2)_p/x_0^2$	0.27E-1	3.63	4.10	3.84	3.64	3.51	3.43	3.27	
k_3	12.61	10.49	10.50	10.39	10.16	9.99	9.87	9.68	9.4395
x_1^3/x_0^3	-0.1 E-4	0.0595	0.591	1.05	1.10	1.10	1.10	1.09	
$a^2(x_1^3)_p/x_0^3$	0.54E-2	0.61	2.99	5.18	5.33	5.26	5.13	4.95	
k_4	14.10	12.43	11.59	11.86	12.62	13.2	13.1	12.9	12.577
x_1^4/x_0^4	-0.6 E-6	0.124	0.378	0.0288	-0.107	-0.78	-0.96	-0.96	
$a^2(x_1^4)_p/x_0^4$	0.6 E-7	0.66	2.59	0.89	0.95	5.43	6.66	6.59	
k_5	16.7	14.03	14.04	13.90	13.65	13.8	14.7	16.1	15.716
x_1^5/x_0^5	-0.2 E-7	-0.0487	-0.600	-0.888	-0.853	-0.19	0.6E-3	0.86	
$a^2(x_1^5)_p/x_0^5$	0.2 E-3	0.79	4.02	6.31	6.26	1.69	0.40	8.16	
	10	8	7	7	7	6	6	4	
	Number of boundary collocation points L								

[1] These eigenvalues are given by Flynn [16] and Weiner [19].

[2] This eigenvalue is given by Leissa [36].

[3] This eigenvalue is given by Conway and Farnham [37].

[4] $(\ )\,E\pm(\ ) \equiv (\ )10^{\pm(\ )}$

Table 4.2

Symmetric Eigenvalues and Modal Participation Functions for Simply Supported Polygonal Plates

	Number of Sides p								
	3	4	5	6	7	8	9	12	∞[1]
k_1	4.189 4.19[2]	3.1416 3.14[2]	2.821	2.676 2.67[2]	2.60[3]	2.50[4]	2.45[5]	2.42	2.1080
x_1^1/x_0^1	1.39	1.590	1.605	1.61	1.60	1.61	1.61	1.61	
$a^2(x_1^1)_p/x_0^1$	2.91	1.961	1.615	1.46	1.38	1.32	1.27	1.24	
k_2	8.378	7.025	6.43	6.12	5.95	5.82	5.74	5.65	5.4188
x_1^2/x_0^2	-0.795	-1.056	-1.08	-1.08	-1.07	-1.06	-1.05	-1.05	
$a^2(x_1^2)_p/x_0^2$	3.33	3.91	3.60	3.34	3.18	3.08	2.99	2.91	
k_3	11.08	9.425	9.56	9.49	9.30	9.14	9.01	8.87	8.5920
x_1^3/x_0^3	-0.3E-4	0.1768	0.514	0.83	0.86	0.86	0.85	0.84	
$a^2(x_1^3)_p/x_0^3$	6.19	1.96	2.99	4.80	4.88	4.78	4.67	4.55	
k_4	12.57	11.33	10.7	11.0	11.8	12.3	12.3	12.1	11.747
x_1^4/x_0^4	-0.1E-5	0.6016	0.354	0.017	-0.09	-0.61	-0.72	-0.72	
$a^2(x_1^4)_p/x_0^4$	0.2E-10	3.71	2.87	0.80	0.92	5.19	6.21	6.22	
k_5	15.10	12.95	13.1	13.0	12.8	13.0	13.9	15.3	14.896
x_1^5/x_0^5	0.2E-4	-0.2433	-0.50	-0.70	-0.65	-0.12	-0.1E-2	0.63	
$a^2(x_1^5)_p/x_0^5$	7.17	4.50	4.11	6.07	5.83	1.40	0.50	7.80	
	10	8	7	6	6	6	6	4	
	Number of boundary collocation points L								

[1] These eigenvalues are given by Weiner [19] for $\nu = 0$.

[2] These eigenvalues are given by Conway [35].

[3] This eigenvalue should be 2.59 according to results given in Section 4.4.

[4] This eigenvalue should be 2.53 according to results given in Section 4.4.

[5] This eigenvalue should be 2.49 according to results given in Section 4.4.

present values. As the number of plate sides increases, these eigenvalues converge to the values given by Flynn [16] and Weiner [19] for circular plates. The eigenvalues given in Table 4.3b for a clamped square plate all lie within the previous best limits given by Bazley, Fox and Stadter [102], and the eigenvalues given in Tables 4.4a and 4.4b for simply supported triangular and square plates are accurate according to the exact solutions [103,21].

The values of the modal participation functions χ_1^i/χ_0^i for uniformly distributed loads and $(\chi_1^i)_p/\chi_0^i$ for central point loads, given in Tables 4.1 and 4.2, were obtained using the eigenvalues in the same tables and their associated eigenvectors where $A_0^i = 1$. Integral values for the coefficients $\phi_1 \ldots \phi_{10}$ were determined using the generalized Simpson's formula with 56 equal increments of θ for the equilateral triangle, 46 increments for the square and 36 for the other polygons. The summation with respect to α was truncated when the values of ϕ_9 and ϕ_{10} converged to five digit accuracy.

The eigenvectors $\bar{\eta}^i$ associated with the eigenvalues for clamped plates in Table 4.1 are given in Tables 4.3a to 4.3h and the eigenvectors associated with the eigenvalues for simply supported plates in Table 4.2 are given in Tables 4.4a to 4.4h. The elements A_{pn}^i and B_{pn}^i of the eigenvectors converged to the accuracy shown in these tables for the number of collocation points indicated. Some of the higher order elements which are given to only one significant figure may be accurate only to an order of magnitude.

Table 4.3a

Eigenvalues, Modal Participation Functions and Eigenvectors for a Clamped Plate With 3 Sides

10 Collocation Points at 0°, 5°, 10°, 20°, 30°, 40°, 50°, 55°, 60°

		Mode i				
		1	2	3	4	5
k_i		5.74514	9.92048	12.6123	14.104	16.7
X_1^i/X_0^i	n=0, ...8	0.2756	-0.00637	-0.109E-04	-0.6E-06	-0.2E-07
	n=0	1.217	-0.369	-0.0910	-0.627E-03	0.0178
	Order n					
A_{pn}^i	0	0.100000E 01	0.100000E 01	0.100000E 01	0.100000E 01	0.100000E 01
	1	-0.107208E 01	0.120809E 01	-0.616653E 00	-0.14 E 03	0.84 E 00
	2	-0.191699E 01	-0.197501E 01	0.832254E 00	-0.32 E 01	-0.27 E 00
	3	-0.3441 E 01	-0.125825E 01	-0.10945 E 01	0.14 E 03	0.71 E 00
	4	0.171 E 03	0.175 E 01	-0.134 E 01	0.55 E 01	-0.18 E 01
	5	-0.7 E 04	0.13 E 02	-0.4 E 00	-0.1 E 03	-0.1 E 01
	6	0.4 E 06	-0.4 E 03	0.3 E 01	-0.1 E 03	0.3 E 01
	7	0.2 E 09	0.19 E 05	-0.7 E 02	0.4 E 03	-0.3 E 02
	8	-0.2 E 11	-0.4 E 06	0.2 E 05	-0.6 E 06	0.4 E 04
B_{pn}^i	0	0.626205E-01	-0.460099E-02	-0.131683E-02	-0.46 E-01	0.13 E-03
	1	0.281451E 00	0.690642E-03	-0.485718E-02	-0.13 E 00	0.26 E-03
	2	0.202315E 01	0.116084E 00	-0.161995E-01	-0.55 E 00	-0.9 E-04
	3	0.22420 E 02	0.133132E 01	-0.4698 E-01	-0.50 E 01	-0.25 E-02
	4	0.183 E 03	0.14160 E 02	0.165 E 00	-0.52 E 02	-0.2 E-02
	5	0.3 E 04	0.1472 E 03	0.66 E 01	-0.55 E 03	0.3 E 00
	6	0.4 E 04	0.157 E 04	0.11 E 03	-0.573 E 04	0.61 E 01
	7	-0.2 E 09	0.14 E 05	0.2 E 04	-0.6 E 05	0.1 E 03
	8	-0.8 E 10	-0.8 E 05	0.2 E 05	-0.5 E 06	0.9 E 03

Table 4.3b

Eigenvalues, Modal Participation Functions and Eigenvectors for a Clamped Plate With 4 Sides

8 Collocation Points at 0°, 5°, 10°, 20°, 30°, 35°, 40°, 45°

		Mode i				
		1	2	3	4	5
k_i		4.24177	8.13038	10.4890	12.432	14.03
X_1^i/X_0^i	n=0, ...6	1.58140	-1.0256	0.0595	0.1244	-0.0487
	n=0	1.667	-1.444	-0.0692	0.7878	0.4576
	Order n					
A_{pn}^i	0	0.100000E 01	0.100000E 01	0.100000E 01	0.100000E 01	0.100000E 01
	1	-0.170804E 01	0.57297 E 00	-0.20308 E 01	0.13977 E 01	-0.1118 E 01
	2	-0.1283 E 02	-0.1522 E 01	0.19797 E 01	0.64 E-02	-0.7869 E 00
	3	0.390 E 04	-0.468 E 01	-0.1494 E 01	-0.1335 E 01	0.193 E 01
	4	-0.4 E 07	0.3 E 03	-0.1 E 02	-0.3 E 01	-0.9 E 00
	5	0.1 E 11	-0.1 E 06	0.2 E 04	0.5 E 02	-0.2 E 02
	6	0.5 E 14	-0.4 E 07	-0.4 E 05	0.7 E 03	-0.9 E 02
B_{pn}^i	0	0.581239E-01	-0.31469 E-02	-0.2224 E-03	0.17938 E-03	0.156 E-04
	1	0.59685 E 00	-0.71190 E-02	-0.32379 E-02	0.5047 E-03	0.939 E-04
	2	0.1662 E 02	0.897 E-01	-0.4401 E-01	0.21304 E-02	0.134 E-03
	3	-0.176 E 04	0.422 E 01	-0.638 E 00	0.416 E-01	-0.106 E-01
	4	0.2 E 07	0.7 E 02	-0.8 E 01	0.13 E 01	-0.341 E 00
	5	-0.1 E 11	0.3 E 05	-0.4 E 03	0.4 E 02	-0.8 E 01
	6	-0.5 E 14	0.1 E 08	-0.4 E 05	0.8 E 03	-0.1 E 03

Table 4.3c

Eigenvalues, Modal Participation Functions and Eigenvectors for a Clamped Plate With 5 Sides

7 Collocation Points at 0°, 5°, 10°, 20°, 26°, 31°, 36°

		Mode i				
		1	2	3	4	5
k_i		3.78397	7.39506	10.5049	11.5889	14.042
X_1^i/X_2^i	n=0, ... 5	1.61783	-1.2945	0.5907	0.3780	-0.6005
	n=0	1.6288	-1.369	1.103	1.202	-1.083
	Order n					
A_{pn}^i	0	0.100000E 01	0.100000E 01	0.100000E 01	0.100000E 01	0.100000E 01
	1	-0.39435 E 01	0.42284 E 00	-0.1422 E 01	0.15750 E 01	-0.13175 E 01
	2	0.195 E 03	-0.44603 E 01	0.2052 E 01	-0.72990 E 00	-0.54046 E 00
	3	0.60 E 06	0.17 E 03	-0.13 E 02	-0.13 E 01	0.290 E 01
	4	-0.8 E 11	-0.8 E 05	0.1 E 04	-0.6 E 02	-0.24 E 02
	5	0.4 E 16	-0.8 E 09	0.5 E 06	-0.6 E 04	-0.7 E 03
B_{pn}^i	0	0.568067E-01	-0.276570E-02	0.12218 E-03	0.10561 E-03	-0.7175 E-05
	1	0.16549 E 01	-0.12898 E-01	-0.646 E-03	0.6166 E-03	0.5610 E-05
	2	0.397 E 02	0.3980 E 00	-0.406 E-01	0.9299 E-02	0.1907 E-03
	3	-0.62 E 06	0.4 E 02	-0.13 E 01	0.35 E 00	-0.141 E-01
	4	0.6 E 11	0.3 E 04	-0.9 E 02	0.2 E 02	-0.117 E 01
	5	-0.3 E 16	0.5 E 09	-0.2 E 06	0.4 E 04	0.4 E 02

Table 4.3d

Eigenvalues, Modal Participation Functions and Eigenvectors for a Clamped Plate With 6 Sides

7 Collocation Points at 0°, 5°, 10°, 15°, 20°, 25°, 30°

		Mode i				
		1	2	3	4	5
k_i		3.57640	7.0267	10.3921	11.857	13.900
X_1^i/X_2^i	n=0, ... 5	1.61710	-1.3048	1.0505	0.02880	-0.88766
	n=0	1.6198	-1.323	1.156	0.440	-1.097
	Order n					
A_{pn}^i	0	0.100000E 01	0.100000E 01	0.100000E 01	0.100000E 01	0.100000E 01
	1	-0.11747 E 02	0.4811 E 00	-0.472 E 00	0.3909 E 01	-0.634 E 00
	2	0.285 E 05	-0.338 E 02	0.2208 E 01	-0.397 E 01	-0.206 E 00
	3	-0.3 E 10	0.5 E 05	-0.19 E 03	0.6 E 02	0.61 E 01
	4	0.3 E 16	-0.8 E 09	0.3 E 06	-0.4 E 05	-0.8 E 03
	5	0.4 E 23	-0.1 E 15	0.2 E 10	-0.1 E 09	-0.4 E 06
B_{pn}^i	0	0.562846E-01	-0.26439 E-02	0.12418 E-03	0.393 E-04	-0.5952 E-05
	1	0.56035 E 01	-0.25649 E-01	0.205 E-03	0.764 E-03	-0.1488 E-04
	2	-0.1459 E 05	0.486 E 01	-0.542 E-01	0.449 E-01	0.82 E-04
	3	0.2 E 10	-0.9 E 04	0.3 E 01	0.31 E 01	-0.5 E-01
	4	-0.2 E 16	0.3 E 09	-0.2 E 05	0.2 E 04	0.1 E 01
	5	-0.4 E 23	0.6 E 14	-0.6 E 09	0.2 E 08	0.6 E 05

Table 4.3e

Eigenvalues, Modal Participation Functions and Eigenvectors for a Clamped Plate With 7 Sides

7 Collocation Points at 0°, 5°, 10°, 15°, 19°, 22.5°, 25.7°

		Mode i				
		1	2	3	4	5
k_i		3.4632	6.8181	10.16	12.621	13.646
X_1^i/X_2^i	n=0, ...5	1.6160	-1.3007	1.099	-0.107	-0.853
	n=0	1.6169	-1.3067	1.125	-0.684	-1.028
	Order n					
A_{pn}^i	0	0.100000E 01	0.100000E 01	0.100000E 01	0.100000E 01	0.100000E 01
	1	-0.427 E 02	0.733 E 00	-0.271 E 00	0.390 E 01	-0.67 E 00
	2	0.27 E 07	-0.46 E 03	0.69 E 01	-0.67 E 01	0.3 E-01
	3	-0.1 E 14	0.13 E 08	-0.8 E 04	0.7 E 03	0.4 E 02
	4	0.2 E 22	-0.1 E 14	0.4 E 09	-0.6 E 07	-0.2 E 06
	5	0.6 E 30	-0.4 E 20	0.6 E 14	-0.1 E 12	-0.2 E 10
B_{pn}^i	0	0.56041 E-01	-0.2593 E-02	0.1179 E-03	-0.8 E-07	-0.527 E-05
	1	0.2237 E 02	-0.579 E-01	0.6217 E-03	0.332 E-03	-0.322 E-04
	2	-0.176 E 07	0.95 E 02	-0.26 E 00	0.61 E-01	-0.911 E-03
	3	0.8 E 13	-0.41 E 07	0.62 E 03	-0.1 E 00	-0.97 E 00
	4	-0.1 E 22	0.6 E 13	-0.7 E 08	0.4 E 06	0.6 E 04
	5	-0.6 E 30	0.2 E 20	-0.2 E 14	0.3 E 11	0.2 E 09

Table 4.3f

Eigenvalues, Modal Participation Functions and Eigenvectors for a Clamped Plate With 8 Sides

6 Collocation Points at 0°, 5°, 10°, 15°, 19°, 22.5°

		Mode i				
		1	2	3	4	5
k_i		3.3944	6.689	9.99	13.17	13.82
X_1^i/X_2^i	n=0, ... 4	1.6154	-1.297	1.10	-0.78	-0.19
	n=0	1.6158	-1.300	1.11	-0.98	-0.90
	Order n					
A_{pn}^i	0	0.100000E 01	0.100000E 01	0.100000E 01	0.100000E 01	0.100000E 01
	1	-0.1816 E 03	0.1377 E 01	-0.240 E 00	0.82 E 00	-0.297 E 01
	2	0.29 E 09	-0.91 E 04	0.41 E 02	-0.42 E 01	0.51 E 01
	3	-0.71 E 17	0.8 E 10	-0.1 E 07	0.5 E 04	-0.2 E 04
	4	-0.3 E 27	0.1 E 18	-0.4 E 12	0.2 E 09	-0.4 E 08
B_{pn}^i	0	0.5592 E-01	-0.2568 E-02	0.1150 E-03	-0.5146 E-05	-0.410 E-05
	1	0.1025 E 03	-0.1465 E 00	0.132 E-02	0.23 E-04	-0.109 E-03
	2	-0.20 E 09	0.24 E 04	-0.23 E 01	0.36 E-01	-0.320 E-01
	3	0.6 E 17	-0.3 E 10	0.1 E 06	-0.1 E 03	0.2 E 02
	4	0.2 E 27	-0.6 E 17	0.1 E 12	-0.2 E 08	0.3 E 07

Table 4.3g

Eigenvalues, Modal Participation Functions and Eigenvectors for a Clamped Plate With 9 Sides

6 Collocation Points at 0°, 5°, 9°, 13°, 17°, 20°

		Mode i				
		1	2	3	4	5
k_i		3.349	6.603	9.872	13.12	14.71
X_1^i/X_2^i	n=0, ... 4	1.615	-1.295	1.098	-0.956	0.0006
	n=0	1.615	-1.297	1.102	-0.979	-0.04
	Order n					
A_{pn}^i	0	0.100000E 01	0.100000E 01	0.100000E 01	0.100000E 01	0.100000E 01
	1	-0.891 E 03	0.309 E 01	-0.285 E 00	0.257 E 00	-0.726 E 01
	2	0.36 E 11	-0.25 E 06	0.39 E 03	-0.95 E 01	0.249 E 02
	3	-0.4 E 21	0.5 E 13	-0.1 E 09	0.2 E 06	-0.6 E 05
	4	-0.7 E 32	0.2 E 22	-0.1 E 16	0.8 E 11	-0.1 E 11
B_{pn}^i	0	0.5585 E-01	-0.2555 E-02	0.1135 E-03	-0.504 E-05	-0.108 E-05
	1	0.53 E 03	-0.414 E 00	0.285 E-02	-0.266 E-04	-0.126 E-03
	2	-0.27 E 11	0.77 E 05	-0.31 E 02	0.118 E 00	-0.124 E 00
	3	0.3 E 21	-0.2 E 13	0.3 E 08	-0.8 E 04	0.1 E 04
	4	0.6 E 32	-0.1 E 22	0.4 E 15	-0.1 E 11	0.7 E 09

Table 4.3h

Eigenvalues, Modal Participation Functions and Eigenvectors for a Clamped Plate With 12 Sides

4 Collocation Points at 0°, 5°, 10°, 15°

		Mode i				
		1	2	3	4	5
k_i		3.279	6.468	9.679	12.89	16.10
X_1^i/X_2^i	n=0, ... 2	1.6145	-1.292	1.092	-0.96	0.86
	n=0	1.6145	-1.293	1.092	-0.96	0.87
	Order n					
A_{pn}^i	0	0.100000E 01	0.100000E 01	0.100000E 01	0.100000E 01	0.100000E 01
	1	-0.21 E 06	0.77 E 02	-0.140 E 01	0.194 E 00	-0.173 E 00
	2	0.3 E 18	-0.2 E 11	0.2 E 07	-0.5 E 04	0.7 E 02
B_{pn}^i	0	0.5574 E-01	-0.2536 E-02	0.1115 E-03	-0.487 E-05	0.212 E-06
	1	0.14 E 06	-0.164 E 02	0.432 E-01	-0.346 E-03	0.33 E-05
	2	-0.24 E 18	0.1 E 11	-0.3 E 06	0.2 E 03	-0.4 E 00

Table 4.4a

Eigenvalues, Modal Participation Functions and Eigenvectors for a Simply Supported Plate With 3 Sides

10 Collocation Points at 0°, 5°, 10°, 20°, 30°, 40°, 45°, 50°, 55°, 60°

		Mode i				
		1	2	3	4	5
k_i		4.18879	8.37758	11.08250	12.56637	15.10290
X_1^i/X_2^i	n=0, ...8	1.3900	-0.79467	-0.000031	-0.0000011	0.00002
	n=0	1.2134	-0.50687	-0.2522	-0.39	0.2993
	Order n					
A_{pn}^i	0	0.100000E 01	0.100000E 01	0.100000E 01	0.100000E 01	0.100000E 01
	1	-0.115470E 01	0.115470E 01	-0.623483E 00	-0.1059 E 07	0.862226E 00
	2	-0.19997 E 01	-0.199999E 01	0.833820E 00	0.7274 E 00	-0.230316E 00
	3	0.110 E 01	-0.115475E 01	-0.114334E 01	0.1059 E 07	0.663646E 00
	4	0.9 E 01	0.20007 E 01	-0.13048 E 01	-0.97 E 01	-0.194695E 01
	5	-0.2 E 05	0.1 E 01	-0.330 E 00	-0.106 E 07	-0.10151 E 01
	6	-0.24 E 08	0.2 E 02	-0.20 E 01	-0.4 E 04	0.679 E 00
	7	-0.5 E 11	0.5 E 04	-0.5 E 01	0.9 E 06	-0.43 E 00
	8	-0.8 E 14	0.6 E 06	-0.4 E 03	-0.1 E 08	0.19 E 01
B_{pn}^i	0	0.1 E-05	0.5 E-08	-0.34 E-09	-0.55 E-04	0.8 E-11
	1	-0.13 E-04	-0.2 E-07	0.13 E-08	0.19 E-03	-0.2 E-10
	2	0.47 E-03	0.2 E-06	-0.7 E-08	-0.8 E-03	0.8 E-10
	3	-0.47 E-01	-0.4 E-05	0.7 E-07	0.7 E-02	-0.4 E-09
	4	0.2 E 02	0.2 E-03	-0.2 E-05	-0.1 E 00	0.6 E-08
	5	0.3 E 03	-0.5 E-01	0.2 E-03	0.8 E 01	-0.3 E-06
	6	0.3 E 08	-0.9 E 01	0.18 E-01	0.5 E 03	-0.1 E-04
	7	0.8 E 11	-0.1 E 04	0.1 E 01	0.3 E 05	-0.4 E-03
	8	0.2 E 15	0.4 E 06	-0.2 E 03	-0.3 E 07	0.2 E-01

Table 4.4b

Eigenvalues, Modal Participation Functions and Eigenvectors for a Simply Supported Plate With 4 Sides

8 Collocation Points at 0°, 5°, 10°, 20°, 30°, 35°, 40°, 45°

		Mode i				
		1	2	3	4	5
k_i		3.14159	7.02482	9.42478	11.32717	12.95312
X_1^i/X_2^i	n=0, ... 6	1.58955	-1.0564	0.17677	0.60157	-0.24331
	n=0	1.5254	-0.87236	0.2728	0.4905	0.0316
	Order n					
A_{pn}^i	0	0.100000E 01	0.100000E 01	0.100000E 01	0.100000E 01	0.100000E 01
	1	-0.200003E 01	0.559996E 00	-0.200001E 01	0.140828E 01	-0.111418E 01
	2	0.2009 E 01	-0.168636E 01	0.199999E 01	-0.167371E-01	-0.758587E 00
	3	-0.2 E 02	-0.1507 E 01	-0.199982E 01	-0.143184E 01	0.195940E 01
	4	0.2 E 06	0.16 E 01	0.199 E 01	-0.200006E 01	-0.142468E 01
	5	-0.9 E 10	-0.1 E 04	0.2 E 01	-0.134 E 01	-0.364 E 00
	6	0.5 E 14	0.3 E 06	-0.4 E 03	-0.2 E 01	0.16 E 01
B_{pn}^i	0	-0.2 E-06	-0.8 E-08	0.1 E-08	0.6 E-10	0.3 E-10
	1	0.9 E-05	0.7 E-07	-0.6 E-08	-0.3 E-09	-0.1 E-09
	2	-0.6 E-02	-0.3 E-05	0.1 E-06	0.3 E-08	0.9 E-09
	3	0.2 E 02	0.4 E-03	-0.6 E-05	-0.1 E-06	-0.2 E-07
	4	-0.1 E 06	-0.2 E 00	0.9 E-03	0.8 E-05	0.9 E-06
	5	0.7 E 10	0.4 E 03	-0.8 E 00	-0.4 E-02	-0.3 E-03
	6	-0.4 E 14	-0.7 E 05	0.2 E 02	0.3 E-02	-0.1 E-02

Table 4.4c

Eigenvalues, Modal Participation Functions and Eigenvectors for a Simply Supported Plate With 5 Sides

7 Collocation Points at 0°, 6°, 12°, 18°, 24°, 30°, 36°

		Mode i				
		1	2	3	4	5
k_i		2.8212	6.4282	9.5642	10.65	13.0870
X_1^i/X_2^i	n=0, ...5	1.6049	-1.0777	0.514	0.3535	-0.5043
	n=0	1.5776	-0.9900	0.7033	0.5678	-0.509
	Order n					
A_{pn}^i	0	0.100000E 01	0.100000E 01	0.100000E 01	0.100000E 01	0.100000E 01
	1	-0.517 E 01	0.4233 E 00	-0.13472 E 01	0.164008E 01	-0.12864 E 01
	2	0.17 E 04	-0.557 E 01	0.2051 E 01	-0.80032 E 00	-0.517632E 00
	3	-0.4 E 08	0.66 E 03	-0.176 E 02	-0.131 E 01	0.303 E 01
	4	-0.1 E 13	-0.2 E 06	0.1 E 04	-0.4 E 02	-0.2 E 02
	5	-0.8 E 19	0.2 E 11	-0.6 E 07	0.1 E 06	0.1 E 05
B_{pn}^i	0	0.6 E-04	-0.37 E-05	0.61 E-06	-0.39 E-07	-0.4 E-07
	1	0.4 E-02	0.5 E-04	-0.44 E-05	0.24 E-06	0.15 E-06
	2	0.2 E 03	-0.2 E-01	0.3 E-03	-0.1 E-04	-0.4 E-05
	3	0.6 E 07	-0.2 E 02	0.3 E-01	-0.6 E-03	-0.5 E-04
	4	0.6 E 13	-0.5 E 06	0.4 E 03	-0.7 E 01	-0.6 E 00
	5	0.1 E 19	-0.1 E 09	0.3 E 06	-0.4 E 04	-0.3 E 03

Table 4.4d

Eigenvalues, Modal Participation Functions and Eigenvectors for a Simply Supported Plate With 6 Sides

6 Collocation Points at 0°, 6°, 12°, 18°, 24°, 30°

		Mode i				
		1	2	3	4	5
k_i		2.676	6.12	9.49	11.0	13.0
X_1^i/X_2^i	n=0, ... 4	1.605	-1.077	0.834	0.017	-0.70
	n=0	1.592	-1.032	0.793	0.13	-0.64
	Order n					
A_{pn}^i	0	0.100000E 01	0.100000E 01	0.100000E 01	0.100000E 01	0.100000E 01
	1	-0.16 E 02	0.49 E 00	-0.45 E 00	0.401 E 01	-0.627 E 00
	2	0.3 E 06	-0.5 E 02	0.2 E 01	-0.420 E 01	-0.197 E 00
	3	0.2 E 12	-0.1 E 05	-0.1 E 03	0.3 E 02	0.54 E 01
	4	0.3 E 19	-0.1 E 11	0.2 E 07	-0.2 E 06	-0.4 E 04
B_{pn}^i	0	0.1 E-03	-0.1 E-04	0.8 E-06	-0.5 E-06	-0.2 E-07
	1	-0.9 E 00	0.8 E-03	-0.2 E-04	0.9 E-05	0.5 E-06
	2	-0.1 E 06	0.1 E 01	0.8 E-03	-0.4 E-03	-0.1 E-04
	3	-0.3 E 12	0.8 E 05	-0.3 E 02	0.4 E 01	0.4 E-01
	4	0.1 E 18	-0.3 E 09	-0.1 E 06	0.1 E 05	0.8 E 02

Table 4.4e

Eigenvalues, Modal Participation Functions and Eigenvectors for a Simply Supported Plate With 7 Sides

6 Collocation Points at 0°, 5°, 10°, 15°, 20°, 25.7°

		Mode i				
		1	2	3	4	5
k_i		2.600	5.9537	9.298	11.80	12.78
X_1^i/X_2^i	n=0, ...4	1.604	-1.075	0.863	-0.090	-0.647
	n=0	1.596	-1.050	0.822	-0.52	-0.673
	Order n					
A_{pn}^i	0	0.100000E 01	0.100000E 01	0.100000E 01	0.100000E 01	0.100000E 01
	1	-0.60 E 02	0.75 E 00	-0.260 E 00	0.383 E 01	-0.684 E 00
	2	0.5 E 08	-0.9 E 03	0.76 E 01	-0.6755 E 01	0.68 E-01
	3	0.2 E 16	-0.4 E 08	-0.1 E 04	0.4 E 03	0.3 E 02
	4	0.3 E 24	-0.8 E 14	0.2 E 10	-0.2 E 08	-0.5 E 06
B_{pn}^i	0	0.8 E-03	-0.3 E-04	0.15 E-05	-0.5 E-06	-0.30 E-07
	1	-0.95 E 01	0.4 E-02	-0.6 E-04	0.1 E-04	0.6 E-06
	2	-0.2 E 08	0.3 E 02	0.3 E-01	-0.229 E-02	-0.9 E-04
	3	-0.3 E 16	0.5 E 08	-0.3 E 04	0.40 E 02	0.1 E 01
	4	0.4 E 24	-0.3 E 14	-0.1 E 09	0.9 E 06	0.2 E 05

Table 4.4f

Eigenvalues, Modal Participation Functions and Eigenvectors for a Simply Supported Plate With 8 Sides

6 Collocation Points at 0°, 5°, 10°, 15°, 19°, 22.5°

		Mode i				
		1	2	3	4	5
k_i		2.50	5.82	9.14	12.33	13.01
X_1^i/X_2^i	n=0, ... 4	1.61	-1.06	0.86	-0.61	-0.12
	n=0	1.605	-1.04	0.83	-0.70	-0.59
	Order n					
A_{pn}^i	0	0.100000E 01	0.100000E 01	0.100000E 01	0.100000E 01	0.100000E 01
	1	-0.1 E 04	0.21 E 01	-0.243 E 00	0.780582E 00	-0.320 E 01
	2	0.7 E 11	-0.6 E 05	0.8 E 02	-0.5 E 01	0.60 E 01
	3	0.8 E 21	-0.5 E 12	0.5 E 07	-0.1 E 05	0.4 E 04
	4	0.2 E 33	-0.2 E 21	0.1 E 14	-0.3 E 10	0.6 E 09
B_{pn}^i	0	-0.8 E-02	0.2 E-03	-0.1 E-05	0.5 E-07	-0.3 E-07
	1	0.5 E 03	-0.7 E-01	-0.1 E-03	0.3 E-05	-0.2 E-05
	2	-0.5 E 11	0.1 E 05	-0.2 E 01	0.6 E-02	-0.2 E-02
	3	-0.7 E 21	0.2 E 12	-0.1 E 07	0.1 E 04	-0.2 E 03
	4	-0.2 E 33	0.9 E 20	-0.1 E 13	0.2 E 09	-0.3 E 08

Table 4.4g

Eigenvalues, Modal Participation Functions and Eigenvectors for a Simply Supported Plate With 9 Sides

6 Collocation Points at 0°, 4°, 8°, 12°, 16°, 20°

		Mode i				
		1	2	3	4	5
	k_i	2.45	5.74	9.01	12.3	13.9
X_1^i/X_2^i	n=0, ... 4	1.61	-1.05	0.85	-0.72	-0.001
	n=0	1.61	-1.04	0.83	-0.70	-0.05
	Order n					
A_{pn}^i	0	0.100000E 01	0.100000E 01	0.100000E 01	0.100000E 01	0.100000E 01
	1	-0.1 E 05	0.6 E 01	-0.4 E 00	0.29 E 00	-0.66 E 01
	2	0.3 E 14	-0.3 E 07	0.1 E 04	-0.2 E 02	0.30 E 02
	3	-0.5 E 25	0.2 E 15	-0.1 E 10	0.6 E 06	-0.1 E 06
	4	0.2 E 39	-0.3 E 25	0.2 E 18	-0.4 E 13	0.3 E 12
B_{pn}^i	0	-0.1 E-01	0.2 E-03	-0.6 E-05	0.3 E-06	-0.2 E-06
	1	0.6 E 04	-0.4 E 00	0.1 E-02	-0.1 E-04	0.6 E-05
	2	-0.2 E 14	0.9 E 06	-0.7 E 02	0.1 E 00	-0.2 E-01
	3	0.4 E 25	-0.1 E 15	0.2 E 09	-0.2 E 05	0.1 E 04
	4	-0.2 E 39	0.2 E 25	-0.6 E 17	0.5 E 12	-0.2 E 11

Table 4.4h

Eigenvalues, Modal Participation Functions and Eigenvectors for a Simply Supported Plate With 12 Sides

4 Collocation Points at 0°, 8°, 12°, 15°

		Mode i				
		1	2	3	4	5
	k_i	2.42	5.65	8.87	12.1	15.3
X_1^i/X_2^i	n=0, ... 2	1.61	-1.05	0.84	-0.72	0.63
	n=0	1.61	-1.05	0.83	-0.70	0.62
	Order n					
A_{pn}^i	0	0.100000E 01	0.100000E 01	0.100000E 01	0.100000E 01	0.100000E 01
	1	-0.40 E 07	0.164 E 03	-0.191 E 01	0.229 E 00	-0.19 E 00
	2	0.31 E 22	-0.2 E 13	0.4 E 08	-0.3 E 05	0.3 E 03
B_{pn}^i	0	-0.83 E-02	0.22 E-03	-0.9 E-05	0.5 E-06	-0.3 E-07
	1	0.22 E 07	-0.13 E 02	0.1 E-01	-0.2 E-04	-0.3 E-06
	2	-0.27 E 22	0.9 E 12	-0.5 E 07	0.9 E 03	-0.9 E 00

Values for modal participation functions χ_1^i/χ_0^i calculated for uniformly distributed loads using only the θ- independent zero order terms in Eqs. (2.22) and (2.23) and henceforth referred to as $(\chi_1^i/\chi_0^i)_0$ are included together with the values calculated using the higher order terms which will be referred to simply as χ_1^i/χ_0^i. The difference between the values of χ_1^i/χ_0^i and $(\chi_1^i/\chi_0^i)_0$ is indicative to some extent of the significance of the errors introduced by the omission of the products of the terms of different orders n in χ_0^i, Eq. (2.22). Results in Tables 4.3 and 4.4 show that the possibility of error in χ_0^i increases with increasing mode number and decreasing number of plate sides.

The Fortran digital computer program used to obtain these results is given in Appendix C.1.

4.2 Effect of Boundary Shape on Symmetric Eigenvalues

The effect of boundary shape on the symmetric eigenvalues k_i^e for plates of equal surface areas is shown in Tables 4.5 and 4.6. These eigenvalues are calculated from the eigenvalues k_i, given in Tables 4.1 and 4.2, using

$$k_i^e = \rho^e k_i \, , \tag{4.1}$$

where

$$\rho^e = \sqrt{\frac{p}{2\pi} \sin \frac{2\pi}{p}} \tag{4.2}$$

and ρ^e is the dimensionless radius of the circular plate having the same area as the regular polygonal plate.

These tables reveal a pattern of fluctuation of k_i^e with the number of the sides of the polygon and the mode number which, with the exception of a few discrepancies, appears to be identical for both simply supported and clamped plates. The direction of decreasing eigenvalue magnitude for either increasing or decreasing number of sides is marked by arrows for each mode. These arrows indicate the polygon having the maximum modal frequency.

Exceptions to this pattern occur in Table 4.6 where the fundamental and some of the higher modal eigenvalues appear to be too low for the simply supported plates with 8 and 9 sides. The same discrepancies also were noticed in these eigenvalues when calculating modal displacements which are discussed later. The magnitude of these discrepancies could be accounted for by the numerical convergence error previously noted for the related eigenvalues in Section 4.1, Table 4.2.

Since the frequency varies as the square of the eigenvalue, these tables show that the fundamental frequency of vibration of polygons of equal area having simply supported or clamped edges decreases with increasing number of sides. The relative difference between the fundamental eigenvalues for a circular plate and a plate with 12

Table 4.5

	Symmetric Eigenvalues for Clamped Polygonal Plates of Equal Area							
	Number of Sides p							
	3	4	5	6	7	8	9	12	∞^1
ρ^e	0.64304	0.79788	0.86996	0.90939	0.93329	0.94885	0.95954	0.97721	1.0
k_1^e	→ 3.694	3.384	3.292	3.252	3.232	3.220	3.213	3.204	3.1962
k_2^e	6.380	↔ 6.487	6.433	6.390	6.363	6.35	6.33	6.32	6.3064
k_3^e	8.109	8.370	9.135	9.449	↔ 9.482	9.48	9.47	9.46	9.4395
k_4^e	9.067	9.918	10.08	10.79	11.78	12.5	12.6	← 12.6	12.577
k_5^e	10.7	11.19	12.21	12.64	12.74	13.1	14.1	15.7	← 15.716

---

[1] These eigenvalues are given by Weiner [19].

Table 4.6

	Symmetric Eigenvalues for Simply Supported Polygonal Plates of Equal Area								
	Number of Sides p								
	3	4	5	6	7	8	9	12	∞[1]
ρ^e	0.64304	0.79788	0.86996	0.90939	0.93329	0.94885	0.95954	0.97721	1.0
k_1^e	→ 2.694	2.507	2.454	2.434	2.43	2.37	2.35	2.37	2.1080($\nu = 0$) 2.2215($\nu = 0.3$)
k_2^e	5.387	↔ 5.605	5.59	5.57	5.55	5.52	5.51	5.52	5.4188($\nu = 0$) 5.4516($\nu = 0.3$)
k_3^e	7.125	7.520	8.32	8.63	↔ 8.68	8.67	8.65	8.67	8.5920($\nu = 0$) 8.6114($\nu = 0.3$)
k_4^e	8.083	9.040	9.31	10.0	11.0	11.7	11.8	← 11.8	11.747 ($\nu = 0$) 11.761 ($\nu = 0.3$)
k_5^e	9.710	10.33	11.4	11.8	11.9	12.3	13.3	← 15.0	14.896 ($\nu = 0$) 14.907 ($\nu = 0.3$)

---

[1] These eigenvalues are given by Weiner [19].

equilateral sides is larger for the simply supported edge condition than the clamped edge condition. This seems reasonable since eigenvalues are independent of Poisson's ratio in the case of simply supported polygonal plates as well as clamped polygonal and circular plates, but are dependent on this ratio in the case of simply supported circular plates, having their smallest values for $\nu = 0$. Rao and Rajaiah [104] have discussed this effect of Poisson's ratio for statically loaded simply supported plates. They showed that inaccuracies can arise for $p>5$ on account of the slow rate of convergence of the solution.

4.3 Symmetric Mode Shapes and Modal Participation Functions

The symmetric mode shapes for the characteristic segments of some clamped and simply supported polygonal plates, computed using the values for the eigenvectors given in Tables 4.3 and 4.4, are shown in Figs. 4.2a through 4.2d. Mode shapes for the complete plates are inferred by the rotational periodicity of the solution. The boundary collocation points used to obtain the eigenvectors are shown as small circles along the plate characteristic segment edge.

The dotted portions of the nodal lines in Figs. 4.2a through 4.2d are considered to result from errors in the satisfaction of the edge conditions. More errors occurred for the clamped plates than the simply supported plates since the satisfaction of the condition of zero edge slope naturally tends to introduce more incorrect

nodal lines near the boundary than the condition of zero edge moment. Since this solution is exact only for circular plates and since a polygonal boundary deviates most from a circle at the corners and this deviation increases with decreasing number of sides, it is consistent that most numerical errors occurred for the triangular plate near the boundary in the corners along generally circular lines emanating from boundary collocation points.

The deviation of the nodal lines from concentric circles increases with decreasing number of sides and increasing mode numbers. The degree of this deviation is reflected in the degree of variation between the values of $(\chi_1^i/\chi_0^i)_{\bar{0}}$ and χ_1^i/χ_0^i given in Tables 4.3 and 4.4.

An attempt was made to relate the nodal areas, defined as the areas between the nodal lines and denoted as ratios of the plate segment area in Figs. 4.2a through 4.2d, to the modal participation functions for uniform loads using

$$(\chi_1^i/\chi_0^i)_a = m_a^i(\chi_1^i/\chi_0^i)_{p=12} , \tag{4.3}$$

where

$$m_a^i = a_d^i/(a_d^i)_{p=12} . \tag{4.4}$$

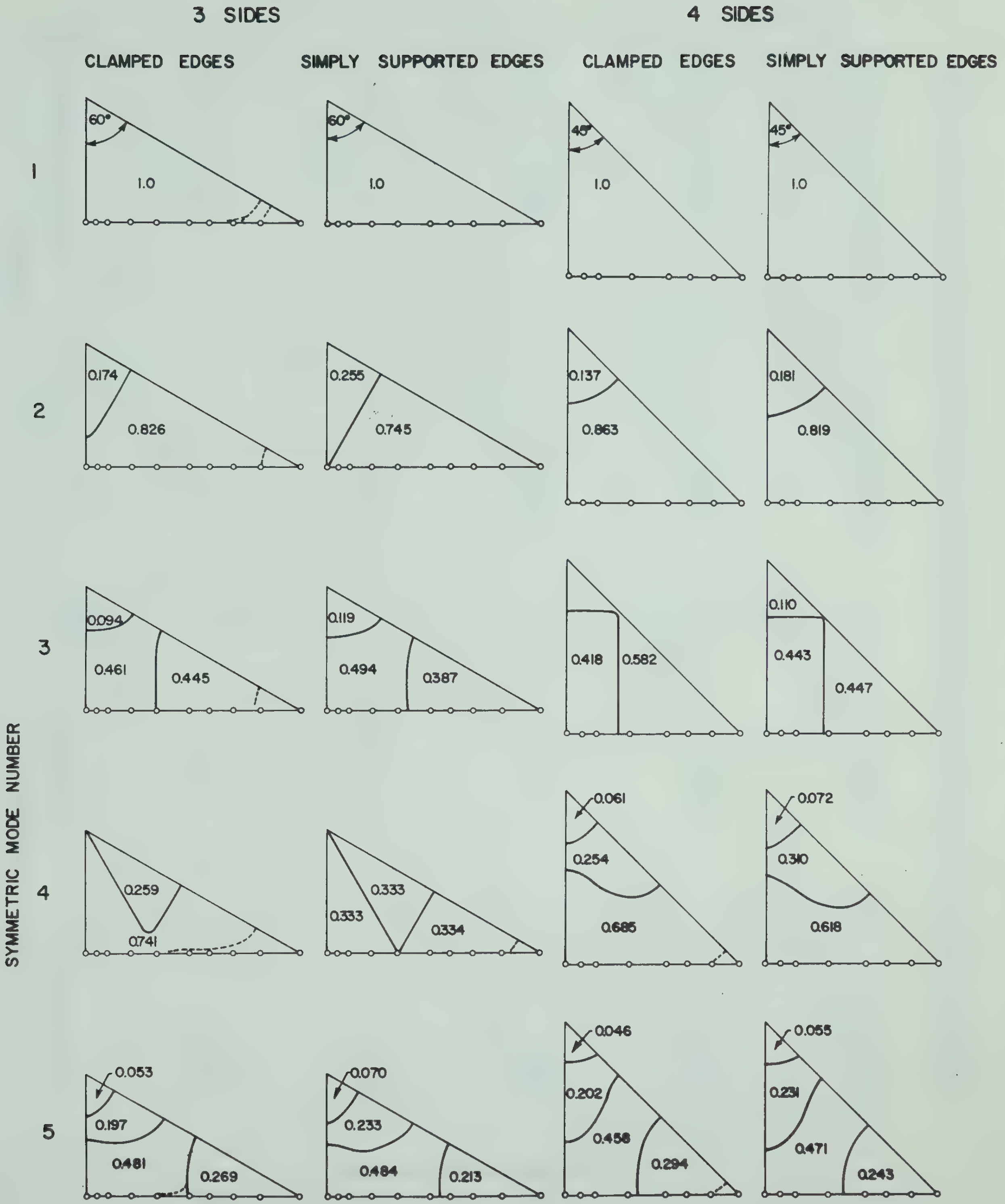

FIG. 4.2a - SYMMETRIC MODE SHAPES FOR THE CHARACTERISTIC SEGMENTS OF REGULAR POLYGONAL PLATES WITH 3 AND 4 SIDES

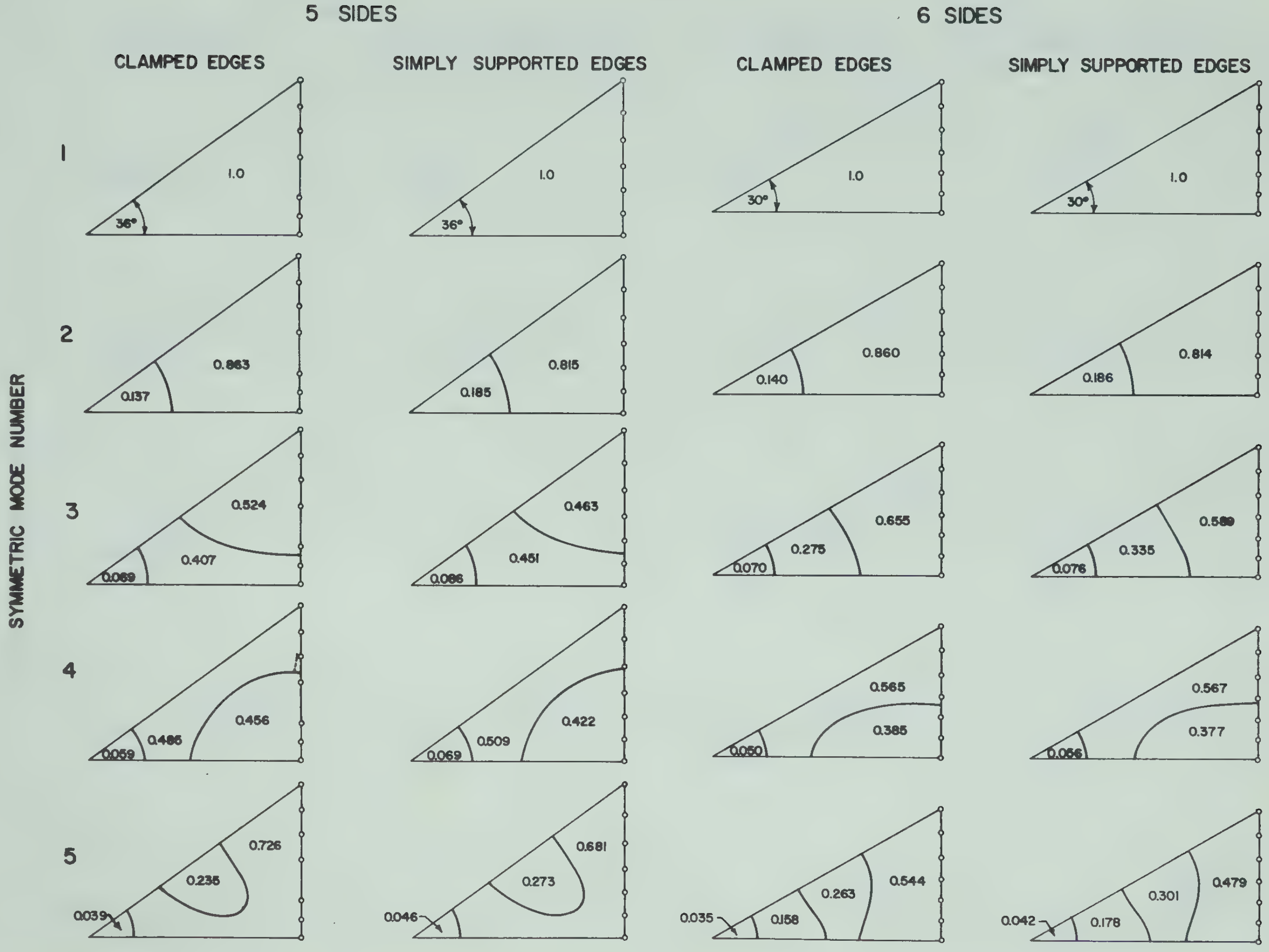

FIG. 4.2b - SYMMETRIC MODE SHAPES FOR THE CHARACTERISTIC SEGMENTS OF REGULAR POLYGONAL PLATES WITH 5 AND 6 SIDES

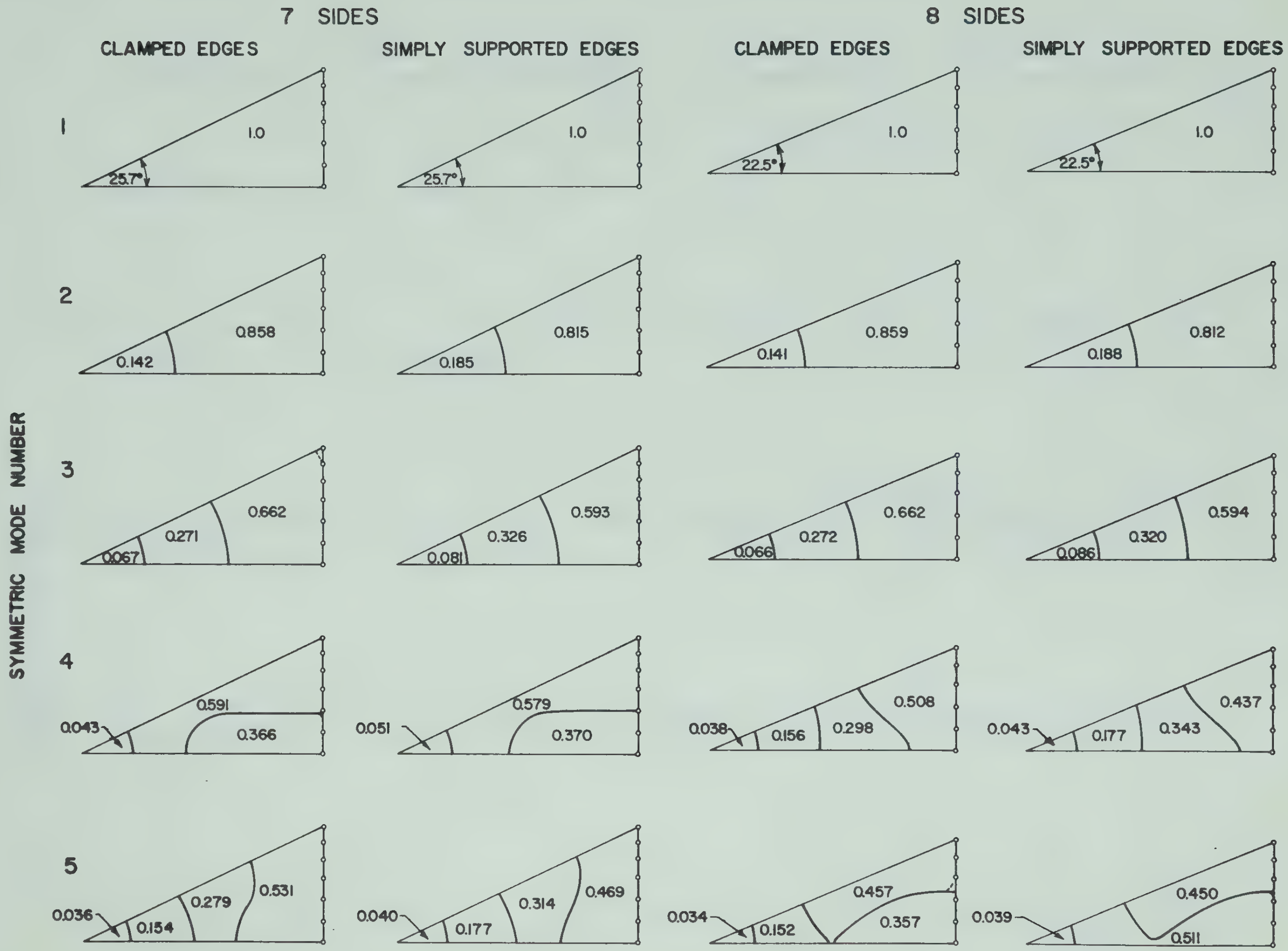

FIG. 4.2C - SYMMETRIC MODE SHAPES FOR THE CHARACTERISTIC SEGMENTS OF REGULAR POLYGONAL PLATES WITH 7 AND 8 SIDES

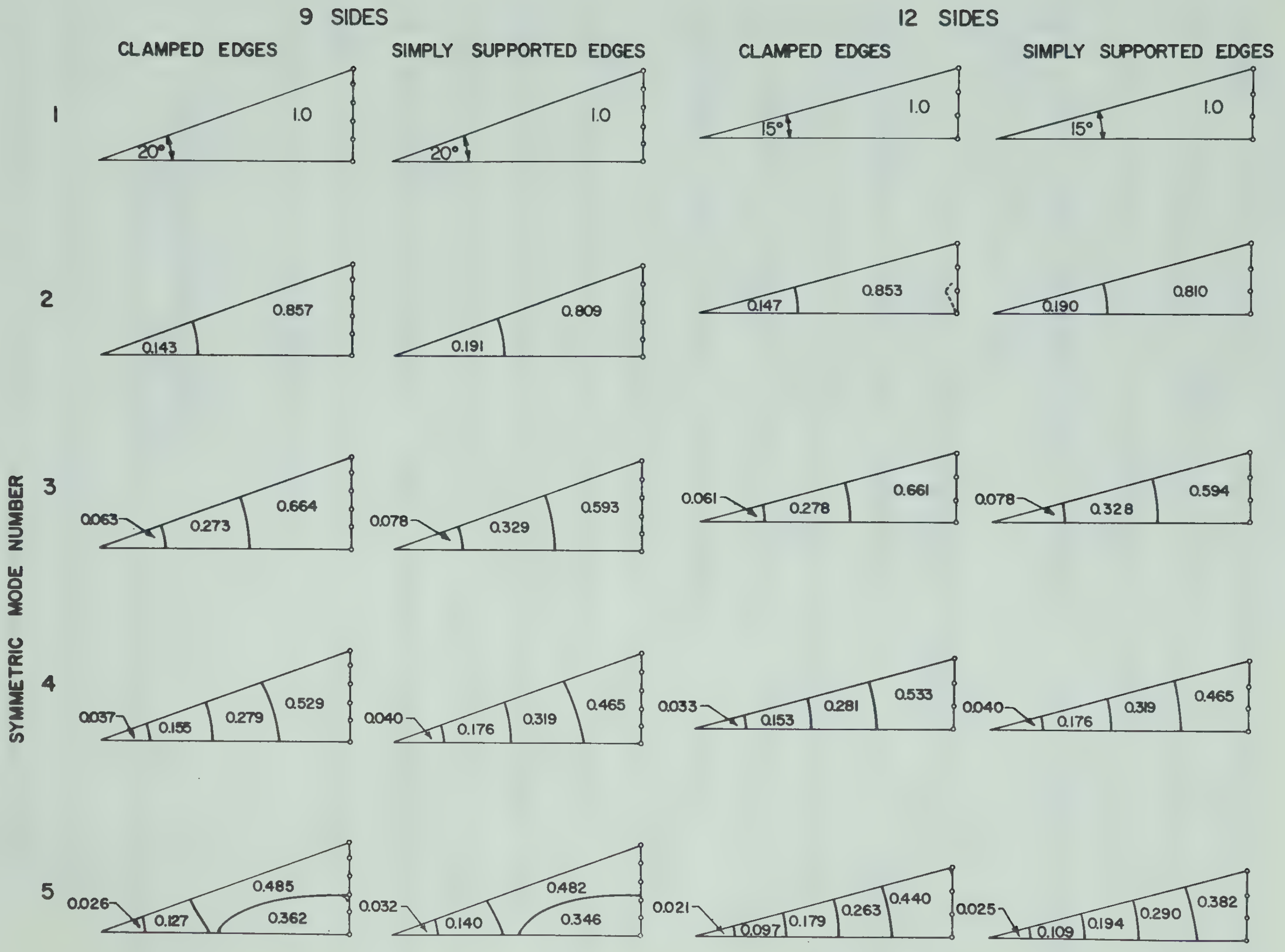

FIG. 4.2d -SYMMETRIC MODE SHAPES FOR THE CHARACTERISTIC SEGMENTS OF REGULAR POLYGONAL PLATES WITH 9 AND 12 SIDES

In Eq. (4.3) $(\chi_1^i/\chi_0^i)_{p=12}$ are the values of χ_1^i/χ_0^i for the 12-sided polygonal plate given in Tables 4.3h and 4.4h. In Eq. (4.4) a_d^i is the difference between the sums of the i-th nodal areas which respond in the same direction under a uniform load.

The modal participation functions χ_1^i/χ_0^i for the 12-sided plate were chosen as the basis for obtaining $(\chi_1^i/\chi_0^i)_a$ for the other polygons since the evaluation of χ_0^i from Eq. (2.22) is most accurate for the polygonal boundary most closely approximating a circle.

The modal participation functions $(\chi_1^i/\chi_0^i)_a$, calculated from Eq. (4.1) and given in Tables 4.7 and 4.8, agree reasonably well with χ_1^i/χ_0^i, with differences generally increasing with decreasing number of sides and increasing mode number. The largest discrepancies occur for the fourth mode of many of the polygons and for all modes of the triangular plates.

4.4 Central Displacement

The static central deflections for the symmetric modes of response of polygonal plates with the same inscribing radius a_o were calculated for uniformly distributed loads using

$$W_i = \frac{A_0^i + B_0^i}{k_i^4 \cos^4\theta_o} \cdot \frac{\chi_1^i}{\chi_0^i} \qquad (4.5a)$$

Table 4.7

Modal Participation Functions for Uniformly Loaded Clamped Polygonal Plates

	Number of Sides p							
	3	4	5	6	7	8	9	12
m_a^1	1.0	1.0	1.0	1.0	1.0	1.0	1.0	1.0
$(\chi_1^1/\chi_0^1)_a$	1.615	1.615	1.615	1.615	1.615	1.615	1.615	1.615
$(\chi_1^1/\chi_0^1)_o$	1.217	1.667	1.6288	1.6198	1.6169	1.6158	1.615	1.6145
χ_1^1/χ_0^1	0.2756	1.58140	1.61783	1.61710	1.6160	1.6154	1.615	1.6145
m_a^2	0.924	1.03	1.03	1.02	1.01	1.02	1.01	1.0
$(\chi_1^2/\chi_0^2)_a$	-1.19	-1.33	-1.33	-1.32	-1.30	-1.32	-1.30	-1.292
$(\chi_1^2/\chi_0^2)_o$	-0.369	-1.444	-1.369	-1.323	-1.3067	-1.300	-1.297	-1.293
χ_1^2/χ_0^2	-0.00637	-1.0256	-1.2945	-1.3048	-1.3007	-1.297	-1.296	-1.292
m_a^3	0.176	0.369	0.419	1.01	1.03	1.03	1.02	1.0
$(\chi_1^3/\chi_0^3)_a$	0.192	0.403	0.458	1.10	1.12	1.12	1.11	1.092
$(\chi_1^3/\chi_0^3)_o$	-0.0910	-0.0692	1.103	1.156	1.125	1.11	1.102	1.092
χ_1^3/χ_0^3	-0.109E-4	0.0595	0.5907	1.0505	1.099	1.10	1.098	1.092
m_a^4	-1.29	-1.32	-0.081	0.349	0.489	0.882	0.989	1.0
$(\chi_1^4/\chi_0^4)_a$	1.24	1.27	0.079	-0.335	-0.469	-0.847	-0.949	-0.960
$(\chi_1^4/\chi_1^4)_o$	-0.627E-3	0.7879	1.202	0.440	-0.684	-0.98	-0.979	-0.96
χ_1^4/χ_0^4	-0.6 E-6	0.1244	0.3780	0.02880	-0.107	-0.78	-0.956	-0.96
m_a^5	0.20	0.03	-1.61	-1.44	-1.32	-0.064	0.079	1.0
$(\chi_1^5/\chi_0^5)_a$	0.17	0.03	-1.40	-1.25	-1.15	-0.056	0.69E-1	0.860
$(\chi_1^5/\chi_0^5)_o$	0.0178	0.4576	-1.083	-1.097	-1.028	-0.90	-0.4 E-1	0.86
χ_1^5/χ_0^5	-0.2 E-7	-0.0487	-0.6005	-0.88766	-0.853	-0.19	0.6 E-3	0.86

Table 4.8

Modal Participation Functions for Uniformly Loaded Simply Supported Polygonal Plates

	Number of Sides p							
	3	4	5	6	7	8	9	12
m_a^1	1.0	1.0	1.0	1.0	1.0	1.0	1.0	1.0
$(\chi_1^1/\chi_0^1)a$	1.610	1.610	1.610	1.610	1.610	1.610	1.610	1.610
$(\chi_1^1/\chi_0^1)o$	1.2134	1.5254	1.5776	1.592	1.596	1.605	1.61	1.61
χ_1^1/χ_0^1	1.3900	1.58955	1.6049	1.605	1.604	1.61	1.61	1.61
m_a^2	0.790	1.03	1.02	1.01	1.02	1.01	0.997	1.0
$(\chi_1^2/\chi_0^2)a$	-0.830	-1.08	-1.07	-1.06	-1.07	-1.06	-1.05	-1.05
(χ_1^2/χ_0^2)	-0.50687	-0.87236	-0.9900	-1.032	-1.050	-1.04	-1.04	-1.05
χ_1^2/χ_0^2	-0.79467	-1.0564	-1.0777	-1.077	-1.075	-1.06	-1.05	-1.05
m_a^3	0.35	0.331	0.285	0.959	1.01	1.05	0.994	1.0
$(\chi_1^3/\chi_0^3)a$	0.029	0.278	0.239	0.806	0.848	0.882	0.835	0.84
$(\chi_1^3/\chi_0^3)o$	-0.2522	0.2728	0.7033	0.793	0.822	0.83	0.83	0.83
χ_1^3/χ_0^3	-0.31E-4	0.17677	0.514	0.834	0.863	0.86	0.85	0.84
m_a^4	-1.18	-1.35	0.064	0.475	0.631	0.809	1.0	1.0
$(\chi_1^4/\chi_0^4)a$	0.850	0.972	-0.046	-0.342	-0.454	-0.582	-0.72	-0.72
$(\chi_1^4/\chi_0^4)o$	-0.39	0.4905	0.5678	0.13	-0.52	-0.70	-0.70	-0.70
χ_1^4/χ_0^4	-0.11E-5	0.60157	0.3535	0.017	-0.090	-0.61	-0.72	-0.72
m_a^5	1.65	0.257	-1.79	-1.55	-1.45	-0.109	0.139	1.0
$(\chi_1^5/\chi_0^5)a$	1.04	0.162	-1.13	-0.977	-0.914	-0.069	0.087	0.63
$(\chi_1^5/\chi_0^5)o$	0.2993	0.0316	-0.509	-0.64	-0.673	-0.59	-0.05	0.62
χ_1^5/χ_0^5	0.2 E-4	-0.24331	-0.5043	-0.70	-0.647	-0.12	-0.001	0.63

and

$$W_i^a = \frac{A_0^i + B_0^i}{k_i^4 \cos^4\theta_0} \cdot \left(\frac{\chi_1^i}{\chi_0^i}\right)_a , \qquad (4.5b)$$

and for central point loads using

$$W_i^p = \frac{A_0^i + B_0^i}{k_i^4 \cos^2\theta_0} \cdot \frac{\left(\chi_1^i\right)_p}{\chi_0^i} \cdot a^2. \qquad (4.6)$$

The convergence of the sums of the modal displacements for polygons with clamped and simply supported edges subjected to uniform pressures q_o

$$W = \sum_i W_i = wD/q_o a_0^4 \qquad (4.7a)$$

and

$$W^a = \sum_i W_i^a \qquad (4.7b)$$

to the values given by Leissa, Lo and Niedenfuhr [77] is shown in Tables 4.9 and 4.10 for the first five modes.

The agreement between the values of W, W^a and the values given in [77] is quite good for all polygons in Tables 4.9 and 4.10 except the triangular plates and the simply supported plates with eight and nine sides. The disagreement between central displacements calculated for these simply supported plates with eight and nine sides by the static approach in [77] and the present dynamic approach could be eliminated

by using the slightly larger fundamental eigenvalues indicated by the discrepancies previously noted in Table 4.6. Good agreement could have been obtained between the static central displacements computed by the two methods for the simply supported plates with seven, eight and nine sides if the fundamental eigenvalues were, respectively, 2.59, 2.53 and 2.49 rather than the values 2.60, 2.50 and 2.45 given in Table 4.2. Consequently, it seems that the modal participation functions for these plates should be reliable. However, for the triangular plates the values of χ_1^i/χ_0^i appear to be incorrect while the values of $(\chi_1^i/\chi_0^i)_a$ provide good convergence of the sum of static central modal displacements W^a to the values given in [77].

From these results it appears that the values of $(\chi_1^i/\chi_0^i)_a$ which were calculated from the nodal areas provide very reliable estimates of at least the first two modal participation functions for the symmetric response of uniformly loaded regular polygonal plates.

The convergence of the sums of the modal displacements for polygons with simply supported and clamped edges subjected to central point loads P_o

$$W^P = \sum_i W_i^P = wD/P_o a_0^2 \qquad (4.8)$$

is shown in Tables 4.11 and 4.12 for the first five

Table 4.9

Static Center Modal Deflections of Uniformly Loaded Clamped Polygonal Plates

	Number of Sides p								
	3	4	5	6	7	8	9	12	∞ [2]
W_1	0.430 E -2	0.207 E -1	0.1947E-1	0.1856E-1	0.1800E-1	0.1764E-1	0.1738E-1	0.1694E-1	
W_1^a	0.252 E -1	0.211 E -1	0.1944E-1	0.1854E-1	0.1799E-1	0.1764E-1	0.1738E-1		
W	0.430 E -2	0.207 E -1	0.1947E-1	0.1856E-1	0.1800E-1	0.1764E-1	0.1738E-1	0.1694E-1	
W^a	0.252 E -1	0.211 E -1	0.1944E-1	0.1854E-1	0.1799E-1	0.1764E-1	0.1738E-1		
W_2	-0.10 E -4	-0.94 E -3	-0.101 E-2	-0.949 E-3	-0.911 E-3	-0.887 E-3	-0.872 E-3	-0.850 E-3	
W_2^a	-0.205 E -2	-0.122 E -2	-0.104 E-2	-0.960 E-3	-0.911 E-3	-0.903 E-3	-0.875 E-3		
W	0.429 E -2	0.197 E -1	0.1846E-1	0.1761E-1	0.1709E-1	0.1675E-1	0.1651E-1	0.1609E-1	
W^a	0.232 E -1	0.199 E -1	0.1840E-1	0.1758E-1	0.1708E-1	0.1674E-1	0.1651E-1		
W_3	-0.7 E -8	0.20 E -4	0.113 E-3	0.160 E-3	0.156 E-3	0.151 E-3	0.148 E-3	0.143 E-3	
W_3^a	0.12 E -3	0.14 E -3	0.876 E-4	0.167 E-3	0.160 E-3	0.154 E-3	0.150 E-3		
W	0.429 E -2	0.198 E -1	0.1857E-1	0.1777E-1	0.1725E-1	0.1690E-1	0.1666E-1	0.1623E-1	
W^a	0.233 E -1	0.200 E -1	0.1849E-1	0.1775E-1	0.1724E-1	0.1689E-1	0.1666E-1		
W_4	-0.2 E -9	0.21 E -4	0.49 E-4	0.26 E-5	-0.64 E-5	-0.36 E-4	-0.41 E-4	-0.40 E-4	
W_4^a	0.41 E -3	0.21 E -3	0.10 E-4	-0.30 E-4	-0.28 E-4	-0.39 E-4	-0.41 E-4		
W	0.429 E -2	0.198 E -1	0.1862E-1	0.1777E-1	0.1724E-1	0.1686E-1	0.1662E-1	0.1619E-1	
W^a	0.237 E -1	0.202 E -1	0.1853E-1	0.1772E-1	0.1721E-1	0.1685E-1	0.1662E-1		
W_5	-0.5 E -11	-0.5 E -5	-0.36 E-4	-0.42 E-4	-0.37 E-4	-0.7 E-5	0.2 E-7	0.15 E-4	
W_5^a	0.34 E -4	0.3 E -5	-0.84 E-4	-0.59 E-4	-0.50 E-4	-0.2 E-5	0.2 E-5		
W	0.429 E -2	0.198 E -1	0.1858E-1	0.1773E-1	0.1721E-1	0.1685E-1	0.1662E-1	0.1621E-1	
W^a	0.237 E -1	0.202 E -1	0.1845E-1	0.1766E-1	0.1716E-1	0.1685E-1	0.1662E-1		
W^1	0.2414E-1	0.2024E-1	0.1861E-1	0.1774E-1	0.1722E-1	0.1687E-1	0.1663E-1		0.15625E-1
W^e	0.0882E-1	0.1249E-1	0.1392E-1	0.1459E-1	0.1495E-1	0.1516E-1	0.1530E-1	0.1547E-1	

---

[1] These static deflections are given by Leissa, Lo and Niedenfuhr [77].

[2] This static deflection is given by Timoshenko and Woinowsky-Krieger [78].

Table 4.10

Stätic Center Modal Deflections of Uniformly Loaded Simply Supported Polygonal Plates

	Number of Sides p								
	3	4	5	6	7	8	9	12	∞^2
W_1	0.722E-1	0.653E-1	0.591E-1	0.557E-1	0.533E-1	0.559E-1	0.572E-1	0.530E-1	
W_1^a	0.837E-1	0.661E-1	0.593E-1	0.559E-1	0.535E-1	0.559E-1	0.572E-1		
W	0.722E-1	0.653E-1	0.591E-1	0.557E-1	0.533E-1	0.559E-1	0.572E-1	0.530E-1	
W^a	0.837E-1	0.661E-1	0.593E-1	0.559E-1	0.535E-1	0.559E-1	0.572E-1		
W_2	-0.258E-2	-0.174E-2	-0.147E-2	-0.136E-2	-0.130E-2	-0.126E-2	-0.125E-2	-0.120E-2	
W_2^a	-0.269E-2	-0.178E-2	-0.146E-2	-0.134E-2	-0.129E-2	-0.126E-2	-0.125E-2		
W	0.697E-1	0.635E-1	0.577E-1	0.543E-1	0.520E-1	0.547E-1	0.560E-1	0.518E-1	
W^a	0.810E-1	0.643E-1	0.578E-1	0.545E-1	0.522E-1	0.547E-1	0.560E-1		
W_3	-0.34 E-7	0.90 E-4	0.14 E-3	0.18 E-3	0.18 E-3	0.17 E-3	0.16 E-3	0.16 E-3	
W_3^a	0.31 E-4	0.14 E-3	0.65 E-4	0.17 E-3	0.18 E-3	0.17 E-3	0.16 E-3		
W	0.697E-1	0.636E-1	0.578E-1	0.545E-1	0.522E-1	0.548E-1	0.562E-1	0.520E-1	
W^a	0.810E-1	0.645E-1	0.579E-1	0.547E-1	0.524E-1	0.548E-1	0.562E-1		
W_4	0.7 E-9	0.15 E-3	0.64 E-4	0.21 E-5	-0.7 E-5	-0.36 E-4	-0.41 E-4	-0.38 E-4	
W_4^a	0.56 E-3	0.24 E-3	-0.8 E-5	-0.42 E-4	-0.35 E-4	-0.34 E-4	-0.41 E-4		
W	0.697E-1	0.638E-1	0.578E-1	0.545E-1	0.521E-1	0.548E-1	0.561E-1	0.520E-1	
W^a	0.817E-1	0.647E-1	0.579E-1	0.547E-1	0.524E-1	0.548E-1	0.561E-1		
W_5	0.6 E-8	-0.35 E-4	-0.40 E-4	-0.43 E-4	-0.37 E-4	-0.60 E-5	-0.3 E-7	0.13 E-4	
W_5^a	0.32 E-3	0.23 E-4	-0.90 E-4	-0.61 E-4	-0.52 E-4	-0.35 E-5	0.3 E-5		
W	0.697E-1	0.638E-1	0.578E-1	0.544E-1	0.521E-1	0.548E-1	0.561E-1	0.520E-1	
W^a	0.820E-1	0.649E-1	0.578E-1	0.546E-1	0.523E-1	0.548E-1	0.561E-1		
W^1	0.833E-1	0.650E-1	0.581E-1	0.548E-1	0.532E-1	0.525E-1	0.523E-1		0.781E-1(ν= 0) 0.626E-1(ν=0.33)
W^e	0.304E-1	0.401E-1	0.435E-1	0.451E-1	0.462E-1	0.472E-1	0.481E-1	0.496E-1	0.573E-1(ν=0.5)

[1] These static deflections are given by Leissa, Lo and Niedenfuhr [77].

[2] These static deflections are given by Timoshenko and Woinowsky-Krieger [78].

Table 4.11

Static Center Modal Deflections of Centrally Point Loaded Clamped Polygonal Plates

	Number of Sides p								
	3	4	5	6	7	8	9	12	∞[1]
W_1^P	0.332E-2	0.182E-1	0.181E-1	0.177E-1	0.175E-1	0.173E-1	0.172E-1	0.170E-1	
W^P	0.332E-2	0.182E-1	0.181E-1	0.177E-1	0.175E-1	0.173E-1	0.172E-1	0.170E-1	
W_2^P	0.11 E-4	0.166E-2	0.209E-2	0.209E-2	0.207E-2	0.205E-2	0.204E-2	0.200E-2	
W^P	0.333E-2	0.199E-1	0.202E-1	0.198E-1	0.196E-1	0.194E-1	0.192E-1	0.190E-1	
W_3^P	0.9 E-6	0.10 E-3	0.37 E-3	0.59 E-3	0.62 E-3	0.62 E-3	0.61 E-3	0.60 E-3	
W^P	0.333E-2	0.200E-1	0.205E-1	0.204E-1	0.202E-1	0.200E-1	0.198E-1	0.196E-1	
W_4^P	0.5 E-11	0.55 E-4	0.22 E-3	0.60 E-4	0.46 E-4	0.21 E-3	0.25 E-3	0.26 E-3	
W^P	0.333E-2	0.200E-1	0.208E-1	0.205E-1	0.202E-1	0.202E-1	0.201E-1	0.199E-1	
W_5^P	0.1 E-7	0.41 E-4	0.16 E-3	0.23 E-3	0.22 E-3	0.54 E-4	0.98 E-5	0.13 E-3	
W^P	0.333E-2	0.201E-1	0.209E-1	0.207E-1	0.204E-1	0.202E-1	0.201E-1	0.200E-1	
W^P [1]		0.224E-1							0.1989E-1
$W^{P,e}$		0.176E-1	0.181E-1	0.188E-1	0.190E-1	0.192E-1	0.193E-1	0.195E-1	

---

[1] These values are given by Timoshenko and Woinowsky-Krieger [78].

Table 4.12

Static Center Modal Deflections of Centrally Point Loaded Simply Supported Polygonal Plates

	Number of Sides p								
	3	4	5	6	7	8	9	12	∞[1]
W_1^P	0.378E-1	0.403E-1	0.389E-1	0.379E-1	0.371E-1	0.392E-1	0.399E-1	0.381E-1	
W^P	0.378E-1	0.403E-1	0.389E-1	0.379E-1	0.371E-1	0.392E-1	0.399E-1	0.381E-1	
W_2^P	0.270E-2	0.321E-2	0.322E-2	0.317E-2	0.312E-2	0.314E-2	0.312E-2	0.306E-2	
W^P	0.405E-1	0.435E-1	0.422E-1	0.411E-1	0.402E-1	0.423E-1	0.430E-1	0.412E-1	
W_3^P	0.164E-2	0.50 E-3	0.55 E-3	0.79 E-3	0.80 E-3	0.80 E-3	0.80 E-3	0.79 E-3	
W^P	0.421E-1	0.440E-1	0.427E-1	0.419E-1	0.410E-1	0.431E-1	0.438E-1	0.420E-1	
W_4^P	0.2 E-14	0.45 E-3	0.34 E-3	0.73 E-4	0.58 E-4	0.26 E-3	0.31 E-3	0.31 E-3	
W^P	0.421E-1	0.444E-1	0.431E-1	0.420E-1	0.411E-1	0.434E-1	0.441E-1	0.423E-1	
W_5^P	0.55 E-3	0.32 E-3	0.21 E-3	0.28 E-3	0.27 E-3	0.57 E-4	0.15 E-4	0.15 E-3	
W^P	0.427E-1	0.447E-1	0.433E-1	0.423E-1	0.413E-1	0.434E-1	0.441E-1	0.424E-1	
W^P [1]	0.518E-1	0.464E-1							0.5968(ν = 0) 0.4981(ν = 0.33) 0.4642(ν = 0.5)
$W^{P,e}$	0.313E-1	0.364E-1	0.374E-1	0.384E-1	0.385E-1	0.411E-1	0.423E-1	0.414E-1	

[1] These values are given by Timoshenko and Woinowsky-Krieger [78].

modes. As far as is known, static deflections for centrally loaded regular polygons have been calculated only for triangular, square and circular shapes. These values have been given by Timoshenko and Woinowsky-Krieger [78]. Agreement with present values is poor for the simply supported triangular plate and fair for the square plate reaffirming that errors exist in values of χ_0^i calculated from Eq. (2.22) for these plates. Better agreement for these plates could be obtained by using values of χ_0^i for the first two symmetric modes which are derived from values of $(\chi_1^i/\chi_0^i)_a$ given in Tables 4.7 and 4.8 along with the values of χ_1^i calculated from Eq. (2.23). However, values of χ_0^i calculated in this way provide unacceptable values for the modal participation functions $(\chi_1^i)_p/\chi_0^i$ for centrally loaded triangular plates for $i \geq 3$. Values of W_i^p should be reliable for the polygons with $p > 4$ except for the errors previously mentioned in the eigenvalues for the first mode of response of the simply supported plates with eight and nine sides.

Comparison of the static central displacements for the first five symmetric modes for each plate in Tables 4.9 to 4.12 reveals that usually only the first two modes must be considered for computing the response of these plates to most uniformly distributed dynamic

loads while the first five modes may be needed for central dynamic point loads. Naturally, the response of the higher modes becomes more significant as the load duration becomes short compared to the lower modal response periods.

Static central displacements of polygonal plates having the same surface area and subjected to uniform and central point loads, termed W^e and $W^{P,e}$, respectively, have been calculated from the values given in [77], [78] and from present values where existing ones are not available, using

$$W^e = W \cos^4\theta_o/(\rho^e)^4 = wD/q_o(\rho^e a)^4 \qquad (4.9a)$$

and

$$W^{P,e} = W^P \cos^2\theta_o/(\rho^e)^2 = wD/P_o(\rho^e a)^2. \qquad (4.9b)$$

Comparison of the values of W^e and $W^{P,e}$ given in Tables 4.9 through 4.12 shows that central displacement increases with the number of polygon sides with the exception of the value of $W^{P,e}$ for the simply supported plate with nine sides which can be ignored for the reason given previously. This implies that for simply supported and clamped polygons of equal area the effective plate flexural bending stiffness increases as the number of boundary sides decreases.

The convergence of the central displacements W^e and $W^{P,e}$ to the values for circular plates as the number of sides of the polygon increases is not as rapid for simply supported plates as it is for clamped plates. This can be explained partially by the fact that the displacements W and W^P are dependent on Poisson's ratio only for simply supported circular plates, decreasing with increasing values of ν.

The undamped forced motions of some clamped plates with the same circumscribing radius a and subjected to the initial conditions given in Eqs. (2.20a) and (2.20b) are depicted in Fig. 4.3 for a typical blast wave of incident load intensity q_o and duration of the positive loading phase t_o. These displacements were computed using the values of χ_1^i/χ_o^i given in Tables 4.3 and 4.4. The smoothness of the theoretical response curves is indicative of the small influence of the higher modes on displacement for this transient load. However, the influence of the higher modes on stress couple response is more significant, as is shown in Chapter 5 for a square plate.

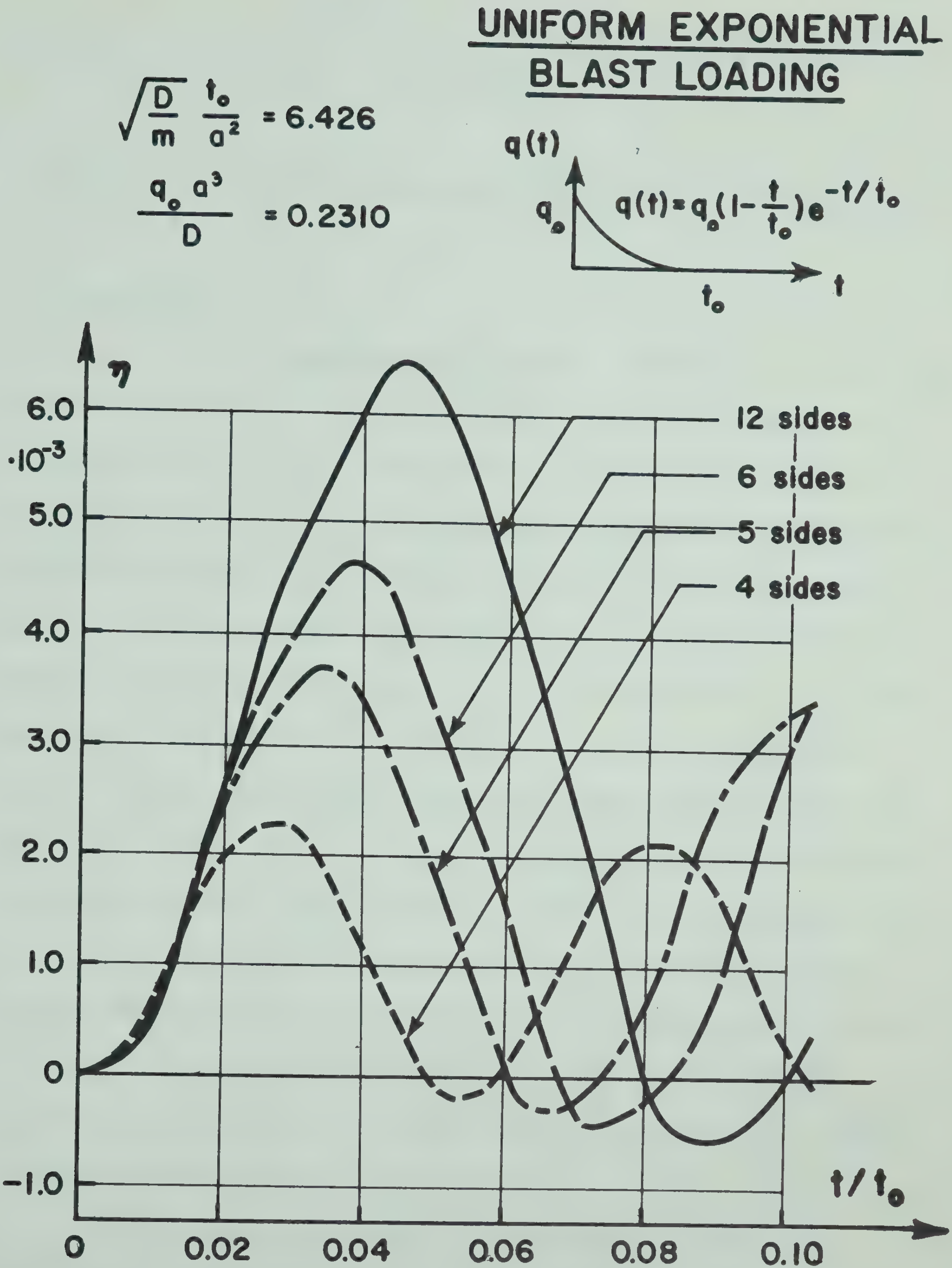

FIG. 4.3 Theoretical Undamped Center Deflections of Some Clamped Polygonal Plates vs. Time

CHAPTER 5

EXPERIMENTAL COMPARISON WITH THEORY FOR A SQUARE PLATE

5.1 Procedure

5.1.1 Experimental Plate. A 34.0 in. (±0.1 in.) square aluminium alloy 65S-T6 plate having a uniform thickness of 0.757 in. (±0.004 in.) was mounted in the rolling section of the DRES six-foot diameter shock tube as shown in Fig. 5.1. Young's molulus E and Poisson's ratio ν were measured statically for two plate material samples as 10.03×10^6 psi and 0.31, and 10.10×10^6 psi and 0.306, respectively. Since the small differences between these values and the Alcan specified values for E and ν of 10.0×10^6 psi and 0.33, respectively, theoretically would have little effect on the plate response, it was decided to use the manufacturer's specified values throughout the theoretical analysis. Strain rate effects for aluminium, as pointed out by Kolsky [79], are not significant for elastic vibrations and consequently were ignored in the theoretical analysis.

The plate was held in position by one inch thick steel clamping plates and rested on a wooden block. These clamping plates partially restricted plate edge rotation while permitting in-plane motion subject to

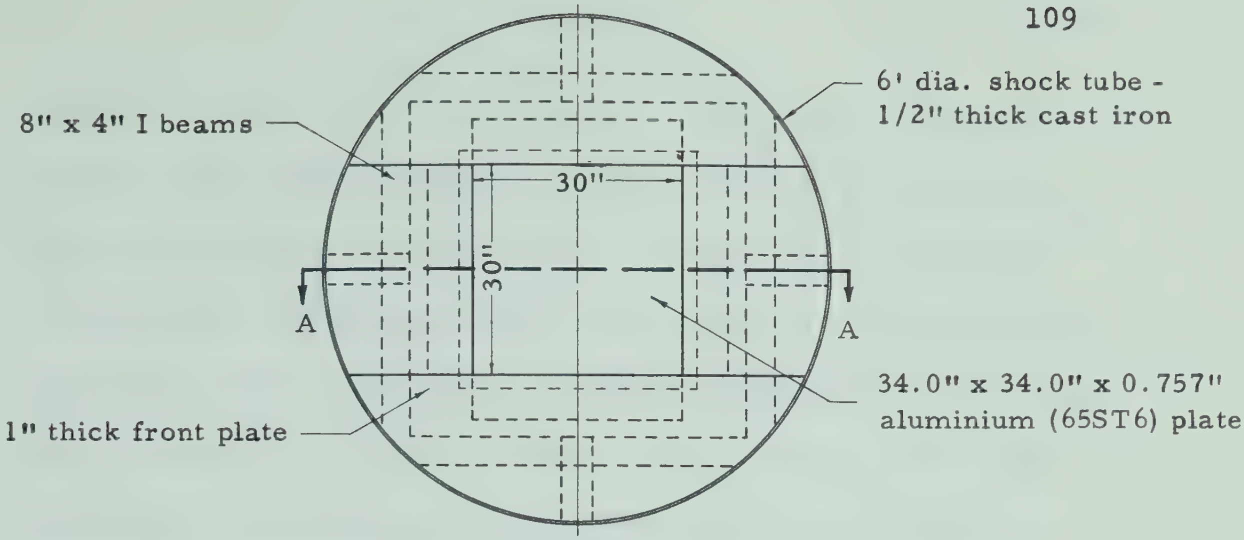

Front View

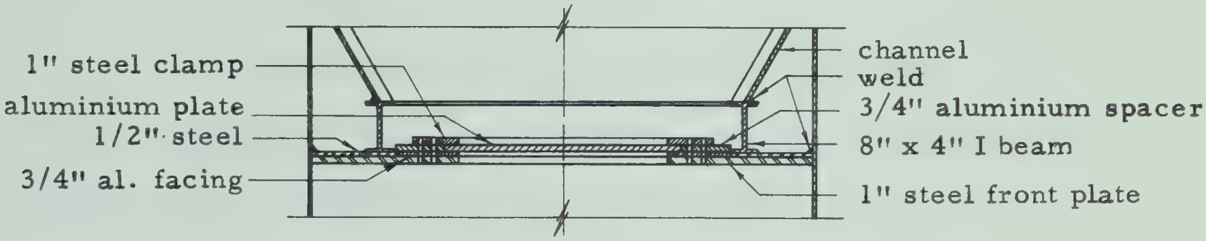

Section A-A

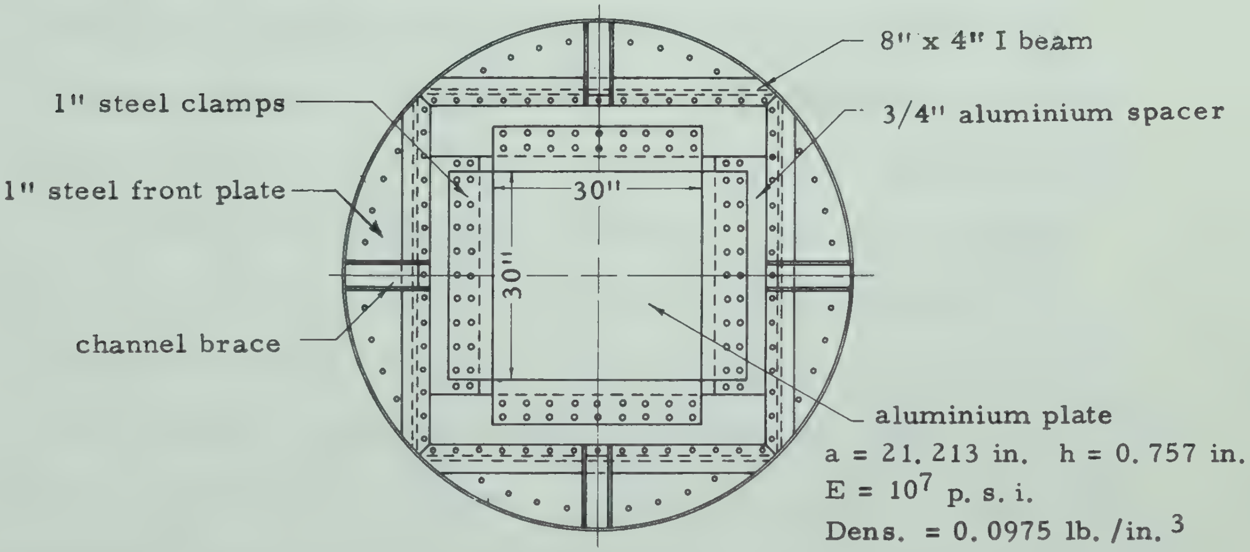

Back View

FIG. 5.1 - Plate Mounting Assembly

resistance by frictional forces. The edge clamping pressure was made as uniform as possible by shimming and by adjusting the tightness of the bolts passing through the clamping plates and the 3/4 in. aluminium spacer plates. By means of this arrangement the plate was elastically clamped along its boundary with fair uniformity and had an exposed surface area 30.0 in. (± 0.1 in.) square.

As demonstrated by Lassiter and Hess [1], initial curvature in plates increases the complexity of analysing deformation by introducing middle surface membrane strains even for small deflections. The experimental plate initially had a maximum deviation from the flat of 0.013 in. over an 8 inch span or a minimum radius of curvature R of approximately 2500 in. An estimate of the effect of this initial curvature on the transverse vibration frequencies can be obtained from the equations for the first two frequencies of transverse vibration of an infinitely long barrel vault simply supported along its lateral edges which are a distance $2a_0$ apart. These equations are given by Hubbard and Houbolt [80] as

$$\omega_1^2 = \left(\frac{\pi}{2a_0}\right)^4 \frac{D}{m}\left[1 - \frac{2}{\pi^2}\left(\frac{2a_0}{R}\right)^2 + \frac{1}{\pi^4}\left(\frac{2a_0}{R}\right)^4 + \right.$$

$$\left. + \frac{96(1-\nu^2)}{\pi^6}\left(\frac{2a_0}{R}\right)^2\left(\frac{2a_0}{h}\right)^2\right] \qquad (5.1)$$

and

$$\omega_2^2 = 16\left(\frac{\pi}{2a_0}\right)^4 \frac{D}{m}\left[1 - \frac{1}{2\pi^2}\left(\frac{2a_0}{R}\right)^2 + \right.$$

$$\left. + \frac{1}{16\pi^4}\left(\frac{2a_0}{R}\right)^4\right]. \qquad (5.2)$$

For the experimental plate

$$2a_0/R = 0.012$$

and

$$2a_0/h = 39.63.$$

Hence

$$\omega_1^2 = \left(\frac{\pi}{2a_0}\right)^4 \frac{D}{m}\,[1.014]$$

and

$$\omega_2^2 = 16\left(\frac{\pi}{2a_0}\right)^4 \frac{D}{m}\,[1.000].$$

It appears from these values of ω_1 and ω_2 that the maximum deviation from the flat plate fundamental frequency due to initial curvature effects is less than one per cent and that the deviation in higher frequencies is even smaller. These calculations indicate that the deviations of the middle surface of the experimental plate from a flat surface were not sufficiently large to introduce significant membrane strains.

The effect of transverse shear and rotatory inertia on the plate's linear response could be neglected according to Reismann and Greene [20] since the plate

thinness ratio h/a of 0.05 was less than 0.1.

One hundred strain gauges were fixed to the plate using Eastman 910 cement. These gauges were placed at twenty unique r,θ locations in each of two characteristic plate sectors along the radial lines θ = 0°, 15°, 30°, and 45°, measuring strain in the radial and circumferential directions as shown in Fig. 5.2. Gauges were placed on both sides of the plate at five of these locations in each sector. Budd strain gauges, type C12-121A, having gauge factors of 2.07 and 2.08 (± 0.5%), a gauge resistance of 120 ohms and a gauge length of 0.125 in., were used at most of the positions. Micro-measurement strain gauges, type EA-06-250-BF-30 having a gauge factor of 2.105 (± 0.5%), a gauge resistance of 350 ohms and a gauge length of 0.250 in., were used at the positions nearest the boundary on the four radial lines where strains were relatively smaller.

5.1.2 Static Response. Static pressures ranging from 0 to 20 psi[1] were applied uniformly over the front surface of the experimental plate by bolting a steel pressure plate to the one inch steel front plate shown in Fig. 5.1, sealing all joints and

---

[1] All pressures refer to pressures relative to atmospheric pressure (i.e., psig) unless otherwise stated.

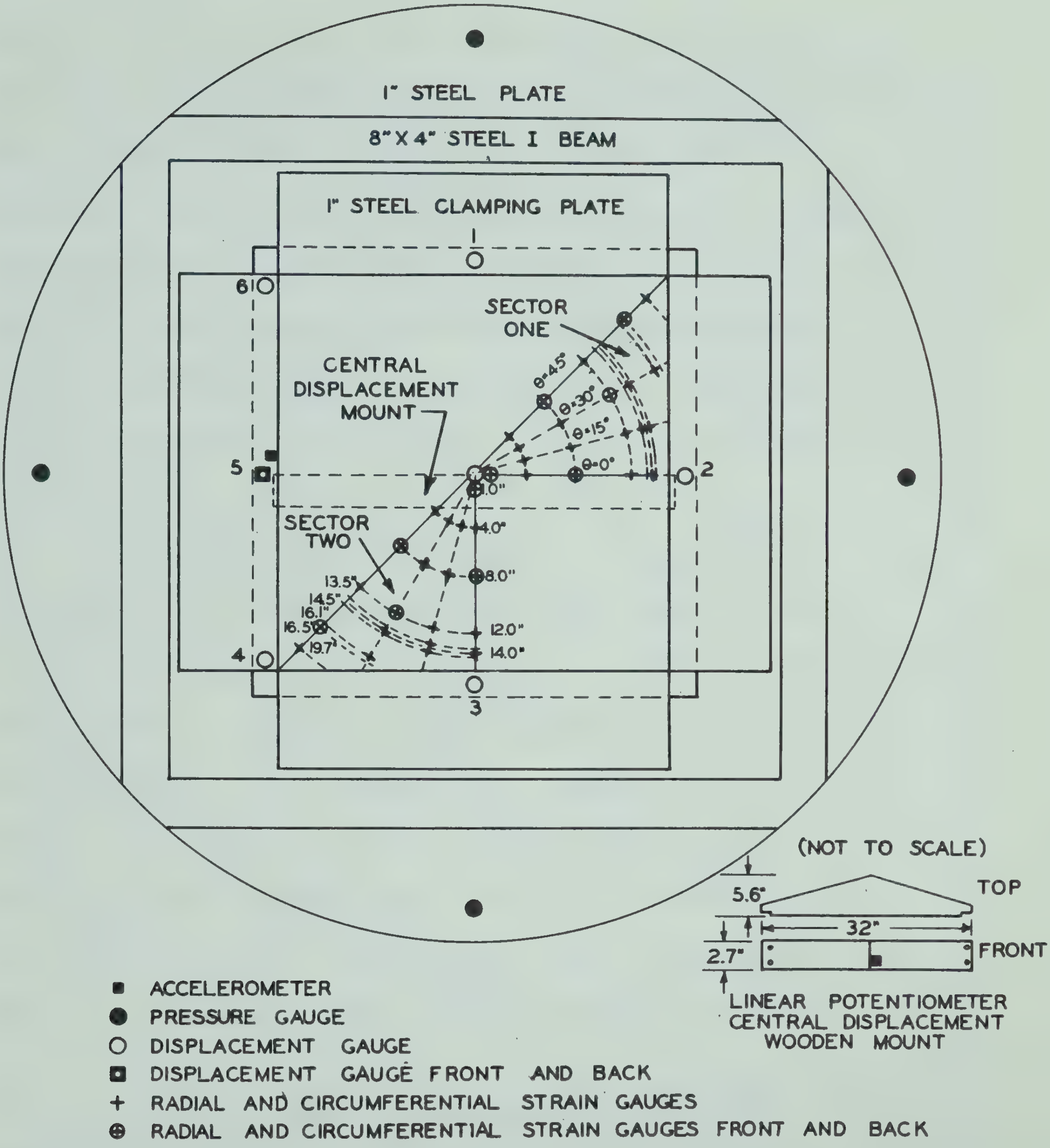

FIG. 5.2 Plate Instrumentation

connecting a pressure line from high pressure air cylinders to the resulting pressure vessel. In this way, uniform pressures were applied only over the 30 x 30 in. plate surface and the mount was supported against displacement at a distance approximately three inches from the plate edges. Pressures were measured with a Wallace and Tiernan bourdon tube gauge, model FA223, having a range of 0 to 50 psi and an accuracy of ± 0.05 psi.

Deflections were measured over the plate profile and around the boundary using Starret model 656-617 dial gauges, each having a 0.0001 in. graduation and a 0.400 in. range. These gauges were mounted as shown in Fig. 5.3. Strains were measured with a Budd P-350 strain indicator and two Budd SB-1 switch and balance units. Strains and deflections were recorded at 5 psi increments from 0 to 20 psi for both the load and the unload portions of the loading cycle.

5.1.3 Transient Response. The cross section of the shock tube shown in Fig. 5.1 was subjected to air blast waves having normally reflected peak overpressures q_o ranging from approximately 5 to 30 psi. The blast waves were formed by the detonation of charges of 60/40 RDX/TNT positioned at the central axis of a 16 inch bore Naval gun barrel which served as the compression chamber for the shock tube. The

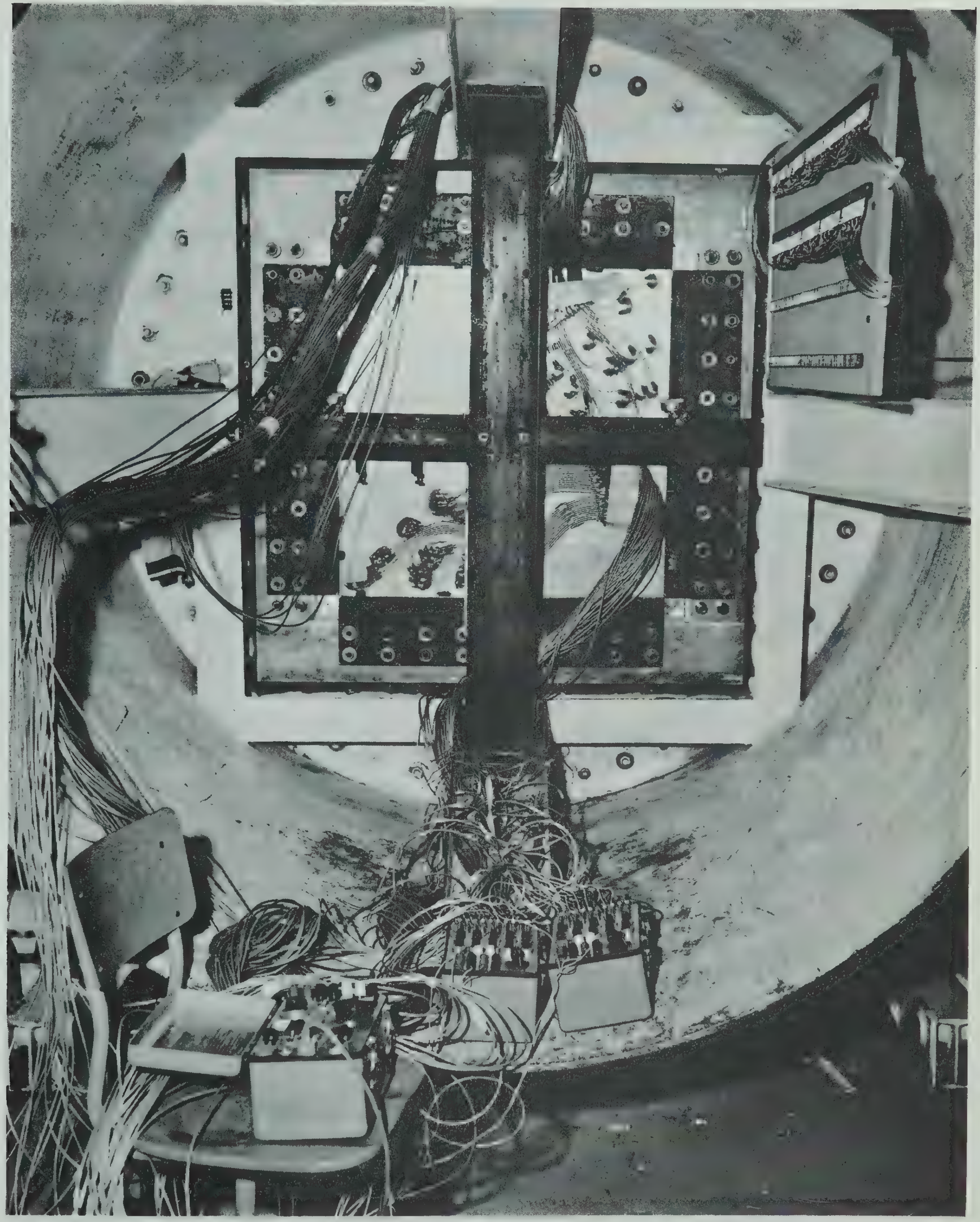

FIG. 5.3 Plate Static Testing Arrangement

waves travelled through a 15 degree conical expansion chamber into a 6 ft. diameter 1/2 in. thick cylindrical tube. The plate test section was located approximately 160 ft. downstream from the compression chamber. A more detailed explanation of the characteristics of this shock tube is given by Campbell, Jones and Watson [81].

This test section was located in the rolling portion of the shock tube. Impingement of the blast waves caused the section to move very slowly along rail tracks. Noticeable motion of the rolling test section started approximately 12 to 20 msec. (sec. x 10^{-3}) after the blast wave arrived at the plate. It was considered that these rigid body accelerations produced negligible forces on the experimental plate in comparison to the forces of the blast loads.

The blast waves at the test section were characterized by a shock front rising to a peak magnitude in a few nanoseconds (sec. x 10^{-9}) and subsequently decaying exponentially to zero magnitude in 20 to 90 msec. depending upon the charge weight. The positive overpressure phase, having an initial normally reflected pressure at the plate q_o and a duration t_o, was followed by a smaller amplitude negative overpressure phase. This characteristic shape of an air blast shock wave is the result of a flat

compression wave pulse being reduced in magnitude approximately exponentially by an ensuing rarefaction wave. The ratio of the initial reflected blast overpressure q_o to which the plate actually was subjected, to the initial incident or free field overpressure, increases with incident overpressure from a value of 2.0 for normal reflection. A succession of smaller amplitude shock waves followed the initial shock wave. These secondary waves were caused by longitudinal reflections of the original shock wave within the shock tube. The period of interest for the plate response, including the oscillation of maximum response plus several smaller amplitude oscillations, always occurred well within the positive phase t_o of the initial shock wave.

Four Ampex 14-track instrumentation magnetic tape recorders, having a total of 56 data channels, were used in this experiment. The recorders use frequency modulation electronics with d.c. response range of 0 to 20,000 cps and amplitude accuracy and linearity of ± 1 per cent. Signals were recorded at a tape speed of 60 inches per second and were reproduced at 1 7/8 inches per second thereby expanding the time scale and reducing the apparent recorded frequencies by a factor of 32. Visual reproduction was obtained using a Honeywell model 1508 moving light paper chart

oscilloscope with a variable chart speed giving a time scale ranging from 0.125 msec./in. to 0.26 msec./in. and galvanometers with a response range of 0 to 2,000 cps.

Some paper chart oscilloscope records were reproduced directly on to graphs while other records were digitized with random time-spacing on to computer tape using a Telecordex chart reader. The data from the chart reader were read into the DRES IBM 1130 computer and then plotted with a Calcomp model 565 X-Y digital plotter. Radial and circumferential digitized strain data from the front and back surfaces of the plate were interpolated linearly in a computer program to yield data with equal time-spacing. Two hundred equitime-spaced points were obtained from each strain record for the first 15 msec. of plate response. The program then correlated strain data from the different gauges to yield membrane and bending strains and sectional resultants at the 20 locations on the plate surface. It was estimated that plate response data associated with frequencies of up to 6,667 cps would be reproduced using this technique.

Pressure variations at the test section over the central 30 in. square were measured for a series of shots using five shear tube piezoelectric pressure transducers of DRES design [82] which were shock mounted

in a dummy plate. These gauges were calibrated after each series of shots to determine gauge signal-to-pressure factors. The gauges had a response capability of up to 10,000 cps with pressure magnitudes accurate to ± 5 per cent. Each pressure signal was amplified and recorded on magnetic tape. Three seconds before a shot, a known electrical charge was applied to the input of the pressure gauge amplifier and after amplification was recorded on each tape channel. In conjunction with the gauge factors,this procedure provided known pressure calibration signals on each pressure channel. It was found that time and spatial variations in the pressure over the 30 in. square were within the possible gauge errors. Consequently, the transient load was assumed to be uniformly distributed over the experimental plate surface.

During the experimental plate tests, reflected overpressures were recorded by four shear tube gauges shock mounted in the one inch steel front plate as shown in Fig. 5.2. As a further check, pressures were computed from the shock front velocities (as measured by side-on pressure gauges mounted in the tube wall upstream from the test section) used in conjunction with atmospheric temperature, pressure and relative humidity measurements taken immediately upstream from the plate.

Fifty strain gauge signals were amplified and recorded on individual tape channels for each shot involving strain measurements. The plate's response symmetry was checked for some shots by recording strain gauge responses at the same 'characteristic segment' radial and circumferential positions in the plate sectors designated 1 and 2 in Fig. 5.2. Strain gauge responses were recorded at all twenty positions in either sector 1 or sector 2 for other shots. Known calibration voltage signals, which took into account gauge and line resistance of the four-armed strain bridge circuit used, were produced with resistance-capacitance shunts of DRES design [83]. The calibration signals were amplified and recorded on each tape channel three seconds before a shot.

The central displacement was measured with a Bourns model 156 Aligno-pot linear potentiometer having an accuracy of ± 0.75 per cent for 0 to 1 inch travel and a maximum range of 1 1/2 inches. This potentiometer was mounted on the wooden box beam shown in Fig. 5.2, which was bolted to the back clamping plates so that displacement was measured relative to the edge. The travelling shaft of the potentiometer was attached to a small circular disk which was glued to the plate center. Edge displacements were measured at the positions shown in Fig. 5.2 using six Bourns

model 141 Linipot linear potentiometers with a range of 7/16 inch. These potentiometers were mounted on 6 in. long 1 1/2 x 1 1/2 in. steel angles which were welded to the 8 x 4 in. I beams and their travelling shafts were held against the clamping plates by compression springs. Linear potentiometer signals were recorded on separate tape channels without amplification. Signals were calibrated over the range of interest by displacing the travelling shafts known amounts using feeler gauges.

Accelerations were measured at the positions shown in Fig. 5.2 with two Endevco model 221D piezoelectric accelerometers having a frequency response range of from 2 to 7,000 cps. Accelerometer signals were amplified and recorded on magnetic tape. Calibration signals were obtained in the same way as for the pressure transducers.

A portion of the instrumentation bunker is shown in Fig. 5.4. A complete instrumentation block diagram is shown in Fig. 5.5.

5.2 Theoretical and Experimental Results

5.2.1 Theoretical Elastically Clamped Square Plate.

Eigenvalues, modal participation functions and static central deflections are given in Table 5.1 for the first five symmetric modes

[illegible]

[illegible]

[illegible]

[illegible]

[illegible]

[illegible]

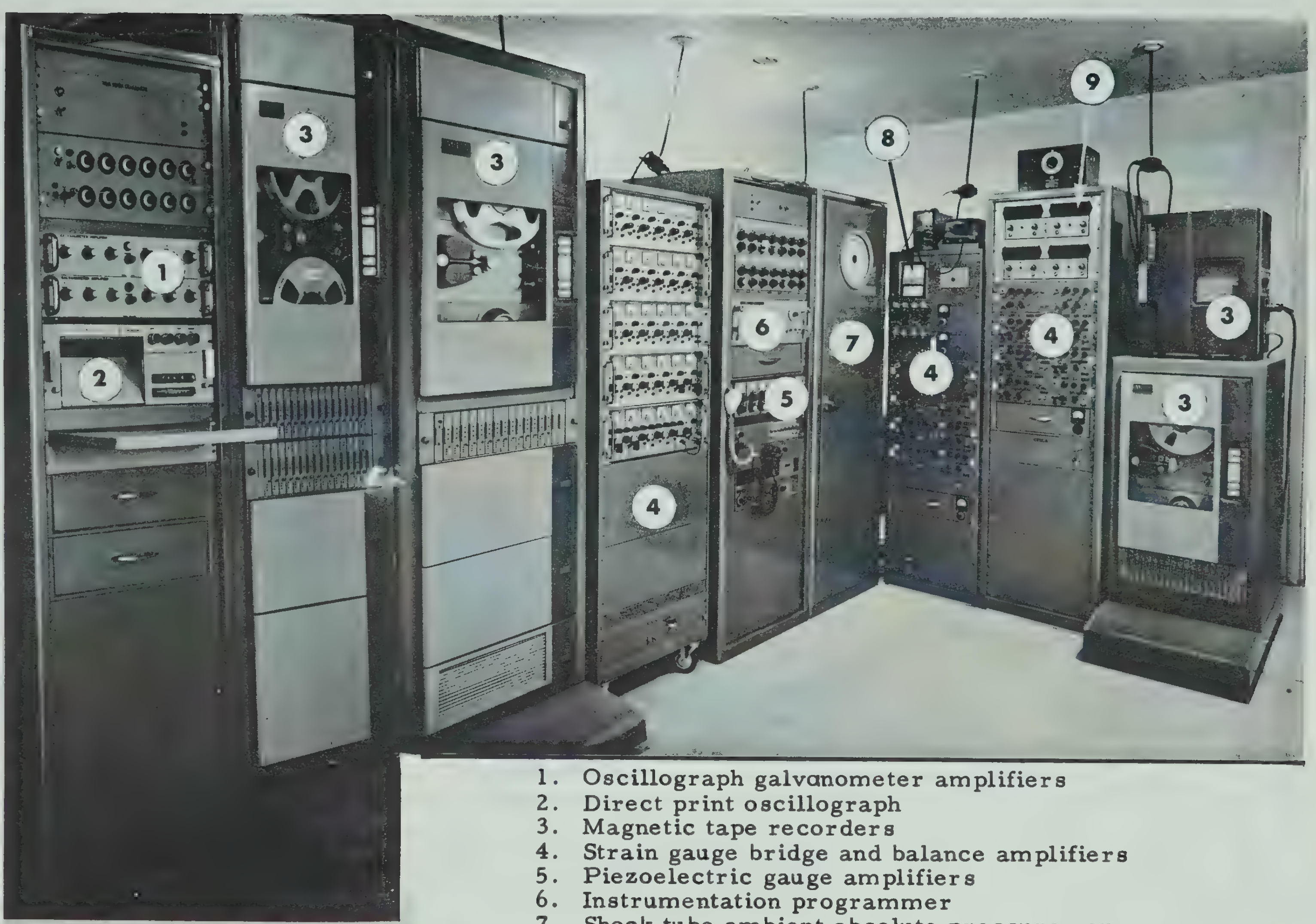

1. Oscillograph galvanometer amplifiers
2. Direct print oscillograph
3. Magnetic tape recorders
4. Strain gauge bridge and balance amplifiers
5. Piezoelectric gauge amplifiers
6. Instrumentation programmer
7. Shock tube ambient absolute pressure gauge
8. Shock tube ambient temperature gauge
9. Shock front velocity counters

FIG. 5.4 - Instrumentation Bunker for Six-Foot Diameter Shock Tube

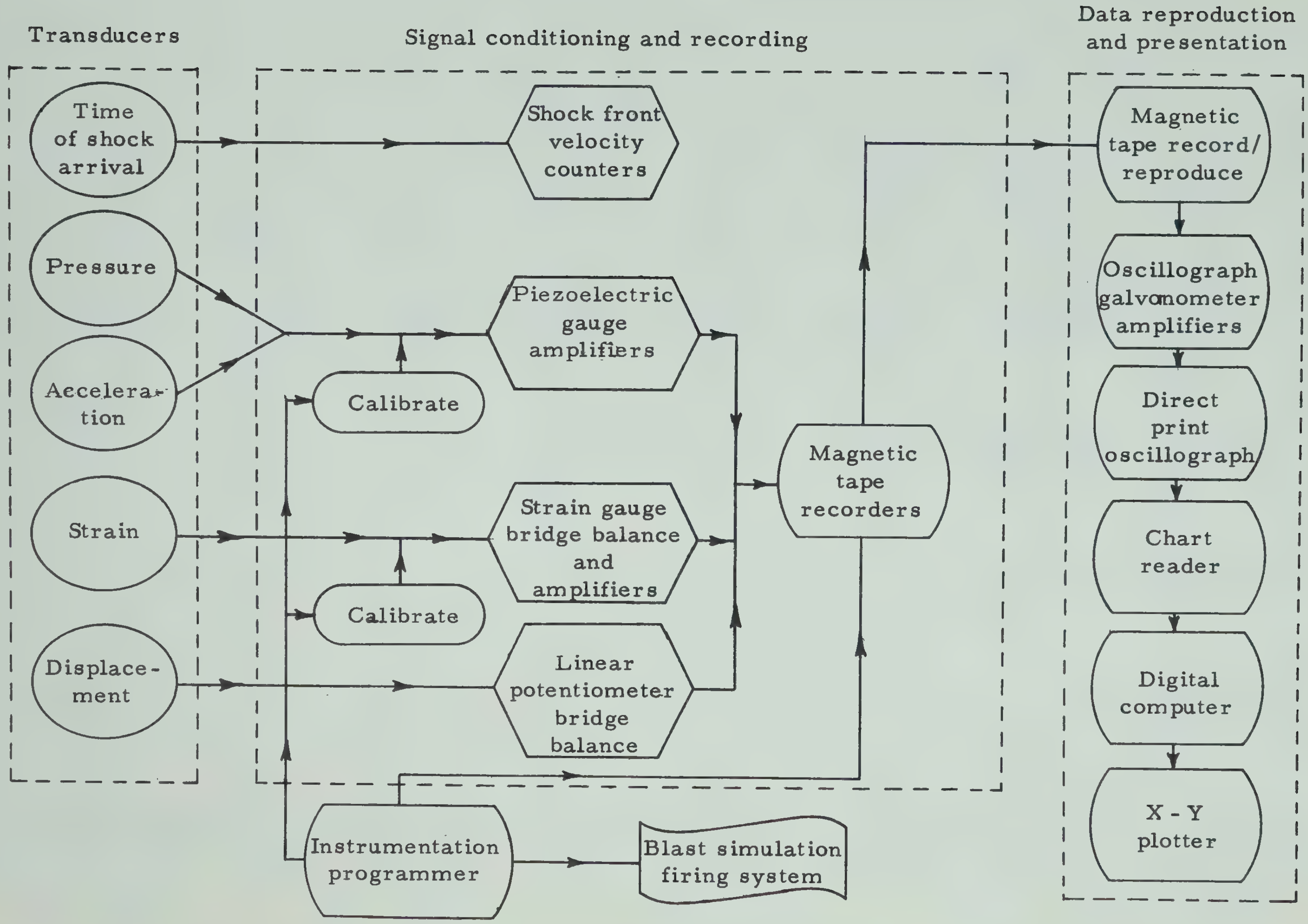
Transducers
Signal conditioning and recording
Data reproduction and presentation
Time of shock arrival
Pressure
Accelera-tion
Strain
Displace-ment
Shock front velocity counters
Piezoelectric gauge amplifiers
Calibrate
Strain gauge bridge balance and amplifiers
Calibrate
Linear potentiometer bridge balance
Magnetic tape recorders
Instrumentation programmer
Blast simulation firing system
Magnetic tape record/ reproduce
Oscillograph galvanometer amplifiers
Direct print oscillograph
Chart reader
Digital computer
X - Y plotter

FIG. 5.5 Block Diagram of Plate Transient Response Instrumentation

Table 5.1

Eigenvalues, Modal Participation Functions and Central Displacements for Uniformly Loaded Elastically Clamped Square Plates

	$\beta_1 a/D$							
	0	0.52289	1.56867	3.13734	5.2289	10.4578	26.1445	∞
k_1	3.14159	3.2468	3.4034	3.5604	3.6948	3.8736	4.0549	4.2418
X_1^1 / X_0^1	1.5896	1.5876	1.5908	1.5988	1.6069	1.6143	1.6100	1.5814
$W_1 \cos^4 \theta_o$	0.1632 E-1	0.1447E-1	0.1219E-1	0.1035E-1	0.9029E-2	0.7554E-2	0.6295E-2	0.5169E-2
k_2	7.0248	7.0752	7.1639	7.2728	7.3859	7.5715	7.8124	8.1304
X_1^2 / X_0^2	-1.056	-1.084	-1.128	-1.170	-1.211	-1.230	-1.198	-1.026
$W_2 \cos^4 \theta_o$	-0.434 E-3	-0.432 E-3	-0.428 E-3	-0.417 E-3	-0.406 E-3	-0.373 E-3	-0.321 E-3	-0.234 E-3
k_3	9.425	9.463	9.531	9.618	9.713	9.879	10.12	10.49
X_1^3 / X_0^3	0.177	0.183	0.193	0.200	0.200	0.180	0.126	0.0595
$W_3 \cos^4 \theta_o$	0.22 E-4	0.23 E-4	0.23 E-4	0.23 E-4	0.22 E-4	0.19 E-4	0.12 E-4	0.49 E-5
k_4	11.33	11.36	11.42	11.50	11.58	11.75	12.00	12.43
X_1^4 / X_0^4	0.602	0.624	0.655	0.674	0.641	0.549	0.306	0.124
$W_4 \cos^4 \theta_o$	0.37 E-4	0.38 E-4	0.39 E-4	0.39 E-4	0.36 E-4	0.29 E-4	0.15 E-4	0.52 E-5
k_5	12.95	12.98	13.03	13.10	13.18	13.33	13.58	14.03
X_1^5 / X_0^5	-0.24	-0.249	-0.258	-0.272	-0.256	-0.223	-0.136	-0.049
$W_5 \cos^4 \theta_o$	-0.86 E-5	-0.88 E-5	-0.89 E-5	-0.92 E-5	-0.85 E-5	-0.71 E-5	-0.40 E-5	-0.13 E-5
$W \cos^4 \theta_o$	0.159 E-1 0.163 E-1 [1]	0.141 E-1	0.118 E-1	0.999 E-2	0.867 E-2	0.722 E-2	0.600 E-2	0.494 E-2 0.506 E-2 [1]

---

[1] These values for $\beta_1 = 0$ and ∞ are given by Leissa, Lo and Niedenfuhr [77].

of vibration of a uniformly loaded square plate having uniform elastic edge clamping ranging from the simply supported to the clamped condition. These values were obtained using seven collocation points on the boundary of the characteristic segment. Values for the coefficients $\phi_1 \ldots \phi_{10}$, required for modal participation functions, were obtained using 46 equal increments of θ for the numerical integration according to Simpson's rule.

Theoretical symmetric frequencies are given in Table 5.2 for the experimental plate subject to various degrees of elastic clamping. These results show that modal frequencies increase relatively more rapidly with values of β_1 for decreasing mode number.

5.2.2 Transient Pressures. Peak reflected overpressures q_o and associated durations of the positive overpressure phase t_o are given in Table 5.3 for 24 separate blast loads on the experimental plate resulting from the detonation of charges of RDX/TNT weighing from 0.5 to 10.0 lbs. Average values of q_o and t_o, obtained from the four shear tube pressure records for each shot, were quite consistent for each charge weight as were values of q_o obtained from the shock front velocity measurements using [84]

TABLE 5.2

Theoretical Frequencies of the Experimental Plate for Various Degrees of Elastic Clamping

		$\beta_1 a/D$							
		0	0.52289	1.56867	3.13734	5.2289	10.4578	26.1445	∞
Frequency, cps	$\omega_1/2\pi$	160.9	171.8	188.8	206.6	222.5	244.6	268.0	293.3
	$\omega_2/2\pi$	804.3	815.9	836.5	862.1	889.2	934.4	994.8	1077
	$\omega_3/2\pi$	1448	1459	1481	1508	1538	1591	1669	1793
	$\omega_4/2\pi$	2091	2103	2125	2156	2187	2250	2348	2520
	$\omega_5/2\pi$	2735	2747	2769	2798	2832	2898	3005	3210

$$\sqrt{\frac{D}{ma^4}} = 102.412$$

Table 5.3

Plate Transient Pressures

Shot	Charge Weight (lb)	Experiment			Theory	
		q_o(psi)		t_o(msec)	q_o(msec)	t_o(msec)
		Average of 4 Measured Values	Calculated from Shock Front Velocity			
1	0.5	5.2	4.0	21	4.8	21
2		5.0	3.9	22		
3		5.2	4.0	22		
4		4.8	4.1	21		
5		5.2		22		
6	1.5	8.9	7.8	32	8.6	33
7		8.7	7.9	33		
8		8.6	7.8	33		
9		8.8	7.5	32		
10		8.9	7.7			
11		9.1	7.8			
12		9.0	7.7			
13		8.5	7.5			
14		8.7	7.8			
15	3.0	12.9	11.6	33	12.9	37
16		13.1	12.5	36		
17		13.0	12.1	38		
18		12.4		38		
19	6.0	20.9	20.5	75	20.9	73
20		20.8	19.5	72		
21		20.9	19.7	72		
22	10.0	29.5	28.0	88	29.8	91
23		29.7	28.1	93		
24		30.2	29.6	94		

$$q_o = q_{atm} \left(\frac{3\kappa M^2 - M^2 + 2 - 2\kappa}{\kappa M^2 - M^2 + 2} \right) \left(\frac{2\kappa M^2 - \kappa + 1}{\kappa + 1} \right) , \qquad (5.3)$$

where

$$M = V/c_{air} \qquad (5.4)$$

and

$$c_{air} = \sqrt{\kappa R T} . \qquad (5.5)$$

In Eqs. (5.3) through (5.5) $\kappa = C_p/C_v$ and C_p and C_v are the specific heats of air at constant pressure and volume, respectively, R is the gas constant, T is the absolute temperature, c_{air} is the velocity of sound and q_{atm} is the atmospheric pressure, all measured immediately upstream from the plate in the undisturbed air, V is the velocity of the incident shock front and M is the shock front Mach number.

The experimental values of q_o measured by the pressure transducers were consistently larger by approximately 1 psi than the values calculated using measured shock front velocities. Initial values of q_o predicted using Eq. (5.3) tended to be less reliable at lower Mach numbers due to the lower accuracy of shock front velocity measurements. They usually did not represent the peak overpressures, in any case, since boundary layer effects introduced a small secondary rise in the reflected compression wave overpressure before it began decaying approximately exponentially.

Values of positive phase duration t_o measured from the pressure transducer records were quite consistent for different shots having the same charge weight. Variations between the values of q_o obtained from either pressure transducer records or shock front velocity measurements for different shots having the same charge weight were usually smaller than variations between the values of q_o obtained for each shot using the two different techniques. Consequently, it was considered reasonable to use one value for q_o and t_o for each charge weight in the theoretical plate transient response calculations, with q_o being chosen nearer to the values measured by the pressure transducers. It is seen from Table 5.3 that the possible errors in theoretical values chosen for q_o range from approximately + 19 per cent to - 8 per cent for a 0.5 lb. shot to + 6 per cent to - 1 per cent for a 10.0 lb. shot.

In view of the errors possible in q_o, it seemed reasonable to assume a transient load history of the form

$$q(t) = q_o(1 - t/t_o) \exp(- t/t_o), \; t \leq t_o, \qquad (5.6)$$

for the theoretical response calculations rather than to numerically integrate the Duhamel integral, Eq. (3.33a), for individual pressure records. Typical experimental and theoretical transient blast pressures

for a 1.5 lb. shot are shown in Fig. 5.6. At least some of the higher frequencies present in this experimental pressure-time record resulted from gauge 'ringing'. For this shot, an initial reflected overpressure q_o of approximately 8.0 psi would have been obtained from accurate shock front velocity measurements. However, a value of 8.6 psi was used for the theoretical initial pressure q_o in order to obtain a more reasonable pressure impulse for the period of interest which was approximately 15 msec.

5.2.3 Damping.

Damping introduces nonconservative forces which dissipate energy in a system undergoing cyclic stressing, usually by converting mechanical energy to heat. It was considered that both structural and air damping would affect the transient response of the experimental plate.

Structural damping is composed of material damping, also termed internal, hysteritic or viscoelastic damping, and interface or Coulomb sliding damping, both of which are described in detail by Lazan and Goodman [85]. Generally, structural damping is nonlinear and is not representable by a viscous damping model.

Air damping, as discussed by Hubbard and Houbolt [80], is composed of a component in-phase with acceleration producing an apparent "added mass" and a

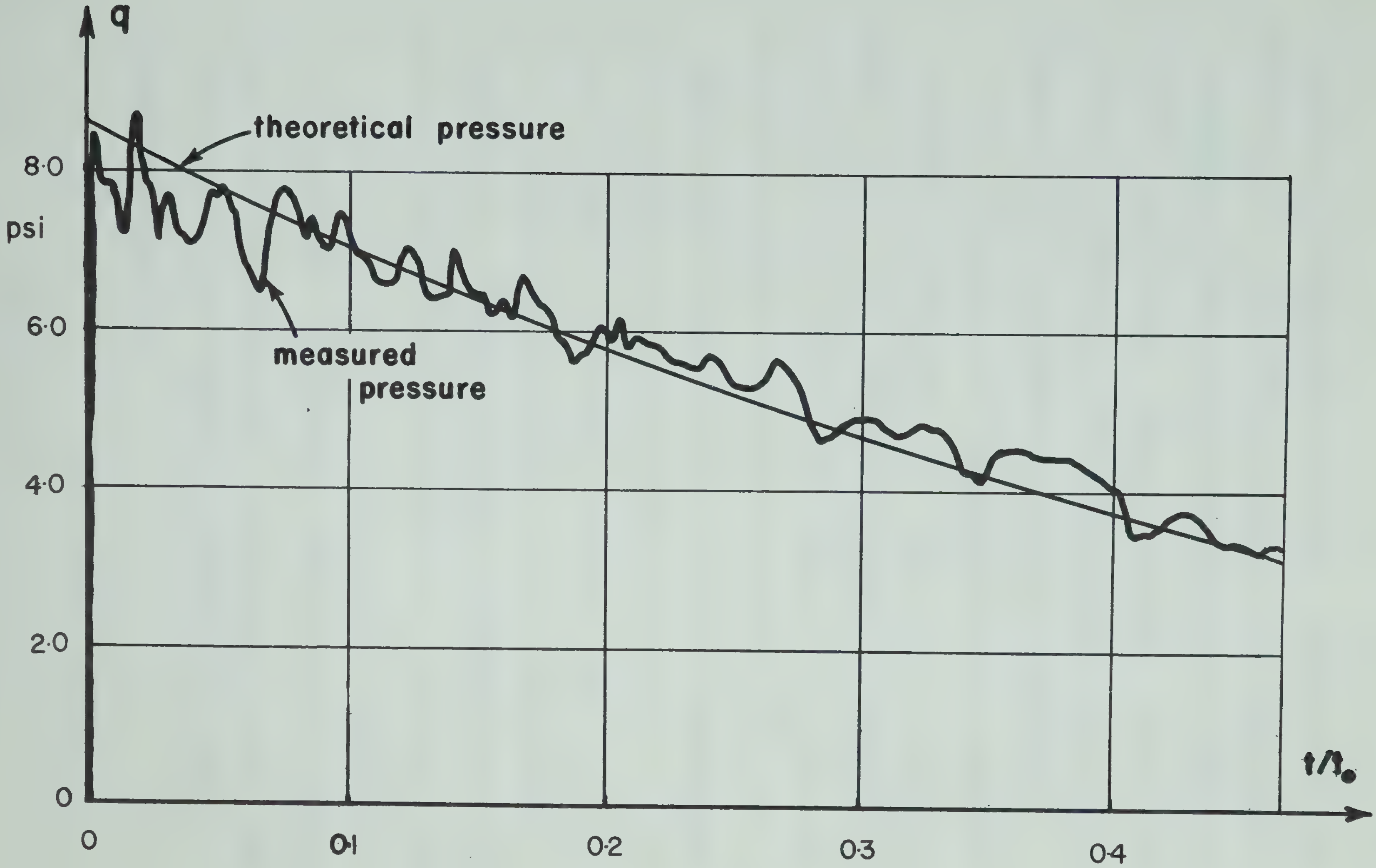

FIG. 5.6 Typical Theoretical and Measured Pressure vs. Time for a 1.5 lb. Shot for Face-on Loading in Six-Foot Diameter Shock Tube

component in-phase with velocity termed "radiation resistance". According to Hubbard and Houbolt, the acceleration component of air damping is negligible for the experimental plate since $2a_0/h = 39.6 < 500$. However, particularly for blast waves, the velocity component of air damping may not be negligible.

The method of calculating the radiation resistance is dependent upon the value of $\omega a_0/c_{air}$, where c_{air} is the velocity of sound in the air surrounding the plate. The values of c_{air} ranged from approximately 1100 to 1300 fps for the air blast overpressures associated with the plate experiments. Radial strain vs. time records at $\rho = 0.377$, $\theta = 15°$ for 1.5 and 6.0 lb. shots, shown in Figs. 5.7 and 5.8, respectively, indicate that the fundamental frequency of vibration of the experimental plate was approximately 165 cps for the 1.5 lb. shot and 160 cps for the 6.0 lb. shot. Relating these frequencies to the theoretical fundamental frequencies for different edge clamping values given in Table 5.2, shows that the experimental edge clamping approached the simply supported condition.

Thus for the experimental plate

$$0.96 < \omega_1 a_0/c_{air} < 1.17.$$

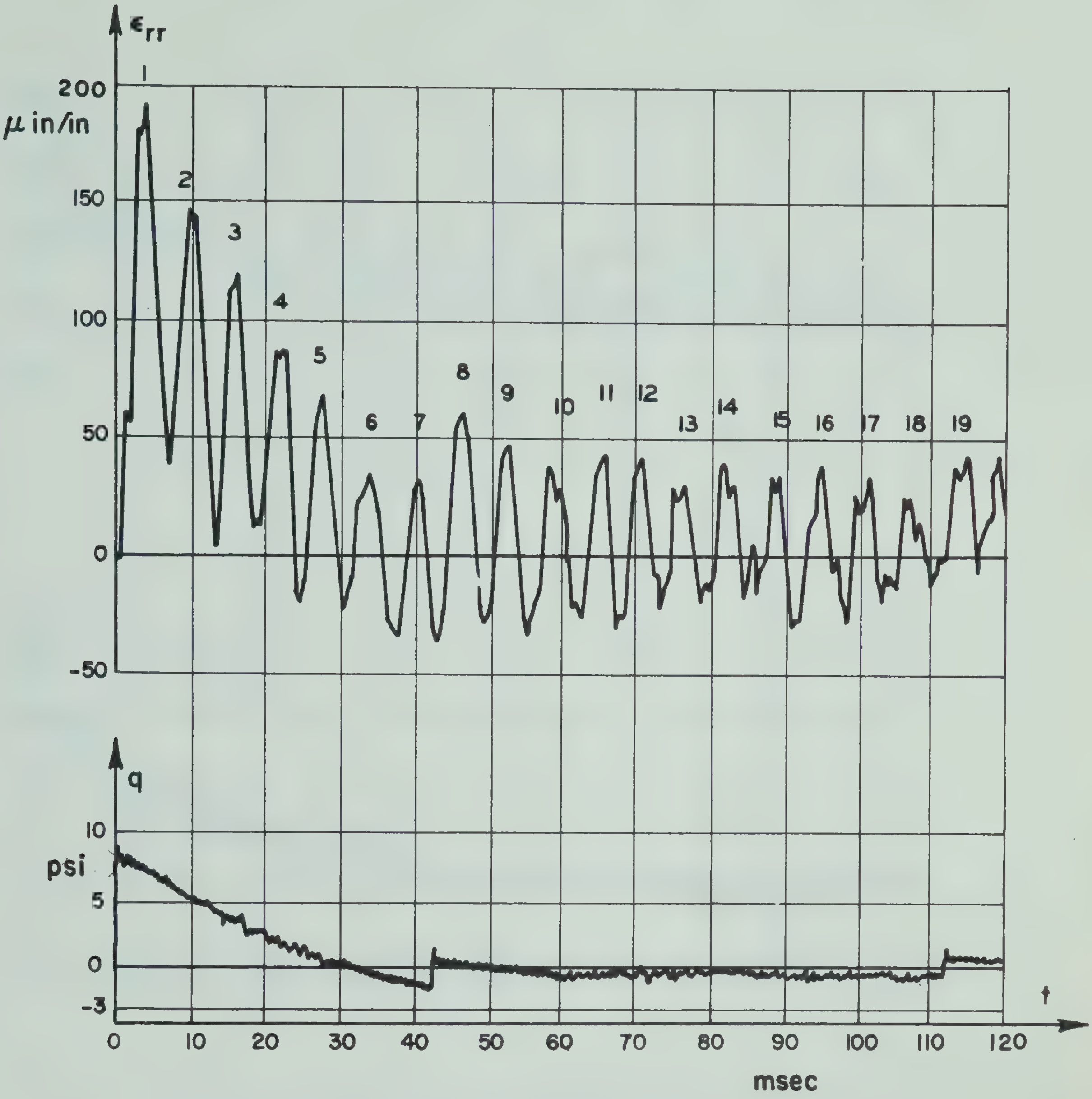

FIG. 5.7 - Plate Experimental Radial Strain at $\rho = 0.377$, $\theta = 15^{\circ}$, sector 1 and Pressure vs. Time for a 1.5 lb. Shot

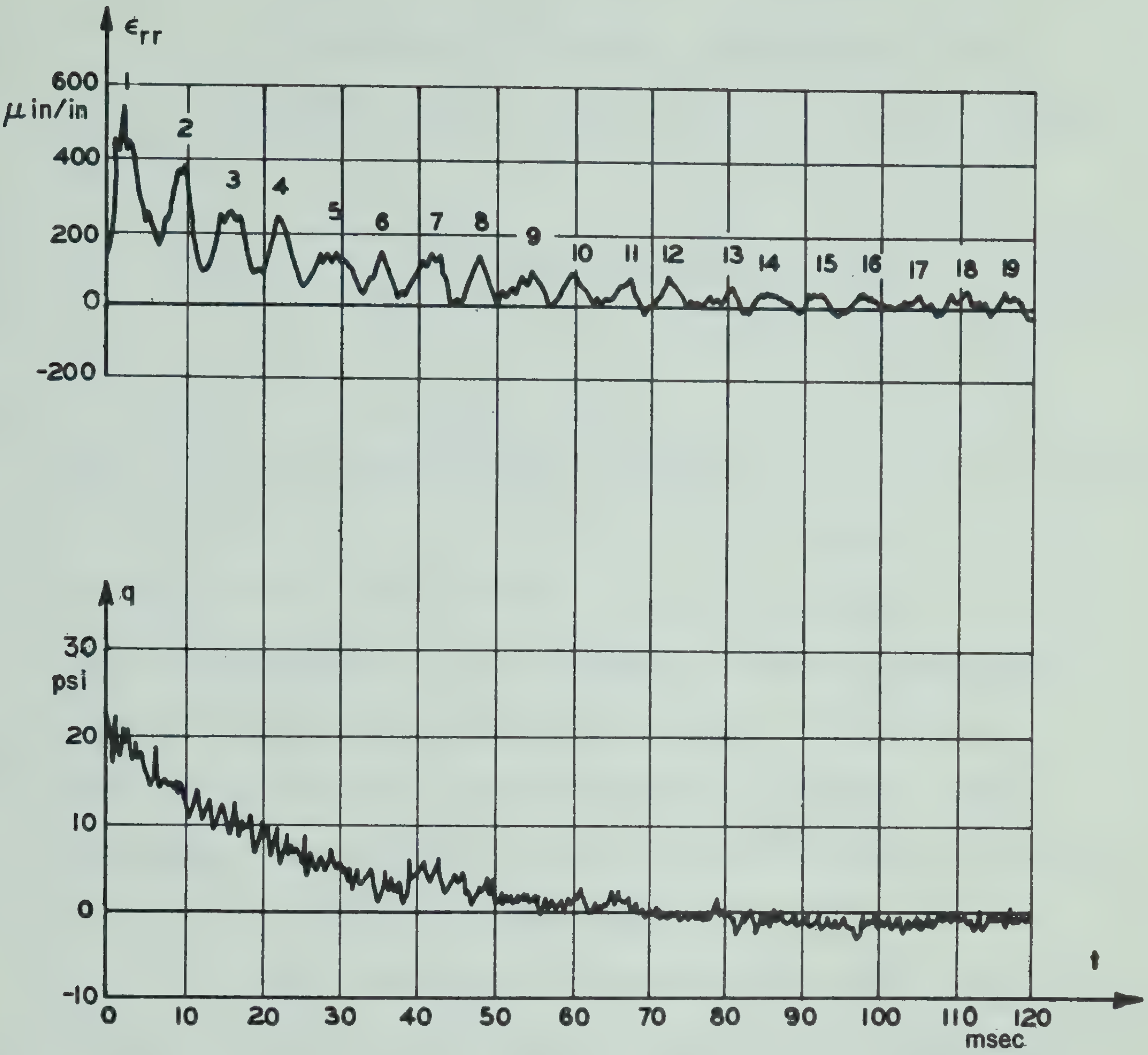

FIG. 5.8 Plate Experimental Radial Strain at $\rho = 0.377$, $\theta = 15^\circ$, sector 1 and Pressure vs. Time for a 6.0 lb. Shot

According to Hubbard and Houbolt, for a simply supported square plate having a Poisson's ratio $\nu = 0.3$,

$$(\zeta_1/\omega_1)_{air} = 0.312\left(\frac{\gamma_{air}}{\gamma}\right)\left(\frac{c}{c_{air}}\right), \quad \frac{\omega a_0}{c_{air}} < 1, \tag{5.7a}$$

$$(\zeta_1/\omega_1)_{air} = 0.350\left(\frac{\gamma_{air}}{\gamma}\right)\left(\frac{c_{air}}{c}\right)\left(\frac{a_0}{h}\right)^2, \quad \frac{\omega a_0}{c_{air}} > 3. \tag{5.7b}$$

In Eqs. (5.7a) and (5.7b) $(\zeta_1/\omega_1)_{air}$ is the ratio of viscous damping of the fundamental mode to critical damping computed for air on one side of the plate only, γ_{air} and γ are the densities of air and plate material, respectively, and $c = \sqrt{E/\gamma}$ is the velocity of sound in the plate material.

At atmospheric pressure and 70°F., $(c_{air})_{atm}$ is approximately 1100 fps and $(\gamma_{air})_{atm}$ is 0.12×10^{-6} lb.sec.^{2} in.$^{-4}$. For the aluminium plate c is 16,600 fps and γ is 0.25×10^{-3} lb.sec.^{2}in.$^{-4}$. For a normally reflected air shock wave, $(\gamma_{air})_{ref}$ and $(c_{air})_{ref}$ are given by [84] as

$$\frac{(\gamma_{air})_{ref}}{(\gamma_{air})_{atm}} = \frac{(7M^2 - 1)3M^2}{(M^2 + 2)(M^2 + 5)} \tag{5.8}$$

and

$$\frac{(c_{\text{air ref}})}{(c_{\text{air atm}})} = \frac{\sqrt{(4M^2 - 1)(M^2 + 2)}}{3M}. \qquad (5.9)$$

Theoretical values of plate viscous damping due to air coupling are given in Table 5.4 for a range of blast loads. Assuming one side of the plate was exposed to atmospheric pressure ($q = 0$ psi) while the other was subjected to air blast loads, theoretical initial values of air damping of the fundamental mode, obtained by adding the damping on each surface given by Eq. (5.7a), ranged from 0.50 per cent of critical for a blast load having $q_o = 4.8$ psi to 0.67 per cent for a blast load having $q_o = 29.8$ psi. Even for a blast load having $q_o = 463$ psi, initial air damping would have been only 1.3 per cent of critical. If Eq. (5.7b) had governed, then air damping would have been slightly larger for all blast overpressures and it would have increased more rapidly with blast overpressure. However, even assuming that Eq. (5.7b) governed, air damping never exceeded 1.6 per cent of critical for a blast load with q_o as large as 29.8 psi.

Experimental values of viscous damping computed from the strain transients in Figs. 5.7 and 5.8 using

$$\frac{\zeta/\omega}{\sqrt{1 - (\zeta/\omega)^2}} = \frac{1}{2\pi(m-n)} \ln\left(\frac{x_m}{x_n}\right), \; n > m, \qquad (5.10)$$

Table 5.4

Plate Theoretical Air Damping On One Surface

q_o(psi)	M	$\frac{(\gamma_{air})_{ref}}{(\gamma_{air})_{atm}}$	$\frac{(c_{air})_{ref}}{(c_{air})_{atm}}$	$\left(\frac{\zeta_1}{\omega_1}\right)_{air}$	
				Eq.(5.7a)	Eq.(5.7b)
0	0	1.0	1.0	0.0023	0.0044
4.8	1.06	1.20	1.02	0.0027	0.0054
8.6	1.12	1.42	1.07	0.0031	0.0067
12.9	1.16	1.60	1.10	0.0033	0.0078
20.9	1.24	1.94	1.14	0.0039	0.0098
29.8	1.31	2.27	1.19	0.0044	0.012
463	2.63	9.27	1.96	0.011	0.080

are given in Table 5.5. In Eq. (5.10) x_m is the amplitude of oscillation m for free vibration. Values of x_m used in the viscous damping calculations were obtained from the forced response strain transients by measuring the strain amplitudes between successive minimum and maximum strain values of the fundamental mode, where the maximum value is labelled oscillation m. In this manner the effect of the time decaying pressure transient on vibration amplitude was partially removed and values of the ratios x_m/x_n for the different strain

[illegible]

[illegible]

[illegible]		[illegible]	[illegible]		[illegible]
[illegible]	[illegible]				
[illegible]	[illegible]	[illegible]	[illegible]		
[illegible]	[illegible]	[illegible]	[illegible]	[illegible]	[illegible]
[illegible]	[illegible]	[illegible]	[illegible]	[illegible]	[illegible]
[illegible]	[illegible]	[illegible]	[illegible]	[illegible]	[illegible]
[illegible]	[illegible]	[illegible]	[illegible]	[illegible]	[illegible]
[illegible]	[illegible]	[illegible]	[illegible]	[illegible]	[illegible]
[illegible]	[illegible]	[illegible]	[illegible]	[illegible]	[illegible]

[illegible]

amplitudes were thought to approximate closely the related free vibration values.

Table 5.5

Plate Experimental Viscous Damping

Peak m to Peak n		1,2	1,3	1,4	1,5	2,4	3,5
ζ_1/ω_1	q_o= 8.6psi	0.087	0.038	0.049	0.028	0.030	0.023
	q_o=20.9psi	0.15	0.096	0.065	0.079	0.026	0.062
Peak m to Peak n		8,9	8,10	8,11	11,12	11,13	12,13
ζ_1/ω_1	q_o= 8.6psi	0.038	0.022	0.018	0	0.025	0.049

Damping measurements for the 1.5 lb. shot commencing at the maximum strain levels occurring for oscillations 1, 8, and 11 which were associated with shock waves arriving at 0, 42 and 111 msec., indicate that viscous damping decayed with the stress amplitude but was considerably larger than the values estimated for air damping at all blast overpressures. Comparison of the damping values for the 1.5 and 6.0 lb. shots when q_o was 8.6 and 20.9 psi, respectively, reveals the nearly linear increase of initial values of viscous damping with stress amplitude. The rapid decay with

time of viscous damping for both shots indicates that initial values of damping could have been considerably larger than the values measured from the first two oscillation peaks. This linear increase in viscous damping with stress amplitude did not occur for the 10.0 lb. shot when plate damping levels were nearly equivalent to those for the 6.0 lb. shot. It was thought that this was a result of a decrease in the plate edge clamping friction. This is discussed further in Section 5.2.5.

The strain response magnitudes of the higher modes, as shown in Fig. 5.7, appear to have remained at least as significant relative to the fundamental mode magnitude after several oscillations of the fundamental mode as they were for the first oscillation. This indicates that the higher modes were subjected to considerably less viscous damping than the fundamental mode, because of the smaller amplitudes associated with the higher modes.

It was considered from these results that most of the experimental damping resulted from the interface damping which occurred at the plate edges in the mounting assembly. Since the experimental values of viscous damping were so large, it is possible that these values represent not only damping but also the effect of the presence of in-plane tensile strains which

are discussed in Section 5.2.5. However, Lassiter and Hess [1] found that combined structural and radiation damping increased rapidly with stress at higher maximum stress levels for a rectangular panel subject to random acoustic input and obtained similarly large values of damping at similar stress levels.

Coupling between the symmetric transverse modes due to damping was not considered to be important, even at these high damping levels, since the modal frequencies were 'well separated'.

5.2.4 Displacement. The theoretical variation of static dimensionless central displacement with edge clamping factor β_1^i is shown in Fig.5.9 for the values given in Tables 5.1. Static central deflections measured at 10 and 20 psi show that values of β_1^i decreased slightly with increased load. While the value of β_1^i a/D was approximately 8 for the static loads as indicated by central deflections, it decreased to between 0 and 0.523 for the blast loads as indicated by values of fundamental frequencies. The reduction of edge stiffness for the blast loads resulted for two reasons. Firstly, for the dynamic loads the mount was supported against displacement by the 8 x 4 in. I beams at a distance of approximately 11 in. from the plate edges, while for the static loads the

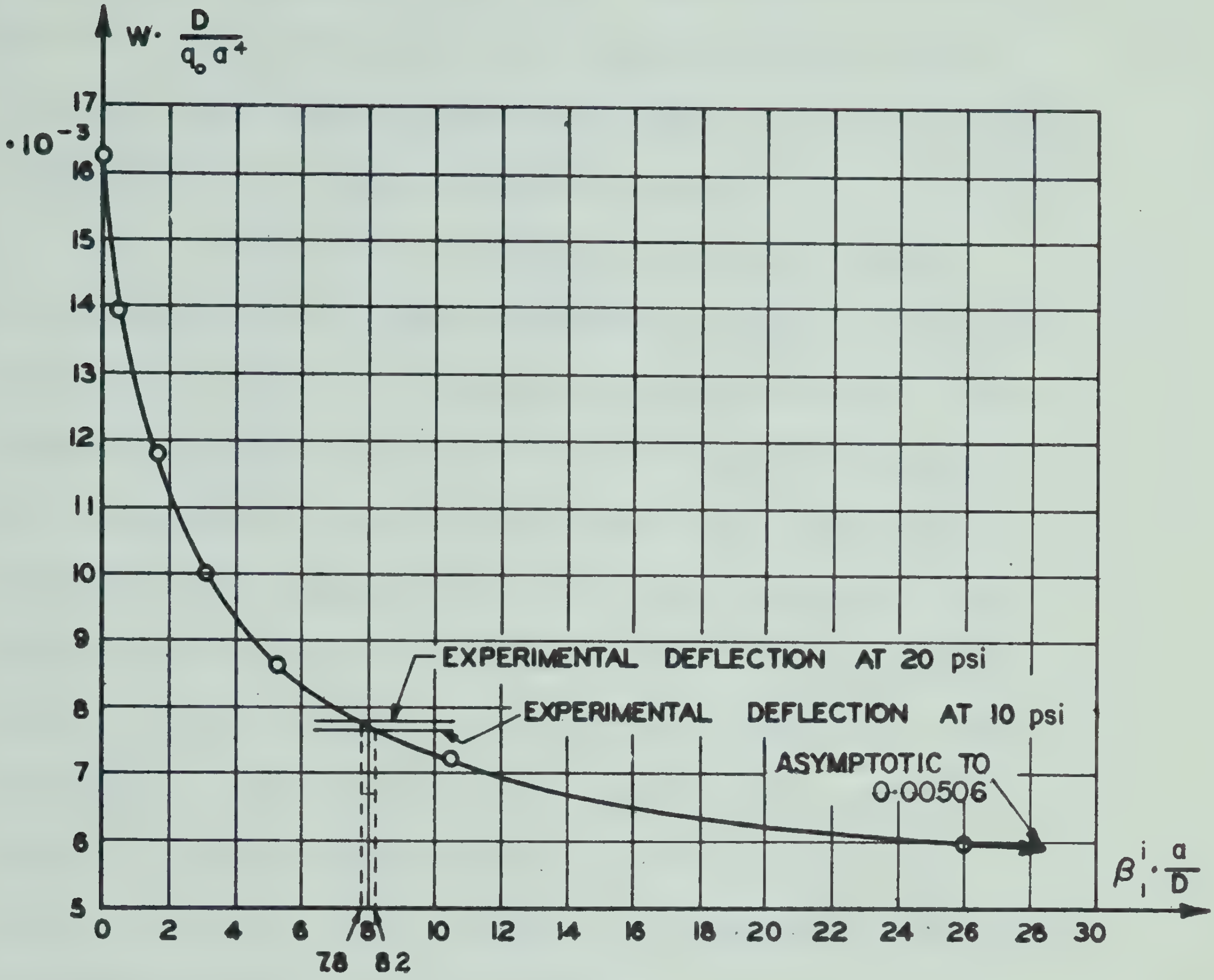

FIG. 5.9 Theoretical Variation of Static Central Displacement with Clamping Factor β_1^i for a Square Plate

mount was supported only 3 in. from the plate edges. Further, the complete 6 ft. diameter section was subjected to blast loads while only the 30 in. square plate was subjected to static loads.

Theoretical and experimental central displacements vs. time are shown in Figs. 5.10 and 5.11 for 0.5 and 1.5 lb. shots, respectively. Since maximum response occurred during the first cycle of the fundamental mode, theoretical and experimental results were compared for the first few cycles only. Theoretical transient displacements computed using $\beta_1^i \, a/D = 0.523$ and $\zeta_i/\omega_i = 0.1$ agree well with the results for the 0.5 lb. shot, however for the 1.5 lb. shot the experimental clamping was slightly more flexible and the viscous damping exceeded 10 per cent of critical for the first cycle.

Dimensionless central displacements are shown in Figs. 5.12 for static and blast loads. Since ratios of maximum dynamic-to-static displacement exceeded the maximum dynamic load factor of two for a flat pulse, it is evident that the elastic edge clamping was more flexible for the blast loads. Non-linear effects were almost unnoticeable for static central displacements ranging up to one-tenth the plate thickness although there appeared to be slight non-linear softening, likely resulting from an edge

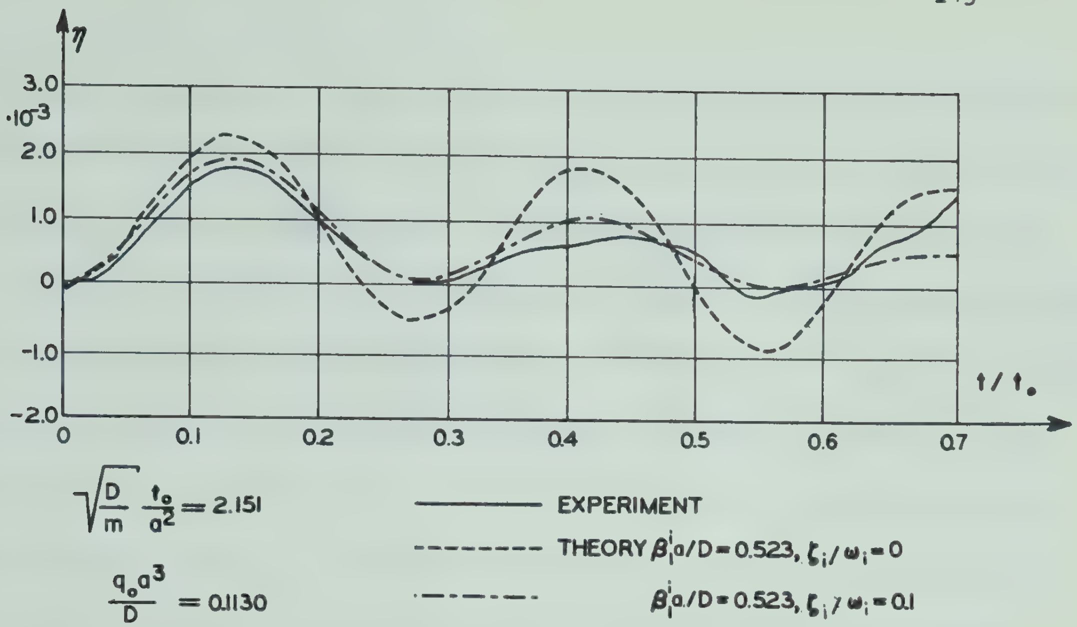

FIG. 5.10 Plate Theoretical and Experimental Central Displacement vs. Time for a 0.5 lb. Shot

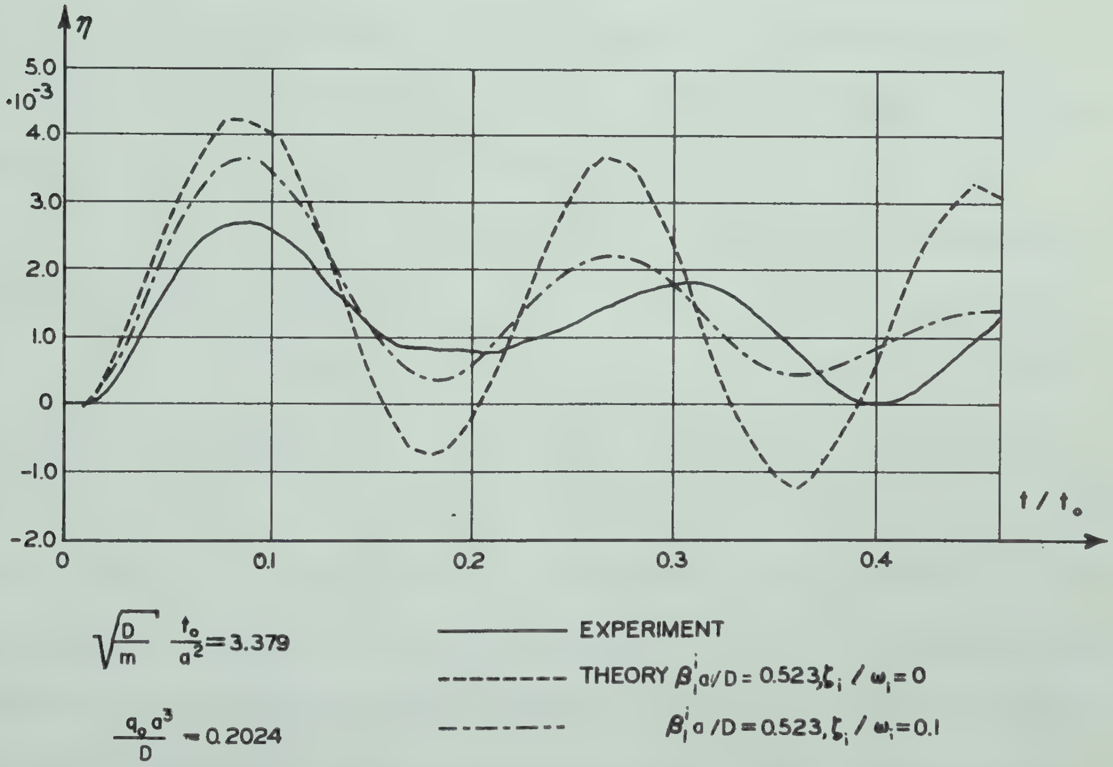

FIG. 5.11 Plate Theoretical and Experimental Central Displacement vs. Time for a 1.5 lb. Shot

flexural softening. However, there was a general hardening of plate response with increasing blast load for all values of w/h with one exception. This hardening was observed previously by Lassiter and Hess [1] for a rectangular plate subjected to acoustical loading. Theoretical results given by Bauer [86] for a simply supported square plate with a stress-free boundary and $h/a_o = 0.08$ ($h/a_o = 0.05$ for the experimental plate) indicate that nonlinear hardening effects for a flat pressure pulse are not significant until the central displacement-to-thickness ratio exceeds 0.3. Consequently, this hardening nonlinearity is probably a result of a combination of the increase in damping with blast load and the softening in the ratio of edge-to-central transverse displacement discussed below.

Ratios of maximum transverse edge displacements-to-central displacements for the blast loads are shown in Fig. 5.13 for the edge positions labelled 3 and 6 in Fig. 5.2. Displacements measured at the other boundary positions 1, 2 and 5, had values ranging up to 30 per cent smaller than the values measured at position 3. However, the increase in the proportion of edge-to-central displacement with the load was observed at all boundaries. This increase was noticed for the static loads as well, but the static edge displacements were approximately one-tenth the value of the dynamic edge displacements as a result of the two different loading arrangements. These results indicate that an elastic edge

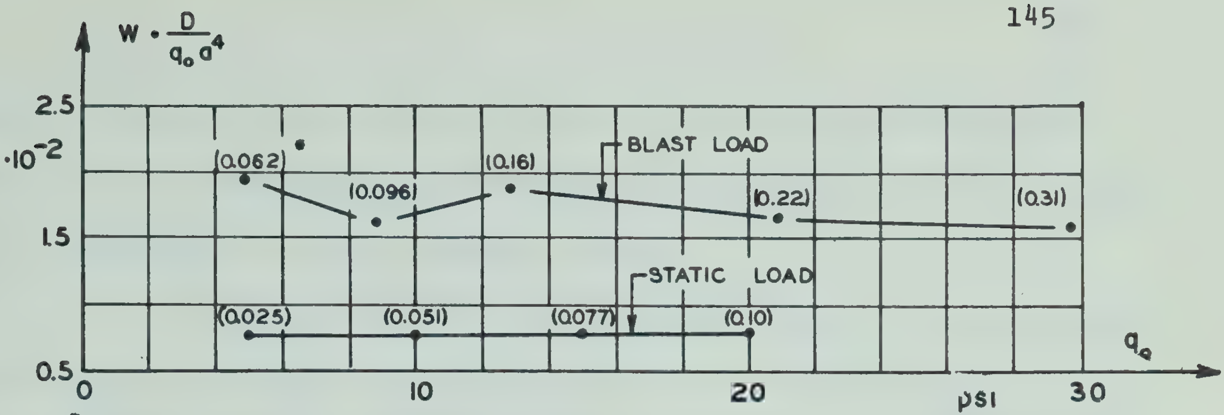

*NUMBERS IN BRACKETS REPRESENT RATIOS OF MAXIMUM CENTRAL DISPLACEMENT TO PLATE THICKNESS w/h.

FIG. 5.12 Plate Experimental Static and Maximum Dynamic Central Displacements vs. Load

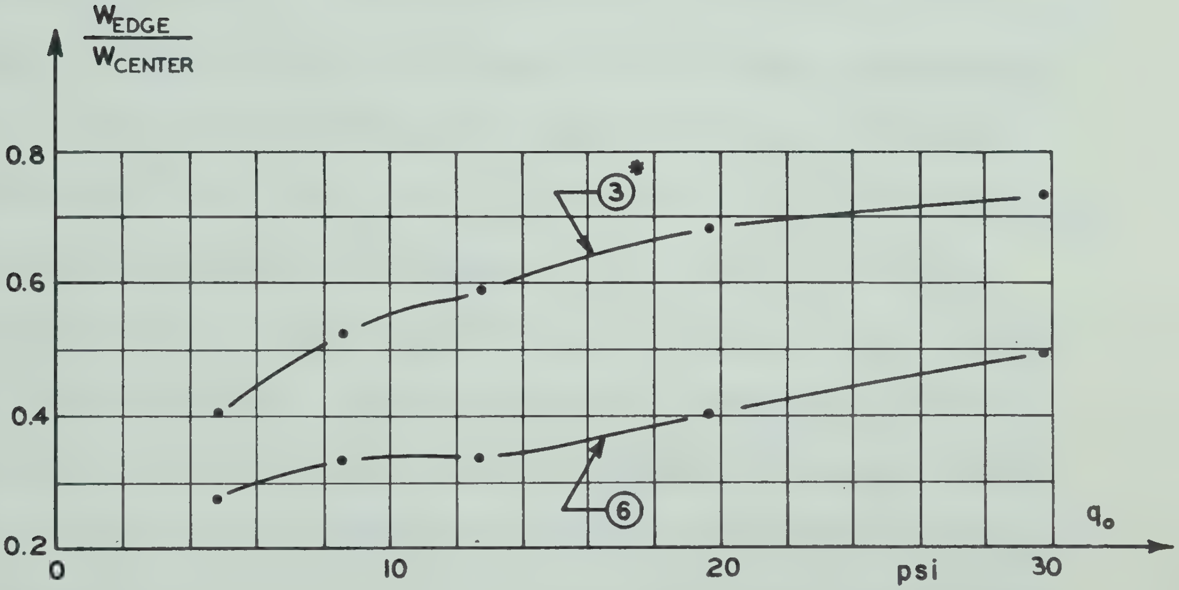

*LOCATIONS OF EDGE DEFLECTION MEASUREMENTS ARE SHOWN IN FIG. 5·2

FIG. 5.13 Plate Experimental Ratio of Maximum Dynamic Edge Displacement-to-Central Displacement vs. Load

condition relating transverse displacement to Kirchoff's effective transverse shear force should also be considered theoretically for the dynamic case.

Integration of accelerometer records corroborated the values of edge motion obtained from the linear potentiometer records and indicated that the wooden mount for the potentiometer which measured central displacement followed the edge displacement motion fairly rigidly.

Fundamental frequencies measured at the plate center and the boundary positions labelled 1 and 5 in Fig. 5.2 are given in Table 5.6. The fundamental frequency at the plate center for the first peak-to-peak cycle was consistently lower than the other measured frequencies. A freqency reduction to 161 cps could be explained by a reduction in the elastic clamping constant β_1 so that the boundary approached the simply supported condition. Large values of viscous damping could reduce the frequency further. However, a reduction in the fundamental frequency from 161 to 147 cps, for example, requires a linear viscous damping of 41 per cent of critical, which is considerably larger than measured values. Consequently, this low initial plate frequency probably resulted from the fact that initially the edge displacement did not vanish completely, as noted previously, and also that the edge conditions were time-dependent.

Table 5.6

Plate Experimental Fundamental Frequencies

			Frequency $\omega_1/2\pi$ (cps ± 4 cps)				
Cycle peak-to-peak	1,2	Plate Center	150	143	143	136	134
		Edge 1	167	167	161	157	162
		Edge 5	169	169	161	154	147
	2,6	Plate center	166	168	160	158	154
		Edge 1	166	165	161	164	157
		Edge 5	165	162	161	164	154
			4.8	8.6	12.9	20.9	29.8
			q_o (psi)				

5.2.5 Strain. Typical experimental bending and membrane strains vs. time are shown in Fig. 5.14 for a 1.5 lb. shot. The frequency of the first peak-to-peak cycle of the fundamental mode was approximately 143 cps for the bending strain while for the membrane strain it was 166 cps. Comparison of these frequencies with the frequencies given in Table 5.6 for q_o = 8.6 psi indicates that the membrane strain frequency had the same value as the plate edge transverse motion frequency. Similar correlations between membrane and transverse edge motion frequencies occurred for the other blast loads.

[illegible]

[illegible]

[illegible]	[illegible]							
[illegible]	[illegible]	[illegible]	[illegible]	[illegible]	[illegible]	[illegible]		[illegible]
[illegible]	[illegible]	[illegible]	[illegible]	[illegible]		[illegible]	[illegible]	
[illegible]	[illegible]	[illegible]	[illegible]	[illegible]		[illegible]		
[illegible]	[illegible]	[illegible]	[illegible]	[illegible]	[illegible]	[illegible]		
[illegible]	[illegible]	[illegible]	[illegible]	[illegible]		[illegible]	[illegible]	
[illegible]	[illegible]	[illegible]	[illegible]	[illegible]		[illegible]		
[illegible]	[illegible]	[illegible]	[illegible]	[illegible]				
[illegible]								

[illegible]

[illegible]

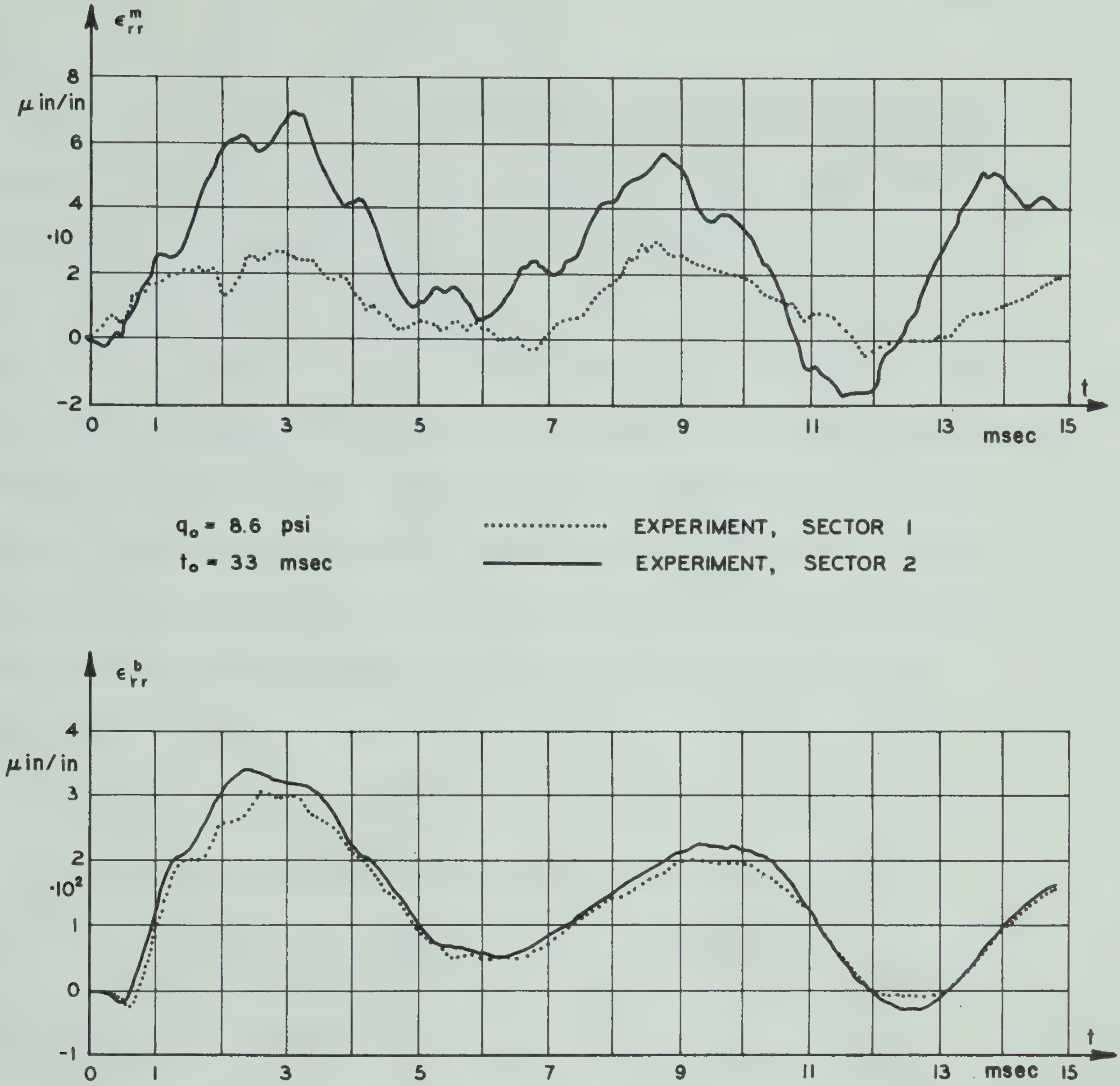

FIG. 5.14 Plate Experimental Bending and Membrane Strains vs. Time at ρ = 0.047, θ = 0° for a 1.5 lb. Shot

Typical values of maximum bending and membrane strains recorded at the ten positions on the plate surface having strain gauges front and back which are shown in Fig. 5.2, are given in Table 5.7 for a static load of 10 psi and in Table 5.8 for a blast load of 8.6 psi initial reflected overpressure. These results show that although membrane strains were quite small in proportion to associated bending strains for static loads, they had significant tensile values for blast loads even when the maximum center displacement-to-plate thickness ratio was less than 0.1.

Table 5.7

Plate Experimental Bending and Membrane Strains

for Uniform Static Load of 10 psi

Position r,θ (in.-deg.)	Sector	ε_{rr}^{b}	ε_{rr}^{m}	$\varepsilon_{\theta\theta}^{b}$	$\varepsilon_{\theta\theta}^{m}$
		(με)			
1 - 0	1	179	-5	192	7
	2	193	11	182	-2
8 - 0	1	91	0	123	7
	2	80	8	100	2
12 - 30	1	-59	-3	119	0
	2	-58	-2	114	-5
8 - 45	1	58	0	166	0
	2	50	-8	168	2
16.5- 45	1	-145	3	101	0
	2	-134	14	94	-7

Table 5.8

Plate Experimental Maximum Bending and Membrane Strains for Uniform Blast Load, $q_o = 8.6$ psi and $t_o = 0.033$ sec.

Position r,θ (in.-deg.)	Sector	ε_{rr}^{b}	ε_{rr}^{m}	$\varepsilon_{\theta\theta}^{b}$	$\varepsilon_{\theta\theta}^{m}$
		(με)			
1 - 0	1	305	26	320	53
	2	340	69	305	34
8 - 0	1	185	25	240	62
	2	155	56	185	37
12 - 30	1	-45	42	235	31
	2	-95	51	225	35
8 - 45	1	100	92	315	39
	2	100	54	325	64
16.5- 45	1	-180	50	220	49
	2	-195	44	215	55

The large variation in the values of membrane strains recorded at the same r,θ positions in sectors 1 and 2, in comparison with the reasonably symmetric values for bending strains, and the correspondence of the values of the plate membrane and transverse edge frequencies, indicate that the membrane strains principally resulted from a nonsymmetric boundary stretching motion associated with the boundary transverse motion. In contrast to this

conclusion, Eikrem and Doige [87], who also observed membrane strains for the small deflection response of a simply supported square plate to blast loads in a recent test conducted at DRES, seemingly attributed these membrane strains to some coupling effect with the transverse motion of the plate itself.

Results given in Section 5.2.4 which showed that transverse edge motion was not symmetric and was approximately ten times larger for blast loads than comparable static loads, further corroborate the postulate that the membrane strains result from in-plane boundary motion. Using this postulate these results explain both the increased magnitude of the membrane strains for the blast loads in comparison to the static loads and the nonsymmetry of the membrane strains. Since a simultaneous in-plane outward displacement of only 0.00075 in. at each of two opposite boundaries was required to produce a tensile membrane strain of 50 $\mu\varepsilon$, it is quite conceivable that this plate stretching could result from boundary rotation in conjunction with an absence of free slippage of the experimental plate between the edge clamping plates.

Plots in Fig. 5.15 of the radial and circumferential bending strains near the plate corner vs. load reveal the general nonlinear softening of the edge support resistance to rotation normal to the boundaries with increasing blast loads.

Variation of membrane strains recorded near the plate corners with blast loading is shown in Fig. 5.16. Generally, the membrane strains reduced nonlinearily with increasing blast load. However, the in-plane motion of the edge clamping plates probably increased nonlinearly with the load, in conjunction with edge transverse motion. Therefore, the boundary clamping friction must have decreased with increasing load as was concluded in Section 5.2.3.

The present theoretical solution can predict correct flexural mode shapes for the experimental plate only if the membrane and bending stress actions were completely uncoupled. Theoretical results given by Dawe [47] for the response of rectangular plates show that the degree of coupling between the membrane and bending stress actions depends not only upon the magnitude of the membrane stresses and their distribution but also upon the plate edge conditions. Even if there was complete uncoupling for the experimental plate response, the presence of the membrane stresses would change the modal frequencies of transverse vibration. Results given by Dawe for $\nu = 0.3$ show that transverse vibration frequencies decrease with the ratio of the membrane stress factor $K = \frac{\sigma(2a_o)^2\, h}{\pi^2 D}$ to the critical

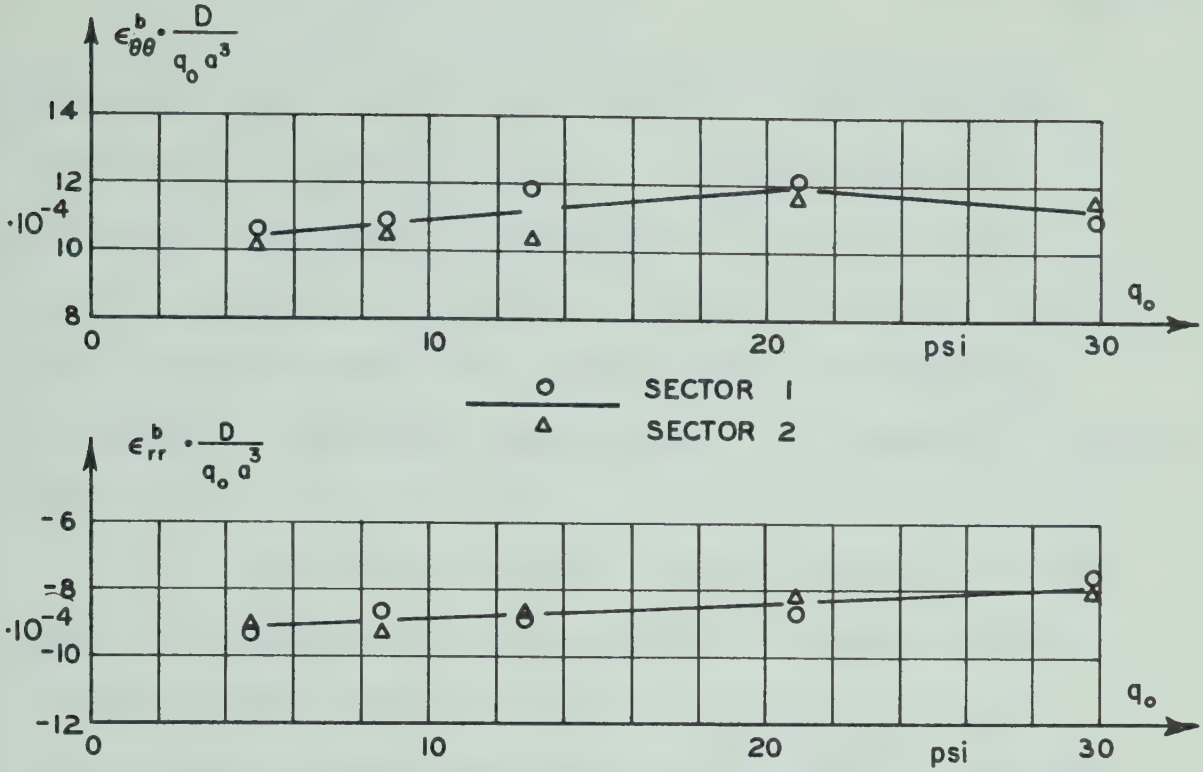

FIG. 5.15 Plate Experimental Maximum Dynamic Bending Strains vs. Load at $\rho = 0.778$, $\theta = 45^{\circ}$

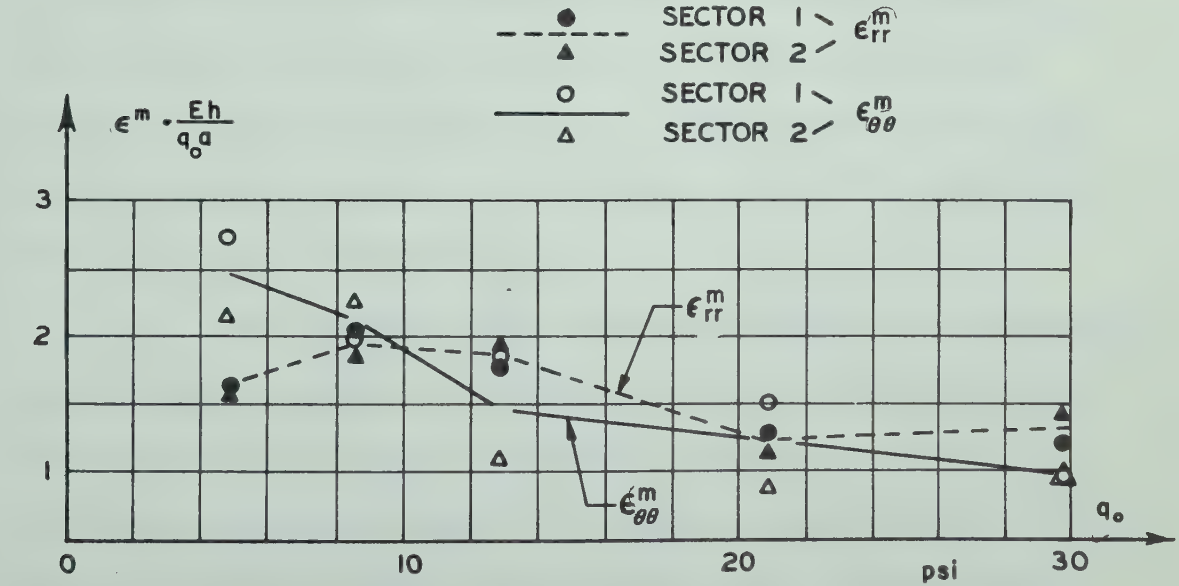

FIG. 5.16 Plate Experimental Maximum Dynamic Membrane Strains vs. Load at $\rho = 0.778$, $\theta = 45^{\circ}$

buckling stress factor K_{cr}, where K is positive for compressive membrane stress σ. A modal frequency approaches zero when K approaches K_{cr} for the mode, as was pointed out for shallow shells in Section 1.3.2. Dawe indicates that mode shapes remain essentially unchanged if the modal frequencies vary linearly with $\sqrt{K}$.

According to Dawe, the mode shapes of simply supported square plates subjected to uniform uniaxial stress remain unchanged for all values of $K < K_{cr}$ and the modal frequencies vary as $\sqrt{1 - K/K_{cr}}$. For the fundamental mode of a simply supported square plate $K_{cr} = 4$. Consequently, for a uniform uniaxial strain of 50 $\mu\varepsilon$ in the experimental plate, $K = 0.085$ and the theoretical fundamental frequency increases by 1.05 per cent from the value given by the present theory for simply supported edges in which the effect of membrane stresses is not considered.

Dawe showed that the mode shapes of a clamped square plate subjected to uniform biaxial stresses are affected only slightly by these stresses for $|K| \leq 5$. His results indicate that the fundamental flexural frequency of the experimental plate with clamped edges would increase by approximately 0.8 per cent from the value given by the present theory for a uniform biaxial strain of 50 $\mu\varepsilon$.

From these results it appears that the flexural response of the experimental plate to blast loads can be predicted reasonably accurately using the present theory.

5.2.6 Stress Couples. Experimental values of static and dynamic flexural stress couples recorded near the plate center vs. load are shown in Fig. 5.17. These stress couples were computed from the 'true' bending strains with membrane strains removed. Although there appears to be some plate elastic hardening for incident blast loads between 4.8 and 8.6 psi, most nonlinearity is within the pressure measurement errors. Consequently, the effect of the nonlinear decay of membrane strain and the elastic softening of the edge clamping with blast load must have been offset by increased viscous damping.

Dimensionless static experimental and maximum dynamic experimental and theoretical flexural stress couples formulated in Appendix A.1 are plotted along the radial lines $\theta = 0°$, 15°, 30° and 45° in Figs. 5.18 to 5.21, respectively. The experimental values were obtained for a 10 psi static load and an 8.6 psi reflected overpressure blast load. Since all dynamic membrane strains were tensile, dynamic stress couples calculated from 'true' bending strains were

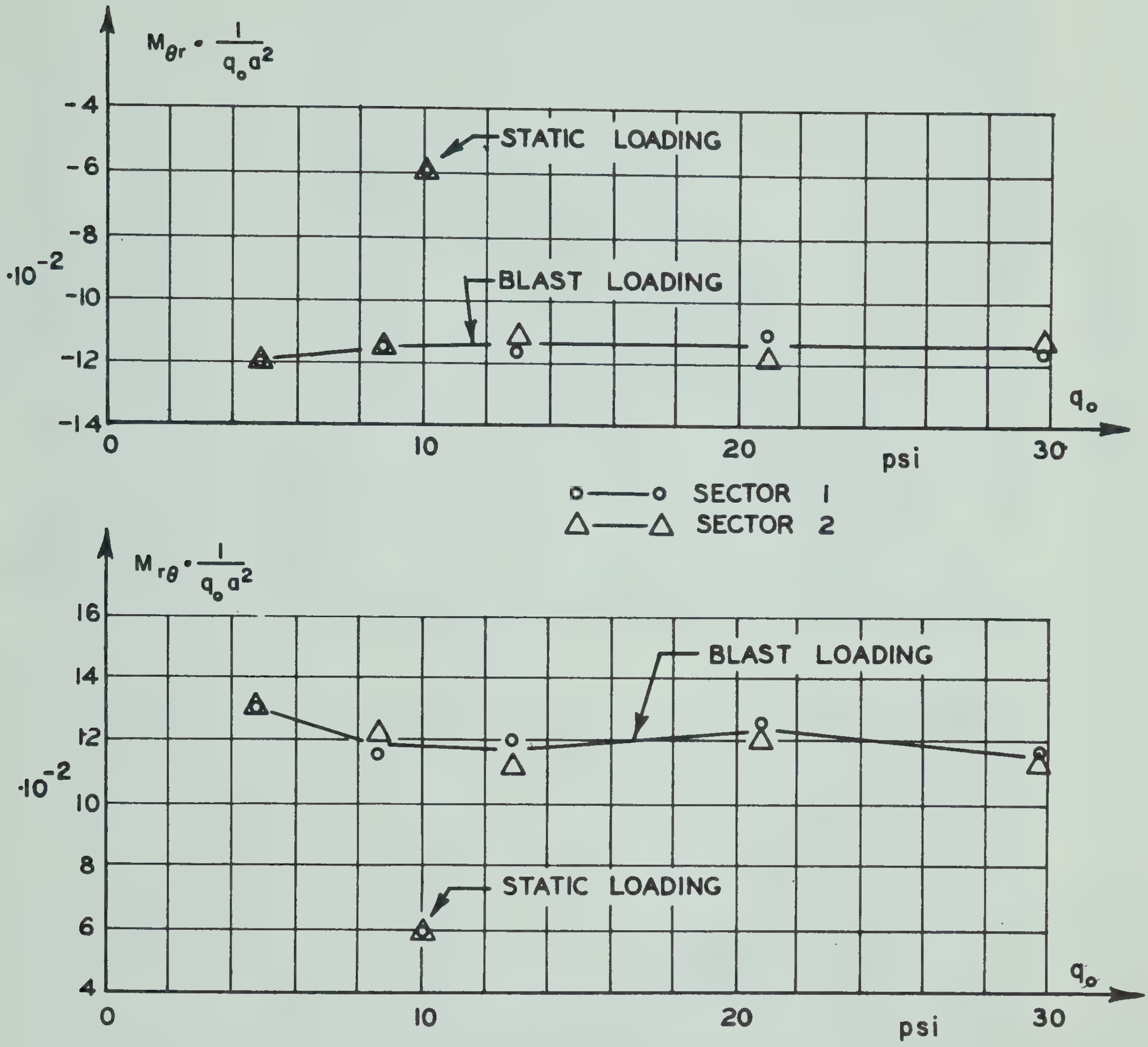

FIG 5.17 Static and Maximum Dynamic Plate Experimental Flexural Stress Couples vs. Load at $\rho = 0.047$, $\theta = 0^{\circ}$

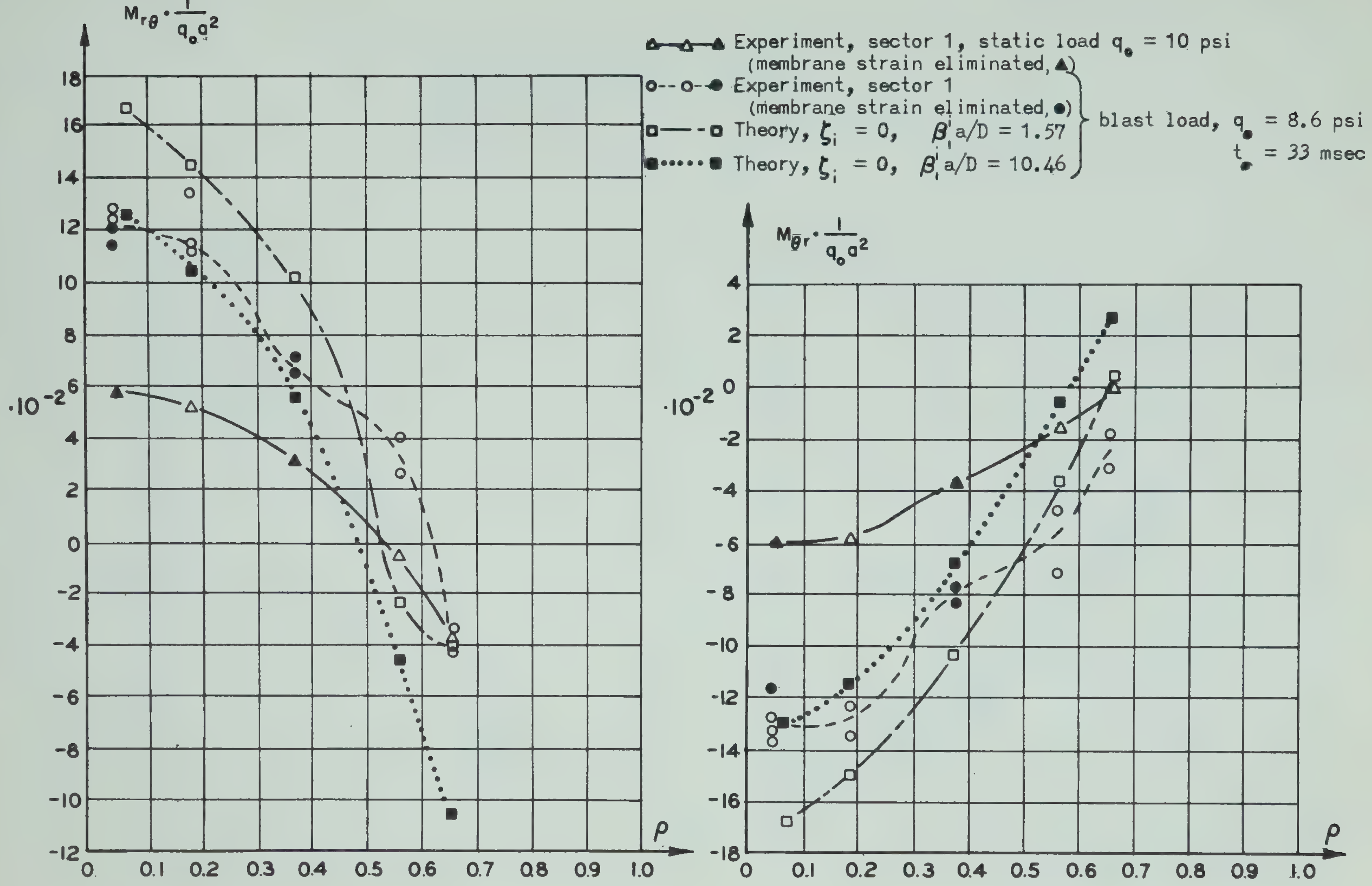

FIG 5.18 Plate Static Experimental and Maximum Dynamic Experimental and Theoretical Flexural Stress Couples on $\theta = 0^o$ for a 1.5 lb. Shot

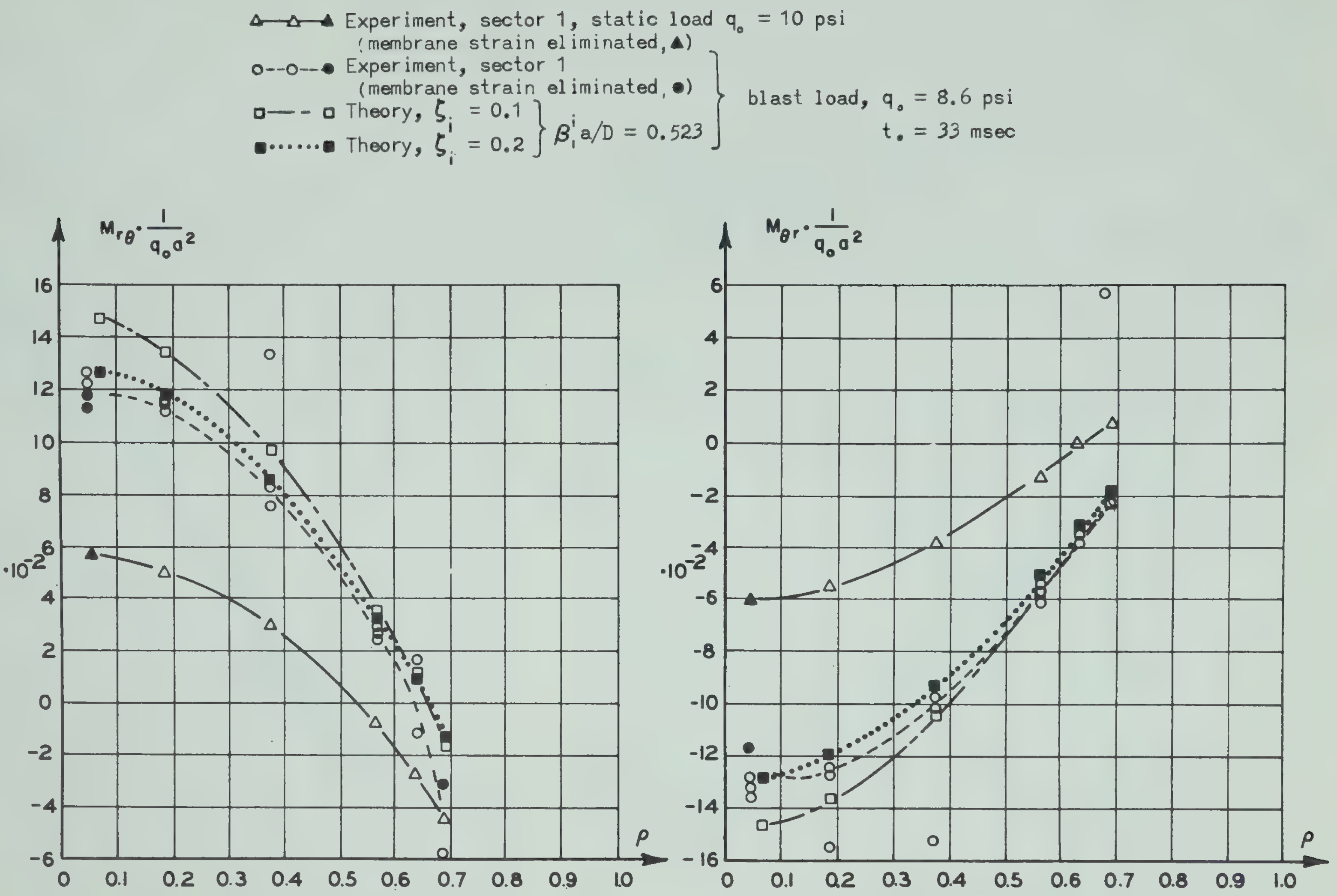

FIG. 5.19 Plate Static Experimental and Maximum Dynamic Experimental and Theoretical Flexural Stress Couples on $\theta = 15^{\circ}$ for a 1.5 lb. Shot

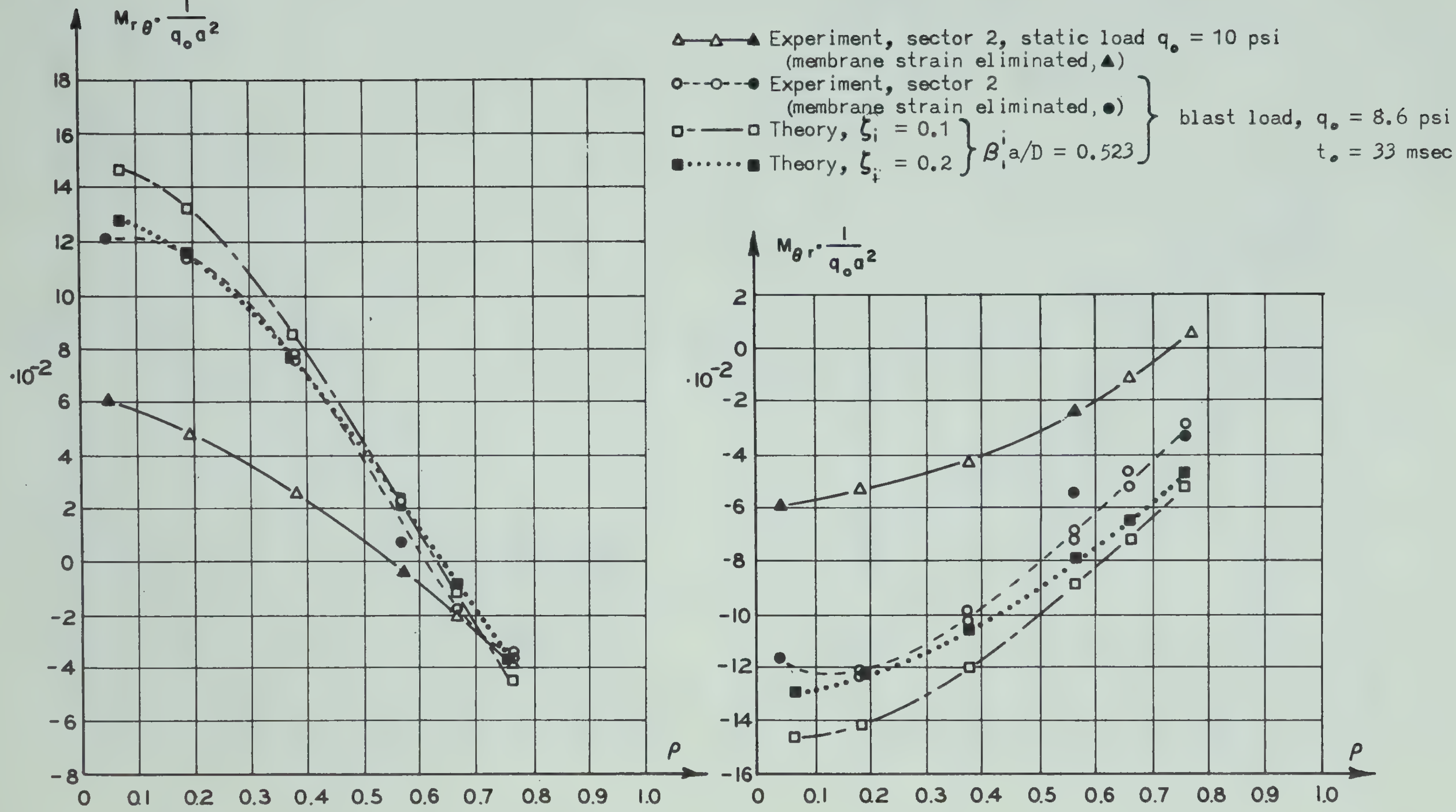

FIG. 5.20 Plate Static Experimental and Maximum Dynamic Experimental and Theoretical Flexural Stress Couples on $\theta = 30^{\circ}$ for a 1.5 lb. Shot

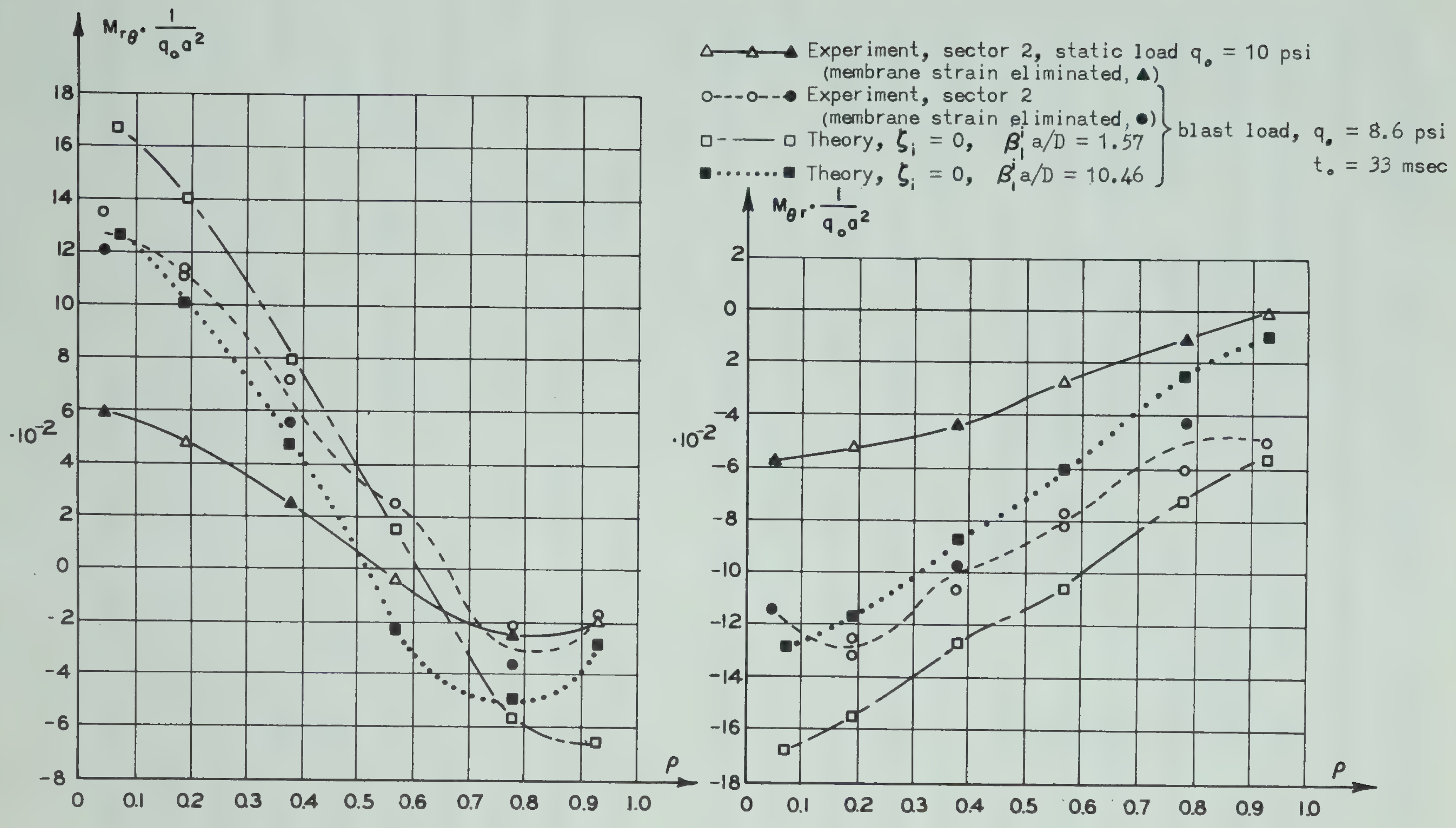

FIG. 5.21 Plate Static Experimental and Maximum Dynamic Experimental and Theoretical Flexural Stress Couples on $\theta = 45^{\circ}$ for a 1.5 lb. Shot

always smaller than stress couples calculated from 'apparent' bending strains which were measured on the back of the plate remote from the blast. The uneven variation in the experimental maximum dynamic stress couples with radius appears to result entirely from the elimination of membrane strains from the stress couple calculations at some positions but not at others. The smooth variation in experimental maximum dynamic stress couples shown in Fig. 5.19 is likely representative of the true variation assuming uniform membrane strains. However, the true magnitudes of the dynamic stress couples would be approximately 0.5 ordinate divisions smaller in magnitude than the stress couples given in this figure.

Theoretical stress couple variations along the four radial lines are shown for edge clamping values β_1^i a/D = 0.523, 1.57 and 10.46 and for viscous damping values ζ_i/ω_i = 0, 0.1 and 0.2. Theoretical results calculated using an edge rigidity of β_1^i a/D = 10.46 shown in Figs. 5.18 and 5.21 appear to give the best agreement with the static experimental results. Stress couples computed for β_1^i a/D = 0.523 and ζ_i/ω_i = 0.2 shown in Figs. 5.19 and 5.20 give the best agreement with the peak magnitudes of stress couples recorded for the blast loading.

Theoretical and experimental flexural stress couples vs. time are compared at four different positions on the plate in Figs. 5.22 through 5.25 for the blast load having $q_o = 8.6$ psi and $t_o = 33$ msec. Experimental stress couples were calculated from 'true' bending strains in Figs. 5.22, 5.23 and 5.25. Theoretical flexural stress couples could not be computed accurately in the region $0<\rho<0.06$. However, experimental results in Fig. 5.18 for uniform static loads indicate that the stress couples varied little with radius for $\rho < 0.1$. Consequently, comparisons in Fig. 5.22 of theoretical stress couples computed at $\rho = 0.0707$ with experimental stress couples computed at $\rho = 0.0471$ should be valid for uniform dynamic loads. Membrane strains were not eliminated from the experimental stress couple calculations at $\rho = 0.5657$, $\theta = 45°$ in Fig. 5.24. This gave larger magnitude experimental stress couples which agree quite closely with the theoretical values. Theoretical and experimental results agree reasonably well at the other positions, however for this blast load initial experimental viscous damping appeared to be greater than 10 per cent of critical and the edge clamping value of $\beta_1^i a / D$ was less than 0.523.

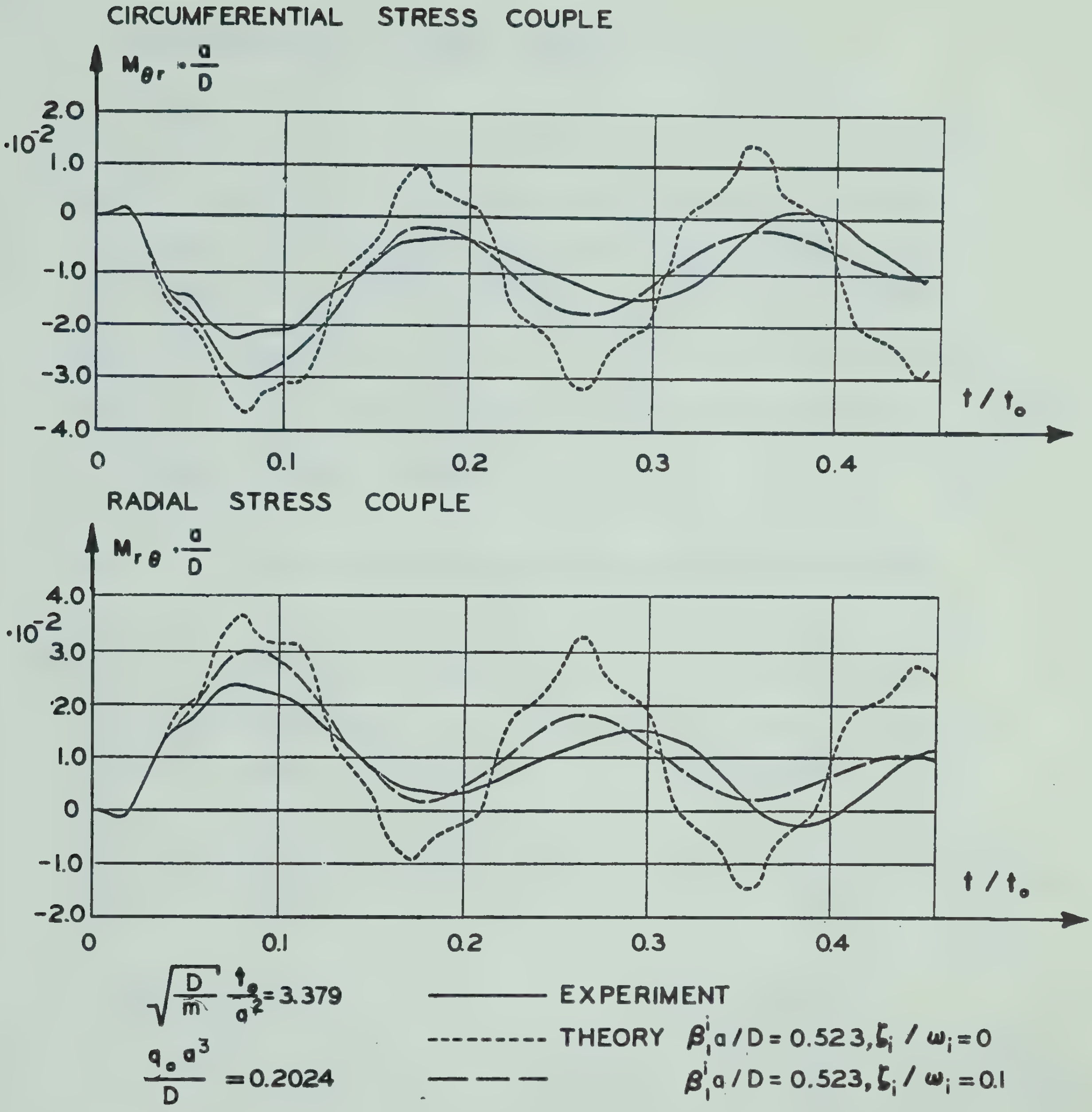

FIG. 5.22 Plate Experimental and Theoretical Flexural Stress Couples vs. Time at $\rho = 0.0471$, $\theta = 0^{\circ}$ and $\rho = 0.0707$, $\theta = 0^{\circ}$, respectively, for a 1.5 lb. Shot

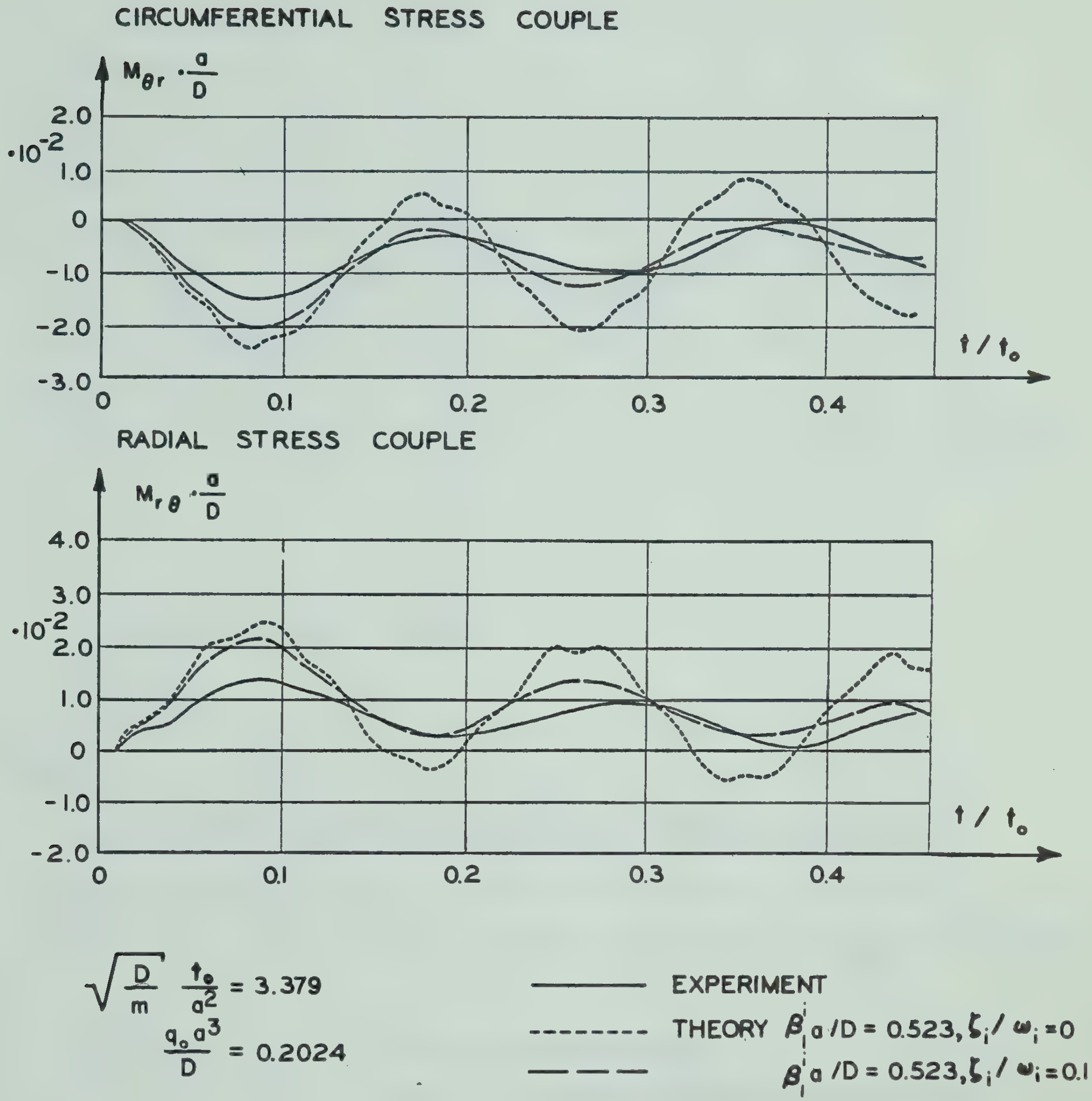

FIG. 5.23 Plate Experimental and Theoretical Flexural Stress Couples vs. Time at $\rho = 0.3771$, $\theta = 0^o$ for a 1.5 lb. Shot

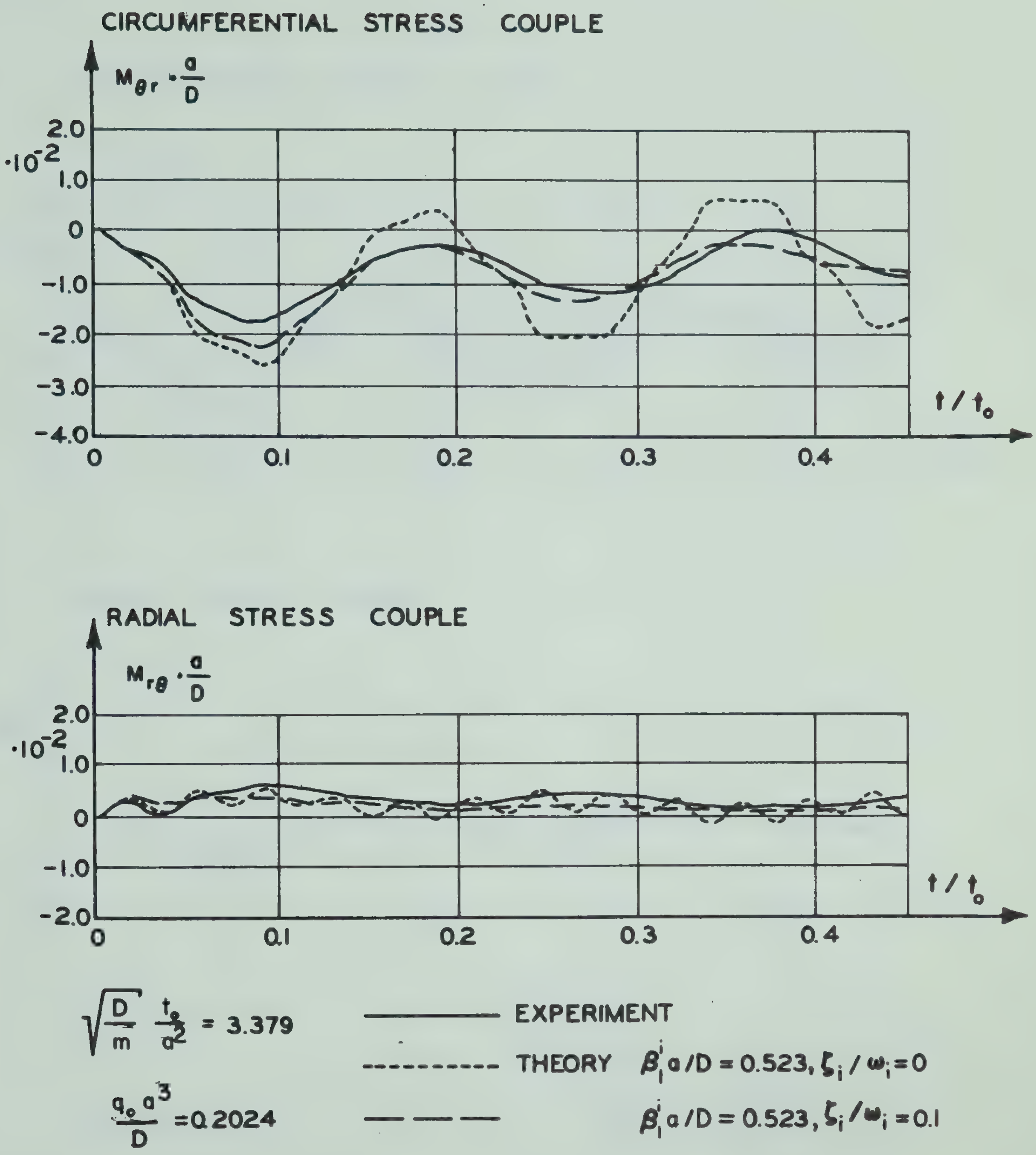

FIG. 5.24 Plate Experimental and Theoretical Flexural Stress Couples vs. Time at $\rho = 0.5657$, $\theta = 45^{\circ}$ for a 1.5 lb. Shot

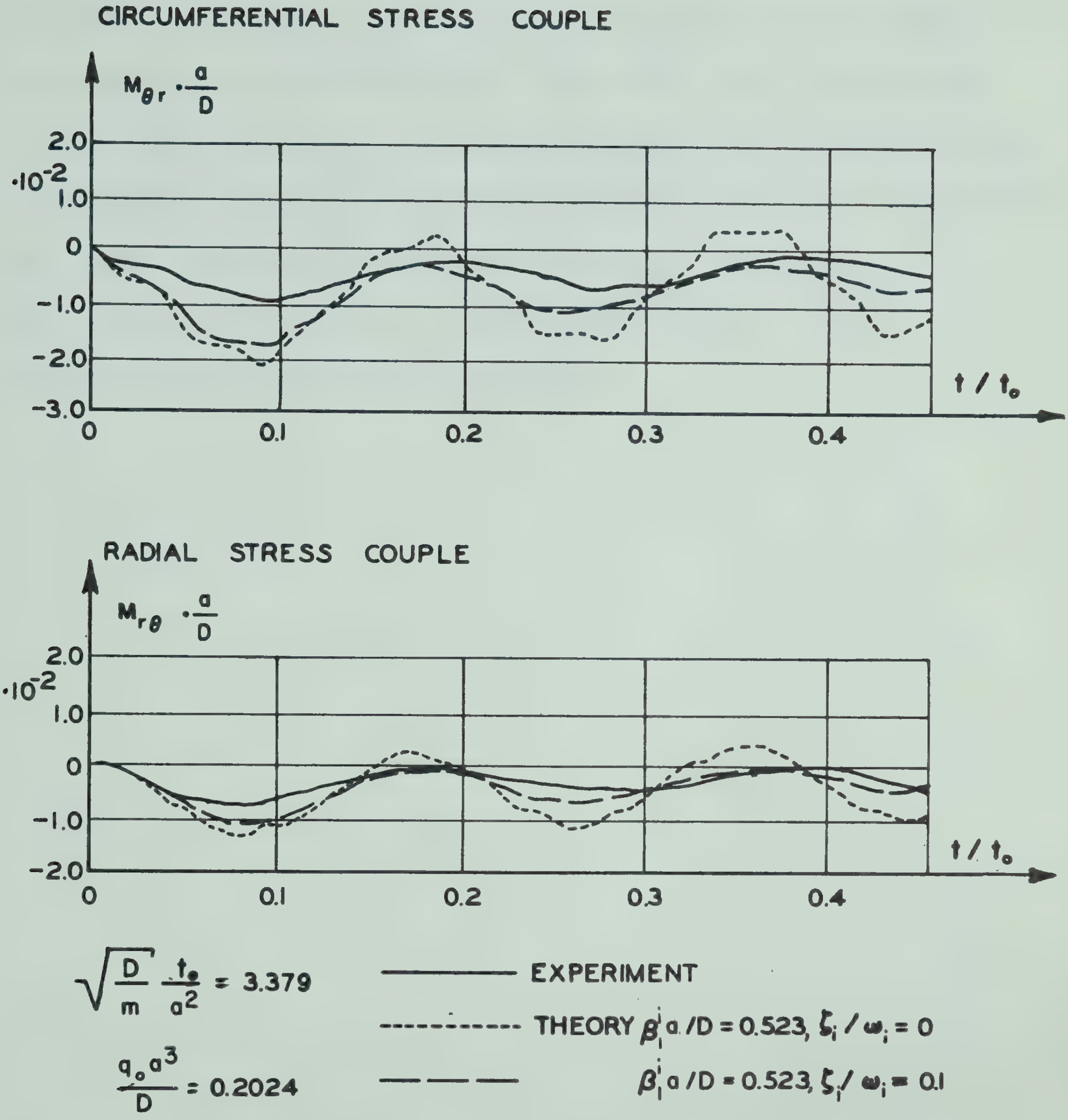

FIG. 5.25 Plate Experimental and Theoretical Flexural Stress Couples vs. Time at $\rho = 0.7778$, $\theta = 45^{\circ}$ for a 1.5 lb. Shot

These results indicate that satisfactory theoretical predictions for stress couples can be made for the entire plate surface, even when edge transverse displacement does not vanish completely and some membrane strains are present, providing viscous damping coefficients and edge spring constants relating the normal slope to the tangential flexural stress couple vector can be estimated with reasonable accuracy.

CHAPTER 6

SHELL NUMERICAL RESULTS

6.1 Transverse Vibrations of Thin Shallow Shells with Homogeneous Edge Conditions

Symmetric eigenvalues for shallow spherical shells with regular polygonal plan were obtained for various values of the geometric parameters a/h and a/R and a range of edge conditions which were satisfied using the boundary collocation technique. Four edge conditions were satisfied at (L-1) boundary collocation points while only the first three edge conditions were satisfied at the remaining collocation point which was always chosen at the shell corner. Consequently, an equal number of simultaneous boundary equations and unknown integration constants was obtained with L collocation points on the boundary of the characteristic segment when the series solutions for $\bar{\eta}^i$ and $\bar{\xi}^i$ in Eqs. (3.27a) and (3.27b) were truncated with n ranging from 0 to (L-1).

Modal participation functions were computed for some of the shells for uniformly distributed and central point loads. Numerical solutions were obtained using the digital computer program given in Appendix C.2 and machine computation using 16 figure accuracy.

Some eigenvalues were obtained using only 10 figure computational accuracy.

The sets of edge conditions satisfied and the associated terminology, well established only for the simply supported and clamped shells, are listed below:

a) Clamped shell:

$$w(\tilde{\rho},\tilde{\theta}) = \frac{\partial w(\tilde{\rho},\tilde{\theta})}{\partial v} = F_{vs}(\tilde{\rho},\tilde{\theta}) = \varepsilon_{ss}(\tilde{\rho},\tilde{\theta}) = 0. \tag{6.1}$$

b) Simply supported shell:

$$w(\tilde{\rho},\tilde{\theta}) = M_{vs}(\tilde{\rho},\tilde{\theta}) = F_{vs}(\tilde{\rho},\tilde{\theta}) = \varepsilon_{ss}(\tilde{\rho},\tilde{\theta}) = 0. \tag{6.2}$$

c) Clamped shell with sliding free edges:

$$w(\tilde{\rho},\tilde{\theta}) = \frac{\partial w(\tilde{\rho},\tilde{\theta})}{\partial v} = F_{vv}(\tilde{\rho},\tilde{\theta}) = F_{vs}(\tilde{\rho},\tilde{\theta}) = 0. \tag{6.3}$$

d) Clamped shell with sliding clamped edges:

$$w(\tilde{\rho},\tilde{\theta}) = \frac{\partial w(\tilde{\rho},\tilde{\theta})}{\partial v} = F_{vv}(\tilde{\rho},\tilde{\theta}) = \varepsilon_{ss}(\tilde{\rho},\tilde{\theta}) = 0. \tag{6.4}$$

e) Simply supported shell with sliding free edges:

$$w(\tilde{\rho},\tilde{\theta}) = M_{vs}(\tilde{\rho},\tilde{\theta}) = F_{vv}(\tilde{\rho},\tilde{\theta}) = F_{vs}(\tilde{\rho},\tilde{\theta}) = 0. \qquad (6.5)$$

f) Simply supported shell with sliding clamped edges:

$$w(\tilde{\rho},\tilde{\theta}) = M_{vs}(\tilde{\rho},\tilde{\theta}) = F_{vv}(\tilde{\rho},\tilde{\theta}) = \varepsilon_{ss}(\tilde{\rho},\tilde{\theta}) = 0. \qquad (6.6)$$

The terminology applied to edge condition Eqs. (6.3) through (6.6) in each case describes successively the edge conditions in transverse displacement and stress function. Thus, for example, a shell satisfying edge condition Eq. (6.3) is referred to as a 'clamped shell with sliding free edges' where 'clamped' refers to the conditions $w(\tilde{\rho},\tilde{\theta}) = \partial w(\tilde{\rho},\tilde{\theta})/\partial v = 0$, 'sliding' refers to the condition $F_{vv}(\tilde{\rho},\tilde{\theta}) = 0$ and 'free' refers to the condition $F_{vs}(\tilde{\rho},\tilde{\theta}) = 0$.

In the numerical analysis, edge condition Eqs. (6.1) and (6.2) were never satisfied at $\theta = 0°$ since, if they were, the determinant value of the boundary equation matrix would vanish for all k as F_{vs} is zero by definition (see Eqs. (3.14b), (3.17c) and (3.19c)) along the radial line $\theta = 0°$. However, edge condition Eqs. (6.3) and (6.5) could be satisfied at $\theta = 0°$ since the fourth edge condition was never satisfied numerically

at the last collocation point.

Satisfaction of the edge condition $\varepsilon_{ss}(\tilde{\rho},\tilde{\theta}) = 0$ in conjunction with the condition $w(\tilde{\rho},\tilde{\theta}) = 0$ is equivalent, for symmetric shell response, to satisfaction of the edge conditions $u_s(\tilde{\rho},\tilde{\theta}) = w(\tilde{\rho},\tilde{\theta}) = 0$, where u_s represents in-plane displacement tangential to the boundary. Satisfaction of the edge condition $F_{vs}(\tilde{\rho},\tilde{\theta}) = 0$ in conjunction with the conditions $u_s(\tilde{\rho},\tilde{\theta}) = \partial u_s(\tilde{\rho},\tilde{\theta})/\partial v = 0$ is equivalent, for symmetric response, to satisfaction of $u_v(\tilde{\rho},\tilde{\theta}) = u_s(\tilde{\rho},\tilde{\theta}) = 0$. Here u_v represents in-plane displacement perpendicular to the boundary. Consequently, specifying only

$$w(\tilde{\rho},\tilde{\theta}) = F_{vs}(\tilde{\rho},\tilde{\theta}) = \varepsilon_{ss}(\tilde{\rho},\tilde{\theta}) = 0 \qquad (6.7)$$

is not equivalent to specifying

$$w(\tilde{\rho},\tilde{\theta}) = u_v(\tilde{\rho},\tilde{\theta}) = u_s(\tilde{\rho},\tilde{\theta}) = 0 \qquad (6.8)$$

and the edge condition Eqs. (6.1) and (6.2) are not equivalent to the usual conditions specified for clamped and simply supported shells. Physically, satisfaction of edge condition Eq. (6.7) eliminates edge elongation and in-plane shear but permits edge curving while satisfaction of edge condition Eq. (6.8) eliminates edge elongation and curving but permits edge in-plane shear. As far as is known, the edge condition of the

function $\partial u_s/\partial v$ has never been considered analytically. However, it is felt that the effect of satisfying either Eq. (6.7) or Eq. (6.8) is almost equivalent for symmetric shell response, except possibly for small values of p, since values of $\partial u_s(\tilde{\rho},\tilde{\theta})/\partial v$ should be small. This near-equivalency is confirmed in Sections 6.1.2 and 6.1.3 for simply supported and clamped shells with 12 and 15 sides.

Oniashvili [88] and Nowacki [33], in analysing the vibrations of a shallow spherical segment with a circular boundary, used the edge conditions

$$\frac{\partial F}{\partial \rho} = \frac{\partial F}{\partial \theta} = w = \frac{\partial w}{\partial \rho} = 0 \qquad (6.9)$$

as being the equivalent of

$$u_\rho = u_\theta = w = \frac{\partial w}{\partial \rho} = 0. \qquad (6.10)$$

However, this equivalency does not appear to be correct, even assuming that $\frac{\partial u_\theta}{\partial \rho} = 0$ at the boundary, since integration of the stress resultant-displacement relations at the boundary yields

$$u_\rho = c_1 \frac{\partial F}{\partial \rho} + f(\theta) \qquad (6.11)$$

and

$$u_\theta = c_2 \frac{\partial F}{\partial \theta} + c_3 \frac{\partial f(\theta)}{\partial \theta} . \qquad (6.12)$$

In these equations $f(\theta)$ is an arbitrary function of θ and c_1, c_2, and c_3 are constants. A numerical check on the correctness of edge condition Eq. (6.9) applied to a shell with a polygonal boundary having 12 sides as an alternative to edge condition Eq. (6.10) applied to a shell with a circular boundary, appeared to give unsatisfactory modal frequencies when compared to values given by Kalnins [56].

Weinitschke [89], in analysing the asymmetric buckling of a clamped shallow spherical shell with a circular boundary, used the edge conditions

$$\varepsilon_{\theta\theta} = r\frac{\partial}{\partial r}[\varepsilon_{\theta\theta}] - \varepsilon_{rr} - \frac{\partial}{\partial \theta}[\varepsilon_{r\theta}] = w = \frac{\partial w}{\partial r} = 0 \qquad (6.13)$$

as being the equivalent of edge condition Eq. (6.10). Although these two edge conditions in strain are the equivalent of satisfying the edge conditions $u_r = u_\theta = 0$ for a clamped shell with a circular boundary, they are not applicable for a simply supported shell since they must be satisfied in conjunction with the two edge conditions $w = \frac{\partial w}{\partial r} = 0$ in order to be valid.

In the numerical results which follow, varying degrees of difficulty were encountered in obtaining fundamental eigenvalues for different edge conditions, shell geometries and boundary collocation sets. It is

postulated that essentially it was the insensitivity of λ to changes in k for small k which made it difficult to find accurately the lowest values of k for which the various boundary equation matrices had vanishing determinant values. The decreasing sensitivity of λ to changes in k as k^4 becomes small in comparison to $12(1 - \nu^2)a^4/(Rh)^2$ is apparent from the relation

$$\omega = \sqrt{\frac{D}{m}\left[\left(\frac{k}{a}\right)^4 + \frac{Eh}{DR^2}\right]}$$

where

$$\lambda = Eh/(maR\omega^2).$$

The function λ is present in boundary equations involving the transverse displacement and its derivatives. Inaccuracies in calculating derivatives of $J_{pn}(k\rho)$ and $I_{pn}(k\rho)$ for k<<1 using lower order derivatives of these functions further amplify the problems caused by this insensitivity of λ.

This postulate explains the variation in the degree of difficulty encountered in the numerical analysis in solving k_1 for the different edge conditions. Fundamental eigenvalues associated with shells satisfying edge condtion Eqs. (6.1) or (6.2) were found relatively easily since the shell edges were reasonably well restricted against in-plane normal

boundary motion and consequently had values of k_1^4 which were large in comparison to $12(1 - \nu^2)a^4/(Rh)^2$. Values of k_1 associated with shells satisfying edge condition Eqs. (6.4) or (6.6) were found for many shell geometries since $u_v(\tilde{\rho},\tilde{\Theta})$ was still partially restricted and consequently values of k_1^4 usually were not too small in comparison to $12(1 - \nu^2)a^4/(Rh)^2$. However, values of k_1 associated with edge condition Eqs. (6.3) or (6.5) were not found for most shell geometries since $u_v(\tilde{\rho},\tilde{\Theta})$ was unrestricted and consequently values of k_1^4 must have been small in comparison to $12(1 - \nu^2)a^4/(Rh)^2$.

This postulate also explains the increasing difficulty encountered in obtaining k_1 as p increased, since the magnitude of k_1 generally decreases with increasing p, at least for the shells for which k_1 was obtained, while $12(1 - \nu^2)a^4/(Rh)^2$ is independent of p. In addition, it explains why the value of k_1 for any particular shell boundary shape and edge condition was solved more accurately for smaller magnitude values of the product of the shell geometry parameters $\frac{a}{R}$ and $\frac{a}{h}$.

The difficulty in solving k_1 for edge condition Eqs. (6.4) and (6.6) for larger values of p might also be explained partially by the fact that, as p increases, the in-plane shear F_{vs} and slope $\frac{\partial u_s}{\partial v}$

decrease and finally vanish for a circular boundary. But the edge conditions

$$w(\tilde{\rho},\tilde{\theta}) = F_{vs}(\tilde{\rho},\tilde{\theta}) = \varepsilon_{ss}(\tilde{\rho},\tilde{\theta}) = \frac{\partial u_s}{\partial v}(\tilde{\rho},\tilde{\theta}) = 0 \qquad (6.16)$$

imply that in-plane displacement normal to the boundary vanishes so that $F_{vv}(\tilde{\rho},\tilde{\theta})$ cannot vanish as well. Thus, it becomes increasingly difficult to satisfy $F_{vv}(\tilde{\rho},\tilde{\theta}) = 0$ as the polygonal boundary approaches the circular shape if $\varepsilon_{ss}(\tilde{\rho},\tilde{\theta}) = 0$.

6.1.1 *Simply Supported Shells with Sliding Clamped Edges*. The only previous analysis of the transverse vibrations of a shallow shell of noncircular planform, as far as is know, has been given by Reissner [50], who solved the natural frequencies of a shallow thin paraboloidal cap with a square base. Neglecting the effects of longitudinal and rotatory inertia and transverse shear and employing the edge conditions

$$w(\tilde{v},\tilde{s}) = \frac{\partial^2 w(\tilde{v},\tilde{s})}{\partial v^2} = \frac{\partial^2 F(\tilde{v},\tilde{s})}{\partial s^2} = \frac{\partial^2 F(\tilde{v},\tilde{s})}{\partial v^2} = 0, \qquad (6.14)$$

Reissner obtained the frequency equation

$$\omega_{ij}^2 = \frac{\pi^4(i^2+j^2)^2}{192(1-\nu^2)} \frac{E}{\gamma} \frac{h^2}{a_0^4}\left[1 + \frac{192(1-\nu^2)}{\pi^4(i^2+j^2)^2}\frac{H^2}{h^2}\right]. \qquad (6.15)$$

In Eq. (6.15), i, j = 1, 3, 5... for symmetric modes and H is the shell height or sagitta.

Although Reissner states that Eq. (6.15) applies to a spherical middle surface, the surface to which it actually applies is slightly paraboloidal since the quantity $(H/a_0)^2$ has been neglected with respect to unity in the curvature calculation. For a truly spherical middle surface, Eq. (6.15) becomes

$$\omega_{ij}^2 = \frac{\pi^4(i^2+j^2)^2}{192(1-\nu^2)} \frac{E}{\gamma} \frac{h^2}{a_0^4}\left[1 + \frac{192(1-\nu^2)}{\pi^4(i^2+j^2)^2} \frac{H^2}{h^2} \frac{1}{(1+H^2/a_0^2+H^4/4a_0^4)}\right] \quad (6.15^*)$$

Solutions were obtained for a shallow spherical shell having the same H/h and a_0/h values as the paraboloidal shell. Edge conditions given in Eq. (6.6), the equivalent of those in Eq. (6.14), were satisfied at four and five collocation points on the boundary of the characteristic segment. Good numerical convergence was obtained for as few as four collocation points. The first five symmetric frequencies calculated using the present theory agree closely with the values calculated from Eq. (6.15) as shown in Table 6.1, and they agree with the values calculated from Eq. (6.15*) to at least four figure accuracy.

It should be noted that the eigenvalues k_i given in Table 6.1 for the spherical shell are identical to the eigenvalues given in Table 4.2 for a simply supported square plate. According to Koplik and Yu [60], higher modal frequencies for clamped shells with circular plan

Table 6.1

Symmetric Eigenvalues and Modal Participation Functions for Simply Supported Shallow Spherical Shells with Sliding Clamped Edges having 4, 5 and 6 Sides[1]

	p	4	5[2]	6[3]				
	a/R	0.390625	0.5	0.1	0.390625	0.5	0.5	
	a/h	66.667	10	66.667	66.667	10	66.667	
mode i	1	3.14159	3.39	2.66	2.62	2.67	2.59	k_i
	2	7.0248	6.44	6.12	6.11	6.12	6.11	
	3	9.4248	9.56	9.49	9.48	9.49	9.48	
	4	11.327	10.64	10.99	10.99	10.99	10.99	
	5	12.95	13.08	12.99	12.99	12.99	12.99	
	6		14.6	14.8	14.8	14.8		
	1	0.3932(0.4093)[4]	0.612	0.105	0.392	0.545	0.501	$a\sqrt{\frac{\gamma}{E}}\,\omega_i$
	2	0.4515(0.4655)	1.36	0.199	0.427	1.25	0.528	
	3	0.5645(0.5758)	2.84	0.425	0.568	2.80	0.648	
	4	0.7064(0.7154)	3.50	0.563	0.678	3.73	0.746	
	5	0.8631(0.8705)	5.25	0.780	0.866	5.19	0.922	
	6		6.57	1.01	1.08	6.75		
	1	-96.5	-61.8		-145.5	-140.1	-149.6	$\left(\frac{X_1^i}{X_0^i}\right)_0$
	2	11.0	15.7		17.2	17.2	17.2	
	3	-1.9	-5.0		-5.47	-5.48	-5.47	
	4	-2.3	-3.1		-0.76	-0.74	-0.77	
	5	-0.14	1.87		2.3	2.3		
	6				-0.21	-0.21		
	1	-100.7	-62.9		-146.8	-141.2	-150.9	$\frac{X_1^i}{X_0^i}$
	2	13.4	17.0		17.9	17.9	17.9	
	3	-1.2	-3.6		-5.75	-5.76	-5.75	
	4	-2.9	-1.9		-0.10	-0.10	-0.10	
	5	0.9	1.86		2.6	2.6		
	6				-0.13	-0.13		
	1	-0.19869	-0.104		-0.210	-0.205	-0.215	$a^2\frac{(X_1^i)_p}{X_0^i}$
	2	-0.07923	-0.0847		-0.0894	-0.0893	-0.0894	
	3	-0.0221	-0.0325		-0.0531	-0.0532	-0.0531	
	4	-0.0290	-0.0254		-0.0068	-0.0068	-0.0068	
	5	-0.0269	-0.0238		-0.0359	-0.0359		
	6				-0.0092	-0.0091		

[1] $\nu = 0.33$ for all calculations.

[2] Edge conditions satisfied at 5 collocation points at $\theta = 36^\circ, 30^\circ, 20^\circ, 10^\circ, 0^\circ$.

[3] Edge conditions satisfied at 4 collocation points at $\theta = 5^\circ, 15^\circ, 25^\circ, 30^\circ$.

[4] Frequencies in brackets were obtained from Eq.(6.15) with $i,j = 1, 3, 5\ldots$ This equation was given by Reissner [50] for shallow parabolodial shells.

converge to the frequencies for clamped circular plates as the curvature effect decreases with higher modes. Consequently, it is likely that the eigenvalues for this shell would be identical to the plate eigenvalues for all modes. Mode shapes computed for this spherical shell are identical with the simply supported square plate mode shapes shown in Fig. 4.2a, as well. Variation of the thinness parameter a/h between 10 and 66.667 and the shallowness parameter a/R between 0.1 and 0.5 had no effect on the eigenvalues and mode shapes.

In the remainder of Table 6.1, eigenvalues are given for spherical shells with 5 and 6 sides having different a/R and a/h values. The eigenvalues found for these shells are almost identical to the values for simply supported plates with the same number of sides which are given in Table 4.2, with the exception of k_1 for the 5-sided shell which likely is in error. The boundary collocation point sets used for these shells with 5 and 6 sides are noted in the table since fundamental eigenvalues were not found for every set used.

It appears from the results given in Table 6.1 that eigenvalues for the edge conditions in Eq. (6.6) are almost independent of the values of a/h and a/R within the limits of thin shallow shells and that they agree

closely with eigenvalues for simply supported plates with the same boundary shape.

Modal participation functions, given in Table 6.1 for uniformly distributed and central point loads, were obtained using the eigenvalues given in the same table and their associated eigenvectors $\bar{\eta}^i$ where $A_0^i = 1$. Integral values for the coefficients $\phi_1 \ldots \phi_{18}$ were determined using the generalized Simpson's formula with 46 increments of θ for the shell with 4 sides and 36 increments of θ for the shells with 5 and 6 sides. Since eigenvalues and eigenvectors were nearly independent of a/h and a/R values, it appears that for these edge conditions the fundamental mode contributions will dominate shallow shell response for most uniform dynamic loads and that contributions of modes higher than the third will be insignificant for practical purposes. The reasonably close agreement between the values of $(\chi_1^i/\chi_0^i)_0$ and χ_1^i/χ_0^i for most modes indicates that the modal participation functions computed from Eq. (3.34a) should be reliable, at least for these boundary shapes. For modes higher than the first, modal participation functions appear to be almost independent of a/R and a/h values, at least for $p = 6$.

6.1.2 Simply Supported Shells. Kraus and Kalnins [66] analysed the transverse vibrations of a simply supported shallow spherical shell with circular plan, including the effect of longitudinal inertia. The shell had a shallowness parameter $R/h = 20$, a thinness parameter $a/h = 5.17638$ and a Poisson's ratio $\nu = 0.3$. Employing the edge conditions

$$w(a,\theta) = M_{r\theta}(a,\theta) = u_r(a,\theta) = u_\theta(a,\theta) = 0, \qquad (6.16)$$

they obtained the first twelve symmetric frequencies and associated static center modal displacements for a load uniformly distributed over the shell surface area.

Theoretical solutions were obtained for shells with regular polygonal bases having 12 and 15 sides. These shells had the same shallowness parameter R/h and Poisson's ratio ν as the circular shell, however the thinness parameter a/h was varied so that the shells with circular and polygonal bases had the same surface area as calculated from the relations

$$A_{\text{circular}} = 2\pi R^2 \left[1 - \sqrt{1 - (a/R)^2}\right] \qquad (6.17)$$

and

$$A_{\text{polygonal}} = 2\pi R^2 \left[1 - \frac{p}{\pi}\int_0^{\pi/p} \sqrt{1 - \left(\frac{a \cos \theta}{R \cos \theta_0}\right)^2}\, d\theta\right]. \qquad (6.18)$$

In Eqs. (6.17) and (6.18), A_{circular} represents the surface area of a spherical shell with a circular plan and $A_{\text{polygonal}}$ represents the surface area of a spherical shell with a regular polygonal plan. $A_{\text{polygonal}}$ was evaluated numerically using Simpson's formula. Edge conditions given in Eq. (6.2) were satisfied at three and four boundary collocation points on the characteristic segment. Convergence of the eigenvalues and static center modal deflections to two or three figure accuracy was obtained for all modes except the fundamental. Poor convergence of the fundamental eigenvalues may have resulted partly from the Poisson's ratio effect previously noted for simply supported plates and partly from errors in the higher orders of the Bessel functions required (orders up to 45 are required for the 15-sided shell with $L = 4$).

Frequencies and static modal displacements obtained for the three collocation point sets are compared in Table 6.2 with the values given by Kraus and Kalnins. In contrast to the results for three collocation points, fundamental modal eigenvalues for the shells with 12 and 15 sides obtained for four collocation points were slightly smaller and fundamental modal deflections were slightly larger than the values

Table 6.2

Symmetric Frequencies and Static Central Modal Deflections for Uniformly Loaded Simply Supported Shallow Spherical Shells with Polygonal and Circular Boundaries and Equivalent Surface Areas[1]

		$R\sqrt{\gamma/E}\,\omega_i$				$[D/(R^4q_o)]w_i$				$\sum_i [D/(R^4q_o)]w_i$		
	p	12	15	∞[2]		12	15	∞[2]		12	15	∞[2]
	a/R	0.26485	0.26265	0.258819		0.26485	0.26265	0.258819		0.26485	0.26265	0.258819
	a/h	5.297	5.253	5.17638		5.297	5.253	5.17638		5.297	5.253	5.17638
	mode type[3]	T	T	T	L	T	T	T	L	T	T	L + T
mode i	1	2.02	2.03	1.863		0.906E-4	0.896E-4	0.10536E-3		0.906E-4	0.896E-4	0.10536E-3
	2	6.90	6.88	6.618		-0.517E-5	-0.519E-5	-0.54763E-5		0.854E-4	0.844E-4	0.99889E-4
	3				15.35				0.62351E-7			0.99951E-4
	4	16.87	16.84	16.43		0.683E-6	0.682E-6	0.65117E-6		0.861E-4	0.851E-4	0.10060E-3
	5				28.15				-0.38542E-8			0.10059E-3
	6	31.3	31.3	30.56		-0.170E-6	-0.169E-6	-0.17090E-6		0.859E-4	0.849E-4	0.10042E-3
	7				40.84				0.21479E-9			0.10042E-3
	8	50.1	50.2	49.01		0.59 E-7	0.59 E-7	0.59038E-7		0.860E-4	0.850E-4	0.10048E-3
	9				53.56				0.85282E-9			0.10048E-3
	10				65.98				-0.52845E-9			0.10048E-3
	11	62.9	73.5	72.06		-0.4 E-9	-0.25 E-7	-0.24530E-7		0.860E-4	0.850E-4	0.10046E-3
	12				78.73				-0.26872E-9			0.10046E-3

[1] $\nu = 0.3$ for all calculations.

[2] These values are given by Kraus and Kalnins [66].

[3] T indicates modes due to transverse inertia effects and L indicates modes due to longitudinal or in-plane inertia.

given by Kraus and Kalnins. However, for modes higher than the first, convergence of frequencies and displacements with increasing number of sides p to the values for a circular boundary was consistent for either collocation set. The results given by Kraus and Kalnins for the shell with the circular boundary show that the largest static center modal displacement due to longitudinal inerta effects (i = 3) has approximately the same magnitude as the fifth modal displacement due to transverse inertia effects (i = 8). Consequently, longitudinal inertia effects can be ignored for these shells for most uniformly distributed transverse dynamic loads.

The dependence of eigenvalues and modal participation functions upon the geometric parameters a/R and a/h for simply supported shallow shells is shown in Table 6.3. For the thinner shells (a/h = 66.667 and 62.0459), the third and fourth modes dominate the response to uniform loads, while for the thicker shells (a/h = 5.2) the fundamental mode dominates the response. Of course, increasing the shallowness parameter a/R would increase the relative importance of the higher modes as well, as pointed out by Kraus and Kalnins [66] who compared modal displacements for a shallow and a hemispherical shell. In contrast, the relative

Table 6.3

Symmetric Eigenvalues and Modal Participation Functions for Simply Supported Shallow Spherical Shells with 6, 12 and 15 Sides

p	6	12		15	
ν	0.33	0.33	0.3	0.3	
a/R	0.390625	0.36355	0.26485	0.26265	
a/h	66.667	62.0459	5.297	5.253	
mode i					
1	5.94	5.38	2.85	2.84	k_i
2	9.51	8.61	5.63	5.57	
3	10.99	10.44	8.83	8.75	
4	11.76	12.15	12.04	11.94	
5	13.01	15.26	15.24	15.12	
6	14.99	17.2	17.1	18.3	
7	16.6				
1	1.05	-1.26	-4.05	-3.96	$\left(\frac{X_1^i}{X_0^i}\right)_0$
2	-1.70	4.46	0.956	0.958	
3	-7.96	-7.92	-0.303	-0.303	
4	-7.87	5.02	0.139	0.139	
5	2.32	-1.76	-0.077	-0.077	
6	3.96	-0.9	0.014	0.05	
7	-1.30				
1	1.80	-1.21	-4.05	-3.96	$\frac{X_1^i}{X_0^i}$
2	-2.32	4.42	0.959	0.959	
3	-7.79	-7.93	-0.305	-0.304	
4	-7.53	5.05	0.141	0.140	
5	2.63	-1.78	-0.078	-0.078	
6	1.53	-0.03	0.0006	0.05	
7	-1.34				
1	-0.113	-0.115	-0.113	-0.110	$a^2\frac{(X_1^i)_p}{X_0^i}$
2	-0.0549	-0.0496	-0.0900	-0.0900	
3	-0.0153	-0.016	-0.0579	-0.0580	
4	-0.0194	-0.038	-0.0425	-0.0423	
5	-0.0371	-0.033	-0.033	-0.033	
6	-0.0106	-0.001	-0.001	-0.03	
7	-0.023				
	5	3	3	3	
	number of boundary collocation points				
	equal surface area		equal surface area		

importance of the higher modes to the response of shells subjected to central point loads increases with decreasing values of a/h. The decrease of eigenvalues k_i with increasing number of sides p for modes 1 and 2 and the increase for modes 4 and 5 (except for p = 15) for these shells follows the pattern exhibited by plates in Tables 4.5 and 4.6. The increase in k_3 with p decreasing from 12 to 6 for mode 3 was not observed for polygonal plates, however.

6.1.3 Clamped Shells. Kalnins [56] obtained the nonsymmetric frequencies of free transverse vibration of some clamped shallow spherical shells with circular plan including the effect of longitudinal inertia. Employing the edge conditions

$$w(a,\theta) = \frac{\partial w(a,\theta)}{\partial r} = u_r(a,\theta) = u_\theta(a,\theta) = 0, \qquad (6.19)$$

he obtained natural frequencies for shells with $\nu = 0.3$, a/h = 10 and a/R = 0.1, 0.3 and 0.5.

The symmetric frequencies given by Kalnins are compared in Table 6.4 with theoretical values for shells with regular polygonal bases having 12 and 15 sides. All shells had the same shallowness parameter R/h and Poisson's ratio ν, however, the thinness parameter a/h was varied so that the shells with

Table 6.4

Symmetric Frequencies of Clamped Shallow Spherical Shells with Polygonal and Circular Boundaries and Equivalent Surface Areas[1]

	p	12	15	∞ [2]			12	15	∞ [2]			12	15	∞ [2]			
	a/R	0.102331	0.101481	0.1			0.306993	0.304443	0.3			0.511655	0.507405	0.5			
	a/h	10.2331	10.1481	10			10.2331	10.1481	10			10.2331	10.1481	10			
	mode type[3]	T	T	T	L_t	L_r	T	T	T	L_t	L_r	T	T	T	L_t	L_r	
mode i	1	0.344	0.344	0.3386			0.541	0.543	0.5205			0.790	0.792	0.7515			$a\sqrt{\gamma/E}\,\omega_i$
	2	1.214	1.212	1.205			1.260	1.258	1.247			1.353	1.352	1.331			
	3				2.376					2.376					2.376		
	4	2.707	2.703	2.698			2.724	2.721	2.711			2.759	2.756	2.737			
	5					4.018					4.032					4.060	
	6				4.351					4.351					4.351		
	7	4.797	4.794	4.789			4.806	4.803	4.796			4.825	4.822	4.814			

[1] $\nu = 0.3$ for all calculations.

[2] These frequencies are given by Kalnins [56] .

[3] T indicates modes due to transverse inertia effects, L_t indicates modes due to longitudinal torsional effects and L_r indicates modes due to longitudinal radial effects.

circular and polygonal bases had the same surface area. Edge conditions given in Eq. (6.1) were satisfied at three and four boundary collocation points. Good numerical convergence was obtained for all frequencies.

Frequencies obtained for these polygonal shells were slightly larger than the values given by Kalnins for the circular shells just as they were for polygonal and circular plates. The largest frequency differences occurred for the fundamental mode and the largest a/R value.

Eigenvalues and modal participation functions are given in Table 6.5 for shells of regular polygonal plan with 6, 12 and 15 sides and a range of a/R and a/h values. The increasing relative importance of the higher modes for uniform and central point loads for increasing values of a/R is shown for shells with 12 and 15 sides and $a/h \approx 10$ and for shells with 6 sides and $a/h = 66.667$. The significant increase in the relative importance of the higher modes with increasing values of a/h for uniform loads and the decrease of their importance with increasing values of a/h for central point loads is shown for shells with 12 sides and $a/R \approx 0.33$. The pattern of variation of the eigenvalues for shells of equal surface area with 6 and 12 sides is the same as it was for the simply supported shells, at least for the first five modes.

Table 6.5

Symmetric Eigenvalues and Modal Participation Functions for Clamped Shallow Spherical Shells with 6, 12 and 15 Sides

p		6		12				15			
ν		0.33	0.33	0.33	0.3	0.3	0.3	0.3	0.3	0.3	
a/R		0.25	0.390625	0.36355	0.102331	0.306993	0.511655	0.101481	0.30443	0.507405	
a/h		66.667	66.667	62.0459	10.2331	10.2331	10.2331	10.1481	10.1481	10.1481	
mode i	1	6.42	6.55	5.99	3.38	3.95	4.60	3.35	3.92	4.57	k_i
	2	8.76	9.96	9.03	6.47	6.51	6.59	6.41	6.45	6.54	
	3	10.53	11.22	10.59	9.68	9.68	9.69	9.59	9.59	9.60	
	4	12.00	12.22	12.99	12.88	12.88	12.88	12.77	12.77	12.78	
	5	13.92	13.97	16.11							
	6	15.76	15.82	17.9							
	7		17.5								
	1	-6.21	-1.21	-3.142	-1.266	-0.748	-0.507	-1.265	-0.742	-0.504	$\left(\frac{X_1^i}{X_0^i}\right)_0$
	2	12.6	4.88	8.325	0.293	0.307	0.329	0.294	0.307	0.330	
	3	-8.51	-9.99	-9.51	-0.110	-0.112	-0.116	-0.110	-0.112	-0.116	
	4	-6.72	-8.12	4.66	0.0549	0.0553	0.0559	0.0547	0.0550	0.0557	
	5	3.82	4.40	-2.14							
	6		2.5	-0.3							
	7		-2.5								
	1	-6.32	-1.36	-3.143	-1.266	-0.748	-0.507	-1.265	-0.742	-0.504	$\frac{X_1^i}{X_0^i}$
	2	12.6	4.93	8.325	0.293	0.307	0.329	0.294	0.307	0.330	
	3	-7.83	-9.30	-9.51	-0.110	-0.112	-0.116	-0.110	-0.112	-0.116	
	4	-1.43	-5.50	4.66	0.0548	0.0552	0.0558	0.0547	0.0550	0.0557	
	5	3.12	3.68	-2.12							
	6		0.6	-0.008							
	7		-1.5								
	1	-0.108	-0.109	-0.110	-0.146	-0.0951	-0.0744	-0.145	-0.0921	-0.0743	$a^2\frac{(X_1^i)_p}{X_0^i}$
	2	-0.015	-0.041	-0.033	-0.0782	-0.0742	-0.0650	-0.0782	-0.0741	-0.0645	
	3	-0.047	-0.030	-0.028	-0.0532	-0.0527	-0.0526	-0.0529	-0.0528	-0.0526	
	4	-0.010		-0.036	-0.0396	-0.0396	-0.0395	-0.0397	-0.0396	-0.0396	
	5	-0.032		-0.031							
	6			-0.0009							
	7										
		5	5	3	3	3	3	3	3	3	
		number of boundary collocation points									
			equal surface area		equal surface area						

Nodal lines for the first four symmetric modes of response of a clamped shallow shell with 12 sides and a/R = 0.102331, a/h = 10.2331 and $\nu = 0.3$ are shown in Fig. 6.1. The nodal areas agree closely with the values for a clamped plate with 12 sides given in Fig. 4.2d.

Nodal lines for the first seven symmetric modes of response of a clamped shallow shell with 6 sides and a/R = 0.390625 and a/h = 66.667 are shown in Fig. 6.2. The first four mode shapes are quite different from the mode shapes for a clamped plate with 6 sides shown in Fig.4.2b. The fundamental mode shape has an interior nodal line which was observed also by Chow and Popov [90] for a shallow shell with a circular boundary and a/R = 0.4422, a/h = 24.04 and $\nu = 0.3$.

Hoppmann and Baronet [91] studied free rotationally symmetric vibrations of simply supported and clamped shallow spherical shells with circular boundaries. They found that, for values of a/R of 0.1655 and 0.399 and a/h of 24 and 48, the interior nodal circle of the fundamental mode approached closer to the boundary with decreasing a/R(a/h) for the same a/h(a/R).

6.1.4 Other Edge Conditions. Eigenvalues and modal participation functions for some shallow spherical shells of regular polygonal plan are given in

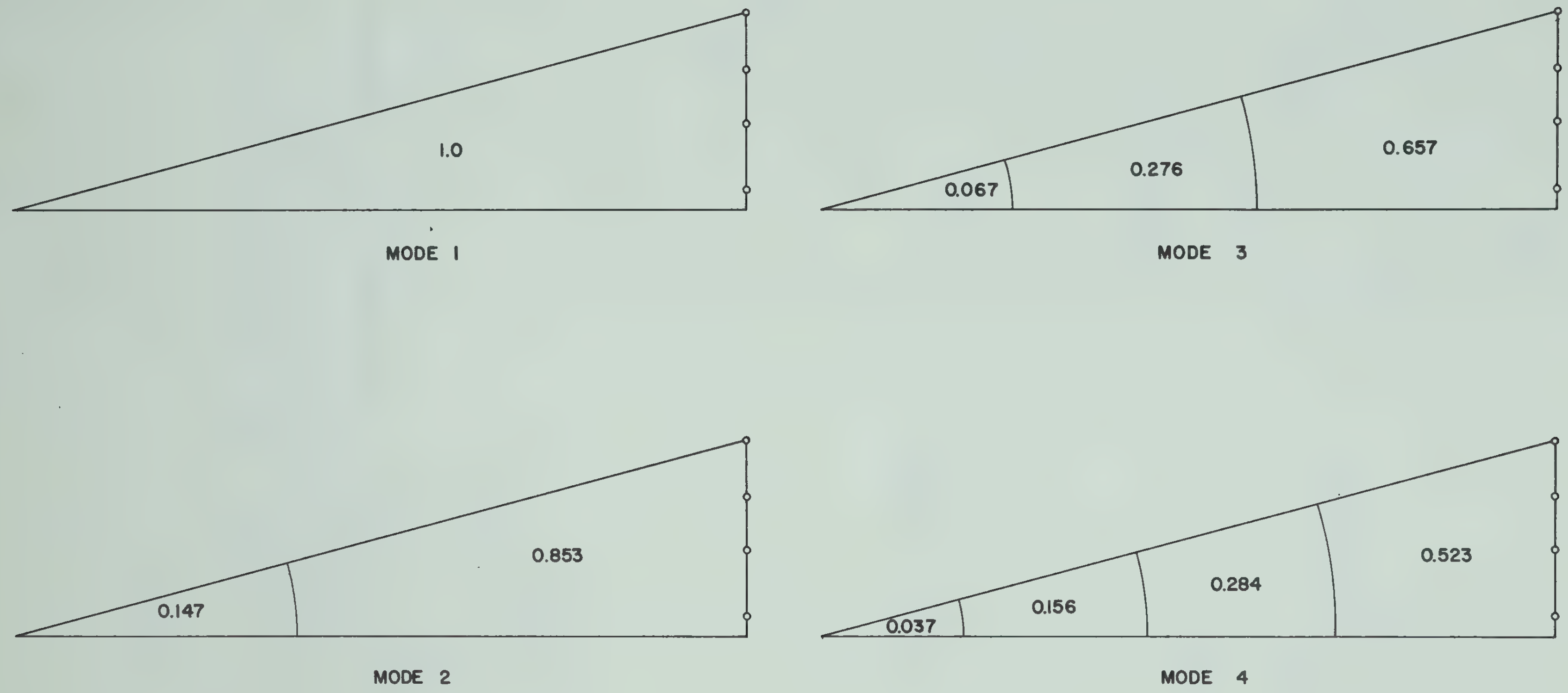

FIG. 6.1 Symmetric Mode Shapes for the Characteristic Segment of a Clamped Shallow Spherical Shell with 12 Sides and $a/R = 0.102331$, $a/h = 10.2331$ and $\nu = 0.3$

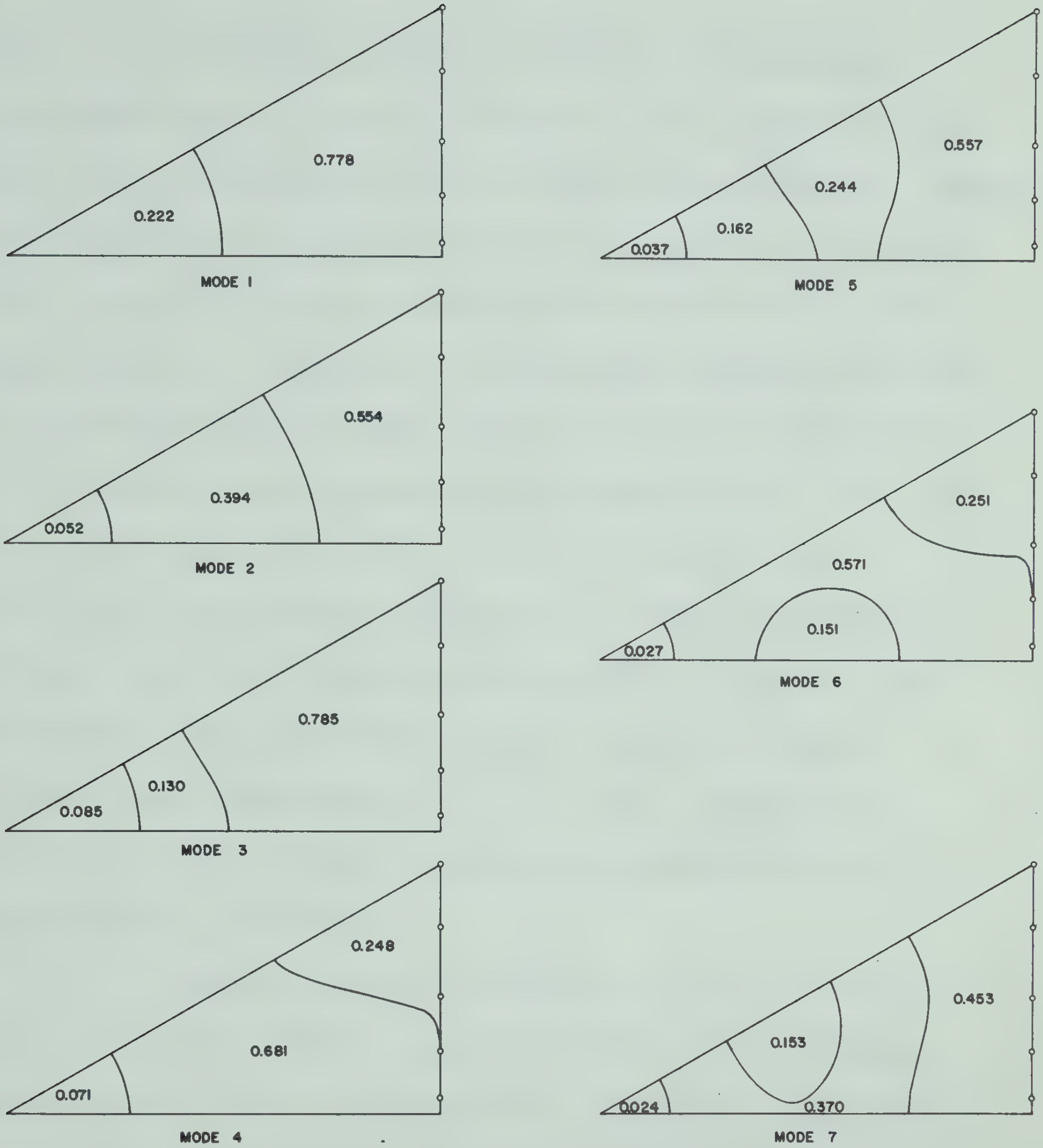

FIG. 6.2 Symmetric Mode Shapes for the Characteristic Segment of a Clamped Shallow Spherical Shell with 6 Sides and $a/R = 0.390625$, $a/h = 66.667$ and $\nu = 0.33$

Table 6.6 for simply supported shells with sliding free edges and in Tables6.7 and 6.8 for clamped shells with sliding free and clamped edges, respectively. These edge conditions, which are given in Eqs. (6.3) through (6.5), were difficult to satisfy numerically for the lower modes of vibration. Fundamental eigenvalues were not obtained for the edge conditions in Eq. (6.5) and were obtained for the edge conditions in Eqs. (6.3) and (6.4) only for some values of p, a/R and a/h and particular collocation point sets. Eigenvalues given without associated modal participation functions were obtained on the IBM 1130 computer using 10 figure computational accuracy while all other values were obtained on the IBM 360/67 computer using 16 figure computational accuracy.

Comparison of eigenvalues given in Tables 6.1 and 6.6 for simply supported shells with sliding edges having 4 and 6 sides shows that eigenvalues and frequencies for the second and third modes increase when the sliding edge is clamped against extension while higher modal values are unaffected. This increase becomes more significant with decreasing number of boundary sides. Fundamental eigenvalues were not obtained for the edge conditions in Eq. (6.5), however these results indicate that there would be a larger increase in the fundamental eigenvalues than observed

Table 6.6

Symmetric Eigenvalues and Modal Participation Functions for Simply Supported Shallow Spherical Shells with Sliding Free Edges having 4, 5, 6 and 12 Sides[1]

p		4		5		6		12		
a/R		0.390625	0.5	0.390625	0.5	0.390625[2]	0.5	0.36355[2]	0.5	
a/h		66.667	10	66.667	10	66.667	10	62.0459	10	
mode i	1									k_i
	2	6.10	6.990	6.07	6.39	5.87	6.08	5.44	5.58	
	3	8.57	9.40	8.94	9.54	9.31	9.48	8.78	8.83	
	4	11.2	11.3	10.5	10.6	10.6	11.0	12.0	12.1	
	5	12.7	12.9	13.0	13.1	13.0	13.0	15.2	15.2	
	6	16.9	16.9	14.6	14.6	14.8	14.8	17.0	17.0	
	1									$\left(\frac{X_1^i}{X_0^i}\right)_0$
	2					3.9		3.78		
	3					-3.9		-3.53		
	4					0.4		2.26		
	5					2.0		-1.40		
	6					-0.5		0.7		
	1									$\frac{X_1^i}{X_0^i}$
	2					4.7		3.84		
	3					-4.0		-3.58		
	4					0.06		2.30		
	5					2.2		-1.42		
	6					-0.2		0.03		
	1									$a^2\frac{(X_1^i)_p}{X_0^i}$
	2					-0.111		-0.113		
	3					-0.049		-0.058		
	4					-0.011		-0.043		
	5					-0.036		-0.033		
	6					-0.01		-0.001		
number of boundary collocation points		5		5		5		3		

[1] $\nu = 0.33$ for all calculations.

[2] These shells have the same surface area.

Table 6.7

Symmetric Eigenvalues and Modal Participation Functions for Clamped Shallow Spherical Shells with Sliding Free Edges having 4, 5, 6 and 12 Sides[1]

p		4		5		6		12		
a/R		0.390625	0.5	0.390625	0.5	0.390625[2]	0.5	0.36355[2]	0.5	
a/h		66.667	10	66.667	10	66.667	10	62.0459	10	
mode i	1		3.64		2.76					k_i
	2	7.72	8.11	7.05	7.367	6.70	6.995	6.18	6.43	
	3	10.1	10.48	10.3	10.50	10.3	10.39	9.59	9.67	
	4	12.3	12.4	11.5	11.6	11.7	11.85	12.86	12.88	
	5	13.9	14.0	14.0	14.0	13.9	13.90	16.07	16.08	
	6	16.7	16.6	15.6	15.6	15.7	15.7	17.8	17.8	
	7	17.9	18.0	17.2	17.2	17.4	17.4			
	1		-108.6		-281.3					$\left(\frac{X_1^i}{X_0^i}\right)_0$
	2		13.4		15.2	6.27		5.97		
	3		0.45		-6.2	-5.0		-4.52		
	4		-3.2		-5.6	-1.3		2.77		
	5		-1.5		3.4	3.2		-1.74		
	6					0.09		0.6		
	7					-2.2				
	1		-102.0		-279.0					$\frac{X_1^i}{X_0^i}$
	2		9.5		14.3	6.10		5.97		
	3		-0.33		-3.3	-4.4		-4.52		
	4		-0.50		-1.7	-0.04		2.77		
	5		0.15		1.9	2.5		-1.73		
	6					-0.2		0.02		
	7					-1.3				
	1		-0.278		-0.602					$a^2\frac{(X_1^i)_p}{X_0^i}$
	2		-0.056		-0.078	-0.104		-0.105		
	3		-0.005		-0.027	-0.048		-0.053		
	4		-0.004		-0.019	-0.007		-0.040		
	5		-0.004		-0.020	-0.033		-0.031		
	6					-0.008		-0.008		
	7					-0.019				
number of boundary collocation points		6		5		5		3		

[1] $\nu = 0.33$ for all calculations.

[2] These shells have the same surface area.

Table 6.8

Symmetric Eigenvalues and Modal Participation Functions for Clamped Shallow Spherical Shells with Sliding Clamped Edges having 4, 5 and 6 Sides[1]

p		4[2]		5[3]		6[4]		
a/R		0.390625	0.5	0.390625	0.5	0.390625	0.5	
a/h		66.667	10	66.667	10	66.667	10	
mode i	1	4.66	4.24	6.00	4.00		3.48	k_i
	2	8.127	8.129	7.86	7.41	6.92	7.02	
	3	10.49	10.49	10.53	10.51	10.36	10.39	
	4	12.41	12.40	11.59	11.59	11.85	11.86	
	5	13.86	13.85	14.05	14.04	13.89	13.90	
	6	16.6	16.6	15.6	15.6	15.71	15.71	
	1	-41.4	-58.0	-19.3	-57.6		-87.5	$\left(\frac{X_1^i}{X_0^i}\right)_0$
	2	13.7	13.7	17.6	15.9	14.5	16.7	
	3	0.32	0.42	-8.7	-6.3	-6.3	-6.7	
	4	-3.2	-3.1	-5.6	-5.6	-2.3	-2.0	
	5	-1.5		3.9		3.5	3.5	
	6			2.4		0.2	0.2	
	1	-39.7	-55.0	-19.4	-57.2		-87.4	$\frac{X_1^i}{X_0^i}$
	2	9.70	9.70	16.9	15.0	14.3	16.4	
	3	-0.34	-0.33	-3.8	-3.4	-5.7	-6.1	
	4	-0.50	-0.49	-1.8	-1.8	-0.2	-1.3	
	5	0.19		2.1		2.8	2.9	
	6			0.4		-0.1	-0.1	
	1	-0.116	-0.155	-0.080	-0.132		-0.177	$a^2\frac{(X_1^i)_p}{X_0^i}$
	2	-0.055	-0.055	-0.036	-0.074	-0.087	-0.078	
	3	-0.006	-0.006	-0.021	-0.027	-0.048	-0.048	
	4	-0.004	-0.004	-0.019	-0.019	-0.007	-0.006	
	5	-0.004		-0.019		-0.033	-0.033	
	6			-0.010		-0.008	-0.008	

[1] $\nu = 0.33$ for all calculations.

[2] Edge conditions satisfied at 5 collocation points at $\theta = 45^\circ, 32^\circ, 23^\circ, 10^\circ, 0^\circ$.

[3] Edge conditions satisfied at 5 collocation points at $\theta = 36^\circ, 30^\circ, 20^\circ, 10^\circ, 0^\circ$.

[4] Edge conditions satisfied at 5 collocation points at $\theta = 5^\circ, 12^\circ, 18^\circ, 25^\circ, 30^\circ$.

for the second and third modal eigenvalues when the sliding edge is clamped against extension. Since values of k_1 could not be obtained for any of the simply supported shells with sliding free edges analysed, it would be logical to assume that k_1 is smaller for this edge condition set than for any of the other edge condition sets analysed, for any particular shell geometry, providing that the arguments given in Section 6.1 are valid. Eigenvalues for the lower modes of these shells were more sensitive to variations in the values of a/R and a/h for simply supported shells with sliding free edges than they were for simply supported shells with sliding clamped edges.

Comparison of eigenvalues for clamped shells with sliding edges having 4, 5 and 6 sides in Tables 6.7 and 6.8 shows, as well, that the eigenvalues for the lower modes increase when the sliding edge is clamped against extension. This increase appears to be most significant for the fundamental mode and affects only the first two or three modes, depending upon the values of a/R and a/h. Eigenvalues for the clamped shallow shells with sliding clamped edges agree to two or three digit accuracy with eigenvalues for clamped plates with the same boundary shape for modes higher than the first. Eigenvalues for the lower modes are more sensitive to

changes in values of a/R and a/h for clamped shells with sliding free edges than for clamped shells with sliding clamped edges.

Nodal lines for the first seven symmetric modes of response of a clamped shell with sliding free edges having 6 sides are shown in Fig. 6.3. These mode shapes are quite similar to the shapes for a clamped plate with 6 sides shown in Fig. 4.2b for the first five modes only.

The results given in Tables 6.1, 6.6, 6.7 and 6.8 indicate that the two stress function edge conditions $F_{vv} = \varepsilon_{ss} = 0$ can be satisfied numerically more accurately for the lower modes of vibration than can the edge conditions $F_{vv} = F_{vs} = 0$, likely because the former edge conditions are associated with higher eigenvalues than are the latter edge conditions. The accuracy of satisfaction of both sets of edge conditions in the stress function is dependent upon the values of a/R and a/h, especially for the edge conditions $F_{vv} = F_{vs} = 0$, and decreases with increasing value of the product of a/R and a/h.

For polygonal shells with sliding edges and as few as 4 sides, these stress function edge conditions usually have little effect on eigenvalues for modes higher than the third. Consequently, higher modal eigenvalues can be calculated from the uncoupled plate frequency equations in transverse displacement for these edge conditions. This uncoupling of the transverse displacement and stress function solutions does not occur

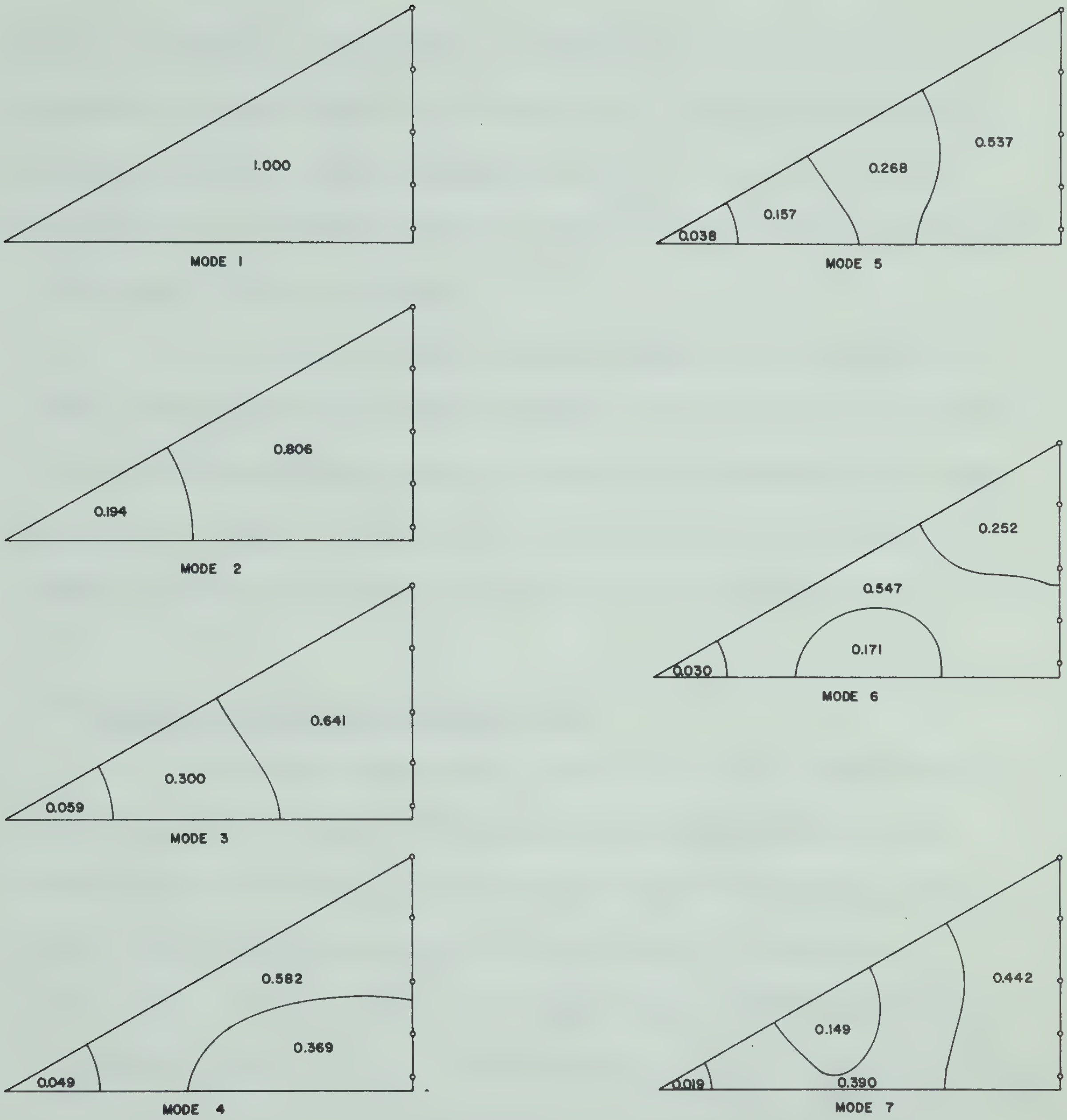

FIG. 6.3 Symmetric Mode Shapes for the Characteristic Segment of a Clamped Shallow Spherical Shell with Sliding Free Edges having 6 Sides and $a/R = 0.390625$, $a/h = 66.667$ and $\nu = 0.33$

for the simply supported or clamped shallow shells studied in Sections 6.1.2 and 6.1.3, which satisfy the stress function edge conditions $F_{vs} = \varepsilon_{ss} = 0$, until the fifth or sixth mode for shells with 6 sides and the fourth mode for 12 sides.

Values of modal participation functions for shells with sliding edges having 6 and 12 sides indicate that the fundamental mode governs the response of these shells to uniform loads while contributions of modes higher than the third are relatively insignificant.

6.2 Edge Condition Satisfaction

In the numerical solution of the transverse vibrations of plates and shallow shells with regular polygonal boundaries, edge conditions have been satisfied approximately using the boundary collocation technique. Using this technique, edge conditions were satisfied exactly only at discrete boundary points rather than along the entire boundary. The effect of the resultant numerical errors in the prescribed edge condition functions will be small in the interior for a stable solution, according to St. Venant's principle, if these errors or edge disturbances are small relative to maximum interior functional values.

It was found that the accuracy of satisfaction of a prescribed edge condition for a particular

function depends not only upon the number and location of the boundary collocation points and the degree of deviation of the boundary from a circle but also upon the interior spacial variation of the function and the functional derivative order when expressed in terms of the transverse displacement or stress function solutions.

Numerical satisfaction of homogeneous edge conditions is illustrated in Figs. 6.4 through 6.7 for the first three modes of vibration of a shallow spherical clamped shell with hexagonal plan having $a/h = 66.667$, $a/R = 0.390625$ and $\nu = 0.33$. Eigenvalues and modal participation functions were given for this shell in Table 6.5.

Plots of ratios of prescribed 'vanishing' edge functions $w(\tilde{\rho},\tilde{\theta})$, $\frac{\partial w}{\partial v}(\tilde{\rho},\tilde{\theta})$, $F_{vs}(\tilde{\rho},\tilde{\theta})$ and $\varepsilon_{ss}(\tilde{\rho},\tilde{\theta})$ to maximum interior values $(w)_{max}$, $(\frac{\partial w}{\partial v})_{max}$, $(F_{vs})_{max}$ and $(\varepsilon_{ss})_{max}$, respectively, for 3, 4 and 5 collocation points on the boundary of the characteristic shell segment show that edge condition satisfaction generally improves with increasing number of boundary collocation points. Of course, since each solution is found by inversion of a boundary equation matrix whose order depends upon the number of boundary collocation points used, there is a practical limit to the number of collocation points which can be satisfied. This limit

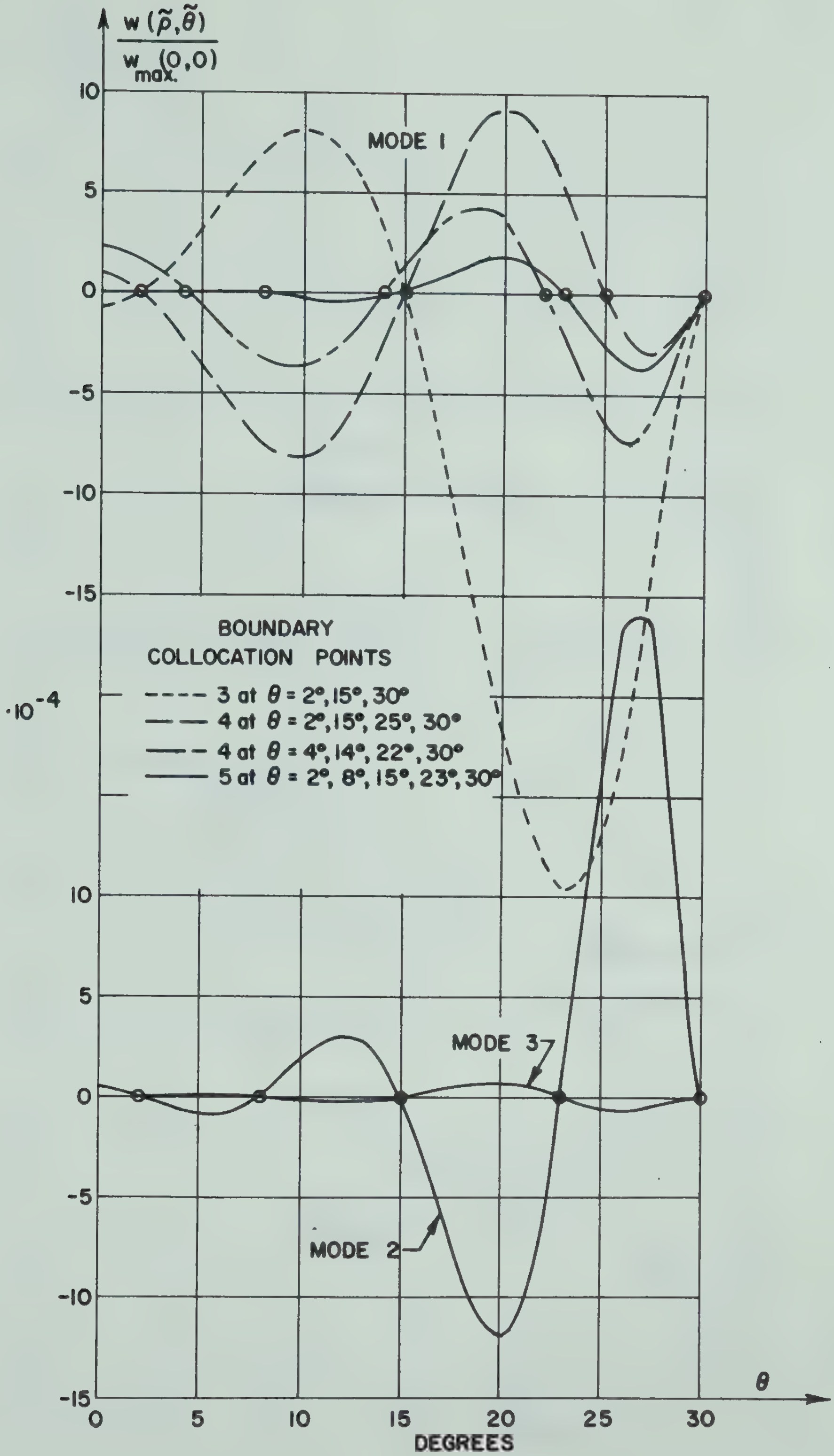

Fig. 6.4 Numerical Satisfaction of Vanishing Transverse Edge Displacement for a Clamped Shallow Spherical Shell with 6 Sides and a/R = 0.390625, a/h = 66.667 and ν = 0.33

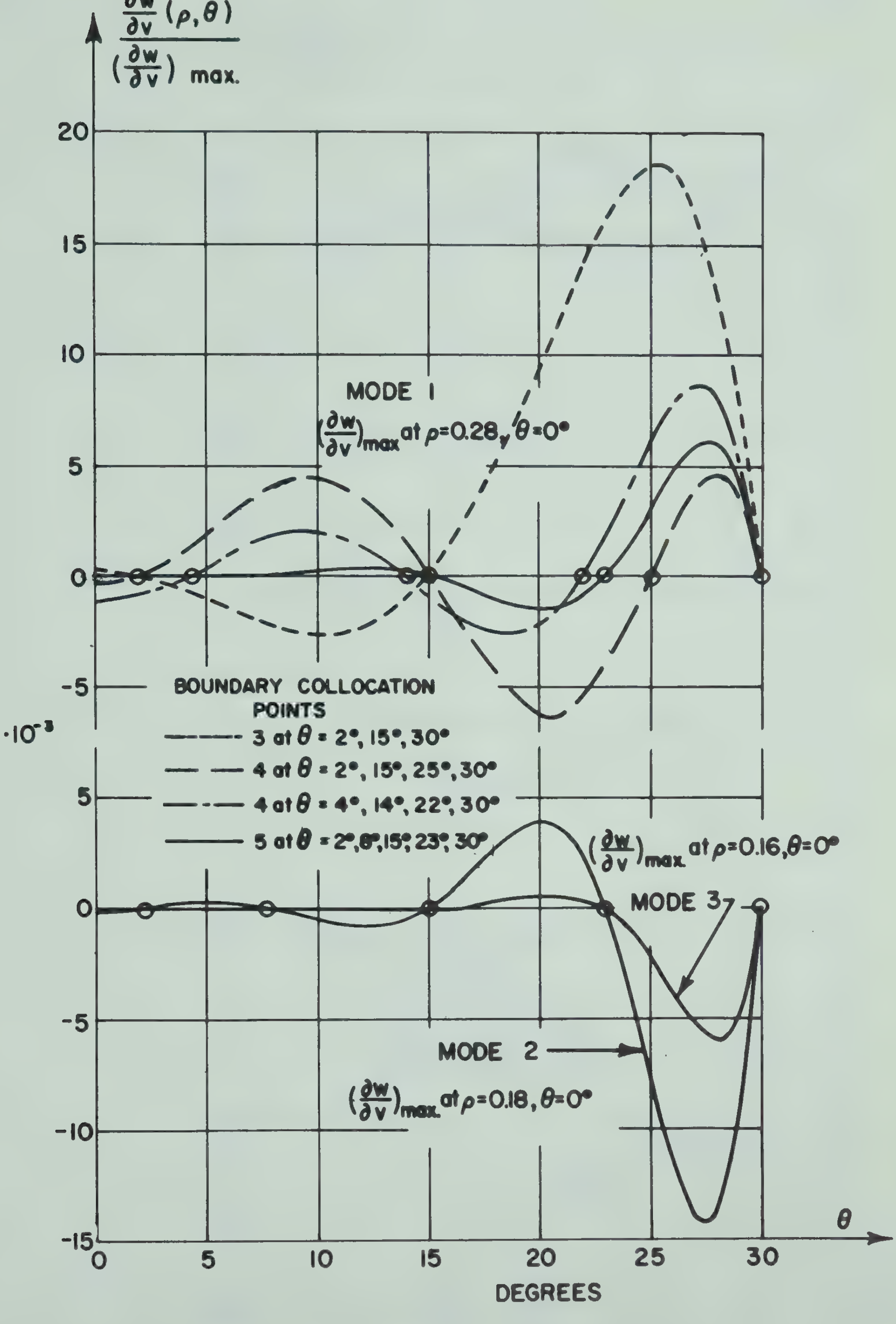

Fig. 6.5 Numerical Satisfaction of Vanishing Normal Slope for a Clamped Shallow Spherical Shell with 6 Sides and $a/R = 0.390625$, $a/h = 66.667$ and $\nu = 0.33$

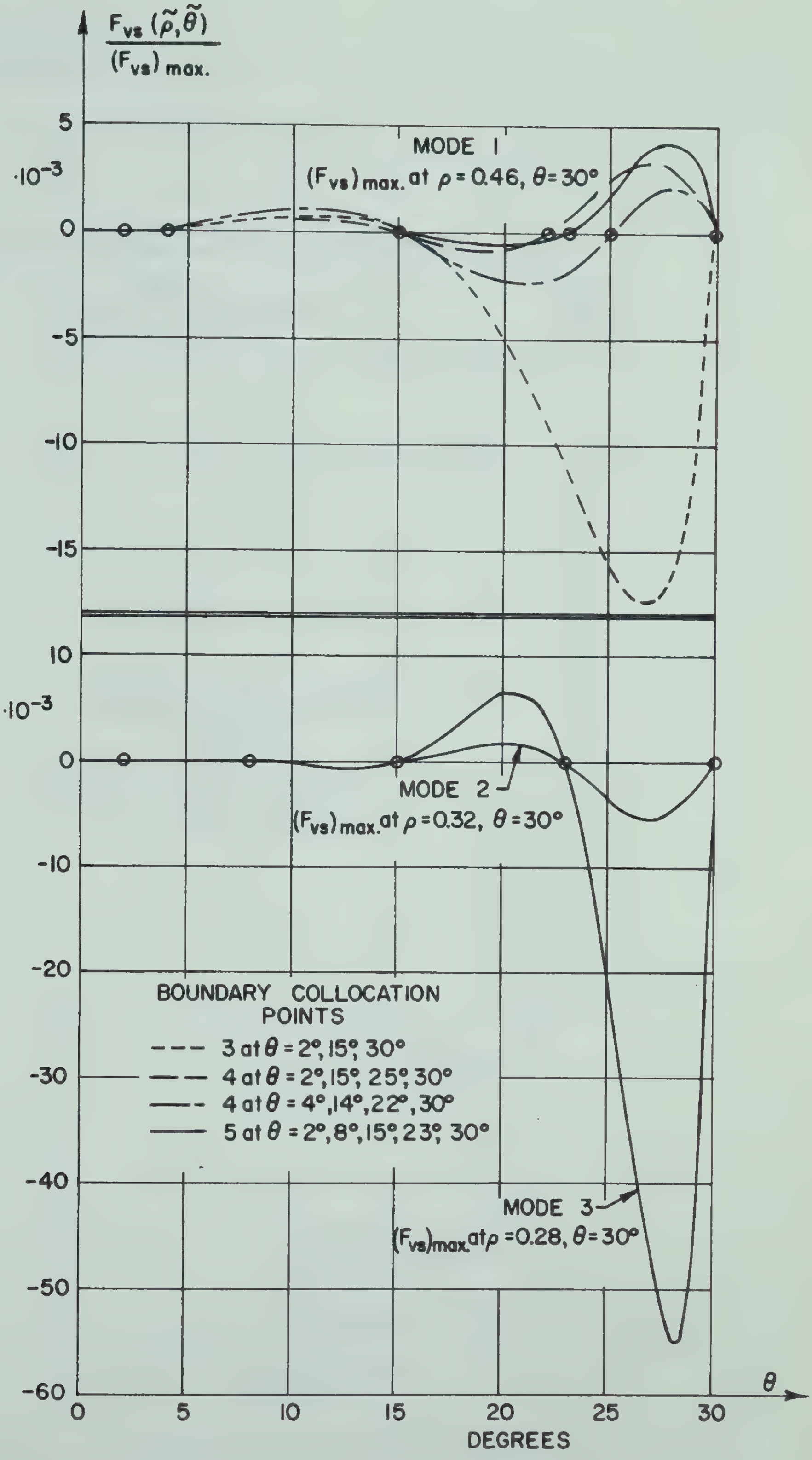

Fig. 6.6 Numerical Satisfaction of Vanishing Tangential Edge Shear for a Clamped Shallow Spherical Shell with 6 Sides and $a/R = 0.390625$, $a/h = 66.667$ and $\nu = 0.33$

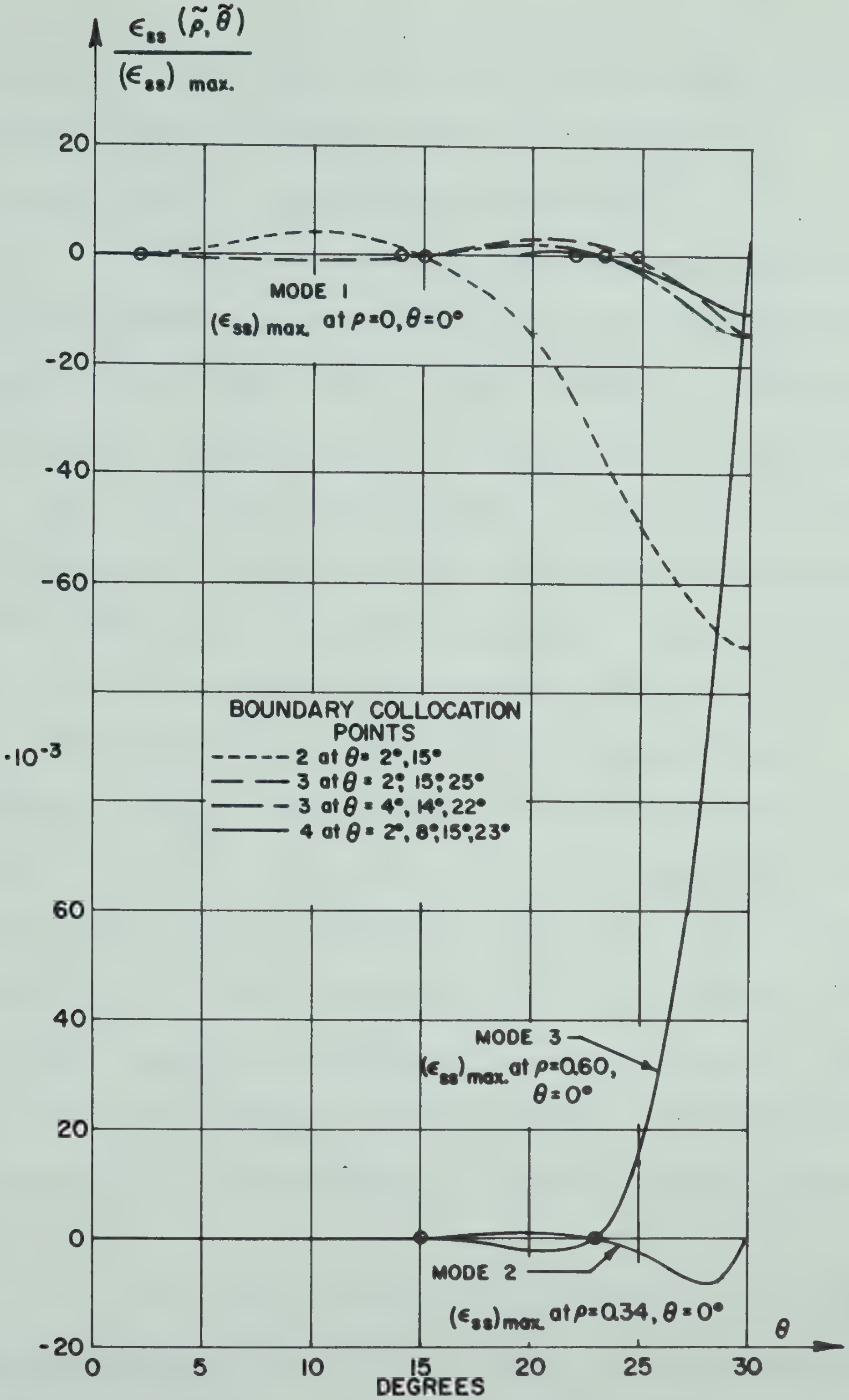

FIG. 6.7 - Numerical Satisfaction of Vanishing Tangential Edge Strain for a Clamped Shallow Spherical Shell with 6 Sides and a/R = 0.390625, a/h = 66.667 and $\nu = 0.33$

is dependent upon the relative 'conditioning' of the boundary equation matrix and the computational accuracy used in the numerical solution.

Plots of edge condition satisfaction for the first mode show that the degree of satisfaction generally decreases towards the boundary corners for equiangular spacing between collocation points. Thus, best edge condition satisfaction is achieved in general by decreasing the angular spacing between collocation points towards the boundary corners. In this example, the set of 4 boundary collocation points at $\theta = 2°, 15°, 25°, 30°$ gave smaller maximum deviations for all functions except displacement than did the set of 4 points at $\theta = 4°, 14°, 22°, 30°$. Consequently, for decreasing number of boundary sides and associated increasing boundary deviation from the circular shape, the total number of boundary collocation points satisfied over the complete shell boundary must be increased to maintain the same degree of edge condition satisfaction.

For the 5 collocation point set, the maximum edge condition errors for the first 3 modes occur in the second mode for the transverse displacement and normal slope functions and in the third mode for the tangential in-plane shear and strain functions. These

errors reflected the relative magnitude and proximity to the boundary of interior functional variations. In general, the degree of edge condition satisfaction expressed in terms of maximum interior values will decrease with increasing mode number.

In this example, maximum edge condition functional errors for the first three modes were 0.24 per cent of the maximum interior value for displacement, 1.43 per cent for normal slope, 5.5 per cent for tangential in-plane shear and 18.5 per cent for tangential strain. Since the maximum error for tangential strain occurred at the shell corner where strain was not prescribed to vanish, maximum boundary errors for strain are not indicative of the accuracy of the boundary collocation method. However, since slope is a first order derivative of transverse displacement and in-plane shear is a second order derivative of stress function, it is apparent that the degree of satisfaction of edge conditions tends to decrease with increasing order of the functional derivative of the transverse displacement and stress function solutions.

6.3 Series Convergence

The convergence of the series solutions for the functions describing each mode of response is illustrated for some edge condition functions in Table 6.9.

Table 6.9

Functional Series Convergence for the Third Mode of Response of a Uniformly Loaded Clamped Shell with 6 Sides

	position ρ,θ						
	0.16, 0°	0.16, 30°	0.56, 0°	0.56, 30°	0.84, 0°	0.96, 30°	order n
w (in.)	0.38699E-03	0.38699E-03	0.30796E-03	0.30796E-03	0.52606E-04	0.41145E-04	0
	0.38675E-03	0.38722E-03	0.20447E-03	0.41144E-03	-0.72300E-05	0.32116E-05	1
	0.38675E-03	0.38722E-03	0.20508E-03	0.41206E-03	0.68555E-05	-0.11849E-04	2
	0.38675E-03	0.38722E-03	0.20508E-03	0.41206E-03	0.55351E-05	0.53700E-07	3
	0.38675E-03	0.38722E-03	0.20508E-03	0.41206E-03	0.55532E-05	0.13821E-05	4
$\frac{\partial w}{\partial v}$	-0.16764E-03	-0.14518E-03	0.61413E-04	0.53186E-04	-0.50153E-04	0.36952E-04	0
	-0.16798E-03	-0.14489E-03	0.42922E-04	0.69199E-04	-0.17342E-04	0.12937E-04	1
	-0.16798E-03	-0.14489E-03	0.43360E-04	0.69579E-04	-0.16095E-04	-0.13727E-04	2
	-0.16798E-03	-0.14489E-03	0.43359E-04	0.69580E-04	-0.17138E-04	-0.67057E-05	3
	-0.16798E-03	-0.14489E-03	0.43359E-04	0.69580E-04	-0.17106E-04	-0.52990E-05	4
F_{vs} $\left(\frac{\text{lb.}}{\text{in.}}\right)$	0	0.49707E 01	0	-0.46926E 01	0	0.28051E 01	0
	0	0.50840E 01	0	-0.23259E 01	0	0.11217E 01	1
	0	0.50840E 01	0	-0.23593E 01	0	0.35879E 01	2
	0	0.50840E 01	0	-0.23590E 01	0	0.92675E 00	3
	0	0.50840E 01	0	-0.23590E 01	0	0.66602E 00	4
ε_{ss}	0.18926E-05	0.29105E-05	0.54364E-05	0.44755E-05	0.73852E-06	0.15437E-05	0
	0.19378E-05	0.28885E-05	0.58404E-05	0.45561E-05	0.20617E-06	0.22866E-05	1
	0.19378E-05	0.28885E-05	0.58556E-05	0.45645E-05	0.60507E-06	0.61585E-05	2
	0.19378E-05	0.28885E-05	0.58558E-05	0.45644E-05	0.53542E-06	0.13056E-05	3
	0.19378E-05	0.28885E-05	0.58558E-05	0.45644E-05	0.53312E-06	0.13912E-05	4

$q_o = 1$ psi, $a/R = 0.390625$, $a/h = 66.667$, $D = 0.49315$ E + 5 lb.-in., $\nu = 0.33$

These functions were calculated for the third mode of response of the uniformly loaded clamped shell with 6 sides and $a/R = 0.390625$, $a/h = 66.667$ and $\nu = 0.33$. Eigenvalues, eigenvectors and modal participation functions were obtained using 5 collocation points on the characteristic segment boundary. Consequently, the series solutions for $\bar{\eta}^i$ and $\bar{\xi}^i$, given in Eqs. (3.27a) and (3.27b), and their functional derivatives were all truncated with n ranging from 0 to 4.

Finite 'exact' solutions were obtained at the origin for $\bar{\eta}^i$ and $\bar{\xi}^i$ from the zero-order terms only, since all higher order terms vanish. Functional derivatives of $\bar{\eta}^i$ and $\bar{\xi}^i$ were difficult to obtain numerically in a small region about the origin. The number of terms in each series required to obtain a specified functional accuracy increased with radial distance from the origin, as these results show. Comparison of functional series convergence at $\rho = 0.84$, $\theta = 0°$ (0.027 from the boundary) and $\rho = 0.96$, $\theta = 30°$ (0.020 from the boundary) in Table 6.9 shows that convergence in the boundary region was less rapid towards the corners. Convergence of derivatives of the $\bar{\eta}^i$ and $\bar{\xi}^i$ functional series appeared to be slightly less rapid than the convergence of the functional series, themselves.

For this example, series solutions converged within two or three terms to an accuracy sufficient for most practical applications over most of the shell interior. Results did not converge so rapidly near the boundary, especially in the corner region, however the degree of accuracy obtained with five functional series terms is probably at least comparable to the consistency of results which would be obtained in practice. In general, the number of series terms necessary to obtain comparable functional accuracy increased with decreasing number of boundary sides p. It was felt also that the number of series terms required would increase with shallowness and thinness parameters a/R and a/h, respectively, although results for the shells analysed in Section 6.1 did not indicate any significant differences for these parameters.

6.4 Auxiliary Edge Conditions

The auxiliary edge conditions given in Eqs. (3.21) and (3.23) for the functions $\bar{g}^{\ell}(\rho,\theta)$ and $\bar{h}^{\ell}(\rho,\theta)$ which were assumed in the form

$$\bar{g}^{\ell}(\rho,\theta) = \sum_{n=0}^{\infty} \left[E^{1,\ell}_{pn}\, \rho^{pn} + E^{2,\ell}_{pn}\, \rho^{pn+2}\right] \cos pn\theta$$

$$\bar{h}^{\ell}(\rho,\theta) = \sum_{n=0}^{\infty} \left[F^{1,\ell}_{pn}\, \rho^{pn+2} + F^{2,\ell}_{pn}\, \rho^{pn+4}\right] \cos pn\theta$$

in Eqs. (3.25a) and (3.25b), were satisfied using the boundary collocation technique. The DRES IBM 1130 digital computer was employed for these calculations using 10 figure computational accuracy. The results are summarized in Table 6.10 and the coefficients $E^{1,\ell}_{pn}$, $E^{2,\ell}_{pn}$, $F^{1,\ell}_{pn}$, and $F^{2,\ell}_{pn}$ are given in Tables 6.11 through 6.16.

Convergent solutions for $\bar{h}^{\ell}(\rho,\theta)$ were not obtained for all edge conditions, especially for small values of p. Better results might be obtained for these cases by increasing the accuracy of the computer calculations, thereby permitting larger auxiliary edge condition matrices to be inverted accurately, or by choosing some different functional form for $\bar{h}^{\ell}(\rho,\theta)$ which will converge more rapidly.

The solutions obtained for $\bar{g}^{\ell}(\rho,\theta)$ can be used for both plates and shells with regular polygonal boundaries which are subjected to time-dependent edge conditions involving transverse displacement, slope normal to the edge or flexural stress couple tangential to the edge.

The function $\bar{g}^{\ell}(\rho,\theta)$ which is associated with time-dependent transverse edge displacement $\eta(\tilde{\rho},\tilde{\theta},t)$ is given by an exact one term solution in Table 6.10. The functions $\bar{h}^{1}(\rho,\theta)$ and $\bar{h}^{2}(\rho,\theta)$ which are associated with time-dependent edge stress resultant $F_{vv}(\tilde{\rho},\tilde{\theta},t)$ and

Table 6.10

Solutions for $\bar{g}^{\ell}(\rho,\theta)$ and $\bar{h}^{\ell}(\rho,\theta)$ for Auxiliary Edge Conditions

Auxiliary Edge Conditions	Solution
$L_1[\bar{g}^1(\tilde{\rho},\tilde{\theta})] = 1,\ L_2[\bar{g}^1(\tilde{\rho},\tilde{\theta})] = 0$	$\bar{g}^1(\rho,\theta) = 1$ for all p and ν
$L_1[\bar{g}^2(\tilde{\rho},\tilde{\theta})] = 0,\ L_2[\bar{g}^2(\tilde{\rho},\tilde{\theta})] = D/a$	$\bar{g}^2(\rho,\theta) = \sum_{n=0}^{L-1}\left[E_{pn}^{1,2}\rho^{pn} + E_{pn}^{2,2}\rho^{pn+2}\right]\cos pn\theta$, where $E_{pn}^{j,2} = E_{pn}^{j,2}(p)$; see Table 6.11
$L_1[\bar{g}^1(\tilde{\rho},\tilde{\theta})] = 1,\ L_3[\bar{g}^1(\tilde{\rho},\tilde{\theta})] = 0$	$\bar{g}^1(\rho,\theta) = 1$ for all p and ν
$L_1[\bar{g}^2(\tilde{\rho},\tilde{\theta})] = 0,\ L_3[\bar{g}^2(\tilde{\rho},\tilde{\theta})] = -1$	$\bar{g}^2(\rho,\theta) = \sum_{n=0}^{L-1}\left[E_{pn}^{1,2}\rho^{pn} + E_{pn}^{2,2}\rho^{pn+2}\right]\cos pn\theta$, where $E_{pn}^{j,2} = E_{pn}^{j,2}(p)$; see Table 6.12
$L_4[\bar{h}^1(\tilde{\rho},\tilde{\theta})] = Eh,\ L_5[\bar{h}^1(\tilde{\rho},\tilde{\theta})] = 0$	$\bar{h}^1(\rho,\theta) = \sum_{n=0}^{L-1}\left[F_{pn}^{1,1}\rho^{pn+2} + F_{pn}^{2,1}\rho^{pn+4}\right]\cos pn\theta$, where $F_{pn}^{j,1} = F_{pn}^{j,1}(p,\nu)$; see Table 6.13
$L_4[\bar{h}^2(\tilde{\rho},\tilde{\theta})] = 0,\ L_5[\bar{h}^2(\tilde{\rho},\tilde{\theta})] = 1$	$\bar{h}^2(\rho,\theta) = F_0^{1,2}\rho^2$, where $F_0^{1,2} = F_0^{1,2}(\nu)$; see Table 6.14
$L_6[\bar{h}^1(\tilde{\rho},\tilde{\theta})] = Eh,\ L_4[\bar{h}^1(\tilde{\rho},\tilde{\theta})] = 0$	$\bar{h}^1(\rho,\theta) = \rho^2$ for all p and ν
$L_6[\bar{h}^2(\tilde{\rho},\tilde{\theta})] = 0,\ L_4[\bar{h}^2(\tilde{\rho},\tilde{\theta})] = Eh$	$\bar{h}^2(\rho,\theta) = \sum_{n=0}^{L-1}\left[F_{pn}^{1,2}\rho^{pn+2} + F_{pn}^{2,2}\rho^{pn+4}\right]\cos pn\theta$, where $F_{pn}^{j,2} = F_{pn}^{j,2}(p)$; no convergent solutions obtained using the IBM 1130 digital computer
$L_6[\bar{h}^1(\tilde{\rho},\tilde{\theta})] = Eh,\ L_5[\bar{h}^1(\tilde{\rho},\tilde{\theta})] = 0$	$\bar{h}^1(\rho,\theta) = \sum_{n=0}^{L-1}\left[F_{pn}^{1,1}\rho^{pn+2} + F_{pn}^{2,1}\rho^{pn+4}\right]\cos pn\theta$, where $F_{pn}^{j,1} = F_{pn}^{j,1}(p,\nu)$; see Table 6.15
$L_6[\bar{h}^2(\tilde{\rho},\tilde{\theta})] = 0,\ L_5[\bar{h}^2(\tilde{\rho},\tilde{\theta})] = -1$	$\bar{h}^2(\rho,\theta) = \sum_{n=0}^{L-1}\left[F_{pn}^{1,2}\rho^{pn+2} + F_{pn}^{2,2}\rho^{pn+4}\right]\cos pn\theta$, where $F_{pn}^{j,2} = F_{pn}^{j,2}(p,\nu)$; see Table 6.16

Note

L_1 is associated with η, L_2 with M_{vs}, L_3 with $\partial\eta/\partial v$, L_4 with F_{vs}, L_5 with ϵ_{ss} and L_6 with F_{vv}.

Table 6.11

Coefficients $E_{pn}^{j,2}(p)^{*}$ for Auxiliary Edge Conditions $L_1[\bar{g}^2(\tilde{\rho},\tilde{\theta})] = 0,\ \frac{a}{D} L_2[\bar{g}^2(\tilde{\rho},\tilde{\theta})] = 1$

	Order n	Number of sides p							
		3	4	5	6	7	8	12	15
$E_{pn}^{1,2}$	0	0.833333E-01	0.1472E 00	0.1828E 00	0.205 E 00	0.222E 00	0.235E 00	0.27E 00	0.30E 00
	1	-0.166667E 00	-0.910 E-01	-0.566 E-01	-0.395 E-01	-0.31 E-01	-0.22 E-01	-0.14E-01	-0.4 E-02
	2		0.75 E-02	0.75 E-02	0.72 E-02	0.66 E-02	0.1 E-01	0.8 E-02	0.2 E-01
	3		-0.18 E-02	-0.3 E-02	-0.35 E-02	-0.59 E-02	0.1 E-01	-0.1 E-02	0.2 E-01
	4		0.63 E-03	0.2 E-02	0.3 E-02	-0.9 E-04	0.2 E-01	0.1 E-01	0.2 E-01
	5		-0.2 E-03	-0.3 E-03	-0.4 E-02	-0.1 E-01			
	6		0.3 E-03	0.8 E-02	0.5 E-02				
	7		0.1 E-02						
	8		0.4 E-02						
$E_{pn}^{2,2}$	0	-0.250000E 00	-0.2498E 00	-0.2507E 00	-0.2532E 00	-0.258E 00	-0.262E 00	-0.28E 00	-0.31E 00
	1		-0.2 E-03	0.6 E-03	0.2 E-02	0.33 E-02	0.2 E-02	0.5 E-02	-0.1 E-02
	2		0.2 E-03	-0.4 E-03	-0.1 E-02	-0.20 E-02	-0.8 E-02	-0.5 E-02	-0.2 E-01
	3		-0.2 E-03	0.2 E-03	0.1 E-02	0.4 E-02	-0.1 E-01	0.4 E-03	-0.2 E-01
	4		0.2 E-03	-0.7 E-03	-0.2 E-02	0.1 E-02	-0.2 E-01	-0.1 E-01	-0.2 E-01
	5		-0.3 E-03	-0.9 E-03	0.3 E-02	0.1 E-01			
	6		0.1 E-04	-0.8 E-02	-0.5 E-02				
	7		-0.2 E-02						
	8		-0.5 E-02						

* Values given for $E_{pn}^{j,2}$ were obtained using $\nu = 0.5$. Although $E_{pn}^{j,2}$ is independent of ν, best series convergence of $\bar{g}^2(\rho,\theta)$ was obtained for $\nu = 0.5$.

Table 6.12

Coefficients $E_{pn}^{j,2}(p)$ for Auxiliary Edge Conditions $L_1[\bar{g}^2(\tilde{\rho},\tilde{\theta})] = 0$, $L_3[\bar{g}^2(\tilde{\rho},\tilde{\theta})] = -1$

			Number of sides p							
			3	4	5	6	7	8	12	15
$E_{pn}^{1,2}$	Order n	0	0.23577E 00	0.3337E 00	0.384E 00	0.4147E 00	0.44E 00	0.46 E 00	0.47E 00	0.48E 00
		1	-0.661 E 00	-0.376 E 00	-0.258E 00	-0.192 E 00	-0.15E 00	-0.15 E 00	-0.8 E-01	-0.6 E-01
		2	0.287 E 00	0.16 E 00	0.1 E 00	0.1 E 00	0.7 E-01	-0.2 E-01	0.1 E-01	0.1 E 00
		3	-0.163 E 00	-0.1 E 00	-0.5 E-01	-0.6 E-01	-0.6 E-01	-0.3 E 00		
		4	0.11 E 00	0.7 E-01	0.2 E-01	0.2 E-02	-0.2 E-01			
		5	-0.8 E-01	-0.7 E-01	0.7 E-02	-0.2 E 00	-0.2 E 00			
		6	-0.1 E 00	-0.1 E 00	0.1 E-01	0.6 E 00				
		7	-0.6 E 00	-0.1 E 01	0.2 E 00	0.7 E 00				
		8	-0.2 E 01	-0.2 E 01	0.4 E 00					
		9	-0.4 E 00	-0.2 E 01						
$E_{pn}^{2,2}$		0	-0.68245E 00	-0.5527E 00	-0.519E 00	-0.507 E 00	-0.51E 00	-0.52 E 00	-0.49E 00	-0.49E 00
		1	0.446 E 00	0.25 E 00	0.177E 00	0.13 E 00	0.1 E 00	0.10 E 00	0.6 E-01	0.5 E-01
		2	-0.166 E 00	-0.1 E 00	-0.8 E-01	-0.9 E-01	-0.7 E-01	0.2 E-01	-0.1 E 00	-0.1 E 00
		3	0.15 E 00	0.9 E-01	0.4 E-01	0.6 E-01	0.5 E-01	0.3 E 00		
		4	-0.9 E-01	-0.7 E-01	-0.9 E-02	0.3 E-01	0.2 E-01			
		5	0.9 E-01	0.6 E-01	-0.2 E-01	0.3 E 00	0.2 E 00			
		6	0.4 E 00	0.2 E 00	-0.6 E-02	0.6 E 00				
		7	0.2 E 01	0.2 E 01	-0.3 E 00	0.7 E 00				
		8	0.5 E 01	0.4 E 01	-0.5 E 00					
		9	0.3 E 01	0.2 E 01						

Table 6.13

Coefficients $F_{pn}^{j,1}(p,\nu)$* for Auxiliary Edge Conditions $\frac{1}{Eh} L_4[\bar{h}^1(\tilde{\rho},\tilde{\theta})] = 1,\ L_5[\bar{h}^1(\tilde{\rho},\tilde{\theta})] = 0$

		Number of Sides p							
		7				8			
		Poisson's ratio ν							
	order n	0.0	0.1	0.33	0.5	0.0	0.1	0.33	0.5
$F_{pn}^{1,1}$	0	0.106 E 01	not convergent	not convergent	not convergent	0.138E 01	0.16 E 01	0.21 E 01	0.24 E 01
	1	0.12 E 00				0.91 E-01	0.97 E-01	0.115E 00	0.136E 00
	2	0.5 E-01				0.33 E-01	0.414E-01	0.561E-01	0.72 E-01
	3	0.3 E-01				0.16 E-01	0.262E-01	0.37 E-01	0.48 E-01
	4	0.1 E-01				0.5 E-02	0.172E-01	0.237E-01	0.32 E-01
	5						0.5 E-02	0.6 E-02	0.1 E-01
	6								0.2 E-02
$F_{pn}^{2,1}$	0	-0.250 E 00				-0.292E 00	-0.32 E 00	-0.34 E 00	-0.34 E 00
	1	-0.9 E-01				-0.69 E-01	-0.76 E-01	-0.94 E-01	-0.114E 00
	2	-0.5 E-01				-0.30 E-01	-0.388E-01	-0.542E-01	-0.709E-01
	3	-0.3 E-01				-0.16 E-01	-0.262E-01	-0.38 E-01	-0.50 E-01
	4	-0.1 E-01				-0.5 E-02	-0.176E-01	-0.248E-01	-0.33 E-01
	5						-0.5 E-02	-0.6 E-02	-0.1 E-01
	6								-0.3 E-02

		Number of Sides p							
		12				15			
		Poisson's ratio ν							
	order n	0.0	0.1	0.33	0.5	0.0	0.1	0.33	0.5
$F_{pn}^{1,1}$	0	0.2269E 01	0.246E 01	0.313E 01	0.401E 01	0.292E 01	0.318E 01	0.407E 01	0.517E 01
	1	0.473 E-01	0.521E-01	0.664E-01	0.811E-01	0.346E-01	0.387E-01	0.510E-01	0.605E-01
	2	0.141 E-01	0.164E-01	0.235E-01	0.317E-01	0.988E-02	0.117E-01	0.173E-01	0.20 E-01
	3	0.67 E-02	0.77 E-02	0.111E-01	0.15 E-01	0.501E-02	0.587E-02	0.863E-02	0.5 E-02
	4	0.3 E-02	0.3 E-02	0.5 E-02	0.6 E-02	0.29 E-02	0.34 E-02	0.51 E-02	
	5	0.7 E-03	0.8 E-03	0.1 E-02	0.1 E-02	0.11 E-02	0.13 E-02	0.16 E-02	
$F_{pn}^{2,1}$	0	-0.4175E 00	-0.425E 00	-0.444E 00	-0.461E 00	-0.518E 00	-0.528E 00	-0.552E 00	-0.564E 00
	1	-0.377 E-01	-0.423E-01	-0.556E-01	-0.692E-01	-0.285E 00	-0.323E-01	-0.437E-01	-0.526E-01
	2	-0.128 E-01	-0.151E-01	-0.222E-01	-0.302E-01	-0.907E-02	-0.108E-01	-0.164E-01	-0.19 E-01
	3	-0.64 E-02	-0.75 E-02	-0.11 E-01	-0.15 E-01	-0.479E-02	-0.565E-02	-0.842E-02	-0.5 E-02
	4	-0.3 E-02	-0.3 E-02	-0.5 E-02	-0.6 E-02	-0.28 E-02	-0.33 E-02	-0.50 E-02	
	5	-0.7 E-03	-0.8 E-03	-0.1 E-02	-0.1 E-02	-0.11 E-02	-0.12 E-02	-0.16 E-02	

* Convergent series for $\bar{h}^1(\rho,\theta)$ were not obtained for $p < 7$.

Table 6.14

Coefficients $F_0^{1,2}(\nu)$* for Auxiliary Edge Conditions $L_4[\bar{h}^2(\tilde{\rho},\tilde{\theta})] = 0,\ L_5[\bar{h}^2(\tilde{\rho},\tilde{\theta})] = 1$

ν	0.0	0.1	0.2	0.3	0.33	0.4	0.5
$F_0^{1,2}$	0.500000	0.555556	0.625000	0.714286	0.746269	0.833333	1.0

* $F_0^{1,2}$ is given approximately by $F_0^{1,2} = 0.18393 \exp[\exp(1.0531\nu)]$.

Table 6.15

Coefficients $F_{pn}^{j,1}(p,\nu)^*$ for Auxiliary Edge Conditions $\frac{1}{Eh}L_6[\bar{h}^1(\tilde{\rho},\tilde{\theta})] = 1,\ L_5[\bar{h}^1(\tilde{\rho},\tilde{\theta})] = 0$

			Number of Sides p							
			5				6			
			Poisson's ratio ν							
			0.0	0.1	0.33	0.5	0.0	0.1	0.33	0.5
$F_{pn}^{1,1}$	order n	0	0.1767E 01	0.1705E 01	0.1562E 01	0.1448E 01	0.170E 01	0.163E 01	0.1476E 01	0.1363E 01
		1	0.94 E-01	0.83 E-01	0.61 E-01	0.47 E-01	0.413E-01	0.377E-01	0.282 E-01	0.211 E-01
		2	-0.15 E-01	-0.17 E-01	-0.23 E-01	-0.25 E-01	-0.1 E-01	-0.9 E-02	-0.8 E-02	-0.70 E-02
		3	0.7 E-02	0.8 E-02	0.9 E-02	0.81 E-02	-0.2 E-02	-0.4 E-03	0.1 E-02	0.13 E-02
		4	-0.4 E-02	-0.4 E-02	-0.4 E-02	-0.24 E-02	-0.9 E-02	-0.6 E-02	-0.3 E-02	-0.2 E-02
		5	0.4 E-02	0.3 E-02	0.2 E-02	0.1 E-02	-0.1 E-01	-0.8 E-02	-0.3 E-02	-0.1 E-02
		6	-0.1 E-02	-0.1 E-02	-0.8 E-03	-0.4 E-03	-0.3 E-01	-0.2 E-01	-0.7 E-02	-0.4 E-02
		7	0.7 E-02	0.5 E-02	0.2 E-02	0.9 E-03	-0.2 E-01	-0.1 E-01	-0.4 E-02	-0.2 E-02
		8	0.5 E-02	0.3 E-02	0.1 E-02	0.6 E-03				
$F_{pn}^{2,1}$		0	-0.481 E 00	-0.444 E 00	-0.357 E 00	-0.2864E 00	-0.387E 00	-0.351E 00	-0.2684E 00	-0.2052E 00
		1	-0.62 E-01	-0.51 E-01	-0.29 E-01	-0.18 E-01	-0.296E-01	-0.267E-01	-0.180 E-01	-0.127 E-01
		2	0.8 E-02	0.11 E-01	0.19 E-01	0.24 E-01	0.8 E-02	0.7 E-02	0.7 E-02	0.63 E-02
		3	-0.6 E-02	-0.7 E-02	-0.8 E-02	-0.73 E-02	0.3 E-02	0.9 E-03	-0.8 E-03	-0.11 E-02
		4	0.4 E-02	0.4 E-02	0.3 E-02	0.20 E-02	0.1 E-01	0.6 E-02	0.3 E-02	0.2 E-02
		5	-0.4 E-02	-0.3 E-02	-0.2 E-02	-0.1 E-02	0.2 E-01	0.9 E-02	0.4 E-02	0.2 E-02
		6	0.7 E-03	0.9 E-03	0.6 E-03	0.3 E-03	0.3 E-01	0.2 E-01	0.8 E-02	0.5 E-02
		7	-0.8 E-02	-0.6 E-02	-0.2 E-02	-0.1 E-02	0.2 E-01	0.1 E-01	0.5 E-02	0.3 E-02
		8	-0.6 E-02	-0.4 E-02	-0.2 E-02	-0.9 E-03				

			Number of Sides p							
			7				8			
			Poisson's ratio ν							
			0.0	0.1	0.33	0.5	0.0	0.1	0.33	0.5
$F_{pn}^{1,1}$	order n	0	0.161 E 01	0.155 E 01	0.140 E 01	0.130 E 01	0.157E 01	0.152E 01	0.139 E 01	0.129 E 01
		1	0.27 E-01	0.24 E-01	0.18 E-01	0.14 E-01	0.18 E-01	0.17 E-01	0.13 E-01	0.99 E-02
		2	0.1 E-02	0.1 E-02	0.3 E-02	0.4 E-02	0.1 E-02	0.1 E-02	0.1 E-02	0.1 E-02
		3	0.4 E-02	0.4 E-02	0.4 E-02	0.4 E-02	0.3 E-02	0.3 E-02	0.3 E-02	0.3 E-02
		4	0.4 E-02	0.4 E-02	0.5 E-02	0.6 E-02	0.4 E-02	0.5 E-02	0.4 E-02	0.4 E-02
		5	0.5 E-02	0.5 E-02	0.6 E-02	0.7 E-02	0.4 E-02	0.4 E-02	0.4 E-02	0.3 E-02
$F_{pn}^{2,1}$		0	-0.335 E 00	-0.303 E 00	-0.229 E 00	-0.173 E 00	-0.309E 00	-0.279E 00	-0.210 E 00	-0.158 E 00
		1	-0.20 E-01	-0.17 E-01	-0.12 E-01	-0.9 E-02	-0.14 E-01	-0.13 E-01	-0.95 E-02	-0.73 E-02
		2	-0.2 E-02	-0.2 E-02	-0.3 E-02	-0.4 E-02	-0.1 E-02	-0.1 E-02	-0.1 E-02	-0.1 E-02
		3	-0.3 E-02	-0.4 E-02	-0.4 E-02	-0.4 E-02	-0.3 E-02	-0.3 E-02	-0.3 E-02	-0.3 E-02
		4	-0.4 E-02	-0.5 E-02	-0.6 E-02	-0.7 E-02	-0.4 E-02	-0.5 E-02	-0.5 E-02	-0.4 E-02
		5	-0.5 E-02	-0.5 E-02	-0.6 E-02	-0.7 E-02	-0.4 E-02	-0.4 E-02	-0.4 E-02	-0.3 E-02

			Number of Sides p							
			12				15			
			Poisson's ratio ν							
			0.0	0.1	0.33	0.5	0.0	0.1	0.33	0.5
$F_{pn}^{1,1}$	order n	0	0.155 E 01	0.149 E 01	0.137 E 01	0.128 E 01	0.154E 01	0.149E 01	0.136 E 01	0.127 E 01
		1	0.3 E-02	0.3 E-02	0.2 E-02	0.1 E-02	0.6 E-03	0.5 E-03	0.3 E-03	0.2 E-03
		2	-0.6 E-03	-0.6 E-03	-0.5 E-03	-0.4 E-03	-0.8 E-03	-0.7 E-03	-0.6 E-03	-0.5 E-03
		3	-0.1 E-04	-0.1 E-04	-0.2 E-04	-0.1 E-04	-0.3 E-03	-0.3 E-03	-0.3 E-03	-0.2 E-03
		4	-0.3 E-03	-0.3 E-03	-0.2 E-03	-0.2 E-03	-0.2 E-03	-0.2 E-03	-0.2 E-03	-0.1 E-03
$F_{pn}^{2,1}$		0	-0.276 E 00	-0.249 E 00	-0.186 E 00	-0.139 E 00	-0.268E 00	-0.242E 00	-0.180 E 00	-0.134 E 00
		1	-0.3 E-02	-0.2 E-02	-0.2 E-02	-0.1 E-02	-0.6 E-03	-0.5 E-03	-0.3 E-03	-0.2 E-03
		2	0.5 E-03	0.5 E-03	0.4 E-03	0.3 E-03	0.7 E-03	0.7 E-03	0.5 E-03	0.4 E-03
		3	0.2 E-04	0.2 E-04	0.2 E-04	0.2 E-04	0.3 E-03	0.3 E-03	0.2 E-03	0.2 E-03
		4	0.3 E-03	0.3 E-03	0.2 E-03	0.2 E-03	0.2 E-03	0.2 E-03	0.2 E-03	0.1 E-03

* Convergent series for $\bar{h}^1(\rho,\theta)$ were not obtained for $p < 5$.

Table 6.16

Coefficients $F^{j,2}_{pn}(p,\nu)$* for Auxiliary Edge Conditions $L_6[\bar{h}^2(\tilde{\rho},\tilde{\theta})] = 0$, $L_5[\bar{h}^2(\tilde{\rho},\tilde{\theta})] = -1$

	order n	Number of Sides p **											
		5				6				7	8	12	15
		Poisson's ratio ν											
		0.0	0.1	0.33	0.5	0.0	0.1	0.33	0.5				
$F^{1,2}_{pn}$	0	0.767E 00	0.783E 00	0.838E 00	0.896 E 00	0.684E 00	0.690 E 00	0.707 E 00	0.723 E 00	0.66 E 00	0.607E 00	0.55 E 00	0.54 E 00
	1	0.94 E-01	0.92 E-01	0.91 E-01	0.94 E-01	0.42 E-01	0.422 E-01	0.416 E-01	0.415 E-01	0.20 E-01	0.12 E-01	0.3 E-02	0.4 E-03
	2	-0.15 E-01	-0.19 E-01	-0.34 E-01	-0.504 E-01	-0.7 E-02	-0.75 E-02	-0.10 E-01	-0.129 E-01	-0.7 E-02	-0.16 E-02	-0.7 E-03	-0.9 E-03
	3	0.7 E-02	0.9 E-02	0.13 E-01	0.163 E-01	0.7 E-03	0.1 E-02	0.25 E-02	0.32 E-02	-0.1 E-02	0.9 E-04	-0.3 E-04	-0.4 E-03
	4	-0.4 E-02	-0.5 E-02	-0.6 E-02	-0.48 E-02	-0.3 E-02	-0.3 E-02	-0.2 E-02	-0.2 E-02	-0.4 E-02	0.1 E-03	-0.3 E-03	-0.3 E-03
	5	0.4 E-02	0.4 E-02	0.3 E-02	0.21 E-02	-0.2 E-02	-0.2 E-02	-0.8 E-03	-0.4 E-03	-0.6 E-02	-0.2 E-03		
	6	-0.1 E-02	-0.1 E-02	-0.1 E-02	-0.7 E-03	-0.5 E-02	-0.4 E-02	-0.3 E-02	-0.2 E-02	-0.1 E-01	0.1 E-03		
	7	0.7 E-02	0.5 E-02	0.3 E-02	0.2 E-02	-0.7 E-02	-0.6 E-02	-0.3 E-02	-0.3 E-02	-0.2 E-01	-0.1 E-03		
	8	0.5 E-02	0.4 E-02	0.2 E-02	0.1 E-02	-0.1 E-01	-0.9 E-02	-0.6 E-02	-0.5 E-02	-0.1 E-01	0.7 E-04		
	9					-0.6 E-02	-0.5 E-02	-0.3 E-02	-0.2 E-02	-0.5 E-02	-0.5 E-04		
$F^{2,2}_{pn}$	0	-0.481E 00	-0.493E 00	-0.533E 00	-0.5728E 00	-0.385E 00	-0.3890E 00	-0.4004E 00	-0.4103E 00	-0.352E 00	-0.320E 00	-0.277E 00	-0.268E 00
	1	-0.62 E-01	-0.57 E-01	-0.44 E-01	-0.35 E-01	-0.30 E-01	-0.290 E-01	-0.263 E-01	-0.245 E-01	-0.13 E-01	-0.80 E-02	-0.2 E-02	-0.3 E-03
	2	0.8 E-02	0.12 E-01	0.28 E-01	0.47 E-01	0.5 E-02	0.56 E-02	0.85 E-02	0.115 E-01	0.6 E-02	0.13 E-02	0.7 E-03	0.9 E-03
	3	-0.6 E-02	-0.8 E-02	-0.12 E-01	-0.15 E-01	-0.3 E-03	-0.9 E-03	-0.2 E-02	-0.27 E-02	0.1 E-02	-0.1 E-04	0.4 E-04	0.4 E-03
	4	0.4 E-02	0.4 E-02	0.5 E-02	0.40 E-02	0.3 E-02	0.3 E-02	0.2 E-02	0.2 E-02	0.5 E-02	-0.2 E-03	0.3 E-03	0.3 E-03
	5	-0.4 E-02	-0.4 E-02	-0.3 E-02	-0.19 E-02	0.3 E-02	0.2 E-02	0.1 E-02	0.7 E-03	0.6 E-02	0.2 E-03		
	6	0.7 E-03	0.1 E-02	0.1 E-02	0.6 E-03	0.6 E-02	0.5 E-02	0.3 E-02	0.3 E-02	0.1 E-01	-0.1 E-03		
	7	-0.8 E-02	-0.7 E-02	-0.4 E-02	-0.2 E-02	0.9 E-02	0.7 E-02	0.4 E-02	0.3 E-02	0.2 E-01	0.1 E-03		
	8	-0.6 E-02	-0.5 E-02	-0.3 E-02	-0.2 E-02	0.1 E-01	0.1 E-01	0.7 E-02	0.5 E-02	0.2 E-01	-0.8 E-04		
	9					0.7 E-02	0.5 E-02	0.3 E-02	0.3 E-02	0.5 E-02	0.6 E-04		

* Convergent series for $\bar{h}^2(\rho,\theta)$ were not obtained for $p < 5$.

** F_{pn} are independent of ν to accuracy given for $p > 6$.

strain $\varepsilon_{ss}(\tilde{\rho},\tilde{\theta},t)$, respectively, are given by one term solutions in Table 6.10, also, when either edge condition is used in conjunction with shear $F_{vs}(\tilde{\rho},\tilde{\theta})$ as the second edge condition in stress function. The evaluation of the modal participation functions $\chi_2^{\ell,i}$, associated with $\bar{h}^{\ell}(\rho,\theta)$ in Eq. (3.31c), and $\chi_3^{1,i}$, associated with $\bar{g}^{1}(\rho,\theta)$ in Eq. (3.31d), simplifies considerably for these time-dependent edge conditions.

For the time-dependent edge condition $\eta(\tilde{\rho},\tilde{\theta},t)$, Eq. (3.34d) becomes

$$\chi_3^{1,i} = A_0^i\,\phi_{13} + B_0^i\,\phi_{14} + C_0^i\,\phi_{15}\,. \tag{6.20}$$

Thus $\chi_3^{1,i}$ is given simply by the zero-order terms of χ_1^i.

For the time-dependent edge condition $\varepsilon_{ss}(\tilde{\rho},\tilde{\theta},t)$ used in conjunction with the edge condition $F_{vs}(\tilde{\rho},\tilde{\theta})$, Eq. (3.34c) becomes

$$\chi_2^{2,i} = 4\,F_0^{1,2}\left[A_0^i\,\phi_{13} + B_0^i\,\phi_{14} + C_0^i\,\phi_{15}\right]. \tag{6.21}$$

Thus $\chi_2^{2,i}$ is simply a constant $4\,F_0^{1,2}$ times the zero-order terms of χ_1^i where $F_0^{1,2}$ is given in Table 6.14.

For the time-dependent edge condition $F_{vv}(\tilde{\rho},\tilde{\theta},t)$ used in conjunction with the edge condition $F_{vs}(\tilde{\rho},\tilde{\theta})$, Eq. (3.34c) becomes

$$\chi_2^{1,i} = 4\left[A_0^i \phi_{13} + B_0^i \phi_{14} + C_0^i \phi_{15}\right] . \tag{6.22}$$

Thus $\chi_2^{1,i}$ is simply four times the zero-order terms of χ_1^i.

CHAPTER 7

EXPERIMENTAL COMPARISON WITH THEORY FOR A SHALLOW SPHERICAL SHELL ENCLOSING AN HEXAGONAL BASE

7.1 Procedure

7.1.1 Experimental Shell. A shallow spherical spun aluminium alloy 65S-T4 shell with hexagonal planform was mounted in the rolling section of the DRES six-foot diameter shock tube using the two support arrangements shown in Figs. 7.1a and 7.1b. The shell thickness h, nominally 0.375 in., was checked with calipers at a few positions near the boundary and appeared to be 0.375 in. (± 0.005 in.). For Trial 1, the shell had a base circle circumscribing diameter 2a of 50.0 in. (± 0.02 in.) and a spherical radius R of approximately 64 in., and for Trial 2 the diameter increased to 50.20 in. (± 0.05 in.) and the spherical radius ranged between 64 and 70 in. For theoretical comparison purposes, the experimental shell geometric shallowness and thinness parameters a/R and a/h will be quoted as 0.390625 and 66.667, respectively, in reference to nominal values for a, R and h of 25 in., 64 in. and 0.375 in., respectively. Young's modulus E and Poisson's ratio ν for the shell were assumed to be 10^7 psi and 0.33, respectively.

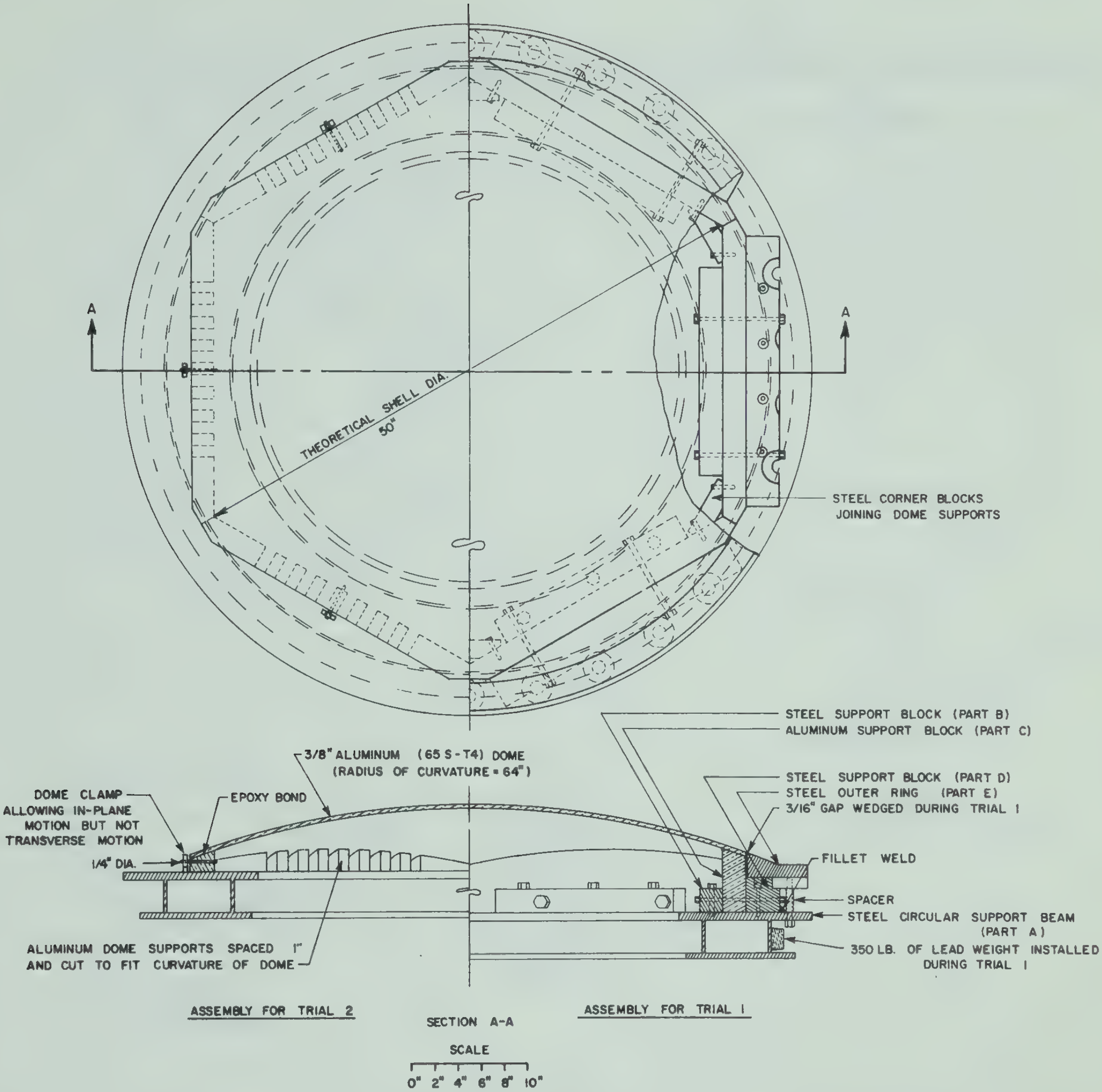
A
A
THEORETICAL SHELL DIA.
50"
STEEL CORNER BLOCKS
JOINING DOME SUPPORTS
STEEL SUPPORT BLOCK (PART B)
ALUMINUM SUPPORT BLOCK (PART C)
3/8" ALUMINUM (65 S-T4) DOME
(RADIUS OF CURVATURE = 64")
DOME CLAMP
ALLOWING IN-PLANE
MOTION BUT NOT
TRANSVERSE MOTION
EPOXY BOND
STEEL SUPPORT BLOCK (PART D)
STEEL OUTER RING (PART E)
3/16" GAP WEDGED DURING TRIAL 1
1/4" DIA.
FILLET WELD
SPACER
STEEL CIRCULAR SUPPORT BEAM
(PART A)
ALUMINUM DOME SUPPORTS SPACED 1"
AND CUT TO FIT CURVATURE OF DOME
350 LB. OF LEAD WEIGHT INSTALLED
DURING TRIAL 1
ASSEMBLY FOR TRIAL 2
ASSEMBLY FOR TRIAL 1
SECTION A-A
SCALE
0" 2" 4" 6" 8" 10"

FIG. 7.1a SHELL TEST ASSEMBLY

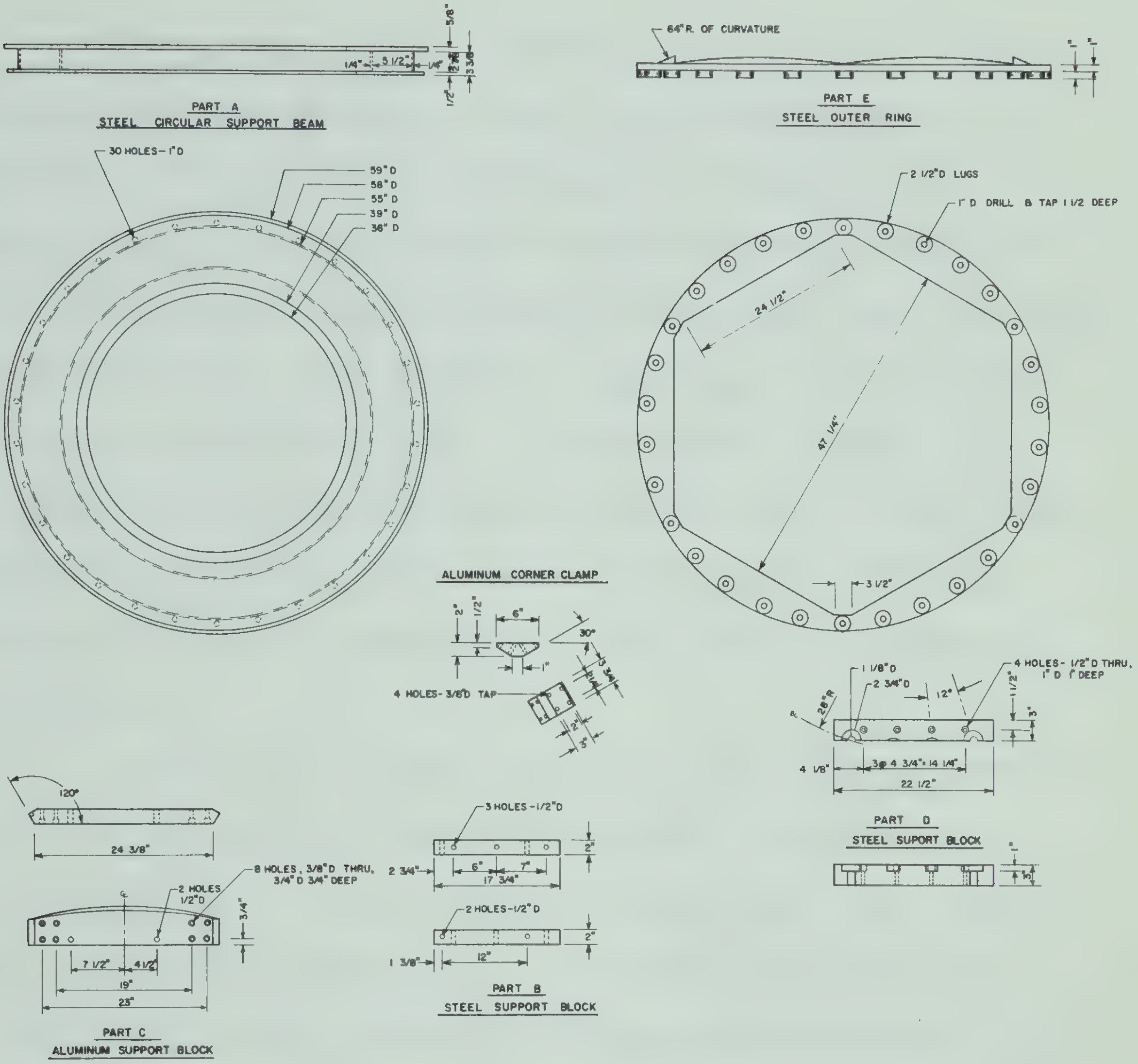

FIG. 7.1 b SHELL TEST ASSEMBLY

The present theory neglects the effects of transverse shear and rotatory inertia (thickness-shear effect). Theoretical results given by Reismann and Culkowski [68] show that the thickness-shear effect can be ignored for symmetric modes of response lower than the fourth mode for clamped shallow spherical shells with circular planform for $a/h > 30$ and a/R as large as 0.5. Consequently, neglecting the thickness-shear effect when computing the experimental shell's transient response likely is valid as long as the lower modes governed the response.

In the first trial, an attempt was made to obtain the shell's transient response subject to the edge conditions for a clamped shell given in Eq. (6.1) and in the second trial, subject to the edge conditions for a clamped shell with sliding free edges given in Eq. (6.3).

For the first trial, 2 x 6 in. aluminium (65S-T4) support blocks were attached with epoxy adhesive to the outer 2 inches of the shell surface. These edge support blocks were clamped between steel blocks which were bolted and welded to a steel circular box-beam. Shell in-plane edge motion was restricted further for some tests by shimming between the shell edge and a steel circular member which had an inner boundary shape matching the shell's hexagonal boundary. Also, for some tests, 350 lb. of lead weights were attached to the

circular box-beam to reduce support ringing. In this way, the shell was clamped reasonably well against edge transverse displacement and normal rotation, and at least partially clamped against edge extension parallel to the boundary as well as against normal in-plane motion. The shell and mount assembly was positioned on its side in the shock tube, resting on a wooden block. The circular box-beam was bolted to the 1 inch steel front plates as shown in Fig. 7.2. These steel front plates were used for the plate experiment and are shown in Fig. 5.1. The space between the shell steel outer ring and the tube wall was closed with 5/8 in. steel plate and all cracks were sealed with adhesive tape as shown in Fig. 7.3. The six 60 degree shell segments are labelled 1 to 6 in this figure for future reference. In this way the air blast was reflected completely at the shell test section. For one series of tests, aluminium shims were placed between the 5/8 in. steel plate and the shell steel outer ring in an attempt to obtain better edge clamping.

For the second trial, the 2 x 6 in. aluminium edge support blocks were cut away in alternate 1 inch blocks. The remaining legs of the support blocks rested on the steel circular box-beam. Heavy duty Krylon silicone lubricant was applied to the contacting sliding

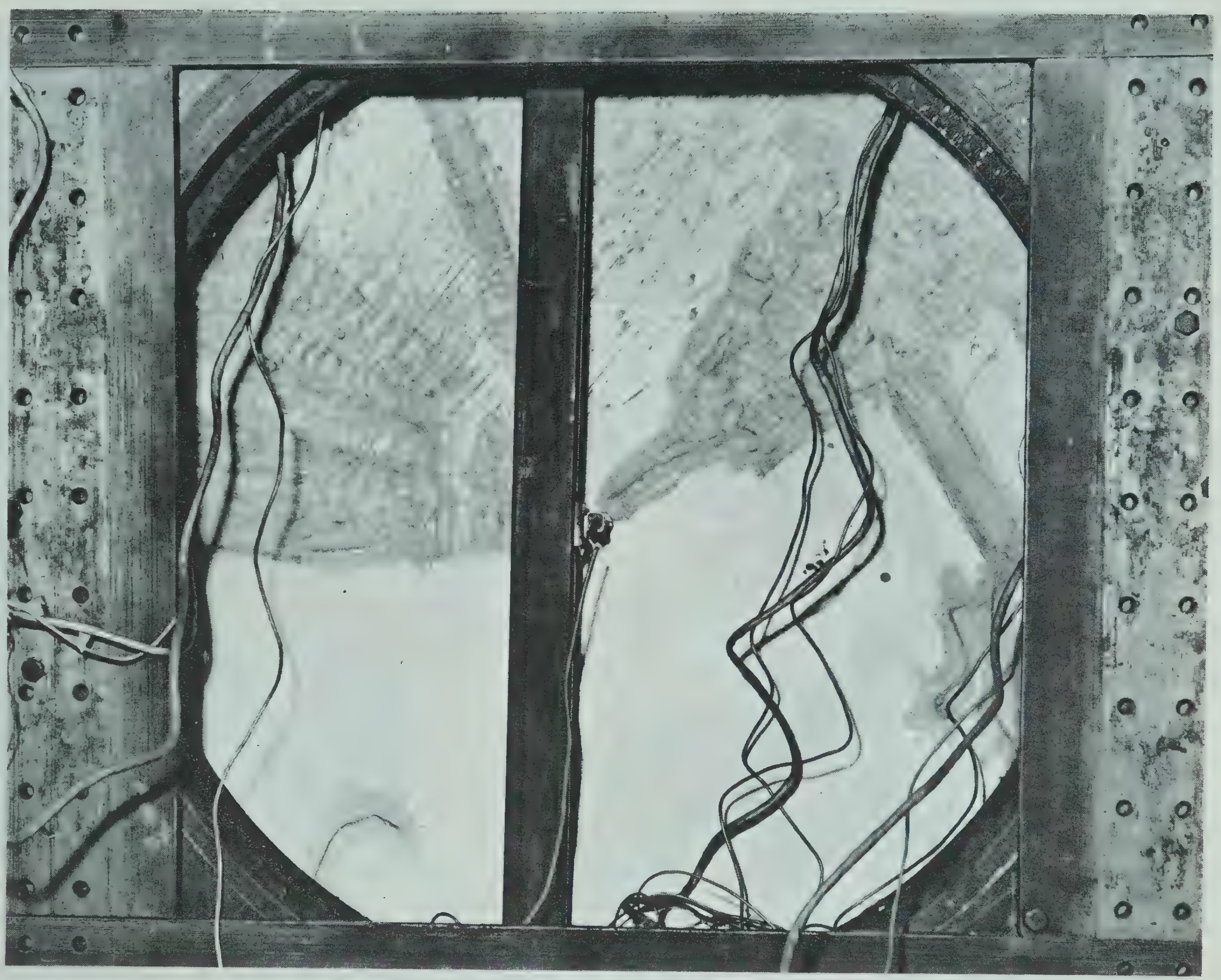

FIG. 7.2 Back View of Shell Mounted in Shock Tube for Trial 1

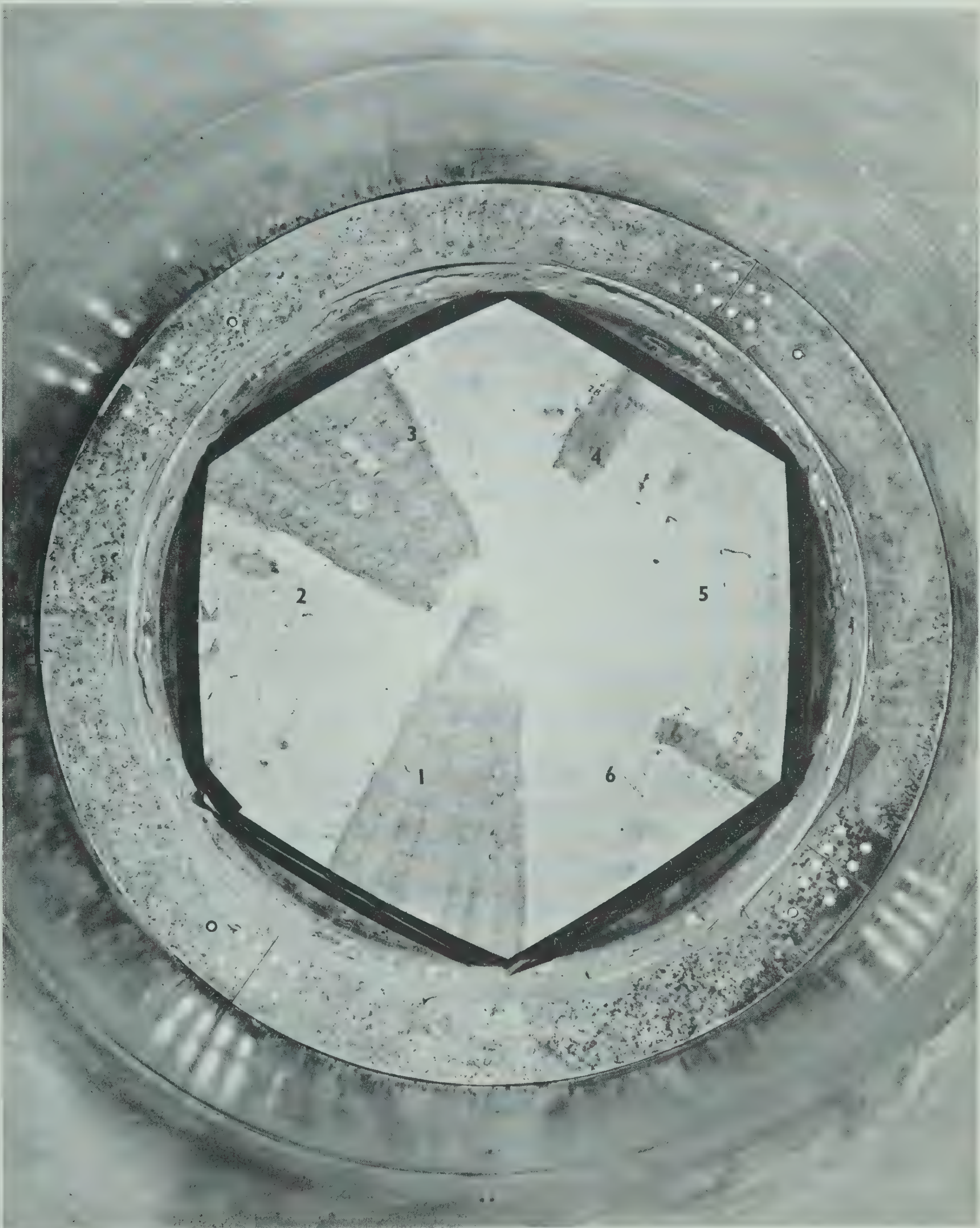

FIG. 7.3 Front View of Shell Mounted in Shock Tube for Trial 1

surfaces. Edge piston-type clamps prevented the shell from falling off the circular box-beam when the shell and mount assembly was positioned on its side in the shock tube. By means of this arrangement, the shell was clamped reasonably well against transverse edge displacement and normal rotation. Edge extension parallel to the boundary was restricted by the outer 2 inch portion of the shell, itself, and normal edge in-plane motion was resisted by the inertial forces of the boundary support mass and frictional forces. The boundary support mass which followed the edge in-plane motion of the shell weighed approximately 34 lb. including the 11 lb. outer 2 in. portion of the shell, while the shell weighed 62 lb. The shell and mount assembly was positioned on its side in the shock tube, resting on a wooden block as shown in Fig. 7.4. The shell assembly was not connected by bolts or welds to the shock tube walls in any way. Instead, the shell assembly was restricted from transverse motion by four clamping angles which are shown in Fig. 7.4. In this manner, shock tube expansion and contraction under blast loading had little effect on the shell boundary motion. The test section was completely sealed against the air blast, however the portion between the shell boundary and the shock tube wall was not a smooth continuous surface as it was for Trial 1. Resistance of the shell boundary to edge transverse motion and normal rotation was reduced from

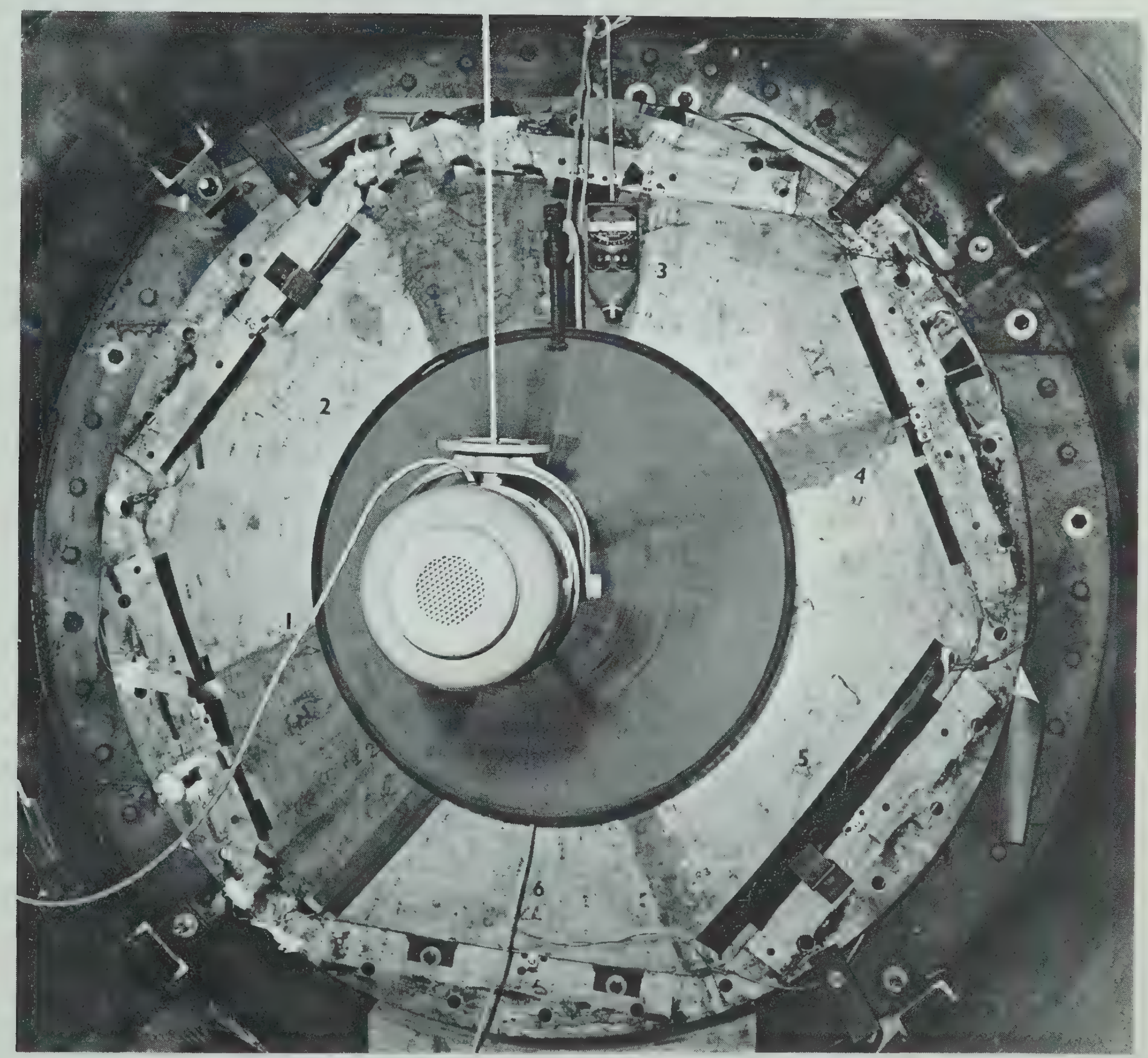

FIG. 7.4 Front View of Shell Mounted in Shock Tube for Trial 2

Trial 1 since the 1 inch steel plates supporting the circular box-beam were partially removed as shown in Fig. 7.5.

Previously, Walkinshaw, Riley, Siddal and Oravas [92] obtained the static response of this shell subjected to uniformly distributed loads using the edge conditions for a clamped shell with sliding clamped edges as given by Eq. (6.4), using heavy steel edge rollers and support clamps. The mounting arrangement used in this static test was considered impractical for tests in the shock tube since the shell and mount assembly had to be positioned on its side. Furthermore, the inertia of the heavy boundary roller-support mass likely would have a considerable influence on the shell's dynamic response characteristics which could not be accounted for using the present theory.

The shell's spherical curvature was formed by spinning to obtain a nominal shallowness parameter a/R of 0.390625 which was within the accepted limits for shallow shells of $0 \leq a/R \leq 0.5$. Spinning, as pointed out by Hossack [69], introduces residual stresses and variations in thickness.

The removal of portions of the aluminium support blocks for Trial 2 permitted some stress relaxation in the shell with an associated shell 'flattening' or an increase in R, near the boundary. A plot of the shell profile

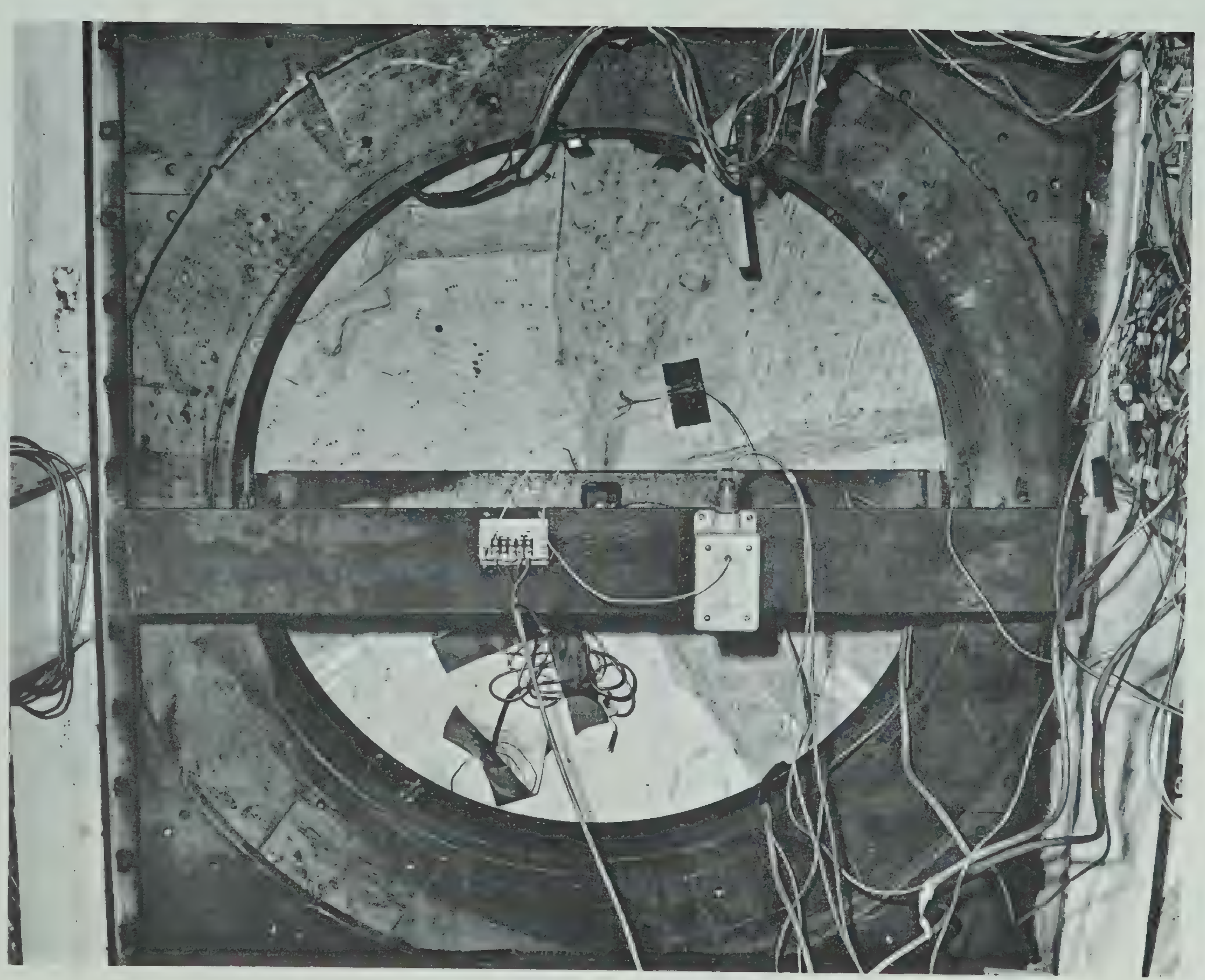

FIG. 7.5 Back View of Shell Mounted in Shock Tube for Trial 2

measured along one of its radial lines in Fig. 7.6 shows this 'flattening'. The variation of the shell radius of curvature, measured along two radial lines with a Cenco spherometer, is shown in Fig. 7.7. This spherometer measured spherical radius of curvatures over 1 inch radius circular segments on the shell surface to an accuracy of ± 3 per cent. The radius of curvature measured on the convex surface of the shell appeared to oscillate three or four times between the apex and the boundary with maximum variations of approximately ± 25 per cent about the average value of R which varied from approximately 65 in. near the apex to 70 in. near the boundary.

For Trial 1, the average spherical middle surface radius of curvature was approximately 64 in., however variations in curvature over the shell surface were not measured. It was felt that the extent of the curvature variations was similar to that measured for Trial 2.

The effect of surface curvature variations or surface 'rippling' on the transient response of shallow shells has not been studied either experimentally or theoretically in the shallow shell literature, as far as is known, and measured variations have not even been quoted. Okubo and Whittier [74], as a result of measurements for the static buckling of clamped spherical shells using the nondestructive technique, concluded that the lowering of

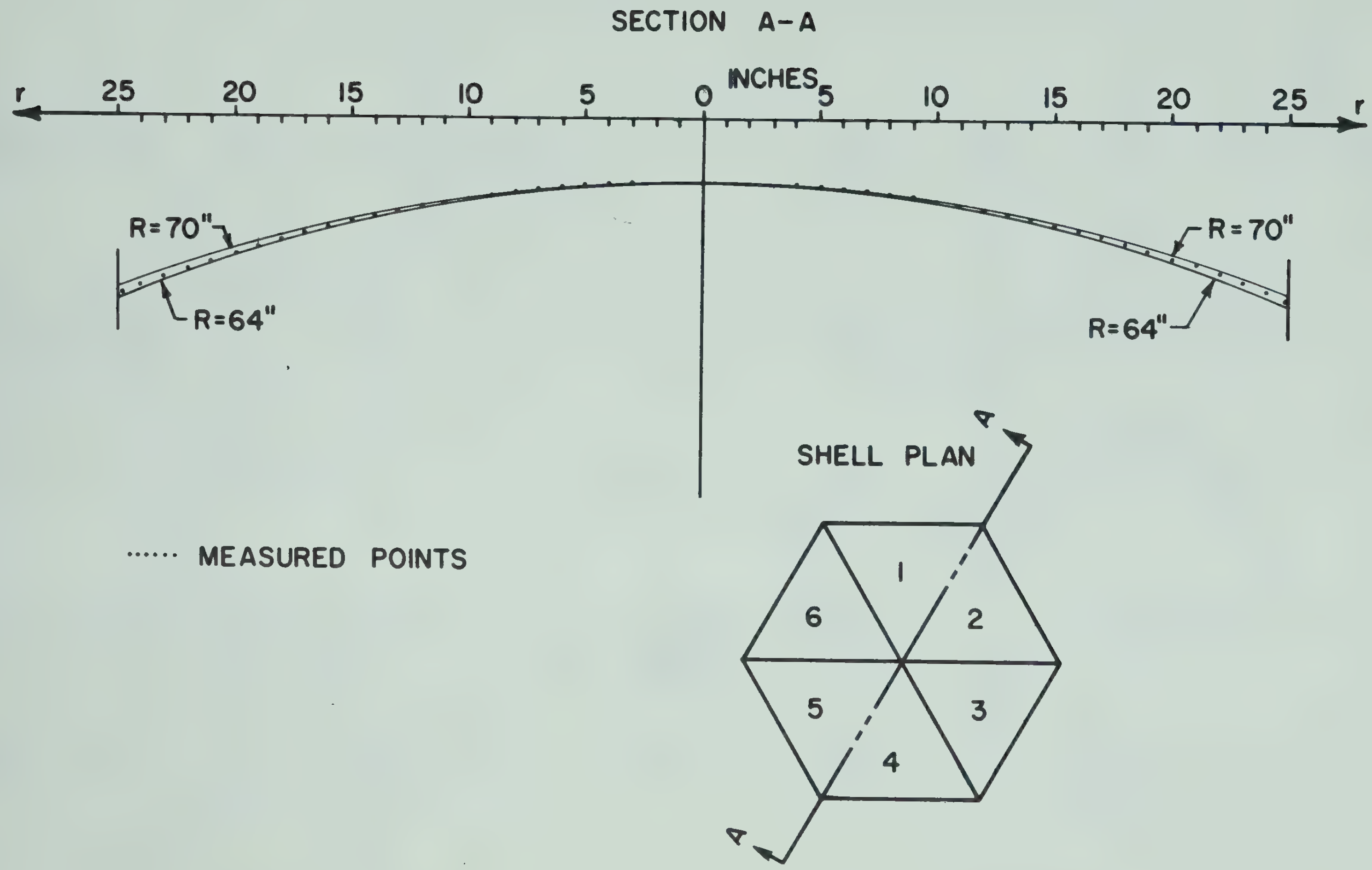

FIG 7.6 Experimental Shell Middle Surface Profile for Trial 2

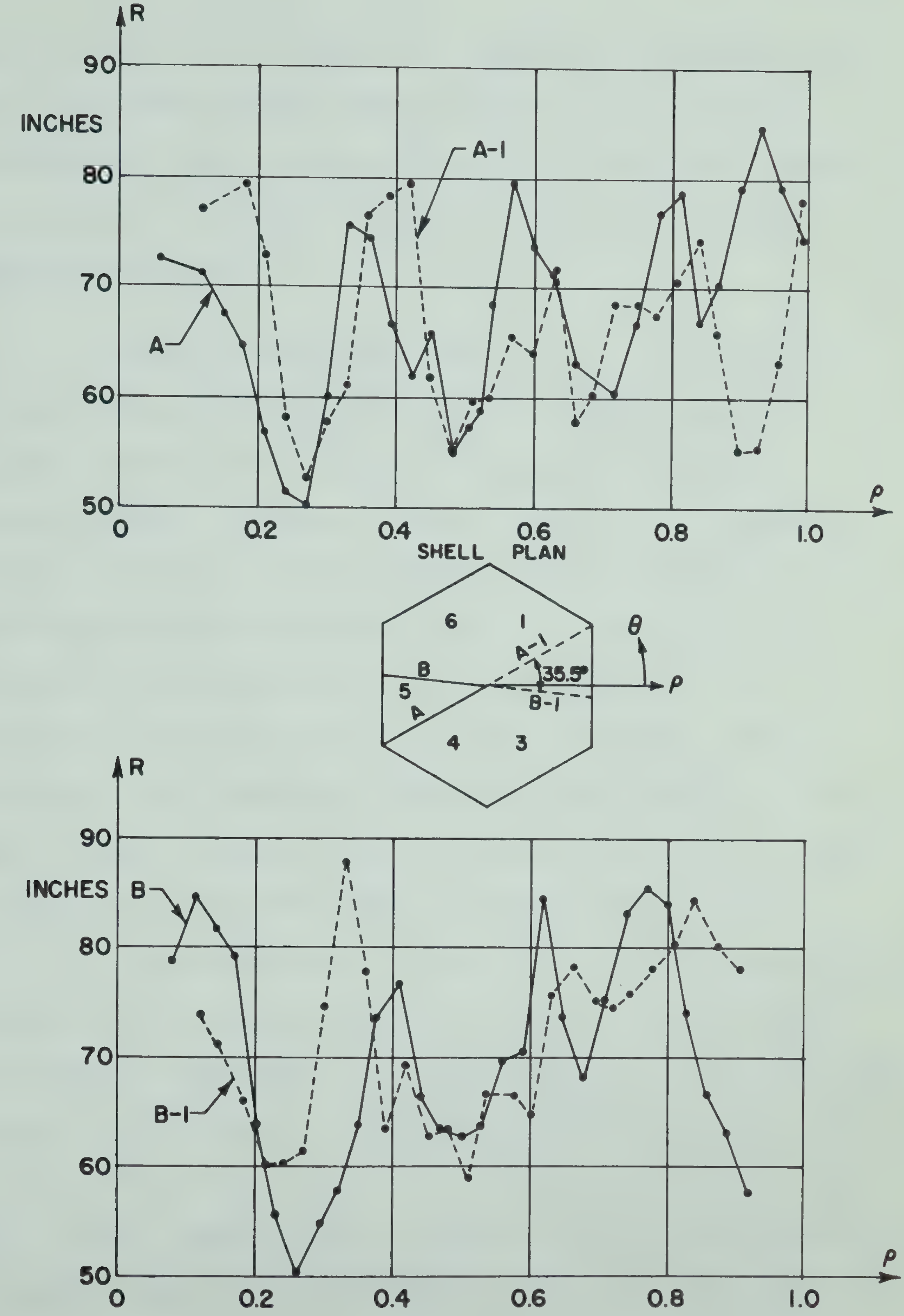

FIG. 7.7 Variation of Experimental Shell Radius of Curvature R with Radius ρ for Trial 2

their experimental frequencies compared with those predicted by theory might have resulted from curvature variations. However, they did not include measurements of the actual curvature variations present in their experimental shells.

Intuitively, 'rippling' of the shell middle surface should decrease the shell's rigidity against in-plane stress and increase it against transverse bending stress relative to the rigidity of a perfect spherical surface. It was felt that the significance of this variation-in-curvature effect upon the transient response of shallow shells would increase with the number and magnitude of the surface 'ripples' and the values of shell geometric parameters a/h and a/R. The significance of this effect likely depends upon the edge conditions to which the shell is subjected, as well.

One hundred and fifty Tatnall strain gauges, type C12-121, having gauge factors of 2.09 (± 0.5 %), gauge resistance of 120 ohms and gauge length of 0.125 in., were mounted on both sides of the shell along the radial lines $\theta = 0°$, $10°$, $20°$ and $30°$ at the positions shown in Fig. 7.8a. Radial bending and membrane strains were measured in one shell characteristic segment at 36 different positions including the shell apex. These strains were used in conjunction with circumferential bending and membrane strains measured at related positions in another shell

PLAN VIEW OF SHELL'S CONVEX (FRONT) SURFACE

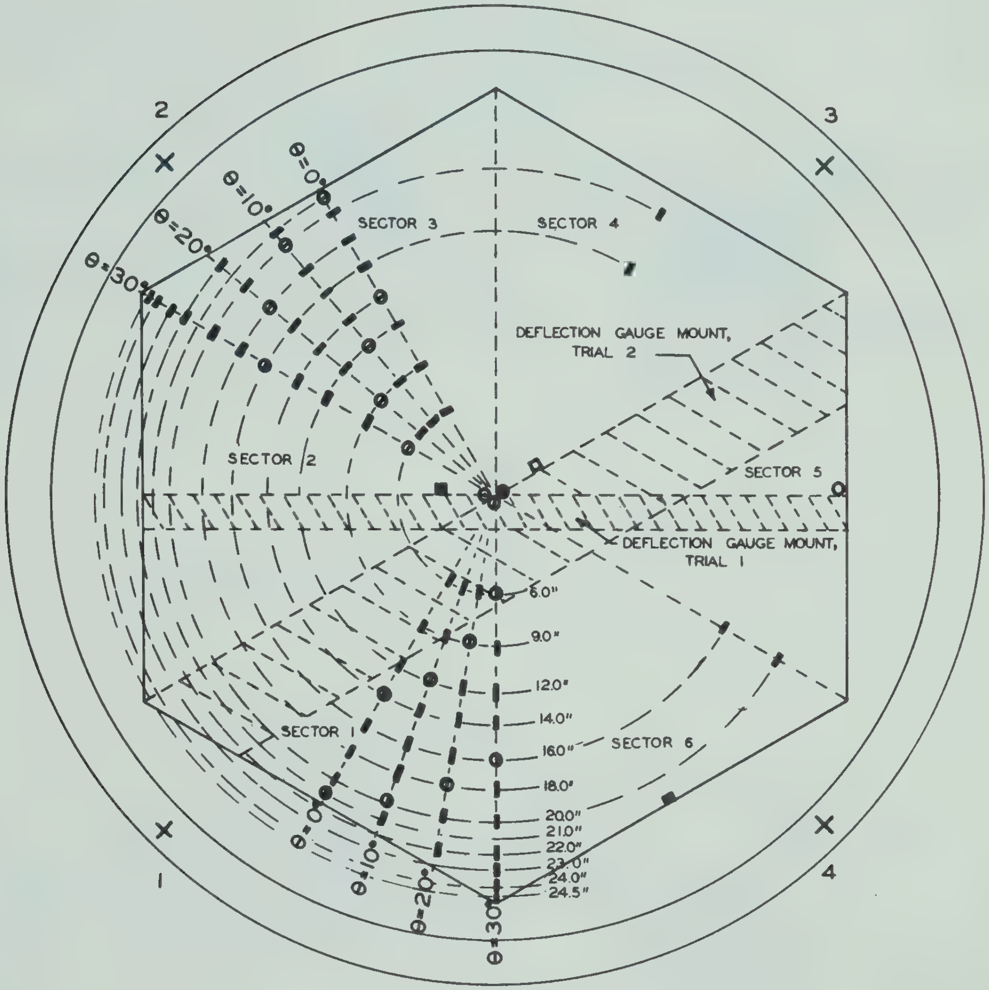

Notes

1. All dimensions are horizontal.

2. Radial distances refer to middle surface. Corrections were applied to locate strain gauges.

✕ Pressure-gauge, Trials 1 and 2
■ Accelerometer, Trial 1
□ Accelerometer, Trial 2
● Linear potentiometer deflection gauge, Trial 1
⊙ Bently Nevada deflection gauge, Trials 1 and 2
○ Bently Nevada deflection gauge, Trial 2
▬ Radial and circumferential strain gauges front and back, Trial 1
⊖ Radial and circumferential strain gauges front and back, Trial 2

Fig. 7.8a Shell Instrumentation

DEFLECTION GAUGE MOUNT, TRIAL 1 (not to scale)

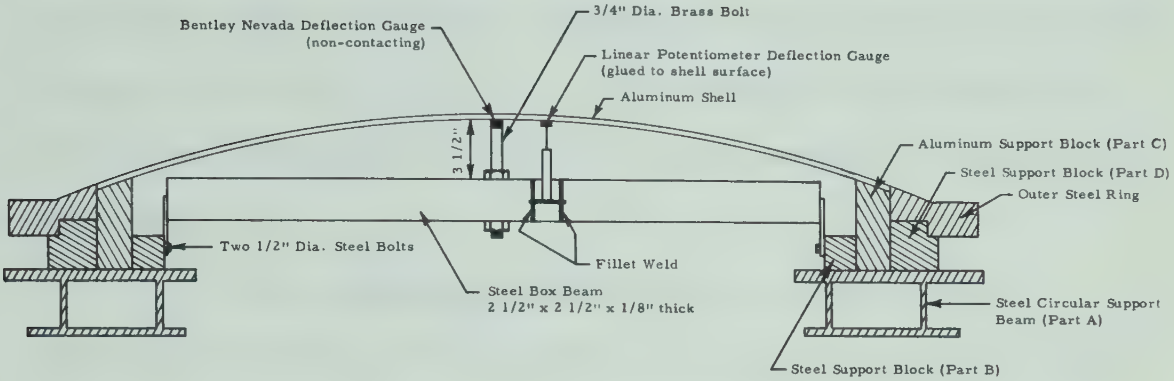
3/4" Dia. Brass Bolt
Bentley Nevada Deflection Gauge
(non-contacting)
Linear Potentiometer Deflection Gauge
(glued to shell surface)
Aluminum Shell
3 1/2"
Aluminum Support Block (Part C)
Steel Support Block (Part D)
Outer Steel Ring
Two 1/2" Dia. Steel Bolts
Fillet Weld
Steel Box Beam
2 1/2" x 2 1/2" x 1/8" thick
Steel Circular Support
Beam (Part A)
Steel Support Block (Part B)

DEFLECTION GAUGE MOUNT, TRIAL 2 (not to scale)

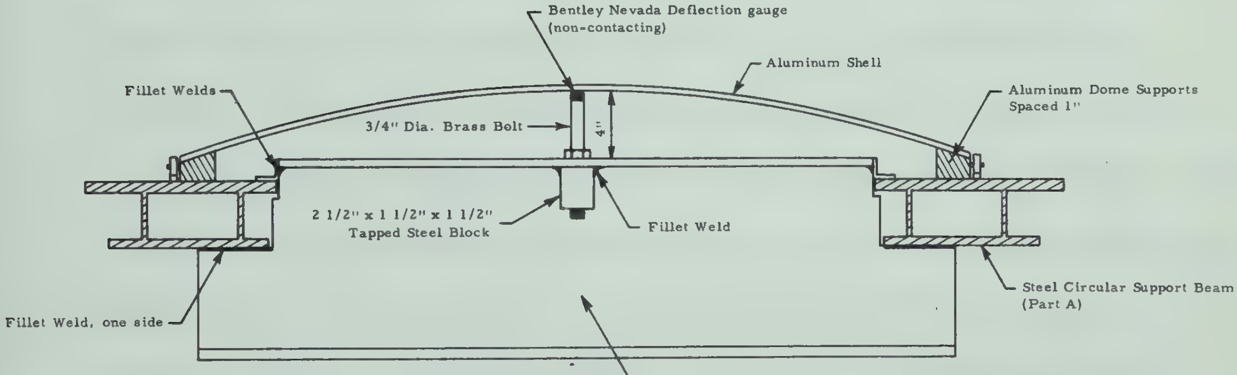

Note - Refer to Fig. 7.1 for detail
of shell test assembly

Fig. 7.8b Shell Instrumentation

characteristic segment to obtain normal stress resultants and flexural stress couples at the 36 positions assuming perfectly symmetric shell response. The shell's symmetry of response was checked at 4 of these 36 positions by measuring radial and circumferential strains in two other segments.

7.1.2 Natural Frequencies. Shell natural frequencies were obtained using acoustic excitation with sound pressures ranging between 100 and 130 decibels at the shell surface. These sound pressures were applied over a large portion of the shell surface area. In this manner, the suppression of some resonant frequencies, which McConnell [93] showed could occur for concentrated excitation forces such as those given by shakers, was avoided. The shell base plane was placed perpendicular to the axis of the exponential horn in order to increase the intensity of pressure loading by using standing waves to advantage; a procedure pointed out by Hubbard and Houbolt [80]. Placing the axis of the acoustic horn parallel to the shell base plane would have provided a more uniform sound pressure level distribution over the shell's front (convex) surface, however the pressure level obtained was too low to excite some of the lower shell modes. Excitation frequencies ranged from 200 to 3,000 cps. Strain and acceleration responses at different positions on

the shell surface indicated the various resonance values. Nodal lines were established for several symmetric modes of response of the shell subject to the edge conditions obtained in Trial 1 from the phase changes observed for the Lissajous figures for acceleration signals recorded at many different positions on the shell's convex surface.

In Trial 1, three Electro-Voice model 848, 30 watt, 10 x 12 in. rectangular horn-type speakers with frequency ranges of 150 to 10,000 cps were used to excite the shell symmetrically. In Trial 2, symmetric excitation was obtained with a Geloso model 2579, 200 watt, 29 in. diameter circular horn-type speaker with a frequency range of 120 to 12,000 cps.

The sweep-frequency was obtained using a Nelson-Ross model PSA-021 spectrum analyser in conjunction with a Nelson-Ross model 601 synchro-sweep generator. The sound pressure level at the shell surface was kept constant over the frequency range for some of the tests by regulating the amplitude of the sine wave generated using a General Radio model 1569 automatic regulator in conjunction with a General Radio model 1565-A sound level meter having an operating range of 44 to 140 decibels. The sine wave signal from the regulator was amplified by a General Radio model 1308-A power amplifier and then fed to the horn-type speakers.

In order to maintain a constant sound pressure level over the entire frequency range using these speakers, the sound pressure level had to be kept at approximately 100 decibels. However, some lower shell resonances were not distinguishable from system noise at this pressure level. Consequently, for many tests constant power amplifier output voltage rather than constant acoustic pressure level was maintained over the frequency range giving pressures as high as 130 decibels at the lower frequencies. However, using this technique, response amplitudes for different modes were not indicative directly of the relative modal participation factors as they were when constant sound pressure was maintained over the frequency range.

Acceleration signals were obtained using a Kistler model 818 piezoelectric accelerometer. Strain signals were amplified with DRES designed amplifiers having gains of 150 to 5,000 and frequency response of 0 to 20,000 cps. Acceleration and strain signals were converted from a.c. to d.c. using a Hewlett-Packard model 400E voltmeter and then recorded on the y-axis of an Autograph model 65 two-axis recorder. At the same time, the sweep-frequency produced by the synchro-sweep generator was recorded on the x-axis. This frequency was monitored by a Hewlitt-Packard model 3734A electronic counter, as well. Lissajous figures, obtained from accelero-

meter signals, were displayed on a Tektronix model 502 oscilloscope.

The acoustic excitation equipment is shown in Fig. 7.9. The Geloso horn speaker and the General Radio sound level meter are shown in Fig. 7.4, positioned on the convex side of the shell which is mounted in the shock tube for Trial 2. A complete instrumentation block diagram is shown in Fig. 7.10.

Since the shell edge supports were too stiff to be excited acoustically, natural frequencies were obtained by striking the shell edge with different rubber and metal hammers while recording acceleration and strain signals on a Tektronix model 564 storage oscilloscope.

7.1.3 Transient Response. The shell was positioned at the same section in the six-foot diameter shock tube as the square plate was tested previously, with the central axis of the shell aligned with the axis of the shock tube. The characteristics of the shock tube at this location are described in Section 5.1.3. For this set of experiments, the test section was subjected to air blast waves having peak normally reflected overpressures q_o and positive durations t_o of approximately 10 psi and 32 msec., respectively. All blast overpressures resulted from the detonation of 1.5 lb. charges of 60/40 RDX/TNT. Higher overpressures were experienced at the test section for this charge weight than during the plate experiment as a

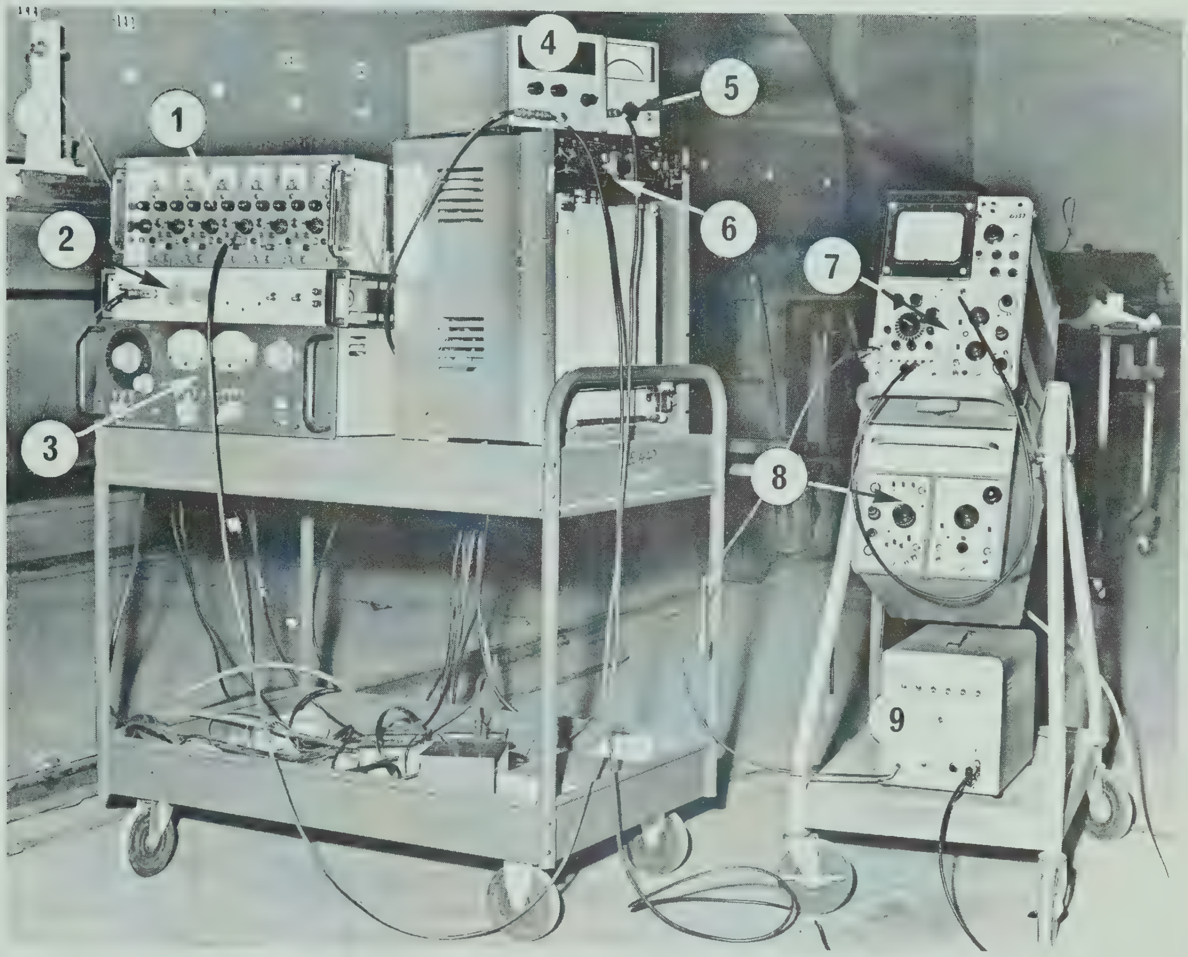

1 Strain gauge amplifiers
2 Automatic level regulator
3 Power amplifier
4 Electronic Counter
5 Voltmeter converting a.c. to d.c.
6 Two-axis recorder
7 Oscilloscope
8 Spectrum analyser
9 Synchro-sweep generator

FIG. 7.9 Acoustic Excitation Equipment

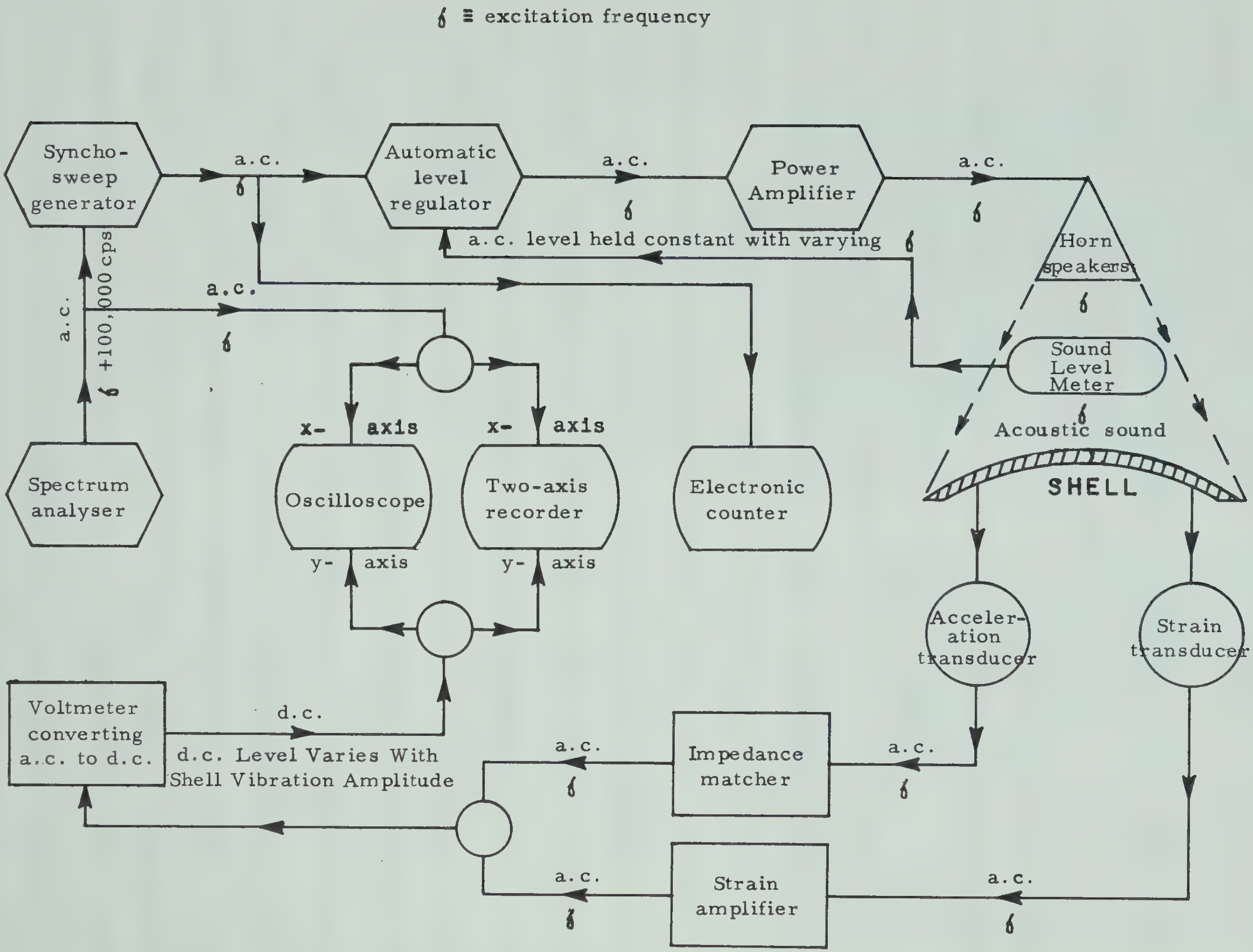

Fig. 7.10 Block Diagram of Shell Acoustic Excitation Instrumentation

result of modifications to the shock tube compression chamber.

The transient loading function for the plate experiment had the form $q = q_o Q(t)$, where $Q(t) = (1 - t/t_o) \exp(-t/t_o)$. However, for the shell experiment, the transient loading function was described by a more complex function having the form $q = q_o \bar{q}(\rho) Q^*(\rho, t)$, as a result of the shell surface curvature. The assumption of axial symmetry of the load was exact for Trial 1 since geometric symmetry was maintained over the complete shock tube cross section, as shown in Fig. 7.3. In Trial 2, geometric asymmetry was introduced at the shell's polygonal boundary, as shown in Fig. 7.4, however its effect on the symmetry of the shell surface loading function was thought to be insignificant.

The effect of surface curvature on the reflection of an air blast wave is demonstrated in the schlieren photographs in Fig. 7.11 and in the pressure-time records in Fig. 7.12 for a cylindrical surface which had a radius of curvature of 11.7 in. and the same angle of opening of 23 degrees as the spherical shell. This test was conducted in the DRES 2 x 12 in. rectangular shock tube for an incident air blast overpressure of approximately 10 psi at the shell surface. This shock wave had a peak normally reflected overpressure of 26 psi and a shock front velocity of 17,300 ips at the cylindrical surface.

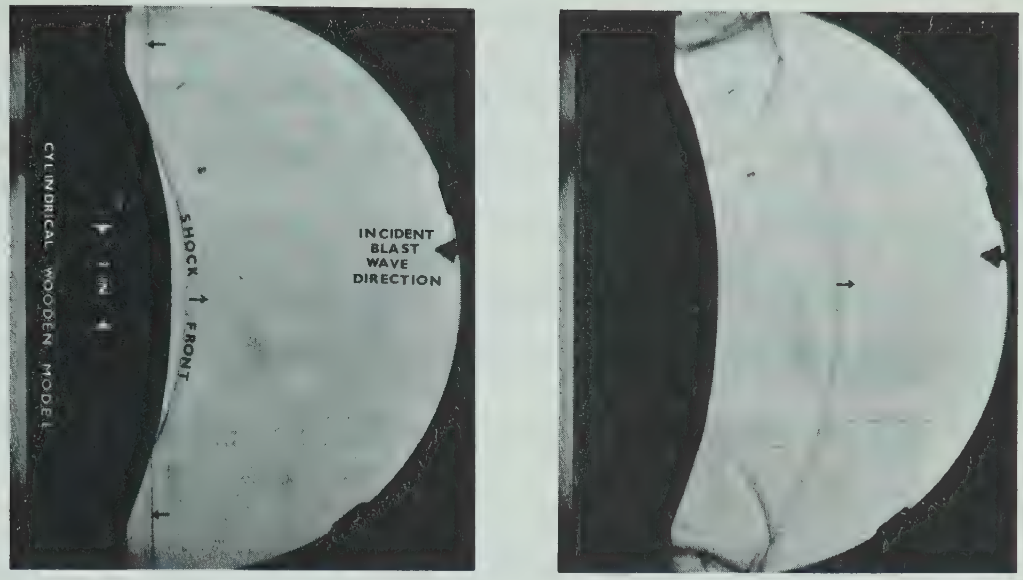

(a) t = 0.017 msec (b) t = 0.140 msec

Fig. 7.11 Schlieren Photographs Showing Air Shock Front Reflection by a Cylinderical Surface in a 2 x 12 in. Shock Tube

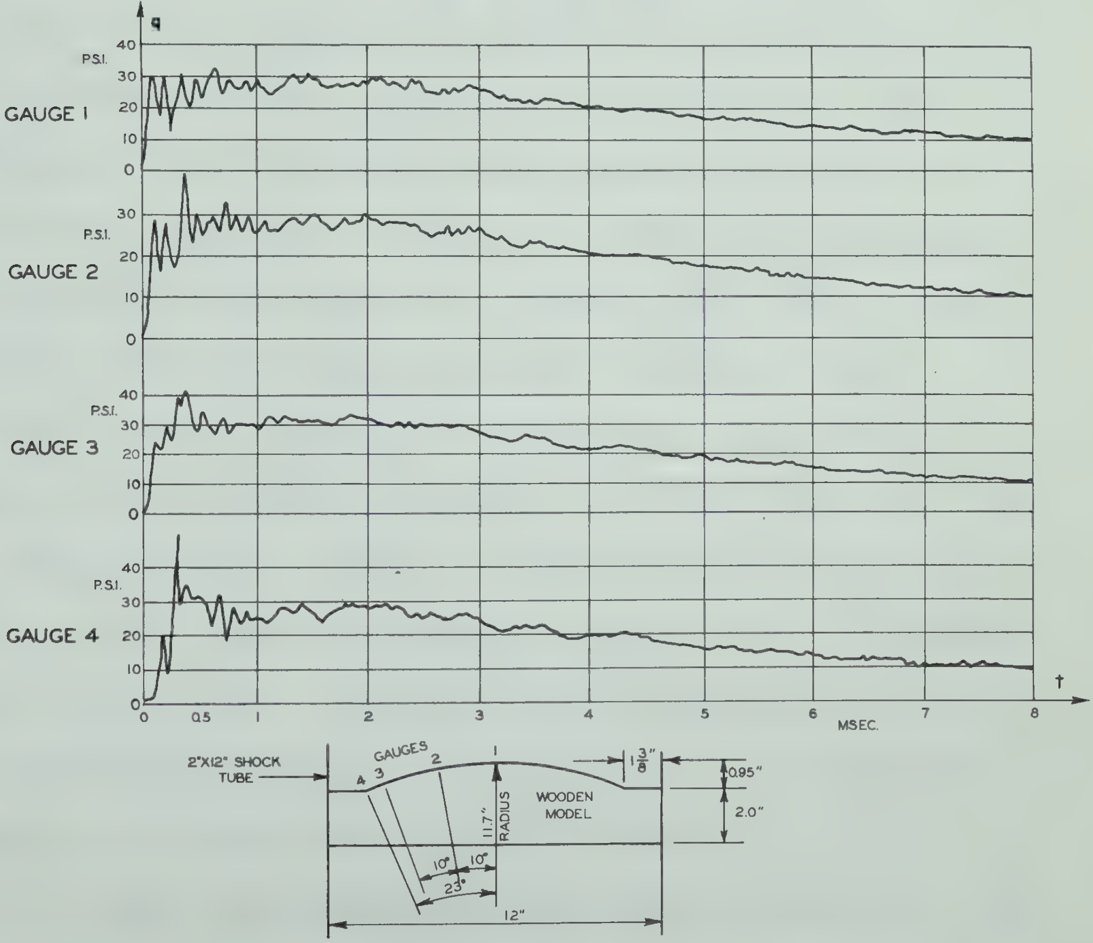

Fig. 7.12 Variation of Measured Pressure vs. Time Over a Cylinderical Surface in 2 x 12 in. Shock Tube

The rectilinear incident and curvilinear reflected shock fronts, which appear as dark lines in schlieren photographs, are shown in Fig. 7.11a at t = 0.017 msec. after the incident shock first reached the shell apex. The curvilinear shock fronts, reflected from the shell surface and the rectilinear shock tube walls, are shown in Fig. 7.11b at t = 0.140 msec.

The overpressure magnitudes of the shock fronts travelling across the shell surface are a function of the spatial variation of the obliquely reflected shock wave magnitude. Theoretically, the reflected overpressure magnitude generally decreases with increasing angle between the shock front and the reflecting surface, and the relative magnitude of this decrease in overpressure generally increases with incident blast overpressure magnitude. Calculations from equations given by Bleakney and Taub [94] show that the magnitude of a normally reflected overpressure of 26 psi at the shell apex would decrease by 1.5 per cent at the shell edges. Extrapolating from curves given in the "Effects of Nuclear Weapons" [95], this decrease appears to be approximately 2 per cent.

The four pressure-time histories in Fig. 7.12, which were recorded perpendicular to the cylindrical surface, indicate that there was a larger decrease in the

magnitude of the initial reflected overpressure with increasing angle of incidence of the shock front than is predicted by [94] or [95]. However, the pressure records are distorted by gauge 'ringing' which makes initial overpressure values difficult to estimate. Consequently, these records serve merely as an indication of the general comportment of the transient blast overpressure for this curved surface. These records show that pressure disturbances travelling across the cylindrical surface were not important after t = 0.4 msec. This implies that, at least for this shell curvature and blast overpressure, the transient overpressure was distributed almost uniformly over the shell surface after the incident shock wave had travelled past the shell apex to the shell boundary, reflected to the shock tube wall and then travelled back across the shell surface to its apex which was located at the central axis of the shock tube.

In the shallow spherical shell experiment, the shock front arrived at the shell apex 0.34 msec. before reaching the shell boundary corners which were 5.1 in. further downstream. Reflections from the shock tube wall crossed the shell apex approximately 3 msec. after the incident wave first reached the shell. However, according to equations given by Bleakney and Taub [94], the normally reflected overpressure at the shell apex of

10 psi would decrease in magnitude by only 0.4 per cent at the shell boundaries. Curves given in [95], Fig. 3.71b, p. 147, show that the maximum decrease in the reflected overpressure for this shell would range between 0 and 3.5 per cent, respectively, for incident overpressures between 2 and 5 psi which are associated with normally reflected overpressures between 4.25 and 11.5 psi, respectively. It was felt that pressure disturbances travelling across the shell's surface would not be important for such small variations in reflected overpressure magnitude. Consequently, radial variations in the pressure magnitude $\overline{q}(\rho)$ were ignored.

The importance of the radial variation in the time of shock arrival of up to 0.34 msec. which can be represented by a function $Q^*(\rho,t)$, depends upon the values of the shell's governing periods of response. Generally, for most transient loads it is assumed that structural response can be determined with sufficient accuracy using values of the load impulse which are averaged over time intervals as large as one-tenth of the natural period of a one-degree system (see, for example, Biggs [96]). Therefore, it is reasonable to assume that if the shell governing periods of response were greater than 34 msec. (i.e., shell governing frequencies were less than about 300 cps), then the function $Q^*(\rho,t)$ could be replaced by the function $Q(t)$. Other-

wise, radial variations of the loading time function should be included in the theoretical analysis. For normal mode theory, the shell's response to a load function $Q^*(\rho,t)$ can be obtained only approximately. This is done by superimposing the shell's response to loads applied on different portions of the surface associated with different loading time functions $Q(t)$, which combine to give an approximate representation of $Q^*(\rho,t)$.

In the shell Trials 1 and 2, pressures, displacements, strains and accelerations were recorded at the locations shown in Fig. 7.8 with three Ampex 14-track tape recorders, using the techniques described in Section 5.1.3 for the plate experiment. Face-on reflected overpressures were measured at four positions around the shell boundary using DRES shear tube piezoelectric pressure transducers. Shell central displacement was measured with a Bently Nevada non-contacting inductance transducer. This transducer had a model 3500N detector-driver and a model 308 proximeter coil with a range of 0.250 inches. Central displacement also was measured with a linear potentiometer in Trial 1. The transverse accelerations of the mounts for these central displacement transducers shown in Fig. 7.8b were measured with an Endevco piezoelectric accelerometer. For Trial 2, in-plane boundary motion of the shell was measured with a

Bentley Nevada transducer having a model 302 proximeter coil with a range of 0.100 inches. For Trial 1, in-plane boundary acceleration was measured with an Endevco accelerometer. Strains were measured with 150 strain gauges at 36 unique r,θ middle surface positions in Trial 1 and with 34 strain gauges at 9 unique positions in Trial 2.

The instrumentation block diagram shown in Fig. 5.5 for the plate experiment is representative of the instrumentation set-up for the shell experiment except that the Bentley Nevada displacement transducer signals were conditioned with DRES strain gauge bridge balances and amplifiers. Also, some data recorded on magnetic tape for Trial 2 were read directly into the DRES IBM 1130 digital computer. This was accomplished with an SYS model 2113 data acquisition and control system having a Miniverter 8 channel, 13 bit analogue-to-digital (A-D) converter multiplexer. The signals, recorded at 60 ips on magnetic tape for frequencies of up to 20,000 cps, were played back on the converter at 3 3/4 ips giving a 16 to 1 speed ratio. The 8 tape channels were read sequentially at a rate of 10,222 samples per second. Thus, 20,444 samples per second of actual shell response were digitized and stored in the computer for each tape channel. Assuming two samples are required to define one response cycle, this gave an A-D

digitizing capability for response frequencies up to 10,222 cps.

Other magnetic tape data were digitized with the chart reader and plotted in the manner explained for the plate experiment in Section 5.1.3. Experimental strain data and theoretical and experimental sectional resultants were represented graphically for 8 msec. with response frequency reproduction of up to 10,222 cps for Trial 1 and for 10 msec. with frequency reproduction of up to 10,000 cps for Trial 2.

7.2 Theoretical Shell Enclosing an Hexagonal Base

Theoretical modal frequencies and static central deflections, computed from eigenvalues and modal participation functions given in Chapter 6, are given in Table 7.1 for the first six or seven symmetric modes of vibration of uniformly loaded shells with hexagonal plan satisfying the six different edge condition Eqs. (6.1) through (6.6). Fundamental eigenvalues could not be found when satisfying Eqs. (6.3) through (6.5) for values of a/R and a/h of 0.390625 and 66.667, respectively, as explained previously.

It should be recalled that the evaluation of the modal participation functions was simplified by integrating over the shell plan area rather than the actual surface area. However, the errors introduced by

using this simplification were not large since the shell plan surface area of 1624 in.^{2} is only 3.29 per cent smaller than the actual surface area, assuming a = 25 in. and R = 64 in.

Comparison of the results given previously in Table 5.2 for the natural frequencies of a square plate with those in Table 7.1, reveals that the lower modal frequencies of a shallow shell do not vary as much with the type of edge conditions satisfied as they do for a plate. However, changing the geometric parameters a/R and a/h causes significant variations in the shell lower modal frequencies, as shown in Table 7.1 when a/R changes from 0.390625 to 0.25. Comparison of values of central modal displacements indicates that for a shell with a/R = 0.390625 and a/h = 66.667 satisfying edge condition Eqs. (6.1) or (6.2), modes 2 through 5 govern shell response with mode 3 dominating, while it appears that if any of edge condition Eqs. (6.3) through (6.6) are satisfied, modes 1 through 3 govern response with mode 1 dominating.

7.3 Theoretical and Experimental Results for Trial 1

7.3.1 Natural Frequencies and Mode Shapes. Some of the shell's natural frequencies for Trial 1 are indicated in Figs. 7.13 through 7.15 by the various resonances recorded with strain and accelerometer gauges

Table 7.1

Theoretical Modal Frequencies and Static Central Displacements for Uniformly Loaded Experimental Shell[1]

	Edge Condition Equations Satisfied						
	Eq. (6.1)		Eq. (6.2)	Eq. (6.3)	Eq. (6.4)	Eq. (6.5)	Eq. (6.6)
R (in.)	100 [2]	64	64	64	64	64	64
$\omega_1/2\pi$ (cps)	397	554	536				497
$W_1 \cos^4\theta_0$	0.113E-3	0.125E-4	-0.137E-4				0.219E-3
$\omega_2/2\pi$ (cps)	547	760	722	560	568	534	541
$W_2 \cos^4\theta_0$	-0.101E-3	-0.377E-4	0.207E-4	-0.538E-4	-0.119E-3	-0.345E-4	-0.124E-3
$\omega_3/2\pi$ (cps)	718	883	860	788	797	706	720
$W_3 \cos^4\theta_0$	0.947E-4	0.102E-3	0.105E-3	0.395E-4	0.517E-4	0.365E-4	0.539E-4
$\omega_4/2\pi$ (cps)	895	1000	944	937	955	823	859
$W_4 \cos^4\theta_0$	0.154E-4	0.556E-4	0.884E-4	0.36 E-6	0.156E-5	-0.52 E-6	0.90 E-6
$\omega_5/2\pi$ (cps)	1170	1239	1101	1223	1226	1096	1099
$W_5 \cos^4\theta_0$	-0.237E-4	-0.248E-4	-0.198E-4	-0.178E-4	-0.195E-4	-0.171E-4	-0.194E-4
$\omega_6/2\pi$ (cps)	1478	1537	1398	1510	1518	1358	1372
$W_6 \cos^4\theta_0$	-0.68 E-6	-0.32 E-5	-0.85 E-5	0.88 E-6	0.64 E-6	0.13 E-5	0.80 E-6
$\omega_7/2\pi$ (cps)	1800	1843	1668	1836			1667
$W_7 \cos^4\theta_0$		0.73 E-5	0.72E-5	0.62 E-5			0.67E-5
$W \cos^4\theta_0$	0.977E-4	0.112E-3	0.179E-3				0.138E-3

[1] Shell parameters used in the calculations are:

$p = 6$, $\nu = 0.33$, $a = 25$ in., $h = 0.375$ in., $E = 10^7$ psi.

[2] Average shell radius R for Trials 1 and 2 was approximately 64 in. Calculations are given for R = 100 in. to indicate effects of increasing R.

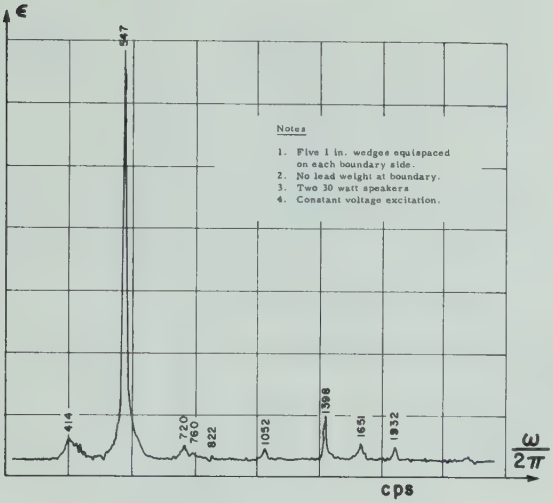

Notes

1. Five 1 in. wedges equispaced on each boundary side.
2. No lead weight at boundary.
3. Two 30 watt speakers
4. Constant voltage excitation.

(A) FRONT STRAIN

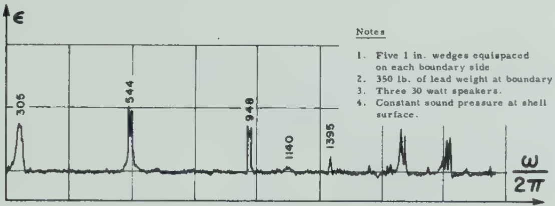

Notes

1. Five 1 in. wedges equispaced on each boundary side
2. 350 lb. of lead weight at boundary
3. Three 30 watt speakers.
4. Constant sound pressure at shell surface.

(B) FRONT STRAIN

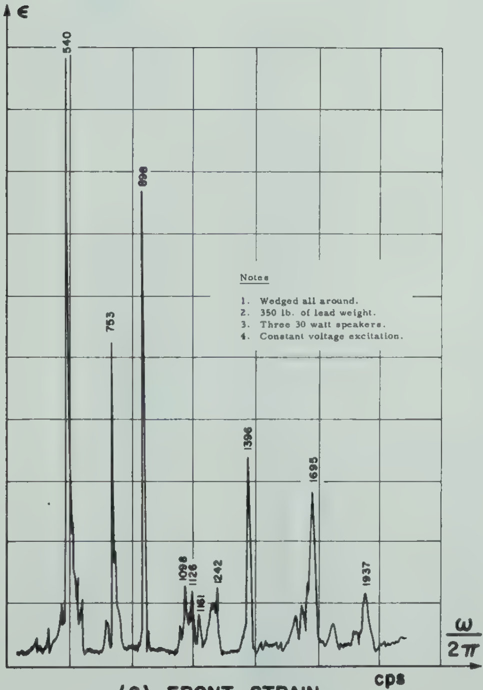

Notes

1. Wedged all around.
2. 350 lb. of lead weight.
3. Three 30 watt speakers.
4. Constant voltage excitation.

(C) FRONT STRAIN

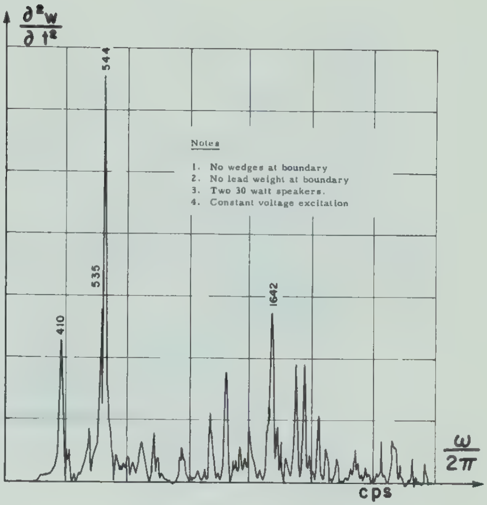

Notes

1. No wedges at boundary
2. No lead weight at boundary
3. Two 30 watt speakers.
4. Constant voltage excitation

(D) TRANSVERSE ACCELERATION

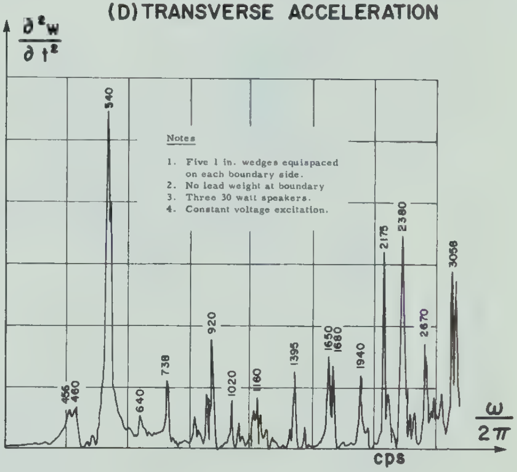

Notes

1. Five 1 in. wedges equispaced on each boundary side.
2. No lead weight at boundary
3. Three 30 watt speakers.
4. Constant voltage excitation.

(E) TRANSVERSE ACCELERATION

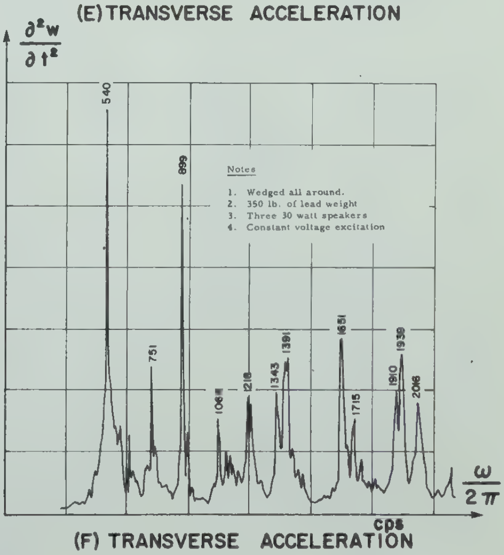

Notes

1. Wedged all around.
2. 350 lb. of lead weight
3. Three 30 watt speakers
4. Constant voltage excitation

(F) TRANSVERSE ACCELERATION

FIG. 7.13 VIBRATION OF ACOUSTICALLY EXCITED SHELL AT APEX FOR TRIAL I

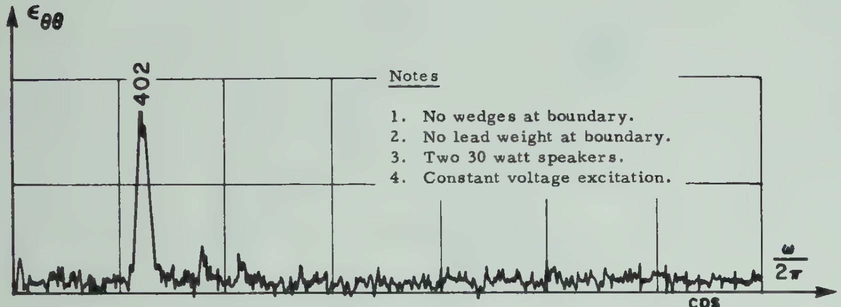

Notes

1. No wedges at boundary.
2. No lead weight at boundary.
3. Two 30 watt speakers.
4. Constant voltage excitation.

(A) TOP CIRCUMFERENTIAL STRAIN AT r=21", θ=0°, SECTOR 3

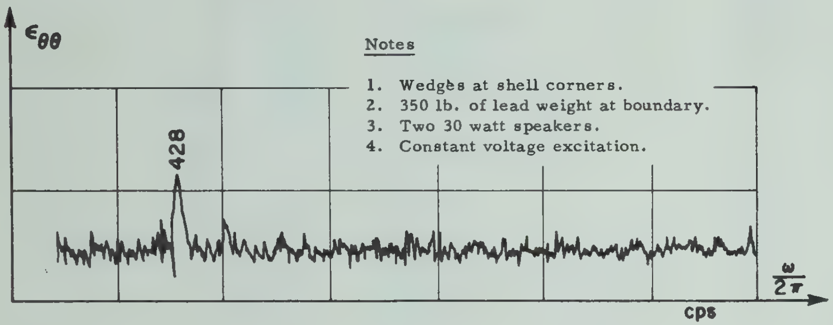

Notes

1. Wedges at shell corners.
2. 350 lb. of lead weight at boundary.
3. Two 30 watt speakers.
4. Constant voltage excitation.

(B) TOP CIRCUMFERENTIAL STRAIN AT r=21", θ=0°, SECTOR 3

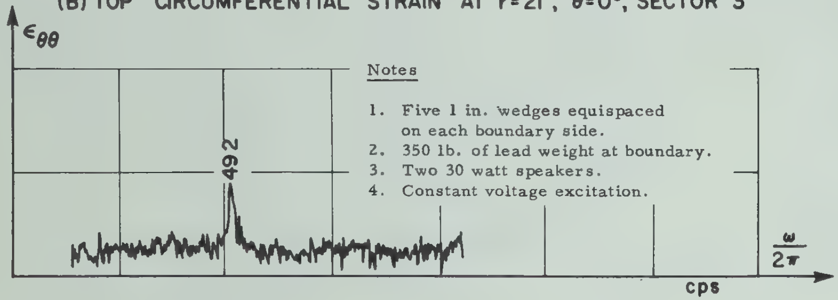

Notes

1. Five 1 in. wedges equispaced on each boundary side.
2. 350 lb. of lead weight at boundary.
3. Two 30 watt speakers.
4. Constant voltage excitation.

(C) TOP CIRCUMFERENTIAL STRAIN AT r = 21", θ=0°, SECTOR 3

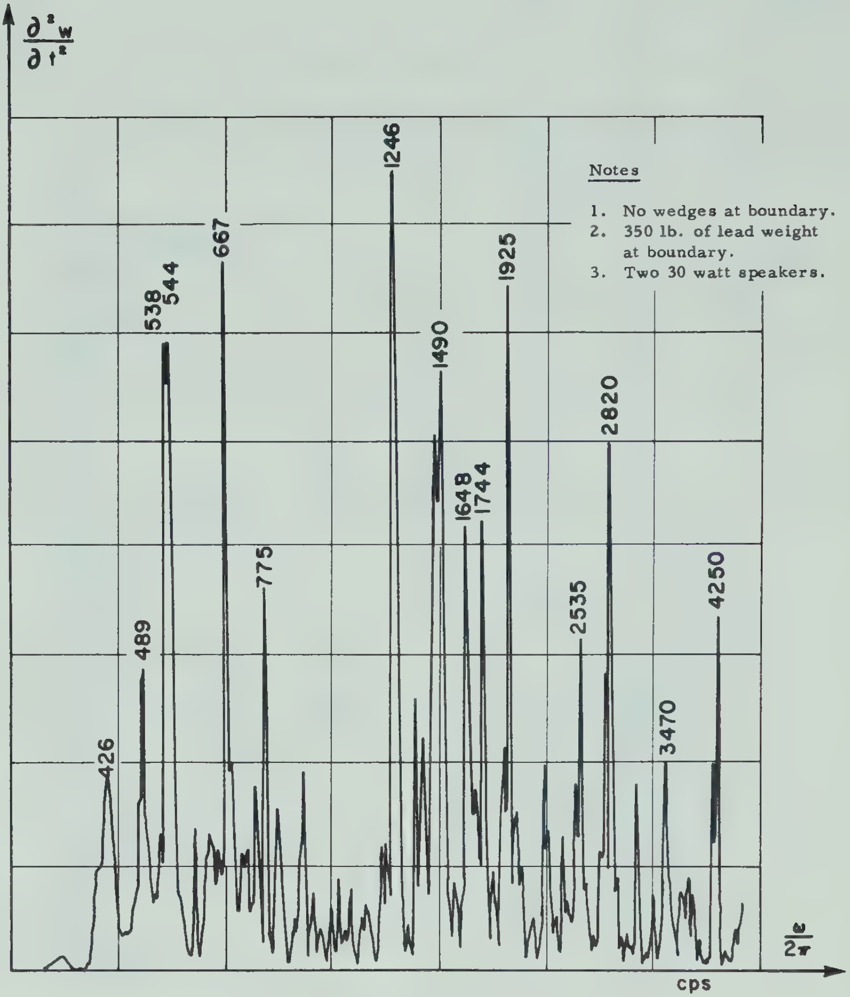

Notes

1. No wedges at boundary.
2. 350 lb. of lead weight at boundary.
3. Two 30 watt speakers.

(D) ACCELERATION AT r = 16", θ=0°, SECTOR 3

FIG. 7.14 VIBRATION OF ACOUSTICALLY EXCITED SHELL AT r=16", θ=0° AND r=21", θ=0°, SECTOR 3, FOR TRIAL 1

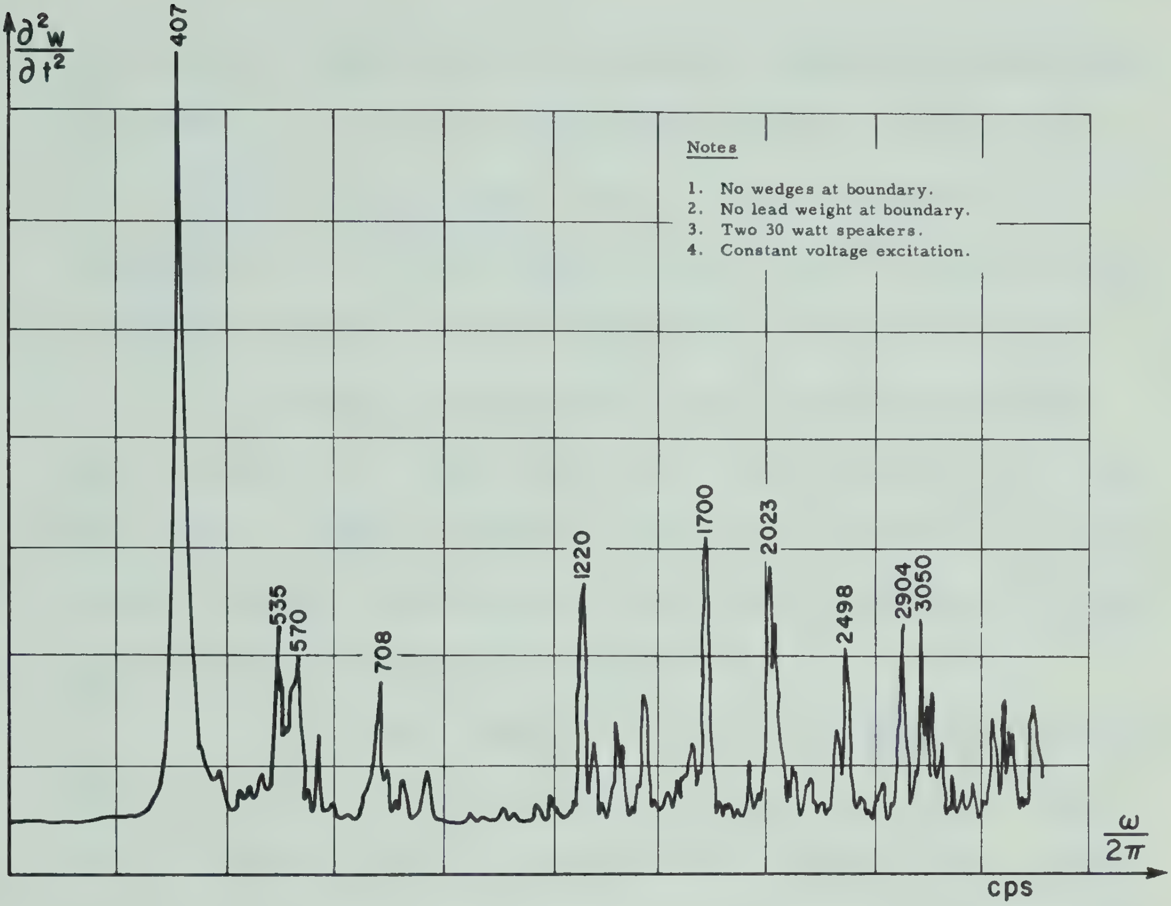

Notes

1. No wedges at boundary.
2. No lead weight at boundary.
3. Two 30 watt speakers.
4. Constant voltage excitation.

(A) TRANSVERSE ACCELERATION

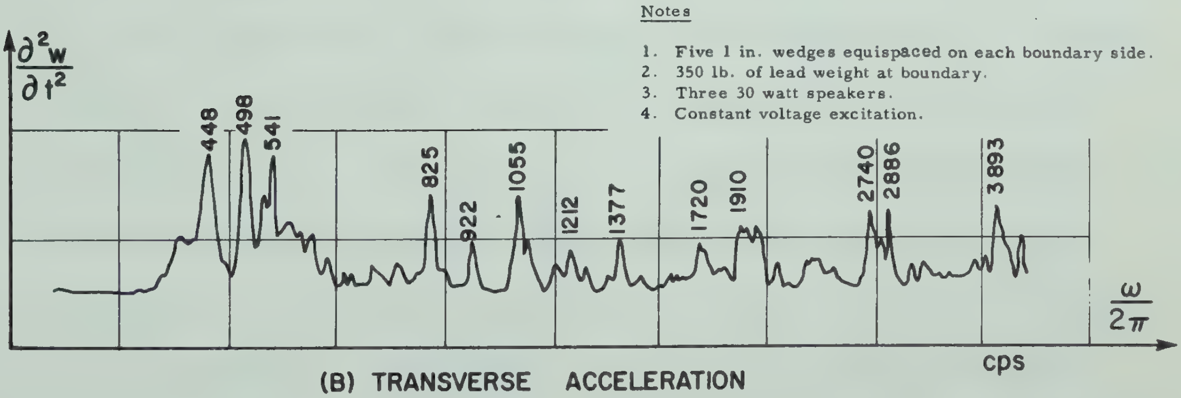

Notes

1. Five 1 in. wedges equispaced on each boundary side.
2. 350 lb. of lead weight at boundary.
3. Three 30 watt speakers.
4. Constant voltage excitation.

(B) TRANSVERSE ACCELERATION

FIG. 7.15 VIBRATION OF ACOUSTICALLY EXCITED SHELL AT BOUNDARY OF SECTOR 3 FOR TRIAL 1.

for acoustic excitation frequencies ranging between 200 and 3000 cps. Although the abscissa scales have not been calibrated in these figures, the excitation frequencies have been noted for most of the significant resonances in cps and are accurate to approximately ± 5 cps. Ordinate scales were not calibrated either since sound level pressures were not kept constant for most tests. Modal response amplitudes cannot be related between graphs even approximately since different signal amplifications may have been used.

The large number of higher resonances obtained may have resulted in part from increases in the sound level overpressure occurring when standing waves were formed at different excitation frequencies. Of course, shell longitudinal inertia modes were excited in addition to the transverse inertia modes predicted by the theory. However, the larger number of resonances obtained at positions away from the shell edge, as shown in Fig. 7.14d for example, indicates that antisymmetric as well as symmetric modes may have been excited. The occurrence of nonsymmetric resonances could have resulted from asymmetries in the sound pressure distribution as well as in the shell geometry and edge fixity.

The attempt to attain better edge clamping by shimming and adding mass at the shell edges in order to simulate the edge conditions in Eq. (6.1) produced some

changes in the modal frequencies. The resonant frequency ranges obtained for the various clamping attempts are summarized in Table 7.2 along with comparable modal frequency ranges for shells with $a/R = 0.390625$ and $a/h = 66.667$ satisfying edge condition Eqs. (6.1), (6.2), (6.4) and (6.6).

The experimental resonant frequency ranging between 400 and 460 cps was not predictable for this shell geometry and these theoretical edge conditions. Oniashvili [88] pointed out that eigenvalues k_i must be real as the frequencies of a shell which can resist bending are always higher than its membrane frequency. Theoretically then, the lowest possible shell frequency occurs for $k = 0$ and has the value $\omega = 1/R \sqrt{E/\gamma}$. Assuming R was 64 in., the minimum shell frequency for any edge conditions would be 495.1 cps. Therefore, it is felt that the occurrence of this low resonant frequency resulted from either coupling between the shell and its mount or an effective increase in the shell radius of curvature R.

Results from Trial 2, which will be given in Section 7.4, indicate that the occurrence of this low resonant frequency resulted from properties of the shell itself rather than the mounting system. However, it should be noted that the dominant resonant frequency of the shell aluminium support blocks was about 230 cps when the steel

Table 7.2

Shell Experimental and Theoretical Natural Frequencies for Trial 1

		Approximate Experimental Modal Frequency Ranges (cps)	Mode Numbers and Frequencies of Theoretical Shells with a/R = 0.390625 and a/h = 66.667 which have Frequencies Comparable to Experimental Shell			
			Edge Conditions Satisfied			
			Eqs. (6.1) and (6.2)		Eqs. (6.4) and (6.6)	
			Mode	Frequency Range (cps)	Mode	Frequency Range (cps)
Position on Experimental Shell Surface where Resonances were Measured	Apex	410 to 460				
		535 to 560 (2 resonances)	1	536 to 554	1,2	497 to ( )[1], 541 to 568
		720 to 760	2	722 to 760	3	720 to 797
		898 to 948	4	944 to 1000	4	859 to 955
		1064 to 1242(4 resonances)	5	1101 to 1239	5	1099 to 1226
		1340 to 1395	6	1398 to 1537	6	1372 to 1518
		+ higher resonances				
	Boundary	402 to 448				
		492 to 498			1	497 to ( )[1]
		535 to 570 (2 resonances)	1	536 to 554	2	541 to 568
		708	2	722 to 760	3	720 to 797
		825				
		922	3,4	860 to 883, 944 to 1000	4	895 to 955
		1055 1212 to 1220	5	1101 to 1239	5	1099 to 1226
		+ higher resonances				

[1] This frequency could not be calculated.

clamping blocks and wedges were removed. These blocks were excited by a hammer striking the shell surface rather than by acoustic sound pressure, in order to obtain a measureable resonance.

The effective shell radius of curvature R would have to be approximately 80 in. in order to predict a natural frequency as low as 400 cps using Eq. (6.6) while it would have to be 100 in. to predict this low frequency using Eq. (6.1). It was felt that R approximated 64 in. much more closely over the shell surface in Trial 1 than it did in Trial 2 although actual variations were not measured in Trial 1. Therefore, it is postulated that the resonant frequencies between 400 and 460 cps were introduced as a result of surface 'rippling' which was discussed in Section 7.1.1.

The dominance near the apex of a resonant frequency of approximately 540 cps and the occurrence of another resonant frequency of approximately 500 cps indicate that there might have been a homogeneous elastic restraint condition relating $F_{vs}(\tilde{\rho},\tilde{\Theta})$ and $F_{vv}(\tilde{\rho},\tilde{\Theta})$, and also that edge condition Eqs. (6.4) and (6.6) were more applicable than Eqs. (6.1) and (6.2).

This closer approximation of the experimental shell edge conditions to the roller rather than the clamped edge conditions is confirmed by the mode shapes

shown in Fig. 7.16. These mode shapes agree more closely with the theoretical mode shapes of a shell satisfying edge condition Eq. (6.6) shown in the same figure than they do with the mode shapes of a shell satisfying edge condition Eq. (6.1) which were shown in Fig. 6.2. Complete experimental nodal lines could not be obtained in all cases, especially for those near the boundary where the vibration amplitude was smallest. The asymmetry of some of these mode shapes probably is indicative of the nonuniformity of the edge condition satisfaction around the boundary.

7.3.2 Transient Pressures. The average peak normally reflected overpressures q_o and associated durations t_o, as measured for each of the seven 1.5 lb. RDX/TNT shots in Trial 1 by three shear tube pressure gauges located around the circumference of the shell mount assembly, were 10.3 psi (± 0.3 psi) and 32 msec. (± 2 msec.), respectively.

It was not considered worthwhile to include variations in the time of arrival of the shock front over the shell surface since theoretical solutions could not be obtained for some of the roller-edge conditions which were thought to best simulate the experimental edge conditions. Therefore, the transient load history over the complete shell surface was assumed to have the form

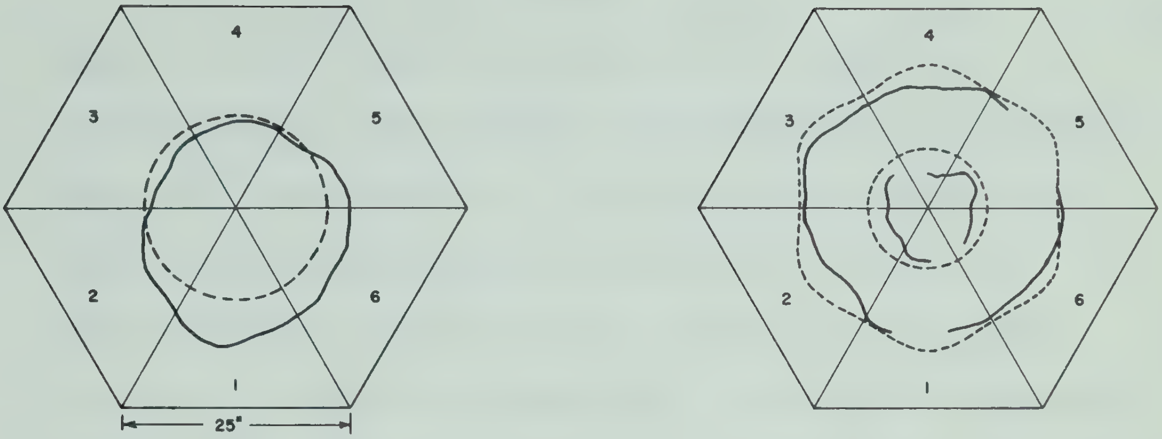

a) Experimental Resonant Frequency — 540 cps

Theoretical Frequency, Mode 2 — 541 cps

b) Experimental Resonant Frequency — 750 cps

Theoretical Frequency, Mode 3 — 720 cps

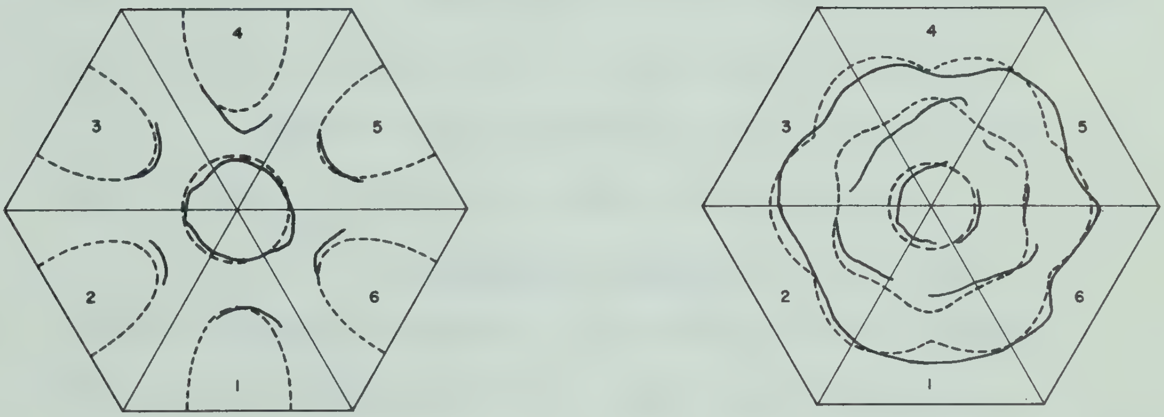

c) Experimental Resonant Frequency — 900 cps

Theoretical Frequency, Mode 4 — 859 cps

d) Experimental Resonant Frequency — 1098 cps

Theoretical Frequency, Mode 5 — 1099 cps

Notes

1. Three 30 watt speakers used for excitation.
2. 350 lb. of lead weight at shell boundary.
3. Wedges all around shell edge.

——— Experimental nodal lines

- - - - Theoretical nodal lines for a simply supported shell with sliding clamped edges and $a/R = 0.390625$, $a/h = 66.667$ and $\nu = 0.33$

FIG. 7.16 Some Experimental and Theoretical Shell Mode Shapes for Trial I

$$q(t) = q_o(1 - t/t_o)\exp(- t/t_o) \ , \ \ t < t_o, \qquad (7.1)$$

where q_o and t_o were -10.0 psi and 32 msec., respectively. The negative overpressure sign signifies that the transverse or $\bar{e}_n$ coordinate was chosen as positive in a direction outward from the front or convex surface of the shell. The value for q_o was chosen as - 10.0 psi rather than -10.3 psi to account for the slightly lower obliquely reflected overpressures which would be initially experienced over much of the shell surface in comparison to the normally reflected overpressure experienced by the pressure gauges.

Typical experimental blast overpressure and shell strain records are shown in Fig. 7.17.

7.3.3 Transient Response. Solutions for transverse displacements and sectional resultants, formulated in Appendix A.2, have been computed for a clamped shell and a simply supported shell with sliding clamped edges. These solutions, obtained by summing the first seven symmetric modes of response, will be referred to as Theory 1 and Theory 2, respectively. Geometric parameters used in the calculations were $a = 25$ in., $R = 64$ in. and $h = 0.375$ in. The experimental sectional resultants were computed by relating radial strains in sector 1 to circumferential strains in sector 3 using the assumption that each of the six sectors of the shell surface responded identically.

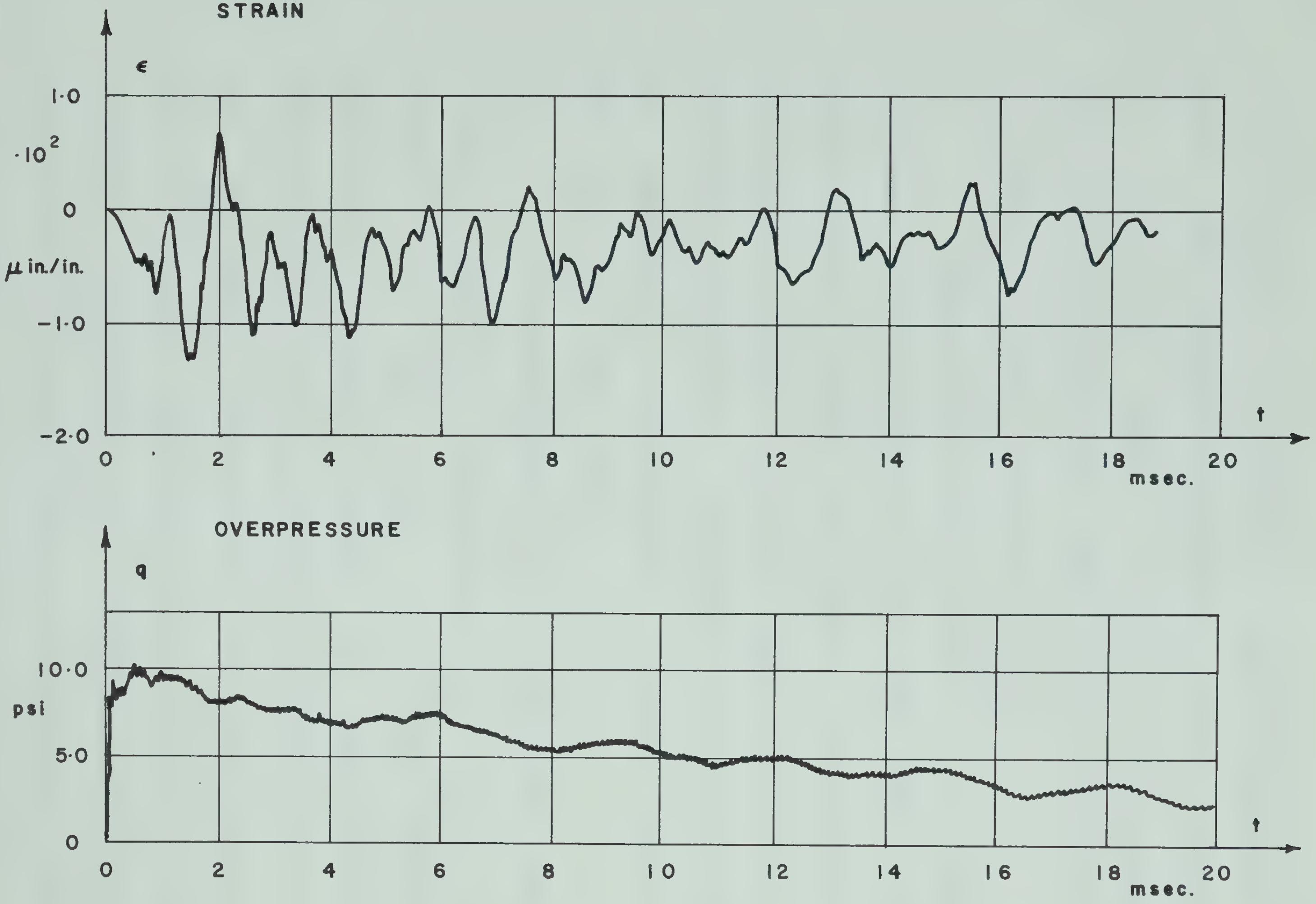

FIG. 7.17 Shell Experimental Central Back Strain and Pressure vs. Time for Trial 1

This assumption of symmetric response appeared to be very good on the basis of comparison of the radial strains at $\rho = 0.64$, $\theta = 0°$ and $\rho = 0.80$, $\theta = 0°$ in sectors 1 and 4 and the circumferential strains at $\rho = 0.64$, $\theta = 30°$ and $\rho = 0.80$, $\theta = 30°$ in sectors 3 and 6.

Damping was not included in the theoretical response calculations as it was felt that the edge conditions of Theory 1 and Theory 2 did not simulate the experimental edge conditions closely enough to make its inclusion worthwhile. Damping effects, although they were not negligible, did not appear to be as significant as for the plate experiment.

Dimensionless theoretical static and maximum dynamic transverse displacements are plotted along the radial line $\theta = 0°$ in Fig. 7.18. It is interesting to note that, because of beating, the ratio of maximum dynamic-to-static displacement exceeds 2 in the region of the shell apex. In contrast, this ratio would not usually exceed 2 for plates since for most transient loads the fundamental mode dominates plate response. The inclusion of viscous damping for the shell would cause a greater reduction in the maximum values near the apex than in the values closer to the boundary since maximum values near the apex occurred several oscillations after maximum values were attained near the boundary.

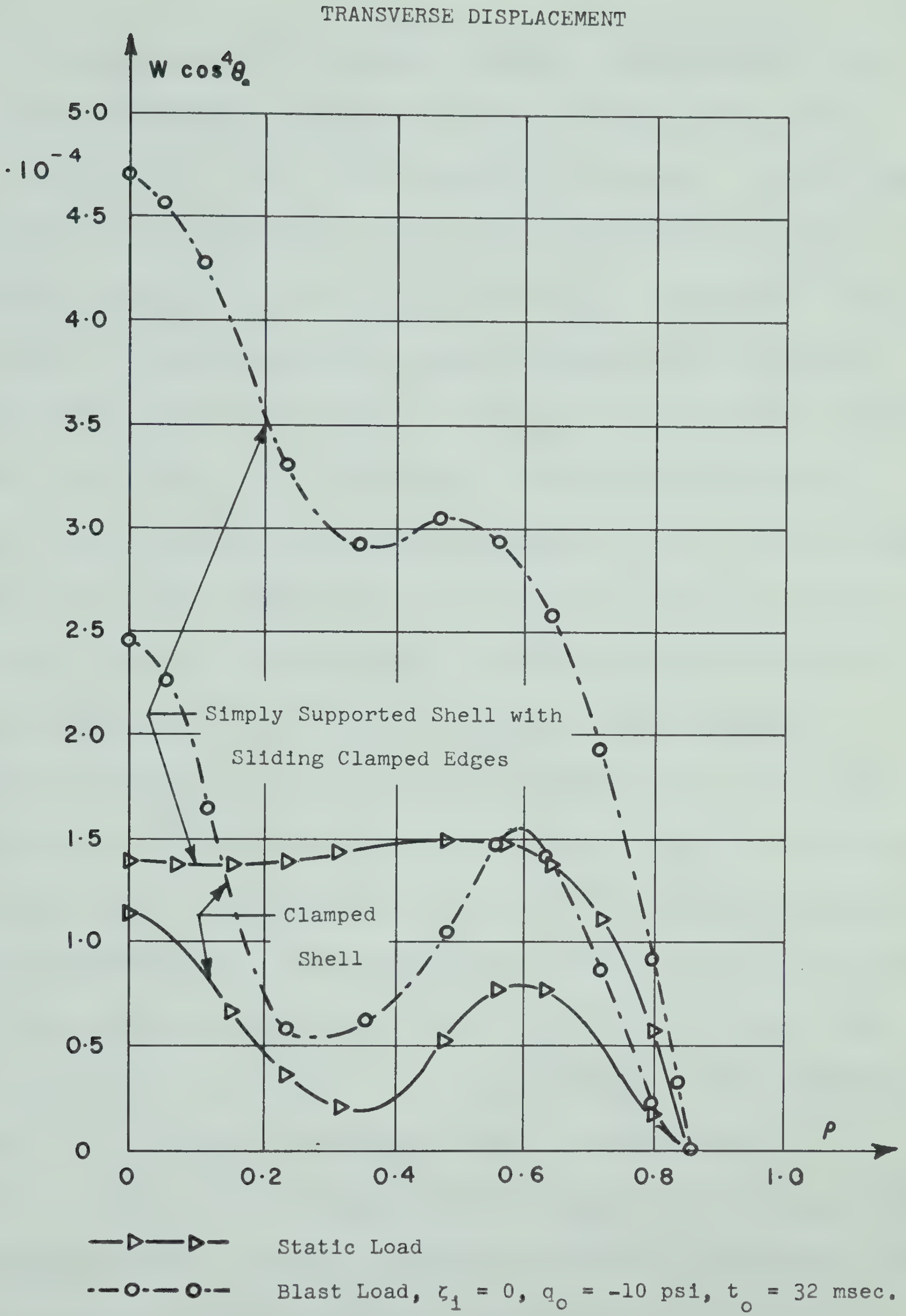

FIG. 7.18 Shell Theoretical Static and Maximum Dynamic Transverse Displacements on $\theta = 0^o$

Dimensionless maximum dynamic experimental and theoretical sectional resultants are plotted along the radial lines $\theta = 0°$, $10°$, $20°$ and $30°$ in Figs. 7.19 through 7.22. The edge conditions which were satisfied by the experimental shell at $\theta = 0°$ can be readily inferred from a comparison of the theoretical and experimental values of the sectional resultants shown in Fig. 7.19 near the shell boundary ($\tilde{\rho} = 0.866$, $\tilde{\theta} = 0°$) since the r,θ coordinates coincide with the v,s coordinates along $\theta = 0°$. Deviations from the prescribed edge condition values in this figure are larger for Theory 2 than Theory 1 primarily because the numerical solution for Theory 1 was obtained using a collocation point at $\theta = 0°$ while the solution for Theory 2 did not use a collocation point at $\theta = 0°$. It is apparent from a comparison of values of the radial stress resultants that the boundary of the experimental shell satisfied more closely the roller edge condition $F_{vv}(\tilde{\rho},\tilde{\theta}) = 0$ than the clamped condition $u_v(\tilde{\rho},\tilde{\theta}) = 0$. Eliminating edge extension by setting $\varepsilon_{ss}(\tilde{\rho},\tilde{\theta}) = 0$ is equivalent to setting $F_{ss}(\tilde{\rho},\tilde{\theta}) = \nu\, F_{vv}(\tilde{\rho},\tilde{\theta})$. Comparison of the experimental radial and circumferential stress resultants reveals that the shell boundary was not well restricted against edge extension. Comparison of the values of the radial flexural stress couples indicates that the experimental shell boundary satisfied the condition $\frac{\partial w}{\partial v}(\tilde{\rho},\tilde{\theta}) = 0$ quite well. Setting

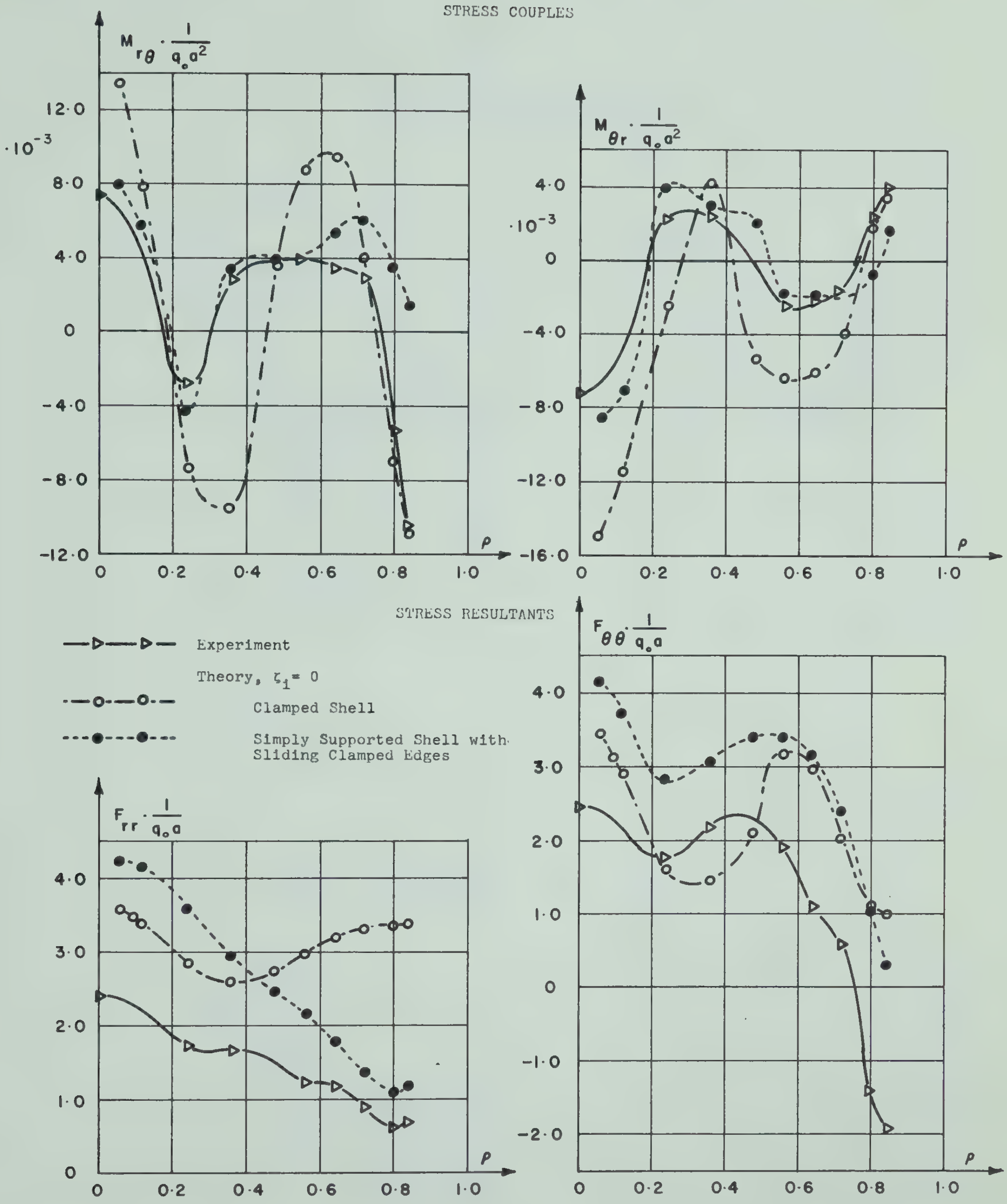

FIG. 7.19 Shell Maximum Dynamic Experimental and Theoretical Sectional Resultants on $\theta = 0^{\circ}$ for Trial 1

STRESS COUPLES

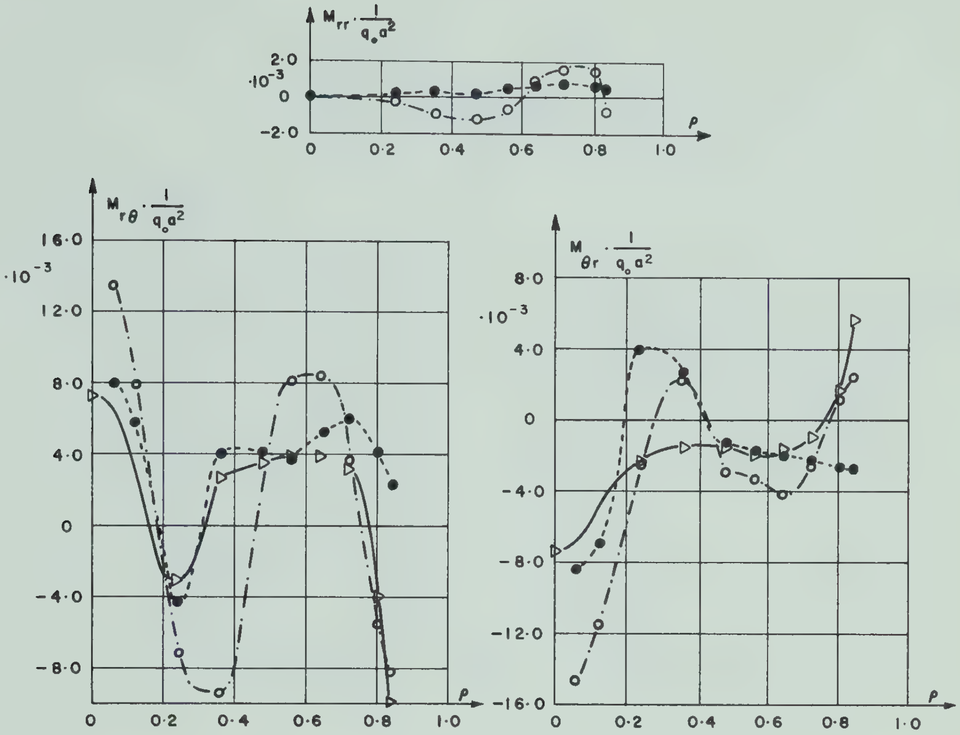

STRESS RESULTANTS

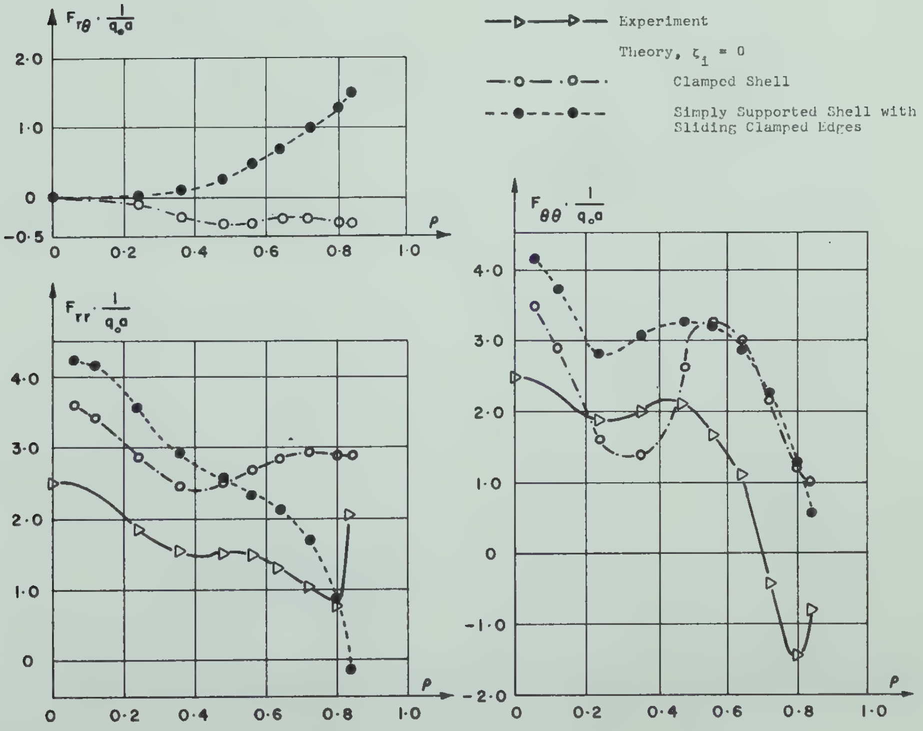

FIG. 7.20 Shell Maximum Dynamic Experimental and Theoretical Sectional Resultants on θ = 10° for Trial 1

STRESS COUPLES

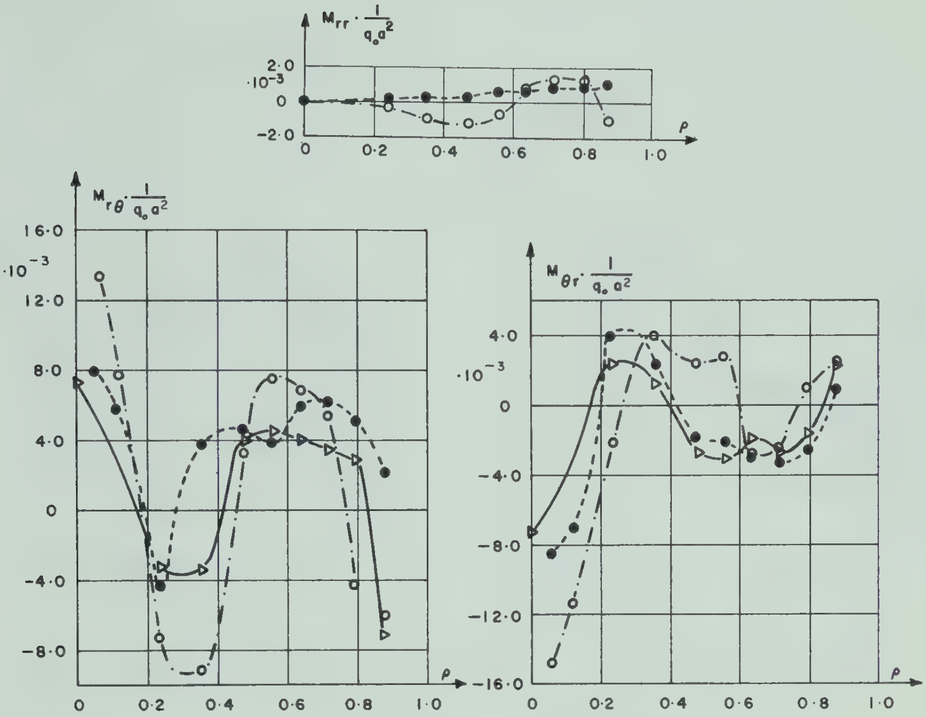

STRESS RESULTANTS

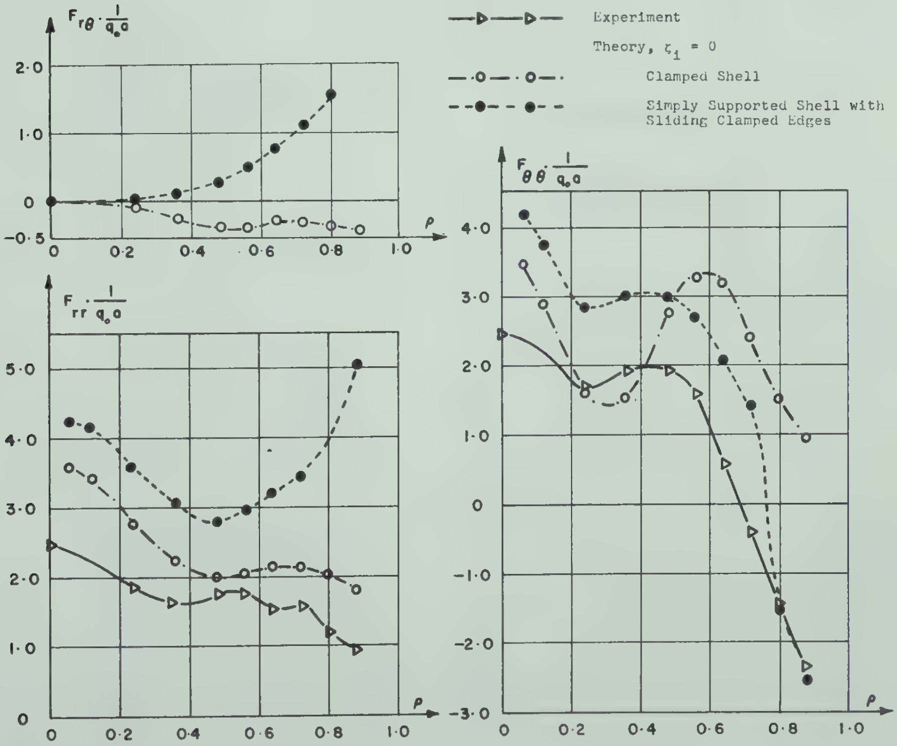

FIG. 7.21 Shell Maximum Dynamic Experimental and Theoretical Sectional Resultants on $\theta = 20^o$ for Trial 1

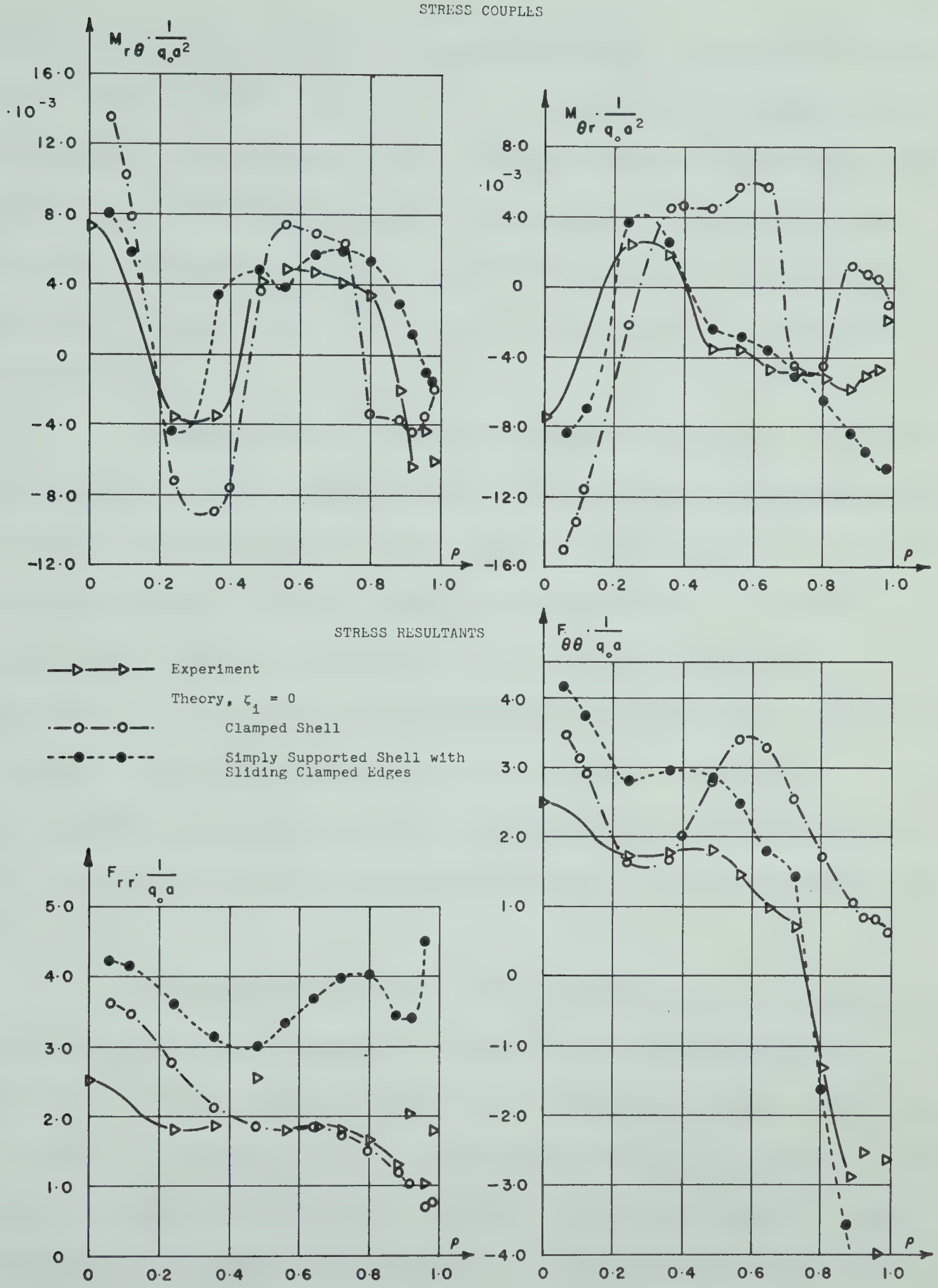

FIG. 7.22 Shell Maximum Dynamic Experimental and Theoretical Sectional Resultants on $\theta = 30^{\circ}$ for Trial 1

$w(\tilde{\rho},\tilde{\theta}) = 0$ results in the relation between the edge flexural stress couples that $M_{sv}(\tilde{\rho},\tilde{\theta}) = -\nu M_{vs}(\tilde{\rho},\tilde{\theta})$. Comparison of the values of the radial and circumferential flexural stress couples at the boundary shows that the condition of edge transverse displacement was satisfied quite well for the experimental shell and for Theory 1 but not quite so well for Theory 2.

It appears from this discussion of edge condition satisfaction that a theoretical solution for a clamped shell with sliding free edges would provide better agreement with the experimental results than the predictions of either Theory 1 or Theory 2. However, it probably would be necessary to use elastic restraints for both edge conditions in stress function in order to obtain the theoretical solution most compatible with the experimental results, at least with reference to the satisfaction of homogeneous edge conditions.

Theoretical values of the twisting stress couples $M_{rr} = - M_{\theta\theta}$ shown in Figs. 7.20 and 7.21 are larger in magnitude for the edge conditions of Theory 1 than for those of Theory 2, however they are smaller than the values of the flexural stress couples $M_{r\theta}$ and $M_{\theta r}$ for either set of edge conditions. Theoretical values of shear stress resultants $F_{r\theta} = F_{\theta r}$ shown in the same figures are generally smaller in magnitude than the values of the normal stress resultants F_{rr} and $F_{\theta\theta}$, although the magnitude of $F_{r\theta}$ approaches that

of $F_{\Theta\Theta}$ near the boundary for Theory 2.

Experimental and theoretical central transverse displacements vs. time are compared in Fig. 7.23. The experimental displacement record is not too reliable as it is composed of some gauge mount vibration as well. Experimental and theoretical sectional resultants vs. time are compared at six different positions on the shell surface in Figs. 7.24 through 7.29. It is apparent that there were experimental frequencies present which are lower than any predictable theoretically for the shell geometry assumed. Although the experimental stress couples responded at frequencies similar to those for Theory 2 over most of the shell's surface except near the boundary where they responded at a frequency of about 400 cps, the stress resultants were governed by frequencies ranging between only 350 and 450 cps which generally decreased towards the boundary. It is from these results that the hypothesis regarding the significance of variations in the middle surface radius of curvature in the form of 'surface rippling', discussed in Section 7.1.1, arose.

A spectral analysis was performed on some of the combined membrane plus bending strain data recorded in the radial direction on the front (convex) surface of the shell using a digital computer program developed at DRES which employs the fast Fourier transform. Record lengths of 50 msec. were analysed at a rate of 20,776 samples per second

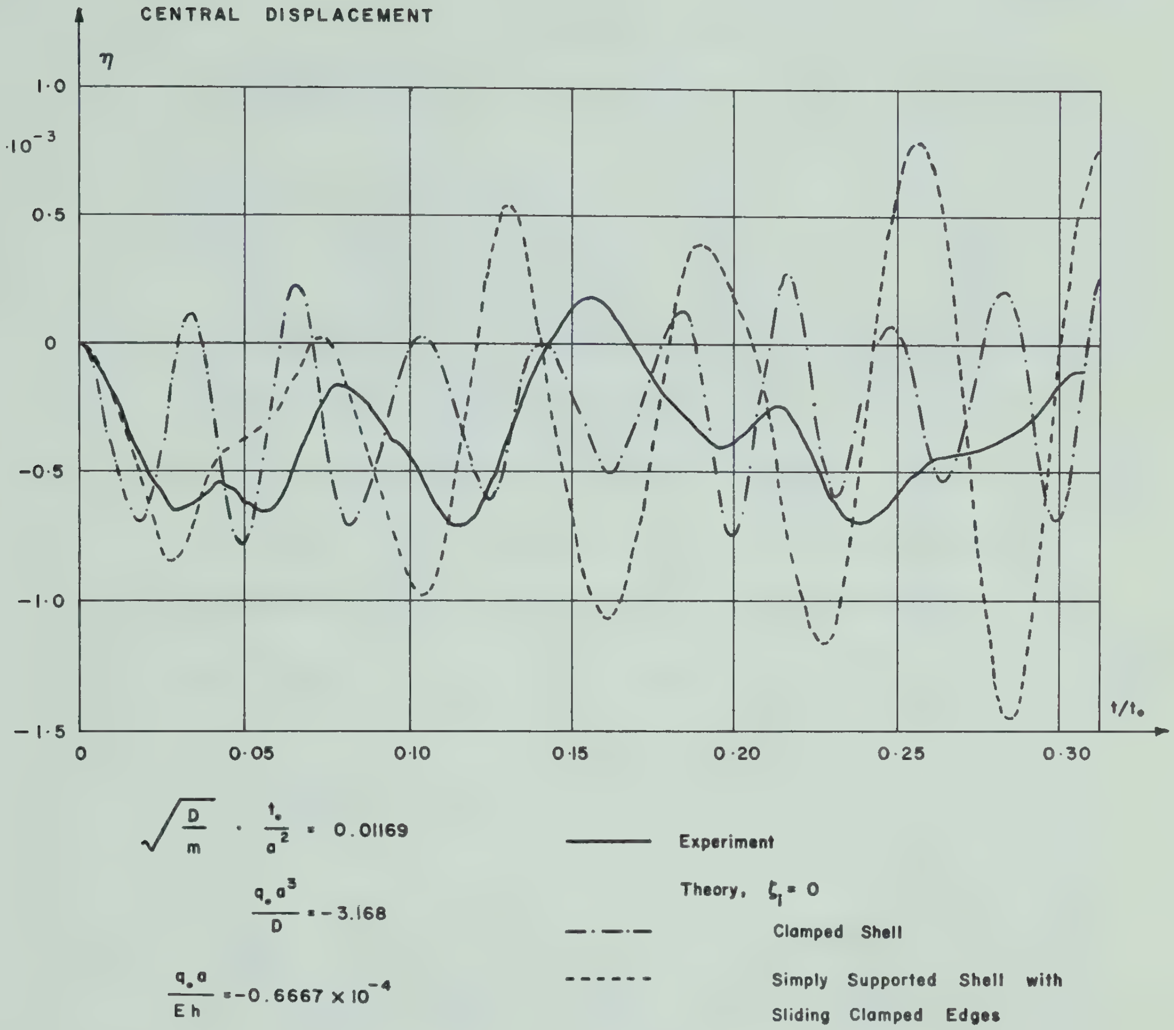

FIG. 7.23 Shell Experimental and Theoretical Central Displacement vs. Time for Trial 1

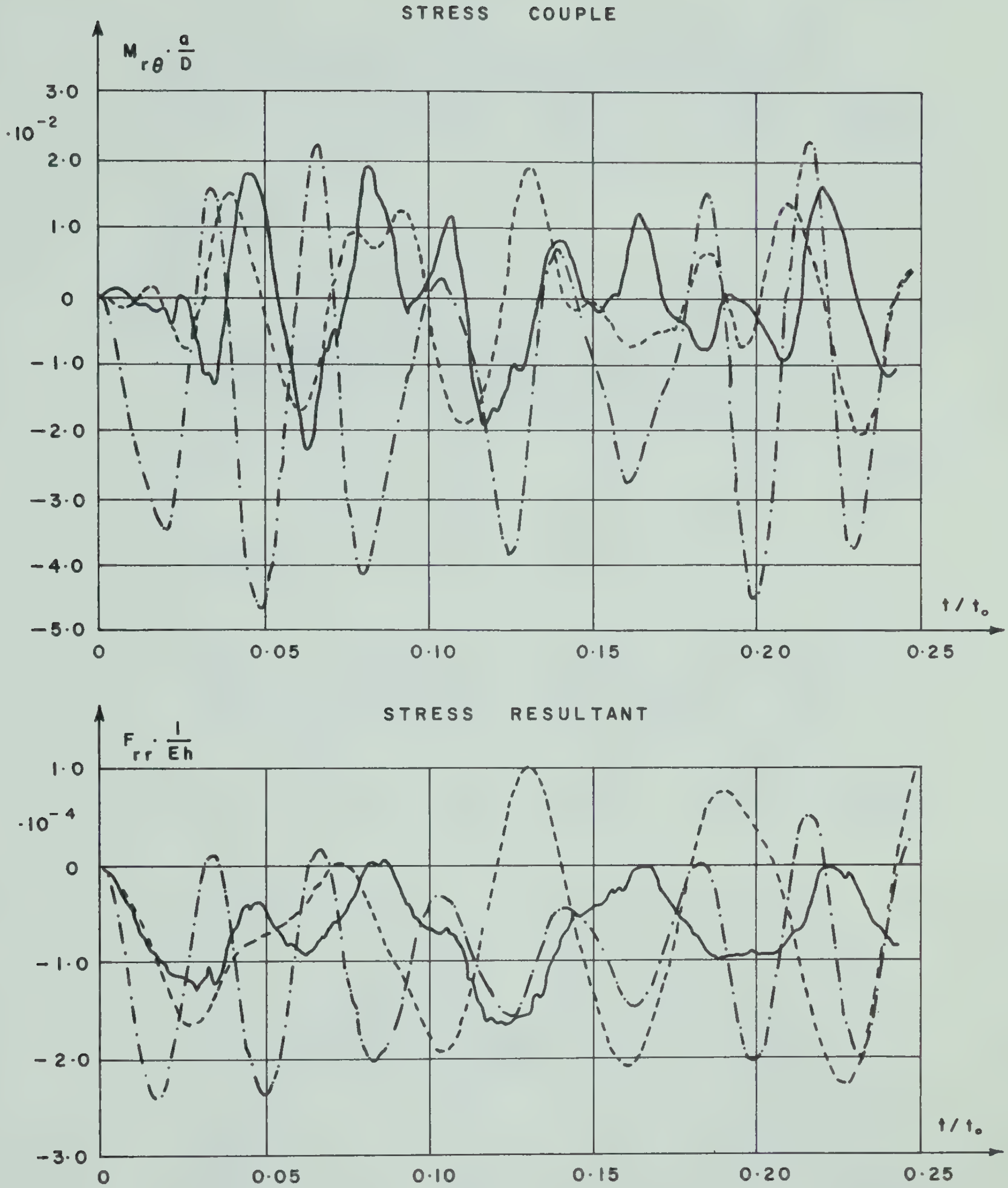

$$\sqrt{\frac{D}{m}} \cdot \frac{t_o}{a^2} = 0.01169$$

$$\frac{q_o a^3}{D} = -3.168$$

$$\frac{q_o a}{Eh} = -0.6667 \times 10^{-4}$$

——— Experiment

Theory, $\zeta_1 = 0$

—·—·— Clamped Shell

------ Simply Supported Shell with Sliding Clamped Edges

FIG· 7·24 Shell Experimental and Theoretical Sectional Resultants vs· Time at $\rho = 0, \theta = 0^\circ$ and $\rho = 0{\cdot}06, \theta = 0^\circ$, respectively, for Trial I

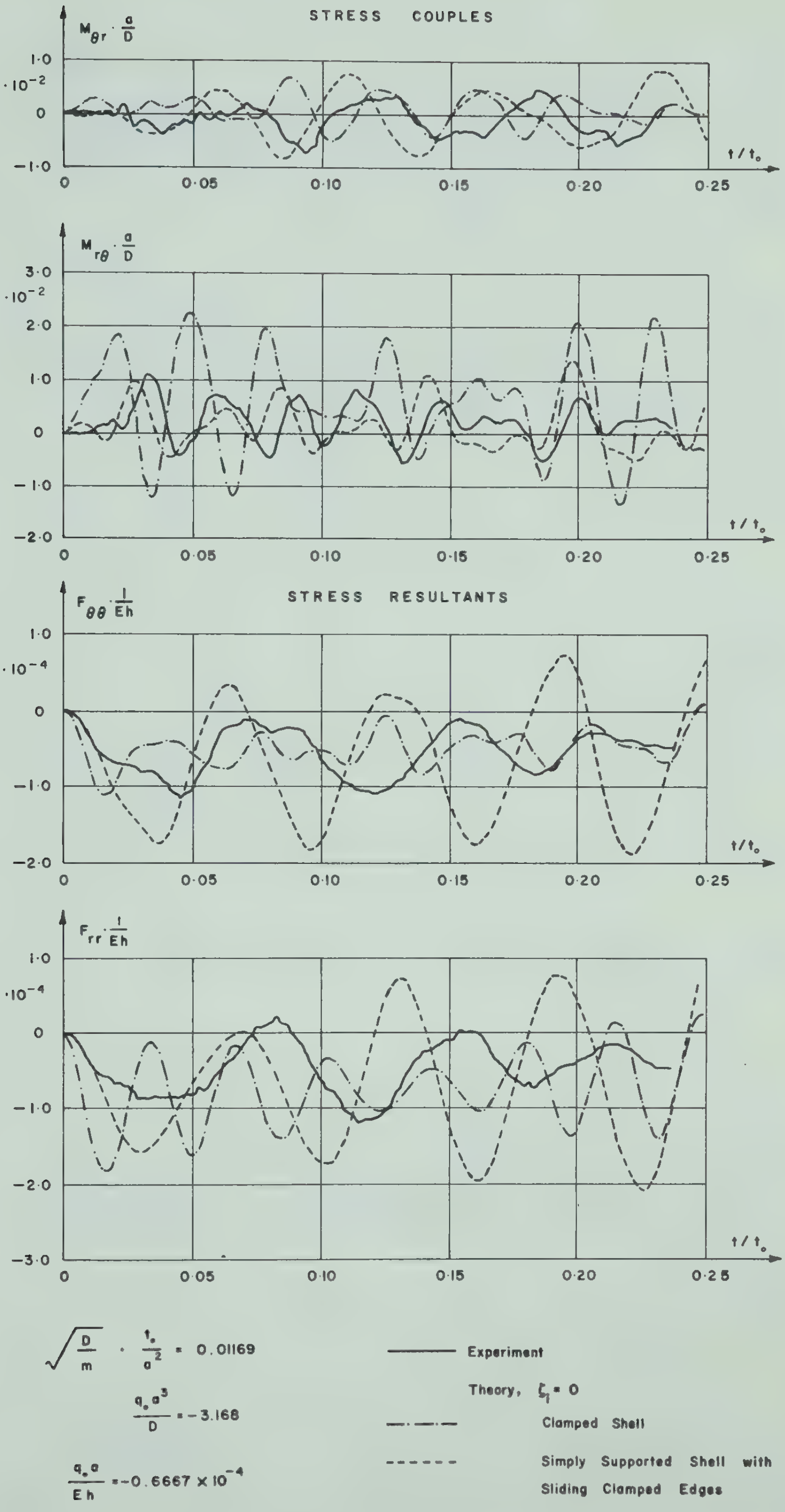

$$\sqrt{\frac{D}{m}} \cdot \frac{t_0}{a^2} = 0.01169$$

$$\frac{q_0 a^3}{D} = -3.168$$

$$\frac{q_0 a}{Eh} = -0.6667 \times 10^{-4}$$

FIG· 7·25 Shell Experimental and Theoretical Sectional Resultants vs· Time at $\rho = 0{\cdot}24$, $\theta = 30°$ for Trial I

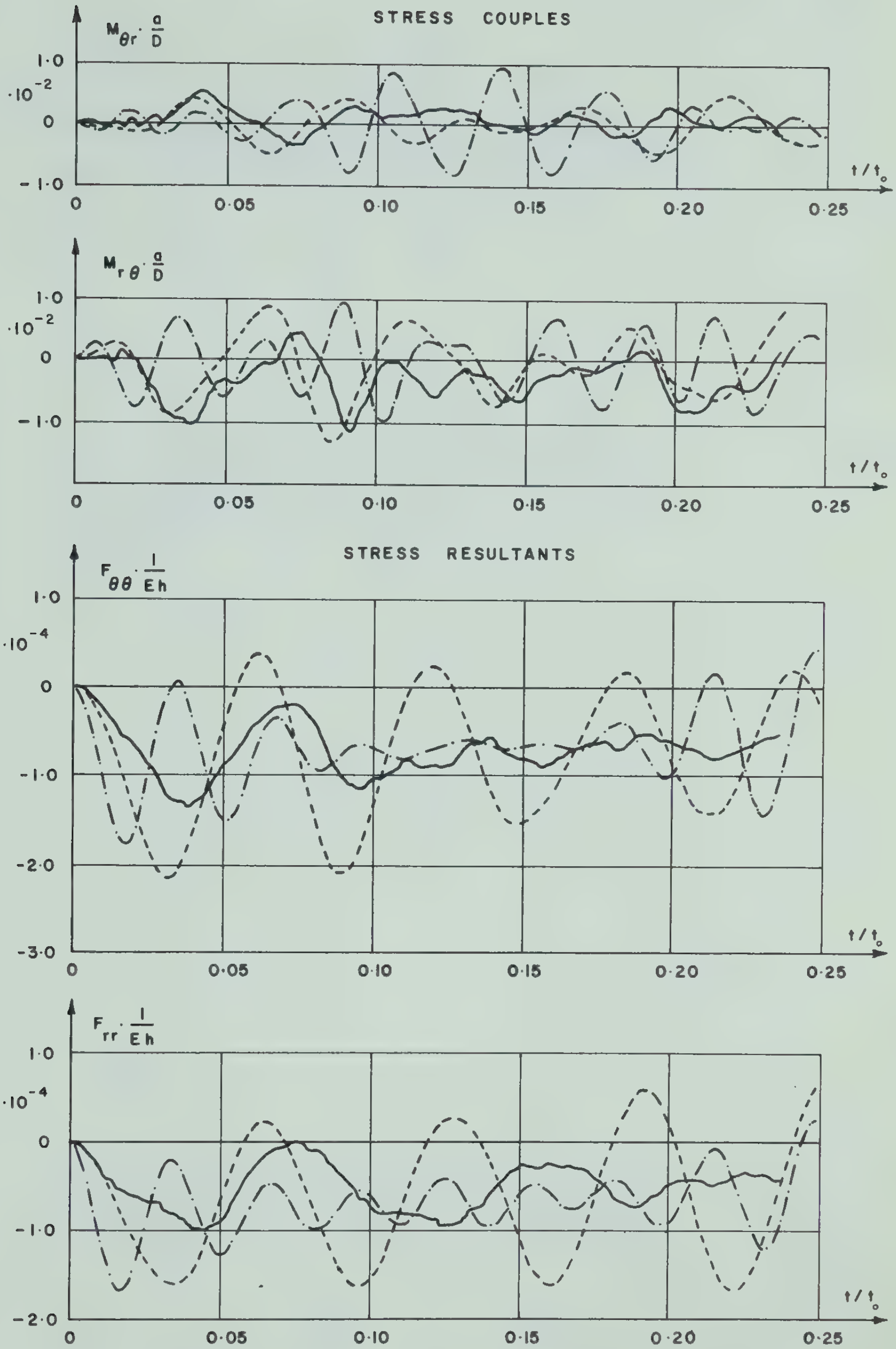

$$\sqrt{\frac{D}{m}} \cdot \frac{t_o}{a^2} = 0.01169$$

$$\frac{q_o a^3}{D} = -3.168$$

$$\frac{q_o a}{Eh} = -0.6667 \times 10^{-4}$$

———— Experiment

Theory, $\zeta_1 = 0$

—·—·— Clamped Shell

- - - - - - Simply Supported Shell with Sliding Clamped Edges

FIG· 7·26 Shell Experimental and Theoretical Sectional Resultants vs· Time at $\rho = 0{\cdot}48$, $\theta = 10^\circ$ for Trial I

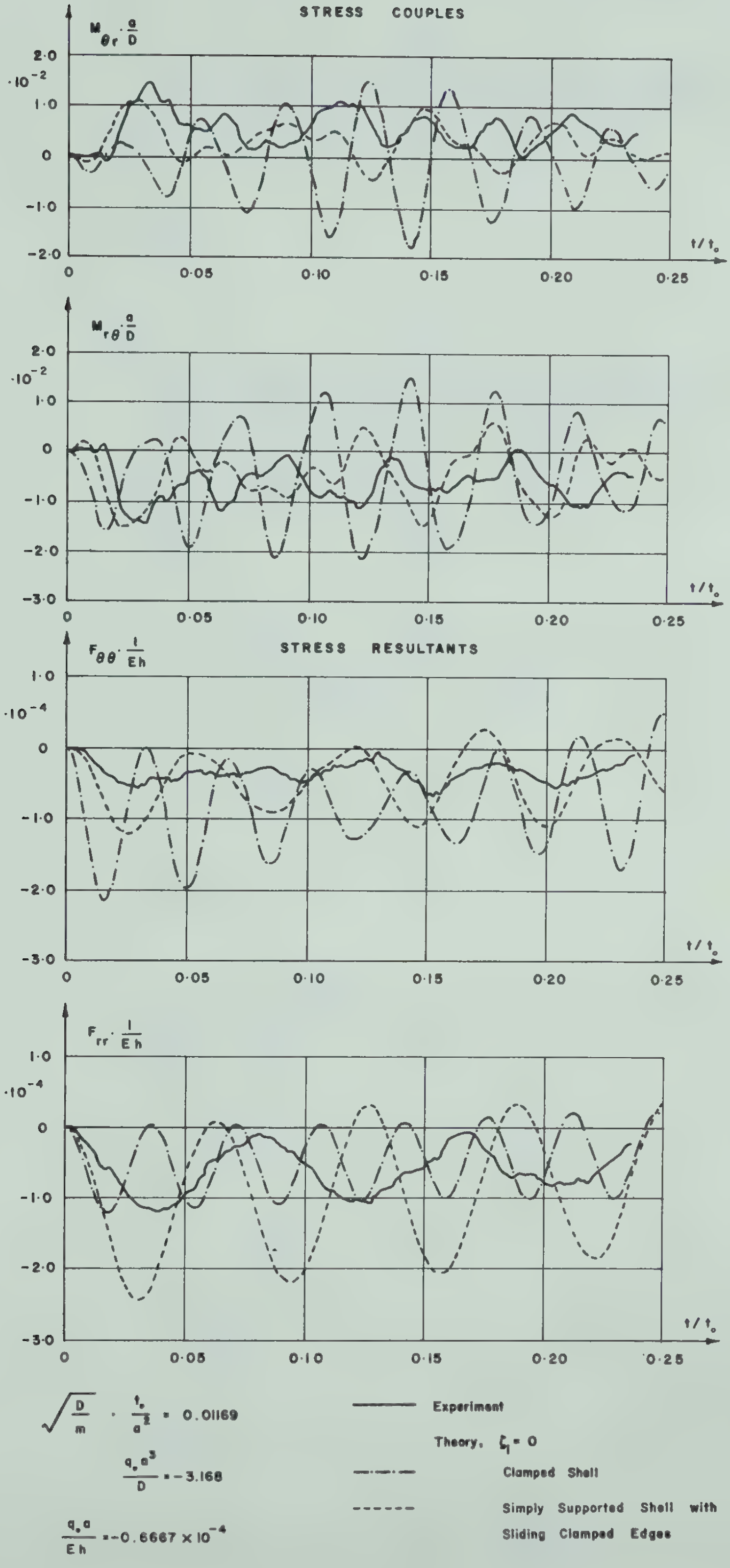

FIG. 7.27 Shell Experimental and Theoretical Sectional Resultants vs. Time at $\rho = 0.64$, $\theta = 30°$ for Trial I

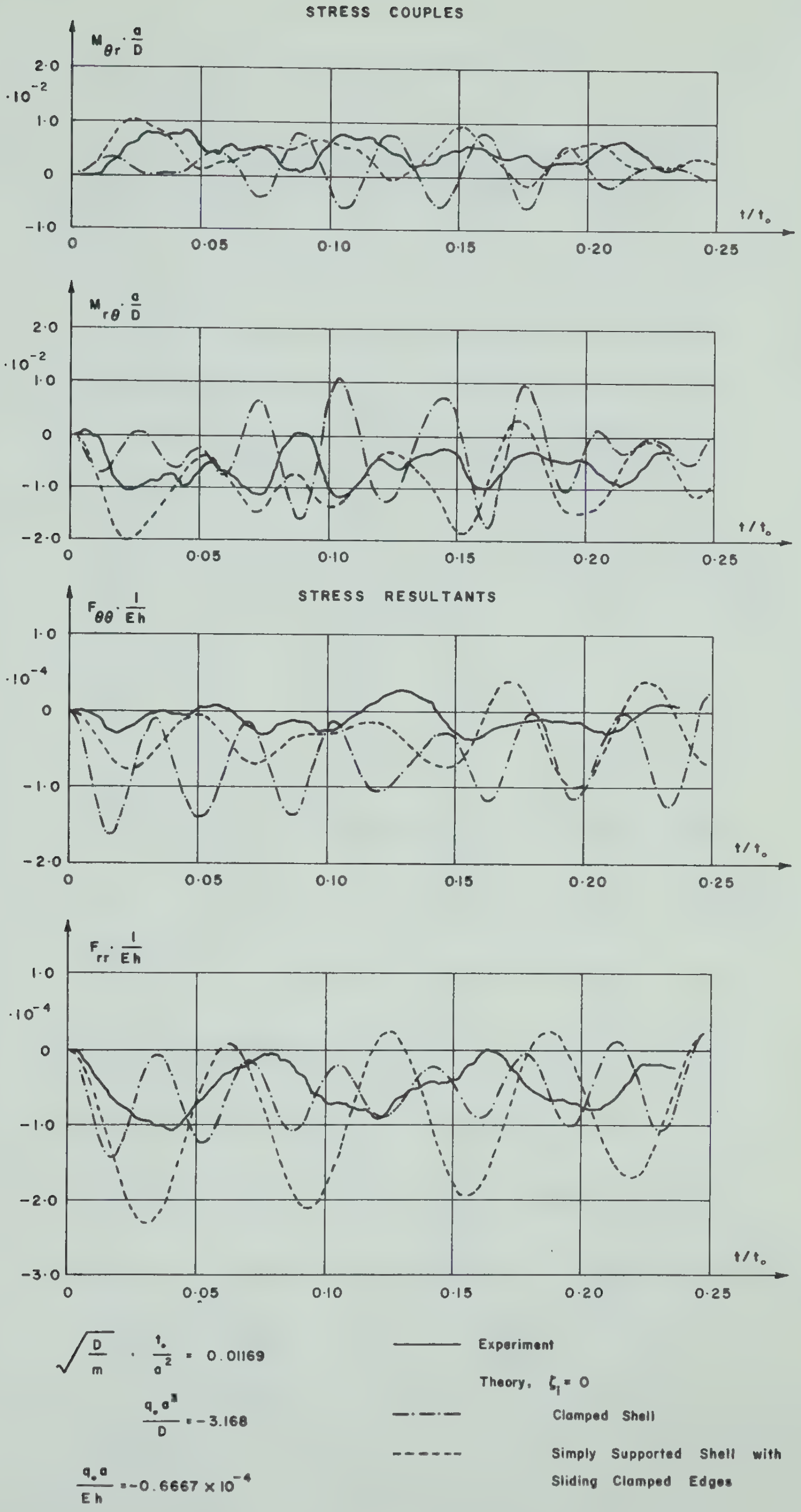

FIG· 7·28 Shell Experimental and Theoretical Sectional Resultants vs· Time at $\rho = 0{\cdot}72$, $\theta = 20^\circ$ for Trial 1

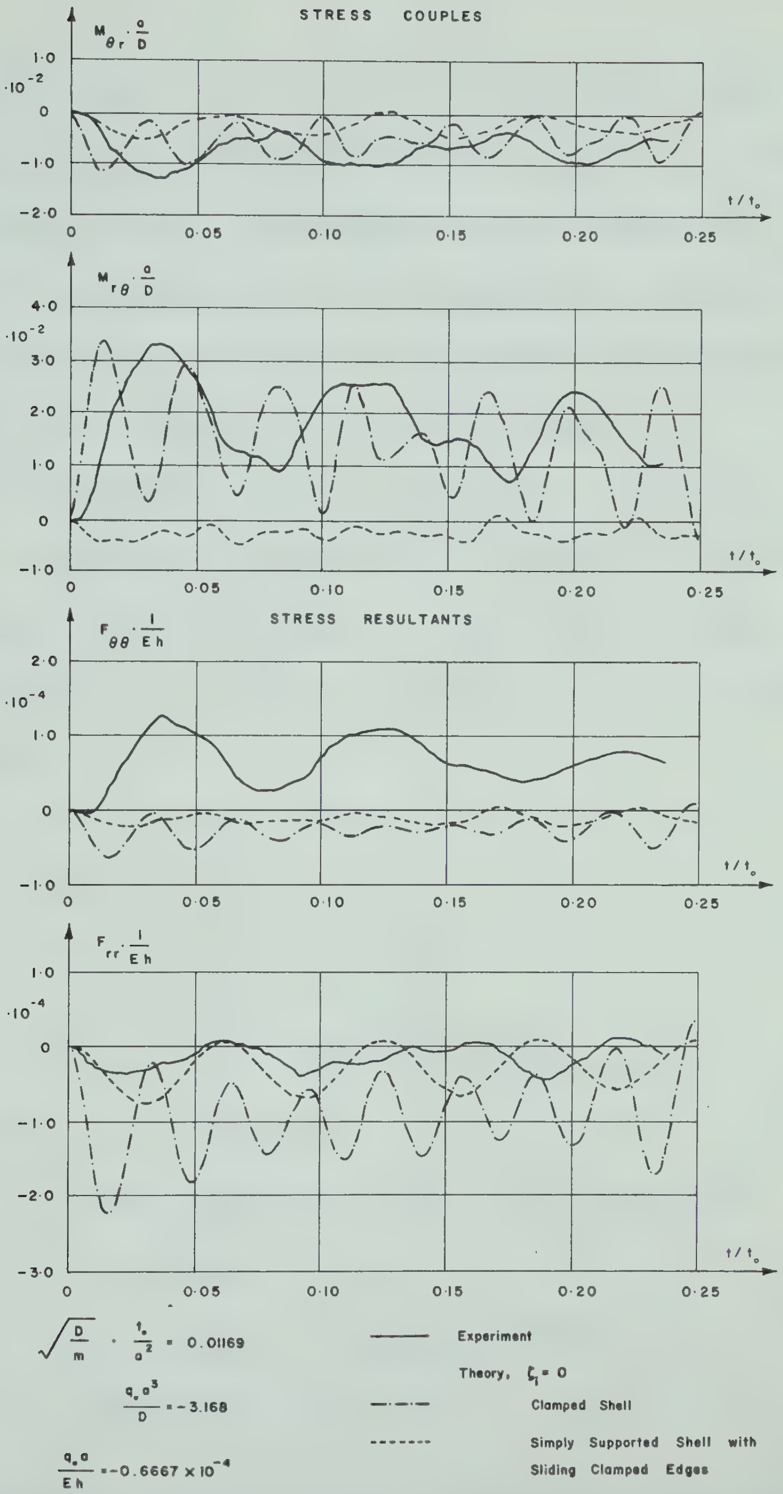

FIG· 7·29 Shell Experimental and Theoretical Sectional Resultants vs· Time at $\rho = 0{\cdot}84$, $\theta = 0^\circ$ for Trial I

giving a maximum frequency reproduction of 10,388 cps, an accuracy of ± 20 cps and a resolvability of 40 cps. Consequently, the presence of frequencies associated with the first two modes of vibration of the experimental shell for sliding edge conditions, theoretically separated only by approximately 40 cps (see Table 7.1), might not be detected from the analysis of a single strain record.

Some of the more significant response frequencies in cps can be summarized in groups of decreasing importance with respect to strain at different positions on the shell's surface as follows:

$\rho = 0, \theta = 0°$	1)	549
	2)	386, 732, 1098
	3)	488, 894, 264
	4)	610, 1687, 2378, 346, 122
$\rho = 0.48, \theta = 10°$	1)	407, 529
	2)	366, 122, 752, 1138, 305, 468
$\rho = 0.84, \theta = 0°$	1)	407
	2)	142, 529, 285, 752, 894
	3)	203, 610, 1138

Frequencies underlined were considered to arise from 'beating' of certain modes. For example, the frequencies of 122 and 142 cps likely represent beating between the modes with frequencies of 407 and 529 cps, and 407 and 549 cps, respectively. These results show that there were

dominant response frequencies at 407, 529 and 549 cps (± 20 cps). This analysis of the spectral representation of the shell's forced response characteristics agrees reasonably well with the acoustic excitation measurements shown in Figs. 7.13 through 7.15.

7.4 Theoretical and Experimental Results for Trial 2

7.4.1 Natural Frequencies. Some of the shell's natural frequencies for Trial 2 are indicated in Fig. 7.30 by the various resonances recorded over the shell surface with strain gauges for acoustic excitation frequencies ranging between 200 and 1200 cps.

The governing frequency of response over most of the shell surface occurred at 530 cps with other significant resonances occurring at approximately 580, 710 and 950 cps. However, as in Trial 1 when a relatively low frequency of around 400 cps dominated response near the shell boundary, a frequency of around 300 cps dominated response in the boundary region for this trial. This low resonant frequency must have resulted from properties of the shell itself rather than of the mount, since in-plane edge rigidity of the mount had been virtually eliminated for this trial.

Accurate experimental mode shapes could not be obtained for this trial since the boundary was not well restrained against free transverse vibration. However, the

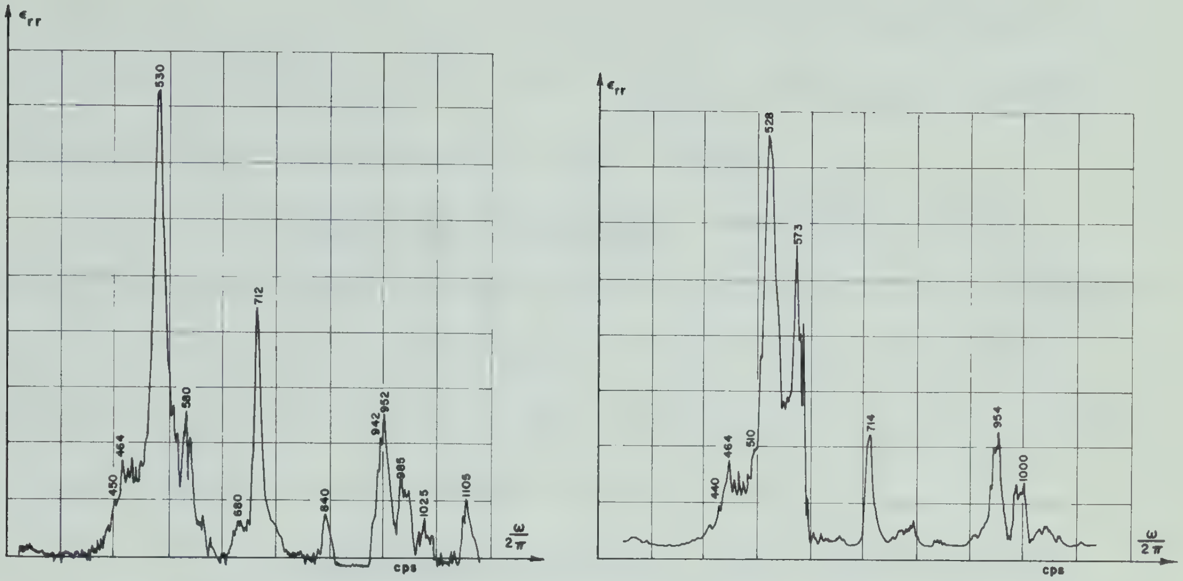

(A) FRONT CENTER STRAIN

(B) FRONT RADIAL STRAIN AT r = 6", θ = 45°

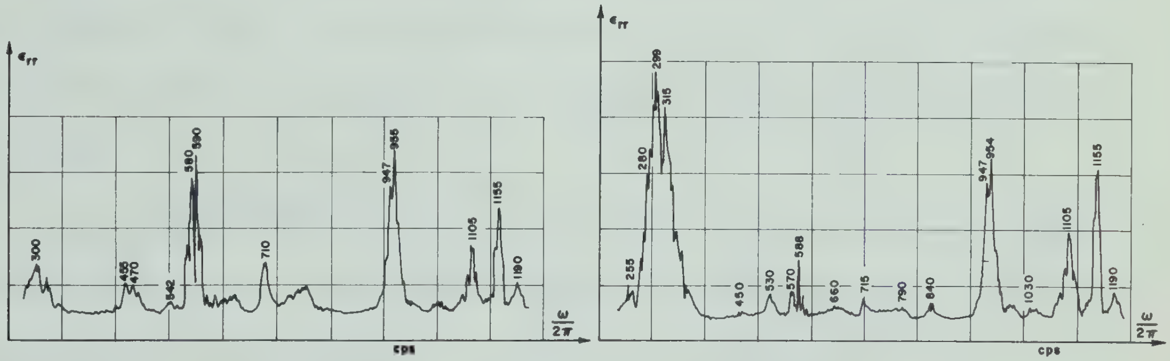

(C) FRONT RADIAL STRAIN AT r = 14", θ = 0°

(D) FRONT RADIAL STRAIN AT r = 21", θ = 0°

NOTES
1. SHELL MOUNTED IN SHOCK TUBE.
2. ONE 200 WATT SPEAKER.
3. CONSTANT VOLTAGE EXCITATION.

FIG. 7.30 VIBRATION OF ACOUSTICALLY EXCITED SHELL FOR TRIAL 2

mode shape for the 530 cps resonant frequency appeared to be nearly the same as that for the 540 cps resonant frequency of Trial 1 which was shown in Fig. 7.16a.

7.4.2 Transient Pressures. Transient overpressures on the shell as measured by two shear tube pressure gauges were unchanged from Trial 1 and consequently were represented theoretically by Eq. (7.1) where q_o and t_o were -10.0 psi and 32 msec., respectively.

7.4.3 Transient Response. Experimental transverse displacement and sectional resultants are compared in this section with the theoretical solution for the simply supported shell with sliding clamped edges used previously for Trial 1.

Experimental and theoretical central transverse displacements vs. time are compared in Fig. 7.31. This experimental displacement record is considered to be reliable since the gauge mount vibration was almost completely eliminated for these tests. The maximum experimental deflection-to-shell thickness ratio of 0.05 was well within the linear response range. The experimental edge in-plane displacement normal to the boundary shown in the same figure was almost as large as the transverse central displacement. This edge displacement appears to have undergone considerable damping.

Since strains were measured at only nine unique r,θ positions, it was not possible to plot variations of the

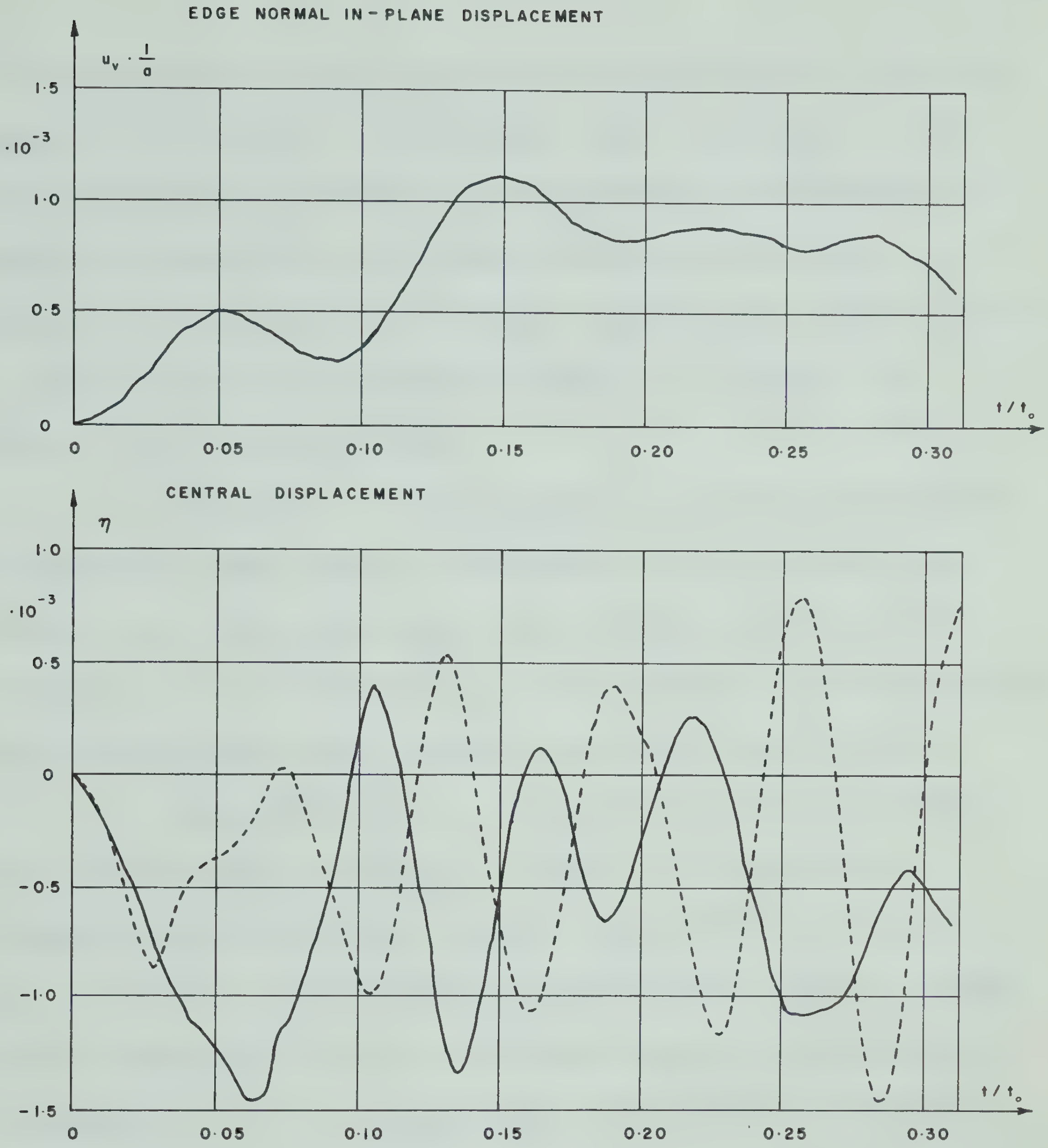

$$\sqrt{\frac{D}{m}} \cdot \frac{t_o}{a^2} = 0.01169$$

$$\frac{q_o a^3}{D} = -3.168$$

$$\frac{q_o a}{Eh} = -0.6667 \times 10^{-4}$$

——— Experiment

------ Theory, $\zeta_1 = 0$

Simply Supported Shell with Sliding Clamped Edges

FIG· 7·31 Shell Experimental and Theoretical Central Transverse Displacement and Experimental Edge In-Plane Displacement vs. Time for Trial 2

values of the sectional resultants along radial lines as was done for Trial 1 when strains were recorded at 36 unique positions. However, experimental and theoretical sectional resultants vs. time are compared in Figs. 7.32 through 7.37 at the same six positions on the shell surface at which they were compared in Trial 1 in Figs. 7.24 through 7.29, respectively.

Comparison of experimental sectional resultants at the shell apex for two different shots in Fig. 7.32 reveals that there was some sensitivity, especially in values of stress resultants, to the changes in edge support conditions which could occur between successive shots.

Comparison of the values of stress resultants near the boundary in Figs. 7.29 and 7.37 shows that, although more edge extension was permitted in Trial 2 than in Trial 1, the normal boundary force did not change significantly for the two different support arrangements, at least at $\theta = 0°$. Comparison of the values of radial stress couples in these two figures shows that the support arrangement of Trial 2 introduced an edge stress couple of opposite sign to the couple which occurs for a clamped edge with $\partial w(\tilde{\rho},\tilde{\theta})/\partial v = 0$. Comparison of the radial and circumferential stress couples near the boundary in Fig. 7.37 indicates that the condition of vanishing transverse edge displacement was not well satisfied since

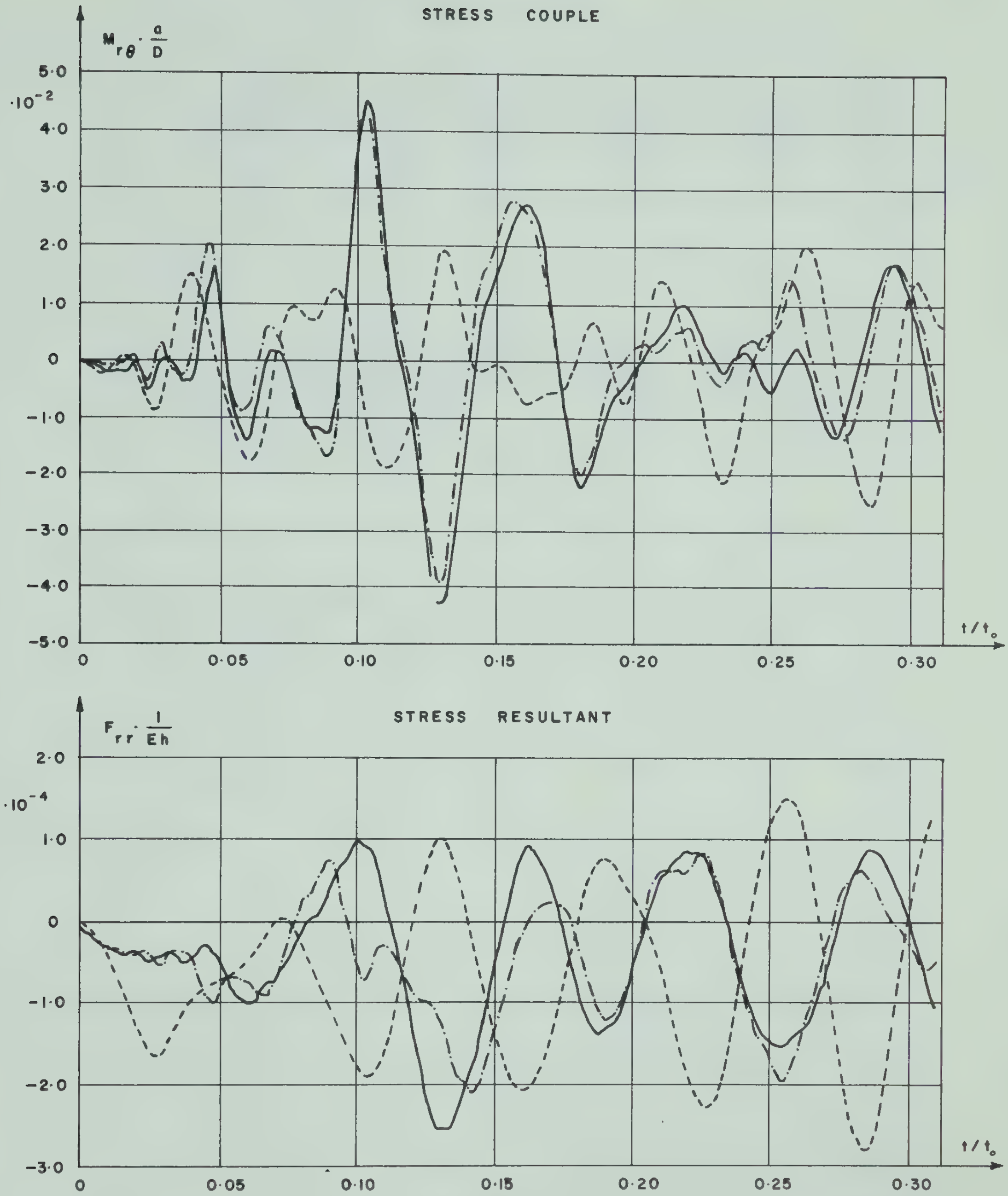

$$\sqrt{\frac{D}{m}} \cdot \frac{t_o}{a^2} = 0.01169$$

$$\frac{q_o a^3}{D} = -3.168$$

$$\frac{q_o a}{Eh} = -0.6667 \times 10^{-4}$$

——— Experiment

—·—·—

- - - - - - Theory, $\zeta_1 = 0$

Simply Supported Shell with Sliding Clamped Edges

FIG· 7·32 Shell Experimental and Theoretical Sectional Resultants vs· Time at $\rho = 0$, $\theta = 0°$ and $\rho = 0{\cdot}06$, $\theta = 0°$, respectively, for Trial 2

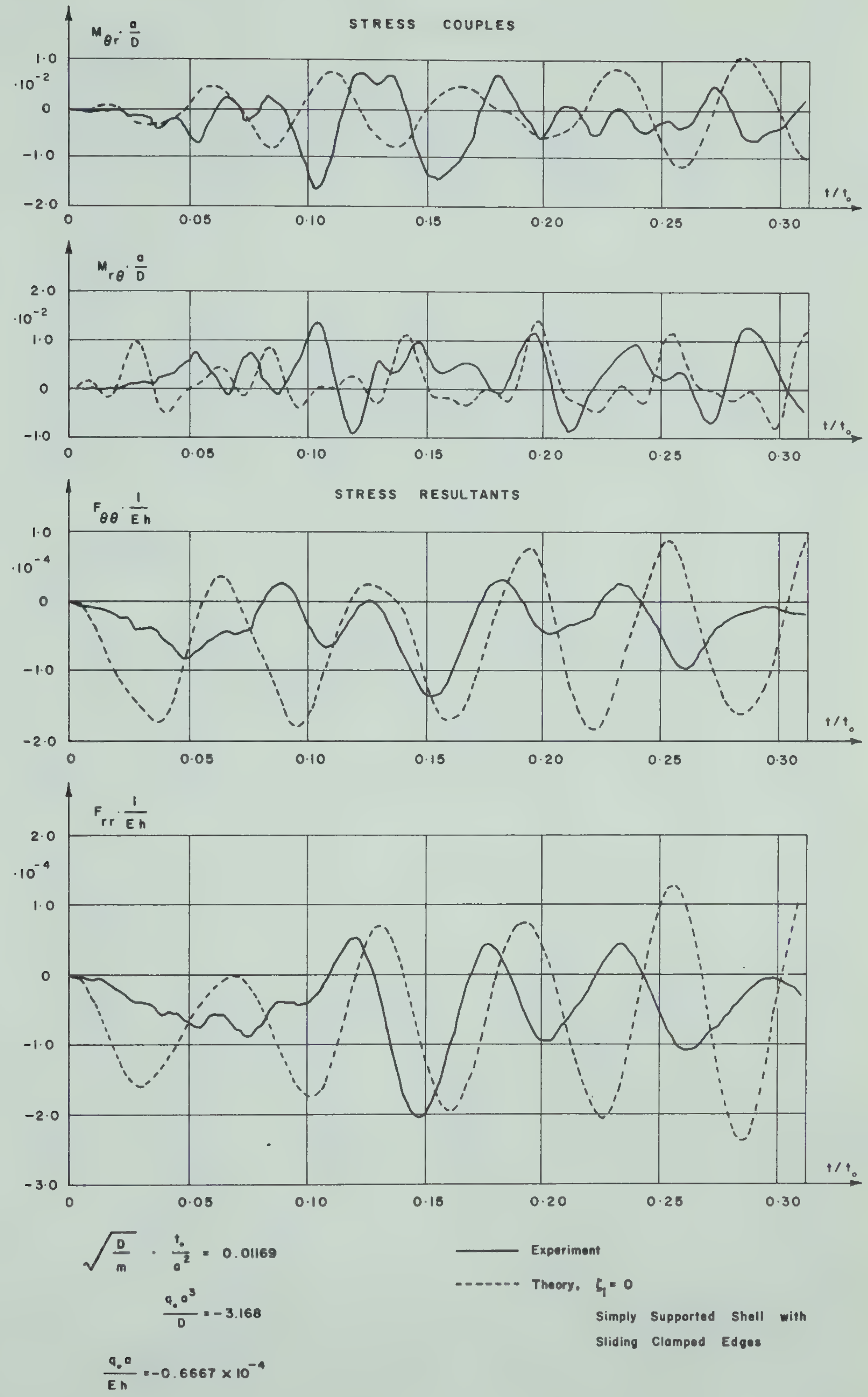

FIG· 7·33 Shell Experimental and Theoretical Sectional Resultants vs· Time at $\rho = 0{\cdot}24$, $\theta = 30°$ for Trial 2

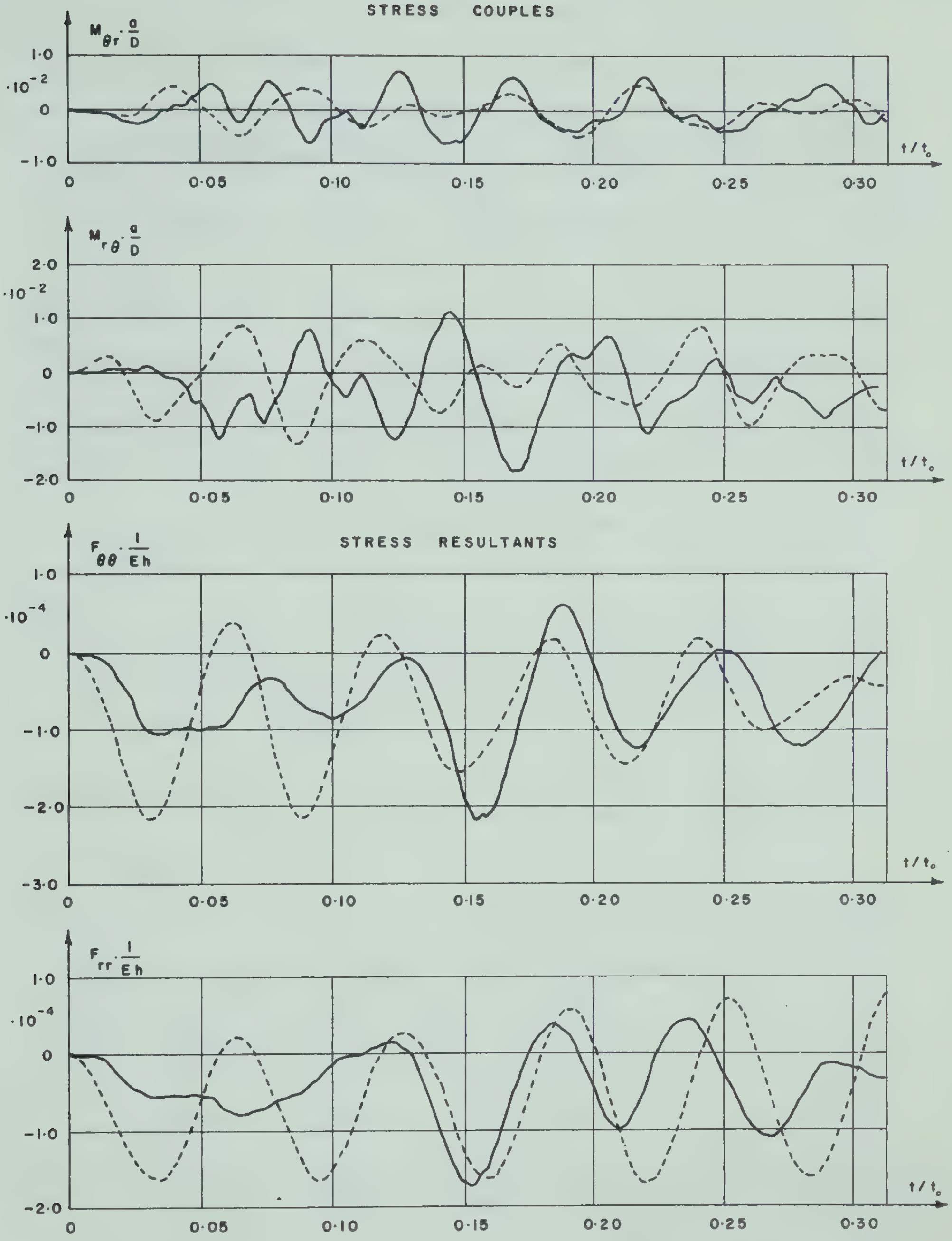

$\sqrt{\frac{D}{m}} \cdot \frac{t_o}{a^2} = 0.01169$

$\frac{q_o a^3}{D} = -3.168$

$\frac{q_o a}{Eh} = -0.6667 \times 10^{-4}$

——— Experiment

- - - - - Theory, $\zeta_1 = 0$

Simply Supported Shell with
Sliding Clamped Edges

FIG·7·34 Shell Experimental and Theoretical Sectional Resultants vs· Time at $\rho = 0{\cdot}48$, $\theta = 10°$ for Trial 2

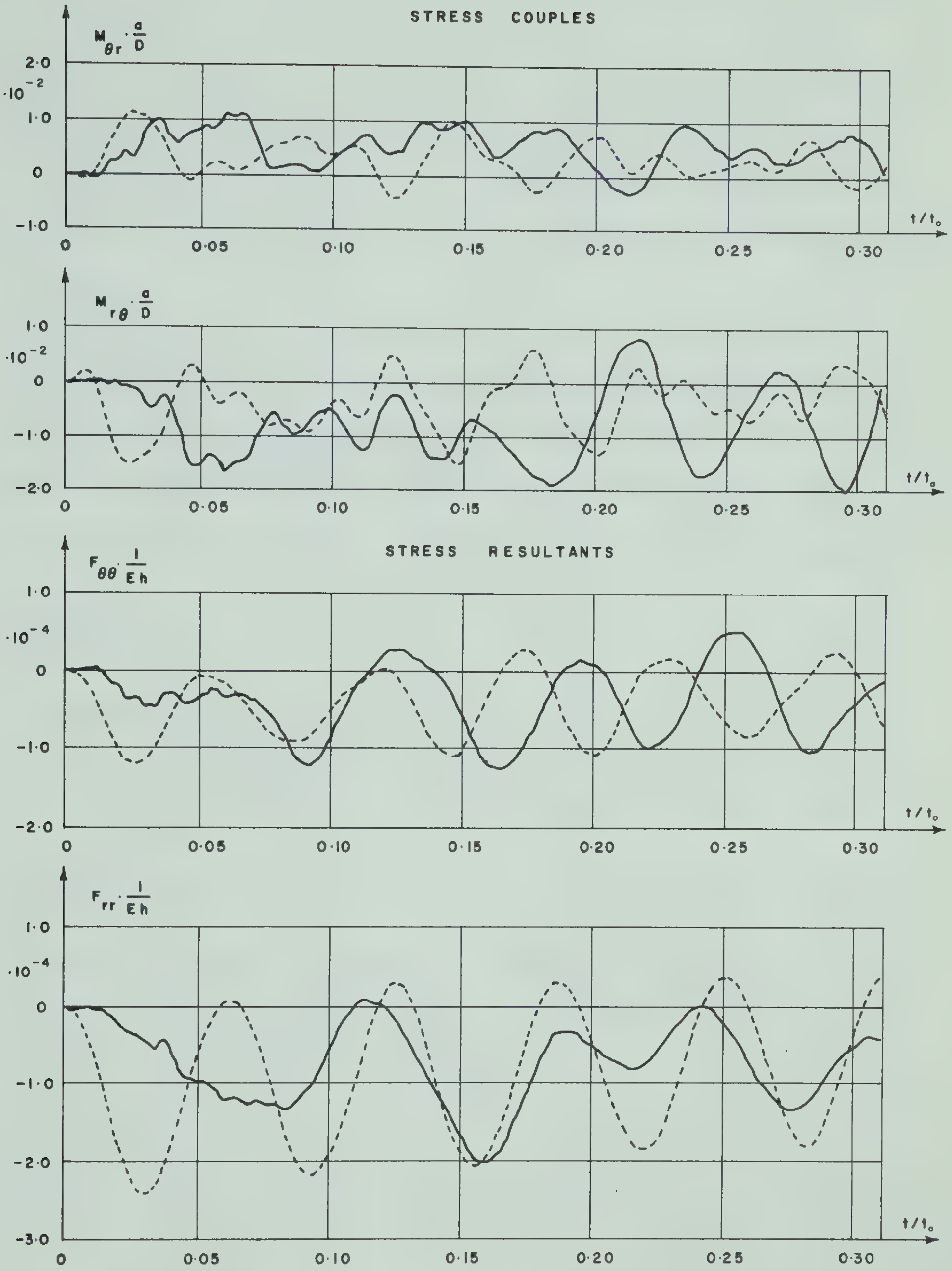

$$\sqrt{\frac{D}{m}} \cdot \frac{t_o}{a^2} = 0.01169$$

$$\frac{q_o a^3}{D} = -3.168$$

$$\frac{q_o a}{Eh} = -0.6667 \times 10^{-4}$$

——— Experiment

– – – – – – Theory, $\zeta_1 = 0$

Simply Supported Shell with
Sliding Clamped Edges

FIG· 7·35 Shell Experimental and Theoretical Sectional Resultants vs· Time at $\rho = 0{\cdot}64$, $\theta = 30°$ for Trial 2

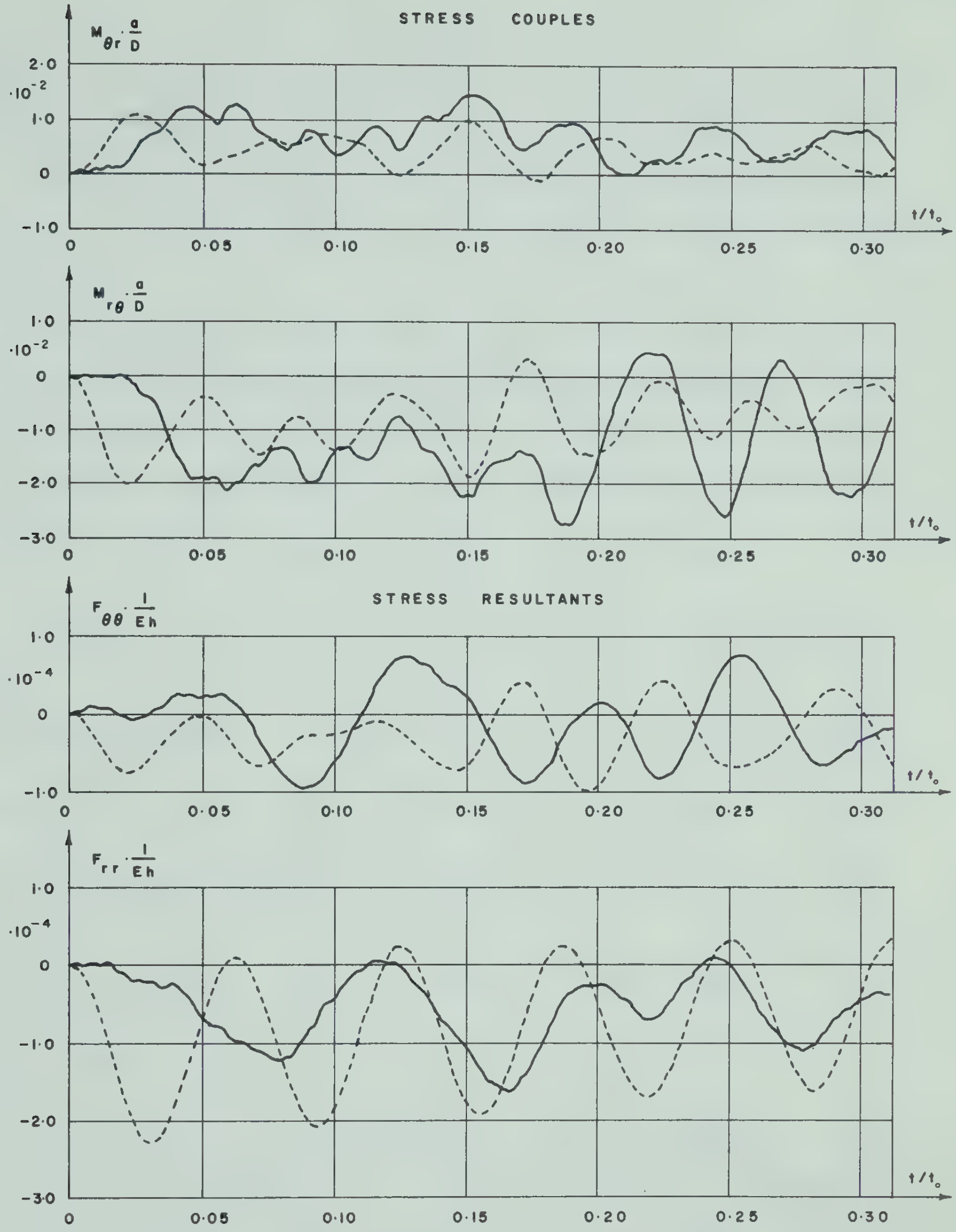

$\sqrt{\frac{D}{m}} \cdot \frac{t_0}{a^2} = 0.01169$

$\frac{q_0 a^3}{D} = -3.168$

$\frac{q_0 a}{Eh} = -0.6667 \times 10^{-4}$

——— Experiment

------ Theory, $\zeta_1 = 0$

Simply Supported Shell with
Sliding Clamped Edges

FIG· 7·36 Shell Experimental and Theoretical Sectional Resultants vs· Time at $\rho = 0{\cdot}72$, $\theta = 20^\circ$ for Trial 2

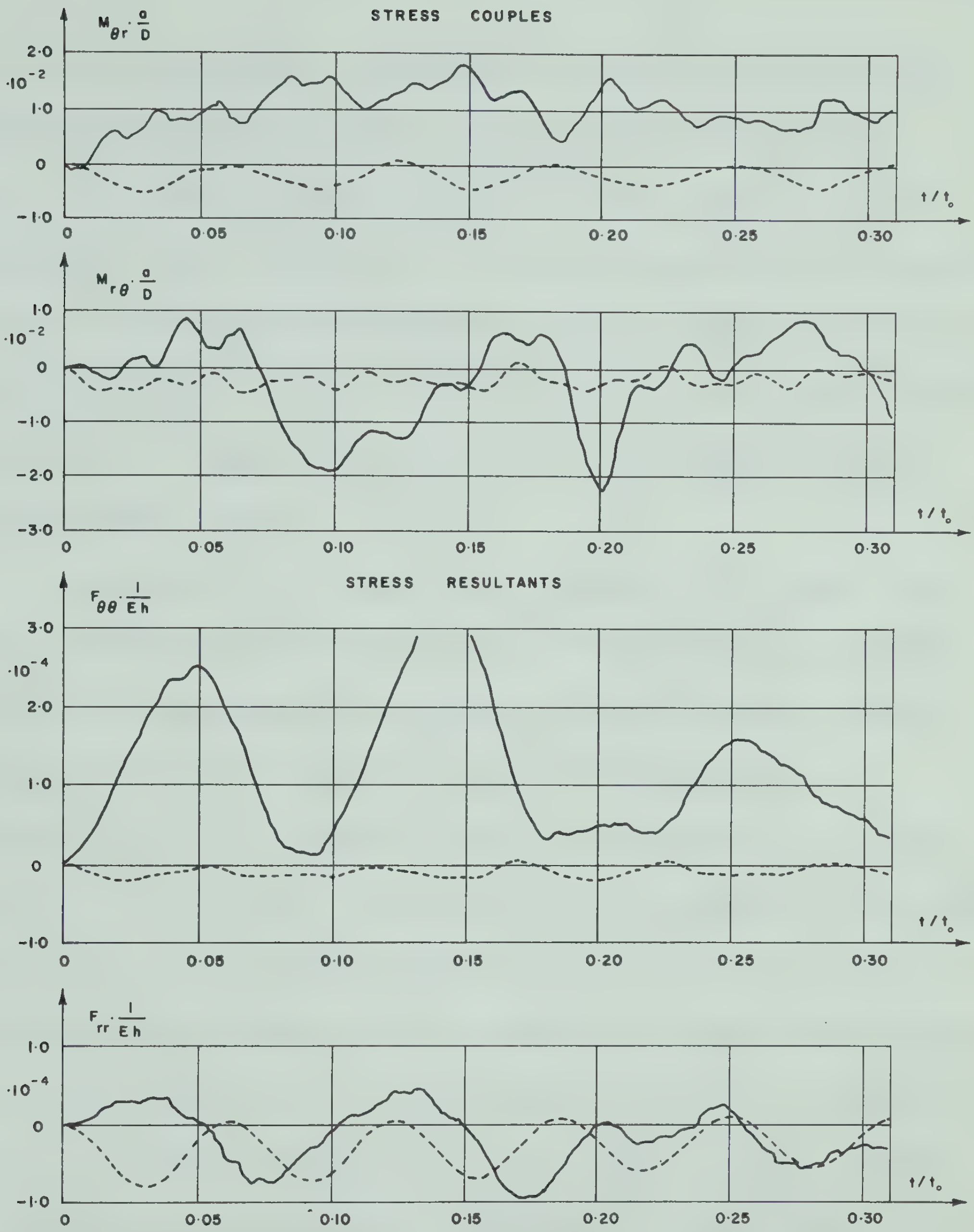

$\sqrt{\frac{D}{m}} \cdot \frac{t_o}{a^2} = 0.01169$

$\frac{q_o a^3}{D} = -3.168$

$\frac{q_o a}{Eh} = -0.6667 \times 10^{-4}$

——— Experiment

------- Theory, $\zeta_1 = 0$

Simply Supported Shell with
Sliding Clamped Edges

FIG· 7·37 Shell Experimental and Theoretical Sectional Resultants vs· Time at $\rho = 0{\cdot}84$, $\theta = 0°$ for Trial 2

$M_{\Theta r}(\tilde{\rho},\tilde{\Theta}) \neq -\nu M_{r\Theta}(\tilde{\rho},\tilde{\Theta})$. Transverse edge displacement was not eliminated completely for Trial 2 since the shell boundary was supported against transverse motion only in one direction over alternate one inch intervals as shown in Fig. 7.1a. It appears from these results that the theory for a simply supported shell with sliding free edges would provide a better approximation of the experimental edge conditions than Theory 2.

The results in Figs. 7.31 through 7.36 show that the shell transverse displacement and sectional resultants responded at frequencies comparable to the theory after a relatively slow first quarter cycle of response. It is considered that this initial frequency response, noticed particularly for stress resultants which responded initially at frequencies even slower than those for Trial 1, was too much lower than any possible theoretical frequencies to be accounted for completely by the variation over the shell surface of the time of arrival of the shock front. This time of arrival had a maximum variation of only 0.01 divisions on the time scale of these figures. Near the shell boundary the governing response frequency was about 300 cps as seen from results in Fig. 7.37. This frequency was predicted from the acoustic excitation tests.

Some of the more significant response frequencies in cps obtained by spectral analysis can be summarized in groups of decreasing importance with respect to front radial

strain at different positions on the shell's surface as follows:

$\rho = 0, \theta = 0°$ 1) 529
2) 691
3) 610, 1016, 447
4) 976, $\underline{264}$, 833
5) 1403, 325, $\underline{81}$, 1098, 1159, 1240, 1362
6) 1870, 1769, 1687, 1545

$\rho = 0.56, \theta = 0°$ 1) 285
2) 325, 529, $\underline{81}$, 468
3) 610, 651
4) 1016, $\underline{163}$, 976, 1138, 1240
5) 813, 1423, 894

$\rho = 0.84, \theta = 0°$ 1) $\underline{102}$
2) 325, 529
3) $\underline{264}$, $\underline{183}$, 610
4) 386, 854, 1016, 1403

Frequencies underlined were considered to arise from beating. This spectral representation of the shell's forced response agrees reasonably closely with the acoustic excitation measurements shown in Figs. 7.30a, 7.30c and 7.30d.

CHAPTER 8

OBSERVATIONS, CONCLUSIONS AND RECOMMENDATIONS

8.1 Observations and Conclusions

8.1.1 Theoretical Analysis of Plates. Some of the more important results obtained in this thesis from the theoretical analysis of the linear dynamic symmetric response of thin elastic plates with regular polygonal boundaries can be summarized as follows:

1. Eigenvalues, eigenvectors, mode shapes and modal participation functions, many of which previously were unavailable in the literature, are obtained for a number of different simply supported, clamped and elastically clamped polygonal plates subjected to uniformly distributed and central point loads.

2. The trends apparent in the changes of eigenvalues and mode shapes with boundary shape often agree quite closely with the trends observed in these functions for shallow spherical shells. In fact, in many cases eigenvalues and mode shapes as defined by the nodal lines are identical for these two structural types for higher modes when they have the same boundary plan.

3. The pattern of change in the modal frequencies ω_i with number of plate sides p was observed to be the same for both the simply supported and clamped edge conditions. It was found that for polygons of equivalent surface area,

increasing p has the following effect on the associated values of ω_i: ω_1 decreases; ω_2 increases up to p = 4 and then decreases; ω_3 increases up to p = 7 and then decreases; ω_4 increases up to p = 9 to 12 and then decreases; and ω_5 increases.

It was observed that the maximum modal frequency occurs for the polygon with the least number of sides for which the nodal lines do not deviate significantly from circles concentric with the origin, and is generally associated with the polygon having the largest difference between nodal areas responding in the same direction. This observation can be explained physically in the following way. As p decreases, the relative proportion of 'inactive' corner area increases, so that, as long as the nodal lines maintain their circular shape, there is an associated increase in the plate stiffness and modal frequency. However, the deviation of a nodal line from the circular shape in order to adjust to the polygonal boundary shape, is accompanied by a relaxation in plate stiffness. The increase in the nodal area function relative to that for a circular boundary is specified by the function m_a^i, and has a maximum value of about 3 per cent for any of the first five modes.

This correlation between the maximum modal frequency and the mode shape, vs. the number of boundary sides, likely occurs for shallow shells as well, although enough shells were not investigated numerically to be certain.

4. The products of terms of different orders n were omitted in the evaluation of χ_0^1 which involves integration over the plate surface area of the square of the displacement eigenvector. The omission of these terms considerably simplifies the numerical evaluation of χ_0^1 and, it appears, still provides reasonably accurate values of χ_0^1 for boundaries with as few as four sides.

5. An approximate method is introduced whereby modal participation functions are calculated for different polygonal plates using known values of these functions for a particular polygonal plate with large p. In this method, changes in the areas between the nodal lines pertaining to the different boundary shapes are related to changes in the modal participation functions. Reasonably accurate modal participation functions are obtained for plates with more than three sides using this simple technique in spite of the approximations made with regard to the modal geometry.

6. The results indicate that plate response will be represented adequately for practical requirements for most uniformly distributed load transients when contributions of modes higher than the second are ignored, and for most central

point load transients when modes higher than the third are ignored.

7. It was observed that the static central deflections of plates having equal surface areas increase with the number of boundary sides p while the associated values of the fundamental frequencies decrease. Likely, these variations can be attributed to the decrease in the relative proportion of 'inactive' corner areas with increasing p.

8.1.2 Comparison of Theoretical Predictions and Experimental Results for a Square Plate. A comparison of theoretical predictions with the experimental results obtained when an elastically clamped square plate was subjected to blast loading revealed the following points:

1. Satisfactory theoretical predictions for flexural stress couples can be made for the entire plate surface even when some membrane strains are present, providing edge spring constants and viscous damping coefficients can be estimated with reasonable accuracy.

2. High levels of damping which increased rapidly with stress level up to a limit, occurred in the experimental model. This nonlinear damping likely was attributable to structural interface damping in the plate mounting system. Air damping was considered to be relatively insignificant for most blast overpressures.

3. The fundamental frequency of the experimental plate initially decreased with increasing load even more than could be explained by the large values of viscous damping observed. It is felt that this experimental frequency decrease might have been an effect of edge conditions in transverse displacement and normal slope being time-dependent rather than homogeneous, since it could not be a nonlinear effect. Theoretically, nonlinear geometry effects will cause an increase in the frequency with load. However, this nonlinear hardening effect should have been practically unnoticeable in this experiment since the maximum displacement-to-thickness ratio was always less than 0.3.

4. The presence of membrane strains in the experimental plate is not accounted for in the present linear theory nor is it predictable by other nonlinear theories at these deflections. Measurements of plate boundary motion indicated that these strains could have arisen from in-plane time-dependent boundary loading. It is possible that the in-plane boundary loading frequency was not constant and could have accounted for the initial plate frequency decrease with increasing load which was discussed above. However, the experimental results seem to confirm, as predicted by Dawe [47], that the effects of bending and membrane action were essentially uncoupled at the relatively low levels of membrane strains encountered.

8.1.3 Theoretical Analysis of Shells. Results obtained from the theoretical analysis of the linear dynamic symmetric response of thin shallow spherical shells having regular polygonal planforms can be summarized by the following points:

1. Eigenvalues, mode shapes and modal participation functions are obtained for a number of shells with different polygonal plans subjected to uniformly distributed and central point loads, for a wide range of geometric parameters a/R and a/h and edge condition sets simulating variations of clamped and roller edges. The only results previously available, as far as is known, concern the free vibrations of shells with square and circular plan and the forced response of shells with circular plan, for just a few of these edge conditions.

2. Numerical problems which arose in the determination of fundamental eigenvalues k_1, appear to be associated with an insensitivity of the circular frequency ω to changes in k which occurs when k^4 is small in comparison to $12(1 - \nu^2)a^4/(Rh)^2$. Consequently, values of k_1 were not always found for small values of k_1 or large values of the product of a/R and a/h. The results show that smaller values of k_1 are associated with a relaxation in edge restraints and an increase in the number of boundary sides p, as would be expected.

3. Eigenvalues, eigenvectors and modal participation functions for shells with roller edges satisfying $F_{vv}(\tilde{\rho},\tilde{\theta}) = 0$ are unaffected by edge conditions in stress function and its derivatives, usually after only the first two or three modes. This uncoupling of the stress and transverse displacement functions for the higher modes is associated with an insensitivity of the eigenvalues, eigenvectors and modal participation functions to changes in a/R and a/h. It is associated also with an interchangeability of eigenvalues and mode shapes for shells and plates having the same boundary shape and subjected to the same edge conditions in transverse displacement and its derivatives.

4. The importance of the contributions of modes higher than the first to shell response and the response sensitivity to values of a/R and a/h, both increase significantly for shells satisfying $\varepsilon_{ss}(\tilde{\rho},\tilde{\theta}) = 0$ when the second edge condition in stress function is $F_{vs}(\tilde{\rho},\tilde{\theta}) = 0$ rather than $F_{vv}(\tilde{\rho},\tilde{\theta}) = 0$. Physically, this implies that even though edge extension is completely eliminated by satisfying $\varepsilon_{ss}(\tilde{\rho},\tilde{\theta}) = 0$ in conjunction with $w(\tilde{\rho},\tilde{\theta}) = 0$ so that in-plane motion normal to the edge will be very small in comparison to that associated with the edge conditions $F_{vv}(\tilde{\rho},\tilde{\theta}) = F_{vs}(\tilde{\rho},\tilde{\theta}) = 0$, for example, the additional 'wrinkling' permitted when $F_{vv}(\tilde{\rho},\tilde{\theta}) = 0$ is satisfied as the second edge condition rather than $F_{vs}(\tilde{\rho},\tilde{\theta}) = 0$, drastically changes the shell response

characteristics.

5. The edge conditions $F_{vs}(\tilde{\rho},\tilde{\theta}) = u_s(\tilde{\rho},\tilde{\theta}) = 0$ were satisfied in an attempt to simulate the conditions $u_v(\tilde{\rho},\tilde{\theta}) = u_s(\tilde{\rho},\tilde{\theta}) = 0$. The equivalence is not exact since the function $\partial u_s(\tilde{\rho},\tilde{\theta})/\partial v$ is not necessarily zero for either set of edge conditions. However, the numerical results indicate that effects of satisfying either edge condition set may be equivalent for $p = 12$ and that differences might not be large for smaller p.

It was discovered at a late date that expressions for in-plane displacements in terms of the stress function had been obtained for the static case by Reissner [97] and Fettahlioğlu [98]. Therefore, it should be possible to check the effect of satisfying the two different edge conditions for any polygonal boundary.

6. The numerical satisfaction of a prescribed homogeneous edge condition using the boundary collocation technique generally improves with increasing number of boundary sides p, with decreasing functional derivative order of w or F, and with increasing number of boundary collocation points L up to a maximum number, the value of which increases with the digital computational accuracy used. Best satisfaction is achieved when boundary collocation points are located with closer angular spacing towards the boundary corners where larger magnitude errors always tend to occur. However, it would be very difficult to

specify the one best spacing for each boundary shape and number of boundary collocation points used, since any particular collocation point spacing will give best overall satisfaction for only one edge condition function. This is true since the degree of edge condition satisfaction depends upon the interior spatial variations of the edge condition functions, and these functions are linearly independent.

These observations and conclusions, made specifically from observing the edge condition satisfaction of a clamped shell, should apply in general.

Although the application of the boundary collocation technique is not new, even today few investigations have been made specifically into the most suitable choice of collocation points, as Collatz [99] pointed out in 1959. It has been stated for the static solution of these shells that the number and location of the collocation points is not of paramount significance [92]. However, in the present dynamic solution these factors are not always negligible. For example, both the number and the location of the points influenced considerably the ability to determine k_1 for some shells with roller edges. Consequently, in many cases the number and sometimes the location of the collocation points have been given along with the associated numerical results.

Lo, Niedenfuhr and Leissa [100] have suggested that overall edge condition satisfaction can be improved

by obtaining more edge condition equations than unknown integration constants and then using a least squares procedure to minimize errors in the integration constants solved. This approach does not appear to be valid since it is impossible to simultaneously minimize the errors in two linearly independent functions with one condition. In addition, since the practical application of the boundary collocation technique depends upon the truncation of the functional series, it might be more advantageous to use the extra edge condition equations to compute additional terms in the functional series, depending upon the rapidity of the series convergence.

8.1.4 Comparison of Theoretical Predictions and Experimental Results for a Shallow Shell with an Hexagonal Base. Comparisons of theoretical predictions with the experimental results obtained when a shallow spherical shell was subjected to acoustic and blast loading for two different sets of boundary restraints, revealed the following points:

1. Shell governing modal frequencies for uniform loads as measured from acoustic excitation tests provided a good estimation of the governing frequency components of the shell's response to blast loads.

2. Comparison of experimental and theoretical mode shapes along with natural frequencies provided a good indication as to the experimental edge conditions which actually governed shell response. The comparison of mode shapes is considered to be essential, since for certain edge conditions some modal frequencies are not 'well separated' and could be overlooked in an analysis of the frequency spectrum alone. Closely spaced modal frequencies occur, for example, for the first two modes of a shell with roller edges. Also, frequencies of different modes of the same shell satisfying different theoretical edge conditions could be almost identical, making it difficult to ascertain from a frequency comparison alone the actual experimental edge conditions satisfied. This difficulty arose for the experimental shell as the theoretical frequencies of the first three modes for the simply supported shell are almost identical to the frequencies of modes 2, 3 and 4, respectively, for the simply supported shell with sliding clamped edges.

3. Comparison of theoretical predictions and experimental results for the response of the shell to blast loading revealed only fair agreement. Some experimental frequencies of response occurred which were much lower than any predictable using the present theory. These lower response frequencies became more dominant

[illegible]

[illegible]

[illegible]

[illegible]

toward the shell boundary and affected the response of the stress resultants more than the stress couples.

The discrepancies between theory and experiment occurred for several reasons. First, theoretical solutions could not be obtained for the edge conditions best simulating the two different sets of experimental edge conditions. Second, spatial and time variations in the blast overpressure over the shell surface were not accounted for in the theory. Third, damping was not included in the thoeretical calculations, although it could have been quite readily. Fourth, the experimental shell geometry deviated from the properties of perfect symmetry, uniform shell thickness and constant middle surface radius of curvature, all of which were assumed in the theory. Fifth, experimental edge conditions were not uniform around the boundary and were nonhomogeneous.

The occurrence of the low experimental response frequencies was considered to be attributable principally to variations in the shell's radius of curvature and not to mount vibrations since these low frequencies occurred even when in-plane boundary rigidity had been virtually eliminated.

4. It appears that it is not practical to simulate the clamped edge conditions in stress function $u_v(\tilde{\rho},\tilde{\theta}) = u_s(\tilde{\rho},\tilde{\theta}) = 0$, at least for a shell having a surface area as large as that of the experimental shell

(i.e. 1670 in.^{2}) which is subjected to uniform loads. It is felt that in most practical applications the edge conditions in stress function will more closely approximate the sliding free edge conditions $F_{vv}(\tilde{\rho},\tilde{\theta}) = F_{vs}(\tilde{\rho},\tilde{\theta}) = 0$ than the clamped edge conditions.

8.2 Recommendations

Certain limitations in the theory presented for the dynamic response of these plate and shell structures became apparent from the numerical and experimental investigations. However, the major effort extended to investigate the ability of the theory to predict the response of the wide range of structural shapes for which it is applicable to the variety of transient load distributions which are permissable, naturally curtailed detailed investigations in particular areas. Consequently, there are several problems which are recommended for future investigation. These are:

1. Modal participation functions χ_0^i should be evaluated without neglecting the products of terms of different orders n, for modes having nodal lines which deviate significantly from circles concentric with the origin. This should be done for all modes of response of plates and shells with 3 and 4 sides.

2. The accuracy of the approximate solutions for these problems is dependent upon the degree of satisfaction of edge conditions achieved using the boundary collocation technique. The accuracy of the solutions obtained in this thesis generally decreases with the number of boundary sides p, since the general solutions have been formulated in polar coordinates. However, errors in fundamental eigenvalues do increase with p for large p. Therefore, it should prove beneficial to formulate solutions to these problems in Cartesian coordinates, especially for plates and shells having boundaries with 3 and 4 sides. In addition, the use of general solutions formulated in Cartesian rather than polar coordinates should yield more readily approximate solutions for plates and shells having rectangular boundaries with large aspect ratios and rhombic boundaries with small acute angles. This has been shown for the statical case by Y. R. Kan [101] in the analysis of uniformly loaded rectangular and rhombic plates. Kan obtained approximate solutions for these problems by applying the boundary collocation technique to the general solution of the biharmonic equation formulated in Cartesian coordinates.

3. The effect of introducing time-dependent edge conditions should be investigated theoretically. It will be relatively easy to introduce the time-dependent edge conditions $\eta(\tilde{\rho},\tilde{\theta},t) = \bar{e}^1(t)$ and $F_{vv}(\tilde{\rho},\tilde{\theta},t) = \bar{f}^1(t)$

or $\varepsilon_{ss}(\tilde{\rho},\tilde{\theta},t) = \bar{f}^2(t)$ when either of the latter two edge conditions is associated with $F_{vs}(\tilde{\rho},\tilde{\theta}) = 0$, since the associated modal participation functions $\chi_3^{1,i}$, $\chi_2^{1,i}$ and $\chi_2^{2,i}$ are simply multiples of the zero-order terms of χ_1^i, the modal participation functions related to the load distribution. The experimental results given for the elastically clamped square plate subjected to blast loading should provide a model for testing the practical applicability of introducing the time-dependent edge conditions $\eta(\tilde{\rho},\tilde{\theta},t) = \bar{e}^1(t)$ and $M_{vs}(\tilde{\rho},\tilde{\theta},t) - \beta_1 \, \partial\eta(\tilde{\rho},\tilde{\theta},t)/\partial v = \bar{e}^{2*}(t)$.

4. The theory for the dynamic response of plates should be extended to include the possibility of in-plane loading and membrane stresses. This will prove useful in practice even for cases where only the transient transverse loads are thought to be significant, since in-plane loading will always occur to some degree at the edge of the plate as the plate will be elastically clamped to a mount which will be excited at its natural frequencies as well.

5. There are three areas related specifically to the dynamic response of shallow spherical shells which require further investigation.

Firstly, there should be additional numerical studies in which the satisfaction of some of the various theoretical boundary conditions presented in this thesis are attempted in more detail. In particular, the effect

of varying the elastic clamping coefficients β_1^i and β_2^i should be evaluated and additional effort should be made to obtain fundamental eigenvalues for shells with roller edges. Edge conditions in stress function which are the equivalent of the conditions $u_s(\tilde{\rho},\tilde{\theta}) = u_v(\tilde{\rho},\tilde{\theta}) = 0$ and $F_{vv}(\tilde{\rho},\tilde{\theta}) - \beta_3^i u_v(\tilde{\rho},\tilde{\theta}) = 0$, where β_3^i is an elastic clamping constant, should be formulated and satisfied for some numerical examples.

Secondly, modal participation functions should be computed for loads distributed over annular rings on the shell surface, so that different load time functions Q(t) can be applied simultaneously to different portions of the shell surface using superposition. Then the effect of variations in time of arrival at the shell surface of a rectilinear shock front, for example, can be studied and the maximum variations in load time functions over the shell surface which can be ignored without introducing significant errors in the theoretical solution can be tabulated versus shell governing frequencies.

Thirdly, the effect of variations in shell geometry from the ideal, particularly variations in radius of curvature, should be studied both experimentally and theoretically in relation to values of the shell parameters a/R and a/h.

6. Experimental values of viscous damping given in this thesis indicate the desirability of

including the possibility of nonlinear amplitude-dependent damping in the theoretical models.

7. An elastic edge condition relating transverse displacement to Kirchoff's effective transverse shearing force should be formulated for both plates and shells. The applicability of this condition can be tested by a theoretical comparison with the experimental results for the plate.

8. A study should be conducted into the antisymmetric vibrations of these plates and shells. This can be done theoretically by replacing $\cos pn\theta$ by $\sin pn\theta$ in the expressions for transverse displacement w and stress function F, and replacing $\cos pm\theta$ by $\sin pm\theta$ in the expression for the transverse loading function q. In this analysis, p will represent the number of antisymmetries in the load over the surface, while the characteristic segment for which the edge conditions must be satisfied numerically will still be defined by $0 \leq \theta \leq \pi/p$. For example, $p = 1$ for a load which is antisymmetric about a shell plan diameter while p equals the number of sides of the regular polygonal boundary for a load which is antisymmetric about each of the radial lines passing through the midpoints of the boundary sides.

9. Predictions for the response of these plates and shells to central point loads using regular solutions do not satisfy the mathematical requirement of infinite transverse shear at the point load. Consequently, results using solutions which retain the singular terms should be compared to the present results. Inclusion of an inner boundary solution will be relatively easy as long as the outer boundary solution remains unchanged.

BIBLIOGRAPHY

1. L. W. Lassiter and R. W. Hess, "Calculated and Measured Stresses in Simple Panels Subject to Intense Random Acoustic Loading Including the Near Noise Field of a Turbojet Engine," National Advisory Committee for Aeronautics Report 1367, 1958, 10 p.

2. M. J. Crocker, "Multimode Response of Panels to Normal and to Travelling Sonic Booms," Journal of Acoustical Society of America, Vol. 42, No. 5, 1967, pp. 1070 - 1079.

3. M. J. Crocker, "Response of Panels to Oscillating and to Moving Shock Waves," Journal of Sound and Vibrations, Vol. 6, No. 1, 1967, pp. 38 - 58.

4. D. S. Walkinshaw and J. S. Kennedy, "On Forced Response of Polygonal Plates," Ingenieur-Archiv, Vol. 38, 1969, pp. 358 - 369.

5. S. D. Poisson, "Sur le Movement des Corps Élastique," Memoires de L'Academie Royale des Sciences de L'Institut de France, Vol. 8, 1829, pp. 357 - 370.

6. G. Kirchoff, "Über das Gleichgewicht und die Bewegung einer elastichen Scheibe," Journal für die reine angewandte Mathematik, Crelle, Vol. 40, 1850, p. 51.

7. J. R. Airey, "The Vibrations of Circular Plates and Their Relation to Bessel Functions," Proceedings of the Physics Society, Vol. 23, 1911, pp. 225 - 232.

8. J. W. S. Rayleigh, "The Theory of Sound," Dover, New York, second American edition, Vol. 1, 1945, pp. 127 - 128, 359 - 383.

9. R. D. Mindlin, "Influence of Rotatory Inertia and Shear on Flexural Motions of Isotropic Elastic Plates," Journal of Applied Mechanics, Vol. 18, Trans. ASME, Vol. 73, 1951, pp. 31 - 38.

10. H. Deresiewicz and R. D. Mindlin, "Axially Symmetric Flexural Vibrations of a Circular Disk," Journal of Applied Mechanics, Vol. 22, 1955, pp. 86 - 88.

11. H. Deresiewicz, "Symmetric Flexural Vibrations of a Clamped Circular Disk," Journal of Applied Mechanics, Vol. 23, 1956, p. 319.

12. P. N. Raju, "Vibrations of Annular Plates," Journal of the Aeronautical Society of India, Vol. 14, No. 2, 1962, pp. 37 - 52.

13. W.P. Reid, "Free Vibrations of a Circular Plate," Journal of the Society of Industrial and Applied Mathematics, Vol. 10, No. 4, 1962, pp. 668 - 674.

14. G. S. Harris, "The Normal Modes of a Circular Plate of Variable Thickness," Quarterly Journal of Mechanics and Applied Mathematics, Vol. 21, Part 3, 1968, pp. 321 - 327.

15. I. N. Sneddon, "Fourier Transforms," McGraw-Hill, New York, first edition, 1951, pp. 150 - 153.

16. P. D. Flynn, " Elastic Response of Simple Structures to Pulse Loading," Ballistic Research Laboratories Memorandum Report No. 525, November, 1950.

17. H. Reismann, "Forced Vibrations of a Circular Plate," Journal of Applied Mechanics, Vol. 26, Trans. ASME, Vol. 81, Series E, 1959, pp. 526 - 527.

18. A. J. McLeod and R. E. D. Bishop, "The Forced Vibration of Circular Flat Plates," Journal of Mechanical Engineering Science, Monograph No. 1, 1965, 33 p.

19. R. S. Weiner, "Forced Axisymmetric Motions of Circular Elastic Plates," Journal of Applied Mechanics, Trans. ASME, Vol. 32, Series E, No. 4, 1965, pp. 893 - 898.

20. H. Reismann and J.E. Greene, "Forced Motion of Circular Plates," State University of New York, Buffalo, Division of Interdisciplinary Studies and Research, Sunyber-2, AFOSR 67-0565, March, 1967, 108 p.

21. S. Timoshenko, "Vibration Problems in Engineering," third edition, D. Van Nostrand, New York, 1955, pp. 443 - 444.

22. W. Voight, "Bemerkung zu dem Problem der transversalen Schwingungen rechteckiger Platten," Göttingen Nachrichten, 1893, pp. 225 - 230.

23. R. D. Mindlin, A. Schacknow, and H. Deresiewicz, "Flexural Vibrations of Rectangular Plates,"Journal of Applied Mechanics, Vol. 23, 1956, pp. 430 - 436.

24. J. R. Desai, "A Survey of Numerical Procedures for the Analysis of Plate and Shell Problems," The Institution of Engineers (India), Civil Engineering Division, Part CI5, Vol. 46, No. 9, 1966, pp. 481 - 488.

25. L. Meirovitch, "Analytical Methods in Vibrations," MacMillan, New York, 1967.

26. W. Ritz, "Über eine neue Method zur Lösung gewisser Variationsprobleme der Mathematische Physik," Journal für reine und angewandte Mathematik, Vol. 135, 1909, pp. 1 - 61.

27. W. Ritz, "Theorie der Transversalschwingungen einer quadratischen Platten mit frien Randern," Annalan der Physik, Vierte Folge, Vol. 28, 1909, pp. 737 - 786.

28. S. Iguchi, "Die Biegungsschwingungen der Vierseitig eingespannten rechteckigen Platte," Ingenieur-Archiv, Vol. 8, 1937.

29. S. Iguchi, "Die Eigenwertsprobleme für die elastiche rechteckigen Platte," Memoirs of the Faculty of Engineering, Hokkaido Imperial University, Vol. 4, 1938, p. 305.

30. D. Young, "Vibration of Rectangular Plates by the Ritz Method," Journal of Applied Mechanics, Trans. ASME, Vol. 17, 1950, pp. 448 - 453.

31. T. Ota and M. Hamada, "Fundamental Frequencies of Simply Supported but Partially Clamped Square

Plates," Bulletin of Journal of Structural and Mechanical Engineering, Vol. 6, No. 23, 1963, pp. 397 - 403.

32. W. Nowacki, "Free Vibration and Buckling of a Rectangular Plate with All the Edges Clamped," Bulletin de L'Academie Polonaise des Sciences, Série des sciences techniques, Vol. 7, No. 4, 1959, pp. 249 - 256.

33. W. Nowacki, "Dynamics of Elastic Systems," Chapman and Hall, London, 1963, pp. 206 - 218, and 269 - 271.

34. F. Tölke, "Über Spannungszustände in dünnen Rechtecksplatten," Ingenieur-Archiv, Vol. 5, 1934, pp. 187 - 237.

35. H. D. Conway, "The Bending, Buckling and Flexural Vibration of Simply Supported Polygonal Plates by Point-Matching," Journal of Applied Mechanics, Vol. 28, 1961, pp. 288 - 291.

36. A. W. Leissa, "A Method for Analyzing the Vibrations of Plates," Journal of the Aerospace Sciences, Vol. 29, 1962, p. 475.

37. H. D. Conway and K. A. Farnham, "The Free Flexural Vibrations of Triangular, Rhombic and Parallelogram Plates and Some Analogies," International Journal of Mechanical Sciences, Vol. 7, 1965, pp. 811 - 816.

38. S. S. H. Chen and G. Pickett,"Bending of Plates of Any Shape and With Any Variation in Boundary Conditions," Journal of Applied Mechanics, Trans. ASME, Vol. 34, Series E, No. 1, 1967, pp. 217 - 218.

39. M. V. Barton, "Vibration of Rectangular and Skew Cantilever Plates," Journal of Applied Mechanics, Vol. 18, 1951, pp. 129 - 134.

40. B. W. Anderson, "Vibration of Triangular Cantilever Plates by the Ritz Method," Journal of Applied Mechanics, Vol. 21, 1954, pp. 365 - 370.

41. C. V. J. Rao and G. Pickett, "Vibrations of Plates of Irregular Shapes and Plates with Holes," Journal of the Aeronautical Society of India, Vol. 13, No. 3, 1961, pp. 83 - 88.

42. Z. Reipert, "Application of Simple Functional Series to the Solution of Problems Concerning

Statics, Stability, and Vibration of Plates Having Non-Typical Forms," Archiwum Mechaniki Stosowanej, Vol. 15, No. 6, 1963, pp. 791 - 815.

43. R. Solecki, "Bending and Vibration of Non-Rectangular Plates," Acta Polytechnica Scandinavica, Mechanical Engineering Series, No. 13, 1963, pp. 3 - 20.

44. P. A. Shahady, R. Passarelli, and P. A. Laura, "Application of Complex-Variable Theory to the Determination of the Fundamental Frequency of Vibrating Plates," Journal of the Acoustical Society of America, Vol. 42, No. 4, 1967, pp. 806 - 809.

45. K. A. V. Pandalai and S. A. Patel, "Natural Frequencies of Orthotropic Circular Plates," AIAA Journal, Vol. 3, No. 4, 1965, pp. 780 - 781.

46. A. P. Salzman and S. A. Patel, "Asymmetric Natural Vibrations of Orthotropic Circular Plates of Variable Thickness," Polytechnic Institute of Brooklyn, PIBAL Report No. 69-6, March, 1969, 29 p.

47. D. J. Dawe, "Discrete Element Analysis of the Lateral Vibration of Rectangular Plates in the

Presence of Membrane Stresses," Royal Aircraft Establishment, TR 68233, September, 1968, 23 p.

48. A. Kalnins, "Dynamic Problems of Elastic Shells," Applied Mechanics Reviews, Vol. 18, No. 11, 1965, pp. 867 - 872.

49. E. Reissner, "On Vibration of Shallow Spherical Shells," Journal of Applied Physics, Vol. 17, 1946, pp. 1038 - 1042.

50. E. Reissner, "On Transverse Vibrations of Thin, Shallow Elastic Shells," Quarterly of Applied Mathematics, Vol. 13, No. 2, 1955, pp. 169 - 176.

51. E. Reissner, "On Axi-Symmetrical Vibrations of Shallow Spherical Shells," Quarterly of Applied Mathematics, Vol. 13, No. 3, 1955, pp. 279 - 290.

52. M. W. Johnson and E. Reissner, "On Transverse Vibrations of Shallow Spherical Shells," Quarterly of Applied Mathematics, Vol. 15, No. 4, 1958, pp. 367 - 380.

53. P. M. Naghdi, "Note on the Equations of Shallow Elastic Shells," Quarterly of Applied Mathematics, Vol. 14, No. 3, 1956, pp. 331 - 333.

54. A. Kalnins and P. M. Naghdi, "Axisymmetric Vibrations of Shallow Spherical Shells," Journal of the Acoustical Society of America, Vol. 32, No. 3, 1960, pp. 342 - 347.

55. A. Kalnins, "On Vibrations of Shallow Spherical Shells," Journal of the Acoustical Society of America, Vol. 33, No. 8, 1961, pp. 1102 - 1107.

56. A. Kalnins, "Free Nonsymmetric Vibrations of Shallow Spherical Shells," Proceedings of the Fourth U.S. National Congress of Applied Mechanics, ASME, 1962, pp. 225 - 233.

57. G. A. Van Fo Fy, "Free Vibrations of a Shallow Spherical Segment," Prikladnaya Meckhanika, Vol. 7, No. 1, 1961.

58. T. H. Lee, "Vibrations of Shallow Spherical Shells with Concentrated Mass," Journal of Applied Mechanics, Trans. ASME, Vol. 33, Series E, No. 4, 1966, pp. 938 - 939.

59. K. A. V. Pandalai and C. L. Dym, "On the Equations for Axisymmetric Deformation of Shallow Shells of Revolution," Department of Aeronautics and Astronautics, Stanford University, California, AFOSR-66-0724, Sudaar No. 267, 1966, 34 p.

60. B. Koplik and Yi-Yuan Yu, "Axisymmetric Vibrations of Homogeneous and Sandwich Spherical Caps," Journal of Applied Mechanics, Trans. ASME, Vol. 34, Series E, No. 3, 1967, pp. 667 - 673.

61. B. Koplik and Yi-Yuan Yu, "Approximate Solutions for Frequencies of Axisymmetric Vibrations of Spherical Caps," Journal of Applied Mechanics, Trans. ASME, Vol. 34, Series E, No. 3, 1967, pp. 785 - 787.

62. Yi-Yuan Yu and B. Koplik, "Torsional Vibrations of Homogeneous and Sandwich Spherical Caps and Circular Plates," Journal of Applied Mechanics, Trans. ASME, Vol. 34, Series E, No. 3, 1967, pp. 787 - 789.

63. M. H. Lock, J. S. Whittier, and H. A. Malcom, "Transverse Vibrations of a Shallow Spherical Dome," Journal of Applied Mechanics, Trans. ASME, Vol. 35, Series E, No. 2, 1968, pp. 402 - 403.

64. P. M. Naghdi and W. C. Orthwein, "Response of Shallow Viscoelastic Spherical Shells to Time-Dependent Axisymmetric Loads," Quarterly of Applied Mathematics, Vol. 18, No. 2, 1960, pp. 107 - 121.

65. G. A. Van Fo Fy and V. N. Buibol, "Vibrations of Shallow Spherical Shells," Theory of Plates and Shells, No. 4, Erevan, 1964, pp. 309-312.

66. H. Kraus and A. Kalnins, "Transient Vibration of Thin Elastic Shells," Journal of the Acoustical Society of America, Vol. 37, 1965, pp. 994 - 1002.

67. H. Kraus, "Thin Elastic Shells," John Wiley and Sons, New York, 1967, pp. 362 - 393.

68. H. Reismann and P. M. Culkowski, "Forced Axi-symmetric Motion of Shallow Spherical Shells," Journal of the Engineering Mechanics Division, Proceedings of the American Society of Civil Engineers, Vol. 94, EM2, 1968, pp. 653 - 670.

69. J. D. W. Hossack, "Experimental Investigation of the Nonlinear Behaviour of Shallow Spherical Shells," Nuclear Structural Engineering, Vol. 1, 1965, pp. 285 - 294.

70. J. S. Humphreys, R. S. Roth, and J. Zatlers, "Experiments on Dynamic Buckling of Shallow Spherical Shells Under Shock Loading," AIAA Journal, Vol. 3, No. 1, 1965, pp. 33 - 39.

71. B. Budiansky and R. Roth, "Axisymmetric Dynamic

Buckling of Clamped Shallow Spherical Shells," NASA TN-D-1510, 1962, pp. 597 - 600.

72. N. C. Huang, "Unsymmetrical Buckling of Thin Shallow Spherical Shells," Journal of Applied Mechanics, Trans. ASME, Vol. 31, Series E, No. 13, 1964, pp. 447 - 457.

73. R. R. Archer and J. Famili, "On the Vibration and Stability of Finitely Deformed Shallow Spherical Shells," Journal of Applied Mechanics, Trans. ASME, Vol. 32, Series E, No. 1, 1965, pp. 116 - 120.

74. S. Okubo and J. S. Whittier, "A Note on Buckling and Vibrations of an Externally Pressurized Shallow Spherical Shell," Journal of Applied Mechanics, Trans. ASME, Vol. 34, Series E, 1967, pp. 1032 - 1034.

75. A. E. H. Love, "A Treatise on the Mathematical Theory of Elasticity," Dover, New York, fourth edition, 1944, p. 279.

76. N. W. McLachlan, "Bessel Functions for Engineers," Oxford, second edition, 1961.

77. A. W. Leissa, C. C. Lo and F. W. Niedenfuhr, "Uniformly Loaded Plates of Regular Polygonal Shape," AIAA Journal, Vol. 3, No. 3, 1965, pp. 566 - 567.

78. S. P. Timoshenko and S. Woinowsky-Krieger, "Theory of Plates and Shells," McGraw-Hill, second edition, 1959.

79. H. Kolsky, "Experimental Studies in Stress Wave Propagation," Proceedings of the Fifth U.S. National Congress of Applied Mechanics, ADME, 1966, pp. 21 - 36.

80. H. H. Hubbard and J. C. Houbolt, "Vibration Induced by Acoustic Waves," Shock and Vibration Handbook, Vol. 3, Section 48, edited by C. M. Harris and C. E. Crede, McGraw-Hill, 1961, pp. 25-57.

81. R. L. Campbell, W. A. Jones and J. S. Watson, "DRES Blast Simulation Complex," DRES Suffield Technical Note No. 233, 1969.

82. J. C. Muirhead and W. J. Fenrick, "Piezoelectric Blast Pressure Transducer," Canadian Patent No. 806,818, 1969.

83. R. Naylor, J. J. Vesso and H. P. Hudema, "An Amplifier-Conditioner for Strain Gauges and Transducers," DRES Suffield Technical Note No. 209, 1969.

84. J. C. Muirhead, "A Listing of Basic Shock Wave Relations," DRES Suffield Memorandum No. 8/67, May, 1967.

85. B. J. Lazan and L. E. Goodman, "Material and Interface Damping," Shock and Vibration Handbook, Vol. 2, Section 36, edited by C. M. Harris and C. E. Crede, McGraw-Hill, 1961, pp. 1 - 46.

86. H. F. Bauer, "Nonlinear Response of Elastic Plates to Pulse Excitations," Journal of Applied Mechanics, Trans. ASME, Vol. 35, Series E, No. 1, 1968, pp. 47 - 52.

87. A. K. A. Eikrem and A. G. Doige, "Response of a Simply Supported Square Plate to a Blast Load," Department of Mechanical Engineering, University of Calgary, April, 1969.

88. O. D. Oniashvili, "Certain Dynamic Problems of the Theory of Shells," Press of the Academy of Sciences of the USSR, Moscow, 1957, Translated by M. D. Friedman, Inc., West Newton, Mass., 1959, pp. 40 - 44.

89. H. J. Weinitschke, "Asymmetric Buckling of Clamped Shallow Spherical Shells," Collected papers on Instability of Shell Structures, NASA TN-D-1510, December, 1962, pp. 481 - 490.

90. H. Y. Chow and E. P. Popov, "Finite Element Solution

of Axisymmetric Dynamic Problems of Shells of Revolution," Structural Engineering Laboratory, California University, Berkeley, April,1966, 53 p.

91. W. H. Hoppmann II and C. N. Baronet, "A Study of the Vibrations of Shallow Spherical Shells," Ballistic Research Laboratories, Report No. 1188, January, 1963, 26 p.

92. D. S. Walkinshaw, G. E. Riley, J. N. Siddall and G.AE. Oravas, "On Thin Shallow Elastic Shells over Polygonal Bases," International Association for Bridge and Structural Engineering, Vol. 28-1, 1968, pp. 175 - 192.

93. K. G. McConnell, "Some Implications of Vibration Testing of Continuous Systems for Resonant Frequencies," Journal of Society of Experimental Stress Analysis, Vol. 9, No. 7, 1969, pp. 321 - 326.

94. W. Bleakney and A. H. Taub, "Interaction of Shock Waves," Reviews of Modern Physics, Vol. 21, No. 4, 1949.

95. "The Effects of Nuclear Weapons," edited by S. Glasstone, prepared by U.S. Department of Defense,

published by the U.S. Atomic Energy Commission, revised edition, April, 1962, p. 147.

96. J. M. Biggs, "Introduction to Structural Dynamics," McGraw-Hill, Toronto, 1964, pp. 1 - 31.

97. E. Reissner, "On the Determination of Stresses and Displacements for Unsymmetrical Deformations of Shallow Spherical Shells," Journal of Mathematics and Physics, Vol. 38, 1959, pp. 16 - 35.

98. Ö. A. Fettahlioğlu, "Analysis of Shallow Spherical Cantilevered Shells and Shallow Spherical Domes with Polar Openings under Antisymmetrically Distributed Loads," Sandia Laboratories, SCL-RR-69-80, September, 1969.

99. L. Collatz, "The Numerical Treatment of Differential Equations," Springer-Verlag, Berlin, 1966, p. 29.

100. C. C. Lo, F. W. Niedenfuhr and A. W. Leissa, "Further Studies on the Application of the Point Matching Technique to Plate Bending and Other Harmonic and Biharmonic Boundary Value Problems," Department of Eng. Mechanics, Ohio State University, Tech. Report AFFDL-TR-65-114, January, 1966.

101. Y. R. Kan, "Point-Matching Solutions for a Class of

Boundary-Value Problems Using Biharmonic Functions in Cartesian Coordinates," M.Sc. Thesis, University of Alberta, Edmonton, Canada, April, 1968.

102. N.W. Bazley, D.W. Fox and J. T. Stadter, "Upper and Lower Bounds for the Frequencies of Rectangular Clamped Plates," The Johns Hopkins University, Applied Physics Laboratory, Technical Memorandum, TG-626, May 1965, 20 p.

103. J.L. Taylor, "Buckling and Vibration of Triangular Flat Plates," Journal of the Royal Aeronautical Society, Vol. 71, October, 1967, pp. 727 - 728.

104. A. K. Rao and K. Rajaiah, "Polygon-Circle Paradox of Simply Supported Thin Plates Under Uniform Pressure," AIAA Journal, Vol. 6, No. 1, 1968, pp. 155 - 156.

APPENDIX A

SECTIONAL RESULTANTS

A.1 Plate Sectional Resultants

The sectional resultants for plates subject to time-dependent edge condition Eqs. (3.15a) and (3.15b), obtained by substituting Eqs. (2.3), (2.12), (2.13) and (2.19) into Eqs. (2.11a) through (2.11e), are:

$$\begin{aligned}
-\frac{a}{D} M_{r\theta}(r,\theta,t) = {} & \sum_{i=1}^{\infty}\sum_{n=0}^{\infty}\left\{k_i^2\left[A^i_{pn}J''_{pn}(\mu) + B^i_{pn}I''_{pn}(\mu)\right] - \nu\left(\frac{pn}{\rho}\right)^2 \times\right. \\
& \times\left[A^i_{pn}J_{pn}(\mu) + B^i_{pn}I_{pn}(\mu)\right] + \nu\frac{k_i}{\rho}\left[A^i_{pn}J'_{pn}(\mu) +\right. \\
& \left.\left. + B^i_{pn}I'_{pn}(\mu)\right]\right\}\cos pn\theta\, T^i(t) + \sum_{\ell=1}^{2}\sum_{n=0}^{\infty}\left\{pn \times\right. \\
& \times (pn-1)(1-\nu)E^{1,\ell}_{pn}\rho^{pn-2} + (pn+1) \times \\
& \left.\times\left[pn + 2 - \nu(pn-2)\right]E^{2,\ell}_{pn}\rho^{pn}\right\}\cos pn\theta\,\bar{e}^{\ell}(t),
\end{aligned}$$

$$\begin{aligned}
\frac{a}{D} M_{\theta r}(r,\theta,t) = {} & \sum_{i=1}^{\infty}\sum_{n=0}^{\infty}\left\{-\left(\frac{pn}{\rho}\right)^2\left[A^i_{pn}J_{pn}(\mu) + B^i_{pn}I_{pn}(\mu)\right] + \frac{k_i}{\rho}\times\right. \\
& \times\left[A^i_{pn}J'_{pn}(\mu) + B^i_{pn}I'_{pn}(\mu)\right] + \nu k_i^2\left[A^i_{pn}J''_{pn}(\mu) +\right. \\
& \left.\left. + B^i_{pn}I''_{pn}(\mu)\right]\right\}\cos pn\theta\, T^i(t) - \sum_{\ell=1}^{2}\sum_{n=0}^{\infty}\left\{pn(pn-1)\times\right. \\
& \times(1-\nu)E^{1,\ell}_{pn}\rho^{pn-2} + (pn+1)\left[pn - 2 - \nu(pn+2)\right]\times \\
& \left.\times E^{2,\ell}_{pn}\rho^{pn}\right\}\cos pn\theta\,\bar{e}^{\ell}(t),
\end{aligned}$$

$$\frac{a}{D(1-\nu)} M_{rr}(r,\theta,t) = -\frac{a}{D(1-\nu)} M_{\theta\theta}(r,\theta,t) =$$

$$= \sum_{i=1}^{\infty} \sum_{n=1}^{\infty} \left\{ -k_i \frac{pn}{\rho} \left[A^i_{pn} J'_{pn}(\mu) + \right.\right.$$

$$\left. + B^i_{pn} I'_{pn}(\mu) \right] + \frac{pn}{\rho^2} \left[A^i_{pn} J_{pn}(\mu) + \right.$$

$$\left.\left. + B^i_{pn} I_{pn}(\mu) \right] \right\} \sin pn\theta \, T^i(t) - \sum_{\ell=1}^{2} \sum_{n=1}^{\infty} pn \times$$

$$\times \left[(pn-1) E^{1,\ell}_{pn} \rho^{pn-2} + \right.$$

$$\left. + (pn+1) E^{2,\ell}_{pn} \rho^{pn} \right] \sin pn\theta \, \bar{e}^{\ell}(t),$$

$$-\frac{a^2}{D} F_{rn}(r,\theta,t) = \sum_{i=1}^{\infty} \sum_{n=1}^{\infty} k_i \left\{ k_i^2 \left[A^i_{pn} J'''_{pn}(\mu) + B^i_{pn} I'''_{pn}(\mu) \right] + \right.$$

$$+ \frac{k_i}{\rho} \left[A^i_{pn} J''_{pn}(\mu) + B^i_{pn} I''_{pn}(\mu) \right] -$$

$$\left. - \left(\frac{pn}{\rho} \right)^2 \left[A^i_{pn} J'_{pn}(\mu) + B^i_{pn} I'_{pn}(\mu) \right] \right\} \cos pn\theta \, T^i(t) +$$

$$+ \; 4 \sum_{\ell=1}^{2} \sum_{n=1}^{\infty} pn(pn+1) E^{2,\ell}_{pn} \rho^{pn-1} \cos pn\theta \, \bar{e}^{\ell}(t),$$

$$\frac{a^2}{D} F_{\theta n}(r,\theta,t) = \sum_{i=1}^{\infty} \sum_{n=1}^{\infty} \frac{pn}{\rho} \left\{ k_i^2 \left[A^i_{pn} J''_{pn}(\mu) + B^i_{pn} I''_{pn}(\mu) \right] + \right.$$

$$+ \frac{k_i}{\rho} \left[A^i_{pn} J'_{pn}(\mu) + B^i_{pn} I'_{pn}(\mu) \right] - \left(\frac{pn}{\rho} \right)^2 \times$$

$$\left. \times \left[A^i_{pn} J_{pn}(\mu) + B^i_{pn} I_{pn}(\mu) \right] \right\} \sin pn\theta \, T^i(t) +$$

$$+ \sum_{\ell=1}^{2} \sum_{n=1}^{\infty} pn(pn+1) E^{2,\ell}_{pn} \rho^{pn-1} \sin pn\theta \, \bar{e}^{\ell}(t),$$

where $\mu = k_i \rho$.

The derivatives of Bessel functions can be expressed in terms of lower order derivatives as

$$J'_n(\mu) = \frac{1}{2} [J_{n-1}(\mu) - J_{n+1}(\mu)],$$

$$I'_n(\mu) = \frac{1}{2} [I_{n-1}(\mu) + I_{n+1}(\mu)],$$

$$J''_n(\mu) = -\frac{1}{\mu} J'_n(\mu) + [(\frac{n}{\mu})^2 - 1] J_n(\mu),$$

$$I''_n(\mu) = -\frac{1}{\mu} I'_n(\mu) + [(\frac{n}{\mu})^2 + 1] I_n(\mu),$$

$$J'''_n(\mu) = -\frac{1}{\mu} J''_n(\mu) + [(\frac{n}{\mu})^2 + \frac{1}{\mu^2} - 1] J'_n(\mu) - \frac{2n^2}{\mu^3} J_n(\mu),$$

$$I'''_n(\mu) = -\frac{1}{\mu} I''_n(\mu) + [(\frac{n}{\mu})^2 + \frac{1}{\mu^2} + 1] I'_n(\mu) - \frac{2n^2}{\mu^3} I_n(\mu).$$

A.2 Shell Sectional Resultants

The sectional resultants for shells subject to time-dependent edge condition Eqs. (3.15) and (3.16), obtained by substituting Eqs. (3.3), (3.25), (3.27) and (3.28) into Eqs. (3.19a) through (3.19f), are:

$$\begin{aligned}
\frac{1}{Eh} F_{\theta\theta}(r,\theta,t) = {} & \sum_{i=1}^{\infty} \sum_{n=0}^{\infty} \Big\{ \frac{a}{R} k_i^2 \Big[A^i_{pn} J''_{pn}(\mu) + B^i_{pn} I''_{pn}(\mu) \Big] + \\
& + (pn + 2)(pn + 1) C^i_{pn} \rho^{pn} + pn(pn - 1) \times \\
& \times D^i_{pn} \rho^{pn-2} \Big\} \cos pn\theta \, T^i(t) + \sum_{\ell=1}^{2} \sum_{n=0}^{\infty} \times \\
& \times \Big[(pn + 2)(pn + 1) F^{1,\ell}_{pn} \rho^{pn} + (pn + 4) \times \\
& \times (pn + 3) F^{2,\ell}_{pn} \rho^{pn+2} \Big] \cos pn\theta \, \bar{f}^{\ell}(t),
\end{aligned}$$

$$\begin{aligned}
\frac{1}{Eh} F_{rr}(r,\theta,t) = {} & \sum_{i=1}^{\infty} \sum_{n=0}^{\infty} \Big\{ \frac{a}{R} A^i_{pn} \Big[\frac{k_i}{\rho} J'_{pn}(\mu) - \Big(\frac{pn}{\rho}\Big)^2 J_{pn}(\mu) \Big] + \\
& + \frac{a}{R} B^i_{pn} \Big[\frac{k_i}{\rho} I'_{pn}(\mu) - \Big(\frac{pn}{\rho}\Big)^2 I_{pn}(\mu) \Big] - (pn + 1) \times \\
& \times (pn - 2) C^i_{pn} \rho^{pn} + pn(1 - pn) D^i_{pn} \rho^{pn-2} \Big\} \times \\
& \times \cos pn\theta \, T^i(t) + \sum_{\ell=1}^{2} \sum_{n=0}^{\infty} \Big\{ - (pn + 1)(pn - 2) \times \\
& \times F^{1,\ell}_{pn} \rho^{pn} + \Big[pn + 4 - (pn)^2 \Big] F^{2,\ell}_{pn} \rho^{pn+2} \Big\} \times \\
& \times \cos pn\theta \, \bar{f}^{\ell}(t),
\end{aligned}$$

$$\frac{1}{Eh} F_{r\theta}(r,\theta,t) = \frac{1}{Eh} F_{\theta r}(r,\theta,t) = \sum_{i=1}^{\infty} \sum_{n=1}^{\infty} \Big\{ \frac{a}{R} A^{i}_{pn} \times$$

$$\times \Big[k_i \frac{pn}{\rho} J'_{pn}(\mu) - \frac{pn}{\rho^2} J_{pn}(\mu) \Big] +$$

$$+ \frac{a}{R} B^{i}_{pn} \Big[k_i \frac{pn}{\rho} I'_{pn}(\mu) - \frac{pn}{\rho^2} I_{pn}(\mu) \Big] +$$

$$+ pn(pn + 1)\, C^{i}_{pn}\, \rho^{pn} + pn(pn - 1) \times$$

$$\times D^{i}_{pn}\, \rho^{pn-2} \Big\} \sin pn\theta\, T^{i}(t) + \sum_{\ell=1}^{2} \sum_{n=1}^{\infty} \times$$

$$\times \Big[pn(pn + 1)\, F^{1,\ell}_{pn}\, \rho^{pn} + pn(pn + 3) \times$$

$$\times F^{2,\ell}_{pn}\, \rho^{pn+2} \Big] \sin pn\theta\, \bar{f}^{\ell}(t) ,$$

$$- \frac{a}{D} M_{r\theta}(r,\theta,t) = \sum_{i=1}^{\infty} \sum_{n=0}^{\infty} \Big\{ k_i^4 A^{i}_{pn} \Big[\Big[\Big(\frac{pn}{\mu}\Big)^2 J_{pn}(\mu) - \frac{1}{\mu} J'_{pn}(\mu) -$$

$$- \nu J''_{pn}(\mu) \Big] - k_i^4 B^{i}_{pn} \Big[\Big[\Big(\frac{pn}{\mu}\Big)^2 I_{pn}(\mu) - \frac{1}{\mu} I'_{pn}(\mu) -$$

$$- \nu I''_{pn}(\mu) \Big] + 4\lambda_i (pn + 1) pn(pn - 1)(1 - \nu) \times$$

$$\times C^{i}_{pn}\, \rho^{pn-2} \Big\} \cos pn\theta\, T^{i}(t) + \sum_{\ell=1}^{2} \sum_{n=0}^{\infty} \Big\{ pn(pn - 1)$$

$$\times (1 - \nu)\, E^{1,\ell}_{pn}\, \rho^{pn-2} + (pn + 1)\, [pn + 2 -$$

$$- \nu(pn - 2)]\, E^{2,\ell}_{pn}\, \rho^{pn} \Big\} \cos pn\theta\, \bar{e}^{\ell}(t) ,$$

$$\begin{aligned}
-\frac{a}{D} M_{\theta r}(r,\theta,t) = \sum_{i=1}^{\infty}\sum_{n=0}^{\infty}\Big\{ & k_i^4 A_{pn}^i \Big[\Big(\frac{pn}{\mu}\Big)^2 J_{pn}(\mu) - \frac{1}{\mu} J'_{pn}(\mu) - \\
& - \nu J''_{pn}(\mu)\Big] - k_i^4 B_{pn}^i \Big[\Big(\frac{pn}{\mu}\Big)^2 I_{pn}(\mu) - \frac{1}{\mu} I'_{pn}(\mu) - \\
& - \nu I''_{pn}(\mu)\Big] - 4\lambda_i (pn+1)pn(pn-1)(1-\nu) \times \\
& \times C_{pn}^i \rho^{pn-2}\Big\} \cos pn\theta\, T^i(t) + \sum_{\ell=1}^{2}\sum_{n=0}^{\infty}\Big\{pn(pn-1) \times \\
& \times (1-\nu) E_{pn}^{1,\ell} \rho^{pn-2} + (pn+1)\,[pn-2-\nu \times \\
& \times (pn+2)]\, E_{pn}^{2,\ell} \rho^{pn}\Big\} \cos pn\theta\, \bar{e}^{\ell}(t),
\end{aligned}$$

$$\begin{aligned}
\frac{a}{D(1-\nu)} M_{rr}(r,\theta,t) = -\frac{a}{D(1-\nu)} M_{\theta\theta}(r,\theta,t) = \sum_{i=1}^{\infty}\sum_{n=1}^{\infty} & \times \\
\times\Big\{ & k_i^4 A_{pn}^i \Big[-\frac{pn}{\mu^2} J_{pn}(\mu) + \frac{pn}{\mu} J'_{pn}(\mu)\Big] - \\
& - k_i^4 B_{pn}^i \Big[-\frac{pn}{\mu^2} I_{pn}(\mu) + \frac{pn}{\mu} I'_{pn}(\mu)\Big] - \\
& - 4\lambda_i (pn+1)pn(pn-1) C_{pn}^i \rho^{pn-2}\Big\} \times \\
& \times \sin pn\theta\, T^i(t) - \sum_{\ell=1}^{2}\sum_{n=1}^{\infty} pn \times \\
& \times \Big[(pn-1) E_{pn}^{1,\ell} \rho^{pn-2} + (pn+1) \times \\
& \times E_{pn}^{2,\ell} \rho^{pn}\Big] \sin pn\theta\, \bar{e}^{\ell}(t),
\end{aligned}$$

where $\mu = k_i \rho$.

APPENDIX B

ORTHOGONALITY OF EIGENVECTORS

B.1 Orthogonality of Plate Eigenvectors

The orthogonality of the eigenvectors for plates, Eq. (2.13),

$$\bar{\eta}^{i}(\rho,\theta) = \sum_{n=0}^{\infty} \left[A^{i}_{pn} J_{pn}(k_{i}\rho) + B^{i}_{pn} I_{pn}(k_{i}\rho) \right] \cos pn\theta \tag{B.1}$$

which are associated with homogeneous edge conditions can be shown by means of the approach used by Nowacki [33].

The equation of free undamped plate vibrations, Eq. (2.5), is

$$\nabla^{4}\eta_{1}(\rho,\theta,t) + \frac{ma^{4}}{D} \frac{\partial^{2}\eta_{1}(\rho,\theta,t)}{\partial t^{2}} = 0. \tag{B.2}$$

Introducing

$$\eta_{1}(\rho,\theta;t) = \bar{\eta}(\rho,\theta) \exp(i\omega t) \tag{B.3}$$

and considering two different symmetric modes of vibration $\bar{\eta}^{i}(\rho,\theta)$ and $\bar{\eta}^{j}(\rho,\theta)$ yields

$$\nabla^{4}\bar{\eta}^{i}(\rho,\theta) = k^{4}_{i}\, \bar{\eta}^{i}(\rho,\theta) \tag{B.4}$$

and

$$\nabla^4 \bar{\eta}^j(\rho,\theta) = k_j^4 \bar{\eta}^j(\rho,\theta), \tag{B.5}$$

where

$$k_i^4 = \frac{ma^4}{D}\omega_i^2.$$

Comparison of Eqs. (B.4) and (B.5) with the differential equation of static plate deflection

$$\nabla^4 \eta(\rho,\theta) = \frac{a^3}{D} q(\rho,\theta) \tag{B.6}$$

shows that $\bar{\eta}^i(\rho,\theta)$ and $\bar{\eta}^j(\rho,\theta)$ can be considered as the deflections for the loads

$$\frac{D}{a^3}k_i^4\,\bar{\eta}^i(\rho,\theta) \quad \text{and} \quad \frac{D}{a^3}k_j^4\,\bar{\eta}^j(\rho,\theta), \text{ respectively.}$$

Applying Betti's reciprocal theorem for stable conservative elastic systems with respect to the external work done on the characteristic plate segment area S yields

$$\iint_S \bar{\eta}^j(\rho,\theta)\,\frac{D}{a^3}\,k_i^4\,\bar{\eta}^i(\rho,\theta)\,dS = \iint_S \bar{\eta}^i(\rho,\theta)\,\frac{D}{a^3}k_j^4\bar{\eta}^j(\rho,\theta)\,dS, \tag{B.7}$$

and thus

$$(\omega_i^2 - \omega_j^2)\iint_S \gamma\,\bar{\eta}^i(\rho,\theta)\,\bar{\eta}^j(\rho,\theta)\,dS = 0. \tag{B.8}$$

If the motions represented by $\bar{\eta}^i(\rho,\theta)$ and $\bar{\eta}^j(\rho,\theta)$ have different frequencies and $\gamma \neq \gamma(\rho,\theta)$, then

$$\iint\limits_S \bar{\eta}^i(\rho,\theta)\ \bar{\eta}^j(\rho,\theta)dS = 0,\ i \neq j, \qquad \text{(B.9)}$$

proving orthogonality of the plate eigenvectors.

B.2 Orthogonality of Shell Eigenvectors

The orthogonality of the transverse displacement eigenvectors for shells, Eq. (3.28a),

$$\bar{\eta}^i(\rho,\theta) = \sum_{n=0}^{\infty}\Big[-k_i^2\, A^i_{pn}\, J_{pn}(k_i\rho) + k_i^2 B^i_{pn}\, I_{pn}(k_i\rho) + 4\lambda_i\,(pn+1)C^i_{pn}\, \rho^{pn}\Big]\cos pn\theta \qquad \text{(B.10)}$$

which are associated with homogeneous edge conditions can be shown by means of the variational approach used by Rayleigh [8].

The principle of virtual work for dynamic systems states

$$\delta\Pi + \iint\limits_S \gamma\ \frac{\partial^2\eta_1(\rho,\theta,t)}{\partial t^2}\ \delta\eta_1(\rho,\theta,t)dS = 0, \qquad \text{(B.11)}$$

where Π is the total potential energy of deformation and, for symmetric response, S is the surface area of the shell characteristic segment.

Substituting

$$\eta_1(\rho,\theta,t) = \bar{\eta}(\rho,\theta)\exp(i\omega t) \tag{B.12}$$

into Eq. (B.11) yields

$$\delta\Pi = \omega^2 \iint_S \gamma \eta_1(\rho,\theta,t)\delta\eta_1(\rho,\theta,t)dS \ . \tag{B.13}$$

Assuming $\eta_1(\rho,\theta,t)$ refers to the motion corresponding to the i-th eigenvector $\bar{\eta}^i(\rho,\theta)$ and $\delta\eta_1(\rho,\theta,t)$ refers to the motion corresponding to the j-th eigenvector $\bar{\eta}^j(\rho,\theta)$ yields

$$\delta\Pi = \omega_i^2 \ \exp(2i\omega t)\iint_S \gamma\bar{\eta}^i(\rho,\theta)\bar{\eta}^j(\rho,\theta)dS \ . \tag{B.14}$$

Conversely, assuming $\eta_1(\rho,\theta,t)$ varies as $\bar{\eta}^j(\rho,\theta)$ and $\delta\eta_1(\rho,\theta,t)$ as $\bar{\eta}^i(\rho,\theta)$ yields

$$\delta\Pi = \omega_j^2 \ \exp(2i\omega t)\iint_S \gamma\bar{\eta}^i(\rho,\theta)\bar{\eta}^j(\rho,\theta)dS \ , \tag{B.15}$$

and thus

$$(\omega_i^2 - \omega_j^2) \iint_S \gamma\bar{\eta}^i(\rho,\theta)\bar{\eta}^j(\rho,\theta)dS = 0 \ . \tag{B.16}$$

If the motions represented by $\bar{\eta}^i(\rho,\theta)$ and $\bar{\eta}^j(\rho,\theta)$ have different frequencies and $\gamma \neq \gamma(\rho,\theta)$, then

$$\iint_S \bar{\eta}^i(\rho,\theta)\bar{\eta}^j(\rho,\theta)dS = 0 \ , \tag{B.17}$$

proving orthogonality of the shell transverse displacement eigenvectors.

APPENDIX C

COMPUTER PROGRAMS

C.1 Plate Program

The plate digital computer program calculates the symmetric eigenvalues, eigenvectors, modal participation functions for uniformly distributed and central point loads, transverse displacements and sectional resultants vs. time including viscous damping effects for regular polygonal plates subjected to various idealized transient load shapes and the elastically clamped homogeneous edge condition Eqs. (2.10a) and (2.10b).

The program has been written for use on the University of Alberta IBM 360/67 digital computer. Double precision (16 figure) accuracy is used in all computations. It has been modified for use on the DRES IBM 1130 digital computer on which it uses only ten figure computational accuracy. A high order computational accuracy and a large underflow-overflow exponent range ($10^{\pm 76}$ on the IBM 360/67) are features required in order to invert accurately some of the larger boundary equation matrices which are ill-conditioned principally due to the presence of higher orders of the Bessel functions J_{pn} and I_{pn}.

Other computer programs which input experimental analogue data and output experimental and

theoretical strains, stresses, displacements and sectional resultants vs. time in the form of X-Y plots and determine theoretical mode shapes have been written for the DRES IBM 1130 computer but are not included in this section.

The plate program compilation from the Fortran source deck,which uses approximately 52,000 core bytes, program listing and formation of an object deck require a total of 2.0 minutes execution time on the IBM 360/67. Program execution on this computer involving the search for one eigenvalue and the calculation of the response of the associated mode of vibration, excluding compilation time, requires approximately 0.5 minutes for a solution using three collocation points on the characteristic segment boundary, 0.8 minutes for four collocation points, 1.4 minutes for six collocation points and 4.8 minutes for ten collocation points. The largest portion of the computer time required for each of these solutions is used to solve the modal participation functions.

A typical data set which causes the program to search for two symmetric modes of vibration of the partially clamped square plate discussed in Chapter 5 and compute the undamped modal response at two positions on the plate for an exponentially decaying blast load is listed by card number below:

```
Data
Card

  1    4   97.5E-3 2121.3E-2   75.7E-2    3.3E-1     1.0E+7

  2       1.E-50   45

  3       7  0.0 10.0 20.0 30.0 35.0 40.0 45.0

  4       4.6E-1     6.5E-1     0.1E-1     0.5E-6

  5    1   0.1E+05   0.0E+00

  6    46 20 20

  7    3

  8     0.00E+00

  9       1.0E+3

 10    1 50    0.1E-3   15.0E-3 1.00

 11    1

 12    2

 13         0.00       0.000

 14       13.859      0.000

 15    1 50    0.1E-3   15.0E-3 1.00

 16    1

 17    2

 18         0.00       0.000

 19       13.859      0.000

 20   99
```

A description of the data correlation to the general polygonal plate vibration problem is given in Table C.1. Problems of determinant value underflow (i.e. values $<10^{-76}$ on the IBM 360/67 or $<10^{-36}$ on the IBM 1130), are automatically corrected by the program which obtains a finite determinant value by incrementing the magnitude of the matrix element multiplier, data number {9a} by multiples of 10^{2}. However, an initial choice of the matrix element multiplier which results in determinant value overflow (i.e. values $>10^{76}$ on the IBM 360/67 or $>10^{36}$ on the IBM 1130) will cause a computer 'hang-up'.

The program consists of a mainline routine which supervises the program execution according to options specified in the data, and nine subroutines. Three of these subroutines DMINV, BESJ and BESI are modifications of standard IBM subroutines. The principal functions of each of these routines are listed in Table C.2. A flow diagram of the possible program execution paths through the routines is shown in Fig. C.1.

In order to facilitate data input and output on any computer, card input and line output variables termed IREAD and IPRIN, respectively, are defined in routine VIBRA and are used in all input/output Fortran statements. The computer line output is labelled appropriately with the exception that the values O1 to

Table C.1

Explanation of Computer Data for Plates

Data Card	Number	Format	Use
1	a	I2	Number of boundary sides p
	b	E10.1	Density γg
	c	E10.1	Circumscribing boundary radius a (in.)
	d	E10.1	Thickness h (in.)
	e	E10.1	Poisson's ratio ν
	f	E10.1	Young's modulus E (psi)
2	a	E10.0	= 1.E-50 for IBM 360/67; = 1.E-32 for IBM 1130. A constant used for the backward recurrence series computation of J_{pn} and I_{pn}
	b	I5	Number of terms calculated in backward recurrence series. This number should be at least an order of 10 greater than the highest order Bessel function required (i.e. $\geq p(L-2) + 11$)
3	a	I5	Number of boundary collocation points L
	b,... ({3a} numbers)	F5.1,...	θ locations of boundary collocation points (degrees). Program is dimensioned for a maximum of 10 collocation points on the characteristic segment boundary
4	a	E10.1	Initial k/a value starting search for eigenvalues
	b	E10.1	Final k/a value ending search for eigenvalues

Table C.1 (continued)

Data Card	Number	Format	Use
4	c	E10.1	Increment in k/a value
	d	E10.1	Decimal place error in eigenvalues, k_i/a
5	a	I2	=1≡ clamped or partially clamped edge condition =2≡ simply supported edge condition
	b	E10.1	Edge clamping factor β_1^i (lb.)
	c	E10.1	Viscous damping ratio of critical damping ζ_i/ω_i
6	a	I3	Even number of boundary points used in Simpson's formula for numerical integration over θ when calculating modal participation functions
	b,c	I3,I3	Maximum number of terms α used in calculating ϕ_9 and ϕ_{10}
7	a	I2	=1≡ search for eigenvalues only and omit cards 10 to 19... =2≡ use the sum of values {4a}[1] and {4b} as an eigenvalue and compute the associated eigenvector and a forced solution =3≡ search for eigenvalues, compute eigenvectors and forced solutions
8	a	E10.0	=0≡ compute modal participation functions = any value ≡ use this value as X_1^i/X_0^i and omit calculation of modal participation functions
9	a	E10.0	Controls the magnitude of the boundary equation matrix determinant value. Each element of the matrix is multiplied by this value thereby eliminating some computer underflow and overflow.

[1] {4a} represents the first number on the fourth data card.

Table C.1 (continued)

Data Card	Number	Format	Use
10	a	I2	=1≡ exponentially time-decaying load =2≡ linearly time-decaying load =3≡ flat impulse =4≡ viscously damped structure subject to a linearly time-decaying load =5≡ viscously damped structure subject to an exponentially time-decaying load
	b	I3	Number of time instants for which transverse displacement and sectional resultants are calculated at each r,θ location
	c	E10.1	Time interval (seconds) between calculation of transverse displacement and sectional resultants at each r,θ location
	d	E10.1	Positive duration of overpressure (seconds). Response cannot be calculated after this time
	e	E10.1	Reference overpressure q_o (psi)
11	a	I2	Number controlling output of transverse displacement and sectional resultants versus time to be on disk or paper. This feature was used on the IBM 1130 but is not shown in the program listing. Changes must be made in subroutine RESUL for its use.

Table C.1 (continued)

Data Card	Number	Format	Use
12	a	I2	Number of r,θ locations at which transverse displacement and sectional resultants are calculated
13,14, ... ({12a} cards)	a	F10.3	Radius r of position of calculation (in.)
	b		Angle θ of position of calculation (deg.)
15,16, 17,18, 19,...			Cards 10 to 14... are repeated once for each symmetric mode of vibration which will be found between the initial k/a value given by {4a} and the final k/a value given by {4b}
20	a	I2	=0≡ program restarted with a new data set following =99≡ end of program execution. This card will be read when the k/a value exceeds the final k/a value given by {4b}.

Table C.2

Functions of Plate Computer Program Subroutines

		Functions
Mainline Routine	VIBRA	Supervises the sequence of program execution according to the options specified. Reads cards 10 to 19 ... . Writes χ_1^1/χ_0^1, q_o and t_o.
Subroutines	INPUT	Calculates plate parameters. Reads cards 1 to 9. Writes edge condition type, p, γg, a, h, ν, E, D, L, angles of collocation points, constant for backward recurrence, number of terms in backward recurrence series, β_1^1, number of points for numerical integration, and maximum value of α in series for ϕ_9 and ϕ_{10}^1.
	BLOND	Calculates higher order Bessel functions J_{pn} and I_{pn} by backward recurrence technique. Computes boundary equation matrix.
	BLONI	Modifies elements of boundary equation matrix to improve conditioning before inverting. Computes eigenvector. Writes k/a, determinant value, matrix element multiplier, k_1/a, k_1, ω_1, ω_1^d and $\bar{\eta}^1$ (first, A_{pn}^1 for n = 0...(L-2), then, B_{pn}^1 for n = 0... (L-2)).
	FOURI	Computes modal participation functions. Writes ϕ_1 to ϕ_{10} (times certain constants), $(\chi_1^1/\chi_0^1)_0$, $(\chi_1^1)_p/\chi_0^1$, and χ_1^1/χ_0^1.
	RESUL	Calculates higher order Bessel functions J_{pn} and I_{pn} by backward recurrence technique. Calculates transverse displacement and sectional resultants for various transient loads. Writes load type, r, θ, t, w, M_{rr}, $M_{r\theta}$, and $M_{\theta r}$ for particular mode.
	DMINV	Calculates inverse matrices and determinant values.
	BESJ	Calculates Bessel function J_{pn} for all orders.
	BESI	Calculates modified Bessel functions for all orders.
	SIMP	Provides weighting factors for Simpson's numerical integration formula.

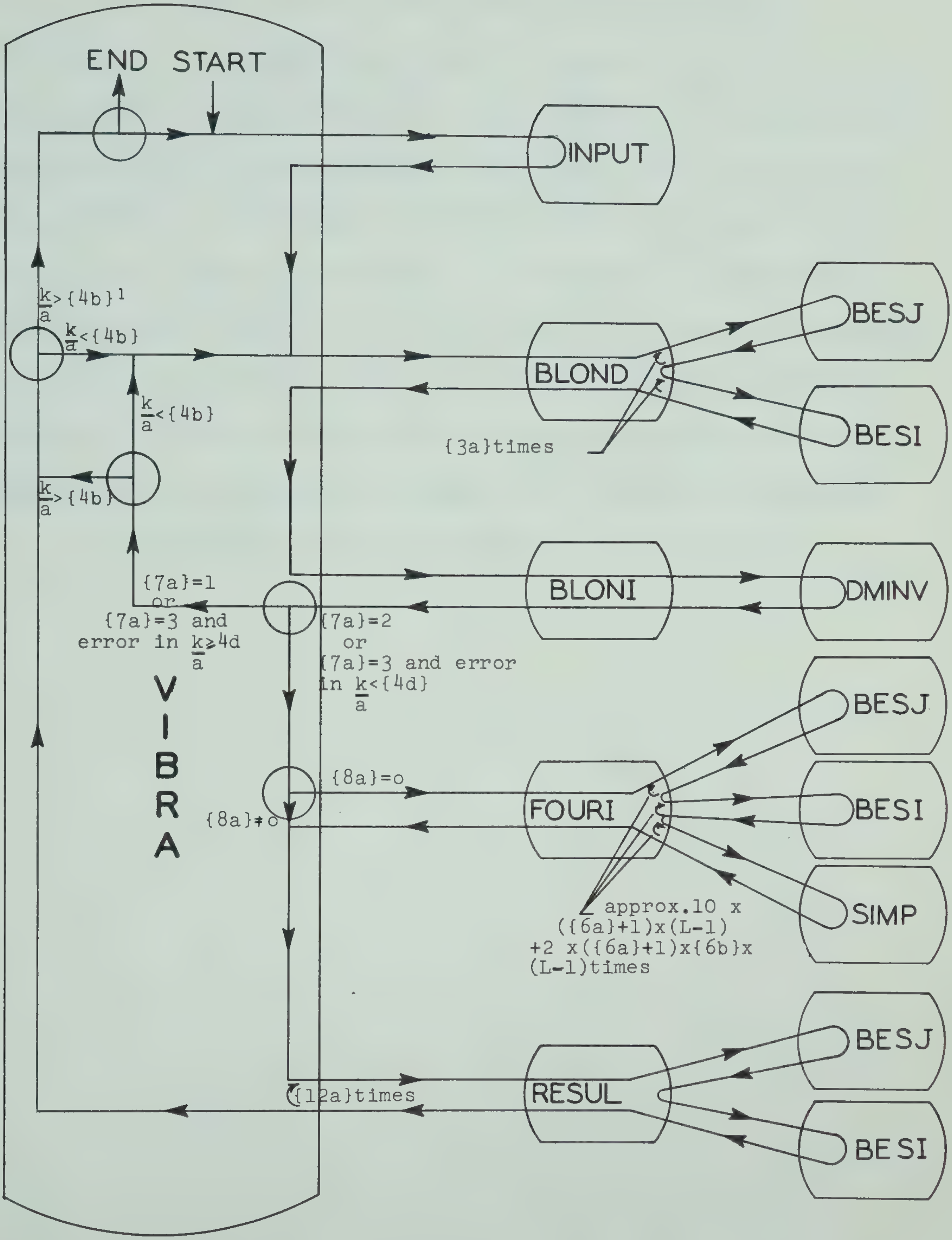

---

[1] Numbers in brackets { } refer to data as outlined in Table C.1.

FIG. C.1 Flow Diagram of Plate Computer Program

04 and 05 to 010 refer to the modal participation coefficients ϕ_7 through ϕ_{10} and ϕ_1 through ϕ_6, respectively. Calculation of the sectional resultants is inaccurate in the region near the plate center since the derivatives of the Bessel functions are calculated from their lower order derivatives. If values of sectional resultants are desired in this region, it may be necessary to reduce the accuracy specified for the Bessel functions computed for subroutine RESUL by increasing the order of magnitude of the variable termed ERR in this subroutine.

The Fortran source program is listed below:

```
C     VIBRA   PLATE
C     VIBRATIONS OF POLYGONAL PLATES
      DIMENSION       R(10),Z(10),ZZ(10),RR(18),A(18,18)
      COMMON  DENS,RAD,TH,V,EF,Z,ZZ,RR,DD,FRE,AA,RK,R,ROE,DET1,DET,FRE1,
     1DELF,ACC,FREMX,FREI,DETI,DELFI,G0,G01,PI,OMEGA,CT,BETA,DAMP,
     2L,NN,NN1,N1,N2,IP,IP1,L1,LL1,LL2,LL3,NMAX,NCOND,NI,NIA,NIB,IENT,
     3L2,IREAD,IPRIN
      DOUBLE PRECISION DENS,RAD,TH,V,EF,Z,ZZ,RR,DD,FRE,AA,RK,R,ROE,DET1,
     1DET,FRE1,DELF,ACC,FREMX,FREI,DETI,DELFI,G0,G01,PI,OMEGA,CT,A,SUM1,
     2SUM2,DEL,DLT,POS,PIN,RA,ZZZ,BETA,DAMP
      IREAD=5
      IPRIN=6
   18 CALL INPUT
      ISENS=2
      IF (IENT-2) 19,35,19
   19 CALL BLOND(A)
      CALL BLONI (A,RR,FRE,DET,LL2,LL3,OMEGA,CT,ISENS,IPRIN,RAD,DAMP)
      IF (DET-0.D0) 20,11,20
   11 CT=CT*1.D+2
      GO TO 19
   20 IF (FRE-FREMX) 21,21,39
   21 CALL BLOND(A)
      CALL BLONI (A,RR,FRE,DET,LL2,LL3,OMEGA,CT,ISENS,IPRIN,RAD,DAMP)
      IF (FRE-FREMX) 22,22,39
   22 SUM1=DABS(DET1-DET)
      SUM2=DABS(DET1+DET)
      IF (SUM1-SUM2) 21,23,23
   23 FREI=FRE
      DETI=DET
      DELFI=DELF
      FRE=FRE1
      IF (DET1) 24,24,30
   24 DELF=DELF/2.D0
      CALL BLOND(A)
      CALL BLONI (A,RR,FRE,DET,LL2,LL3,OMEGA,CT,ISENS,IPRIN,RAD,DAMP)
      IF (DELF-ACC) 36,36,25
   25 IF (DET) 24,24,26
   26 FRE=FRE1
      GO TO 24
   30 DELF=DELF/2.D0
      CALL BLOND(A)
      CALL BLONI (A,RR,FRE,DET,LL2,LL3,OMEGA,CT,ISENS,IPRIN,RAD,DAMP)
      IF (DELF-ACC) 36,36,31
   31 IF (DET) 32,30,30
   32 FRE=FRE1
      GO TO 30
   36 IF (IENT-2) 57,35,35
   35 DELF=0.D0
      CALL BLOND(A)
      DAMP=DAMP*OMEGA
      ISENS=1
      CALL BLONI (A,RR,FRE,DET,LL2,LL3,OMEGA,CT,ISENS,IPRIN,RAD,DAMP)
   41 IF(G0-0.D0) 71,37,71
   71 WRITE (IPRIN,72) G0
   72 FORMAT (1H0,20HFOURIER COEFFICIENT=,E12.5,/)
      GO TO 38
   37 CALL FOURI
   38 G0=G0/(DD*FRE**4)
      READ (IREAD,1) ICODE,NDLT,DLT,POS,PIN
    1 FORMAT (I2,I3,2E10.1,F5.2)
      WRITE (IPRIN,61) PIN,POS
   61 FORMAT (1H0,13HREFL. PRESS.=,F6.2,10X,10HPOS. DUR.=,E10.2)
      READ (IREAD,1) IOT
      READ (IREAD,1) NPT
      DO 50 I=1,NPT
      READ (IREAD,52) RA,ZZZ
      CALL RESUL(AA,NN,DD,V,L1,NN1,N1,N2,NMAX,IP,IP1,PI,FRE,G0,RR,OMEGA,
     1RA,ZZZ,ICODE,NDLT,DLT,POS,PIN,I,IOT,IREAD,IPRIN,DAMP)
   50 CONTINUE
   52 FORMAT (2F10.3)
   57 IF (FRE-FREMX) 58,58,39
   58 FRE=FREI
```

```
      DET=DETI
      DELF=DELFI
      CT=CT*1.D-1
      GO=0.DO
      GO TO 19
   39 READ(IREAD,1) IST
      IF (IST-99) 18,40,40
   40 STOP
      END


C     INPUT    PLATE
      SUBROUTINE INPUT
      DIMENSION       R(10),Z(10),ZZ(10),RR(18)
      COMMON  DENS,RAD,TH,V,EF,Z,ZZ,RR,DD,FRE,AA,RK,R,ROE,DET1,DET,FRE1,
     1DELF,ACC,FREMX,FREI,DETI,DELFI,GO,GO1,PI,OMEGA,CT,BETA,DAMP,
     2L,NN,NN1,N1,N2,IP,IP1,L1,LL1,LL2,LL3,NMAX,NCOND,NI,NIA,NIB,IENT,
     3L2,IREAD,IPRIN
      DOUBLE PRECISION DENS,RAD,TH,V,EF,Z,ZZ,RR,DD,FRE,AA,RK,R,ROE,DET1,
     1DET,FRE1,DELF,ACC,FREMX,FREI,DETI,DELFI,GO,GO1,PI,OMEGA,CT,GR,BETA
     2,DAMP,SR1
      READ (IREAD,1) IP,DENS,RAD,TH,V,EF
    1 FORMAT (I2,5E10.1)
      READ (IREAD,2) AA,NN
    2 FORMAT (E10.0,I5)
      READ (IREAD,3) L,(ZZ(I),I=1,L)
    3 FORMAT (I5,15F5.1)
      READ (IREAD,4) FRE,FREMX,DELF,ACC
    4 FORMAT (4E10.1)
      READ (IREAD,1) NCOND,BETA,DAMP
      READ (IREAD,5) NI,NIA,NIB
      READ (IREAD,1) IENT
      READ (IREAD,2) GO
      READ (IREAD,2) CT
    5 FORMAT (3I3)
      IF (NCOND-1) 7,7,8
    7 WRITE (IPRIN,21)
      GO TO 9
    8 WRITE (IPRIN,22)
    9 RK=IP
      PI=3.141592653589793
      NN1=NN-1
      N1=NN+1
      N2=NN+2
      GR=32.2DO*12.DO
      NMAX=(L-2)*IP+1
      IP1=IP+1
      L1=L-1
      L2=L-2
      LL1=2*L-1
      LL2=LL1-1
      LL3=LL2-1
      DD=EF*TH**3/(12.DO*(1.DO-(V**2)))
      ROE=DENS*TH/GR
      SR1 =RAD*DCOS(PI/RK)
      WRITE (IPRIN,10)
   10 FORMAT (1HO,4X,5HSIDES,9X,7HDENSITY,9X,6HRADIUS,7X,9HTHICKNESS,5X,
     17HPOISSON,1X,5HRATIO,2X,5HYOUNG,1X,7HMODULUS,2X,4HFLEX,1X,
     28HRIGIDITY)
      WRITE (IPRIN,11) IP,DENS,RAD,TH,V,EF,DD
   11 FORMAT (6X,I2,5X,6E15.5//)
      WRITE (IPRIN,12) L,(ZZ(I),I=1,L)
   12 FORMAT (1HO,10HCOL. PTS.=,I2,5X,13HANGLES(DEG.)=,15F5.1)
      WRITE (IPRIN,13) AA,NN,BETA,DAMP
   13 FORMAT (1HO,3HAA=,E10.1, 5X,19HSTART OF BACK REC.=,I5, 5X,
     114HCLAMPING BETA=,E10.2,5X,15HDAMPING FACTOR=,E12.5)
      WRITE (IPRIN,14) NI,NIA,NIB
   14 FORMAT (1HO,3HNI=,I3,10X,4HNIA=,I3,10X,4HNIB=,I3)
      DO 20 I=1,L
      Z(I)=ZZ(I)*PI/180.DO
   20 R(I)=SR1 /DCOS(Z(I))
   21 FORMAT (1H1, 10X,15HCLAMPED   PLATE)
```

```
   22 FORMAT (1H1,10X,26HSIMPLY   SUPPORTED   PLATE)
      RETURN
      END


C     BLOND      PLATE
      SUBROUTINE BLOND(A)
      DIMENSION        ARG(10),FJ(60),FI(60),RJ(10,9),RI(10,9),RJ1(10,9),
     1RI1(10,9),RJ2(10,9),RI2(10,9)
      DIMENSION        R(10),Z(10),ZZ(10),RR(18),A(18,18)
      COMMON  DENS,RAD,TH,V,EF,Z,ZZ,RR,DD,FRE,AA,RK,R,ROE,DET1,DET,FRE1,
     1DELF,ACC,FREMX,FREI,DETI,DELFI,G0,G01,PI,OMEGA,CT,BETA,DAMP,
     2L,NN,NN1,N1,N2,IP,IP1,L1,LL1,LL2,LL3,NMAX,NCOND,NI,NIA,NIB,IENT,
     3L2,IREAD,IPRIN
      DOUBLE PRECISION DENS,RAD,TH,V,EF,Z,ZZ,RR,DD,FRE,AA,RK,R,ROE,DELF,
     1ACC,FREMX,FREI,DETI,DELFI,G0,G01,PI,OMEGA,CT,ARG,FJ,FI,RJ,RI,RJ1,
     2RI1,RJ2,RI2,RJ0,RI0,C,CJ,CI,DUM,A,DET1,DET,FRE1,ERR,BETA,DAMP
     3,F1,F2,F3
      F1=1.D0
      F2=2.D0
      F3=3.D0
      FRE1=FRE
      DET1=DET
      FRE=FRE+DELF
      ERR=1.D-15
      DO 6 I=1,L
      ARG(I)=FRE*R(I)
      CALL BESJ(ARG(I),0,RJ0,ERR,IER)
      CALL BESI(ARG(I),0,RI0,ERR,IER)
      FJ(1)=0.D0
      FI(1)=0.D0
      FJ(2)=AA
      FI(2)=AA
      DO 2 J=1,NN1
      C=NN-J
      FJ(J+2)=FJ(J+1)*F2*C/ARG(I)-FJ(J)
    2 FI(J+2)=FI(J+1)*F2*C/ARG(I)+FI(J)
      CJ=FJ(N1)/RJ0
      CI=FI(N1)/RI0
      DO 4 J=1,NMAX,IP
      K=((J-1)/IP)+1
      K1=N2-J
      RJ(I,K)=FJ(K1)/CJ
    4 RI(I,K)=FI(K1)/CI
      K1=N2-2
      RJ1(I,1)=-FJ(K1)/CJ
      RI1(I,1)=FI(K1)/CI
      DO 5 J=IP1,NMAX,IP
      K=((J-1)/IP)+1
      K1=N2-J
      RJ1(I,K)=(FJ(K1+1)-FJ(K1-1))/(F2*CJ)
    5 RI1(I,K)=(FI(K1-1)+FI(K1+1))/(F2*CI)
      DO 6 J=1,L1
      C=(J-1)*IP
      RJ2(I,J)=-RJ1(I,J)/ARG(I)+RJ(I,J)*((C/ARG(I))**2-F1)
    6 RI2(I,J)=-RI1(I,J)/ARG(I)+RI(I,J)*((C/ARG(I))**2+F1)
      IF (NCOND-1) 10,10,12
   10 DO 11 I=1,L1
      DO 11 J=1,L1
      C=IP*(J-1)
      K=J+L1
      A(I,J)=FRE*RJ1(I,J)*DCOS(Z(I))*DCOS(C*Z(I))+(C/R(I))*RJ(I,J)*
     1 DSIN(Z(I))*DSIN(C*Z(I))
   11 A(I,K)=FRE*RI1(I,J)*DCOS(Z(I))*DCOS(C*Z(I))+(C/R(I))*RI(I,J)*
     1DSIN(Z(I))*DSIN(C*Z(I))
      IF (BETA) 12,14,12
   12 DO 13 I=1,L1
      DO 13 J=1,L1
      C=IP*(J-1)
      K=J+L1
      DUM=-   (F1-V)*((C/(R(I)**2))*RJ(I,J)-(FRE*C/R(I))*RJ1(I,J))*
     1        DSIN(F2*Z(I))*DSIN(C*Z(I))
```

```
      A(I,J)=A(I,J)*BETA/DD+
     1         ((FRE**2)*RJ2(I,J)-V*((C/R(I))**2)*RJ(I,J)+V*(FRE/R(I))*
     2         RJ1(I,J))*((DCOS(Z(I)))**2)*DCOS(C*Z(I))    +
     3         (V*(FRE**2)*RJ2(I,J)-((C/R(I))**2)*RJ(I,J)+(FRE/R(I))*
     4         RJ1(I,J))*((DSIN(Z(I)))**2)*DCOS(C*Z(I))    +DUM
      DUM= -   (F1-V)*((C/(R(I)**2))*RI(I,J)-(FRE*C/R(I))*RI1(I,J))*
     1         DSIN(F2*Z(I))*DSIN(C*Z(I))
   13 A(I,K)=A(I,K)*BETA/DD+
     1         ((FRE**2)*RI2(I,J)-V*((C/R(I))**2)*RI(I,J)+V*(FRE/R(I))*
     2         RI1(I,J))*((DCOS(Z(I)))**2)*DCOS(C*Z(I))    +
     3         (V*(FRE**2)*RI2(I,J)-((C/R(I))**2)*RI(I,J)+(FRE/R(I))*
     4         RI1(I,J))*((DSIN(Z(I)))**2)*DCOS(C*Z(I))    +DUM
   14 DO 15 J=1,L1
      C=IP*(J-1)
      I=1
      K=J+L1
      I1=I+L1
      A(I1,J)=RJ(I,J)*DCOS(C*Z(I))
   15 A(I1,K)=RI(I,J)*DCOS(C*Z(I))
      DO 16 I=3,L
      DO 16 J=1,L1
      C=IP*(J-1)
      I1=I+L1-1
      K=J+L1
      A(I1,J)=RJ(I,J)*DCOS(C*Z(I))
   16 A(I1,K)=RI(I,J)*DCOS(C*Z(I))
      OMEGA=DSQRT(DD*FRE**4/ROE)
      RETURN
      END


C     BLONI    PLATE
      SUBROUTINE BLONI(A,RR,FRE,DET,LL2,LL3,OMEGA,CT,ISENS,IPRIN,
     1RAD,DAMP)
      DIMENSION      A(18,18),RR(18),LW(18),MW(18),D(18),CC(18),CR(18)
      DOUBLE PRECISION D,DV,A,RR,FRE,DET,OMEGA,CT,CC,CR,CF,RF,RAD,
     1DAMP,XYZ,OMEDA
C    DEFINE COLUMN CONSTANTS
      CF=1.0D0
      DO 1 J=1,LL2
      CC(J)=A(1,J)
      IF (CC(J))8,9,8
    9 CC(J)=1.D0
    8 CF=CF*CC(J)*CT/DABS(CC(J))
    1 CONTINUE
      DO 2 I=1,LL2
      DO 2 J=1,LL2
      A(I,J)=A(I,J)/CC(J)
    2 CONTINUE
C    DEFINE ROW CONSTANTS
      RF=1.0D0
      DO 3 I=1,LL2
      CR(I)=A(I,1)
      IF (CR(I)) 10,11,10
   11 CR(I)=1.D0
   10 RF=RF*CR(I)/DABS(CR(I))
    3 CONTINUE
      DO 4 I=1,LL2
      DO 4 J=1,LL2
      A(I,J)=A(I,J)/CR(I)
    4 CONTINUE
      IF (ISENS-1) 22,22,20
   20 CALL DMINV (A,LL2,DET,LW,MW)
      DET=DET*CF*RF
      WRITE (IPRIN,21) FRE,DET,CT
   21 FORMAT (1H0,11HFREQUENCY =,E18.8,5X,19HDETERMINANT VALUE =,E18.8,
     15X,12HCONSTANT-CT=,E10.1)
      GO TO 29
   22 ISENS=2
      DO 23 J=1,LL3
   23 D(J)=-A(J,1)
```

```
      DO 24 I=1,LL3
      DO  24 J=1,LL3
      J1=J+1
   24 A(I,J)=A(I,J1)
      CALL DMINV (A,LL3,DV,LW,MW)
      DO 25 I=2,LL2
   25 RR(I)=0.0D0
      RR(1)=1.0D0
      DO 26 I=2,LL2
      DO 26 J=1,LL3
      I1=I-1
   26 RR(I)=RR(I)+A(I1,J)*D(J)
      DO 35 I=2,LL2
      RR(I)=RR(I)*CC(1)/CC(I)
   35 CONTINUE
      XYZ=RAD*FRE
      OMEDA=DSQRT(OMEGA**2-DAMP**2)
      WRITE (IPRIN,27) FRE,XYZ,OMEGA,OMEDA
   27 FORMAT (1H0,15HEIGENFREQUENCY=,2E18.8,/,5X,19HANGULAR FREQUENCY= ,
     1E18.8,5X,17HDAMPED ANG. FRE.=,E18.8)
      WRITE (IPRIN,28) (RR(I),I=1,LL2)
   28 FORMAT (1H0,11HEIGENVECTOR,/,(4E18.8/))
   29 RETURN
      END


C    DMINV    PLATE
      SUBROUTINE DMINV (A,N,D,L,M)
      DIMENSION  A(324),L(18),M(18)
      DOUBLE PRECISION BIGA,HOLD,A,D
      IS=18
      K=0
      DO 9 I=1,N
      DO 9 J=1,N
      I1=I-1
      K=K+1
      NI=IS*I1+J
    9 A(K)=A(NI)
C        SEARCH FOR LARGEST ELEMENT
      D=1.0D0
      NK=-N
      DO 80 K=1,N
      NK=NK+N
      L(K)=K
      M(K)=K
      KK=NK+K
      BIGA=A(KK)
      DO 20 J=K,N
      IZ=N*(J-1)
      DO 20 I=K,N
      IJ=IZ+I
   10 IF (DABS(BIGA)-DABS(A(IJ))) 15,20,20
   15 BIGA=A(IJ)
      L(K)=I
      M(K)=J
   20 CONTINUE
C        INTERCHANGE ROWS
      J=L(K)
      IF(J-K) 35,35,25
   25 KI=K-N
      DO 30 I=1,N
      KI=KI+N
      HOLD=-A(KI)
      JI=KI-K+J
      A(KI)=A(JI)
   30 A(JI) =HOLD
C        INTERCHANGE COLUMNS
   35 I=M(K)
      IF(I-K) 45,45,38
   38 JP=N*(I-1)
      DO 40 J=1,N
      JK=NK+J
```

```
      JI=JP+J
      HOLD=-A(JK)
      A(JK)=A(JI)
   40 A(JI) =HOLD
C        DIVIDE COLUMN BY MINUS PIVOT (VALUE OF PIVOT ELEMENT IS
C        CONTAINED IN BIGA)
   45 IF(BIGA) 48,46,48
   46 D=0.0D0
      RETURN
   48 DO 55 I=1,N
      IF(I-K) 50,55,50
   50 IK=NK+I
      A(IK)=A(IK)/(-BIGA)
   55 CONTINUE
C        REDUCE MATRIX
      DO 65 I=1,N
      IK=NK+I
      IJ=I-N
      DO 65 J=1,N
      IJ=IJ+N
      IF(I-K) 60,65,60
   60 IF(J-K) 62,65,62
   62 KJ=IJ-I+K
      A(IJ)=A(IK)*A(KJ)+A(IJ)
   65 CONTINUE
C        DIVIDE ROW BY PIVOT
      KJ=K-N
      DO 75 J=1,N
      KJ=KJ+N
      IF(J-K) 70,75,70
   70 A(KJ)=A(KJ)/BIGA
   75 CONTINUE
C        PRODUCT OF PIVOTS
      D=D*BIGA
C        REPLACE PIVOT BY RECIPROCAL
      A(KK)=1.0D0/BIGA
   80 CONTINUE
C        FINAL ROW AND COLUMN INTERCHANGE
      K=N
  100 K=(K-1)
      IF(K) 150,150,105
  105 I=L(K)
      IF(I-K) 120,120,108
  108 JQ=N*(K-1)
      JR=N*(I-1)
      DO 110 J=1,N
      JK=JQ+J
      HOLD=A(JK)
      JI=JR+J
      A(JK)=-A(JI)
  110 A(JI) =HOLD
  120 J=M(K)
      IF(J-K) 100,100,125
  125 KI=K-N
      DO 130 I=1,N
      KI=KI+N
      HOLD=A(KI)
      JI=KI-K+J
      A(KI)=-A(JI)
  130 A(JI) =HOLD
      GO TO 100
  150 K=N*N+1
      NI=IS*N+1
      DO 8 I=1,N
      NI=NI-(IS-N)
      DO 8 J=1,N
      K=K-1
      NI=NI-1
    8 A(NI)=A(K)
      RETURN
      END
```

```
C    BESJ      PLATE
      SUBROUTINE BESJ(X,N,BJ,D,IER)
      DOUBLE PRECISION BPREV,FM1,ALPHA,BMK,S,FM,DBLN,X,BJ,D
      BJ=.0D0
      IF(N)10,20,20
   10 IER=1
      RETURN
   20 IF(X)30,30,31
   30 IER=2
      RETURN
   31 IF(X-15.D0) 32,32,34
   32 NTEST=20.D0+10.D0*X-X**2/3.D0
      GO TO 36
   34 NTEST=90.D0+X/2.D0
   36 IF(N-NTEST)40,38,38
   38 IER=4
      RETURN
   40 IER=0
      N1=N+1
      BPREV=.0D0
C        COMPUTE STARTING VALUE OF M
      IF(X-5.D0)50,60,60
   50 MA=X+6.D0
      GO TO 70
   60 MA=1.4D0*X+60.D0/X
   70 MX=X
      MB=N+MX/4+2
      MZERO=MA
      IF(MA-MB)80,90,90
   80 MZERO=MB
C        SET UPPER LIMIT OF M
   90 MMAX=NTEST
  100 DO 190 M=MZERO,MMAX,3
C        SET F(M),F(M-1)
      FM1=1.0D-40
      FM=.0D0
      ALPHA=.0D0
      IF(M-(M/2)*2)120,110,120
  110 JT=-1
      GO TO 130
  120 JT=1
  130 M2=M-2
      DO 160 K=1,M2
      MK=M-K
      DBLN=MK
      BMK=2.D0*DBLN*FM1/X-FM
      FM=FM1
      FM1=BMK
      IF(MK-N-1)150,140,150
  140 BJ=BMK
  150 JT=-JT
      S=1+JT
  160 ALPHA=ALPHA+BMK*S
      BMK=2.D0*FM1/X-FM
      IF(N)180,170,180
  170 BJ=BMK
  180 ALPHA=ALPHA+BMK
      BJ=BJ/ALPHA
      IF(DABS(BJ-BPREV)-DABS(D*BJ))200,200,190
  190 BPREV=BJ
      IER=3
  200 RETURN
      END
```

```
C    BESI      PLATE
      SUBROUTINE BESI(X,N,BI,TOL,IER)
      DOUBLE PRECISION XX,FACTN,FI,TERM,FK,FN,PI,DBLN,FLN,X,BI,TOL
C        CHECK FOR ERRORS IN N AND X AND EXIT IF ANY ARE PRESENT
      IER=0
```

```
      BI=1.0D0
      IF(N)150,15,10
   10 IF(X)160,20,20
   15 IF(X)160,17,20
   17 RETURN
C          DEFINE TOLERANCE
C          IF ARGUMENT GT 12 AND GT N, USE ASYMPTOTIC FORM
   20 IF(X-12.D0)40,40,30
   30 FLN=N
      IF (X-FLN) 40,40,110
C          COMPUTE FIRST TERM OF SERIES AND SET INITIAL VALUE OF THE SUM
   40 XX=X/2.D0
   50 TERM=1.0D0
      IF(N) 70,70,55
   55 DO 60 I=1,N
      FI=I
      IF (DABS(TERM)-1.D-68)56,60,60
   56 IER=3
      BI=0.0D0
      RETURN
   60 TERM=TERM*XX/FI
   70 BI=TERM
      XX=XX*XX
C          COMPUTE TERMS,STOPPING WHEN ABS(TERM) LE ABS(SUM OF TERMS)
C          TIMES TOLERANCE
      DO 90 K=1,1000
      IF(DABS(TERM)-DABS(BI*TOL))100,100,80
   80 FK=K*(N+K)
      TERM=TERM*(XX/FK)
   90 BI=BI+TERM
C          RETURN BI AS ANSWER
  100 RETURN
C          X GT 12 AND X GT N, SO USE ASYMPTOTIC APPROXIMATION
  110 FN=4*N*N
      IF(X-110.0D0)115,111,111
  111 IER=4
      RETURN
  115 XX=1.D0/(8.D0*X)
      TERM=1.D0
      BI=1.D0
      DO 130 K=1,30
      IF (DABS(TERM)-DABS(TOL*BI))140,140,120
  120 FK=(2*K-1)**2
      DBLN=K
      TERM=TERM*XX*(FK-FN)/DBLN
  130 BI=BI+TERM
C          SIGNIFICANCE LOST AFTER 30 TERMS,TRY SERIES
      GO TO 40
  140 PI=3.141592653589793
      BI=BI*DEXP(X)/DSQRT(2.D0*PI*X)
      GO TO 100
  150 IER=1
      GO TO 100
  160 IER=2
      GO TO 100
      END


C     SIMP    PLATE
      SUBROUTINE SIMP (I,O,N,IL)
      DOUBLE PRECISION O
      IF (I-1)1,1,2
    2 IF (I-N)3,1,1
    3 IF (IL-1) 4,4,5
    4 O=O*4.D0
      IL=2
      GO TO 1
    5 O=O*2.D0
      IL=1
    1 RETURN
      END
```

```
C    FOURI    PLATE
      SUBROUTINE FOURI
C     FOURIER COEFFICIENTS
      DIMENSION      R(10),Z(10),ZZ(10),RR(18)
      DIMENSION      O3(8),O4(8),O8(8),O9(8),O10(8),O31(8),O32(8),
     1O41(8),O42(8)
      COMMON  DENS,RAD,TH,V,EF,Z,ZZ,RR,DD,FRE,AA,RK,R,ROE,DET1,DET,FRE1,
     1DELF,ACC,FREMX,FREI,DETI,DELFI,G0,G01,PI,OMEGA,CT,BETA,DAMP,
     2L,NN,NN1,N1,N2,IP,IP1,L1,LL1,LL2,LL3,NMAX,NCOND,NI,NIA,NIB,IENT,
     3L2,IREAD,IPRIN
      DOUBLE PRECISION DENS,RAD,TH,V,EF,Z,ZZ,RR,DD,FRE,AA,RK,R,ROE,DET1,
     1DET,FRE1,DELF,ACC,FREMX,FREI,DETI,DELFI,G0,G01,PI,OMEGA,CT,O3,O4,
     2O8,O9,O10,O31,O32,O41,O42,FAC,ERR,DEL,X,O1,Y,BJ,O2,BI,C,O5,BJ0,
     3BJ1,O6,BI0,BI1,O7,BEJ,BEJ1,BEJ11,BEI,BEI1,BEI11,GOT,GOB,AY,BETA
     4,RJ,ERFOR,ORI,DAMP
     5,F1,F2,F3,F4
      IPRIN=6
      NPRIN=6
      F1=1.D0
      F2=2.D0
      F3=3.D0
      F4=4.D0
      R(1)=R(1)*DCOS(Z(1))
      AY=NI
      FAC=PI/(RK*F3*AY)
      DEL =PI/(RK*AY)
      ERR=1.D-15
      NI1=NI+1
      X=0.D0
      O1=0.D0
      IL=1
      DO 50 I=1,NI1
      Y=FRE*R(1)/DCOS(X)
      CALL BESJ(Y,1,BJ,ERR,IER)
      Y=BJ/DCOS(X)
      CALL SIMP(I,Y,NI1,IL)
      Y=Y*FAC
      X=X+DEL
      O1=O1+Y
   50 CONTINUE
      WRITE (IPRIN,10)O1
      O1=O1*R(1)/FRE
      X=0.D0
      O2=0.D0
      IL=1
      DO 51 I=1,NI1
      Y=FRE*R(1)/DCOS(X)
      CALL BESI(Y,1,BI,ERR,IER)
      Y=BI/DCOS(X)
      CALL SIMP(I,Y,NI1,IL)
      Y=Y*FAC
      X=X+DEL
      O2=O2+Y
   51 CONTINUE
      WRITE (IPRIN,11)O2
      O2=O2*R(1)/FRE
      DO 105 II=1,L2
      O31(II)=0.D0
      ORI=O31(II)
      C=IP*II
      DO 103 J=1,NIA
      IL=1
      X=0.D0
      DO 101 I=1,NI1
      Y=FRE*R(1)/DCOS(X)
      IOR=IP*II+2*(J-1)+1
      CALL BESJ(Y,IOR,BJ,ERR,IER)
      Y=BJ*DCOS(C*X)/DCOS(X)
      CALL SIMP(I,Y,NI1,IL)
      Y=Y*FAC
      X=X+DEL
```

```
      O31(II)=O31(II)+Y
  101 CONTINUE
      ERFOR=DABS((ORI-O31(II))/O31(II))-ACC
      IF (ERFOR) 104,104,102
  102 ORI=O31(II)
  103 CONTINUE
  104 WRITE (IPRIN,12)II,O31(II),J
      O31(II)=O31(II)*F2*R(1)/FRE
  105 CONTINUE
      DO 110II=1,L2
      O32(II)=0.D0
      ORI=O32(II)
      C=IP*II
      DO 108 J=1,NIA
      RJ=J
      IL=1
      X=0.D0
      DO 106 I=1,NI1
      Y=FRE*R(1)/DCOS(X)
      IOR=II*IP+2*J
      CALL BESJ(Y,IOR,BJ,ERR,IER)
      Y=BJ*DCOS(C*X)
      CALL SIMP(I,Y,NI1,IL)
      Y=Y*FAC*RJ
      X=X+DEL
      O32(II)=O32(II)+Y
  106 CONTINUE
      ERFOR=DABS((ORI-O32(II))/O32(II))-ACC
      IF (ERFOR) 109,109,107
  107 ORI=O32(II)
  108 CONTINUE
  109 WRITE (IPRIN,13) II,O32(II),J
      O32(II)=-O32(II)*F4/FRE**2
      O3(II)=O32(II)+O31(II)
  110 CONTINUE
      DO 120 II=1,L2
      O41(II)=0.D0
      ORI=O41(II)
      C=IP*II
      DO 118 J=1,NIA
      IL=1
      X=0.D0
      DO 116 I=1,NI1
      Y=FRE*R(1)/DCOS(X)
      IOR=IP*II+2*(J-1)+1
      CALL BESI(Y,IOR,BI,ERR,IER)
      Y=BI*DCOS(C*X)/DCOS(X)
      CALL SIMP(I,Y,NI1,IL)
      Y=Y*FAC
      X=X+DEL
      O41(II)=O41(II)+Y*((-F1)**(J-1))
  116 CONTINUE
      ERFOR=DABS((ORI-O41(II))/O41(II))-ACC
      IF (ERFOR)119,119,117
  117 ORI=O41(II)
  118 CONTINUE
  119 WRITE (IPRIN,14) II,O41(II),J
      O41(II)=O41(II)*F2*R(1)/FRE
  120 CONTINUE
      DO 125 II=1,L2
      O42(II)=0.D0
      ORI=O42(II)
      C=IP*II
      DO 123 J=1,NIA
      RJ=J
      IL=1
      X=0.D0
      DO 121 I=1,NI1
      Y=FRE*R(1)/DCOS(X)
      IOR=II*IP+2*J
      CALL BESI(Y,IOR,BI,ERR,IER)
      Y=BI*DCOS(C*X)
```

```
      CALL SIMP(I,Y,NI1,IL)
      Y=Y*FAC*RJ
      X=X+DEL
      O42(II)=O42(II)+Y*((-F1)**(J-1))
  121 CONTINUE
      ERFOR=DABS((ORI-O42(II))/O42(II))-ACC
      IF (ERFOR)124,124,122
  122 ORI=O42(II)
  123 CONTINUE
  124 WRITE (IPRIN,15) II,O42(II),J
      O42(II)=-O42(II)*F4/FRE**2
      O4(II)=O42(II)+O41(II)
  125 CONTINUE
      X=0.D0
      O5=0.D0
      IL=1
      DO 52 I=1,NI1
      Y=FRE*R(1)/DCOS(X)
      CALL BESJ(Y,0,BJ0,ERR,IER)
      CALL BESJ(Y,1,BJ1,ERR,IER)
      Y=(BJ0**2  +BJ1**2)/(DCOS(X)**2)
      CALL SIMP(I,Y,NI1,IL)
      Y=Y*FAC
      X=X+DEL
      O5=O5+Y
   52 CONTINUE
      WRITE (IPRIN,16)O5
      O5=O5*(R(1)**2)/F2
      X=0.D0
      O6=0.D0
      IL=1
      DO 53 I=1,NI1
      Y=FRE*R(1)/DCOS(X)
      CALL BESI(Y,0,BI0,ERR,IER)
      CALL BESI(Y,1,BI1,ERR,IER)
      Y=(-(BI1**2)+BI0**2)/(DCOS(X)**2)
      CALL SIMP(I,Y,NI1,IL)
      Y=Y*FAC
      X=X+DEL
      O6=O6+Y
   53 CONTINUE
      WRITE (IPRIN,17)O6
      O6=O6*(R(1)**2)/F2
      X=0.D0
      O7=0.D0
      IL=1
      DO 54 I=1,NI1
      Y=FRE*R(1)/DCOS(X)
      CALL BESJ(Y,0,BJ0,ERR,IER)
      CALL BESJ(Y,1,BJ1,ERR,IER)
      CALL BESI(Y,0,BI0,ERR,IER)
      CALL BESI(Y,1,BI1,ERR,IER)
      Y=(BJ0*BI1+BJ1*BI0)/DCOS(X)
      CALL SIMP(I,Y,NI1,IL)
      Y=Y*FAC
      X=X+DEL
      O7=O7+Y
   54 CONTINUE
      WRITE (IPRIN,18)O7
      O7=O7*R(1)/(F2*FRE)
      DO 69 II=1,L2
      O8(II)=0.D0
      IL=1
      X=0.D0
      J=IP*II
      C=J
      J1=J+1
      J11=J-1
      DO 68 I=1,NI1
      Y=FRE*R(1)/DCOS(X)
      CALL BESJ(Y,J,BEJ,ERR,IER)
      CALL BESJ(Y,J1,BEJ1,ERR,IER)
      CALL BESJ(Y,J11,BEJ11,ERR,IER)
```

```
      BEJ1=(BEJ11-BEJ1 )/F2
      Y=(BEJ1**2+BEJ**2*(F1-(C*DCOS(X)/(FRE*R(1)))**2))
     1  *(DCOS(C*X)/DCOS(X))**2
      CALL SIMP(I,Y,NI1,IL)
      Y=Y*FAC
      X=X+DEL
      O8(II)=O8(II)+Y
   68 CONTINUE
      WRITE (NPRIN,19)II,O8(II)
      O8(II)=O8(II)*R(1)**2/F2
   69 CONTINUE
      DO 71 II=1,L2
      O9(II)=0.D0
      IL=1
      X=0.D0
      J=IP*II
      C=J
      J1=J+1
      J11=J-1
      DO 70 I=1,NI1
      Y=FRE*R(1)/DCOS(X)
      CALL BESI(Y,J,BEI,ERR,IER)
      CALL BESI(Y,J1,BEI1,ERR,IER)
      CALL BESI(Y,J11,BEI11,ERR,IER)
      BEI1=(BEI11+BEI1)/F2
      Y=(-(BEI1**2)+BEI**2*(F1+(C*DCOS(X)/(FRE*R(1)))**2))
     1  *(DCOS(C*X)/DCOS(X))**2
      CALL SIMP(I,Y,NI1,IL)
      Y=Y*FAC
      X=X+DEL
      O9(II)=O9(II)+Y
   70 CONTINUE
      WRITE (NPRIN,20)II,O9(II)
      O9(II)=O9(II)*R(1)**2/F2
   71 CONTINUE
      DO 73 II=1,L2
      O10(II)=0.D0
      IL=1
      X=0.D0
      J=IP*II
      C=J
      J1=J+1
      J11=J-1
      DO 72 I=1,NI1
      Y=FRE*R(1)/DCOS(X)
      CALL BESJ(Y,J,BEJ,ERR,IER)
      CALL BESI(Y,J,BEI,ERR,IER)
      CALL BESJ(Y,J1,BEJ1,ERR,IER)
      CALL BESI(Y,J1,BEI1,ERR,IER)
      CALL BESJ(Y,J11,BEJ11,ERR,IER)
      CALL BESI(Y,J11,BEI11,ERR,IER)
      BEJ1=(BEJ11-BEJ1 )/F2
      BEI1=(BEI11+BEI1)/F2
      Y=(BEJ*BEI1-BEJ1*BEI)*DCOS(C*X)**2/DCOS(X)
      CALL SIMP(I,Y,NI1,IL)
      Y=Y*FAC
      X=X+DEL
      O10(II)=O10(II)+Y
   72 CONTINUE
      WRITE (IPRIN,21)II,O10(II)
      O10(II)=O10(II)*R(1)/(F2*FRE)
   73 CONTINUE
      GOT =RR(1)*O1+RR(L)*O2
      GOB =RR(1)**2*O5+RR(L)**2*O6+F2*RR(1)*RR(L)*O7
      GO1=GOT/GOB
      DO 75 I=1,L2
      I1=I+1
      II=I1+L1
      GOT=GOT+RR(I1)*O3(I)+RR(II)*O4(I)
      GOB=GOB+RR(I1)**2*O8(I)+RR(II)**2*O9(I)+F2*RR(I1)*RR(II)*O10(I)
   75 CONTINUE
      GO=GOT/GOB
      GO2=(RR(1)+RR(L))*(RAD**2)/(2.*RK*GOB)
```

```
      WRITE (IPRIN,22) G01,G0,G02
   22 FORMAT (1H0,19HG01(APPROX. COEF.)=,E18.8,5X, 18HG0(FOURIER COEF.)=
     1,E18.8,24HFOURIER COEF.(PT. LOAD)=,E18.8/)
   10 FORMAT (1H0,3HO1=,E18.7)
   11 FORMAT (1H ,3HO2=,E18.7)
   12 FORMAT (1H ,4HO31(,I2,2H)=,E18.7,10X,5HAMAX=,I2)
   13 FORMAT (1H ,4HO32(,I2,2H)=,E18.7,10X,5HAMAX=,I2)
   14 FORMAT (1H ,4HO41(,I2,2H)=,E18.7,10X,5HAMAX=,I2)
   15 FORMAT (1H ,4HO42(,I2,2H)=,E18.7,10X,5HAMAX=,I2)
   16 FORMAT (1H ,3HO5=,E18.7)
   17 FORMAT (1H ,3HO6=,E18.7)
   18 FORMAT (1H ,3HO7=,E18.7)
   19 FORMAT (1H ,3HO8(,I2,2H)=,E18.7)
   20 FORMAT (1H ,3HO9(,I2,2H)=,E18.7)
   21 FORMAT (1H ,4HO10(,I2,2H)=,E18.7)
      R(1)=R(1)/DCOS(Z(1))
      RETURN
      END


C     RESUL   PLATE
      SUBROUTINE RESUL(AA,NN,DD,V,L1,NN1,N1,N2,NMAX,IP,IP1,PI,FRE,G0,VEC
     1,OMEGA,R,ZZ,ICODE,NDLT,DLT,POS,PIN,IA,IOT,IREAD,IPRIN,DAMP)
C     SECTIONAL RESULTANTS
      DIMENSION       VEC(18)
      DIMENSION       FJ(60),FI(60),RJ(9),RI(9),RJ1(9),RI1(9),
     1RJ2(9),RI2(9),RJ3(9),RI3(9)
      DOUBLE PRECISION FJ,FI,RJ,RI,RJ1,RI1,RJ2,RI2,RJ3,RI3,Z,UN,BMRR,
     1BMRO,BMOR,FRN,FON,ARG,RJO,ERR,RIO,C,CJ,CI,DUM,TI,Z1,Z2,Z3,Z4,Z5,Z6
     2,AA,DD,V,FRE,G0,VEC,OMEGA,R,ZZ,DLT,POS,PIN,T,PI,DAMP,OMEDA,DAMM
     3,F1,F2,F3,F4
      F1=1.D0
      F2=2.D0
      F3=3.D0
      F4=4.D0
      ERR=1.D-15
      L=L1+1
      OMEDA=DSQRT(OMEGA**2-DAMP**2)
      DAMM=F1/POS-DAMP
      IF (IOT-1) 60,60,61
   60 IF (ICODE-2) 1,2,3
    1 WRITE (IPRIN,48)
      GO TO 7
    2 WRITE (IPRIN,49)
      GO TO 7
    3 IF (ICODE-4) 4,5,6
    4 WRITE (IPRIN,50)
      GO TO 7
    5 WRITE (IPRIN,51) DAMP
      GO TO 7
    6 WRITE (IPRIN,52) DAMP
    7 WRITE (IPRIN,53)
   61 Z=ZZ*PI/180.D0
      UN=0.D0
      BMRO=0.D0
      BMRR=0.D0
      BMOR=0.D0
      FRN=0.D0
      FON=0.D0
      ARG=FRE*R
      IF (ARG) 54,9,10
    9 WRITE (IPRIN,33)
      UN=(VEC(1)+VEC(L))*G0
      GO TO 21
   10 CALL BESJ(ARG,0,RJO,ERR,IER)
      CALL BESI(ARG,0,RIO,ERR,IER)
      FJ(1)=0.D0
      FI(1)=0.D0
      FJ(2)=AA
      FI(2)=AA
      DO 11 J=1,NN1
```

```
      C=NN-J
      FJ(J+2)=FJ(J+1)*F2*C/ARG-FJ(J)
   11 FI(J+2)=FI(J+1)*F2*C/ARG+FI(J)
      CJ=FJ(N1)/RJO
      CI=FI(N1)/RIO
      DO 14  J=1,NMAX,IP
      K=((J-1)/IP)+1
      K1=N2-J
      RJ(K)=FJ(K1)/CJ
   14 RI(K)=FI(K1)/CI
      K1=N2-2
      RJ1(1)=-FJ(K1)/CJ
      RI1(1)=FI(K1)/CI
      DO 16  J=IP1,NMAX,IP
      K=((J-1)/IP)+1
      K1=N2-J
      RJ1(K)=(FJ(K1+1)-FJ(K1-1))/(F2*CJ)
   16 RI1(K)=(FI(K1-1)+FI(K1+1))/(F2*CI)
      DO 17  J=1,L1
      C=(J-1)*IP
      RJ2(J)=-RJ1(J)/ARG+RJ(J)*((C/ARG)**2-F1)
   17 RI2(J)=-RI1(J)/ARG+RI(J)*((C/ARG)**2+F1)
      DO 18  J=1,L1
      C=(J-1)*IP
      RJ3(J)=-RJ2(J)/ARG+RJ1(J)*((C/ARG)**2-F1+(F1/ARG)**2)-RJ(J)*(F2/
     1ARG)*((C/ARG)**2)
   18 RI3(J)=-RI2(J)/ARG+RI1(J)*((C/ARG)**2+F1+(F1/ARG)**2)-RI(J)*(F2/
     1ARG)*((C/ARG)**2)
      DO 20  J=1,L1
      JJ=L1+J
      C=(J-1)*IP
      UN=UN+
     1    (VEC(J)*RJ(J)+VEC(JJ)*RI(J))*DCOS(C*Z)*G0
      BMRR=BMRR+
     1      DD*(F1-V)*(FRE*(-C/R)*(VEC(J)*RJ1(J)
     2      +VEC(JJ)*RI1(J))+(C/R**2)*(VEC(J)*RJ(J)
     3      +VEC(JJ)*RI(J)))*DSIN(C*Z)*G0
      DUM=DCOS(C*Z)*G0
      BMRO=BMRO-
     1      DD*(FRE**2*(VEC(J)*RJ2(J)+VEC(JJ)*RI2(J))
     2      -V*(C/R)**2*(VEC(J)*RJ(J)+VEC(JJ)*RI(J))
     3      +V*FRE/R*(VEC(J)*RJ1(J)+VEC(JJ)*RI1(J)))*DUM
      BMOR=BMOR+
     1      DD*(-(C/R)**2*(VEC(J)*RJ(J)+VEC(JJ)*RI(J))
     2      +FRE/R*(VEC(J)*RJ1(J)+VEC(JJ)*RI1(J))
     3      +V*FRE**2*(VEC(J)*RJ2(J)+VEC(JJ)*RI2(J)))*DUM
      FRN=FRN-
     1      DD*FRE*(FRE**2*(VEC(J)*RJ3(J)+VEC(JJ)*RI3(J))
     2      +FRE/R*(VEC(J)*RJ2(J)+VEC(JJ)*RI2(J))
     3      -(C/R)**2*(VEC(J)*RJ1(J)+VEC(JJ)*RI1(J)))*DUM
      DUM =DSIN(C*Z)*G0
   20 FON=FON+
     1      DD*C/R*(FRE**2*(VEC(J)*RJ2(J)+VEC(JJ)*RI2(J))
     2      +FRE/R*(VEC(J)*RJ1(J)+VEC(JJ)*RI1(J))
     3      -(C/R)**2*(VEC(J)*RJ(J)+VEC(JJ)*RI(J)))*DUM
   21 TI=0.D0
CICODE=1EXPONENTIAL DECAYING LOAD
CICODE=2LINEARLY DECAYING LOAD
CICODE=3FLAT IMPULSE
CICODE=4DAMPED LINEARLY DECAYING LOAD
CICODE=5DAMPED  EXPONENTIALLY DECAYING LOAD
      DO 22 II=1,NDLT
      IF (ICODE-4) 39,30,31
   30 T=PIN*(F1+F2*DAMP/(OMEGA**2*POS)-TI/POS+DEXP(-DAMP*TI)*(
     1    (-DAMP/OMEDA+((OMEDA**2-   DAMP**2)/(OMEGA**2*OMEDA*POS)))
     2   *DSIN(OMEDA*TI)- (F1+F2*DAMP/(OMEGA**2*POS))*DCOS(OMEDA*TI)))
      GO TO 40
   31 T=  DEXP(-TI/POS)*(OMEGA**2/(DAMM**2+OMEDA**2))*(F1-TI/POS-F2*
     1    DAMM/(POS*(DAMM**2+OMEDA**2))+DEXP(+DAMM*TI)*(DSIN(OMEDA*TI)*
     2 (DAMM/OMEDA+(OMEDA**2-   DAMM**2)/(OMEDA*POS*(DAMM**2+OMEDA**2)))
     3    +DCOS(OMEDA*TI)*(-F1+F2*DAMM/(POS*(DAMM**2+OMEDA**2)))))*PIN
      GO TO 40
   39 IF (ICODE-2) 41,42,43
```

```
41 T    =(PIN*POS**2*OMEGA**2/(F1+(OMEGA*POS)**2)**2)*(DEXP(-TI/POS)*
  1      (-F1-TI/POS+(OMEGA*POS)**2-OMEGA**2*TI*POS)
  2      +F2*OMEGA*POS*DSIN(OMEGA*TI)-(OMEGA*POS)**2*DCOS(OMEGA*TI)
  3      +DCOS(OMEGA*TI))
   GO TO 40
42 T   =PIN*(F1-DCOS(OMEGA*TI)-TI/POS+(F1/(OMEGA*POS))*DSIN(OMEGA*TI))
   GO TO 40
43 T     =PIN*(F1-DCOS(OMEGA*TI))
40 Z1=UN*T
   Z2=BMRR*T
   Z3=BMRO*T
   Z4=BMOR*T
   Z5=FRN*T
   Z6=FON*T
   WRITE (IPRIN,32) TI,R,ZZ,Z1,Z2,Z3,Z4,Z5,Z6
   TI=TI+DLT
22 CONTINUE
32 FORMAT (1X,9E13.5)
33 FORMAT (1H0,14HSINGULAR POINT)
48 FORMAT (1H0,27HEXPONENTIALLY DECAYING LOAD)
49 FORMAT (1H0,22HLINEARLY DECAYING LOAD)
50 FORMAT (1H0,12HFLAT IMPULSE)
51 FORMAT (1H0,46HDAMPED LINEARLY DECAYING LOAD VISCOUS DAMPING=,
  1E12.5)
52 FORMAT (1H0,51HDAMPED EXPONENTIALLY DECAYING LOAD VISCOUS DAMPING=
  1,E12.5)
53 FORMAT (1H1,3X,10HTIME(SEC.),5X,6HRADIUS,8X,5HANGLE,8X,5HUN(I),6X,
  17HBMRR(I),6X,7HBMRO(I),6X,7HBMOR(I),7X,6HFRN(I),7X,6HFON(I),/)
54 RETURN
   END
```

C.2 Shell Program

The shell digital computer program calculates the symmetric eigenvalues, eigenvectors, modal participation functions for uniformly distributed and central point loads, transverse displacements and sectional resultants vs. time including viscous damping effects for shallow spherical shells with regular polygonal boundaries subjected to various idealized transient load shapes and the elastically clamped homogeneous edge condition Eqs. (3.22) and (3.24).

The program has been written for the University of Alberta IBM 360/67 digital computer using double precision computation. The free vibration part of the program has been modified for use on the DRES IBM 1130 computer. Since the boundary equation elements are in dimensional form in this program, ill-conditioning results from the presence of terms of the form r^n as well as from the higher orders of the Bessel functions J_{pn} and I_{pn}.

Other programs used on the DRES IBM 1130 in the plate analysis and mentioned in Appendix C.1 were modified for the shell analysis as well. In addition, a program calculating the functions $\bar{g}^\ell$ and $\bar{h}^\ell$ associated with the nonhomogeneous time-dependent edge conditions, Eqs. (3.21) and (3.23), has been written for the IBM 1130. These programs are not included.

The shell program compilation from the Fortran source deck, which uses approximately 84,000 core bytes, program listing and formation of an object deck require a total of 3.6 minutes execution time on the IBM 360/67. Program execution on the IBM 360/67 for the complete solution of one mode of vibration requires approximately one minute for a solution using three collocation points and two minutes for a solution using five collocation points. Accurate execution times for different solutions are not known since a solution using five collocation points took as long as 4.25 minutes when the computer monitor was at level 13 and as little as 1.15 minutes when the monitor was at level 16.

A typical data set which causes the program to search for one symmetric mode of vibration of a simply supported shell with 12 sides and solve the undamped modal response at three positions on the shell surface for an exponentially decaying blast load is listed by card number below:

```
Data
Card

 1   12  97.5E-323267.2E-3   37.5E-2   3.3E-1    1.0E+7    64.0E+0

 2      1.E-50   50

 3      4  2.0  7.0 11.0 15.0

 4      0.1E-1    3.0E-1    0.2E-1   0.5E-6

 5    6  1.0E-10   0.0E+00   0.0E+00

 6    36 20 20

 7    3

 8       0.0E+0

 9       1.0E+0

10    1 50    0.2E-4  30.0E-3+10.0

11    1

12    3

13        0.000     0.000

14        5.000     0.000

15       22.476     0.000

16   99
```

The data correlation to the general shell vibration problem follows the explanation given for plate data in Table C.1 except for the modifications which are given in Table C.3.

The edge conditions $\frac{\partial F(\tilde{\rho},\tilde{\theta})}{\partial v} = 0$ and $\frac{\partial F(\tilde{\rho},\tilde{\theta})}{\partial s} = 0$ which are employed when data {5a} = 3, 4, 5 or 7, were postulated by Oniashvili [88] to represent vanishing

in-plane displacements perpendicular and tangential to the shell edge, respectively. Satisfaction of these edge conditions did not yield satisfactory fundamental frequencies for clamped shells with 12 and 15-sided polygonal boundaries.

Table C.3

Modifications of Plate Computer Data for Shells

Data Card	Number	Format	Use
1	g	E10.1	Radius of curvature of shell middle surface R (in.)
2	b	I5	Number of terms calculated in backward recurrence series; should be $\geq p(L-1) + 11$
3	b,... ({3a} numbers)	F5.1	θ locations of boundary collocation points (deg.). Program is dimensioned for $L \leq 7$
5	a	I2	Number designating shell homogeneous edge conditions to be satisfied; $=1 \equiv \eta = M_{vs} - \beta_1 \partial\eta/\partial v = F_{vv} = F_{vs} - \beta_2 \varepsilon_{ss} = 0$ $=2 \equiv \eta = M_{vs} = F_{vv} = F_{vs} - \beta_2 \varepsilon_{ss} = 0$ $=3 \equiv \eta = M_{vs} - \beta_1 \partial\eta/\partial v = \partial F/\partial v = \varepsilon_{ss} = 0$ $=4 \equiv \eta = M_{vs} - \beta_1 \partial\eta/\partial v = \partial F/\partial s + \partial F/\partial v = \varepsilon_{ss} = 0$ $=5 \equiv \eta = M_{vs} - \beta_1 \partial\eta/\partial v = \partial F/\partial s - \partial F/\partial v = \varepsilon_{ss} = 0$ $=6 \equiv \eta = M_{vs} - \beta_1 \partial\eta/\partial v = F_{vs} = \varepsilon_{ss} = 0$ $=7 \equiv \eta = M_{vs} - \beta_1 \partial\eta/\partial v = \partial F/\partial v = \partial F/\partial s = 0$ If $\beta_1 = 0$ in {5b} when {5a} = 1, 3, 4, 5, 6, or 7, then edge condition M_{vs} is not computed.

Table C.3 (continued)

Data Card	Number	Format	Use
5	d	E10.1	Edge clamping factor β_2^i(lb./in.)
7	b	I2	=1≡ enter subroutine NONDIS and search for a determinant value which becomes progressively smaller in magnitude but does not change sign =0≡ do not enter subroutine NONDIS

The shell program mainline routine and subroutines perform the same functions as the plate routines with the same names as outlined in Table C.2 and the shell program execution essentially follows the flow diagram for plates shown in Fig. C.1. In order to accommodate the shell program on the IBM 360/67 it was necessary to divide the subroutine BLOND into five shorter subroutines called BLOND, BLOND2, BLOND3, BLOND4, and BLOND5, and the subroutine FOURI into two shorter subroutines called FOURI and FOURI2. One additional subroutine NONDIS was written for the shell program. This routine is entered only when data {7b} = 1. It searches for eigenvalues for which the determinant value magnitude becomes progressively smaller but does not change in sign. This routine was used in an unsuccessful attempt to find eigenvalues for clamped shells

using the edge conditions of vanishing in-plane displacements as postulated by Oniashvili.

The shell computer output is labelled appropriately with the exception that the values of O1 to O12 and O13 to O18 refer to the modal participation coefficients ϕ_7 through ϕ_{18} and ϕ_1 through ϕ_6, respectively.

The Fortran source program, except for the subroutines BESJ, BESI and SIMP which are unchanged from the plate program, is listed below:

```
C    VIBRA    SHELL
C     VIBRATIONS OF POLYGONAL SHELLS
      DIMENSION R(7),Z(7),ZZ(7),RR(27),A(27,27)
      COMMON DENS,RAD,TH,V,EF,Z,ZZ,RR,DD,FRE,AA,RK,R,ROE,DET1,DET,FRE1,
     1DELF,ACC,FREMX,FREI,DETI,DELFI,G0,G01,PI,OMEGA,CT,SR,BB,BETA,DAMP,
     2BETA2,
     3L,NN,NN1,N1,N2,IP,IP1,L1,LL1,LL2,LL3,NMAX,NCOND,NI,NIA,NIB,L2,IENT
     4,IREAD,IPRIN,NDIST
      DOUBLE PRECISION DENS,RAD,TH,V,EF,Z,ZZ,RR,DD,FRE,AA,RK,R,ROE,DET1,
     1DET,FRE1,DELF,ACC,FREMX,FREI,DETI,DELFI,G0,G01,PI,A,OMEGA,CT,SUM1,
     2SUM2,DEL,DLT,POS,PIN,RA,ZZZ,SR1,SR,BB,BETA,DAMP,BETA2
      IREAD=5
      IPRIN=6
   18 CALL INPUT (SR1)
      ISENS=2
      IF (NDIST-1) 101,102,101
  102 CALL NONDIS
      GO TO 35
  101 IF (IENT-2) 19,35,19
   19 CALL BLOND(A)
      CALL BLONI (A,RR,FRE,DET,LL1,LL2,OMEGA,CT,ISENS,IPRIN,BB,L,DAMP,
     1RAD)
      IF (DET-0.D0) 20,11,20
   11 CT=CT*1.D+2
      GO TO 19
   20 IF (FRE-FREMX)21,21,39
   21 CALL BLOND(A)
      CALL BLONI (A,RR,FRE,DET,LL1,LL2,OMEGA,CT,ISENS,IPRIN,BB,L,DAMP,
     1RAD)
      IF (FRE-FREMX)22,22,39
   22 SUM1=DABS(DET1-DET)
      SUM2=DABS(DET1+DET)
      IF (SUM1-SUM2)21,23,23
   23 FREI=FRE
      DETI=DET
      DELFI=DELF
      FRE=FRE1
      IF (DET1)24,24,30
   24 DELF=DELF/2.D0
      CALL BLOND(A)
      CALL BLONI (A,RR,FRE,DET,LL1,LL2,OMEGA,CT,ISENS,IPRIN,BB,L,DAMP,
     1RAD)
      IF (DELF-ACC)36,36,25
   25 IF (DET)24,24,26
   26 FRE=FRE1
      GO TO 24
   30 DELF=DELF/2.D0
      CALL BLOND(A)
      CALL BLONI (A,RR,FRE,DET,LL1,LL2,OMEGA,CT,ISENS,IpRIN,BB,L,DAMP,
     1RAD)
      IF (DELF-ACC) 36,36,31
   31 IF (DET) 32,30,30
   32 FRE=FRE1
      GO TO 30
   36 IF (IENT-2) 57,35,35
   35 DELF=0.D0
      CALL BLOND(A)
      DAMP=DAMP*OMEGA
      ISENS=1
      CALL BLONI (A,RR,FRE,DET,LL1,LL2,OMEGA,CT,ISENS,IPRIN,BB,L,DAMP,
     1RAD)
   41 IF(G0-0.D0)71,37,71
   71 WRITE (IPRIN,72) G0
   72 FORMAT (1H0,20HFOURIER COEFFICIENT=,E12.5,/)
      GO TO 38
   37 CALL FOURI(SR1)
   38 G0=G0/(ROE*OMEGA**2)
      READ(IREAD,1) ICODE,NDLT,DLT,POS,PIN
    1 FORMAT (I2,I3,2E10.1,F5.2)
      WRITE (IPRIN,61) PIN,POS
   61 FORMAT (1H0,13HREFL. PRESS.=,F6.2,10X,10HPOS. DUR.=,E10.2)
      READ (IREAD,1) IOT
      READ (IREAD,1) NPT
```

```
      DO 50 I=1,NPT
      READ (IREAD,52) RA,ZZZ
      CALL  RESUL (AA,NN,DD,V,L1,NN1,N1,N2,NMAX,IP,IP1,PI,FRE,
     1G0,RR,OMEGA,RA,ZZZ,ICODE,NDLT,DLT,POS,PIN,I,IOT,BB,SR,EF,TH,
     2IREAD,IPRIN,DAMP)
   50 CONTINUE
   52 FORMAT  (2F10.3)
   57 IF (FRE-FREMX) 58,58,39
   58 FRE=FREI
      DET=DETI
      DELF=DELFI
      CT=CT*1.D-1
      G0=0.D0
      GO TO 19
   39 READ (IREAD,1) IST
      IF (IST-99) 18,40,40
   40 STOP
      END


C     INPUT    SHELL
      SUBROUTINE INPUT(SR1)
      DIMENSION R(7),Z(7),ZZ(7),RR(27)
      COMMON DENS,RAD,TH,V,EF,Z,ZZ,RR,DD,FRE,AA,RK,R,ROE,DET1,DET,FRE1,
     1DELF,ACC,FREMX,FREI,DETI,DELFI,G0,G01,PI,OMEGA,CT,SR,BB,BETA,DAMP,
     2BETA2,
     3L,NN,NN1,N1,N2,IP,IP1,L1,LL1,LL2,LL3,NMAX,NCOND,NI,NIA,NIB,L2,IENT
     4,IREAD,IPRIN,NDIST
      DOUBLE PRECISION DENS,RAD,TH,V,EF,Z,ZZ ,RR,DD,FRE,AA,RK,R,ROE,ACC,
     1FREMX,FREI,DETI,DELFI,G0,G01,PI,OMEGA,CT,SR,BB,   GR,DET1,DET,
     2FRE1,DELF,BETA,DAMP,SR1,BETA2
      READ(IREAD,1) IP,DENS,RAD,TH,V,EF,SR
    1 FORMAT  (I2,6E10.1)
      READ (IREAD,2) AA,NN
    2 FORMAT (E10.0,I5)
      READ(IREAD,3) L,(ZZ(I),I=1,L)
    3 FORMAT (I5,15F5.1)
      READ (IREAD,4) FRE,FREMX,DELF,ACC
    4 FORMAT (4E10.1)
      READ (IREAD,1) NCOND,BETA,DAMP,BETA2
      READ (IREAD,5) NI,NIA,NIB
      READ (IREAD,15) IENT,NDIST
   15 FORMAT (2I2)
      READ (IREAD,2) G0
      READ (IREAD,2) CT
    5 FORMAT (3I3)
      IF (NCOND-2) 6,7,8
    6 WRITE (IPRIN,21)
      GO TO 9
    7 WRITE (IPRIN,22)
      GO TO 9
    8 WRITE (IPRIN,23)
      IF (NCOND-4) 16,17,18
   16 WRITE (IPRIN,24)
      GO TO 9
   17 WRITE (IPRIN,25)
      GO TO 9
   18 IF (NCOND-6) 19,30,31
   19 WRITE (IPRIN,26)
      GO TO 9
   30 WRITE (IPRIN,27)
      GO TO 9
   31 WRITE (IPRIN,28)
    9 RK=IP
      PI=3.141592653589793
      NN1=NN-1
      N1=NN+1
      N2=NN+2
      GR=32.2D0*12.D0
      NMAX=(L-1)*IP+1
      IP1=IP+1
```

```
      L1=L-1
      L2=L-2
      LL1=4*L-1
      LL2=4*L-2
      LL3=4*L-3
      DD=EF*TH**3/(12.D0*(1.D0-(V**2)))
      ROE=DENS*TH/GR
      SR1 =RAD*DCOS(PI/RK)
      WRITE (IPRIN,10)
   10 FORMAT (1H0,4X,5HSIDES,9X,7HDENSITY,9X,6HRADIUS,7X,9HTHICKNESS,
     14X,58HPOISSON RATIO YOUNG MODULUS FLEX RIGIDITY SPHERICAL RADIUS)
      WRITE (IPRIN,11) IP,DENS,RAD,TH,V,EF,DD,SR
   11 FORMAT (6X,I2,3X,7E15.5//)
      WRITE (IPRIN,12) L,(ZZ(I),I=1,L)
   12 FORMAT (1H0,10HCOL. PTS.=,I2,5X,13HANGLES(DEG.)=,15F5.1)
      WRITE (IPRIN,13) AA,NN,BETA,DAMP,BETA2
   13 FORMAT (1H0,3HAA=,E10.1,10X,19HSTART OF BACK REC.=,I5,5X,
     114HCLAMPING BETA=,E10.2,5X,15HDAMPING FACTOR=,E12.5,/,
     25X,21HSTRAIN CLAMPING BETA=,E10.2)
      WRITE (IPRIN,14) NI,NIA,NIB
   14 FORMAT (1H0,3HNI=,I3,10X,4HNIA=,I3,10X,4HNIB=,I3)
      DO 20 I=1,L
      Z(I)=ZZ(I)*PI/180.D0
   20 R(I)=SR1 /DCOS(Z(I))
   21 FORMAT (1H1,5X,30HCLAMPED   SHELL   ON   ROLLERS)
   22 FORMAT (1H1,5X,41HSIMPLY   SUPPORTED   SHELL   ON   ROLLERS)
   23 FORMAT (1H1,5X,23H  FULLY  CLAMPED  SHELL)
   24 FORMAT (1H0,5X, 46HB.C.=TR. DISP.,SLOPE,NORM. DISP.,TANG. STR. =0)
   25 FORMAT (1H0,5X, 52HB.C.=TR. DISP.,SLOPE,TANG.+NORM. DISP.,TANG. ST
     1R. =0)
   26 FORMAT (1H0,5X, 52HB.C.=TR. DISP.,SLOPE,TANG.-NORM. DISP.,TANG. ST
     1R. =0)
   27 FORMAT (1H0,5X, 46HB.C.=TR. DISP.,SLOPE,TANG. SHEAR,TANG. STR. =0)
   28 FORMAT (1H0,5X, 46HB.C.=TR. DISP.,SLOPE,NORM. DISP.,TANG. DIS. =0)
      RETURN
      END


      SUBROUTINE  NONDIS
C   NONDISTINCT ROOTS  ENTERED WHEN NDIST=1
      DIMENSION R(7),Z(7),ZZ(7),RR(27),A(27,27)
      COMMON DENS,RAD,TH,V,EF,Z,ZZ,RR,DD,FRE,AA,RK,R,ROE,DET1,DET,FRE1,
     1DELF,ACC,FREMX,FREI,DETI,DELFI,G0,G01,PI,OMEGA,CT,SR,BB,BETA,DAMP,
     2BETA2,
     3L,NN,NN1,N1,N2,IP,IP1,L1,LL1,LL2,LL3,NMAX,NCOND,NI,NIA,NIB,L2,IENT
     4,IREAD,IPRIN,NDIST
      DOUBLE PRECISION DENS,RAD,TH,V,EF,Z,ZZ,RR,DD,FRE,AA,RK,R,ROE,DET1,
     1DET,FRE1,DELF,ACC,FREMX,FREI,DETI,DELFI,G0,G01,PI,A,OMEGA,CT,SUM1,
     2SUM2,DEL,DLT,POS,PIN,RA,ZZZ,SR1,SR,BB,DET2,BETA,DAMP,BETA2
      ISENS=2
      FREI=FRE
      DETI=DET
      DELFI=DELF
    1 CALL BLOND(A)
      CALL BLONI (A,RR,FRE,DET,LL1,LL2,OMEGA,CT,ISENS,IPRIN,BB,L,DAMP)
      IF (DET) 3,2,3
    2 CT=CT*1.E+2
      FRE=FRE-DELF
      GO TO 1
    3 DELF=DELF/10.D0
      DO 6 I=1,10
      DET2=DET1
      CALL BLOND(A)
      CALL BLONI (A,RR,FRE,DET,LL1,LL2,OMEGA,CT,ISENS,IpRIN,BB,L)
      IF (DABS(DET)-DABS(DET1)) 6,7,8
    6 CONTINUE
    7 FRE=FRE1
      DET=DET1
      GO TO 3
    8 FRE=FRE1-DELF
      DET=DET2
      DELF=2.D0*DELF
```

```
      IF (DELF-ACC) 10,3,3
   10 RETURN
      END



C    BLOND      SHELL
      SUBROUTINE BLOND(A)
      DIMENSION  ARG(7),                      RJ(7,7),RI(7,7),RJ1(7,7),
     1 RI1(7,7),RJ2(7,7),RI2(7,7)
      DIMENSION R(7),Z(7),ZZ(7),RR(27),A(27,27)
      COMMON DENS,RAD,TH,V,EF,Z,ZZ,RR,DD,FRE,AA,RK,R,ROE,DET1,DET,FRE1,
     1DELF,ACC,FREMX,FREI,DETI,DELFI,G0,G01,PI,OMEGA,CT,SR,BB,BETA,DAMP,
     2BETA2,
     3L,NN,NN1,N1,N2,IP,IP1,L1,LL1,LL2,LL3,NMAX,NCOND,NI,NIA,NIB,L2,IENT
     4,IREAD,IPRIN,NDIST
      DOUBLE PRECISION DENS,RAD,TH,V,EF,Z,ZZ,RR,DD,FRE,AA,RK,R,ROE,DET1,
     1DET,FRE1,DELF,ACC,FREMX,FREI,DETI,DELFI,G0,G01,PI,OMEGA,CT,SR,BB,
     2ARG,FJ,FI,RJ,RI,RJ1,RI1,RJ2,RI2,RJO,RIO,C,CJ,CI,C1,C2,A,ERR,BETA,
     3DAMP,BETA2,DUM
     4,F1,F2,F3,F4
C   NCOND=1  NORMAL SLOPE + BENDING MOMENT TRANSVERSE DISPLACEMENT NORMAL
C            FORCE TANGENTIAL STRAIN + SHEAR  =0
C   NCOND=2  TANGENTIAL BENDING MOMENT TRANSVERSE DISPLACEMENT NORMAL
C            FORCE TANGENTIAL STRAIN + SHEAR  =0
C   NCOND=3  NORMAL SLOPE TRANSVERSE DISPLACEMENT NORMAL DISPLACEMENT
C            TANGENTIAL STRAIN  =0
C   NCOND=4  NORMAL SLOPE TRANSVERSE DISPLACEMENT TANG.+NORM. DISP.,
C            TANGENTIAL STRAIN  =0
C   NCOND=5  NORMAL SLOPE TRANSVERSE DISPLACEMENT TANG.-NORM. DISP.,
C            TANGENTIAL STRAIN  =0
C   NCOND=6  NORMAL SLOPE TRANSVERSE DISPLACEMENT TANGENTIAL SHEAR
C            TANGENTIAL STRAIN  =0
C   NCOND=7  NORMAL SLOPE TRANSVERSE DISPLACEMENT NORMAL DISPLACEMENT
C            TANGENTIAL DISPLACEMENT  =0
      F1=1.D0
      F2=2.D0
      F3=3.D0
      F4=4.D0
      FRE1=FRE
      DET1=DET
      FRE=FRE+DELF
      OMEGA=DSQRT((FRE**4+EF*TH/(DD*SR**2))*DD/ROE)
      BB=F1/(ROE*SR*OMEGA**2)
      ERR=1.D-15
      CALL BLOND2 (ERR,RJ,RI,RJ1,RI1,RJ2,RI2)
      IF (NCOND-2) 10,13,10
   10 J=1
      J1=J+L
      J2=J1+L
      DO 11 I=1,L
      A(I,J) =-(FRE**3)*RJ1(I,J)*DCOS(Z(I))
      A(I,J1)= (FRE**3)*RI1(I,J)*DCOS(Z(I))
   11 A(I,J2) = 0.0D0
      DO 12 I=1,L
      DO 12 J=2,L
      C=IP*(J-1)
      C1=C-1.D0
      J1=J+L
      J2=J1+L
      J3=J2+L1
      A(I,J) = -(FRE**3)*RJ1(I,J)*DCOS(Z(I))*DCOS(C*Z(I))
     1         -(FRE**2)*(C/R(I))*RJ(I,J)*DSIN(Z(I))*DSIN(C*Z(I))
      A(I,J1) =  (FRE**3)*RI1(I,J)*DCOS(Z(I))*DCOS(C*Z(I))
     1         +(FRE**2)*(C/R(I))*RI(I,J)*DSIN(Z(I))*DSIN(C*Z(I))
      A(I,J2) = F4 *BB*C*(C+F1 )*R(I)**C1*(DCOS(Z(I))*DCOS(C*Z(I))
     1          +DSIN(Z(I))*DSIN(C*Z(I)))
   12 A(I,J3) = 0.0D0
      IF (BETA) 13,16,13
   13 J=1
      J1=J+L
      J2=J1+L
      DO 14 I=1,L
```

```
      A(I,J)=A(I,J)*BETA/DD-
     1        (FRE**4*RJ2(I,J)+V*(FRE**3/R(I))*RJ1(I,J))*(DCOS(Z(I)))**2
     2       -(V*FRE**4*RJ2(I,J)+(FRE**3/R(I))*RJ1(I,J))*(DSIN(Z(I)))**2
      A(I,J1)=A(I,J1)*BETA/DD
     1        +((FRE**4*RI2(I,J)+V*(FRE**3/R(I))*RI1(I,J))*(DCOS(Z(I)))
     2 **2+(V*FRE**4*RI2(I,J)+(FRE**3/R(I))*RI1(I,J))*(DSIN(Z(I)))**2)
   14 A(I,J2) = 0.0D0
      DO 15 I=1,L
      DO 15 J=2,L
      C=IP*(J-1)
      C1=C-1.D0
      C2=C-2.D0
      J1=J+L
      J2=J1+L
      J3=J2+L1
      DUM=   -(-(F1-V)*(( C/R(I)  **2)*RJ(I,J)-FRE*(C/R(I))*RJ1(I,J))*
     1        DSIN(F2 *Z(I))*DSIN(C*Z(I)))  *FRE**2
      A(I,J)=A(I,J)*BETA/DD-
     1         FRE**2*((FRE**2*RJ2(I,J)-V*(C/R(I))**2*RJ(I,J)+V*(FRE/R(I
     2         ))*RJ1(I,J))*(DCOS(Z(I)))**2*DCOS(C*Z(I))
     3       +(V*FRE**2*RJ2(I,J)-(C/R(I))**2*RJ(I,J)+(FRE/R(I))*RJ1(I,J)
     4        )*(DSIN(Z(I)))**2*DCOS(C*Z(I)))+DUM
      DUM=  -((F1-V)*(( C/R(I)  **2)*RI(I,J)-FRE*(C/R(I))*RI1(I,J))*
     1        DSIN(F2 *Z(I))*DSIN(C*Z(I)))*FRE**2
      A(I,J1)=A(I,J1)*BETA/DD
     1        +FRE**2*((FRE**2*RI2(I,J)-V*(C/R(I))**2*RI(I,J)+V*(FRE/R(I
     2         ))*RI1(I,J))*(DCOS(Z(I)))**2*DCOS(C*Z(I))
     3       +(V*FRE**2*RI2(I,J)-(C/R(I))**2*RI(I,J)+(FRE/R(I))*RI1(I,J)
     4        )*(DSIN(Z(I)))**2*DCOS(C*Z(I)))+DUM
      A(I,J2)=A(I,J2)*BETA/DD
     1          +F4 *BB*(F1 -V)*C*(C**2-F1)*R(I)**C2*(((DCOS(Z(I)))**2-
     2       (DSIN(Z(I)))**2)*DCOS(C*Z(I))+DSIN(F2*Z(I))*DSIN(C*Z(I)))
   15 A(I,J3) = 0.0D0
   16 J=1
      J1=J+L
      J2=J1+L
      DO 17 I=1,L
      I1=I+L
      I2=I1+L
      I3=I2+L
      A(I1,J) = -(FRE**2)*RJ(I,J)
      A(I1,J1)=  (FRE**2)*RI(I,J)
      A(I1,J2)= F4 *BB
   17 CONTINUE
      DO 19 J=2,L
      C=IP*(J-1)
      C1=C-1.D0
      C2=C-2.D0
      J1=J+L
      J2=J1+L
      J3=J2+L1
      DO 19 I=1,L
      I1=I+L
      I2=I1+L
      I3=I2+L
      A(I1,J) = -(FRE**2)*RJ(I,J)*DCOS(C*Z(I))
      A(I1,J1)=  (FRE**2)*RI(I,J)*DCOS(C*Z(I))
      A(I1,J2)= F4 *BB*(C+F1 )*R(I)**C*DCOS(C*Z(I))
      A(I1,J3)= 0.0D0
   19 CONTINUE
      IF (NCOND-6) 44,43,44
   43 CALL BLOND5(RJ,RI,RJ1,RI1,RJ2,RI2,A)
      GO TO 45
   44 J=1
      J1=J+L
      J2=J1+L
      DO 31 I=1,L
      I1=I+L
      I2=I1+L
      I3=I2+L
      IF (NCOND-2) 41,41,42
   41 A(I2,J) =(EF*TH/SR)*((FRE/R(I))*RJ1(I,J)*(DCOS(Z(I)))**2
```

```
     1          +FRE**2*RJ2(I,J)*(DSIN(Z(I)))**2)
      A(I2,J1)=(EF*TH/SR)*((FRE/R(I))*RI1(I,J)*(DCOS(Z(I)))**2
     1          +FRE**2*RI2(I,J)*(DSIN(Z(I)))**2)
      A(I2,J2)= 2.D0
      GO TO 31
   42 A(I2,J) = (FRE*RJ1(I,J)*DCOS(Z(I)))*EF*TH/SR
      A(I2,J1) = (FRE*RI1(I,J)*DCOS(Z(I)))*EF*TH/SR
      A(I2,J2) = F2*R(I)*DCOS(Z(I))
   31 CONTINUE
   45 CALL BLOND3 (RJ,RI,RJ1,RI1,RJ2,RI2,A)
   40 RETURN
      END


      SUBROUTINE BLOND2 (ERR,     RJ,RI,RJ1,RI1,RJ2,RI2)
      DIMENSION R(7),Z(7),ZZ(7),RR(27)
      DIMENSION  ARG(7),FJ(60),FI(60),RJ(7,7),RI(7,7),RJ1(7,7),
     1 RI1(7,7),RJ2(7,7),RI2(7,7)
      COMMON DENS,RAD,TH,V,EF,Z,ZZ,RR,DD,FRE,AA,RK,R,ROE,DET1,DET,FRE1,
     1DELF,ACC,FREMX,FREI,DETI,DELFI,G0,G01,PI,OMEGA,CT,SR,BB,BETA,DAMP,
     2BETA2,
     3L,NN,NN1,N1,N2,IP,IP1,L1,LL1,LL2,LL3,NMAX,NCOND,NI,NIA,NIB,L2,IENT
     4,IREAD,IPRIN,NDIST
      DOUBLE PRECISION DENS,RAD,TH,V,EF,Z,ZZ,RR,DD,FRE,AA,RK,R,ROE,DET1,
     1DET,FRE1,DELF,ACC,FREMX,FREI,DETI,DELFI,G0,G01,PI,OMEGA,CT,SR,BB,
     2ARG,FJ,FI,RJ,RI,RJ1,RI1,RJ2,RI2,RJ0,RI0,C,CJ,CI,C1,C2,A,ERR,BETA,
     3DAMP,BETA2
     4,F1,F2,F3
      F1=1.D0
      F2=2.D0
      F3=3.D0
      DO 6 I=1,L
      ARG(I)=FRE*R(I)
      CALL BESJ(ARG(I),0,RJ0,ERR,IER)
      CALL BESI(ARG(I),0,RI0,ERR,IER)
      FJ(1)=0.D0
      FI(1)=0.D0
      FJ(2)=AA
      FI(2)=AA
      DO 2 J=1,NN1
      C=NN-J
      FJ(J+2)=FJ(J+1)*F2*C/ARG(I)-FJ(J)
    2 FI(J+2)=FI(J+1)*F2*C/ARG(I)+FI(J)
      CJ=FJ(N1)/RJ0
      CI=FI(N1)/RI0
      DO 4 J=1,NMAX,IP
      K=((J-1)/IP)+1
      K1=N2-J
      RJ(I,K)=FJ(K1)/CJ
    4 RI(I,K)=FI(K1)/CI
      K1=N2-2
      RJ1(I,1)=-FJ(K1)/CJ
      RI1(I,1)= FI(K1)/CI
      DO 5 J=IP1,NMAX,IP
      K=((J-1)/IP)+1
      K1=N2-J
      RJ1(I,K)=(FJ(K1+1)-FJ(K1-1))/(F2*CJ)
    5 RI1(I,K)=(FI(K1-1)+FI(K1+1))/(F2*CI)
      DO 6 J=1,L
      C=(J-1)*IP
      RJ2(I,J)=-RJ1(I,J)/ARG(I)+RJ(I,J)*((C/ARG(I))**2-F1)
    6 RI2(I,J)=-RI1(I,J)/ARG(I)+RI(I,J)*((C/ARG(I))**2+F1)
      RETURN
      END


      SUBROUTINE  BLOND3 (RJ,RI,RJ1,RI1,RJ2,RI2,A)
      DIMENSION  ARG(7),              RJ(7,7),RI(7,7),RJ1(7,7),
     1 RI1(7,7),RJ2(7,7),RI2(7,7)
      DIMENSION R(7),Z(7),ZZ(7),RR(27),A(27,27)
      COMMON DENS,RAD,TH,V,EF,Z,ZZ,RR,DD,FRE,AA,RK,R,ROE,DET1,DET,FRE1,
```

```
  1DELF,ACC,FREMX,FREI,DETI,DELFI,G0,G01,PI,OMEGA,CT,SR,BB,BETA,DAMP,
  2BETA2,
  3L,NN,NN1,N1,N2,IP,IP1,L1,LL1,LL2,LL3,NMAX,NCOND,NI,NIA,NIB,L2,IENT
  4,IREAD,IPRIN,NDIST
   DOUBLE PRECISION DENS,RAD,TH,V,EF,Z,ZZ,RR,DD,FRE,AA,RK,R,ROE,DET1,
  1DET,FRE1,DELF,ACC,FREMX,FREI,DETI,DELFI,G0,G01,PI,OMEGA,CT,SR,BB,
  2ARG,FJ,FI,RJ,RI,RJ1,RI1,RJ2,RI2,RJ0,RI0,C,CJ,CI,C1,C2,A,ERR,BETA,
  3DAMP,BETA2,DUM
  4,F1,F2,F3,F4
   F1=1.D0
   F2=2.D0
   F3=3.D0
   F4=4.D0
   IF (NCOND-6) 41,8,41
41 DO 32 I=1,L
   I1=I+L
   I2=I1+L
   I3=I2+L
   DO 32 J=2,L
   C=IP*(J-1)
   C1=C-1.D0
   J1=J+L
   J2=J1+L
   J3=J2+L1
   IF (NCOND-2)43,43,44
43 A(I2,J) =  (EF*TH/SR)*(((FRE/R(I))*RJ1(I,J)-(C/R(I))**2*RJ(I,J))
  1           *(DCOS(Z(I)))**2*DCOS(C*Z(I))
  2           +FRE**2*RJ2(I,J)*(DSIN(Z(I)))**2*DCOS(C*Z(I))
  3           +((C   /R(I)**2)*RJ(I,J)-(C*FRE/R(I))*RJ1(I,J))*
  4           DSIN(F2*Z(I))*DSIN(C*Z(I)))
   A(I2,J1) =  (EF*TH/SR)*(((FRE/R(I))*RI1(I,J)-(C/R(I))**2*RI(I,J))
  1            *(DCOS(Z(I)))**2*DCOS(C*Z(I))
  2            +FRE**2*RI2(I,J)*(DSIN(Z(I)))**2*DCOS(C*Z(I))
  3           +((C   /R(I)**2)*RI(I,J)-(C*FRE/R(I))*RI1(I,J))*
  4            DSIN(F2*Z(I))*DSIN(C*Z(I)))
   C2=C-2.D0
   A(I2,J2) = R(I)**C*((C+F2-C**2)*(DCOS( Z(I)))**2*DCOS(C*Z(I))
  1          +(C+F2)*(C+F1)*(DSIN(Z(I)))**2*DCOS(C*Z(I))
  2        -C*(C+F1)*DSIN(F2*Z(I))*DSIN(C*Z(I)))
   A(I2,J3) =-C*C1*R(I)**C2*(((DCOS(Z(I)))**2-(DSIN(Z(I)))**2)
  1           *DCOS(C*Z(I))+DSIN(F2*Z(I))*DSIN(C*Z(I)))
   GO TO 32
44 A(I2,J)=(FRE*RJ1(I,J)*DCOS(Z(I))*DCOS(C*Z(I))+(C/R(I))*RJ(I,J)*
  1DSIN(Z(I))*DSIN(C*Z(I)))*EF*TH/SR
   A(I2,J1)=(FRE*RI1(I,J)*DCOS(Z(I))*DCOS(C*Z(I))+(C/R(I))*RI(I,J)*
  1DSIN(Z(I))*DSIN(C*Z(I)))*EF*TH/SR
   C2=C+1.D0
   A(I2,J2)= ((C+F2)*DCOS(Z(I))*DCOS(C*Z(I))+C*DSIN(Z(I))*
  1DSIN(C*Z(I)))*R(I)**C2
   A(I2,J3)= (DCOS(Z(I))*DCOS(C*Z(I))+DSIN(Z(I))*DSIN(C*Z(I)))*C*
  1R(I)**C1
32 CONTINUE
   IF (NCOND-3) 8,8,6
 6 IF (NCOND-5) 7,7,8
 7 CALL BLOND4 (RJ,RI,RJ1,RI1,RJ2,RI2,A)
 8 J=1
   J1=J+L
   J2=J1+L
   J3=J2+L1
   IF (NCOND-6) 33,33,34
33 DO 18 I=1,L1
   I1=I+L
   I2=I1+L
   I3=I2+L
   A(I3,J)  =(EF*TH/SR)*(((FRE/R(I))*RJ1(I,J)-V*FRE**2*RJ2(I,J))*
  1         (DSIN(Z(I)))**2
  2         +(FRE**2*RJ2(I,J)-V*(FRE/R(I))*RJ1(I,J))*(DCOS(Z(I)))**2)
   A(I3,J1)=  (EF*TH/SR)*(((FRE/R(I))*RI1(I,J)-V*FRE**2*RI2(I,J))
  1         *(DSIN(Z(I)))**2
  2         +(FRE**2*RI2(I,J)-V*(FRE/R(I))*RI1(I,J))*(DCOS(Z(I)))**2)
   A(I3,J2)= F2*(F1-V)
18 CONTINUE
   GO TO 36
```

```
34 DO 35 I=1,L1
   I1=I+L
   I2=I1+L
   I3=I2+L
   A(I3,J) =(FRE*RJ1(I,J)*DSIN(Z(I)))*EF*TH/SR
   A(I3,J1) =(FRE*RI1(I,J)*DSIN(Z(I)))*EF*TH/SR
   A(I3,J2) = F2*R(I)*DSIN(Z(I))
35 CONTINUE
36 IF (NCOND-6) 37,37,38
37 DO 20 I=1,L1
   I1=I+L
   I2=I1+L
   I3=I2+L
   DO 20 J=2,L
   C=IP*(J-1)
   C1=C-1.D0
   C2=C-2.D0
   J1=J+L
   J2=J1+L
   J3=J2+L1
   DUM=(      +(F1 +V)*((C/R(I))*FRE*RJ1(I,J)-(C/R(I)**2)*RJ(I,J))
  1           *DSIN(F2 *Z(I))*DSIN(C*Z(I)))*(EF*TH/SR)
   A(I3,J) =(EF*TH/SR)*(((FRE/R(I))*RJ1(I,J)-(C/R(I))**2*RJ(I,J)
  1           -V*FRE**2*RJ2(I,J))*(DSIN(Z(I)))**2*DCOS(C*Z(I))
  2           +(FRE**2*RJ2(I,J)-V*(FRE/R(I))*RJ1(I,J)
  3           +V*(C/R(I))**2*RJ(I,J))*(DCOS(Z(I)))**2* DCOS(C*Z(I)))
  4           +DUM
   DUM=(       +(F1 +V)*((C/R(I))*FRE*RI1(I,J)-(C/R(I)**2)*RI(I,J))
  1           *DSIN(F2 *Z(I))*DSIN(C*Z(I)))*(EF*TH/SR)
   A(I3,J1) =(EF*TH/SR)*(((FRE/R(I))*RI1(I,J)-(C/R(I))**2*RI(I,J)
  1            -V*FRE**2*RI2(I,J))*(DSIN(Z(I)))**2*DCOS(C*Z(I))
  2            +(FRE**2*RI2(I,J)-V*(FRE/R(I))*RI1(I,J)
  3            +V*(C/R(I))**2*RI(I,J))*(DCOS(Z(I)))**2*DCOS(C*Z(I)))
  4            +DUM
   A(I3,J2) =R(I)**C*((C+F2-C**2-V*(C+F1)*(C+F2))*(DSIN(Z(I)))**2
  1            *DCOS(C*Z(I))
  2            +((C+F1)*(C+F2)+V*C**2-V*(C+F2))*(DCOS(Z(I)))**2
  3            *DCOS(C*Z(I))
  4            +(F1+V)*C*(C+F1)*DSIN(F2*Z(I))*DSIN(C*Z(I)))
   A(I3,J3) =C*C1*(F1+V)*R(I)**C2*(((DCOS(Z(I)))**2-(DSIN(Z(I)))**2)
  1            *DCOS(C*Z(I))+DSIN(F2*Z(I))*DSIN(C*Z(I)))
20 CONTINUE
   IF (BETA2-1.E+5) 46,46,40
46 IF (NCOND-2) 45,45,40
45 CALL BLOND5 (RJ,RI,RJ1,RI1,RJ2,RI2,A)
   GO TO 40
38 DO 39 I=1,L1
   I1=I+L
   I2=I1+L
   I3=I2+L
   DO 39 J=2,L
   C=IP*(J-1)
   C1=C-1.D0
   C2=C+1.D0
   J1=J+L
   J2=J1+L
   J3=J2+L1
   A(I3,J) =(FRE*RJ1(I,J)*DSIN(Z(I))*DCOS(C*Z(I))-(C/R(I))*RJ(I,J)*
  1DCOS(Z(I))*DSIN(C*Z(I)))*EF*TH/SR
   A(I3,J1) =(FRE*RI1(I,J)*DSIN(Z(I))*DCOS(C*Z(I))-(C/R(I))*RI(I,J)*
  1DCOS(Z(I))*DSIN(C*Z(I)))*EF*TH/SR
   A(I3,J2) = ((C+F2)*DSIN(Z(I))*DCOS(C*Z(I))-C*DCOS(Z(I))*
  1DSIN(C*Z(I)))*R(I)**C2
   A(I3,J3) = (DSIN(Z(I))*DCOS(C*Z(I))-DCOS(Z(I))*DSIN(C*Z(I)))
  1*C*R(I)**C1
39 CONTINUE
40 RETURN
   END
```

```
   SUBROUTINE  BLOND4 (RJ,RI,RJ1,RI1,RJ2,RI2,A)
```

```
      DIMENSION  ARG(7),                 RJ(7,7),RI(7,7),RJ1(7,7),
     1 RI1(7,7),RJ2(7,7),RI2(7,7)
      DIMENSION R(7),Z(7),ZZ(7),RR(27),A(27,27)
      COMMON DENS,RAD,TH,V,EF,Z,ZZ,RR,DD,FRE,AA,RK,R,ROE,DET1,DET,FRE1,
     1DELF,ACC,FREMX,FREI,DETI,DELFI,G0,G01,PI,OMEGA,CT,SR,BB,BETA,DAMP,
     2BETA2,
     3L,NN,NN1,N1,N2,IP,IP1,L1,LL1,LL2,LL3,NMAX,NCOND,NI,NIA,NIB,L2,IENT
     4,IREAD,IPRIN,NDIST
      DOUBLE PRECISION DENS,RAD,TH,V,EF,Z,ZZ,RR,DD,FRE,AA,RK,R,ROE,DET1,
     1DET,FRE1,DELF,ACC,FREMX,FREI,DETI,DELFI,G0,G01,PI,OMEGA,CT,SR,BB,
     2ARG,FJ,FI,RJ,RI,RJ1,RI1,RJ2,RI2,RJ0,RI0,C,CJ,CI,C1,C2,A,ERR,BETA,
     3DAMP,BETA2
     4,F1,F2,F3,F4
      F1=1.D0
      F2=2.D0
      F3=3.D0
      F4=4.D0
      J=1
      J1=J+L
      J2=J1+L
      J3=J2+L1
      DO 10 I=1,L
      I1=I+L
      I2=I1+L
      I3=I2+L
      A(I2,J)=A(I2,J)*(-F1)**NCOND +
     1          (FRE*RJ1(I,J)*DSIN(Z(I)))*EF*TH/SR
      A(I2,J1)=A(I2,J1)*(-F1)**NCOND +
     1          (FRE*RI1(I,J)*DSIN(Z(I)))*EF*TH/SR
      A(I2,J2)=A(I2,J2)*(-F1)**NCOND +
     1           F2*R(I)*DSIN(Z(I))
   10 CONTINUE
      DO 11 I=1,L
      I1=I+L
      I2=I1+L
      I3=I2+L
      DO 11 J=2,L
      C=IP*(J-1)
      C1=C-1.D0
      C2=C+1.D0
      J1=J+L
      J2=J1+L
      J3=J2+L1
      A(I2,J)=A(I2,J)*(-F1)**NCOND +
     1          (FRE*RJ1(I,J)*DSIN(Z(I))*DCOS(C*Z(I))-(C/R(I))*RJ(I,J)*
     2DCOS(Z(I))*DSIN(C*Z(I)))*EF*TH/SR
      A(I2,J1)=A(I2,J1)*(-F1)**NCOND +
     1          (FRE*RI1(I,J)*DSIN(Z(I))*DCOS(C*Z(I))-(C/R(I))*RI(I,J)*
     2DCOS(Z(I))*DSIN(C*Z(I)))*EF*TH/SR
      A(I2,J2)=A(I2,J2)*(-F1)**NCOND +
     1           ((C+F2)*DSIN(Z(I))*DCOS(C*Z(I))-C*DCOS(Z(I))*
     2DSIN(C*Z(I)))*R(I)**C2
      A(I2,J3)=A(I2,J3)*(-F1)**NCOND +
     1           (DSIN(Z(I))*DCOS(C*Z(I))-DCOS(Z(I))*DSIN(C*Z(I)))
     2*C*R(I)**C1
   11 CONTINUE
      RETURN
      END


      SUBROUTINE  BLOND5 (RJ,RI,RJ1,RI1,RJ2,RI2,A)
      DIMENSION  ARG(7),                 RJ(7,7),RI(7,7),RJ1(7,7),
     1 RI1(7,7),RJ2(7,7),RI2(7,7)
      DIMENSION R(7),Z(7),ZZ(7),RR(27),A(27,27)
      COMMON DENS,RAD,TH,V,EF,Z,ZZ,RR,DD,FRE,AA,RK,R,ROE,DET1,DET,FRE1,
     1DELF,ACC,FREMX,FREI,DETI,DELFI,G0,G01,PI,OMEGA,CT,SR,BB,BETA,DAMP,
     2BETA2,
     3L,NN,NN1,N1,N2,IP,IP1,L1,LL1,LL2,LL3,NMAX,NCOND,NI,NIA,NIB,L2,IENT
     4,IREAD,IPRIN,NDIST
      DOUBLE PRECISION DENS,RAD,TH,V,EF,Z,ZZ,RR,DD,FRE,AA,RK,R,ROE,DET1,
     1DET,FRE1,DELF,ACC,FREMX,FREI,DETI,DELFI,G0,G01,PI,OMEGA,CT,SR,BB,
     2ARG,FJ,FI,RJ,RI,RJ1,RI1,RJ2,RI2,RJ0,RI0,C,CJ,CI,C1,C2,A,ERR,BETA,
```

```
     3 DAMP,C3,BETA2
     4,F1,F2,F3,F4
      F1=1.D0
      F2=2.D0
      F3=3.D0
      F4=4.D0
      J=1
      J1=J+L
      J2=J1+L
      J3=J2+L1
      DO 10 I=1,L
      I1=I+L
      I2=I1+L
      I3=I2+L
      IF (NCOND-2) 6,6,7
    6 I2=I3
    7 A(I2,J)=-A(I2,J)*BETA2+
     1          EF*TH/(F2*SR)*((FRE/R(I))*RJ1(I,J)-FRE**2*RJ2(I,J))*
     2          DSIN(F2*Z(I))
      A(I2,J1 )=-A(I2,J1)*BETA2+
     1           EF*TH/(F2*SR)*((FRE/R(I))*RI1(I,J)-FRE**2*RI2(I,J))*
     2          DSIN(F2*Z(I))
      A(I2,J2)=-A(I2,J2)*BETA2+0.D0
   10 CONTINUE
      DO 11 I=1,L
      I1=I+L
      I2=I1+L
      I3=I2+L
      IF (NCOND-2) 8,8,9
    8 I2=I3
    9 DO 11 J=2,L
      C=IP*(J-1)
      C1=C-1.D0
      C2=C+1.D0
      C3=C-2.D0
      J1=J+L
      J2=J1+L
      J3=J2+L1
      A(I2,J)=-A(I2,J)*BETA2+
     1          EF*TH/(F2*SR)*(((FRE/R(I))*RJ1(I,J)-(C/R(I))**2*RJ(I,J)-
     2          FRE**2*RJ2(I,J))*DSIN(F2*Z(I))*DCOS(C*Z(I)) + (F2*C/R(I))
     3          *(-RJ(I,J)/R(I)+FRE*RJ1(I,J))*DCOS(F2*Z(I))*DSIN(C*Z(I)))
      A(I2,J1)=-A(I2,J1)*BETA2+
     1          EF*TH/(F2*SR)*(((FRE/R(I))*RI1(I,J)-(C/R(I))**2*RI(I,J)-
     2          FRE**2*RI2(I,J))*DSIN(F2*Z(I))*DCOS(C*Z(I)) + (F2*C/R(I))
     3          *(-RI(I,J)/R(I)+FRE*RI1(I,J))*DCOS(F2*Z(I))*DSIN(C*Z(I)))
      A(I2,J2)=-A(I2,J2)*BETA2+
     1           (R(I)**C)*C*C2*(-DSIN(F2*Z(I))*DCOS(C*Z(I))+DCOS(F2*Z(I)
     2          )*DSIN(C*Z(I)))
      A(I2,J3)=-A(I2,J3)*BETA2+
     1          (R(I)**C3)*C*C1*(-DSIN(F2*Z(I))*DCOS(C*Z(I))+DCOS(F2*Z(I)
     2          )*DSIN(C*Z(I)))
   11 CONTINUE
      RETURN
      END


C    BLONI     SHELL
      SUBROUTINE BLONI (A,RR,FRE,DET,LL1,LL2,OMEGA,CT,ISENS,IPRIN,BB,L,
     1DAMP,RAD)
      DIMENSION  A(27,27),RR(27),LW(27),MW(27),D(27),CC(27),CR(27)
      DOUBLE PRECISION  DV,A,D,RR,FRE,DET,OMEGA,CT,BB,CC,CR,CF,RF,DAMP,
     1XYZ,OMEDA,RAD
      L1=L-1
C   DEFINE COLUMN CONSTANTS FOR EACH CALOTTE SHELL
      I2=2
      CF=1.0D0
      DO 1 J=1,LL1
      CC(J)=A(I2,J)
      IF(CC(J)) 8,9,8
    9 CC(J)=1.0D0
    8 CF=CF*CC(J)/DABS(CC(J))
```

```
    1 CONTINUE
      DO 2 I=1,LL1
      DO 2 J=1,LL1
      IF (A(I,J)-0.D0)5,2,5
    5 A(I,J)=A(I,J)/CC(J)
    2 CONTINUE
C     DEFINE ROW CONSTANTS FOR EACH CALOTTE SHELL
      LL4=3*L
      RF=1.0D0
      DO 3 I=1,LL4
      CR(I)=A(I,1)
      IF (CR(I)) 10,11,10
   11 CR(I)=1.D0
   10 RF=RF*CR(I)/DABS(CR(I))
    3 CONTINUE
      DO 12 I=1,L1
      I2=I+2*L
      I3=I2+L
      CR(I3)=CR(I2)
      RF=RF*CR(I3)/DABS(CR(I3))
   12 CONTINUE
      DO 4 I=1,LL1
      DO 4 J=1,LL1
      IF (A(I,J)-0.D0) 6,4,6
    6 A(I,J)=A(I,J)/CR(I)
    4 CONTINUE
      DO 7 I=1,LL1
      DO 7 J=1,LL1
      A(I,J)=A(I,J)*CT
    7 CONTINUE
      IF (ISENS-1) 22,22,20
   20 CALL DMINV (A,LL1,DET,LW,MW)
      DET=DET*CF*RF
      WRITE (IPRIN,21) FRE,DET,CT
   21 FORMAT (1H0,11HFREQUENCY =,E18.8,5X,19HDETERMINANT VALUE =,E18.8,
     15X,12HCONSTANT-CT=,E10.1)
      GO TO 29
   22 ISENS=2
      DO 23 J=1,LL2
   23 D(J)=-A(J,1)
      DO 24 I=1,LL2
      DO 24 J=1,LL2
      J1=J+1
   24 A(I,J)=A(I,J1)
      CALL DMINV(A,LL2,DV,LW,MW)
      DO 25 I=2,LL1
   25 RR(I)=0.0D0
      RR(1)=1.0D0
      DO 26 I=2,LL1
      DO 26 J=1,LL2
      I1=I-1
   26 RR(I)=RR(I)+A(I1,J)*D(J)
      DO 35 I=2,LL1
      RR(I)=RR(I)*CC(1)/CC(I)
   35 CONTINUE
      OMEDA=DSQRT(OMEGA**2-DAMP**2)
      XYZ=RAD*FRE
      WRITE (IPRIN,27) FRE,XYZ,BB,OMEGA,OMEDA
   27 FORMAT (1H0,15HEIGENFREQUENCY=,2E18.8,5X,7HLAMBDA=,E18.8,/,1X,
     119HANGULAR FREQUENCY=  ,E18.8,5X,18HDAMPED ANG. FRE.=  ,E18.8)
      WRITE (IPRIN,28) (RR(I),I=1,LL1)
   28 FORMAT (1H0,11HEIGENVECTOR,/,(4E18.8/))
   29 RETURN
      END


C     DMINV    SHELL
      SUBROUTINE DMINV (A,N,D,L,M)
      DIMENSION  A(729),L(27),M(27)
      DOUBLE PRECISION BIGA,HOLD,A,D
      IS=27
```

```
      K=0
      DO 9 I=1,N
      DO 9 J=1,N
      I1=I-1
      K=K+1
      NI=IS*I1+J
    9 A(K)=A(NI)
C        SEARCH FOR LARGEST ELEMENT
      D=1.0D0
      NK=-N
      DO 80 K=1,N
      NK=NK+N
      L(K)=K
      M(K)=K
      KK=NK+K
      BIGA=A(KK)
      DO 20 J=K,N
      IZ=N*(J-1)
      DO 20 I=K,N
      IJ=IZ+I
   10 IF (DABS(BIGA)-DABS(A(IJ))) 15,20,20
   15 BIGA=A(IJ)
      L(K)=I
      M(K)=J
   20 CONTINUE
C        INTERCHANGE ROWS
      J=L(K)
      IF(J-K) 35,35,25
   25 KI=K-N
      DO 30 I=1,N
      KI=KI+N
      HOLD=-A(KI)
      JI=KI-K+J
      A(KI)=A(JI)
   30 A(JI) =HOLD
C        INTERCHANGE COLUMNS
   35 I=M(K)
      IF(I-K) 45,45,38
   38 JP=N*(I-1)
      DO 40 J=1,N
      JK=NK+J
      JI=JP+J
      HOLD=-A(JK)
      A(JK)=A(JI)
   40 A(JI) =HOLD
C        DIVIDE COLUMN BY MINUS PIVOT (VALUE OF PIVOT ELEMENT IS
C        CONTAINED IN BIGA)
   45 IF(BIGA) 48,46,48
   46 D=0.0D0
      RETURN
   48 DO 55 I=1,N
      IF(I-K) 50,55,50
   50 IK=NK+I
      A(IK)=A(IK)/(-BIGA)
   55 CONTINUE
C        REDUCE MATRIX
      DO 65 I=1,N
      IK=NK+I
      IJ=I-N
      DO 65 J=1,N
      IJ=IJ+N
      IF(I-K) 60,65,60
   60 IF(J-K) 62,65,62
   62 KJ=IJ-I+K
      A(IJ)=A(IK)*A(KJ)+A(IJ)
   65 CONTINUE
C        DIVIDE ROW BY PIVOT
      KJ=K-N
      DO 75 J=1,N
      KJ=KJ+N
      IF(J-K) 70,75,70
   70 A(KJ)=A(KJ)/BIGA
   75 CONTINUE
```

```
C        PRODUCT OF PIVOTS
      D=D*BIGA
C        REPLACE PIVOT BY RECIPROCAL
      A(KK)=1.0D0/BIGA
   80 CONTINUE
C        FINAL ROW AND COLUMN INTERCHANGE
      K=N
  100 K=(K-1)
      IF(K) 150,150,105
  105 I=L(K)
      IF(I-K) 120,120,108
  108 JQ=N*(K-1)
      JR=N*(I-1)
      DO 110 J=1,N
      JK=JQ+J
      HOLD=A(JK)
      JI=JR+J
      A(JK)=-A(JI)
  110 A(JI) =HOLD
  120 J=M(K)
      IF(J-K) 100,100,125
  125 KI=K-N
      DO 130 I=1,N
      KI=KI+N
      HOLD=A(KI)
      JI=KI-K+J
      A(KI)=-A(JI)
  130 A(JI) =HOLD
      GO TO 100
  150 K=N*N+1
      NI=IS*N+1
      DO 8 I=1,N
      NI=NI-(IS-N)
      DO 8 J=1,N
      K=K-1
      NI=NI-1
    8 A(NI)=A(K)
      RETURN
      END


C    FOURI    SHELL
C     FOURIER COEFFICIENTS
      SUBROUTINE FOURI(SR1)
      DIMENSION  Z(7),ZZ(7),R(7),RR(27)
      DIMENSION  O4(9),O5(9),O6(9),O13(9),O14(9),O15(9),O16(9),
     1O17(9),O18(9),O41(9),O42(9),O51(9),O52(9)
      COMMON DENS,RAD,TH,V,EF,Z,ZZ,RR,DD,FRE,AA,RK,R,ROE,DET1,DET,FRE1,
     1DELF,ACC,FREMX,FREI,DETI,DELFI,G0,G01,PI,OMEGA,CT,SR,BB,BETA,DAMP,
     2BETA2,
     3L,NN,NN1,N1,N2,IP,IP1,L1,LL1,LL2,LL3,NMAX,NCOND,NI,NIA,NIB,L2,IENT
     4,IREAD,IPRIN,NDIST
      DOUBLE PRECISION DENS,RAD,TH,V,EF,Z,ZZ,RR,DD,FRE,AA,RK,R,ROE,
     1DELF,ACC,FREMX,FREI,DETI,DELFI,FAC,ERR,BJ,Y,BI,C,BI0,BI1,BEJ,
     2BEI1,BEI11,G0T,G0B,O1,O2,O3,O4,O41,O42,O5,O51,O52,O6,O7,O8,O9,
     3O10,O11,O12,O13,O14,O15,O16,O17,O18,
     4BJ0,BJ1,BEJ1,BEJ11,BEI,DET1,FRE1,DET,G0,G01,PI,OMEGA,CT,SR,BB,
     5DEL,X,AY,SR1,RJ,ERFOR,ORI,BETA,DAMP,BETA2,G02
     6,F1,F2,F3,F4
      F1=1.D0
      F2=2.D0
      F3=3.D0
      F4=4.D0
      R(1)=SR1
      AY=NI
      FAC=PI/(RK*F3*AY)
      DEL =PI/(RK*AY)
      ERR=1.D-15
      NI1=NI+1
      X=0.D0
      O1=0.D0
      IL=1
```

```
      DO 50 I=1,NI1
      Y=FRE*SR1/DCOS(X)
      CALL BESJ(Y     ,1,BJ,ERR,IER)
      Y=BJ/DCOS(X)
      CALL SIMP(I,Y,NI1,IL)
      X=X+DEL
      O1=O1+Y
   50 CONTINUE
      O1=-O1*FRE*R(1)*FAC
      WRITE (IPRIN,10) O1
      X=0.D0
      O2=0.D0
      IL=1
      DO 51 I=1,NI1
      Y=FRE*SR1/DCOS(X)
      CALL BESI(Y     ,1,BI,ERR,IER)
      Y=BI/DCOS(X)
      CALL SIMP(I,Y,NI1,IL)
      X=X+DEL
      O2=O2+Y
   51 CONTINUE
      O2=O2*FRE*R(1)*FAC
      WRITE (IPRIN,11) O2
      O3=F2*BB*R(1)**2*DSIN(PI/RK)/DCOS(PI/RK)
      WRITE (IPRIN,12) O3
      DO 105 II=1,L1
      O41(II)=0.D0
      ORI=O41(II)
      C=IP*II
      DO 103 J=1,NIA
      IOR=IP*II+2*(J-1)+1
      IL=1
      X=0.D0
      DO 101 I=1,NI1
      Y=FRE*SR1/DCOS(X)
      CALL BESJ(Y     ,IOR,BJ,ERR,IER)
      Y=BJ*DCOS(C*X)/DCOS(X)
      CALL SIMP(I,Y,NI1,IL)
      X=X+DEL
      O41(II)=O41(II)+Y
  101 CONTINUE
      ERFOR=DABS((ORI-O41(II))/O41(II))-ACC
      IF (ERFOR) 104,104,102
  102 ORI=O41(II)
  103 CONTINUE
  104 O41(II)=-O41(II)*F2*FRE*R(1)*FAC
      WRITE (IPRIN,13) II,O41(II),J
  105 CONTINUE
      DO 110 II=1,L1
      O42(II)=0.D0
      ORI=O42(II)
      C=IP*II
      DO 108 J=1,NIA
      RJ=J
      IL=1
      X=0.D0
      IOR=II*IP+2*J
      DO 106 I=1,NI1
      Y=FRE*SR1/DCOS(X)
      CALL BESJ(Y     ,IOR,BJ,ERR,IER)
      Y=BJ*DCOS(C*X)
      CALL SIMP(I,Y,NI1,IL)
      O42(II)=O42(II)+Y*RJ
      X=X+DEL
  106 CONTINUE
      ERFOR=DABS((ORI-O42(II))/O42(II))-ACC
      IF (ERFOR) 109,109,107
  107 ORI=O42(II)
  108 CONTINUE
  109 O42(II)=O42(II)*F4*FAC
      WRITE (IPRIN,14) II,O42(II),J
      O4(II)=O41(II)+O42(II)
```

```
  110 CONTINUE
      DO 120 II=1,L1
      O51(II)=0.D0
      ORI=O51(II)
      C=IP*II
      DO 118 J=1,NIA
      IOR=IP*II+2*(J-1)+1
      IL=1
      X=0.D0
      DO 116 I=1,NI1
      Y=FRE*SR1/DCOS(X)
      CALL BESI(Y     ,IOR,BI,ERR,IER)
      Y=BI*DCOS(C*X)/DCOS(X)
      CALL SIMP(I,Y,NI1,IL)
      X=X+DEL
      O51(II)=O51(II)+Y*((-F1)**(J-1))
  116 CONTINUE
      ERFOR=DABS((ORI-O51(II))/O51(II))-ACC
      IF (ERFOR) 119,119,117
  117 ORI=O51(II)
  118 CONTINUE
  119 O51(II)=O51(II)*F2*FRE*R(1)*FAC
      WRITE (IPRIN,15) II,O51(II),J
  120 CONTINUE
      DO 125 II=1,L1
      O52(II)=0.D0
      ORI=O52(II)
      C=IP*II
      DO 123 J=1,NIA
      RJ=J
      IOR=II*IP+2*J
      X=0.D0
      IL=1
      DO 121 I=1,NI1
      Y=FRE*SR1/DCOS(X)
      CALL BESI(Y     ,IOR,BI,ERR,IER)
      Y=BI*DCOS(C*X)
      CALL SIMP(I,Y,NI1,IL)
      Y=Y*RJ
      O52(II)=O52(II)+Y*((-F1)**(J-1))
      X=X+DEL
  121 CONTINUE
      ERFOR=DABS((ORI-O52(II))/O52(II))-ACC
      IF (ERFOR) 124,124,122
  122 ORI=O52(II)
  123 CONTINUE
  124 O52(II)=-O52(II)*F4*FAC
      WRITE (IPRIN,16) II,O52(II),J
      O5(II)=O51(II)+O52(II)
  125 CONTINUE
      CALL        FOURI2 (O6,O7,O8,O9,O10,O11,O12,O13,O14,O15,O16,O17,
     1 O18,SR1,FAC,ERR,NI1,AY,DEL)
      J=1
      J1=J+L
      J2=J1+L
      GOT=RR(J)*O1+RR(J1)*O2+RR(J2)*O3
      GOB=RR(J)**2*O7+RR(J1)**2*O8+RR(J2)**2*O9+F2*RR(J)*RR(J1)*O10 +
     1    F2*RR(J)*RR(J2)*O11+F2*RR(J1)*RR(J2)*O12
      GO1=GOT/GOB
      DO 79 J=2,L
      C=IP*(J-1)
      J1=J+L
      J2=J1+L
      I=J-1
      GOT=GOT+RR(J)*O4(I)+RR(J1)*O5(I)+RR(J2)*O6(I)
      GOB=GOB+RR(J)**2*O13(I)+RR(J1)**2*O14(I)+RR(J2)**2*O15(I)+
     1    F2*RR(J)*RR(J1)*O16(I)+F2*RR(J)*RR(J2)*O17(I)  +
     2    F2*RR(J1)*RR(J2)*O18(I)
   79 CONTINUE
      GO=GOT/GOB
      J1=L+1
      J2=J1+L
      GO2=(-(FRE**2)*RR(1)+FRE**2*RR(J1)+F4*BB*RR(J2))
```

```
      G02=G02/(G0B*2.*RK)
      WRITE (IPRIN,9) G01,G0,G02
    9 FORMAT (1H0,19HG01(APPROX. COEF.)=,E18.8,5X,18HG0(FOURIER COEF.)=,
     1E18.8,24HFOURIER COEF (PT. LOAD)=,E18.8/)
   10 FORMAT (1H0,3HO1=,E18.8)
   11 FORMAT (1H ,3HO2=,E18.8)
   12 FORMAT (1H ,3HO3=,E18.8)
   13 FORMAT (1H ,4HO41(,I2,2H)=,E18.7,10X,5HAMAX=,I2)
   14 FORMAT (1H ,4HO42(,I2,2H)=,E18.7,10X,5HAMAX=,I2)
   15 FORMAT (1H ,4HO51(,I2,2H)=,E18.7,10X,5HAMAX=,I2)
   16 FORMAT (1H ,4HO52(,I2,2H)=,E18.7,10X,5HAMAX=,I2)
      R(1)=SR1/DCOS(Z(1))
      RETURN
      END


      SUBROUTINE FOURI2 (O6,O7,O8,O9,O10,O11,O12,O13,O14,O15,O16,O17,
     1 O18,SR1,FAC,ERR,NI1,AY,DEL)
      DIMENSION  Z(7),ZZ(7),R(7),RR(27)
      DIMENSION                  O6(9),O13(9),O14(9),O15(9),O16(9),
     1O17(9),O18(9),O41(9),O42(9),O51(9),O52(9)
      COMMON DENS,RAD,TH,V,EF,Z,ZZ,RR,DD,FRE,AA,RK,R,ROE,DET1,DET,FRE1,
     1DELF,ACC,FREMX,FREI,DETI,DELFI,G0,G01,PI,OMEGA,CT,SR,BB,BETA,DAMP,
     2BETA2,
     3L,NN,NN1,N1,N2,IP,IP1,L1,LL1,LL2,LL3,NMAX,NCOND,NI,NIA,NIB,L2,IENT
     4,IREAD,IPRIN,NDIST
      DOUBLE PRECISION DENS,RAD,TH,V,EF,Z,ZZ,RR,DD,FRE,AA,RK,R,ROE,
     1DELF,ACC,FREMX,FREI,DETI,DELFI,FAC,ERR,BJ,Y,BI,C,BI0,BI1,BEJ,
     2BEI1,BEI11,G0T,G0B,O1,O2,O3,O4,O41,O42,O5,O51,O52,O6,O7,O8,O9,
     3O10,O11,O12,O13,O14,O15,O16,O17,O18,
     4BJ0,BJ1,BEJ1,BEJ11,BEI,DET1,FRE1,DET,G0,G01,PI,OMEGA,CT,SR,BB,
     5DEL,X,AY,SR1,RJ,ERFOR,ORI,BETA,DAMP ,BETA2
     6,F1,F2,F3,F4,F8
      F1=1.D0
      F2=2.D0
      F3=3.D0
      F4=4.D0
      F8=8.D0
      DO 61 II=1,L1
      X=0.D0
      O6(II)=0.D0
      C=IP*II
      IL=1
      DO 60 I=1,NI1
      Y=DCOS(C*X)/(DCOS(X)**(C+F2))
      CALL SIMP(I,Y,NI1,IL)
      O6(II)=O6(II)+Y
      X=X+DEL
   60 CONTINUE
      O6(II)=O6(II)*F4*BB*R(1)**(C+F2)*((C+F1)/(C+F2))*FAC
      WRITE (IPRIN,17) II,O6(II)
   61 CONTINUE
      O7=0.D0
      X=0.D0
      IL=1
      DO 62 I=1,NI1
      Y=FRE*SR1/DCOS(X)
      CALL BESJ(Y    ,0,BJ0,ERR,IER)
      CALL BESJ(Y    ,1,BJ1,ERR,IER)
      Y=(BJ0**2+BJ1**2)/(DCOS(X)**2)
      CALL SIMP(I,Y,NI1,IL)
      X=X+DEL
      O7=O7+Y
   62 CONTINUE
      O7=O7*FRE**4*R(1)**2*FAC/F2
      WRITE (IPRIN,18) O7
      O8=0.D0
      X=0.D0
      IL=1
      DO 63 I=1,NI1
      Y=FRE*SR1/DCOS(X)
      CALL BESI(Y    ,0,BI0,ERR,IER)
```

```
      CALL BESI(Y     ,1,BI1,ERR,IER)
      Y=(BI0**2-(BI1**2))/(DCOS(X)**2)
      CALL SIMP(I,Y,NI1,IL)
      X=X+DEL
      O8=O8+Y
   63 CONTINUE
      O8=O8*FRE**4*R(1)**2*FAC/F2
      WRITE (IPRIN,19) O8
      O9=BB**2*R(1)**2*F8*(DSIN(PI/RK)/DCOS(PI/RK))
      WRITE (IPRIN,20) O9
      O10=0.D0
      X=0.D0
      IL=1
      DO 64 I=1,NI1
      Y=FRE*SR1/DCOS(X)
      CALL BESJ(Y     ,0,BJ0,ERR,IER)
      CALL BESJ(Y     ,1,BJ1,ERR,IER)
      CALL BESI(Y     ,0,BI0,ERR,IER)
      CALL BESI(Y     ,1,BI1,ERR,IER)
      Y=(BJ0*BI1+BJ1*BI0)/DCOS(X)
      CALL SIMP(I,Y,NI1,IL)
      X=X+DEL
      O10=O10+Y
   64 CONTINUE
      O10=-O10*FRE**3*R(1)*FAC/F2
      WRITE (IPRIN,21) O10
      O11=0.D0
      X=0.D0
      IL=1
      DO 65 I=1,NI1
      Y=FRE*SR1/DCOS(X)
      CALL BESJ(Y     ,1,BJ,ERR,IER)
      Y=BJ/DCOS(X)
      CALL SIMP(I,Y,NI1,IL)
      X=X+DEL
      O11=O11+Y
   65 CONTINUE
      O11=-O11*FRE*BB*R(1)*FAC*F4
      WRITE (IPRIN,22) O11
      O12=0.D0
      X=0.D0
      IL=1
      DO 66 I=1,NI1
      Y=FRE*SR1/DCOS(X)
      CALL BESI(Y     ,1,BI,ERR,IER)
      Y=BI/DCOS(X)
      CALL SIMP(I,Y,NI1,IL)
      X=X+DEL
      O12=O12+Y
   66 CONTINUE
      O12=O12*FRE*BB*R(1)*FAC*F4
      WRITE (IPRIN,23) O12
      DO 68 II=1,L1
      O13(II)=0.D0
      X=0.D0
      IL=1
      J=IP*II
      C=J
      J1=J+1
      J11=J-1
      DO 67 I=1,NI1
      Y=FRE*SR1/DCOS(X)
      CALL BESJ(Y     ,J,BEJ,ERR,IER)
      CALL BESJ(Y     ,J1,BEJ1,ERR,IER)
      CALL BESJ(Y     ,J11,BEJ11,ERR,IER)
      BEJ1=(BEJ11-BEJ1)/F2
      Y=(BEJ1**2+BEJ**2*(F1-(C*DCOS(X)/(FRE*SR1))**2))*(DCOS(C*X)/
     1 DCOS(X))**2
      CALL SIMP(I,Y,NI1,IL)
      X=X+DEL
      O13(II)=O13(II)+Y
   67 CONTINUE
```

```
      O13(II)=O13(II)*FRE**4*R(1)**2*FAC/F2
      WRITE (IPRIN,24) II,O13(II)
   68 CONTINUE
      DO 70 II=1,L1
      O14(II)=0.D0
      X=0.D0
      IL=1
      J=IP*II
      C=J
      J1=J+1
      J11=J-1
      DO 69 I=1,NI1
      Y=FRE*SR1/DCOS(X)
      CALL BESI(Y     ,J,BEI,ERR,IER)
      CALL BESI(Y     ,J1,BEI1,ERR,IER)
      CALL BESI(Y     ,J11,BEI11,ERR,IER)
      BEI1=(BEI11+BEI1)/F2
      Y=(-(BEI1**2)+BEI**2*(F1+(C*DCOS(X)/(FRE*SR1))**2))*(DCOS(C*X)/
     1 DCOS(X))**2
      CALL SIMP(I,Y,NI1,IL)
      X=X+DEL
      O14(II)=O14(II)+Y
   69 CONTINUE
      O14(II)=O14(II)*FRE**4*R(1)**2*FAC/F2
      WRITE (IPRIN,25) II,O14(II)
   70 CONTINUE
      DO 72 II=1,L1
      O15(II)=0.D0
      X=0.D0
      IL=1
      C=IP*II
      DO 71 I=1,NI1
      Y=(DCOS(C*X)**2)/(DCOS(X)**(F2*C+F2))
      CALL SIMP(I,Y,NI1,IL)
      X=X+DEL
      O15(II)=O15(II)+Y
   71 CONTINUE
      O15(II)=O15(II)*BB**2*(C+F1)*R(1)**(F2*C+F2)*FAC*F8
      WRITE (IPRIN,26) II,O15(II)
   72 CONTINUE
      DO 74 II=1,L1
      X=0.D0
      IL=1
      O16(II)=0.D0
      J=IP*II
      C=J
      J1=J+1
      J11=J-1
      DO 73 I=1,NI1
      Y=FRE*SR1/DCOS(X)
      CALL BESJ(Y     ,J,BEJ,ERR,IER)
      CALL BESI(Y     ,J,BEI,ERR,IER)
      CALL BESJ(Y     ,J1,BEJ1,ERR,IER)
      CALL BESI(Y     ,J1,BEI1,ERR,IER)
      CALL BESJ(Y     ,J11,BEJ11,ERR,IER)
      CALL BESI(Y     ,J11,BEI11,ERR,IER)
      BEJ1=(BEJ11-BEJ1)/F2
      BEI1=(BEI11+BEI1)/F2
      Y=(BEJ*BEI1-BEJ1*BEI)*DCOS(C*X)**2/DCOS(X)
      CALL SIMP(I,Y,NI1,IL)
      X=X+DEL
      O16(II)=O16(II)+Y
   73 CONTINUE
      O16(II)=-O16(II)*FRE**3*R(1)*FAC/F2
      WRITE (IPRIN,27) II,O16(II)
   74 CONTINUE
      DO 76 II=1,L1
      X=0.D0
      IL=1
      O17(II)=0.D0
      C=IP*II
      J=IP*II+1
      DO 75 I=1,NI1
```

```
      Y=FRE*SR1/DCOS(X)
      CALL BESJ(Y     ,J,BEJ,ERR,IER)
      Y=BEJ*(DCOS(C*X)**2)/(DCOS(X)**J)
      CALL SIMP(I,Y,NI1,IL)
      X=X+DEL
      O17(II)=O17(II)+Y
   75 CONTINUE
      O17(II)=-O17(II)*(C+F1)*BB*FRE*R(1)**J*FAC*F4
      WRITE (IPRIN,28) II,O17(II)
   76 CONTINUE
      DO 78 II=1,L1
      X=0.D0
      IL=1
      O18(II)=0.D0
      C=IP*II
      J=IP*II+1
      DO 77 I=1,NI1
      Y=FRE*SR1/DCOS(X)
      CALL BESI(Y     ,J,BEI,ERR,IER)
      Y=BEI*(DCOS(C*X)**2)/(DCOS(X)**J)
      CALL SIMP(I,Y,NI1,IL)
      X=X+DEL
      O18(II)=O18(II)+Y
   77 CONTINUE
      O18(II)=O18(II)*(C+F1)*BB*FRE*R(1)**J*FAC*F4
      WRITE (IPRIN,29) II,O18(II)
   78 CONTINUE
   17 FORMAT (1H ,3HO6(,I2,2H)=,E18.7)
   18 FORMAT (1H ,3HO7=,E18.8)
   19 FORMAT (1H ,3HO8=,E18.8)
   20 FORMAT (1H ,3HO9=,E18.8)
   21 FORMAT (1H ,4HO10=,E18.7)
   22 FORMAT (1H ,4HO11=,E18.7)
   23 FORMAT (1H ,4HO12=,E18.7)
   24 FORMAT (1H ,4HO13(,I2,2H)=,E18.7)
   25 FORMAT (1H ,4HO14(,I2,2H)=,E18.7)
   26 FORMAT (1H ,4HO15(,I2,2H)=,E18.7)
   27 FORMAT (1H ,4HO16(,I2,2H)=,E18.7)
   28 FORMAT (1H ,4HO17(,I2,2H)=,E18.7)
   29 FORMAT (1H ,4HO18(,I2,2H)=,E18.7)
      RETURN
      END


C    RESUL     SHELL
      SUBROUTINE RESUL(AA,NN,DD,V,L1,NN1,N1,N2,NMAX,IP,IP1,PI,FRE,G0,RR
     1,OMEGA,R,ZZ,ICODE,NDLT,DLT,POS,PIN,IA,IOT,BB,SR,EF,TH,IREAD,IPRIN,
     2DAMP)
      DIMENSION  RR(39),FJ(60),FI(60),RJ(10),RI(10),RJ1(10),RI1(10),
     1RJ2(10),RI2(10),RJ3(10),RI3(10)
      DOUBLE PRECISION FJ,FI,RJ,RI,RJ1,RI1,RJ2,RI2,RJ3,RI3,Z,ERR,ARG,RJO
     1,RIO,C,CJ,CI,UN,FRR,FOO,FRO,BMRO,BMOR,BMRR,C1,C2,CC1,CC2,TI,T,Z1,
     2Z2,Z3,Z4,Z5,Z6,Z7,AA,DD,V,PI,FRE,G0,RR,OMEGA,R,ZZ,DLT,POS,PIN,BB,
     3SR,EF,TH,DAMP,OMEDA,DAMM
     4,F1,F2,F3,F4
      F1=1.D0
      F2=2.D0
      F3=3.D0
      F4=4.D0
      OMEDA=DSQRT(OMEGA**2-DAMP**2)
      DAMM=F1/POS-DAMP
      IF (ICODE-2) 1,2,3
    1 WRITE (IPRIN,48)
      GO TO 7
    2 WRITE (IPRIN,49)
      GO TO 7
    3 IF (ICODE-4) 4,5,6
    4 WRITE (IPRIN,50)
      GO TO 7
    5 WRITE (IPRIN,51) DAMP
      GO TO 7
    6 WRITE (IPRIN,52) DAMP
```

```
    7 WRITE (IPRIN,53)
      L=L1+1
      Z=ZZ*PI/180.D0
      ERR=1.D-15
      UN=0.D0
      FRR=0.D0
      FOO=0.D0
      FRO=0.D0
      BMRO=0.D0
      BMOR=0.D0
      BMRR=0.D0
      LL=L+1
      LLL=LL+L
      ARG=FRE*R
      IF (ARG) 54, 9,10
    9 WRITE (IPRIN,33)
      UN=-FRE**2*RR(1)+FRE**2*RR(LL)+F4*BB*RR(LLL)
      GO TO 21
   10 CALL BESJ(ARG,0,RJ0,ERR,IER)
      CALL BESI(ARG,0,RI0,ERR,IER)
      FJ(1)=0.D0
      FI(1)=0.D0
      FJ(2)=AA
      FI(2)=AA
      DO 11 J=1,NN1
      C=NN-J
      FJ(J+2)=FJ(J+1)*F2*C/ARG-FJ(J)
   11 FI(J+2)=FI(J+1)*F2*C/ARG+FI(J)
      CJ=FJ(N1)/RJ0
      CI=FI(N1)/RI0
      DO 14 J=1,NMAX,IP
      K=((J-1)/IP)+1
      K1=N2-J
      RJ(K)=FJ(K1)/CJ
   14 RI(K)=FI(K1)/CI
      K1=N2-2
      RJ1(1)=-FJ(K1)/CJ
      RI1(1)= FI(K1)/CI
      DO 16 J=IP1,NMAX,IP
      K=((J-1)/IP)+1
      K1=N2-J
      RJ1(K)=(FJ(K1+1)-FJ(K1-1))/(F2*CJ)
   16 RI1(K)=(FI(K1-1)+FI(K1+1))/(F2*CI)
      DO 17 J=1,L
      C=(J-1)*IP
      RJ2(J)=-RJ1(J)/ARG+RJ(J)*((C/ARG)**2-F1)
   17 RI2(J)=-RI1(J)/ARG+RI(J)*((C/ARG)**2+F1)
      DO 18 J=1,L
      C=(J-1)*IP
      RJ3(J)=-RJ2(J)/ARG+RJ1(J)*((C/ARG)**2-F1+(F1/ARG)**2)-RJ(J)*(F2/
     1ARG)*((C/ARG)**2)
   18 RI3(J)=-RI2(J)/ARG+RI1(J)*((C/ARG)**2+F1+(F1/ARG)**2)-RI(J)*(F2/
     1ARG)*((C/ARG)**2)
      J=1
      LL=L+J
      LLL=LL+L
      LLLL=LLL+L1
      UN = -(FRE**2)*RR(J)*RJ(J)+FRE**2*RR(LL)*RI(J)+F4*BB*RR(LLL)
      FRR = RR(J)*(EF*TH/SR)*(FRE/R)*RJ1(J)+
     1     RR(LL)*(EF*TH/SR)*(FRE/R)*RI1(J) + F2 *RR(LLL)
      FOO = RR(J)*(EF*TH/SR)*(FRE**2)*RJ2(J) +
     1     RR(LL)*(EF*TH/SR)*(FRE**2)*RI2(J) + F2 *RR(LLL)
      FRO = 0.0D0
      BMRO = -DD*(RR(J)*(-(FRE**4)*RJ2(J)-V*(FRE**3/R    )*RJ1(J)) +
     1              RR(LL)*((FRE**4)*RI2(J)+V*(FRE**3/R    )*RI1(J)))
      BMOR =  DD*(RR(J)*(-(FRE**3/R)*RJ1(J)-V*FRE**4*RJ2(J))+
     1              RR(LL)*((FRE**3/R)*RI1(J)+V*FRE**4*RI2(J)))
      BMRR = 0.0D0
      DO 20 J=2,L
      LL=L+J
      LLL=LL+L
      LLLL=LLL+L1
```

```
      C=IP*(J-1)
      C1=C-1.D0
      C2=C-2.D0
      CC1=C+1.D0
      CC2=C+2.D0
      UN = UN-
     1     ((FRE**2)*RR(J)*RJ(J)-FRE**2*RR(LL)*RI(J)-F4*BB*CC1*RR(LLL)*
     2     R**C)*DCOS(C*Z)
      FRR = FRR +
     1     (RR(J)*(EF*TH/SR)*((FRE/R)*RJ1(J)-(C/R)**2*RJ(J))+
     2     RR(LL)*(EF*TH/SR)*((FRE/R)*RI1(J)-(C/R)**2*RI(J))+
     3      RR(LLL)*R**C*(CC2-C**2) +
     4      RR(LLLL)*C*R**C2*(F1-C))*DCOS(C*Z)
      FOO = FOO +
     1     (RR(J)*(EF*TH/SR)*(FRE**2)*RJ2(J)  +
     2     RR(LL)*(EF*TH/SR)*(FRE**2)*RI2(J)+
     3     RR(LLL)*CC2*CC1*R**C+
     4     RR(LLLL)*C*C1*R**C2)*DCOS(C*Z)
      FRO = FRO +
     1      (RR(J)*(EF*TH/SR)*(-(C/R**2)*RJ(J)+(C/R)*FRE*RJ1(J))+
     2      RR(LL)*(EF*TH/SR)*(-(C/R**2)*RI(J)+(C/R)*FRE*RI1(J))+
     3     RR(LLL)*C*CC1*R**C + RR(LLLL)*C*C1*R**C2)*DSIN(C*Z)
      BMRO = BMRO -
     1      DD*(RR(J)*FRE**2*(-(FRE**2)*RJ2(J)+V*(C/R)**2*RJ(J)-V*(FRE/R
     2      )*RJ1(J))      +
     3      RR(LL)*FRE**2*((FRE**2)*RI2(J)-V*(C/R)**2*RI(J)+V*(FRE/R)
     4      *RI1(J))  +
     5      RR(LLL)*F4*BB*CC1*C*C1*(F1-V)*R**C2)*DCOS(C*Z)
      BMOR = BMOR + DD*(
     1   RR(J)*FRE**2*((C/R)**2*RJ(J)-(FRE/R)   *RJ1(J)-V*FRE**2*RJ2(J))
     2 +RR(LL)*FRE**2*(-((C/R)**2)*RI(J)+(FRE/R)   *RI1(J)+V*FRE**2*RI2(J
     3 ))+RR(LLL)*F4*BB*CC1*C*C1*(V-F1)*R**C2)*DCOS(C*Z)
      BMRR = BMRR +DD*(1. -V)*(
     1   RR(J) *FRE**2*(-(C/R**2)*RJ(J)+(C/R)*FRE*RJ1(J))+
     2   RR(LL)*FRE**2*((C/R**2)*RI(J)-(C/R)*FRE*RI1(J)) -
     3   RR(LLL)*F4 *BB*CC1*C1* C*R**C2)*DSIN(C*Z)
   20 CONTINUE
   21 TI=0.D0
CICODE=1EXPONENTIAL DECAYING LOAD
CICODE=2LINEARLY DECAYING LOAD
CICODE=3FLAT IMPULSE
CICODE=4DAMPED LINEARLY DECAYING LOAD
CICODE=5DAMPED  EXPONENTIALLY DECAYING LOAD
      DO 22 II=1,NDLT
      IF (ICODE-4) 39,30,31
   30 T=PIN*(F1+F2*DAMP/(OMEGA**2*POS)-TI/POS+DEXP(-DAMP*TI)*(
     1 (-DAMP/OMEDA+((OMEDA**2-    DAMP**2)/(OMEGA**2*OMEDA*POS)))
     2 *DSIN(OMEDA*TI)- (F1+F2*DAMP/(OMEGA**2*POS))*DCOS(OMEDA*TI)))
      GO TO 40
   31 T=  DEXP(-TI/POS)*(OMEGA**2/(DAMM**2+OMEDA**2))*(F1-TI/POS-F2*
     1    DAMM/(POS*(DAMM**2+OMEDA**2))+DEXP(+DAMM*TI)*(DSIN(OMEDA*TI)*
     2 (DAMM/OMEDA+(OMEDA**2-   DAMM**2)/(OMEDA*POS*(DAMM**2+OMEDA**2)))
     3    +DCOS(OMEDA*TI)*(-F1+F2*DAMM/(POS*(DAMM**2+OMEDA**2)))))*PIN
      GO TO 40
   39 IF(ICODE-2) 41,42,43
   41 T   =(PIN*POS**2*OMEGA**2/(F1+(OMEGA*POS)**2)**2)*(DEXP(-TI/POS)*
     1    (-F1-TI/POS+(OMEGA*POS)**2-OMEGA**2*TI*POS)
     2    +F2*OMEGA*POS*DSIN(OMEGA*TI)-(OMEGA*POS)**2*DCOS(OMEGA*TI)
     3    +DCOS(OMEGA*TI))
      GO TO 40
   42 T  =PIN*(F1-DCOS(OMEGA*TI)-TI/POS+(F1/(OMEGA*POS))*DSIN(OMEGA*TI))
      GO TO 40
   43 T  =PIN*(F1-DCOS(OMEGA*TI))
   40 Z1=UN*T*GO
      Z2=BMRR*T*GO
      Z3=BMRO*T*GO
      Z4=BMOR*T*GO
      Z5=FRR*T*GO
      Z6=FOO*T*GO
      Z7=FRO*T*GO
      WRITE (IPRIN,32) TI,R,ZZ,Z1,Z2,Z3,Z4,Z5,Z6,Z7
      TI=TI+DLT
   22 CONTINUE
```

```
32 FORMAT (1X,10E12.5)
33 FORMAT (1H ,14HSINGULAR POINT)
48 FORMAT (1H0,27HEXPONENTIALLY DECAYING LOAD)
49 FORMAT (1H0,22HLINEARLY DECAYING LOAD)
50 FORMAT (1H0,12HFLAT IMPULSE)
51 FORMAT (1H0,46HDAMPED LINEARLY DECAYING LOAD VISCOUS DAMPING=,
  1E12.5)
52 FORMAT (1H0,51HDAMPED EXPONENTIALLY DECAYING LOAD VISCOUS DAMPING=
  1,E12.5)
53 FORMAT (1H1,1X,10HTIME(SEC.),4X,6HRADIUS,7X,5HANGLE,7X,5HUN(I),
  15X,7HBMRR(I),5X,7HBMRO(I),5X,7HBMOR(I),6X,6HFRR(I),6X,6HFOO(I),6X,
  26HFRO(I),//)
54 RETURN
   END
```

B29948